THÈSE

En vue de l'obtention du

DOCTORAT DE L'UNIVERSITÉ DE TOULOUSE

Délivré par **l'Institut Supérieur de l'Aéronautique et de l'Espace**
Spécialité : Systèmes automatiques

Présentée et soutenue par **Mario Andres HERNANDEZ LOPEZOMOZA**
le 21 septembre 2012

**Cadre de travail généralisé de compensation non-linéaire robuste :
application à la rentrée atmosphérique**

**A generalized framework for robust nonlinear compensation:
Application to an atmospheric reentry control problem**

JURY

M. Franck Cazaurang, président, rapporteur
M. Jean-Marc Biannic, directeur de thèse
M. Frank Jouhaud, co-directeur de thèse
M. Édouard Laroche, rapporteur
M. Guilhem Puyou

Acknowledgements

First of all, I would like to express my very sincere gratitude to all those who made possible the opportunity for this thesis work :

Thanks to Mr. Patrick Fabiani and the people in charge of DCSD at ONERA Toulouse who, through their efforts, were able to materialize all the required resources for this project. Then, I would like to thank Caroline Berard for having supported my candidature for this thesis project after having worked with her and Carsten Döll during my Master's internship at ONERA Toulouse.

My most sincere acknowledgements go also to my thesis directors Jean-Marc Biannic and Frank Jouhaud for having believed in me and for their support till the completion of this thesis work experience.

I would also like to thank the various research members of the DCSD department at ONERA Toulouse, whose warm welcome, remarks and comments made me grow and learn more from their vast variety of knowledge. A special expression of gratitude goes also to all my PhD colleagues whose fun and unconditional moral support made this a better experience every day.

Last but not least, my biggest acknowledgements go to my family members, without whom this experience would not have been the same. Although this is meant to be an extensive expression of gratitude to all my grandparents, uncles and cousins : thank you so much Juan Carlos, Montse, Kris, Luis, Vivi and most specially, *gracias Rosa Magali y Juan por todo su amor, que finalmente es lo que le dio sentido a estos estudios de doctorado.*

To my parents.

Abstract

This thesis work is devoted to extending *Nonlinear Dynamic Inversion* (NDI) for a large scale of nonlinear systems while guaranteeing sufficient stability conditions.

After the mathematical formalization of *feedback linearization* in the 1980's, NDI has been studied in a wide range of applications, including aeronautics and aerospace. NDI allows to compute nonlinear control laws able to decouple and linearize a model at any operating point of its state envelope. However, this method is inherently non-robust to modelling errors and input saturations. Moreover, obtaining a quantifiable guarantee of the attained stability domain in a nonlinear control context is not a very straightforward task. This drives the motivation of the thesis.

In aerospace applications, most well-known linear control design techniques usually struggle to give a satisfying answer to the control problem, unless gain-scheduled controllers are used. In this contribution, to avoid standard difficulties raised by gain-scheduling approaches (lack of guarantee between interpolation points, time-consuming tuning procedure), an alternative methodology, inspired by NDI schemes and linear Robust Control, is then proposed.

Unlike standard NDI approaches, our methodology can be viewed as a generalized nonlinear compensation framework which allows to incorporate uncertainties and input saturations in the design process. Paralleling anti-windup strategies, the controller can be computed through a single multi-channel optimization problem or through a simple two-step process : the first step, thanks to recent advances in nonsmooth optimization techniques, consists of optimizing a structured H_∞ controller ; then in a second phase, an anti-windup strategy is used to enhance the controller properties despite input constraints.

Within this framework, linear fractional transformations of the nonlinear closed-loop can be easily derived for robust stability analysis using standard tools for linear systems.

The proposed method is tested for the flight control of a delta wing type reentry vehicle at hypersonic, transonic and subsonic phases of the atmospheric reentry. For this thesis work, a Flight Mechanics simulator including diverse external factors and modelling errors was developed in Simulink.

In simulation, the longitudinal and lateral dynamics of the vehicle are tested to validate the computation of the NDI-based control laws. A comparison between the standard NDI technique and the general nonlinear compensation approach is also presented along with simulation results which help to validate the proposed methodology.

Résumé

Ce travail de thèse est consacré à l'extension de l'Inversion Dynamique non-linéaire (NDI-Nonlinear Dynamic Inversion) pour un ensemble plus grand de systèmes non-linéaires, tout en garantissant des conditions de stabilité suffisantes.

Après la formalisation mathématique de la "linéarisation par retour d'état" dans les années 80, la NDI a été étudiée dans le cas de diverses applications, y compris en aéronautique et en aérospatiale. La NDI permet de calculer des lois de contrôle capables de linéariser et de découpler un modèle non-linéaire à tout point de fonctionnement de son enveloppe d'état. Cependant cette méthode est intrinsèquement non-robuste aux erreurs de modélisation et aux saturations en entrée. En outre, dans un contexte non-linéaire, l'obtention d'une garantie quantifiable du domaine de stabilité atteint reste à l'heure actuelle complexe. C'est l'ensemble de ces paramètres qui a motivé la rédaction de cette thèse.

Dans les applications aérospatiales, la plus grande partie des approches linéaires pour la conception de lois de pilotage ont, en général, du mal à donner une réponse satisfaisante au problème de contrôle, à moins d'utiliser des gains auto-séquencés. Dans cette contribution, pour éviter les difficultés soulevées par les approches utilisant des gains auto-séquencés (absence de garantie entre les points d'interpolation, procédure de réglage longue...), une autre méthode, inspirée par la NDI, est ensuite proposé.

Contrairement aux approches classiques de la NDI, notre méthodologie peut être considérée comme un cadre de compensation non-linéaire généralisé qui permet d'intégrer les incertitudes et les saturations en entrée dans le processus de conception. En utilisant des stratégies de contrôle anti-windup, la loi de pilotage peut être calculée grâce à un simple processus multi-canaux ou par un simple processus en deux phases. La première, grâce aux avancements récents des techniques d'optimisation non-lisse, consiste à optimiser un correcteur structuré H∞, puis dans une deuxième phase, une stratégie anti-windup est utilisée pour améliorer les propriétés du correcteur en dépit des contraintes sur l'entrée du système.

Dans ce cadre de travail généralisé des transformations linéaires fractionnaires (LFT - Linear Fractional Transformations) de la boucle fermée non-linéaire peuvent être facilement déduites pour l'analyse de la stabilité robuste en utilisant des outils standards pour de systèmes linéaires. La méthode proposée est testée pour le pilotage d'un véhicule de rentrée atmosphérique de type aile delta lors de ses phases hypersonique, transsonique et subsonique. Pour cette thèse, un simulateur du vol incluant divers facteurs externes ainsi que des erreurs de modélisation a été développé dans Simulink.

En simulation, la dynamique longitudinale et latérale du véhicule est testée pour valider le calcul des lois de pilotage. Une comparaison entre la technique standard NDI et l'approche généralisée de compensation non-linéaire est également présentée avec des résultats de simulation permettant de valider la méthodologie proposée.

Contents

ONERA
THE FRENCH AEROSPACE LAB

ISAE
Institut Supérieur de l'Aéronautique et de l'Espace

ONERA
THE FRENCH AEROSPACE LAB

ISae
Institut Supérieur de l'Aéronautique et de l'Espace

Introduction

Thesis context

Control techniques for nonlinear systems have been gaining much attention from the research community in the late years. Compared to advances in Linear Control, the Nonlinear Control field has historically advanced at a lower pace due to the computation capabilities available and to a lack of general frameworks to allow a direct and systematic application on different classes of nonlinear systems. With the advent of powerful computer technologies, most computational difficulties have been wiped-out of the scene and the implementation of nonlinear controllers is simpler nowadays.

There are three main groups of mature nonlinear control approaches that can be foreseen: techniques that attempt to treat the process as a linear system in limited ranges of operation (*e.g.* Gain Scheduling), methods that introduce auxiliary nonlinear feedback loops so that the system can be treated as linear for purposes of control design (*e.g.* Feedback Linearisation with Stability, commonly referred as Nonlinear Dynamic Inversion), and Lyapunov function-based approaches (*e.g.* Backstepping and Lyapunov Redesign).

This thesis work is devoted to extending *Nonlinear Dynamic Inversion* (NDI) for a large scale of nonlinear systems while guaranteeing sufficient stability conditions.

NDI first derived from *noninteracting control* [IKGGM81, Fli85, NS86, IG88, Ha88, IKGGM89] and from *feedback linearization techniques* [Isi85, IMDL86, CLM91, SL91, Vid93, Kha96].

The principle of noninteracting control is to find a decoupled partition of the input vector such that each component of the i–th output is influenced only by the components of the i–th input partition. This can be achieved via static state-feedback, when the full state information is available. Such feedback control laws are said to be *regular* if they are invertible in the entire state envelop [NS86].

The first efforts to extend to nonlinear systems the noninteracting control theory, previously developed for linear systems, appeared at the beginning of the 1970's by Porter [Por70]. In the 1980's, Isidori *et al.* [IKGGM81] formulated and studied for the first time the problem of nonlinear noninteracting control in the framework of differential geometry and distributions theory. Then, the problem of achieving noninteraction and stability was addressed in [IG88, Ha88, IKGGM89].

From the results obtained through noninteracting control with stability, a coordinate transformation allowing to linearize nonlinear systems can also be obtained. Then, a nonlinear system

can be decoupled, linearized and stabilized via state-feedback and a coordinate transformation [Isi85]. This technique, considered nowadays a classic method of Nonlinear Control, is also known as *feedback linearization* [Isi85, SL91, Vid93, Kha96].

In feedback linearization, concepts like the rank and controlled invariance of nonlinear systems play a key role on the mathematical formalization of the technique. The rank was introduced in [Fli85] based on a differential algebraic analysis. The study of controlled invariance was initiated in [Bro78], under static state-feedback laws of the form

$$u = \alpha(x) + v$$

Later on, controlled invariance was tackled in [IKGGM81]. A special class of controlled invariant distributions is given by controllability distributions, which became a basic tool for solving the noninteracting control problem with or without stability. In fact, the controllability distributions allow to characterize the fixed dynamics of the decoupled system via static feedback [IG88]. Then, the group of linearizing laws was extended to regular state-feedbacks of the form

$$u = \alpha(x) + \beta(x)\,v$$

A generalized notion of controlled invariance was introduced in the 1990's by Huijberts *et al.* [HMA97], allowing to enlarge the group of linearizing laws to the class of quasi-static state-feedbacks of the form
$$u = \alpha(x, v, \dot{v}, \ldots, v^{(k)})$$

Finally, sufficient conditions were introduced in [IMDL86, CLM91] to extend the group of linearizing laws to dynamic state-feedbacks of the form

$$\begin{cases} \dot{\varsigma} &=& \varrho(x, \varsigma) + \vartheta(x, \varsigma)\,v \\ u &=& \alpha(x, \varsigma) + \beta(x, \varsigma)\,v \end{cases}$$

In fact, *differentially flat* systems can be inverted via dynamic state-feedback. A general nonlinear system is considered *flat* if the state x and the input u can be recovered from a finite number of derivatives of a vector z, containing a specific choice of system outputs [FLMR95].

NDI has become of great interest in aeronautics and aerospace applications due to the advantages it presents. Some common examples include: high manoeuvrability airplanes [RBG95, RBG96, Pap03, Kol05], atmospheric reentry vehicles [Jou92, IGVW02, DN02, GV03, LRDY07, MCV09], civil transportation [Lav05] and military applications [Har91, SK98]. Before NDI came into play in the Nonlinear Control scene, linear methods such as gain scheduling were successfully used in the aerospace field.

Gain scheduling design typically employs a set of linearized approximations of the nonlinear process which are representative of the operation domain. However, these approximations are only valid in the neighborhood of a specific operating point, which means that there is a lack of guarantee between interpolation points. Moreover, depending on the number of linearized approximations considered, the tuning procedure of such design may turn-out to be time-consuming.

In contrast to gain scheduling, NDI adapts automatically to the present operating point around which the system will be linearised. Next, the nonlinear system in question is decoupled and linearized by a state-feedback controller. This is done by punctually eliminating all nonlinearities

using the inverse of the system, obtained through feedback linearization. Once the system is linearised and decoupled, it is with great simplicity that desired dynamics can be imposed for each decoupled signal to guarantee the closed-loop stability. Finally, NDI is a very straight forward technique where the controller is based on the equations of the open loop nonlinear system, thus allowing to have an insight of the controller behaviour.

In the early 1990's, the first implementations of the NDI theory in the aerospace field were conducted by Honeywell Aerospace Advanced Technology in cooperation with NASA [BEE90]. A Honeywell NDI design was selected for the F-18 High Angle-of-Attack Research Vehicle (HARV) [BEE90, EBHS94]. Then, Honeywell collaborated with Lockheed Martin to produce a Nonlinear Dynamic Inversion controller for the F-35 aircraft. In this case, the NDI controller provided consistent predictable control through the transition from conventional aircraft flight to hover mode.

At the same time, the French space agency CNES started the development of the space vehicle project Hermes which was later on absorbed by the European Space Agency ESA. The Hermes space vehicle was designed to provide independent European manned access to space. NDI design was studied as part of the attitude control system of the vehicle [Jou92] before the project was cancelled due to budgetary constraints.

In the late 1990's, NASA developed an X-38 Crew Rescue Vehicle program [Bos10]. The program consisted of a series of developmental space vehicles that would lead to a production vehicle that would serve as the Space Station lifeboat. The NDI controller was proposed as a good solution for this program since it would provide a generic control approach [IGVW02].

For many reasons, control design for atmospheric reentry vehicles, for example, still remains a challenging task. Typically, because the flight domain is extremely large, nonlinear and time-varying aspects induce nontrivial issues. Most well-known linear control design techniques usually fail to give a satisfying answer to the control problem, unless gain scheduled controllers are used. It is in this type of context that NDI shows to be the most useful.

Despite its remarkable qualities, some drawbacks have kept NDI controllers from being used more widely:
– standard NDI approaches are non robust to modelling errors, environmental factors and to internal unobservable dynamics that may be unstable (including the inversion of non-minimal phase systems). Robust approaches may then require a thorough adaptation of the method and the resulting synthesis structures for "robustifying" NDI can easily become a complex process;
– standard NDI methods are not well adapted for models accounting for input constraints or physical limits. In presence of these physical limits of the process inputs, the NDI controller can only partially eliminate the original process dynamics and therefore residual unexpected dynamics can become critical to the system stability.

These drawbacks drive the motivation of this work. In this contribution, an alternative methodology inspired by NDI schemes, is proposed.

> The main objective of this thesis work is to develop a general framework for nonlinear control allowing to consider diverse uncertainties, varying parameters and input constraints in the controller synthesis procedure, as well as proposing a modelling strategy to enable the use of linear stability analysis tools.

To achieve this goal, a reformulation of the standard NDI method will be introduced to give the synthesis procedure a more linear oriented perspective. This reformulation requires to rewrite nonlinear systems by first extracting their linear parts. Then, the remaining nonlinearities are viewed as residual nonlinear inputs to be compensated by the control law.

Then, strongly inspired from the LPV analysis framework, a single loop controller structure is proposed to compensate the system nonlinearities in presence of modelling errors, varying and uncertain parameters, and in spite of input constraints.

Finally, the robust stability assessment of the interconnection between the nonlinear process and the obtained NDI-based controller is carried out by deriving a Linear Fractional Transformation of the nonlinear closed-loop, which enables the use of linear analysis tools.

In order to validate the proposed method, controllers for the longitudinal and lateral dynamics of air vehicles (including aircrafts, space launchers and reentry vehicles) will be computed and further tested with a 6 degrees-of-freedom Flight Mechanics simulator. In particular, the model of a reentry vehicle will be employed in simulation given the interesting nonlinear characteristics of the atmospheric reentry problem.

Thesis outline

This thesis is organized in two parts and five chapters. On the one hand, the first part is dedicated to present some theoretical preliminaries along with the generalized nonlinear compensation framework which is proposed as a contribution to Nonlinear Control techniques. On the other hand, the second part of this work is devoted to applying the proposed framework to the computation of flight control laws for air vehicles, from which the particular case of the atmospheric reentry problem is treated in simulation.

In Chapter 1, an introduction to NDI techniques is presented for different classes of nonlinear systems, going from the simpler cases to the more complex. Concepts related to the feedback linearization are introduced along with different modelling approaches to solve commonly encountered issues. Standard remedies to the central limitations of the technique and more advanced robust control strategies are also described. The chapter ends with a brief presentation of control input saturations, which are not naturally accounted for by standard NDI techniques, but that will be considered in the generalized framework proposed in Chapter 2.

Then, in Chapter 2, our generalized framework for nonlinear compensation is presented. A fresh reformulation inspired by standard NDI is used to give the nonlinear compensation approach a more linear oriented perspective. Then, robust approaches for linear control design can be readily exploited. A multi-channel design oriented control scheme is introduced as an enhanced alternative to the standard NDI controller design. In a very straightforward manner, anti-windup control strategies are used to increase the stability domain of the nonlinear closed-loop in spite of input saturations. Finally, different stability and robustness analysis tools are presented along with a well-suited LFT modelling of the resulting nonlinear closed-loop.

Chapter 3 is dedicated to the presentation of some fundamental of Flight Mechanics and the modelling of common flight control objectives. General equations of dynamic state models with 6 degrees-of-freedom are presented along with a general description of air vehicle aerodynamic

models. The control objectives, which are fundamentally attitude parameters of the air vehicles, are derived from the general equations of motion. This chapter is concluded by a presentation of the main disturbances which are considered in simulation of air vehicles, either from an environmental source or from a modelling source.

Next, in Chapter 4, standard NDI control laws and generalized Nonlinear Compensation control laws are computed for the longitudinal and lateral control objectives of air vehicles. This allows a direct comparison of both approaches in the design phase, before passing on to the synthesis and simulation phases contained in Chapter 5.

Finally, Chapter 5 presents a general introduction to atmospheric reentry missions and the onboard automatic systems that interact to enable a vehicle to land safely on Earth. Then, the implementation of the previously designed control laws is explained in detail. A thorough comparison of the computed controllers using both, the standard NDI approach and the generalized Nonlinear Compensation framework, is presented. Finally, a robustness assessment is introduced along with simulation results for a final validation of the method.

The general conclusions are presented as a recapitulation of the main results of this work. Some future work perspectives of the generalized framework proposed are also included as a guideline of the actual state of this subject of study. An Appendix with reference information and an international congress paper conclude this thesis work.

Part I

A generalized "NDI inspired" framework

Chapter 1

Introduction to Nonlinear Dynamic Inversion techniques

Introduction

After the mathematical formalization, founded on differential geometry, of *feedback linearization* techniques in the 1980's by Isidori *et al.* [IKGGM81], Nonlinear Dynamic Inversion (NDI) has been studied in a wide range of applications, including aeronautics and aerospace [Har91, Jou92, RBG95, RBG96, SK98, IGVW02, Pap03, GV03, Lav05, Kol05, LRDY07]. In fact, NDI is basically a feedback linearisation technique which uses a double loop structure to decouple, linearize and stabilize a given nonlinear process. The purpose of the inner loop in a standard NDI controller is to eliminate the process nonlinearities, thus linearizing it, while an outer loop is used to stabilize and impose desired dynamics to the resulting decoupled linear system.

The design of the NDI inner loop has its origins in *noninteracting control* for nonlinear systems [IKGGM81, Fli85, Har91]. The basic idea of noninteracting control techniques is to decouple a nonlinear system via regular state-feedback.

As noninteracting control can ultimately lead to a linear canonical form of the decoupled nonlinear system using a coordinate transformation, this particular case of state-feedback became known as *feedback linearization* [Isi85, SL91, Vid93]. There are two main approaches that can be taken into consideration: input-output feedback linearization and input-state feedback linearization.

In the case of input-output feedback linearization [Isi85, Vid93], the objective is to linearize the map between the transformed model input $\tilde{u}$ and the actual model controlled output z. However, given a nonlinear system of dimension n, this approach may result in a linear sub-system of dimension $r < n$ linked to a nonlinear unobservable sub-system of dimension $n - r$, which could turn-out to be a disadvantage as it will be further discussed.

The goal of input-state feedback linearization [Isi85, Mar86, MT95] is to linearize the map between

the transformed input $\tilde{u}$ and the entire vector of transformed state variables $\tilde{x}$. This can be achieved by deriving an artificial output vector $\tilde{y}$ that yields a linearized feedback model with state dimension $r = n$.

A major drawback of this last approach is that the artificial output $\tilde{y}$ is generally not the same as the controlled output z. Then, an input-state linearizing controller with tracking objectives is almost never attainable because a desirable behavior of the artificial output $\tilde{y}$ does not systematically imply a desirable behavior of the actual controlled output z. In fact, input-state linearization is used mainly for stabilization problems in which the controlled output z is not specified *a priori*.

Even though in some particular cases it is possible to simultaneously linearize the input-output and input-state maps of the nonlinear system, in the following, the focus is set on the input-output feedback linearization technique for designing the inner loop of the standard NDI controller.

Once the inner loop has been designed via feedback linearization, a linear controller, which stabilizes the resulting linear mapping of the original nonlinear system, is designed as the outer loop of the standard NDI structure. Different linear techniques, such as standard PID control and $\mathcal{H}_\infty$-based robust control designs, can be foreseen to this end as it will be further explained.

In this chapter, the standard NDI technique is developed for different classes of commonly encountered nonlinear control systems. The main objective is to gradually introduce the reader to the fundamentals of NDI control while highlighting some relevant aspects that will ultimately lead to a generalizing reformulation, which is at the core of this thesis work.

Starting from a simple case in Section 1.1, extensions to NDI controller design for more complex classes of nonlinear systems are introduced in Section 1.2, along with useful approaches that help avoid commonly encountered problems.

Finally, in Section 1.3, a small review on input control saturations in the context of NDI control is presented as it will be an integral part of our generalized nonlinear compensation framework.

To better illustrate the design of NDI controllers, let us begin by introducing the case of square and input-affine systems.

1.1 Input-affine square systems

The case of input-affine square systems is a very straightforward example to explain the standard NDI design technique. The model Σ in equation (1.1) represents such a system.

$$\Sigma: \quad \dot{x} = f(x) + G(x)\,u \tag{1.1}$$

where
– $x \in \mathbb{R}^n$ is the state vector;
– $u \in \mathbb{R}^m$ is the control input, with $n = m$;
– $f(x) \in \mathbb{R}^n$ and $G(x) \in \mathbb{R}^{m \times m}$ are smooth nonlinear functions;

Assumption 1.1 *It is assumed that:*

$det(G(x)) \neq 0 \quad \forall\, x \in \mathcal{D},$

where $\mathcal{D} \subset \mathbb{R}^n$ is the admissible domain of the state vector. Therefore, $G(x)$ is invertible.

A classical example of a square input-affine system, in the context of aerospace applications, is the model of a flying vehicle rotation rates.

Example 1.2 *The 3 degree-of-freedom dynamics model of the rotation rates is obtained from the equation of moments about the center of gravity of a winged flying vehicle as described in Appendix A.*

$$
\begin{bmatrix} \dot{p} \\ \dot{q} \\ \dot{r} \end{bmatrix} = f(x) + G(x) \begin{bmatrix} \delta_{aileron} \\ \delta_{elevator} \\ \delta_{rudder} \end{bmatrix} \tag{1.2}
$$

where $G(x) \in \mathbb{R}^{3 \times 3}$ verifies Assumption 1.1 and $x = \begin{bmatrix} p & q & r \end{bmatrix}^T$ is the state vector containing the roll rate, the pitch rate and the yaw rate respectively. In this example, the input $u = \begin{bmatrix} \delta_{aileron} & \delta_{elevator} & \delta_{rudder} \end{bmatrix}^T$ is defined as a set of independent control signals that represent the effects of the flying vehicle control surfaces on each of its reference axis.

1.1.1 General principle

NDI allows to linearize and decouple a nonlinear system via state-feedback. The general principle is to construct a controller $u(x)$ by explicitly using the functions $f(x)$ and $G(x)$ to eliminate the nonlinear dynamics while enforcing a linear behavior on the closed-loop system. This is classically achieved with two control loops: an inner loop used to eliminate system nonlinearities, and an outer loop used to stabilize the closed loop.

Assumption 1.3 *The full state x is available for controller design. Using this measurement of the full state, exact computations of the real process nonlinear dynamics modelled as $f(x)$ and $G(x)$ can be obtained.*

The NDI controller design is done in two general steps:

Step 1 *Consider the square input-affine representation (1.1). Define the inner loop controller $u(x)$ capable of eliminating the nonlinear dynamics of Σ contained in the functions $f(x)$ and $G(x)$ as*

$$
u(x) = G^{-1}(x)[-f(x) + \tilde{u}] \tag{1.3}
$$

The general interconnection scheme of this nonlinear controller $u(x)$ is depicted on Figure 1.1.
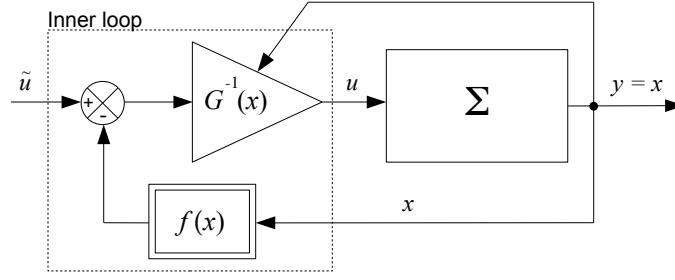
Figure 1.1: Standard NDI inner loop controller structure.

Once the inversion controller (1.3) of the inner loop is defined and applied to system (1.1), the resulting linearized system $\tilde{\Sigma}$ is represented by equation (1.4). Clearly, the nonlinear system is reduced to a set of n decoupled integrators for which a tracking controller needs to be designed.

$$\tilde{\Sigma}: \qquad \dot{x} = \tilde{u}(x_c, x) \tag{1.4}$$

or, using a slight abuse of notation:

$$x = \tilde{\Sigma}(s)\,\tilde{u}(x_c, x), \quad \text{with} \quad \tilde{\Sigma}(s) = \frac{I}{s}$$

Linear dynamics can be imposed to system (1.4) through the new input $\tilde{u}(x_c, x) \in \mathbb{R}^n$ as explained in the next step.

Step 2 *Define an outer-loop controller $C(s)$ capable of enforcing a linear and stable behavior of the inner loop to ensure a good tracking of the setpoint or commanded value x_c, using a linear approach such that:*

$$\tilde{u}(x_c, x) = C(s) \begin{bmatrix} x_c \\ x \end{bmatrix} \tag{1.5}$$

Different linear approaches can be foreseen for designing this outer-loop controller. The choice of the controller $C(s)$ can be based on simple and common control requirements such as: having small or no static error with respect to the setpoint x_c, having a small overshoot in the system transient response, guaranteeing a certain closed loop bandwidth (which is equivalent to fixing a settling time for the system transient response), or allowing a specific pole placement.

By adding this layer to the nonlinear controller obtained in the previous step, the standard NDI controller structure is illustrated on Figure 1.2.
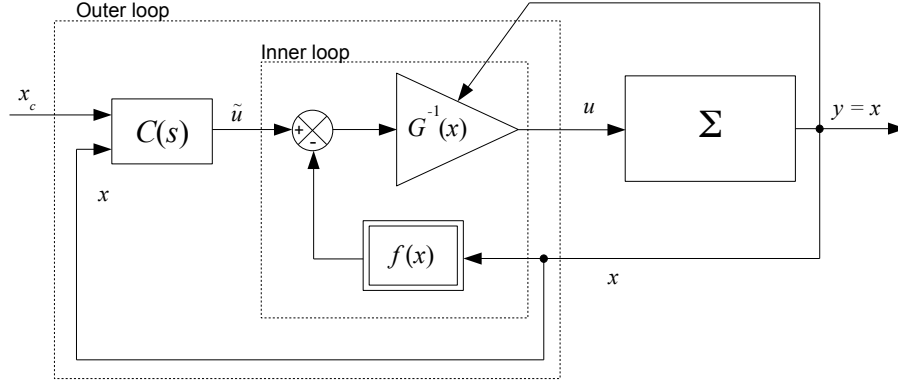
Figure 1.2: Standard NDI control design structure.

The control law resulting from the above procedure is described by:

$$u(x) = G^{-1}(x) \left(-f(x) + C(s) \begin{bmatrix} x_c \\ x \end{bmatrix} \right) \tag{1.6}$$

Example 1.4 *Consider the system described in Example 1.2 concerning the dynamics of a flying vehicle rotation rates. By defining the nonlinear controller*

$$\begin{bmatrix} \delta_{aileron} \\ \delta_{elevator} \\ \delta_{rudder} \end{bmatrix} = G^{-1}(x) \left(-f(x) + \begin{bmatrix} \tilde{u}_p \\ \tilde{u}_q \\ \tilde{u}_r \end{bmatrix} \right) \tag{1.7}$$

the inner closed-loop system becomes

$$\begin{bmatrix} \dot{p} \\ \dot{q} \\ \dot{r} \end{bmatrix} = \begin{bmatrix} \tilde{u}_p \\ \tilde{u}_q \\ \tilde{u}_r \end{bmatrix}$$

Stable dynamics for driving the state $x = \begin{bmatrix} p & q & r \end{bmatrix}^T$ towards the target $x_c = \begin{bmatrix} p_c & q_c & r_c \end{bmatrix}^T$ can be enforced by means of a linear controller. The simplest structure to ensure this convergence is that of a static proportional controller:

$$C(s) = \begin{bmatrix} diag(k_1, \ k_2, \ \dots, \ k_n) & -diag(k_1, \ k_2, \ \dots, \ k_n) \end{bmatrix} \qquad \forall \, k_i \in \mathbb{R}_+^* \tag{1.8}$$

Consider this proportional gain for adjusting the dynamics of the linearized system through the input $\tilde{u}(x_c, x)$, then

$$\begin{bmatrix} \dot{p} \\ \dot{q} \\ \dot{r} \end{bmatrix} = \begin{bmatrix} diag(k_p, \ k_q, \ k_r) & -diag(k_p, \ k_q, \ k_r) \end{bmatrix} \begin{bmatrix} x_c \\ x \end{bmatrix} \tag{1.9}$$

By fixing the constant values of (1.8) as:

$$k_p = \frac{1}{\tau_p}, \ k_q = \frac{1}{\tau_q}, \ k_r = \frac{1}{\tau_r} \tag{1.10}$$

one obtains a first-order behavior for each variable:

$$\dot{p} = \tau_p^{-1}(p_c - p), \quad \dot{q} = \tau_q^{-1}(q_c - q), \quad and \quad \dot{r} = \tau_r^{-1}(r_c - r) \tag{1.11}$$

It becomes clear that the NDI design that has just been described is actually a nonlinear compensation technique. The information on the nonlinear dynamics of the model Σ is exploited to generate the exact signal allowing to compensate for the nonlinearities and turning the original system dynamics into a set of decoupled integrators. Then, suitable linear dynamics can be easily imposed through the outer-loop controller.

1.1.2 Central limitations

Up to now, strong assumptions have been made to clarify the NDI design procedure. For example, Assumption 1.3 deliberately reckons the capacity of having measurements of the state x and being able to compute with this measurements the functions $f(x)$ and $G(x)$ to the point of reproducing *exactly* the real process nonlinear dynamics. It has also been implicitly assumed that the linearizing feedback control input u of equation (1.3) can be realized by the actuators without any constraints, including delays and saturations.

Real life processes present a wide variety of different restrictions that make non-viable to assume such *ideal* conditions. In a more realistic scenario:
– the model Σ is a simplified representation of a real process and its environment;
– the full state measurement of a real process may not be accessible, thus requiring the use of on-line estimations; moreover, these measurements are usually affected by deterministic and stochastic disturbances like noises and biases;
– the inputs of most real life processes are governed by actuators that have physical constraints and inherent dynamics Σ_A that may prevent the system from reacting immediately to any given controller signal.

The main limitation of standard NDI approaches is that the exact compensation of the process nonlinearities usually implies:
– a full access to the entire state vector x;
– a high accuracy of the model so that the on-line computed terms $f(x)$ and $G(x)$ coincide exactly with the reality;
– large bandwidth actuators capable of realizing possibly large and fast control signals without any limitations.

Let us temporarily neglect the impact of actuators and their inherent limitations, to focus primarily on the limitations induced by a non direct access to the nonlinear model. In such a case, the linearizing control law of equation (1.3) becomes

$$u(x) = \hat{G}^{-1}(x)[-\hat{f}(x) + \tilde{u}(x_c, x)] \tag{1.12}$$

where $\hat{f}(x)$ and $\hat{G}(x)$ denote respectively approximated on-line estimations of the nonlinear vector $f(x)$ and the nonlinear control efficiency matrix $G(x)$.

Closing the inner loop between this real scenario controller $u(x)$ and the nonlinear model (1.1) generates the following state equation:

$$\dot{x} = f(x) - G(x)\hat{G}^{-1}(x)\ \hat{f}(x) + G(x)\hat{G}^{-1}(x)\ \tilde{u}(x_c, x)$$

Now let us model the residual part due to the inexact simplification of the function $G(x)$ with a multiplicative uncertainty Δ_G as:

$$\Delta_G = G(x)\hat{G}^{-1}(x) - I \tag{1.13}$$

and let us represent the residual part due to the inexact elimination of the function $f(x)$ as a nonlinear input disturbance

$$w_f(x) = f(x) - (I + \Delta_G)\,\hat{f}(x) \tag{1.14}$$

The dynamics of the system resulting from the inner closed loop can be stated as:

$$\tilde{\Sigma}: \qquad \dot{x} = w_f(x) + (I + \Delta_G)\,\tilde{u}(x_c, x) \tag{1.15}$$

Clearly, the design of the outer tracking loop becomes more demanding since it is now required that the linear controller $C(s)$ exhibits some robustness characteristics with respect to the inversion errors w_f and Δ_G. The control design problem of the outer loop is represented by the scheme of Figure 1.3 where a controller $C(s)$ is sought to ensure the tracking of the setpoint x_c and withstand the inversion errors, thus trying to keep the closed-loop dynamics as linear as possible.
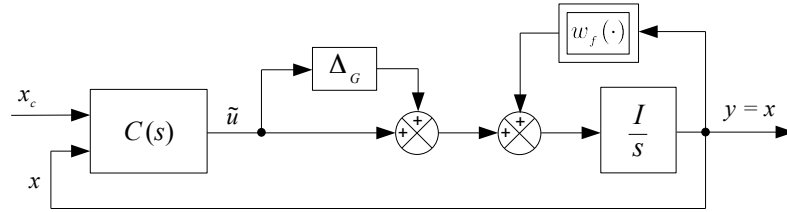
Figure 1.3: Outer-loop controller design scheme for non-exact NDI.

1.1.3 Standard remedies

In Example 1.4, a proportional controller is used to enforce linear dynamics in the system $\tilde{\Sigma}$ through the input $\tilde{u}(x_c, x)$. Yet, in the eyes of the limitations described in the previous section regarding the inversion procedure, this controller strategy is no longer suited for assuring the convergence of the state x towards the commanded value x_c.

Let us denote $\varepsilon = x_c - x$ the error signal between the target x_c and the state x. Then, the proportional controller introduced in Example 1.4 can be re-written under the form:

$$\tilde{u}(x_c, x) = K_P\,\varepsilon \tag{1.16}$$

where

$$K_P = diag\left(\frac{1}{\tau_1},\ \frac{1}{\tau_2},\ \ldots,\ \frac{1}{\tau_n}\right) \tag{1.17}$$

This controller structure, depicted on Figure 1.4, fixes first-order dynamics of time constant τ_i for each state. But given that an exact inversion is unattainable through the inner loop controller, it

can only help fending-off the inversion error Δ_G from the system $\tilde{\Sigma}$ described by equation (1.15). Indeed, by tuning the time constant τ, a desired settling time t_s can be achieved in spite of this inversion error. Still, a steady-state error between x and x_c will be observed due to the inversion error w_f acting as an "exogenous" [1] input disturbance, thus preventing x to converge towards x_c.
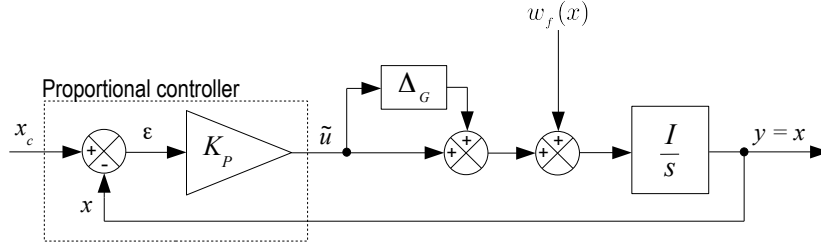
Figure 1.4: Proportional controller structure for the outer loop.

To counteract this issue inherent to the inversion procedure, integral control approaches are commonly employed.

1.1.3.1 The proportional-integral (PI) structure

Rejection of input disturbances is a common problem in linear control. The PI structure proves to be practical for these type of control problems due to the robustness characteristics that it provides.

In the context of the problem established to control the system $\tilde{\Sigma}$ of equation (1.15), besides being capable of reducing the impact of the inversion error Δ_G through a proportional gain, a PI controller helps eliminate the steady-state error between x and x_c induced by w_f using an additional integral signal. This structure can be graphically represented with the block diagram of Figure 1.5 and it is defined as:

$$\tilde{u}(x_c, x) = K_P \, \varepsilon + K_I \int \varepsilon \, dt \tag{1.18}$$

where

$$\begin{aligned} K_P &= diag(k_{P_1}, \ k_{P_2}, \ \ldots, \ k_{P_n}) \\ K_I &= diag(k_{I_1}, \ k_{I_2}, \ \ldots, \ k_{I_n}) \end{aligned}$$

From a time domain perspective, the proportional part of the PI controller uses the present error ε while the integral part uses the accumulation of the error throughout time to try to minimize the present error. Choosing the values of the gains in K_P and K_I becomes a trade-off between the closed-loop settling time and the overshoot in relation to the commanded setpoint x_c. From a frequency domain perspective, this trade-off is translated in terms of the attained system bandwidth versus damping.

---

1. From a synthesis perspective, the function $w_f(x)$ will be modelled as an input disturbance, thus allowing to treat the control problem as linear. Yet, it should be kept in mind that this input depends on the state and further analysis on its stability may be required.
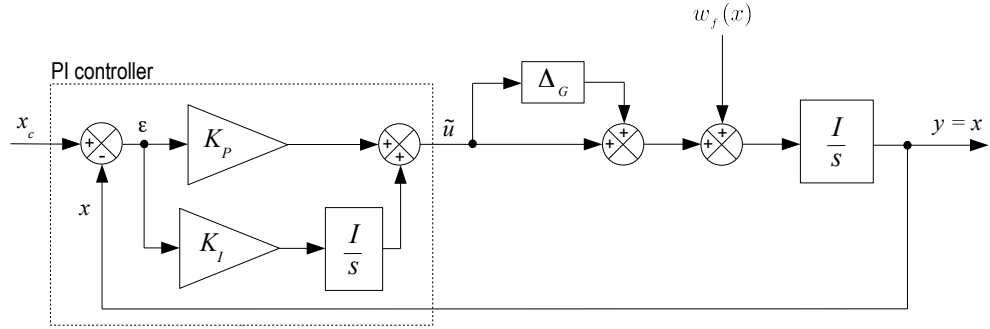
Figure 1.5: PI controller structure for the outer loop.

There are two characteristics that should be pointed out from the implementation of such a controller structure. First, the behavior generated by the PI controller follows second-order stable dynamics if the gains in K_P and K_I are defined as positive constants. In a very convenient manner, the constants k_{P_i} and k_{I_i} can be associated to the cut-off frequency ω_c and the damping coefficient ξ by recalling the characteristic polynomial $p(s)$ of second-order dynamic systems

$$p(s) = s^2 + 2\,s\,\xi\,\omega_c + \omega_c^2$$

To set a desired cut-off frequency ω_{c_i} and damping coefficient ξ_i of each closed-loop state, the gains k_{P_i} and k_{I_i} can be identified as:

$$
\begin{aligned}
k_{P_i} &= 2\,\xi_i\,\omega_{c_i} & (1.19)\\
k_{I_i} &= \omega_{c_i}^2 & (1.20)
\end{aligned}
$$

Second, as a result of the feedback interconnection the PI controller introduces a zero in each closed-loop state at the frequency $\omega_{c_i} = k_{I_i}/k_{P_i}$. If the controller gains in K_P and K_I are defined positive, then the closed-loop is not only stable but also minimum phase.

Remark 1.5 *The proportional and the proportional-integral controllers are unique for a given desired dynamics τ or (ω_c, ξ). This means that the controller gains K_P and K_I can generate only one specific desired dynamics. Having static gains K as adjustment parameters of the control law makes it easy to schedule the controller with respect to any of the system parameters.*

On the downside of this approach, the PI controller produces phase lag which tends to reduce the closed loop stability margins. A more sophisticated solution can be proposed to palliate this slight drawback.

1.1.3.2   The proportional-integral-derivative (PID) structure

The proportional-integral-derivative (PID) controller comes as a more general structure. In fact, the prior two controllers described before can be considered as particular cases of a PID controller.

In the PID structure, the error measurement ε, its integral $\int \varepsilon\,dt$ and its time derivative $\dot{\varepsilon}$ are related to a set of static gains K_P, K_I and K_D as defined in equation (1.21). A proportional

controller can be seen as a particular PID structure where the gains K_I and K_D are null, while a PI controller is the particular case where the gain K_D is null.

$$\tilde{u}(x_c, x) = K_P \, \varepsilon(t) + K_I \int \varepsilon(t) \, dt + K_D \frac{d}{dt} \, \varepsilon(t) \tag{1.21}$$

with

$$
\begin{array}{rcl}
K_P & = & diag(k_{P_1}, \ k_{P_2}, \ \dots, \ k_{P_n}) \\
K_I & = & diag(k_{I_1}, \ k_{I_2}, \ \dots, \ k_{I_n}) \\
K_D & = & diag(k_{D_1}, \ k_{D_2}, \ \dots, \ k_{D_n})
\end{array}
$$

This controller uses not only the present error ε and its accumulation through time, it also employs a prediction of future error based on the present rate-of-variations to try to minimize the present error. The derivative signal of the controller is useful to provide phase lead which in terms offsets the phase lag caused by the integration signal. Because of this property, the derivative signal is considered to help improve the stability margins.

In a similar way to the PI controller, the closed loop produces second-order stable dynamics if the gains in K_P, K_I and K_D are positive constants. In such case, the resulting closed-loop system is also minimum phase.

The interconnection scheme on Figure 1.6 represents the closed loop between the PID controller and the system $\tilde{\Sigma}$ of equation (1.15).
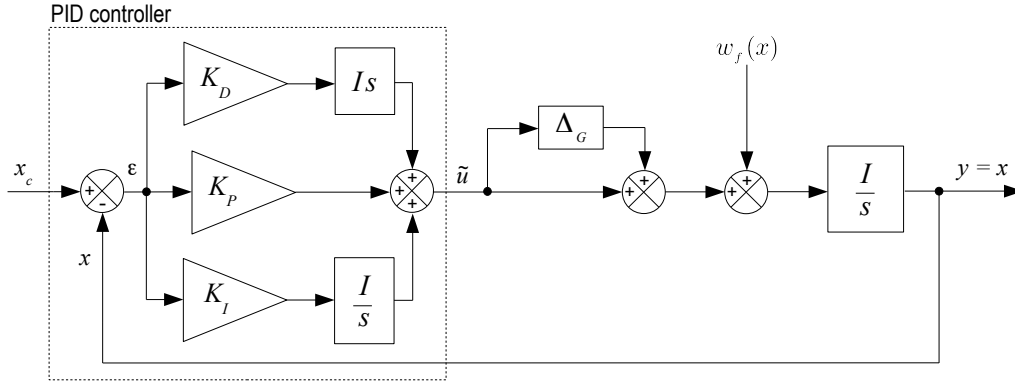
Figure 1.6: PID controller structure for the outer loop.

Remark 1.6 *The derivative operator is represented on Figure 1.6 by a non-causal block Is.*

For implementation, in practice, it is assumed that the derivative $\dot{\varepsilon}$ is available for feedback. Otherwise, the non-causal operator is replaced by a pseudo-derivation filter such as:

$$F_D = \frac{s}{\tau_D \, s + 1} I \tag{1.22}$$

where the time constant τ_D is chosen sufficiently small.

The generated dynamics can also be associated to the second-order characteristic polynomial (1.19). In choosing the values of k_{P_i}, k_{I_i} and k_{D_i}, the trade-off between attained bandwidth versus damping remains present. With the extra degree of freedom introduced by the gain K_D, the cut-off frequencies ω_{c_i} and damping coefficients ξ_i of the closed-loop states can be fixed by identification from the system

$$\frac{k_{P_i}}{1 + k_{D_i}} = 2\,\xi_i\,\omega_{c_i} \tag{1.23}$$

$$\frac{k_{I_i}}{1 + k_{D_i}} = \omega_{c_i}^2 \tag{1.24}$$

From a practical point of view, one of the three gains can be chosen heuristically. Then, it is simply required that the other two gains verify the equations above. Other heuristic methods to choose the value of the constants in K_P, K_I and K_D, such as the Ziegler-Nichol formula [ACL05, Oga02], could also be used.

Although a well tuned PID controller is a very complete solution, one mayor disadvantage comes from the fact that in presence of measurement noise, the derivative signal of the controller may produce large control signals.

A simple way to reduce the magnitude of the derivative signal of the PID controller is to filter the error measurement ε using a low-pass filter, which in term is equivalent compensating the derivative signal of the controller. Therefore, the use of a PI controller structure could be a better-suited alternative. In some cases, discarding the use of the derivative signal has little impact on the closed loop.

Remark 1.7 *For a given desired dynamics, different combinations of the gains K_P, K_I, and K_D are able to produce the same desired dynamics with a PID controller.*

Remark 1.8 *In the three standard controller structures that have been detailed above, even though the inversion errors Δ_G and w_f are considered, they are not explicitly used to fix the controller gains. Instead, the adjustment parameters of the gains K are directly linked to the dynamics that can be realized. As a matter of fact, the choice of the constants in the gains K end up defining the location of the closed-loop system poles, which leads us to consider these linear control designs as pole placement approaches.*

1.1.4 Advanced *robustification* techniques

There are essentially two kinds of techniques to improve the behavior of NDI controllers against inversion errors: adaptive control schemes or robust controllers.

From an adaptive point of view, the main goal is to generate a loop capable of adjusting the base-line model used to invert the system dynamics in presence of modelling errors. The foundations of these adaptive approaches can be found in [SI89], where an asymptotic exact cancellation of the nonlinear dynamics is achieved with a parameter update law. Different on-line adaptive laws and system identification strategies can be foreseen [DN02, HLS06, Tan06]. Evolutionary methods such as neural networks can also be employed as adaptive means of accomplishing an exact system

inversion [CR98, Ple03, SZ03]. In this thesis work, robust control techniques will receive more attention, although our proposed control structure detailed in Chapter 2 has strong connections with indirect adaptive control schemes.

As emphasized in Remark 1.8, standard PI or PID structures exhibit interesting robustness properties which permit, to some extent, to alleviate the adverse effects of inversion errors. However, the available degrees-of-freedom in such structures do not allow to take these errors explicitly into account while simultaneously placing the nominal closed-loop poles as desired.

More advanced linear approaches leading to higher-order controllers can then be foreseen to better exploit the available information on the system and the disturbances that affect its behavior. Particularly, to improve the controller robustness capabilities thanks to the additional degrees-of-freedom offered by higher-order controllers, these linear approaches take into account explicitly the different ways in which the model uncertainties, external disturbances and varying parameters will affect the nominal behavior.

Supplementary efforts to model the disturbances affecting the system in question are usually required. These efforts show to pay-off as the computed controller becomes more sensible to disturbances, thus attaining a better level of robustness. Depending on how the system and considered disturbances are modelled, the robust controllers may sometimes prove to induce conservatism in the control loop, *i.e.*, endowing the controller an overcapacity to react to circumstances that are physically unattainable because of actuator saturation.

Let us elaborate on how these advanced robust control techniques can be used to obtain controllers $C(s)$ that can reduce the effects of the inversion errors Δ_G and $w_f(x)$.

1.1.4.1   A standard $\mathcal{H}_\infty$ approach

Along with the PI structure, the $\mathcal{H}_\infty$ control design technique becomes very practical for linear control problems dealing with disturbance rejection. Still, the latter presents the advantage of using the model structure to establish a mathematical optimization problem where the $\mathcal{H}_\infty$ norms of specific transfer functions are minimized.

The formulation of the $\mathcal{H}_\infty$ control problem is of the utmost importance, since the resulting controllers are optimized in the sense given by the posed problem, which typically consists of:

– specifying the transfer functions to be minimized;
– tuning frequency domain weighting functions to control the closed-loop bandwidth as well as the rejection properties in the frequency domain.

When used to provide improved robustness properties to the outer loop in the context of NDI, the control problem consists on guaranteeing the robust performance of the closed loop by "rejecting" the inversion errors. A closed-loop desired behavior can be enforced in this optimization problem via a reference model $R(s)$ as shown on Figure 1.7.
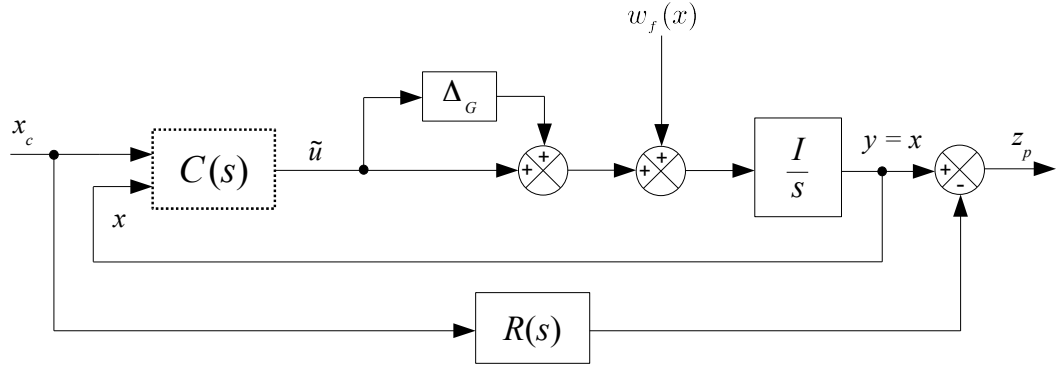
Figure 1.7: $\mathcal{H}_\infty$ control design scheme for system $\tilde{\Sigma}$.

The control design scheme above is then transformed into the *standard form* depicted on Figure 1.8. The latter is a particular kind of *linear fractional transformation* (LFT) used for controller synthesis where

– $P(s)$ is the augmented linear interconnection specifying the $\mathcal{H}_\infty$ design problem. In our context, it contains the dynamics of $\tilde{\Sigma}(s)$, $R(s)$ and other weighting functions $W(s)$;

– $\mathbf{w}$ is a vector regrouping all the exogenous inputs, including the setpoint signal x_c and input disturbances like w_f;

– $\mathbf{z}$ is a vector regrouping all the weighted exogenous outputs. In our context, it consists of the error between the output y and that of the reference model.
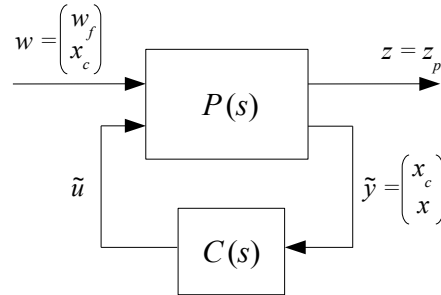
Figure 1.8: Standard form used to formulate $\mathcal{H}_\infty$ optimization problems.

Indeed, the signals of the vector $\mathbf{z}$ (and possibly those of the vector $\mathbf{w}$ as well) are weighted by a series of functions $W(s)$ that contribute to adding information to the optimization process. These weighting functions are part of the loop-shaping approach and they describe the frequency domain characteristics over which the controller should be optimized. When these functions are neglected, the controller is optimized for all frequencies ω which may result unnecessary and infeasible.

The interconnection system $P(s)$ is formalized in such a way that the closed-loop plant describing the multi-variable transfer to be minimized coincides with the following lower LFT expression:

$$
\begin{aligned}
\mathcal{T}_{\mathbf{w} \to \mathbf{z}} &= \mathcal{F}_l(P(s), C(s)) \\
&= P_{11}(s) + P_{12}(s)\, C(s)\, [I - P_{22}(s)\, C(s)]^{-1} P_{21}(s)
\end{aligned}
\tag{1.25}
$$

where $P_{ij}(s)$ denote the elements of a suitable partition of $P(s)$.

In the $\mathcal{H}_\infty$ framework, considering the Small Gain Theorem presented on Appendix B.1 (see page 241), the system illustrated on Figure 1.9 is robustly stable against any unstructured bounded uncertain operator $\Delta(\cdot)$ such that for all z, $||\Delta(z)|| < ||z||$ if:

$$||\mathcal{T}_{\mathbf{w} \to \mathbf{z}}(s)||_\infty < 1 \tag{1.26}$$
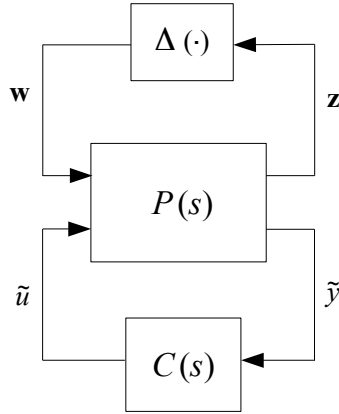
Figure 1.9: Standard form associated to $\mathcal{H}_\infty$ robust stability.

Consequently, resolving the following optimization problem responds directly to the above robust stability constraint:

$$\min_{C(s)} \gamma \,/\, ||\mathcal{F}_l(P(s), C(s))||_\infty < 1 \tag{1.27}$$

But thanks to the time-domain interpretation of the $\mathcal{H}_\infty$ norm (see Appendix B.2), the above problem can also be regarded as a performance preservation issue against disturbing inputs w_f. More precisely, in our context, the $\mathcal{H}_\infty$ outer-loop controller is designed to keep the error between the plant outputs y as close as possible to those of the reference model $R(s)$.

To achieve this goal, in a first approach two transfer functions are minimized. The first one, corresponding to $\mathcal{T}_{x_c \to z_p}(s)$, is directly related to the nominal performance and is to be minimized in the low frequency domain. The second one, corresponding to $\mathcal{T}_{w_f \to z_p}(s)$, reflects the effects of the nonlinear disturbances due to inversion errors on the outputs. In most cases, such a transfer is to be minimized in higher frequency regions where the accuracy of the model is often degraded.

In a next phase, in order to take into account more explicitly the effects of the multiplicative uncertainties Δ_G, an additional transfer $\mathcal{T}_{w_\Delta \to z_\Delta}(s)$, as shown on Figure 1.9, should be integrated to the standard plant $P(s)$. Now, the latter describes the interconnection between the inputs w_Δ, w_f and x_c and the outputs z_Δ, z_p and $\tilde{y}$ as shown on Figure 1.10.
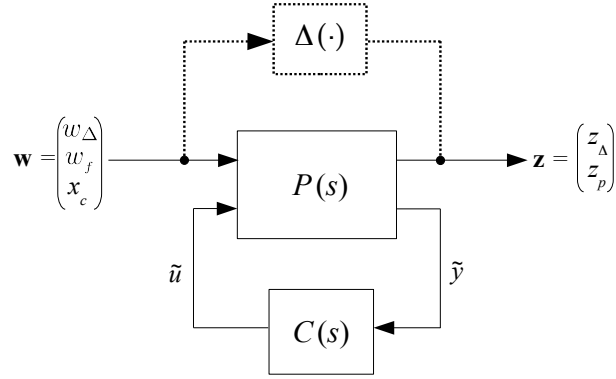
Figure 1.10: Augmented standard form associated to $\mathcal{H}_\infty$ control design.

Once again, invoking the small gain theorem, standard $\mathcal{H}_\infty$ design techniques can be used to attempt to solve the following minimization problem:

$$\min_{C(s)} ||\mathcal{F}_l(P(s), C(s))||_\infty \quad \longleftrightarrow \quad \min_{C(s)} ||\mathcal{T}_{\mathbf{w}\to\mathbf{z}}(s)||_\infty \tag{1.28}$$

where

$$\mathbf{w} = \begin{bmatrix} w_\Delta & w_f & x_c \end{bmatrix}^T, \qquad \mathbf{z} = \begin{bmatrix} z_\Delta & z_p \end{bmatrix}^T$$

But this strategy turns out to produce very conservative results since the structure of Δ is not taken into consideration for controller synthesis. In this case, the uncertainty operator Δ has the following structure:

$$\Delta = \left[\begin{array}{c|cc} \Delta_G & \mathbf{0} & \mathbf{0} \\ \hline \mathbf{0} & \Delta_{w_f} & \Delta_{perf} \end{array} \right] \tag{1.29}$$

1.1.4.2 Enhanced $\mathcal{H}_\infty$ design techniques

A classical approach to relax the conservatism described above, consists of taking explicitly into account the structure of Δ with the help of scaling operators.

As a matter of fact, the main source of conservatism is due to the minimization of non-physical transfers, such as the transfer from w_f to z_Δ. On the considered example, it is desired to minimize the transfer from $\begin{bmatrix} w_f & x_c \end{bmatrix}^T$ to z_p on one hand, and the transfer from w_Δ to z_δ on the other hand.

A standard approach to clearly distinguish these two main transfers is to minimize the influence of the "cross transfers" with the help of scaling operators commuting with the structured Δ block. Because the latter might no be square, as shown in equation (1.29) for our example, left and right scalings must be defined:

$$D_L = \begin{bmatrix} d_{\Delta_G} I_n & \mathbf{0} \\ \mathbf{0} & d_w I_{2n} \end{bmatrix}, \qquad D_R = \begin{bmatrix} d_{\Delta_G} I_n & \mathbf{0} \\ \mathbf{0} & d_w I_n \end{bmatrix} \tag{1.30}$$

such that

$$\Delta D_L = D_R \Delta \tag{1.31}$$
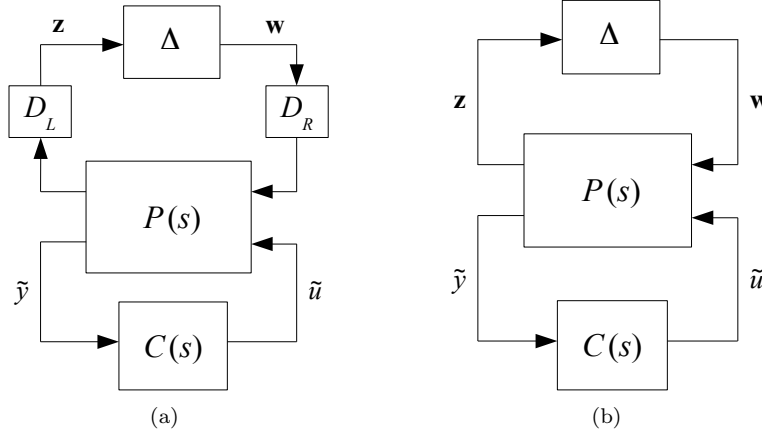
Figure 1.11: LFT representation used for μ-analysis and synthesis optimization problems.

It is clear, from a stability point of view, that the diagrams 1.11(a) and 1.11(b) are equivalent. But the transfer "seen" by the uncertain operator Δ is modified, which then relaxes the small gain theorem stability condition. The optimal controller is now obtained as:

$$\hat{C}(s) = \underset{C(s), D_L, D_R}{\text{Argmin}} \ ||D_L \, \mathcal{F}_l(P(s), C(s)) \, D_R^{-1}||_\infty \tag{1.32}$$

The resolution of the above nonconvex optimization problem, which is often referred to as a complex μ synthesis problem, is usually performed iteratively using the algorithm known as *D-K Iteration* [Doy82, Roo07]. The scaling operators D_i are initially fixed to identity and a preliminary controller is designed. The latter is then fixed and the scaling operators are computed. Such an algorithm is implemented in MatLab [BDG$^+$90]. This approach has been successfully used in the NDI context to compute robust outer-loop controllers $C(s)$ in aerospace applications [AB93, RBG95, RBG96].

To simplify the discussion on this relaxation approach, constant scaling operators D have been considered, which is also the only possible choice when the uncertain operator Δ contains time-varying elements. This is the case of the uncertainties Δ_G and Δ_{w_f}.

Interestingly, it can also be assumed that some elements of the Δ block can be estimated on-line. In such a case, the controller $C(s)$ may depend on an estimated uncertain operator $\hat{\Delta}$.

Assuming, for example, that Δ_G can be modelled and estimated, then the closed-loop scheme can be represented by the block diagram of Figure 1.12. When the estimation of the uncertainties is accurate enough, it comes that

$$\Theta \triangleq \hat{\Delta}_G \approx \Delta_G \tag{1.33}$$

where Θ is a vector of varying parameters.

Then, the robust control problem can be reformulated using readily available design techniques for LPV control. In this case, the convexity of the control problem is ensured. A solution based

on the Scaled Bounded Real Lemma (see Section 2.5.4), can be foreseen to compute a parameter dependent controller $C(s, \Theta)$ [AG95].
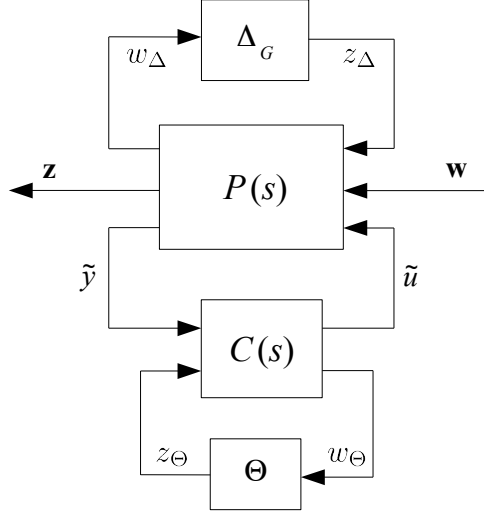
Figure 1.12: LFT representation used to formulate LPV control problems.

Other LPV strategies using polytopic modelling of the inversion errors as varying parameters can be considered [BA99]. In this case, the $\mathcal{H}_\infty$ norm devoted to the class of LTI systems is replaced by the $\mathcal{L}_2$-induced gain which remains valid for LPV models. A parameter dependent polytopic controller $C(s, \Theta) \in \mathcal{C}o\{C(s, \Theta_i)\}_{i=1...N}$ is then computed to guarantee the quadratic $\mathcal{H}_\infty$ performance of the closed loop system.

Remark 1.9 *In robust control approaches, for a given desired dynamics contained in the reference model $R(s)$, a wide range of controllers $C(s)$ can be obtained depending on the weighting functions $W(s)$ used and the way the optimization problem is established. These approaches present a more flexible solution than the previously detailed standard remedies.*

1.2 Extensions to more general nonlinear systems

Let us now present some extensions to NDI for more general nonlinear systems that are not necessarily square or input-affine.

First, the case of single-input single-output (SISO) systems is presented. In such cases, as the number of states of the nonlinear system is $n \neq 1$, the system is no longer square. Next, an extension to more general systems with multiple inputs and multiple outputs (MIMO) is addressed. To simplify the presentation of the MIMO case, the focus will be preliminarily set on the class of input-affine systems. Finally, an extension to non input-affine systems is considered.

1.2.1 A brief review of the SISO case

The general expression of a SISO input-affine nonlinear system is

$$\Sigma: \quad \begin{cases} \dot{x} &= f(x) + g(x)u \\ z &= h(x) \end{cases} \tag{1.34}$$

where
 – $x \in \mathbb{R}^n$ is the state vector of the system;
 – $u \in \mathbb{R}$ is the control input of the system;
 – $z \in \mathbb{R}$ is the controlled output;
 – $f(x) \in \mathbb{R}^n$ and $g(x) \in \mathbb{R}^n$ are smooth nonlinear vector fields;
 – $h(x) \in \mathbb{R}$ is a smooth nonlinear scalar function.

Unlike what has been considered in Section 1.1, the nonlinear process represented in (1.34) is an input-affine system for which the number of states $n > 1$ is no longer equal to the number of inputs $m = 1$.

Example 1.10 *Consider the SISO nonlinear system described by the sate-space equation (1.35) where $x \in \mathcal{D}$ and $\mathcal{D} \subset \mathbb{R}^n$. Consider also that $n = 2$ and, consequently, $n \neq m$. The control tracking objective is $z = x_1$, even though the full state measurement x may be available for controller synthesis.*

$$\Sigma: \begin{cases} \dot{x}_1 &= -\cos x_1 + x_2^2 \\ \dot{x}_2 &= \frac{1}{2}x_1\,x_2^{-1} - x_1\,u - x_2\,u \\ z &= x_1 \end{cases} \tag{1.35}$$

Under the general form of equation (1.34), one can easily identify

$$f(x) = \begin{bmatrix} -\cos x_1 + x_2^2 \\ \frac{1}{2}x_1\,x_2^{-1} \end{bmatrix} \quad,\quad g(x) = \begin{bmatrix} 0 \\ -(x_1 + x_2) \end{bmatrix}$$

1.2.1.1 Fundamentals on input-output feedback linearization

The design of the NDI linearizing inner loop is better known as input-output feedback linearization. It can be defined as follows [Isi85, SL91, Vid93].

Definition 1.11 (Exact input-output feedback linearization) *The nonlinear system (1.34) can be input-output linearized if there exists a coordinate transformation*

$$\tilde{x} = \Phi(x) \tag{1.36}$$

and a static state-feedback control

$$u(x) = \alpha(x) + \beta(x)\,\tilde{u}(z_c, z) \tag{1.37}$$

such that the resulting closed loop of transformed states are decoupled and linear.

To obtain the expression of the linearizing controller $u(x)$, the controlled output z is derived. Let us recall that the derivative operator of a scalar function with respect to a vector field is known as the *Lie Derivative*. The Lie derivative of $h(x)$ with respect to $f(x)$, for example, is defined as:

$$L_f h(x) = \frac{\partial h(x)}{\partial x} f(x) \tag{1.38}$$

ONERA
THE FRENCH AEROSPACE LAB

ISAE
Institut Supérieur de l'Aéronautique et de l'Espace

The derivation process of z continues until the control input u appears explicitly on the expression of the last derivative. The minimum number r of consecutive derivations required is known as the nonlinear system *relative degree* [Isi85].

Definition 1.12 (Relative degree) *The nonlinear system (1.34) has a relative degree r if*
- $L_g L_f^i h(x) = 0 \quad \forall\, i < r - 1 \text{ with } i \in \mathbb{N}$
- $L_g L_f^{r-1} h(x) \neq 0$

As a result of this derivation process, one obtains r linearly independent equations where the input control u appears only in the r-th equation. To clarify this process, let us consider that the nonlinear system Σ has a relative degree r, then

$$\dot{z} = \frac{dh(x)}{dt} = \frac{\partial h(x)}{\partial x}\dot{x} = \frac{\partial h(x)}{\partial x}\left(f(x) + g(x)\,u\right)$$

$$\dot{z} = L_f h(x) + L_g h(x)\,u$$

where $L_g h(x) = 0$. Continuing with the derivation process of z, one gets:

$$\ddot{z} = \frac{\partial L_f h(x)}{\partial x}\left(f(x) + g(x)\,u\right)$$

$$\ddot{z} = L_f^2 h(x) + L_g L_f h(x)\,u$$

where $L_g L_f h(x) = 0$. The derivation process continues until the r-th derivative

$$z^{(r)} = \frac{\partial L_f^{r-1} h(x)}{\partial x}\left(f(x) + g(x)\,u\right)$$

$$z^{(r)} = L_f^r h(x) + L_g L_f^{r-1} h(x)\,u$$

This time, the control input u appears because $L_g L_f^{r-1} h(x) \neq 0$. From this expression of the r-th derivative, the NDI inner loop controller that linearizes the input-output mapping of the nonlinear system Σ is defined as:

$$u(x) = \frac{1}{L_g L_f^{r-1} h(x)}\left(-L_f^r h(x) + \tilde{u}(z_c, z)\right) \tag{1.39}$$

The static controller structure presented in equation (1.37) can be recovered by identification of $\alpha(x)$ and $\beta(x)$ as:

$$\alpha(x) = \frac{-1}{L_g L_f^{r-1} h(x)} L_f^r h(x), \qquad \beta(x) = \frac{1}{L_g L_f^{r-1} h(x)}$$

while the coordinate transformation (1.36) is given by:

$$\Phi(x) = \begin{bmatrix} \phi_1(x) \\ \phi_2(x) \\ \vdots \\ \phi_r(x) \end{bmatrix} = \begin{bmatrix} z \\ \dot{z} \\ \vdots \\ z^{(r-1)} \end{bmatrix} = \begin{bmatrix} h(x) \\ L_f h(x) \\ \vdots \\ L_f^{r-1} h(x) \end{bmatrix} = \begin{bmatrix} \tilde{x}_1 \\ \tilde{x}_2 \\ \vdots \\ \tilde{x}_r \end{bmatrix} \tag{1.40}$$

Consequently, the closed loop SISO nonlinear system (1.34) is immersed into the linear and decoupled representation

$$\begin{cases} \dot{\tilde{x}}_1 = \tilde{x}_2 \\ \qquad \vdots \\ \dot{\tilde{x}}_{r-1} = \tilde{x}_r \\ \dot{\tilde{x}}_r = \tilde{u}(z_c, z) \end{cases} \tag{1.41}$$

The dimension of the resulting transformed system (1.41) is equal to the relative degree r. Naturally, one may be interested in comparing the dimension n of the original nonlinear system Σ and that of the transformed representation. There are three main cases:

a) $r = n$. The first implication of this result is that the nonlinear system Σ can be fully reconstituted from the controlled output z. The input-output feedback linearization is equivalent to the input-state linearization of Σ.

Example 1.13 *Consider the nonlinear system of example 1.10 represented by the state-space equation (1.35) in page 26. Recall that the full state x is measurable and assume an exact estimation of the nonlinear functions $f(x)$ and $g(x)$ is available.*

Based on the procedure that has just been described, the relative degree must first be determined by deriving the controlled output z until the input u appears explicitly in the expression of the r-th derivative.

$$
\begin{aligned}
z &= x_1 \\
\dot{z} &= \dot{x}_1 = -\cos x_1 + x_2^2 \\
\ddot{z} &= \ddot{x}_1 = x_1 + x_2^2 \sin x_1 - \frac{1}{2}\sin 2x_1 - 2x_2(x_1 + x_2)\,u
\end{aligned}
$$

Then, the relative degree is $r = 2$. The immersion of the nonlinear system into a linear representation is achieved by the static feedback controller

$$
u(x) = \frac{-1}{2\,x_2(x_1 + x_2)}\left(x_1 + x_2^2 \sin x_1 - \frac{1}{2}\sin 2x_1 + \tilde{u}(z_c, z)\right) \tag{1.42}
$$

where

$$
\tilde{u}(z_c, z) = \frac{1}{\tau}(z_c - z) \tag{1.43}
$$

and the coordinate transformation

$$
\Phi(x) = \begin{bmatrix} \tilde{x}_1 \\ \tilde{x}_2 \end{bmatrix} = \begin{bmatrix} x_1 \\ -\cos x_1 + x_2^2 \end{bmatrix} \tag{1.44}
$$

The closed-loop transformed representation becomes

$$
\begin{bmatrix} \dot{\tilde{x}}_1 \\ \dot{\tilde{x}}_2 \end{bmatrix} = \begin{bmatrix} 0 & 1 \\ 0 & 0 \end{bmatrix} \begin{bmatrix} \tilde{x}_1 \\ \tilde{x}_2 \end{bmatrix} + \begin{bmatrix} 0 \\ 1 \end{bmatrix} \frac{1}{\tau}(z_c - z) \tag{1.45}
$$

b) $r < n$. In this case, the original system includes unobservable internal dynamics that cannot be reconstituted and linearized by immersion using a static controller $u(x)$ and a coordinate transformation $\Phi(x)$. Yet, it is possible to obtain a linear input-output behavior through state-feedback. The unobservable dynamics end up creating *zero-dynamics*, that may introduce further stability problems as is clarified in Section 1.2.1.2.

Example 1.14 *Consider the second-order SISO nonlinear system described by the sate-space equation*

$$
\Sigma : \begin{cases} \dot{x}_1 &= -x_1^3 + 2x_2 + \frac{1}{10}u \\ \dot{x}_2 &= -x_1 - u \\ z &= x_1 \end{cases} \tag{1.46}
$$

for which

$$f(x) = \begin{bmatrix} -x_1^3 + 2\,x_2 \\ -x_1 \end{bmatrix} \quad , \quad g(x) = \begin{bmatrix} 0.1 \\ -1 \end{bmatrix}$$

Assuming an exact estimation of the nonlinear functions $f(x)$ and $g(x)$ is available, the relative degree r of the nonlinear system is obtained by deriving the objective z until the input u appears explicitly in the expression of the r-th derivative. Since

$$\dot{z} = \dot{x}_1 = -x_1^3 + 2\,x_2 + 0.1\,u$$

the relative degree is $r = 1$ and the coordinate transformation reduces to:

$$\phi(x) = \tilde{x} = x_1 \tag{1.47}$$

The input-output linearizing controller of system (1.46) can be expressed as:

$$u(x) = 10\left(x_1^3 - 2\,x_2 + \frac{1}{\tau}(z_c - z)\right) \tag{1.48}$$

Because in this case $r < n$, only the input-output mapping of the system Σ can be linearized. Then, internal nonlinear dynamics in system (1.46) still remain to be analysed.

c) $r > n$. This case reveals that the relative degree r of the nonlinear system Σ is not well defined, meaning that the input can not be recovered from the output, therefore, the system cannot be input-output linearized.

1.2.1.2 The effects of zero-dynamics

Let us first define what zero-dynamics are [Isi85, Vid93].

Definition 1.15 (zero-dynamics) *The zero-dynamics are the dynamics that characterize the internal behavior of a system when the input u and the initial conditions x_0 have been set in such a way that the output y is strictly zero.*

By regarding the linearizing controller $u(x)$ of the inner loop as the nonlinear equivalent of placing poles at the zeros of a system, the zero-dynamics are dynamics which are made unobservable by state feedback.

As explained in the previous section, when the system dimension n is greater than the relative degree r of the system, the nonlinear system posses internal dynamics that cannot be reconstituted from the controlled output z. The system resulting from the coordinate transformation (1.40)

becomes

$$\begin{cases}
\dot{\tilde{x}}_1 &=& \tilde{x}_2 \\
&\vdots& \\
\dot{\tilde{x}}_{r-1} &=& \tilde{x}_r \\
\dot{\tilde{x}}_r &=& L_f^r h(\zeta, \eta) + L_g L_f^{r-1} h(\zeta, \eta)\, u \\
\dot{x}_{r+1} &=& d_1(\zeta, \eta) \\
&\vdots& \\
\dot{x}_n &=& d_{n-r}(\zeta, \eta)
\end{cases} \tag{1.49}$$

where

$$\zeta = \begin{bmatrix} \tilde{x}_1 \\ \tilde{x}_2 \\ \vdots \\ \tilde{x}_{r-1} \\ \tilde{x}_r \end{bmatrix} \quad , \quad \eta = \begin{bmatrix} x_{r+1} \\ x_{r+2} \\ \vdots \\ x_{n-1} \\ x_n \end{bmatrix} \tag{1.50}$$

This representation can be decomposed into two sub-systems $\dot{\zeta}$ and $\dot{\eta}$. By considering the operating point $\bar{x} = \mathbf{0}$ as an equilibrium of the nonlinear system Σ, the zero-dynamics are characterized by:

$$\dot{\eta} = d(\mathbf{0}, \eta) \tag{1.51}$$

with $d(\mathbf{0}, \eta) \in \mathbb{R}^{n-r}$. When the zero-dynamics (1.51) are asymptotically stable, the control law

$$u(\zeta, \eta) = \frac{1}{L_g L_f^{r-1} h(\zeta, \eta)} \left(-L_f^r h(\zeta, \eta) + \tilde{u}(z_c, z) \right)$$

linearizes and decouples the mapping from the input $\tilde{u}$ to the controlled output z of the nonlinear system Σ.

If the nonlinear system Σ is non-minimum phase, the system inverse is unstable and no input-output linearization with internal stability can be obtained. The dimension of the largest linearizable subsystem can be determined through the computation of controllability distributions [Mar86]. It is also worth mentioning that the choice of the controlled output plays a key role on modifying the residual internal dynamics as explained in [Har91]. By choosing the right output function to be linearized, the resulting unobservable sub-system composed by the differential equation $\dot{\eta}$ may turn out to be stable.

Example 1.16 *Consider the nonlinear system of example 1.14 represented by the state-space equation (1.46).*

In fact, the system Σ is non-minimum phase. This can be proved by obtaining the first-order tangent system about an equilibrium point $(\bar{x}_1, \bar{x}_2)$ such as:

$$\begin{cases}
\delta \dot{x}_1 &=& -3\,\bar{x}_1^2\,\delta x_1 + 2\,\delta x_2 + 0.1\,\delta u \\
\delta \dot{x}_2 &=& -\delta x_1 - \delta u \\
\delta z &=& \delta x_1
\end{cases} \tag{1.52}$$

When this system is expressed in the frequency domain using the Laplace transform, one gets the non-minimum phase transfer function

$$\frac{\delta z}{\delta u} = \frac{0.1\,s - 2}{s^2 + 3\,\bar{x}_1^2\,s + 2} \tag{1.53}$$

ONERA
THE FRENCH AEROSPACE LAB

isae
Institut Supérieur de l'Aéronautique et de l'Espace

As detailed in example 1.14, an input-output linearizing controller for the nonlinear system (1.46) can be defined as:

$$u(x) = 10 \left(x_1^3 - 2\,x_2 + \frac{1}{\tau}(z_c - z) \right)$$

Because the number of states $n = 2$ is greater than the relative degree $r = 1$, one can expect the existence of zero-dynamics. Considering the resulting transformation $\phi(x)$ defined in example 1.14, the closed-loop system becomes

$$\begin{cases} \dot{\tilde{x}} &=& \frac{1}{\tau}(x_c - x) \\ \dot{x}_2 &=& 20\,x_2 - 10\,x_1^3 - x_1 - \frac{10}{\tau}(z_c - z) \end{cases} \tag{1.54}$$

As $z = x_1$ converges towards a constant value $z_c = x_{1_c}$, the zero-dynamics is characterized by the following state equation:

$$\dot{x}_2 = 20\,x_2 - 10\,x_{1_c}^3 - x_{1_c} \tag{1.55}$$

*Clearly, the solution to this differential equation increases exponentially with time. The zero-dynamics is **unstable**.*

At this point, one can choose to solve the problems related to unstable zero-dynamics by explicitly trying to stabilize them. The strategy proposed in [DAOM92], for example, relies on establishing a trade-off between making the input-output mapping as linear as possible, and making some portion of the zero-dynamics "observable" in order to achieve internal stability.

But the issue of creating these unobservable dynamics via state-feedback in the first place, can be associated directly to the system modelling. In this sense, selecting the appropriate type of model to represent a nonlinear system intended to be input-output linearized is relevant.

For example, in some particular cases where the number of states is greater than the relative degree of the nonlinear system $r < n$, the model may allow to obtain a "state-free" inverse [IMDL86]. For such systems, a *dynamic* inner-loop controller

$$\begin{cases} \dot{\varsigma} &=& \varrho(x,\varsigma) + \vartheta(x,\varsigma)\,\tilde{u} \\ u &=& \alpha(x,\varsigma) + \beta(x,\varsigma)\,\tilde{u} \end{cases}$$

can be designed to obtain an input-output linearization via state-feedback that does not generate unobservable internal dynamics. It should be mentioned that the dynamics is not affected in the single input case where $m = 1$ [CLM91].

This is the case of *differentially flat* systems. A general nonlinear system is considered *flat* if the state x and the input u can be recovered from a finite number of derivatives of a vector z, containing a specific choice of system outputs [FLMR95, Lé11]. By obtaining a differentially flat model of the nonlinear system, the creation of zero-dynamics is averted. This approach has been successfully used in aerospace applications [MCV09, Mor09].

A simple modelling approach, natural to various mechanical systems and that helps circumvent partially having to deal with zero-dynamics along with other previously mentioned problems, is introduced next.

ONERA
THE FRENCH AEROSPACE LAB

ISAE
Institut Supérieur de l'Aéronautique et de l'Espace

1.2.1.3 Systems with multiple time scales

The core idea of time-scaling separation consists in assuming that a process can be decomposed into two or more sub-systems, based on a hierarchical time basis. This is done by analysing the open-loop behavior of the states that compose a given process. In other words, the system can be seen as two or more systems, that evolve over different ranges of time, and that are linked one to the other.

Let us assume that the system (1.34) presented on page 26 can be rewritten as follows:

$$\begin{cases} \dot{x}_1 &=& f_1(x_1) + \lambda_1(x_1)\,x_2 \\[2mm] \dot{x}_2 &=& f_2(x_1, x_2) + \lambda_1(x_1, x_2)\,x_3 \\[2mm] &\vdots& \\[2mm] \dot{x}_{k-1} &=& f_{k-1}(x_1, \ldots, x_{k-1}) + \lambda_{k-1}(x_1, \ldots, x_{k-1})\,x_k \\[2mm] \dot{x}_k &=& f_k(x) + \lambda_k(x)\,u \end{cases} \tag{1.56}$$

where x_1 denotes the slowest dynamics while x_k coincides with the fastest. In the above description, the control input u directly affects the fastest dynamics. Then, the state x_k is easily controlled using the standard NDI law (1.6) which in this case becomes

$$u = \lambda_k^{-1}(x)\left(-f_k + C_k(s)\begin{bmatrix} x_{k_c} \\ x_k \end{bmatrix}\right) \tag{1.57}$$

The controller $C_{(s)}$ is tuned such that the convergence of the state x_k towards the target x_{k_c} is fast when compared to the dynamics of the slower states. As a result, in the differential equation describing the evolution of x_{k-1}, the approximation $x_k \approx x_{k_c}$ may be considered. Then, it comes that

$$\dot{x}_{k-1} = f_{k-1}(x_1, \ldots, x_{k-1}) + \lambda_{k-1}(x_1, \ldots, x_{k-1})\,x_{k_c} \tag{1.58}$$

Thus, x_{k_c} may now be viewed as a new control input thanks to which x_{k-1} can be easily driven to $x_{(k-1)_c}$ using a standard NDI control law. Clearly, by a recursive procedure, the slow dynamics x_1 can be finally controlled as well.

Interestingly, most physical systems can be approximated by (1.56) although in practice, the control input u will rarely only affect the fastest dynamics.

Example 1.17 *Consider again the SISO nonlinear system presented in example 1.14 of page 28. The nonlinear system (1.46) has been intentionally formulated in such a way to resemble a mechanical system where the state x_1 depends heavily on the state x_2 rather than on the system input u, and the state x_2 reacts directly to the input commands u.*

Assuming the full state x is measurable and that the system can be decoupled in a time-scale basis, Σ can be expressed as two separate sub-systems such as:

$$\Sigma_1 : \begin{cases} \dot{x}_1 &=& -x_1^3 + 0.1\,u + 2\,x_2 \\ z_1 &=& x_1 \end{cases} \tag{1.59}$$

and

$$\Sigma_2 : \left\{ \begin{array}{rcl} \dot{x}_2 & = & -x_1 - u \\ z_2 & = & x_2 \end{array} \right. \tag{1.60}$$

where the state x_2 represents the fast dynamics and the state x_1 represents the slow dynamics.

First, an input-output linearizing controller $u(x)$ can be designed for the fast dynamics. Deriving z_2, one gets:

$$\dot{z}_2 = \dot{x}_2 = -x_1 - u$$

$$u(x) = -x_1 - \frac{1}{\tau_2}(x_{2_c} - x_2) \tag{1.61}$$

Clearly, $r_2 = n_2$ and $n_2 = m_2$. The closed-loop fast sub-system Σ_2 becomes

$$\dot{x}_2 = \frac{1}{\tau_2}(x_{2_c} - x_2) \tag{1.62}$$

It is reminded that while the slow dynamics evolve, the fast dynamics converge rather quickly towards its setpoint $x_2 = x_{2_c}$.

As for the slow dynamics control, the input of this sub-system is now the state x_2, which means that the system is not controlled through its non-minimal effect any more.

The input-output linearizing controller that eliminates the nonlinear dynamics of the slow sub-system, generates the commanded value of this fast state $x_{2_c}(x)$ such as:

$$\begin{aligned} \dot{z}_1 = \dot{x}_1 &= -x_1^3 + 0.1\, u + 2\, x_2 \\ &= -x_1^3 + 0.1\left(-x_1 - \frac{1}{\tau_2}(x_{2_c} - x_{2_c})\right) + 2\, x_2 \end{aligned}$$

$$x_{2_c}(x) = \frac{1}{2}\left(x_1^3 - 0.1\, x_1 + \frac{1}{\tau_1}(x_{1_c} - x_1)\right) \tag{1.63}$$

Once again, it can be verified that $r_1 = n_1$ and that $n_1 = m_1$. The closed-loop slow sub-system becomes

$$\dot{x}_1 = \frac{1}{\tau_1}(x_{1_c} - x_1) \tag{1.64}$$

Notice that under time-scaling separation, the inversion controller (1.63) is multiplied by a factor of $\frac{1}{2}$ instead of 10, thus requiring smaller control signals to linearize both, the slow state x_1 and the fast state x_2.

Finally, by assembling controllers (1.61) and (1.63), the time-scaled NDI controller that linearizes and decouples the nonlinear system (1.46) without creating zero-dynamics becomes

$$u(x) = -x_1 - \frac{1}{\tau_2}\left(0.5x_1^3 - 0.05x_1 + \frac{0.5}{\tau_1}(x_{1_c} - x_1) - x_2\right) \tag{1.65}$$
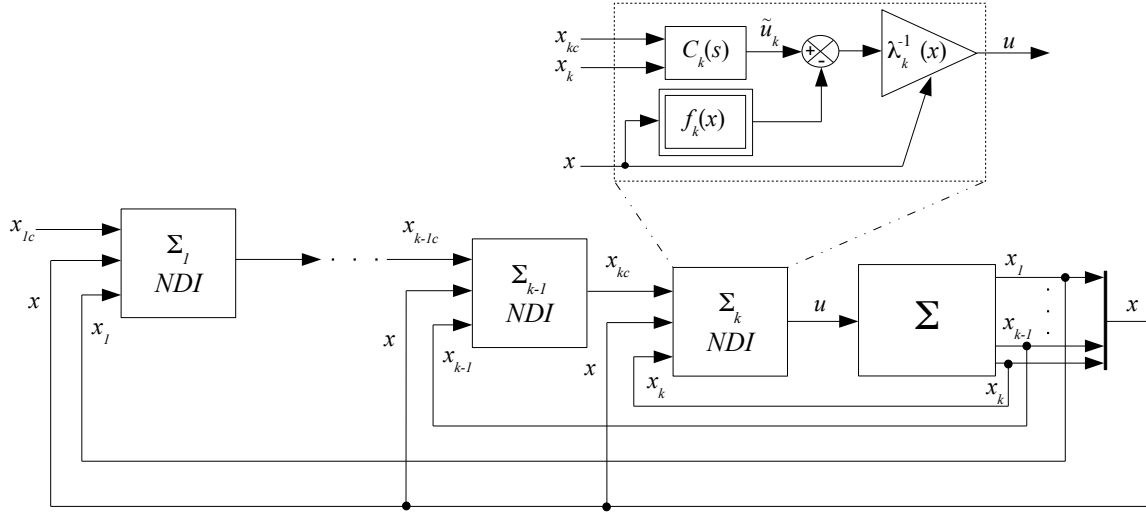
Figure 1.13: Cascade NDI structure of a system Σ with k time scales.

The time-scaling approach generates a very close approximation of the inversion control signal required to compensate the system nonlinear dynamics, thus conferring approximated linearization and decoupling properties to the NDI controller.

It should also be kept in mind that in order for this approach to work in practice along with the NDI control technique, the hypothesis that the system can be decoupled into faster and slower dynamics must hold when the control loop is closed. This means that the open-loop fast dynamics must remain faster than the slower dynamics in closed loop. Generally, the obtained results using NDI with time-scaling separation are adequate and sufficient from a performance perspective.

1.2.2 Overview of the MIMO case

Let us now explain how the NDI inner loop design described in the previous section for SISO nonlinear systems can be extended in a very straightforward manner to the multiple-input multiple-output (MIMO) case. The expression of a MIMO nonlinear system can be

$$\Sigma: \quad \begin{cases} \dot{x} &= f(x) + \sum_{i=1}^{p} g_i(x)\, u_i \\ z &= h(x) \end{cases} \tag{1.66}$$

where
– $x \in \mathbb{R}^n$ is the state vector of the system;
– $u_i \in \mathbb{R}$ are the control input of the system, with $i = 1, \dots, p$ and $n \neq p$;
– $z \in \mathbb{R}^p$ are the controlled outputs;
– $f(x) \in \mathbb{R}^n$ and $g_i(x) \in \mathbb{R}^n$ are smooth nonlinear vector fields;
– $h_j(x) \in \mathbb{R}$ are smooth scalar functions, with $j = 1, \dots, p$.

The fundamentals regarding input-output linearization sustain in the MIMO case. The adaptation of some concepts are nonetheless required. For example, the notion of the relative degree is

extended as the *vector relative degree*. The vector relative degree of a MIMO nonlinear system is expressed as:

$$\mathrm{r} = \begin{bmatrix} r_1 & \cdots & r_j & \cdots & r_p \end{bmatrix}^T \tag{1.67}$$

where r_j represent the minimum number of derivations of the corresponding controlled output z_j required to make at least one of the inputs u_i appear in the expression of its r_i-th derivative. Let us clarify this concept by taking the example of the j-th controlled output z_j. Its first derivative is written as:

$$\dot{z}_j = \frac{dh_j(x)}{dt} = \frac{\partial h_j(x)}{\partial x}\dot{x} = \frac{\partial h_j(x)}{\partial x}\left(f(x) + \sum_{i=1}^{p} g_i(x)\, u_i\right)$$

$$\dot{z}_j = L_f h(x) + \sum_{i=1}^{p} \left(L_{g_i} h_j(x)\right) u_i$$

where each of the $L_{g_i} h_j(x) = 0$. The derivation process of z_j continues until the r_j-th derivative

$$z_j^{(r_j)} = \frac{\partial L_f^{r_j-1} h_j(x)}{\partial x}\left(f(x) + \sum_{i=1}^{p} g_i(x)\, u_i\right)$$

$$z^{(r_j)} = L_f^{r_j} h_j(x) + \sum_{i=1}^{p} L_{g_i} L_f^{r_j-1} h_j(x)\, u_i$$

This time, one of the control inputs u_i appears because at least one $L_{g_i} L_f^{r_j-1} h_j(x) \neq 0$. The same process is applied to the p controlled outputs of the original nonlinear system Σ.

Once all the controlled outputs have been derived and that the vector relative degree is obtained, by regrouping the set of p expressions containing the r_j-th derivatives of z

$$\begin{bmatrix} z_1^{(r_1)} \\ \vdots \\ z_p^{(r_p)} \end{bmatrix} = \begin{bmatrix} L_f^{r_1} h_1(x) \\ \vdots \\ L_f^{r_p} h_p(x) \end{bmatrix} + G(x)\begin{bmatrix} u_1 \\ \vdots \\ u_p \end{bmatrix} \tag{1.68}$$

with $G(x) = \begin{bmatrix} L_{g_1} L_f^{r_1-1} h_1(x) & \cdots & L_{g_p} L_f^{r_1-1} h_1(x) \\ \vdots & \ddots & \vdots \\ L_{g_1} L_f^{r_p-1} h_p(x) & \cdots & L_{g_p} L_f^{r_p-1} h_p(x) \end{bmatrix}$,

the NDI inner loop controller that linearizes the input-output mapping of the MIMO nonlinear system Σ can be deduced as:

$$\begin{bmatrix} u_1(x) \\ \vdots \\ u_p(x) \end{bmatrix} = G^{-1}(x)\left(-\begin{bmatrix} L_f^{r_1} h_1(x) \\ \vdots \\ L_f^{r_p} h_p(x) \end{bmatrix} + \begin{bmatrix} \tilde{u}_1(z_{1_c}, z_1) \\ \vdots \\ \tilde{u}_p((z_{p_c}, z_p)) \end{bmatrix}\right) \tag{1.69}$$

Notice that the matrix $G(x) \in \mathbb{R}^{p \times p}$ is square. It is also generally assumed that $G(x)$ is non-singular $\forall\, x$, thus ensuring that it is invertible. An input-output linearization may still be achieved in some cases where this square matrix $G(x)$ is singular at some operating points by adding integrators before specific inputs u_i as proposed in [DM85].

ONERA
THE FRENCH AEROSPACE LAB

ISae
Institut Supérieur de l'Aéronautique et de l'Espace

However, one may still be confronted with problems associated to the resulting NDI controller generating large control signals if at specific operating point, the determinant of the matrix $G(x)$ becomes small. And in many real life control applications, $G(x)$ may not necessarily be square. In fact, when the number of inputs m and the number of outputs p do not match $m \neq p$, the matrix $G(x)$ becomes rectangular, meaning that the input needs to be allocated or redistributed onto each controllable state to compensate their nonlinear dynamics.

Both issues associated to the size and operating conditions of the matrix $G(x)$, are usually resolved using the modelling approach described in Section 1.2.1.3.

In regards to the coordinate transformation $\Phi(x)$, in the MIMO case, it is constructed from each computed derivative. Let us retake the example of the j-th controlled output z_j. The coordinate transformation $\Phi_j(x)$ related to this controlled output yields

$$\Phi_j(x) = \begin{bmatrix} \phi_{j,1}(x) \\ \vdots \\ \phi_{j,r_j}(x) \end{bmatrix} = \begin{bmatrix} z_j \\ \vdots \\ z_j^{(r_j-1)} \end{bmatrix} = \begin{bmatrix} h_j(x) \\ \vdots \\ L_f^{r_j-1} h_j(x) \end{bmatrix} = \begin{bmatrix} \tilde{x}_{j,1} \\ \vdots \\ \tilde{x}_{j,r_j} \end{bmatrix} \tag{1.70}$$

Then, the coordinate transformation is obtained by reassembling the p functions Φ_j such as:

$$\Phi(x) = \begin{bmatrix} \Phi_1(x) \\ \vdots \\ \Phi_j(x) \\ \vdots \\ \Phi_p(x) \end{bmatrix} \tag{1.71}$$

The dimension of the resulting transformation function $\Phi(x)$, and therefore the dimension of the transformed linear and decoupled system, depends on the number of derivatives r_j of each one of the p output functions z, then

$$dim(\Phi(x)) = \sum_{j=1}^{p} r_j \tag{1.72}$$

Example 1.18 *Consider the MIMO nonlinear system described by the sate-space equation (1.73) where $x \in \mathcal{D}$ and $\mathcal{D} \subset \mathbb{R}^n$. Consider also that $n = 3$, $m = 2$ and $p = 2$. The full state measurement x is available for controller synthesis.*

$$\Sigma : \begin{cases} \dot{x}_1 &= -x_1 x_2 + u_1 - u_2 \\ \dot{x}_2 &= x_2 x_3^2 \\ \dot{x}_3 &= -x_3 - x_2 u_1 - u_2 \\ z &= \begin{bmatrix} x_1 x_2 & x_2 \end{bmatrix}^T \end{cases} \tag{1.73}$$

Under the particular form (1.66), one can identify at first glance

$$f(x) = \begin{bmatrix} -x_1 x_2 \\ x_2 x_3^2 \\ -x_3 \end{bmatrix} \quad , \quad g(x) = \begin{bmatrix} u_1 - u_2 \\ 0 \\ -x_2 u_1 - u_2 \end{bmatrix}$$

The vector relative degree is obtained by deriving each one of the controlled outputs z. Since

$$
\begin{array}{rcl}
z_1 & = & x_1\,x_2 \\
\dot{z}_1 & = & -x_1\,x_2^2 + x_1\,x_2\,x_3^2 + x_2\,u_1 - x_2\,u_2
\end{array}
$$

the relative degree is $r_1 = 1$. Passing on to the second controlled output, one gets that:

$$
\begin{array}{rcl}
z_2 & = & x_2 \\
\dot{z}_2 & = & x_2\,x_3^2 \\
\ddot{z}_2 & = & x_2\,x_3^4 - 2x_2\,x_3^2 - 2x_2^2\,x_3\,u_1 - 2x_2\,x_3\,u_2
\end{array}
$$

The relative degree is $r_2 = 2$. Because $r_1 + r_2 = n$, the obtained input-output feedback linearization is equivalent to the input-state linearization. The immersion of the nonlinear system into a linear and decoupled representation is achieved by the static feedback controller

$$
u(x) = \begin{bmatrix} x_2 & -x_2 \\ -2x_2^2\,x_3\,u_1 & -2x_2\,x_3\,u_2 \end{bmatrix}^{-1} \left(- \begin{bmatrix} -x_1\,x_2^2 + x_1\,x_2\,x_3^2 \\ x_2\,x_3^4 - 2x_2\,x_3^2 \end{bmatrix} + \begin{bmatrix} \tau_1^{-1}(z_{1_c} - z_1) \\ \tau_2^{-1}(z_{2_c} - z_2) \end{bmatrix} \right) \tag{1.74}
$$

and the coordinate transformation

$$
\Phi(x) = \begin{bmatrix} \tilde{x}_1 \\ \tilde{x}_2 \\ \tilde{x}_3 \end{bmatrix} = \begin{bmatrix} x_1\,x_2 \\ x_2 \\ x_2\,x_3^2 \end{bmatrix} \tag{1.75}
$$

The closed-loop transformed representation becomes

$$
\begin{bmatrix} \dot{\tilde{x}}_1 \\ \dot{\tilde{x}}_2 \\ \dot{\tilde{x}}_3 \end{bmatrix} = \begin{bmatrix} 0 & 0 & 0 \\ 0 & 0 & 1 \\ 0 & 0 & 0 \end{bmatrix} \begin{bmatrix} \tilde{x}_1 \\ \tilde{x}_2 \\ \tilde{x}_3 \end{bmatrix} + \begin{bmatrix} 1 & 0 \\ 0 & 0 \\ 0 & 1 \end{bmatrix} \begin{bmatrix} \tau_1^{-1}(z_{1_c} - z_1) \\ \tau_2^{-1}(z_{2_c} - z_2) \end{bmatrix} \tag{1.76}
$$

1.2.3 The case of non input-affine systems

To conclude this section with a more general class of nonlinear systems, which often appear in aerospace control applications, let us now consider the case of non input-affine systems as described by the state-space equation (1.77).

$$
\Sigma: \quad \begin{cases} \dot{x} & = & f(x) + g(x, u) \\ z & = & h(x) \end{cases} \tag{1.77}
$$

where
– $x \in \mathbb{R}^n$ is the state vector of the system;
– $u \in \mathbb{R}^m$ is the control input of the system, with $n \neq m$;
– $z \in \mathbb{R}^p$ is the controlled output;
– $f(x) \in \mathbb{R}^n$, $g(x, u) \in \mathbb{R}^n$ and $h(x) \in \mathbb{R}^p$ are smooth vector fields.

Non-affine representations increase the complexity of the practical application of the NDI standard technique since an explicit inversion, with respect to the input u is not possible. Different approaches, some more sophisticated than the others, can be used to circumvent this issue.

For example, a complex but powerful solution is proposed in [SZ03]. In this case, a multi-layer neural-network is used along with a high-gain observer to generate the nonlinear control signal

u capable of inverting the non-affine system. This solution is an auto-adaptive strategy that compensates the nonlinear dynamics of the input in relation to the system.

Another idea is proposed in [HLS06, YCHL06], where it is considered that for most non-affine systems, the ideal dynamic inversion controller exists but can not be written explicitly. In this sense, the authors introduce an heuristic design that attempts to approximate a dynamic inversion controller based on a time-scaling assumption between the system dynamics and the input dynamics. One disadvantage of this approach is that it does not account for input constraints that may limit the system input dynamics.

A more elegant solution can be found by defining a vector containing the "flat" outputs of the system which allow to recover the state x and the input u from a finite number of its derivatives [SRS04, Lé11]. When the non-affine system is differentially flat, a dynamic state-feedback controller for the inner loop of the NDI control structure can be obtained following [CLM91].

Finally, a simpler adaptation consists in considering the m inputs present in the process Σ as states of an extended state-space representation [HS90]. The idea consists on including the input vector u as part of the system dynamics. This can be achieved by proposing a change of variables $\breve{x}$ in order to obtain an affine representation. In a very natural manner, this approach generates a dynamic linearizing controller when used with the standard NDI inner loop design. Let us illustrate this idea. Starting from the state equation

$$\dot{x} = f(x) + g(x, u)$$

then by posing the change of variables

$$\breve{x} = \begin{bmatrix} x \\ u \end{bmatrix}, \qquad \breve{u} = \dot{u} \tag{1.78}$$

the extended representation of the non-affine system becomes

$$\begin{cases} \dot{\breve{x}} &= \breve{f}(\breve{x}) + \breve{g}(\breve{x})\breve{u} \\ \breve{z} &= \breve{h}(\breve{x}) \end{cases} \tag{1.79}$$

with $\breve{f}(\breve{x}) = \begin{bmatrix} f(x) + g(x, u) \\ 0 \end{bmatrix}$, $\breve{g}(\breve{x}) = \begin{bmatrix} 0 \\ 1 \end{bmatrix}$ and $\breve{h}(\breve{x}) = h(x)$.

The extended system (1.79) is affine, the linearizing controller can be designed in the usual manner but with a slight difference. After computing the vector relative degree r and the set of p equations corresponding to the r_j-th derivative of each controlled output $\breve{z}_j$, the resulting feedback linearizing control law has the following rate

$$\dot{u} = \breve{u} = \breve{G}(\breve{x})^{-1}[-\breve{F}(\breve{x}) + \tilde{u}(z_c, z)] \tag{1.80}$$

with $\breve{F}(\breve{x}) = \begin{bmatrix} L_{\breve{f}}^{r_1} \breve{h}_1(\breve{x}) \\ \vdots \\ L_{\breve{f}}^{r_p} \breve{h}_p(\breve{x}) \end{bmatrix}$ and $\breve{G}(\breve{x}) = \begin{bmatrix} L_{\breve{g}_1} L_{\breve{f}}^{r_1-1} \breve{h}_1(\breve{x}) & \dots & L_{\breve{g}_m} L_{\breve{f}}^{r_1-1} \breve{h}_1(\breve{x}) \\ \vdots & \ddots & \vdots \\ L_{\breve{g}_1} L_{\breve{f}}^{r_p-1} \breve{h}_p(\breve{x}) & \dots & L_{\breve{g}_m} L_{\breve{f}}^{r_p-1} \breve{h}_p(\breve{x}) \end{bmatrix}.$

Finally, this feedback linearization control law can be expressed in the form of a dynamic controller by introducing the controller state $\varsigma \in \mathbb{R}^m$ such as:

$$\left\{ \begin{array}{rcl} \dot{\varsigma} & = & -\breve{G}(\breve{x})^{-1}\breve{F}(\breve{x}) + \breve{G}(\breve{x})^{-1}\tilde{u}(z_c, z) \\ u & = & \varsigma \end{array} \right. \tag{1.81}$$

1.3 On control input saturations

Let us take into account the input constraints that have been neglected up to now, including actuator dynamics Σ_A and physical limitations.

In fact, the control input u of most physical processes involve constraints on the achievable value that can be generated in real-life. These constraints represented by nonsmooth and unfortunately non-invertible nonlinear functions are often referred to as "hard nonlinearities" in the literature [SL91].

Magnitude and rate saturations are the most standard examples of such kinds of hard nonlinearities which are commonly used to model the main physical limitations in actuators.

1.3.1 Representation and effects of control input saturations

In a large majority of control applications, the nominal behavior of actuators is correctly approximated by first or second-order transfer functions. Consider the simpler first-order case

$$\Sigma_A(s) = \frac{1}{\tau_a\, s + 1} \tag{1.82}$$

where τ_a is the time constant of the actuator, which is usually small compared to the closed-loop response.

Let us denote u_c the commanded input delivered by the control laws, and u_r the real output delivered by the actuator to the physical process. The transfer from u_c to u_r described by (1.82) can also be represented by the block diagram presented on Figure 1.14.
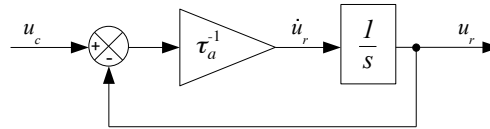
Figure 1.14: A general first-order actuator model.

In a very convenient manner, the derivative signal $\dot{u}_r$ appears explicitly on this diagram. This allows a natural representation of rate limited actuators in a very simple way, using only static nonlinearities. A standard representation of mixed magnitude and rate limited actuators, used for controller design, is depicted on Figure 1.15.
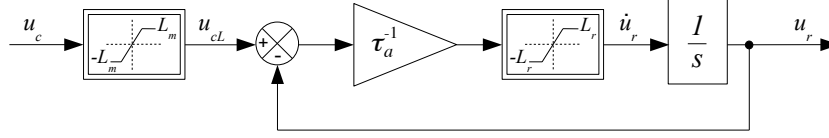
Figure 1.15: A design-oriented first-order saturated actuator model.

For simplicity, let us temporarily assume that the saturation nonlinearities on the diagram above are symmetrical. In the case of the control signal u_c, for example, one gets that:

$$u_{c_L} = \begin{cases} L_m & \text{if} \quad u_c > L_m \\ u_c & \text{if} \quad |u_c| \leq L_m \\ -L_m & \text{if} \quad u_c < -L_m \end{cases} \tag{1.83}$$

This assumption on the symmetry of the saturation bounds generally holds in practice for rate limitations, but not systematically for the magnitude limitations which usually depend on trimming conditions.

The impact of magnitude and rate saturations on the closed-loop behavior is very sever, even for linear systems. As a matter of fact, when saturations occur, the system is no longer controlled by the feedback laws. The behavior is temporarily characterized by the open loop dynamics subject to constant inputs $\pm L_i$. Assume that the open loop system is unstable, then it is easily understood why saturations are often responsible for a dangerous reduction of the size of the stability domain.

In the NDI context, the saturation phenomenon is even more complex since the magnitude and rate limitations will also introduce severe imperfections in the inversion process. As a result, the feedback linearisation which is normally performed by the inner loop controller fails to provide a linear system. Consequently, additional efforts are required from the outer loop to counteract these nonlinear effects.

Whatever the control strategy, there exist essentially two ways to minimize the adverse effects of saturations. The first possibility consists of avoiding saturations by adjusting the control requirement as proposed in [GT91]. Typically, this will result in a significant loss of the attainable performance. Moreover, in the NDI context, this approach is not trivial since, from equation (1.6), one observes that $u(x)$ is not directly controlled. The latter depends on $f(x)$ and $G(x)$.

The second possibility consists of actively controlling the saturated system through the design of an external control loop also known as an *anti-windup* device. Such strategies are briefly reviewed hereafter.

1.3.2 Anti-windup control strategies

Some of the first formal Anti-windup control approaches were introduced in [Hor83, DSE87, HKH87]. To this day, anti-windup strategies have been developed for a variety of systems subject to input saturation: from linear time-invariant (LTI) systems [AR89, ZT02, WL04, GdST05],

passing through LFT representations [FB07, Roo07] and applications to aerospace control systems [BT09, Boa10]. Some works can be found on Anti-windup strategies applied along with NDI control [YPY08, HTM$^+$10]. These particular approaches, which remain in a nonlinear context, require adaptations of the NDI controller inner loop which results in rather complex control structures.

The basic idea of the anti-windup controller is to enlarge the closed-loop stability domain as much as possible by reducing the impact of the saturating inputs. This is achieved by introducing a correction signal from the input saturation to a nominal controller $C(s)$ and its commanded signal u_c. This correction terms coming out of the anti-windup controller $J(s)$ help diminishing the signals that accumulate within the nominal controller states x_C when saturation occurs.

The first anti-windup approaches were basically frequency domain techniques that focused on changing the closed-loop system to prevent limit cycles or instability following the Nyquist criterion, for example [Hor83, AR89]. The main drawback to these techniques is that they applied only to single input saturation systems. More recent adaptations of the anti-windup schemes allow a systematic implementation to multiple input saturation systems through the minimization of the saturated input transfers. Although these last approaches can be considered as more conservative, they are also more general and can be applied to a larger scale of systems.

However, the actuator constrained measurements are not generally available to the anti-windup controller since they are generated inside the actuator internal structure. To generate the anti-windup correction signals for the nominal controller $C(s)$, the input saturation, whether in magnitude or in rate, needs to be reconstituted out of the actuator model. From this recovered saturation or *control limiter*, one can define an input for the anti-windup device.
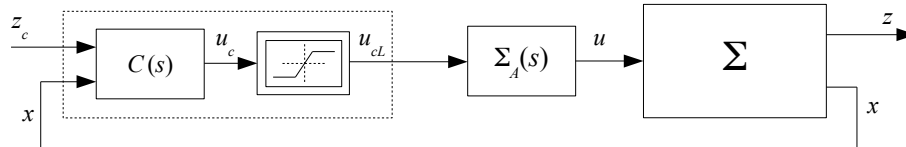
Figure 1.16: Standard tracking control interconnection with control limiter.

Consider, for example, the standard tracking control interconnection illustrated on Figure 1.16. A magnitude saturation nonlinearity that ensures the exact same nominal behavior of the saturated actuator is now part of the controller $C(s)$. As it has been explained, the advantage of adding this saturation to the controller structure is that it can be directly exploited by the anti-windup control loop.

The *Direct Linear Anti-windup* control scheme, that uses the signals measured from the control limiter and that enhances the nominal controller $C(s)$ of the previous interconnection, is illustrated in the following figure:
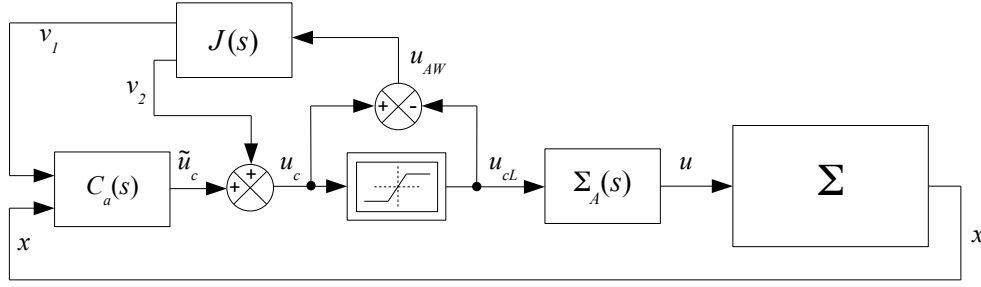
Figure 1.17: Direct Linear Anti-windup scheme.

where,

– $C_a(s)$ is the augmented controller structure enhanced by the anti-windup device;
– $u_{AW} \in \mathbb{R}^m$ is the anti-windup controller input, defined as $u_{AW} = u_c - u_{c_L}$;
– $v_1 \in \mathbb{R}^{n_C}$ is the anti-windup controller output that modifies the states of the nominal controller $C(s)$;
– $v_2 \in \mathbb{R}^m$ is the anti-windup controller output that modifies the commanded signal $\tilde{u}_c$.

The anti-windup controller $J(s)$ activates only when the control input saturates or $u \neq u_{c_L}$, whereas the anti-windup correction signal $v = \begin{bmatrix} v_1 & v_2 \end{bmatrix}^T$ is zero while the control input remains within the linear zone $u = u_{c_L}$.

Different variations of the anti-windup structure can be foreseen. Take, for example, the case of the so called *Model Recovery Anti-windup* structure [ZT02, Boa10], presented on Figure 1.18.
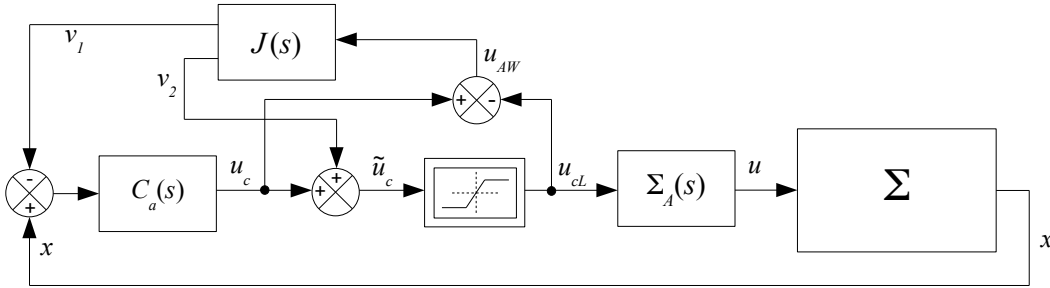
Figure 1.18: Model Recovery Anti-windup scheme.

In this particular case, the anti-windup controller can be seen as a filter that reconstitutes the unconstrained closed-loop dynamics. By exploiting the difference between the commanded value u_c generated by the controller and the saturated input u_{c_L}, this lost control signal $u_{AW} = u_c - u_{c_L}$ can be used to recover the missing closed-loop dynamics due to saturation. Then, the recovered dynamics are fed to the nominal controller in an attempt to reduce the difference between the unconstrained closed loop and the saturated one.

Usually, the computation of the anti-windup control loop is done as a supplementary step after nominal controller synthesis. Although a very recent developed technique, founded on nonsmooth

optimization, allows to synthesize a nominal controller and the anti-windup controller simultaneously [BA11].

Concluding comments

In this chapter, the evolution and foundations of standard Nonlinear Dynamic Inversion have been described. Along with the fundamentals of the technique, some common approaches to "robustify" NDI and to avoid practical problems, such as the time-scaling approach, have been also introduced.

First, the case of square and input-affine nonlinear systems was used to present in a very simple and straightforward manner the general principle behind NDI. The inherent limitations of the technique, which drive the motivation of this thesis work have also been exposed.

Then, extensions to more general nonlinear systems were addressed while presenting the NDI technique in a more formal way. Concepts linked to feedback linearization like the relative degree or the zero-dynamics of a nonlinear system have also been defined and explained. NDI for SISO, MIMO and non input-affine nonlinear systems was explained and illustrated giving simple academic examples.

Finally, a review on systems with input saturations was presented in the context of NDI control design. Anti-windup control schemes were presented as an alternative to enhance the closed-loop stability of such systems.

Nonlinear Dynamic Inversion is basically a nonlinear compensation approach. It has become of great interest in a large number of applications due to the advantages it presents. In contrast to other purely nonlinear control techniques, NDI bridges nonlinear and linear control approaches by proposing state-feedback control laws capable of decoupling, linearizing and stabilizing nonlinear systems.

Yet, some inherent robustness problems arise as wider classes of nonlinear systems are considered, including: uncertainties, time-varying parameters and control input constraints.

In the next chapter, a new perspective will be given to this standard nonlinear compensation method. As a more generic formulation of nonlinear compensation is obtained, a larger scale of nonlinear systems can be ultimately addressed by the novel and interesting framework which will be proposed.

Chapter 2

Towards a generalized nonlinear compensation framework

Introduction

The introduction presented in the previous chapter helps clarify the insight of NDI as a nonlinear compensation technique. The nonlinear dynamics of a system can be compensated through an inner loop that uses the "dynamic inverse" of the known process [Isi85, SL91, Vid93]. But, in trying to linearize a system:

Is it really necessary to use a fixed structure that introduces nonlinear terms punctually to reproduce the system inverse within the controller?

Whereas NDI seeks to compensate nonlinear dynamics by imprinting the system inverse in the controller, other strategies can be devised for this purpose. Inspired from the robust control framework and from the insight of NDI, the goal of compensating nonlinear dynamics could be seen as a disturbance rejection problem (with specific performance requirements), where the nonlinear process is in fact a "linear" system affected by nonlinear "disturbances".

For example, consider the following representation of a nonlinear system:

$$\dot{x} = w(x, \Theta) + \Lambda(x, \Theta)u \tag{2.1}$$

where Θ is a vector of varying parameters. The nonlinear function of the efficiency matrix Λ can be considered as an input gain that varies with the operating conditions defined by (x, Θ), and the nonlinear function w can be considered as a disturbance.

To compensate the nonlinear effects of the term Λ, one can use the gain inverse as proposed in the standard NDI procedure. But the nonlinear function w can be rejected from the system as if it were an input disturbance. This can be achieved using a linear robust controller by making the information on the system nonlinear dynamics available to the control law as input signals. In this sense, the basic idea is to compute a linear nominal controller that receives nonlinear functions as

a part of its input vector, rather than computing a nonlinear controller.

The main objective of this chapter is to present a fresh reformulation of the standard NDI method, which can be viewed as a Generalized Nonlinear Compensation (NLC) Framework that uses linear-oriented techniques for controller design and analysis.

To do so, in Section 2.2, a particular representation of nonlinear systems is proposed. This representation stresses the linear interaction of the state variables with the system nonlinear dynamics. This leads to an easy and systematic implementation of readily available linear robust control tools for systems with uncertainties, varying parameters, external disturbances and input saturations.

Then, in Sections 2.3 and 2.4, multi-channel design-oriented models are derived for robust control design and anti-windup control strategies. General guidelines for weighting functions design are also provided. A generic $\mathcal{H}_\infty$ optimization approach is proposed for controller synthesis.

Finally, in Section 2.5, an LFT modelling approach of the resulting nonlinear closed-loop is proposed for robustness and stability analysis. The linear nature of this modelling approach allows the use of well-suited stability analysis tools, which are also detailed within this section.

But first, an interesting way of refining the standard NDI controller structure by promoting a better balance between the efforts of the inner and outer loops is presented in Section 2.1. This refined linearizing control law design will eventually lead to the linear-oriented framework which is at the core of our generalized nonlinear compensation approach.

2.1 Refined linearizing control laws

Let us take a retrospective look at the NDI design procedure. As is clear from Chapter 1 and the introduction above, a standard NDI-based controller for the nonlinear system of equation (1.1), which is recalled hereafter:

$$\dot{x} = f(x) + G(x)\,u$$

is designed in two steps:

1. A nonlinear inner loop is first determined to cancel the nonlinearities of the system so that the latter behaves like pure decoupled integrators;

2. A linear outer loop is computed to:
   - ensure closed-loop stability and performance,
   - compensate the inversion errors of the inner loop which has been designed on a simplified approximation of the real nonlinear process to be controlled.

From the expression of the linearizing feedback law recalled below:

$$u(x) = G^{-1}(x)[-f(x) + \tilde{u}] \tag{2.2}$$

It is clear that the magnitude and rate-of-variations of each component of the nonlinear vector $f(x)$ directly impact the control inputs u to be realized by the actuators. Consequently, there might be a significant difference between the actual input u and $\tilde{u}$ which is delivered by the outer-loop controller.

As is clarified in Chapter 1, thanks to $\mathcal{H}_\infty$ control techniques, for example, the magnitude of $\tilde{u}$ is rather easily tuned via appropriate weighting functions. Imagine then the case for which $f(x) \equiv 0$, so that a straightforward relationship appears between u and $\tilde{u}$ such that

$$u(x) = G^{-1}(x)\,\tilde{u} \tag{2.3}$$

Exploiting this relationship and the fact that in many applications $G(x)$ is a diagonal dominant matrix, the magnitude and rate-of-variations of u can be controlled by an appropriate choice of the outer-loop controller. If necessary, the latter can be adapted as a function of $G(x)$.

In summary, the standard NDI-based design approach proposed in Chapter 1 is well adapted to nonlinear systems for which the vector $f(x)$ remains close to zero:

$$\dot{x} \approx G(x)\,u \approx \tilde{u} \tag{2.4}$$

This also means that the approach is well-suited for systems whose natural behavior remains close to a pure integrator. In aerospace applications, this is rarely the case. More precisely, in a neighborhood of some given flight conditions Θ, typically fixed as a function of the Mach number and the altitude, the vector $f(x)$ can be re-written given that some linear information can be extracted from this nonlinear function. Consider the following reformulation of the process nonlinear dynamics

$$f(x) = A(\Theta)\,x + \tilde{f}(x) \tag{2.5}$$

The latter is determined so that the norm of the residual nonlinear entry $\tilde{f}(x)$ is minimized. Since the inner loop objective is solely to eliminate the system nonlinearities, with such a formulation, the nonlinear control law of equation (1.3), presented on page 11, is modified as follows:

$$u(x) = \hat{G}^{-1}(x)\left[-\tilde{f}(x) + \tilde{u}\right] \tag{2.6}$$

Consequently, the extracted linear part from the function $f(x)$ remains present in the outer loop design problem. The linearized model to be controlled through the intermediate variable $\tilde{u}$ becomes

$$\tilde{\Sigma}: \qquad \dot{x} = A(\Theta)\,x + \tilde{u} \tag{2.7}$$

and it can be tuned using any LPV control technique.

The control interest of such a procedure is to better balance the efforts between the inner and outer loops. When compared to (1.3), the modified nonlinear control law (2.6) becomes more interesting since $||\tilde{f}(x)|| < ||f(x)||$. This leads to a closer relationship between the magnitude of the physical control input signal $u(x)$ and that of the intermediate variable $\tilde{u}$ which is generated by the LPV outer loop.

Since both, the magnitude and rate-of-variations of $\tilde{u}$ can be rather easily controlled during the LPV design process via an appropriate choice of the weighting functions, this refined procedure offers interesting new perspectives for an improved management of control limitations in NDI-based control techniques. These ideas will be further exploited in the following sections.

2.2   A linear-oriented framework

The control design framework that will be proposed next, allows to compute a linear robust control law with enhanced stability characteristics. This augmented robust controller $K_a(s)$ is presented as a generalized solution to cope with the central limitations of the standard NDI approach. Here, the inversion errors due to defective modelling and input saturation are dealt with in a unified framework.

Based on the proposed modelling approach of Section 2.1, consider the class of affine nonlinear systems presented in equation (2.8). This representation of nonlinear systems can be derived for many practical problems concerning mechanical systems, particularly in the case of aerospace applications.

$$\begin{cases} \dot{x} & = & A(\Theta)\,x + B_1\,f(x,\Theta) + B_2\,\Lambda(x,\Theta)\,u \\ z & = & Cx \end{cases} \tag{2.8}$$

where
– $x \in \mathbb{R}^n$ is the state vector of the system;
– $\Theta \in \mathbb{R}^q$ is a vector of varying parameters;
– $f(x,\Theta) \in \mathbb{R}^{m_1}$ is a state and parametric dependent nonlinear input vector;
– $u \in \mathbb{R}^{m_2}$ is the control input;
– $\Lambda(x,\Theta) \in \mathbb{R}^{m_2 \times m_2}$ is a nonlinear input efficiency matrix;
– $z \in \mathbb{R}^p$ is the controlled output.

Assumption 2.1 *The control efficiency matrix* $\Lambda(x,\Theta)$ *is invertible assuming that*

$det(\Lambda(x,\Theta)) \neq 0 \;\; \forall\,(x,\Theta) \in \mathcal{D} \times \tilde{\mathcal{D}},$

given the admissible domains $\mathcal{D} \subset \mathbb{R}^n$ *and* $\tilde{\mathcal{D}} \subset \mathbb{R}^q$ *of the state and varying parameters respectively.*

Assumption 2.2 *The full state* x *and varying parameters* Θ *are measured and can be used for controller design.*

When modelled by (2.8), the nonlinear system presents a particular structure composed of
– a matrix $A(\Theta) \in \mathbb{R}^{n \times n}$;
– two input matrices $B_1 \in \mathbb{R}^{n \times m_1}$ and $B_2 \in \mathbb{R}^{n \times m_2}$;
– a controlled output matrix $C \in \mathbb{R}^{p \times n}$.

Clearly, the system nonlinear dynamics are concentrated in $f(x,\Theta)$ and $\Lambda(x,\Theta)$. However, the matrix $\Lambda(x,\Theta)$ will be considered as part of the control input u, while the vector $f(x,\Theta)$ will be considered as an external input disturbance acting over the system. To get closer to the linear framework, using a standard abuse of notation, the nonlinear system (2.8) can be rewritten as:

$$z = \Sigma(s) \begin{bmatrix} f \\ \Lambda\,u \end{bmatrix} \tag{2.9}$$

where

$$\Sigma(s) = C\,(sI - A(\Theta))^{-1} \begin{bmatrix} B_1 & B_2 \end{bmatrix} \tag{2.10}$$

Unlike common input disturbances, the vector $f(x,\Theta)$ collects functions that can actually be estimated from measurements and a nominal model. This is the main reason why, from now on, they

will be referred to as *measured disturbances*.

In a first step, a nominal controller $K(s)$ can be designed by using a robust control technique. This robust controller $K(s)$ will be charged of rejecting the system nonlinearities as well as fending-off any modelling errors rising from an inaccurate estimation of the nonlinear functions.

On the one hand, the compensation of the nonlinear matrix $\Lambda(x, \Theta)$ can be tackled in the same way as in the standard NDI procedure, by simplifying it as closely as possible using its inverse $\Lambda^{-1}(x, \Theta)$. On the other hand, based on the $\mathcal{H}_\infty$ optimization framework, the compensation of the nonlinear dynamics contained in $f(x, \Theta)$ can now be formulated as a disturbance rejection problem.

Inspired by the NDI technique, where the nonlinear dynamics of a system are introduced in the inner loop of the controller structure for compensation, the rejection of the measured disturbances $f(x, \Theta)$ can be achieved by making this nonlinear information available to the controller synthesis.

It should be kept in mind that only an approximation of the functions in $f(x, \Theta)$ can be obtained and made accessible to the controller. Then, these measured disturbances can be modelled as:

$$f(x, \Theta) = \hat{f}(x, \Theta) + w_f(x, \Theta) \tag{2.11}$$

where the modelling error $w_f(x, \Theta)$ is considered to be norm bounded.

Finally, the performance criterion of the closed-loop system can be established as a reference model $R(s)$ tracking problem. A general scheme of this linear-oriented control design framework is represented on Figure 2.1.
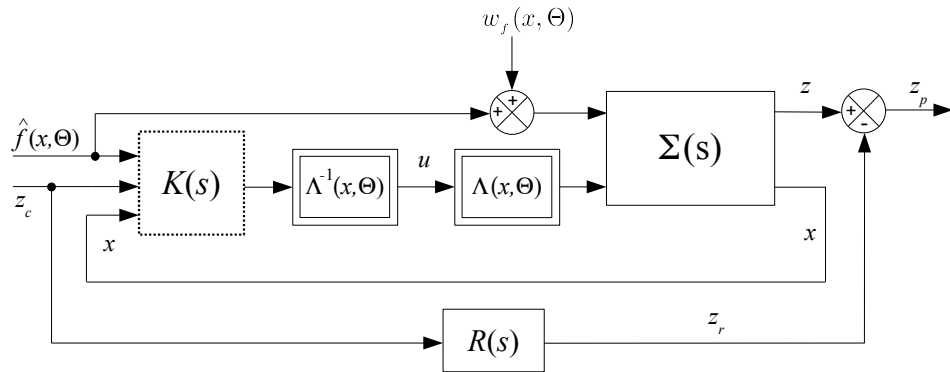
Figure 2.1: A general linear-oriented robust control scheme for nonlinear compensation.

The goal of our robust control design scheme is to find the best controller $K(s)$, such that the control law:

$$u(x, \Theta) = \Lambda^{-1}(x, \Theta) \; K(s) \begin{bmatrix} \hat{f}(x, \Theta) \\ z_c \\ x \end{bmatrix} \tag{2.12}$$

can minimize the error between the controlled output z and z_r delivered by the linear reference model $R(s)$ in spite of the measured disturbances $\hat{f}(x, \Theta)$ and modelling errors w_f.

This linear-oriented framework endows greater flexibility to the controller $K(s)$ synthesis process because more information on the system can be exploited as will be further explained.

Remark 2.3 *The functions contained in the vector $\hat{f}(x, \Theta)$ remain sufficiently small when the operation points remain close to the equilibrium conditions $(\bar{x}, \bar{\Theta})$. Making reference to the control scheme of Figure 2.1, for such operating points, the transfer $\mathcal{T}_{z_c \to z_p}$ becomes the most important one which the controller should seek to minimize in order to guarantee the highest performance level attainable.*

The previous remark gives rise to a particular issue concerning the choice of the best flight conditions that will minimize the size of the signals contained in the vector $\hat{f}(x, \Theta)$ for most operation points. A not necessarily optimal approach, consists in finding worst case scenario conditions at which control requirements are higher and reducing the size of $\hat{f}(x, \Theta)$ becomes relevant. This might not necessarily minimize $\hat{f}(x, \Theta)$ for most operation points but may improve the performance at worse case scenarios while assuring that the size of $\hat{f}(x, \Theta)$ remains bearable for other points of the operation domain.

Another sub-optimal approach that can be foreseen, consists in finding a "central" point of the operation domain from a pole location perspective. This can be done by obtaining a set of matrices A corresponding to *a priori* selected conditions covering a wide range of the operation domain. Then, it is only a matter of finding which matrix A of the set yields "midpoint" eigenvalues.

In a subsequent step to the synthesis of the robust controller $K(s)$, this linear-oriented framework allows to enhance the stability of the closed loop in presence of saturating inputs and actuator dynamics by means of an anti-windup control loop. In contrast with existing approaches regarding anti-windup strategies for NDI controllers [YPY08, HTM+10], in our framework any anti-windup structure can be directly implemented with no particular precautions or adaptations since the nominal controller $K(s)$ is linear.

Consider, for example, the Direct Linear Anti-windup scheme presented in Section 1.3.2. A controller $J(s)$ that modifies the robust controller $K(s)$ is sought as to enlarge the stability domain. A schematic representation of this strategy is presented on Figure 2.2.
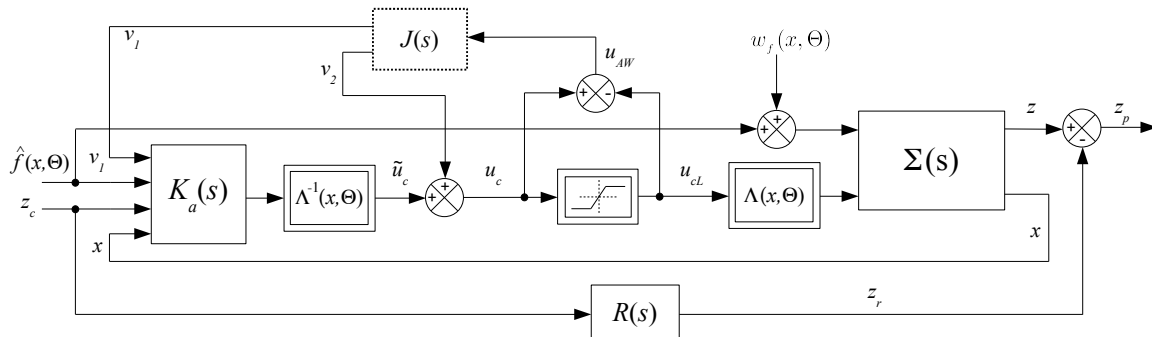
Figure 2.2: A general linear-oriented anti-windup enhancement for nonlinear compensation.

The expression of the robust control law augmented by the anti-windup controller $J(s)$ becomes

$$u_c(x, \Theta) = \Lambda^{-1}(x, \Theta) \ K_a(s) \begin{bmatrix} v_1 \\ \hat{f}(x, \Theta) \\ z_c \\ x \end{bmatrix} + v_2 \tag{2.13}$$

where

$$\begin{bmatrix} v_1 \\ v_2 \end{bmatrix} = J(s) \, u_{AW} \tag{2.14}$$

The goal of this second control design scheme is to find an optimal controller $J(s)$ that enlarges as much as possible the stability domain in spite of saturating inputs and actuator dynamics.

Notice that the NDI control design can be considered as a particular case of a more general nonlinear compensation problem. In fact, the baseline controller

$$u_c(x, \Theta) = \Lambda^{-1}(x, \Theta) \left(-\hat{f}(x, \Theta) + C(s) \begin{bmatrix} z_c \\ x \end{bmatrix} \right)$$

can be recovered for

$$K_a(s) = \begin{bmatrix} \mathbf{0} & -I & C(s) \end{bmatrix}, \qquad v_2 = \mathbf{0}$$

> The novelty of this generalized linear-oriented approach for nonlinear compensation resides in the fact that the nonlinearities of a system are not cancelled by punctually imprinting the system inverse inside a double-loop controller structure, but instead, the information on the nonlinearities is made available to a unified linear control design strategy that will naturally seek to reduce their impact on the system along with modelling errors and in spite of input saturations.

Remark 2.4 *In Figure 2.2, the exact cancellation of $\Lambda(x, \Theta)$ by its inverse which appeared in Figure 2.1 is no longer verified because of the saturation inserted between these two operators. This is also the case when actuator dynamics are considered. In both cases, the diagram looses its linear properties which makes more complex the design of $K(s)$ or $K_a(s)$. These issues are further investigated in the following section.*

2.3 A multi-channel Nonlinear Compensation $\mathcal{H}_\infty$ design procedure

The generalized nonlinear compensation (NLC) framework proposed in the previous section can be enriched for controller synthesis. As more information on the system is made available, greater are the means of the optimization process to generate a more effective controller to comply with the performance requirements.

2.3.1 Design-oriented models

In contrast with the standard NDI control design technique, this generalized framework can account for actuator dynamics in a very natural manner. Let us start by considering the following actuator linear dynamics that does not account for magnitude or rate saturations:

$$u = \Sigma_A(s)u_c, \quad \text{with} \quad \Sigma_A(s) = (sI - A_a)^{-1} B_a \qquad (2.15)$$

When the actual process allows it, the state of the actuator can be made available to the controller as shown in the design-oriented scheme depicted on Figure 2.3.

Furthermore, it is also possible to add to the optimization process the objective of reducing the magnitude of the control signals generated by the controller $K(s)$, thus trying to prevent the actuators from reaching prematurely their saturation limits. This additional optimization objective makes the controller design procedure *multi-channel*. It can be integrated to the control scheme by adding a weighted output z_u directly related to the control signal u, its derivative $\dot{u}$ or any combination of both.

Figure 2.3: A multi-channel $\mathcal{H}_\infty$ design-oriented scheme.
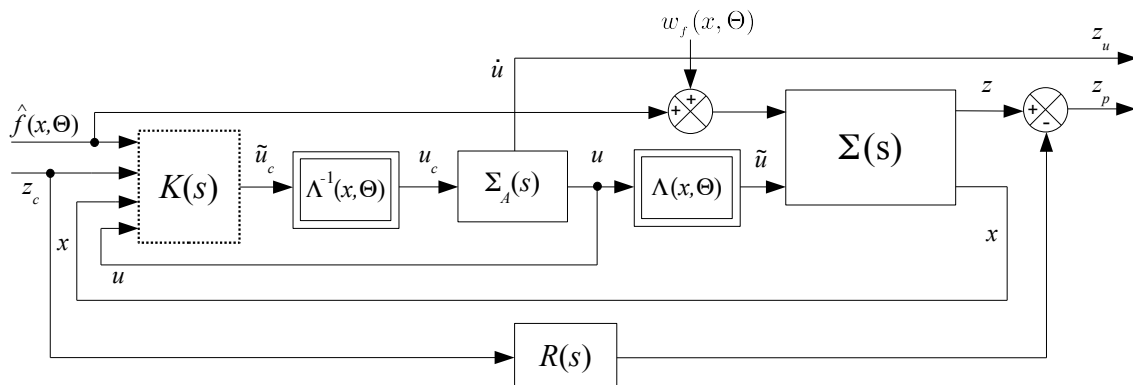
As already emphasized by Remark 2.4, the diagram of Figure 2.3 is not in a fully compatible format to allow the use of $\mathcal{H}_\infty$ design techniques. The main obstacle resides indeed in the fact that Λ and its inverse Λ^{-1} are separated here by the actuator dynamics. As a consequence, they do not compensate each other exactly, which means that some nonlinearities will remain present in the loop.

Yet, in the absence of any saturation, when the actuator dynamics are fast compared to the evolution of the system, the following manipulations show that the compensation of Λ and its inverse can be assumed without any great loss of accuracy. Let us rewrite the state-space equation of the actuator model (2.15) as:

$$\dot{u} = A_a\,u + B_a\,u_c$$

From Figure 2.3, let us identify the scaled variables $\tilde{u}$ and $\tilde{u}_c$ as:

$$\tilde{u} = \Lambda(x,\Theta)\,u, \qquad \tilde{u}_c = \Lambda(x,\Theta)\,u_c \qquad (2.16)$$

Then, the derivative of the scaled input $\tilde{u}$ can be expressed as:

$$\dot{\tilde{u}} \quad = \quad \dot{\Lambda}\,u, + \Lambda\,\dot{u}$$

$$
\begin{aligned}
&= & \dot{\Lambda}\,\Lambda^{-1}\,\tilde{u} + A_a\,\Lambda\,u + B_a\,\Lambda\,u_c \\
&= & (\dot{\Lambda}\,\Lambda^{-1} + A_a)\,\tilde{u} + B_a\,\tilde{u}_c
\end{aligned}
\tag{2.17}
$$

When the variations of the input efficiency matrix Λ are rather low compared to the actuator dynamics and the input efficiency is strong enough, it is without any severe impact that the product $\dot{\Lambda}\,\Lambda^{-1}$ can be considered sufficiently small and the actuator model can be approximated as

$$
\tilde{u} \approx \Sigma_A(s)\,\tilde{u}_c, \quad \text{with} \quad \Sigma_A(s) = (sI - A_a)^{-1}\,B_a
\tag{2.18}
$$

The resulting design-oriented scheme after this simplification becomes:
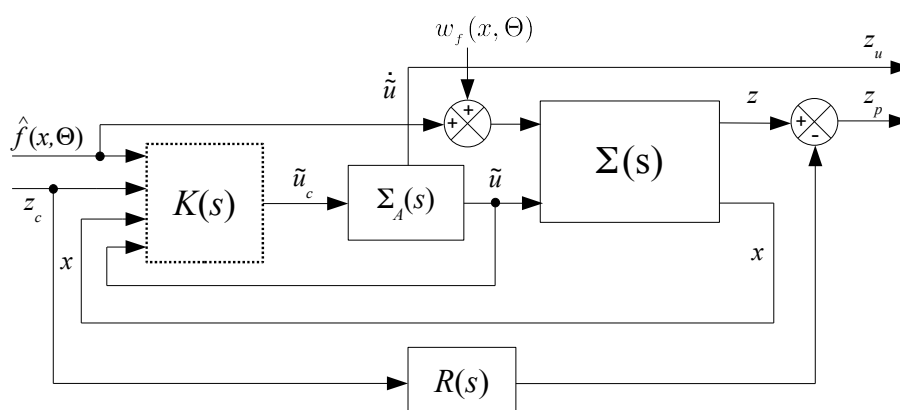
Figure 2.4: Modified multi-channel $\mathcal{H}_\infty$ design-oriented scheme simplifying $\Lambda(x, \Theta)$.

2.3.2 Weighting functions design

Once the controller structure has been enriched with as much information on the system as possible, a set of weighting filters $W(s)$ remain to be designed in order to give the optimization process more details on the frequency domain desired characteristics that will shape the closed-loop.

The tuning of such filters is an essential and often a rather difficult task in the $\mathcal{H}_\infty$ design framework. It requires specific attention since these weighting functions reflect the performance and stability requirements for the design of the robust controller. These requirements may have to be translated from the time domain (rise time, settling time and step overshoot) to the frequency domain (cut-off frequency, low and high frequency gain).

On the one hand, it is desired that the closed-loop system exhibits a high-gain for good setpoint tracking as well as good disturbance rejection. On the other hand, the closed-loop should also present a low-gain to obtain sufficient stability margins and be insensible to neglected system dynamics and other external factors such as measurement noises. The conflicting nature of loop shaping is obvious since, at any given frequency ω, both requirements can not be assured simultaneously by the same controller

Then, it is all a matter of choosing at which bandwidths the closed-loop should present higher and lower gains by filtering the weighted outputs **z**. For example, to ensure a satisfactory disturbance

rejection and a sufficient performance level, usually, the closed-loop gain must be higher at low frequencies. The neglected process dynamics and measurement noises usually appear at high-frequencies, therefore, the closed-loop gain must be lower at these bandwidths to improve the stability margins.

Our multi-channel control scheme of Figure 2.3, is mainly focused on the rejection of the nonlinearities of the system and the tracking of a stable reference model, thus accounting naturally for a stability objective. Another stability issue is raised by the size of the control signals generated by the controller, mainly because of input constraints. Given these specificities of control scheme, the filters of the weighted outputs $\mathbf{z} = \begin{bmatrix} z_u & z_p \end{bmatrix}^T$ can be designed as follows:

– The filter $W_p(s)$, weighting the output z_p, should be chosen such that the low-frequency gain is high, but then attenuated promptly at high frequencies. This can be achieved by defining $W_p(s)$ as a low-pass or lag filter.
 The optimization process will seek to minimize the size of the error signal between the control objective z and the reference model $R(s)$ in the bandwidth where it is expected to be higher, thus ensuring a sufficient disturbance rejection and good performance level at low-frequencies.
– The filter $W_u(s)$, weighting the output $z_u = \dot{u}$, should be chosen such that the low-frequency gain is rather low whereas the high-frequency gain is high. This can be achieved by defining $W_u(s)$ as a high-pass or lead filter.
 The optimization process will seek to diminish the size of the input signals in the bandwidth where they are expected to be higher, thus reducing their activity at higher frequencies while ensuring a sufficient input gain where the performance constraint requires it. By extracting the derivative $\dot{u}$ from the actuator models, one can define filters for this signal which permits to bound the rate-of-variations of the control signals. This is an interesting way of preventing the adverse effects of rate limitations.

As for the exogenous inputs $\mathbf{w}$, the use of weighting filters can be foreseen to translate the fact that, for example, the system nonlinearities may not be significant in an unlimited frequency spectrum. Therefore, lag filters $W_f(s)$ can be used on the disturbances $\hat{f}(x, \Theta)$ to reflect that the system nonlinear dynamics are present mainly at low-frequencies. The loop shaped design-oriented scheme using the weighting functions $W(s)$ is illustrated on Figure 2.5.
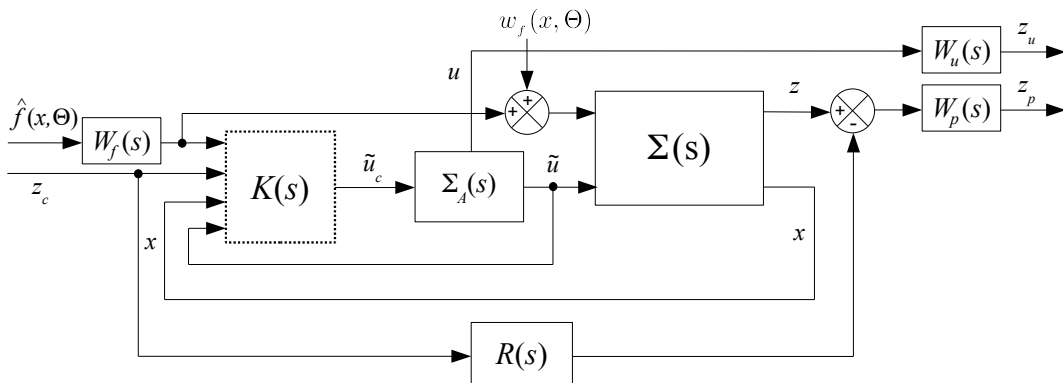

Figure 2.5: Loop shaped multi-channel $\mathcal{H}_\infty$ control scheme.

2.3.3 Controller synthesis through $\mathcal{H}_\infty$ optimization

Once the enriched design-oriented model has been defined and that the weighting functions $W(s)$ have been selected to describe the model frequency domain characteristics, a standard form can be easily deduced from the multi-channel control scheme of Figure 2.6 with the following notation:

– $\mathbf{w} = \begin{bmatrix} w_f & \hat{f} & z_c \end{bmatrix}^T$ is the vector of exogenous inputs;

– $\mathbf{z} = \begin{bmatrix} z_u & z_p \end{bmatrix}^T$ is the vector of weighted outputs;

– $\tilde{y} = \begin{bmatrix} \hat{f} & z_c & x & \tilde{u} \end{bmatrix}^T$ is the vector of controller inputs.
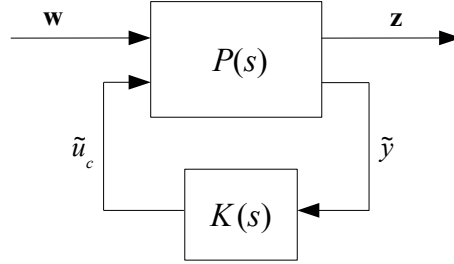
Figure 2.6: Standard form of the multi-channel $\mathcal{H}_\infty$ control scheme.

Invoking arguments developed in Chapter 1, based on the small gain theorem and the time-domain interpretation of the $\mathcal{H}_\infty$ norm, the robust performance problem depicted in Figure 2.6 is satisfied when

$$||\mathcal{T}_{\mathbf{w}\to\mathbf{z}}(s)||_\infty < 1 \tag{2.19}$$

and may thus be solved via $\mathcal{H}_\infty$ optimization:

$$\min_{K(s)} ||\mathcal{F}_l(P(s), K(s))||_\infty \tag{2.20}$$

Depending on the different weighing functions $W(s)$ chosen to establish the frequency domain characteristics of the exogenous inputs $\mathbf{w}$ and the weighted outputs $\mathbf{z}$, the resulting robust controller that minimizes $\mathcal{T}_{\mathbf{w}\to\mathbf{z}}$ should be able to produce the following effects:

– The smaller $\mathcal{T}_{z_c\to z_p}$, the better the model-tracking of the reference model $R(s)$;

– The smaller $\mathcal{T}_{\hat{f}\to z_p}$, the larger the operation domain;

– The smaller $\mathcal{T}_{w_f\to z_p}$, the lower the modelling errors effect;

– The smaller $\mathcal{T}_{\mathbf{w}\to z_u}$, the lower the magnitude of the control input u.

This problem was shown to be convex in the full-order case, that is, when the order of the controller $K(s)$ coincides with that of $P(s)$. In such a case, a famous algorithm based on an iterative resolution of coupled Riccati equations can be used [DGKF89]. The latter is quite efficient even for high-order systems, although it requires some regularity assumptions to be satisfied by $P(s)$. More recently, in 1994, an LMI-based formulation was developed and offered much more flexibility [GA94]. Unfortunately, this approach is also much more demanding numerically and suffers from some drawbacks as the Ricatti-based method: it does not allow to impose constraints neither on the order of $K(s)$ nor on its structure.

In such cases, which of course are very relevant in practice, the optimization problem turns out to be no longer convex. Over the past ten years, many algorithms based on LMI optimization have

been proposed. Most of these implement iterative strategies combining design and analysis steps. In many cases, such algorithms converge to a fixed point that might not even be a local optimum.

In 2006, recent developments in nonsmooth optimization [AN06, BHLO06], have given birth to new and efficient tools to solve this difficult nonconvex problem [GMO08, Mat11b]. Quite interestingly, the flexibility of nonsmooth optimization techniques permits to solve multi-model and multi-channel $\mathcal{H}_\infty$ design problems [GHMO09].

Thus, not only the structure and the order of $K(s)$ can be imposed, but also non desired crossed transfer functions can be avoided. This last property will be of particular interest for a simultaneous design of the feedback controller $K(s)$ and the anti-windup compensator $J(s)$, which will be detailed next.

2.4 Anti-windup design procedure

Once a nominal robust controller $K(s)$ has been obtained from the $\mathcal{H}_\infty$ design approach presented above, the nonlinear closed-loop properties may still require some improvement when input saturations occur. As it was mentioned before, this can be achieved by anti-windup control loops to be further detailed next.

Thanks to the generalized NLC framework, it is shown below that the optimization of these anti-windup loops present strong similarities with the design of the nominal controller $K(s)$. Interestingly, both loops can be tuned simultaneously.

2.4.1 A design-oriented model for rate saturations

In a large majority of control applications, rate limitations are much more restrictive than magnitude bounds inside the actuator. This is why the following is essentially focused on this class of saturations. Note that the results are easily transposed to the more simple case of static magnitude constraints.

In practice, to preserve the actuators, the control signals are preliminarily bounded by an appropriate device within the control law. In the case of rate limitations, the signal u_c illustrated on Figure 2.7 is filtered by a nonlinear operator with first-order dynamics, thus generating a rate limited signal u_{c_L} such that

$$\dot{u}_{c_L} = sat_L \left(\tau_L^{-1}[u_c - u_{c_L}] \right) \tag{2.21}$$
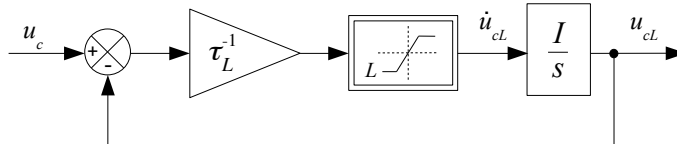
Figure 2.7: General first-order control rate limiter.

Then, the physical actuator remains in a nominal region and can be represented by the linear model $\Sigma_A(s)$ without loss of generality.

Still, with this new device inserted between $\Lambda(x, \Theta)$ and its inverse, the diagram of Figure 2.3 now becomes:

Figure 2.8: Control scheme with first-order rate limiter.

In this context, the manipulations of equation (2.23) allowing to obtain the simplified diagram of Figure 2.4, must be revised. Using the notation of equation (2.16) and also defining similarly the additional rescaled variable $\tilde{u}_{c_L}$ as:

$$\tilde{u}_{c_L} = \Lambda \, u_{c_L} \tag{2.22}$$

one gets from equation (2.21) that:

$$
\begin{aligned}
\dot{\tilde{u}}_{c_L} &= \dot{\Lambda} \, u_{c_L}, + \Lambda \, \dot{u}_{c_L} \\
&= \dot{\Lambda} \, \Lambda^{-1} \, \tilde{u}_{c_L} + \Lambda \, sat_L(\tau_L^{-1}[u_c - u_{c_L}]) \\
&\approx \Lambda \, sat_L(\tau_L^{-1}[u_c - u_{c_L}])
\end{aligned} \tag{2.23}
$$

Next, observing that for any positive diagonal matrix $\Lambda(x, \Theta) \in \mathbb{R}^{m \times m}$, any vector $L \in \mathbb{R}^m$ and any signal $u \in \mathbb{R}^m$ verifies that

$$\Lambda \, sat_L(u) = sat_{\Lambda L}(\Lambda \, u) \tag{2.24}$$

one obtains the simplified rate limiter expression:

$$\dot{\tilde{u}}_{c_L} \approx sat_{\tilde{L}}(\tau_L^{-1}[\tilde{u}_c - \tilde{u}_{c_L}]) \tag{2.25}$$

with

$$\tilde{L} = \Lambda \, L \tag{2.26}$$

Finally, after replacing the saturation-type nonlinearity by a dead-zone operator $\varphi_{\tilde{L}}$, The above developments lead to a simplified of the diagram as shown on Figure 2.9, where the linear interconnection $\Sigma_{RL}(s)$ is given by:

$$\Sigma_{RL}(s) : \begin{cases} \dot{x}_{RL} &= \tau_L^{-1}(\tilde{u}_c - x_{RL}) - w_\varphi \\ \tilde{u}_{c_L} &= x_{RL} \\ z_\varphi &= \tau_L^{-1}(\tilde{u}_c - x_{RL}) \end{cases} \tag{2.27}$$

Figure 2.9: Modified control scheme with first-order rate limiter and simplifying $\Lambda(x, \Theta)$.

Since the saturation-type nonlinearity has been replaced by a dead-zone operator, whose outputs w_φ are null in the linear region, the dynamics of $\Sigma_{RL}(s)$ correspond to the nominal unconstrained case. As a result, this interconnection is stable.

Also, in a very convenient and interesting manner, the output w_φ coincides with the saturation activity given that

$$w_\varphi = z_\varphi - sat(z_\varphi) \tag{2.28}$$

Then, the control scheme of Figure 2.2 can be redrawn and transformed into a design-oriented model as depicted on Figure 2.10, where w_φ can be directly used as the input of the anti-windup device such that

$$u_{AW} = w_\varphi \tag{2.29}$$

Figure 2.10: Design-oriented scheme with rate limiter and anti-windup correction.

Following the $\mathcal{H}_\infty$ formalism introduced for designing the control laws with $K(s)$, This diagram can also be redrawn in a compact standard form as depicted on Figure 2.11.
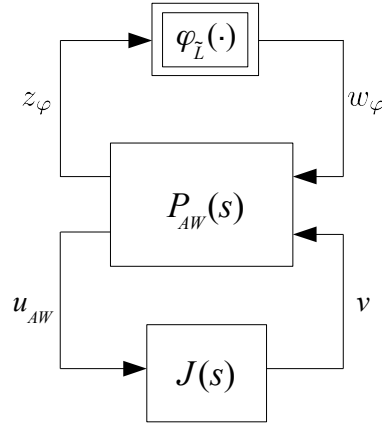
Figure 2.11: LFT representation associated to the anti-windup control scheme.

Let us now discuss how the computation of the Anti-windup controller can be established as an $\mathcal{H}_\infty$ optimization problem.

2.4.2 Optimization aspects

The objective of the control synthesis procedure is to obtain an optimal controller $J(s)$ capable to diminish the impact of the nonlinear signal z_φ in the stability of the closed loop. Consider the following assumption:

Assumption 2.5 *There exists a positive scalar k_φ such that $\forall\ z_\varphi \in \mathbb{R}^m$*

$$||w_\varphi|| = ||\varphi(z_\varphi)|| \le k_\varphi\,||z_\varphi|| \tag{2.30}$$

Invoking once more the small gain theorem, the stability of the closed loop is assured if

$$||\mathcal{T}_{w_\varphi \to z_\varphi}||_\infty < \frac{1}{k_\varphi} \tag{2.31}$$

In the same way as in the case of the nominal controller $K(s)$, the computation of the anti-windup controller $J(s)$ can be done with a nonsmooth optimization method. The standard form, relative to the proposed control scheme on Figure 2.10, that is used for controller synthesis is represented on Figure 2.12, where

– $w_\varphi = u_{AW}$ is the exogenous input corresponding to the nonlinear disturbance, which is also the anti-windup controller activation signal;

– z_φ is the exogenous output corresponding to the nonlinearity input;

– $v = \begin{bmatrix} v_1 & v_2 \end{bmatrix}^T$ is the vector of anti-windup correction signals.
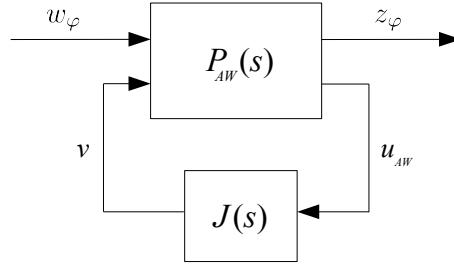
Figure 2.12: Standard form of the anti-windup design-oriented control scheme.

The anti-windup compensator is obtained as the solution of the following $\mathcal{H}_\infty$ minimization problem:

$$\hat{J}(s) = \underset{J(s)}{\mathrm{Argmin}} \, ||\mathcal{F}_l(P_{AW}(s), J(s))||_\infty \tag{2.32}$$

Clearly, the smaller the $\mathcal{H}_\infty$ norm, the less restrictive assumption 2.5 will be. In that case, larger values of k_φ are allowed.

Remark 2.6 *Observing that the dead-zone operator always verifies the assumption for $k_\varphi = 1$, the anti-windup compensator $J(s)$ ensures global stability if:*

$$||\mathcal{F}_l(P_{AW}(s), J(s))||_\infty < 1 \tag{2.33}$$

Conversely, large $\mathcal{H}_\infty$ norms do not necessarily imply smaller stability regions since the representation of the dead-zone nonlinearity by a Lipschitzian operator is rather conservative.

With respect to other anti-windup synthesis approaches, such as those proposed in [Roo07, BT09, GdST05, MTK09] based on convex optimisation, a nonsmooth optimization technique which minimizes the $\mathcal{H}_\infty$ norm of the standard form will be used in this thesis. This synthesis tool allows to fix the structure of the controller $J(s)$.

2.5 On stability and robustness analysis

As it was already emphasized in Section 2.3, our NLC design strategy, thanks to the minimization of the $\mathcal{H}_\infty$ norm of the transfer from the nonlinear inputs $\hat{f}$ to the error output z_p, tends to maximize the operating domain by minimizing the nonlinear effects on the closed-loop.

However, there is no straightforward relationship between the $\mathcal{H}_\infty$ norm of this transfer and the size of the stability domain achieved.

Then, a more specific model is required to perform this type of analysis. In the following, an LFT interconnection composed of a linear closed-loop affected by structured nonlinear feedback signals along with parametric variations and uncertainties will be derived. Then, robustness analysis tools are presented to solve the robust stability problem.

2.5.1 Nonlinear closed-loop LFT modelling

For simplicity of the modelling strategy presentation, consider temporarily a nominal case without modelling errors ($w_f = 0$) which means that an exact estimation of the nonlinear inputs can be obtained such that $\hat{f}(x, \Theta) = f(x, \Theta)$.

Let us suppose the existence of a stable equilibrium state $\bar{x}$ of the closed-loop system presented on Figure 2.10 for a given parametric configuration $\Theta = \bar{\Theta}$. Then, the stability analysis is performed about the equilibrium conditions $(\bar{x}, \bar{\Theta})$ for which $\dot{x} = 0$.

By denoting $\tilde{x} = x - \bar{x}$ the "small" variations of the state x around the equilibrium point $\bar{x}$, the control scheme of Figure 2.10 can be redrawn to generate the diagram of Figure 2.13. The input $w_\Phi \in \mathbb{R}^n$ on this diagram denotes the variation of the nonlinear estimates $\hat{f}(x, \Theta)$ about the equilibrium $(\bar{x}, \bar{\Theta})$ such that:

$$w_\Phi = \hat{f}(x, \Theta) - \hat{f}(\bar{x}, \bar{\Theta}) \tag{2.34}$$

Clearly, when the system is at the equilibrium, this variation becomes $w_\Phi = 0$.
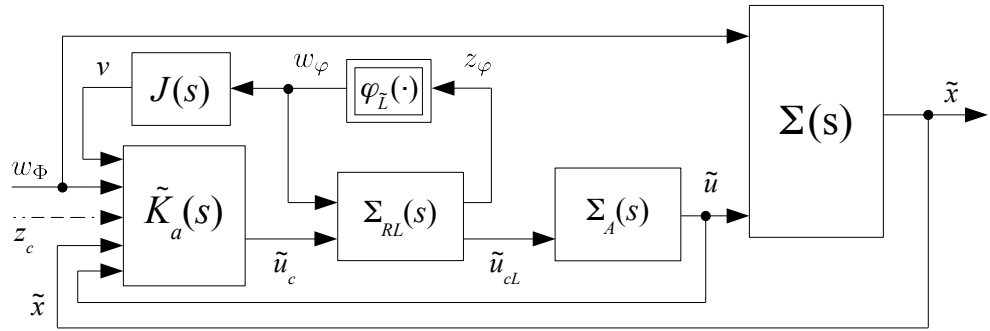

Figure 2.13: Representation of the control scheme about equilibrium conditions $(\bar{x}, \bar{\Theta})$

At the equilibrium, the setpoint signal is $z_c \equiv 0$. Then, by suppressing the latter, the controller $K_a(s)$ becomes $\tilde{K}_a(s)$ as presented on the figure above. Since the focus of this diagram is set on the stability conditions of the closed-loop system around $\bar{x}$, the reference model $R(s)$, the error output z_p and the actuator rate output z_u are also discarded.

Next, let us further detail the nonlinear input w_Φ to obtain a better suited representation for robustness analysis. Assume that this variation can be rewritten as follows:

$$w_\Phi = L_\Phi(\tilde{\Theta})\,\tilde{x} + \Delta_\Phi(\tilde{x}) \tag{2.35}$$

where it is supposed that the remaining nonlinearities contained in Δ_ϕ only depend on $\tilde{x}$, the variation of the state around the equilibrium.

In fact, it can be assumed that the parameter-dependent operator L_Φ rationally depends on the components of the vector $\tilde{\Theta} \in \mathbb{R}^q$. By denoting $\tilde{n}_i$ the size of the rational dependency of L_Φ on

the i-th parameter of the vector $\tilde{\Theta}$, there exists a block-diagonal structure $\Delta_{\tilde{\Theta}}(t) \in \mathbb{R}^{\tilde{q}}$ expressed as:

$$\Delta_{\tilde{\Theta}}(t) = diag(\Delta_{\tilde{\Theta}_1}(t)\, I_{\tilde{n}_1}, \ldots, \Delta_{\tilde{\Theta}}(t)\, I_{\tilde{n}_q}) \tag{2.36}$$

and a linear interconnection T_{L_Φ} of appropriate sizes such that:

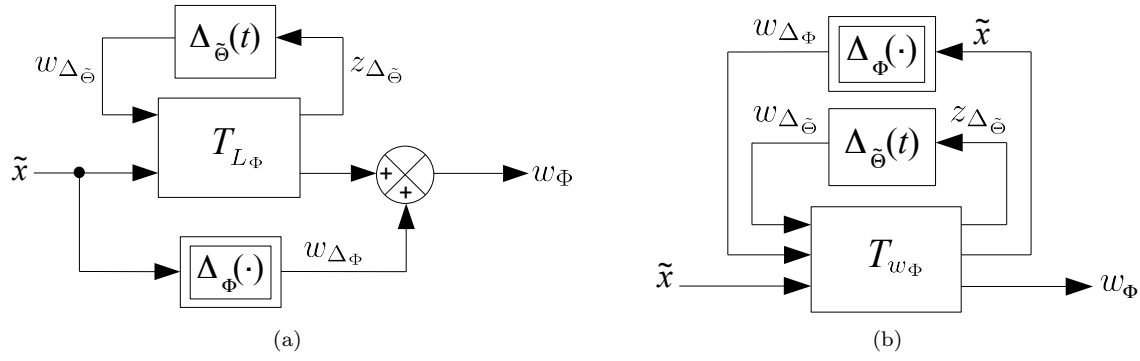$$L_\Phi(\tilde{\Theta}) = \mathcal{F}_u(T_{L_\Phi}, \Delta_{\tilde{\Theta}}(t)) \tag{2.37}$$

Figure 2.14: LFT modelling of the variation w_Φ.

Consequently, as illustrated on Figure 2.14, one can generate a better suited linear interconnection matrix T_{w_Φ} such that:

$$
\begin{aligned}
w_\Phi &= \mathcal{F}_u\left(T_{L_\Phi}, \Delta_{\tilde{\Theta}}(t)\right)\tilde{x} + \Delta_\Phi(\tilde{x}) \\
&= \mathcal{F}_u\left(\mathcal{F}_u(T_{w_\Phi}, \Delta_{\tilde{\Theta}}(t)), \Delta_\Phi(\cdot)\right)\tilde{x}
\end{aligned} \tag{2.38}
$$

Finally, connecting the above diagram with the one of Figure 2.13, one obtains the nonlinear closed-loop scheme depicted on Figure 2.15. In practice, this interconnection can be easily implemented in MatLab and Simulink by defining LFR objects using the Linear Fractional Representation Toolbox (LFRT) [Mag02].
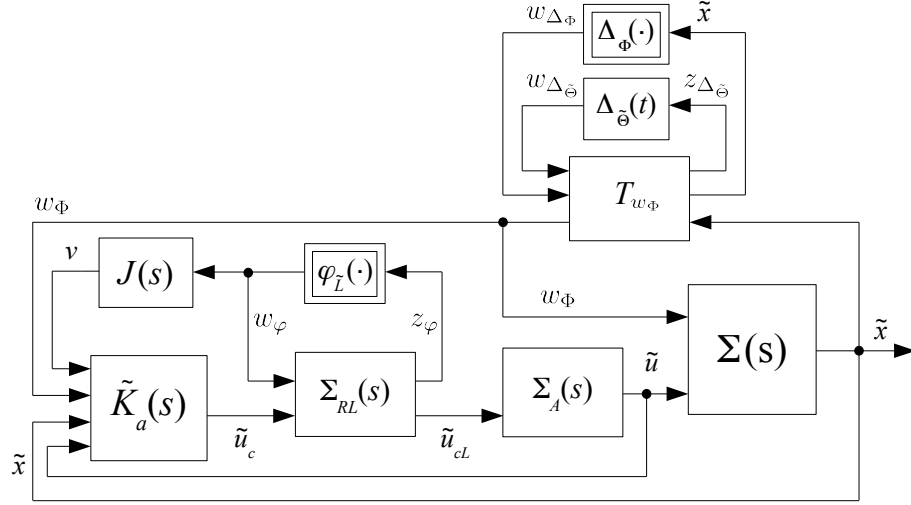
Figure 2.15: Nonlinear closed-loop scheme.

From above scheme, the robustness analysis-oriented LFT form presented on Figure 2.16 can be easily deduced and expressed using a nested upper LFT interconnection as:

$$\mathcal{F}_u\left(\mathcal{F}_u\left(M(s), \Delta_{\tilde{\Theta}}(t)\right), diag\left(\Delta_{\Phi}(\cdot), \varphi_{\tilde{L}}(\cdot)\right)\right) \tag{2.39}$$
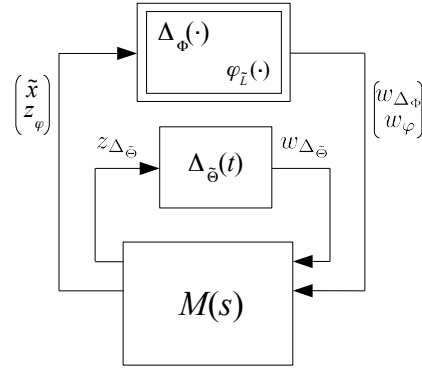
Figure 2.16: Analysis LFT representation of the nonlinear closed-loop.

Now, let us consider the more realistic case where, due to the modelling errors w_f, the estimations $\hat{f}(x, \Theta)$ are only approximations of the real nonlinearities $f(x, \Theta)$. Then, a difference exists between the variation $\hat{w}_\Phi$ "seen" by the controller $K_a(s)$ and the actual system variation w_Φ around the equilibrium conditions $(\bar{x}, \bar{\Theta})$.

A multiplicative uncertainty $\Delta_w(t)$ can be used to represent this modelling discrepancy as depicted on Figure 2.17. In this case, a diagonal block $\Delta_w(t)$ of time-varying parametric uncertainties is

added to the signal w_ϕ which is fed to the robust controller $K_a(s)$ such that:

$$\hat{w}_\Phi = (I + \Delta_w(t))\, w_\Phi, \quad \text{with} \quad \Delta_w(t) = \begin{bmatrix} \delta_{w_1}(t) & & \\ & \ddots & \\ & & \delta_{w_n}(t) \end{bmatrix} \tag{2.40}$$
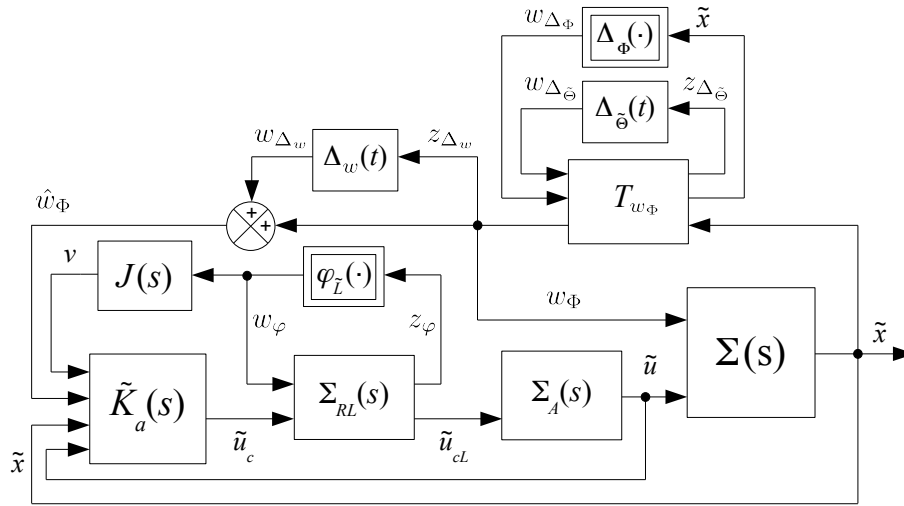
Figure 2.17: Nonlinear closed-loop scheme with parametric uncertainties.
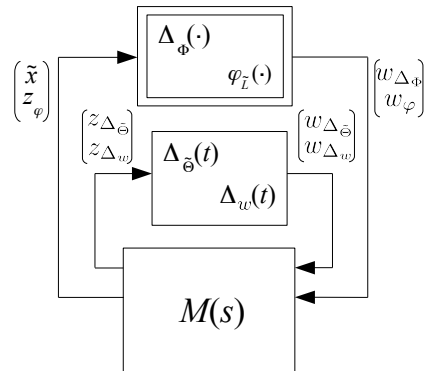
Figure 2.18: Analysis-oriented LFT of the nonlinear closed-loop with parametric uncertainties.

With some simple manipulations on the control scheme of Figure 2.17, the resulting LFT representation of the nonlinear closed-loop with parametric uncertainties is depicted on Figure 2.18 and can be expressed with a nested upper LFT interconnection as:

$$\mathcal{F}_u\left(\mathcal{F}_u\left(M(s), diag(\Delta_{\tilde{\Theta}}(t), \Delta_w(t))\right), diag\left(\Delta_\Phi(\cdot), \varphi_{\tilde{L}}(\cdot)\right)\right) \tag{2.41}$$

2.5.2 Standard Assumptions

Based on the nonlinear closed-loop LFT model presented in the previous section, several robustness analysis tools can be considered to evaluate the stability region of the nonlinear system in feedback loop with our generalized NLC control law.

Hereafter, the time varying operators $\Delta_{\tilde{\Theta}}(t)$ and $\Delta_w(t)$ along with the nonlinear elements $\Delta_\Phi(\cdot)$ and $\varphi_{\tilde{L}}(\cdot)$ are supposed to satisfy the following assumptions:

Assumption 2.7 *The nonlinear operators $\Delta_\Phi(\cdot)$ and $\varphi_{\tilde{L}}(\cdot)$ satisfy the Lipschitz condition. Then, $\forall \ \tilde{x} \in \mathbb{R}^n$ and $\forall \ z_\varphi \in \mathbb{R}^m$, two Lipschitz constants k_Φ and k_φ can be defined such that:*

$\forall \ \rho_\Phi > 0$ and $\forall \ \rho_\varphi > 0$, where

$$||\tilde{x}|| < \rho_\Phi, \qquad ||z_\varphi|| < \rho_\varphi \tag{2.42}$$

one gets that

$$||\Delta_\Phi(\tilde{x})|| \leq k_\Phi(\rho_\Phi) \, ||\tilde{x}|| \tag{2.43}$$

$$||\varphi_{\tilde{L}}(z_\varphi)|| \leq k_\varphi(\rho_\varphi) \, ||z_\varphi|| \tag{2.44}$$

Assumption 2.8 *The time varying operators $\Delta_{\tilde{\Theta}}(t)$ and $\Delta_w(t)$ are normalized, i.e.:*

$$\forall \ i = 1 \ldots q, \ \forall \ t \geq 0, \ |\Delta_{\tilde{\Theta}_i}(t)| \leq 1 \tag{2.45}$$

$$\forall \ j = 1 \ldots n, \ \forall \ t \geq 0, \ |\delta_{w_j}(t)| \leq 1 \tag{2.46}$$

From the previously established assumptions, the following remarks can be made:

Remark 2.9 *Since the nonlinear operator $\varphi_{\tilde{L}}$ is associated to a dead-zone function, the Lipschitz condition in Assumption 2.7 is global for $k_\varphi \geq 1$. Otherwise, as illustrated by Figure 2.19, one only gets a local condition.*
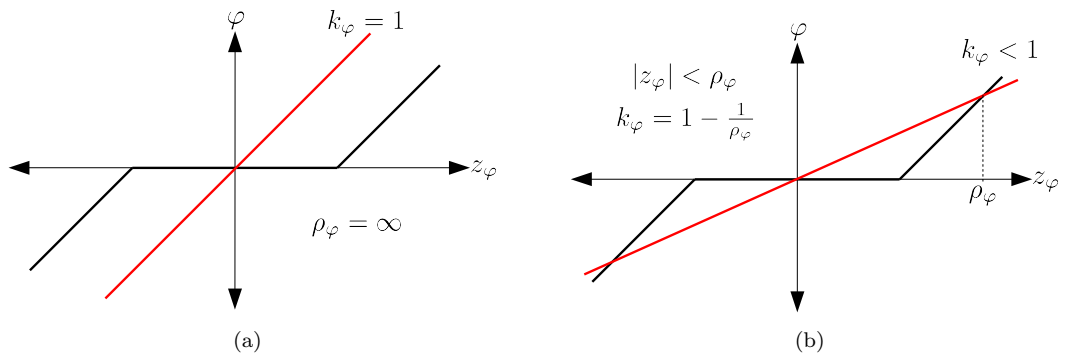

Figure 2.19: Global and local Lipschitz conditions of a dead-zone operator.

Remark 2.10 *Assumption 2.8 is not restrictive since the linear interconnection $M(s)$ can be rescaled to enforce this normalization property.*

2.5.3 A basic result

A first stability test, that yields a rather conservative measure of the stability region, can be proposed by invoking the Small Gain Theorem (see Appendix B.1 on page 243). Based on the $\mathcal{H}_\infty$ norm of the transfer between the exogenous inputs $\mathbf{w} = \begin{bmatrix} w_{\Delta_{\tilde{\Theta}}} & w_{\Delta_w} & w_{\Delta_\Phi} & w_\varphi \end{bmatrix}^T$ and the exogenous outputs $\mathbf{z} = \begin{bmatrix} z_{\Delta_{\tilde{\Theta}}} & z_{\Delta_w} & \tilde{x} & z_\varphi \end{bmatrix}^T$, if

$$||M(s)||_\infty < \gamma \tag{2.47}$$

then, the nonlinear closed-loop is stable for all

$$|\Delta_{\tilde{\Theta}}(t)| < \frac{1}{\gamma}, \quad |\Delta_w(t)| < \frac{1}{\gamma}, \quad k_\Phi(\rho_\Phi) < \frac{1}{\gamma}, \quad \text{and} \quad k_\varphi(\rho_\varphi) < \frac{1}{\gamma} \tag{2.48}$$

This approach allows to obtain a first idea of the size of the constants k_i. From the latter, one can deduce the size of the stability regions ρ_Φ and ρ_φ given that:

$$\forall\, \tilde{x}, \quad |\tilde{x}| < \rho_\Phi \quad \rightarrow \quad |\Delta_\Phi(\tilde{x})| \leq k_\Phi|\tilde{x}| \tag{2.49}$$

$$\forall\, z_\varphi, \quad |z_\varphi| < \rho_\varphi \quad \rightarrow \quad |\varphi_{\tilde{L}}(z_\varphi)| \leq k_\varphi|z_\varphi| \tag{2.50}$$

Furthermore, if the $\mathcal{H}_\infty$ norm of the transfer $\mathcal{T}_{\mathbf{w} \to \mathbf{z}}$ is $\gamma < 1$, the parametric domain of the variation $\tilde{\Theta}$ is cleared by the controller along with any time varying uncertainty $\Delta_w(t)$ admissible in the system. Otherwise, the parametric domain is not clear for all admissible variations of $\tilde{\Theta}$ and the closed-loop stability is only guaranteed for a certain level of uncertainty.

Remark 2.11 *In the case where $\gamma > 1$, since the parametric domain is not cleared by the controller, a refined result can be obtained by weighting separately the transfer "seen" by $\Delta_{\tilde{\Theta}}$.*

Considering the remark above, let us define:

$$M_\rho(s) = diag\left(\frac{1}{\sqrt{\rho}}I_{\tilde{q}}, I_{2\,n+m}\right) \times M(s) \times diag\left(\frac{1}{\sqrt{\rho}}I_{\tilde{q}}, I_{2\,n+m}\right) \tag{2.51}$$

After this modification to the system $M(s)$, the stability conditions in (2.47) and (2.48) can be transformed into the following statement: if

$$||M_\rho(s)||_\infty < \gamma \tag{2.52}$$

then, the nonlinear closed-loop is stable for all

$$|\Delta_{\tilde{\Theta}}(t)| < \frac{\rho}{\gamma}, \quad |\Delta_w(t)| < \frac{1}{\gamma}, \quad k_\Phi(\rho_\Phi) < \frac{1}{\gamma}, \quad \text{and} \quad k_\varphi(\rho_\varphi) < \frac{1}{\gamma} \tag{2.53}$$

The previous restatement of the stability conditions can be solved for different values of ρ. The parametric domain is cleared for all values of ρ that verify that:

$$\rho \leq \gamma \tag{2.54}$$

It is clear that conservatism induced by this approach can become non-trivial if the values of ρ that verify the condition above are too small. In such a case, the transfer $\mathcal{T}_{w_{\Delta_{\tilde{\Theta}}} \to z_{\Delta_{\tilde{\Theta}}}}$ becomes large and preponderant with respect to transfer of the remaining inputs and outputs in $\mathbf{w}$ and $\mathbf{z}$.

2.5.4 A refined approach

Now, let us consider a less conservative approach that relaxes the robustness analysis problem through the use of constant scalings. Once the nonlinear operators $\Delta_\Phi(\cdot)$ and $\varphi_{\tilde{L}}(\cdot)$ have been assumed Lipschitzian, they can be replaced by time-varying linear operators, which enable the use of LTV analysis tools.

Indeed, for any nonlinear function that verifies the Lipschitz continuity condition, a sector associated to that nonlinearity can be deduced. Then, $\Delta_\Phi(\tilde{x})$ and $\varphi_{\tilde{L}}(z_\varphi)$ can be immersed in a linear representation using time-varying uncertainties in diagonal-block structures $\tilde{\Delta}_i(t)$ such that:

$$\forall\, i = 1 \ldots n, \ \forall\ \tilde{x}, \ \exists\, \tilde{\delta}_{\Phi_i}(t) \in \begin{bmatrix} -k_\Phi & k_\Phi \end{bmatrix} \ / \ \Delta_\Phi(\tilde{x}) \ = \ \tilde{\Delta}_\Phi(t)\, \tilde{x} \tag{2.55}$$

$$\forall\, j = 1 \ldots m, \ \forall\, z_\varphi, \ \exists\, \tilde{\delta}_{\varphi_j}(t) \in \begin{bmatrix} -k_\varphi & k_\varphi \end{bmatrix} \ / \ \varphi_{\tilde{L}}(z_\varphi) \ = \ \tilde{\Delta}_\varphi(t)\, z_\varphi \tag{2.56}$$

After replacing the nonlinear functions by LTV operators, the LFT in (2.41) can now be simply expressed as:

$$\mathcal{F}_u\left(M(s), \boldsymbol{\Delta}(t)\right) \tag{2.57}$$

with

$$\boldsymbol{\Delta}(t) = diag\left(\Delta_{\tilde{\Theta}}(t), \Delta_w(t), \tilde{\Delta}_\Phi(t), \tilde{\Delta}_\varphi(t)\right) \tag{2.58}$$
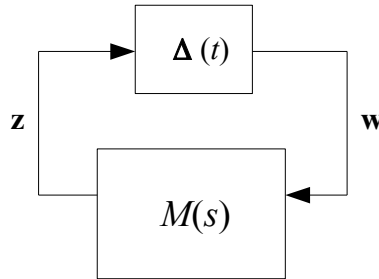
Figure 2.20: Modified analysis LFT representation with LTV operators.

Given the time-varying nature of the operators in the block $\boldsymbol{\Delta}(t)$, an invertible static scaling operator D can be used such that:

$$\boldsymbol{\Delta}(t)\, D = D\, \boldsymbol{\Delta}(t) \tag{2.59}$$

with

$$D = \begin{bmatrix} d_{\tilde{\Theta}}\, I_{\tilde{q}} & & & \mathbf{0} \\ & d_w\, I_n & & \\ & & d_\Phi\, I_n & \\ \mathbf{0} & & & d_\varphi\, I_m \end{bmatrix} \tag{2.60}$$

Thanks to the above commuting property, the closed-loop interconnections of Figures 2.20 and 2.21 are clearly equivalent. But the transfer "seen" by $\Delta(t)$ is modified in this case, which relaxes the small gain theorem.

Figure 2.21: Modified analysis LFT representation with LTV operators and scalings.

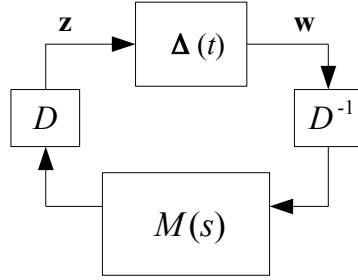Using a similar reasoning as on the previous case, a second test for robustness analysis can indeed be established. Given

$$||D\, M(s)\, D^{-1}||_\infty < \gamma \tag{2.61}$$

then, the nonlinear closed-loop is stable for all

$$|\Delta_{\tilde{\Theta}}(t)| < \frac{1}{\gamma}, \quad |\Delta_w(t)| < \frac{1}{\gamma}, \quad |\tilde{\Delta}_\Phi(t)| < \frac{1}{\gamma}, \quad \text{and} \quad |\tilde{\Delta}_\varphi(t)| < \frac{1}{\gamma} \tag{2.62}$$

This problem can be readily solved using the Scaled Bounded Real Lemma (SBRL). The latter is an adaptation of the well-known Bounded Real Lemma (BRL) which is described in Appendix B.2 (see page 244).

Consider that (A_M, B_M, C_M, D_M) is a realization of the system $M(s)$. The standard BRL can be restated to include the constant scaling D as:

Lemma 2.12 (Scaled Bounded Real) *The gain of the scaled system $D\, M(s)\, D^{-1}$ is bounded by $\gamma > 0$ if and only if there exist $X = X^T$, $L = L^T$ and $Z = Z^T$ such that:*

$$\begin{bmatrix} A_M^T\, X + X\, A_M & X\, B_M & C_M^T\, L \\ B_M^T\, X & -Z & D_M^T\, L \\ L\, C_M & L\, D_M & -Z \end{bmatrix} < 0 \tag{2.63}$$

where $X > 0$, $L = D\, D^T > 0$ and $Z < \gamma\, L$.

Using the SBRL, the solution to the robust stability problem presented by the conditions (2.61) and (2.62), can be expressed as:

$$\hat{D} = \underset{D}{\text{Argmin}}\, ||D\, M(s)\, D^{-1}||_\infty \tag{2.64}$$

Once again, a straightforward link between notion of stability region and the $\mathcal{H}_\infty$ norm γ can be established as described in the previous section.

Concluding comments

In this chapter, a novel Generalized Nonlinear Compensation Framework has been proposed for a large class of nonlinear systems. This framework offers a fresh reformulation of the rather rigid controller structure of standard NDI techniques. In this generalized framework, a linear controller capable of compensating the system nonlinear dynamics in presence of modelling errors, uncertain or varying parameters and input constraints, can be systematically designed.

First, a simple approach to refine the linearizing control laws, by better balancing the efforts of the inner and outer loops of the standard NDI controller structure, was proposed. From this approach, a linear-oriented framework was deduced to design robust controllers capable of "rejecting" the nonlinear dynamics of the system as if they were input disturbances. This new perspective for nonlinear compensation produces linear controllers that proved to generalize the double loop standard NDI controller structure.

Then, design-oriented models resulting from this framework were proposed. In these control schemes, as more information about the system is made available, the better are the chances of obtaining a high performance solution to address the control problem. Also, these design-oriented models allow multi-channel formulations which are helpful to simultaneously optimize a performance criteria and restrictions on the size of control signals.

Given the linear nature of the proposed framework, anti-windup control strategies were also presented as a natural option for enhancing the robustness of the obtained controllers with respect to input saturations. No further adaptation of the existing anti-windup control schemes are required.

Finally, a modelling strategy using Linear Fractional Transformations for robustness and stability analysis was proposed. This LFT representation of the nonlinear closed-loop enables the use of a variety of linear-oriented analysis tests, some of which were detailed. To solve the robustness analysis problem, it should be considered that an exact result is hardly ever found, no matter what approach is used. Even though some tests induce less conservatism than others, the computational burden foregone is usually greater. This remark on stability analysis concludes Part I of this thesis work.

Part II will be devoted to one of the most popular application fields of standard NDI techniques: aerospace applications. In the next chapter, some fundamentals on Flight Mechanics and modelling of aerospace applications will be discussed. Some of the most common control objectives, corresponding to attitude parameters, will be derived from the general equations of motion in a rather convenient way for nonlinear compensation design.

Part II

Application: air vehicles

Chapter 3

Flight Mechanics modelling and control objectives

Introduction

The fundamental laws of motion in classical Mechanics apply to all moving bodies in the same way. The same principle holds for air vehicles (including aircraft, space launchers and spacecrafts such as reentry vehicles). The fundamental equations of motion used in Flight Mechanics [Etk95, Boi98, Taq09] allow to describe the dynamics of such air vehicles despite of their particularities and desired flying qualities.

There are two main models used to represent the motion of any of these air vehicles: 3 degrees-of-freedom models and 6 degrees-of-freedom models. On the one hand, the 3 degrees-of-freedom representation is a simplified model which mainly focuses on the longitudinal motion of the air vehicle. On the other hand, a 6 degrees-of-freedom model describes the complete motion of the air vehicle in the 3 dimensional space. These degrees-of-freedom correspond to the 3 components of forces and moments to which the air vehicle is subject to.

The central objective of this chapter is to introduce the main modelling aspects of air vehicles. In particular, the modelling of the attitude control objectives is stressed. To do so, it is necessary to begin with a description of the fundamental equations of motion used in Flight Mechanics.

First, in Section 3.1, a general representation of an air vehicle as a dynamic system with 6 degrees-of-freedom is presented. Some relevant aspects of this model, mainly related to the air vehicle simulation, are gradually exposed in more detail as the aerodynamic characteristics are introduced in Section 3.2.

Then, in Section 3.3, the target parameters for which the flight control laws are designed are introduced. These control objectives correspond specifically to attitude parameters of air vehicles as it will be explained. An interesting formulation of these objectives is derived. By exploiting measurements that are usually made available by the IMU, such as the acceleration measurement Γ_m, some aerodynamic coefficients and vehicle parameters like the mass can be accounted for

indirectly. This will prove to be very practical for NLC-based flight controller designs in some aerospace applications since the instantaneous mass is usually hard to estimate.

Finally, Section 3.4 presents a list of the main sources of disturbance affecting air vehicles, which should be considered to introduce a realistic scenario in simulation.

3.1 A general dynamic state model (6 degrees-of-freedom)

The dynamic model representing the motion of an air vehicle can be obtained from the general equations of Flight Mechanics that are detailed in Appendix A.1. Such dynamic modelling can be useful for computer simulation and also for deriving the expression of different predominant parameters in specific tasks. The state models are represented as non-autonomous systems in the general form

$$\begin{cases} \dot{\vec{\mathbf{x}}} &= \vec{\mathbf{f}}(t, \vec{\mathbf{x}}(t), \vec{\mathbf{c}}(t), \vec{\mathbf{u}}(t)) \\ \vec{\mathbf{y}}(t) &= \vec{\mathbf{g}}(t, \vec{\mathbf{x}}(t), \vec{\mathbf{c}}(t), \vec{\mathbf{u}}(t)) \end{cases} \tag{3.1}$$

with $\vec{\mathbf{x}}(t) \in \mathbb{R}^n$ as the state vector, $\vec{\mathbf{u}}(t) \in \mathbb{R}^m$ as the input vector, $\vec{\mathbf{y}}(t) \in \mathbb{R}^p$ as the system measurements or output vector, $\vec{\mathbf{c}}(t) \in \mathbb{R}^q$ as a vector of constant or varying parameters, $\vec{\mathbf{f}}$ and $\vec{\mathbf{g}}$ as vector fields containing the system dynamics.

When modelling the 6 degrees-of-freedom motion of air vehicle, the focus is set on the instantaneous position, attitude, translation speed, angular speed, and mass. The state vector $\vec{\mathbf{x}}(t)$ of an air vehicle representation can be defined as:

$$\vec{\mathbf{x}}(t) = \begin{bmatrix} \vec{\mathbf{r}}(t) & \vec{\mathbf{V}}(t) & \mathbf{q}(t) & \vec{\boldsymbol{\Omega}}(t) & m(t) \end{bmatrix}^T \tag{3.2}$$

where $\vec{\mathbf{r}}$ is the position vector, $\vec{\mathbf{V}}$ is the speed vector, $\mathbf{q}$ is an attitude quaternion, $\vec{\boldsymbol{\Omega}}$ is the angular speed vector and m is the mass of the air vehicle.

The input $\vec{\mathbf{u}}(t)$ affecting the states of the dynamic model are mainly: the deflection of the aerodynamic controls, or control surfaces, located on the air vehicle and the thrust levers (when available).

The output $\vec{\mathbf{y}}(t)$ represents the measurements obtained via different on-board instruments such as: the Inertial Measurement Unit (IMU), anemometric units, global positioning systems (GPS), radars, and telemetry, amongst others. For example, the IMU detects the rotation rate $\vec{\boldsymbol{\Omega}}$ through a set of independent gyroscopes and the translational acceleration $\vec{\boldsymbol{\Gamma}}$ by means of accelerometers. The IMU then integrates this measurements to compute other parameters such as: ground position $\vec{\mathbf{r}}_g$, ground speed $\vec{\mathbf{V}}_g$, and the Euler angles ϕ, θ and ψ. The anemometric unit uses a probe [1] to measure the air speed and air-speed linked parameters like the anlge-of-attack and the side-slip angle. The GPS provides information on the inertial position $\vec{\mathbf{r}}$ of an air vehicle and radars are mainly used to determine its altitude.

Given that the moment of inertia tensor $\mathbf{I}$ can be considered constant in the body frame, equation (3.3) contains a general dynamic model with 6 degrees-of-freedom which can be used to

---

1. On high-speed vehicles, the anemometric probe is retracted to protect it from high temperatures, usually, for Mach numbers $\mathcal{M} < 2.5$.

represent the state $\vec{\mathbf{x}}(t)$ of an air vehicle at any given time t.

$$\begin{cases} \dot{\vec{\mathbf{r}}} &= \vec{\mathbf{V}} \\ m\dot{\vec{\mathbf{V}}} &= m\vec{\mathbf{\Gamma}} = \sum\vec{\mathbf{F}} \\ \dot{\mathbf{q}}_i &= \frac{1}{2}\mathbf{q}_i \otimes \vec{\mathbf{\Omega}} \\ \mathbf{I}\dot{\vec{\mathbf{\Omega}}} &= \sum\vec{\mathbf{M}}_G - \vec{\mathbf{\Omega}} \wedge \mathbf{I}\vec{\mathbf{\Omega}} \end{cases} \tag{3.3}$$

where

- $\vec{\mathbf{r}} = (\overrightarrow{\mathbf{OG}})_{/R_i}$: inertial position vector, taken from the origin O of the inertial frame to the air vehicle center of gravity G;
- $\vec{\mathbf{V}} = \vec{\mathbf{V}}_g - \vec{\mathbf{\Omega}}_E \wedge \vec{\mathbf{r}}$: inertial speed vector;
- $\vec{\mathbf{V}}_g = \vec{\mathbf{V}}_a - \vec{\mathbf{V}}_w$: ground speed vector expressed as the difference of the aerodynamic speed and the wind speed;
- $\vec{\mathbf{\Gamma}}$: inertial acceleration vector;
- $\mathbf{q}_i$: attitude quaternion between the body frame and the inertial frame;
- $\vec{\mathbf{\Omega}} = \vec{\mathbf{\Omega}}_i - \vec{\mathbf{\Omega}}_o - \vec{\mathbf{\Omega}}_E$: angular speed vector expressed in body frame as the difference of the inertial angular speed, the local and Earth angular speeds;
- $\vec{\mathbf{\Omega}}_o$: angular speed vector of the local frame rotation with respect to the inertial frame;
- $\vec{\mathbf{\Omega}}_E$: angular speed vector of the Earth;
- $\sum\vec{\mathbf{F}} = \vec{\mathbf{F}}_a + \vec{\mathbf{F}}_p + m\vec{\mathbf{g}}$: sum of aerodynamic, propulsion and gravitational forces;
- $\sum\vec{\mathbf{M}}_G = \vec{\mathbf{M}}_{aG} + \vec{\mathbf{M}}_{pG}$: sum of aerodynamic and propulsion moments;
- $\otimes$: noncommutative product of quaternions.

By setting the inertial frame of reference $\mathcal{R}_i$ with its origin at the center of the Earth (see Appendix A.2), the first equation in (3.3) describes the change in inertial position $\vec{\mathbf{r}}$ of the vehicle center of gravity. Next, the force equation in the inertial frame $\mathcal{R}_i$ contains the dynamics of the translational speed vector $\vec{\mathbf{V}}$ of a vehicle with instantaneous mass m, under the action of the inertial gravity vector $\vec{\mathbf{g}}$. The third equation determines the attitude of the body, using the quaternion $\mathbf{q}$ to avoid non-physical computation problems. The dynamics of the angular speed vector $\vec{\mathbf{\Omega}}$, expressed also in the body frame $\mathcal{R}_b$, is described by the moments equation where the matrix $\mathbf{I}$ represents the constant moment of inertia of the vehicle. Finally, the last equation represents the change of mass of the air vehicle.

3.2 Aerodynamic models

The aerodynamic model contains the information on how the forces and moments are created around a given air vehicle. This model is usually composed of coefficients that affect directly the equations of forces and moments as shown in (3.4).

The model uses aerodynamic coefficients that depend on the body geometry and physical structure. The general definition of the aerodynamic forces and moments about a reference point A show how

these coefficients affect the aerodynamic model:

$$
\begin{aligned}
\vec{\mathbf{M}}_{a_A} &= \bar{q}S_r \begin{bmatrix} l_r C_l \\ b_r C_m \\ l_r C_n \end{bmatrix} = \begin{bmatrix} L \\ M \\ N \end{bmatrix} \\[2mm]
\vec{\mathbf{F}}_a &= \bar{q}S_r \begin{bmatrix} C_x \\ C_y \\ C_z \end{bmatrix} = \begin{bmatrix} X \\ Y \\ Z \end{bmatrix}
\end{aligned}
\tag{3.4}
$$

with
- S_r : reference surface;
- l_r : lateral reference length or wingspan;
- b_r : longitudinal reference length or chord;
- $\bar{q} = \frac{1}{2}\rho V_a^2$: dynamic pressure;
- ρ : instantaneous air density of Earth's atmosphere;
- C_l : roll moment aerodynamic coefficient;
- C_m : pitch moment aerodynamic coefficient;
- C_n : yaw moment aerodynamic coefficient;
- C_x : drag force aerodynamic coefficient;
- C_y : lateral force aerodynamic coefficient;
- C_z : lift force aerodynamic coefficient.

The coefficients C_x and C_z are usually expressed as a function of the coefficients C_{x_a}, C_{y_a} and C_{z_a} defined in the aerodynamic frame $\mathcal{R}_a$ with an opposite sign convention such as:

$$
\begin{aligned}
C_x &= -(C_{x_a}\cos\alpha\cos\beta - C_{y_a}\cos\alpha\sin\beta - C_{z_a}\sin\alpha) \tag{3.5} \\
C_z &= -(C_{x_a}\sin\alpha\cos\beta - C_{y_a}\sin\alpha\sin\beta + C_{z_a}\cos\alpha) \tag{3.6}
\end{aligned}
$$

In the same way, when the coefficient C_y is not expressed in body axis, the following relation with the aerodynamic coefficients C_{x_a} and C_{y_a} can be used:

$$
C_y = C_{x_a}\sin\beta + C_{y_a}\cos\beta \tag{3.7}
$$

The aerodynamic coefficients C_l, C_m and C_n of the equation of moments are expressed in the body frame $\mathcal{R}_b$.

Two main kind of aerodynamic coefficients can be distinguished. In one hand, there are coefficients that depend just on the flight operating conditions (angle-of-attack α, side-slip angle β and Mach number $\mathcal{M}$). On the other hand, there exist effects encountered on the 3 moment components that are due to the aerodynamic controls. As so, 3 conventional controls δ_l, δ_m and δ_n acting on L, M and N respectively are usually defined. Then, there exists a relation between actual aerodynamic controls δ_{real} and the conventional 3 axis controls δ_{pseudo} such that

$$
\delta_{real} = \mathcal{G}\,\delta_{pseudo} \tag{3.8}
$$

As there can be more than just 3 aerodynamic controls in δ_{real}, the matrix $\mathcal{G}$ is usually not invertible. Heuristics and other methods can be used to allocate the efforts from δ_{pseudo} to δ_{real} as it will be explained in Section 5.2.2 for the case of a reentry vehicle.

The effect of the aerodynamic coefficients is often assumed to be additive. As so, this coefficients can be decomposed as:

$$
\begin{bmatrix} C_l \\ C_m \\ C_n \end{bmatrix} = \begin{bmatrix} C_{l_\beta}(\alpha,\mathcal{M})\beta + C_{l_p}(\alpha,\mathcal{M})\tilde{p} + C_{l_r}(\alpha,\mathcal{M})\tilde{r} + C_{l_{\delta_l}}(\alpha,\mathcal{M},\delta_l) + C_{l_{\delta_n}}(\alpha,\mathcal{M},\delta_n) \\ C_{m_0}(\alpha,\mathcal{M}) + C_{m_q}(\alpha,\mathcal{M})\tilde{q} + C_{m_{\delta_m}}(\alpha,\mathcal{M},\delta_m) \\ C_{n_\beta}(\alpha,\mathcal{M})\beta + C_{n_p}(\alpha,\mathcal{M})\tilde{p} + C_{n_r}(\alpha,\mathcal{M})\tilde{r} + C_{n_{\delta_l}}(\alpha,\mathcal{M},\delta_l) + C_{n_{\delta_n}}(\alpha,\mathcal{M},\delta_n) \end{bmatrix}
$$

ONERA
THE FRENCH AEROSPACE LAB

ISAE
Institut Supérieur de l'Aéronautique et de l'Espace

$$\begin{bmatrix} C_{x_a} \\ C_{y_a} \\ C_{z_a} \end{bmatrix} = \begin{bmatrix} C_{x_0}(\alpha, \mathcal{M}) + C_{x_{\delta_m}}(\alpha, \mathcal{M}, \delta_m) \\ C_{y_\beta}(\alpha, \mathcal{M})\beta + C_{y_{\delta_l}}(\alpha, \mathcal{M}, \delta_l) + C_{y_{\delta_n}}(\alpha, \mathcal{M}, \delta_n) \\ C_{z_0}(\alpha, \mathcal{M}) + C_{z_{\delta_m}}(\alpha, \mathcal{M}, \delta_m) \end{bmatrix} \tag{3.9}$$

with $\tilde{p} = \dfrac{l_r}{V_a}p$, $\tilde{q} = \dfrac{b_r}{V_a}q$ and $\tilde{r} = \dfrac{l_r}{V_a}r$.

To express the aerodynamic moments about the actual center of gravity G of the air vehicle, a transmission moments need to be added given $(\overrightarrow{\mathbf{AG}}) = \begin{bmatrix} dg_x & dg_y & dg_z \end{bmatrix}^T$. The equation of the aerodynamic moments in (3.4) can be now expressed in the body frame $\mathcal{R}_b$ as:

$$\vec{\mathbf{M}}_{a_G} = \vec{\mathbf{M}}_{a_A} + \vec{\mathbf{F}}_a \wedge (\overrightarrow{\mathbf{AG}}) \tag{3.10}$$

Now, let us show how to derive the control objectives which are parameters that depend directly on the fundamental equations of movement affected by these aerodynamic coefficients.

3.3 Control objectives

The main objective of the control system of an air vehicle is the modulation of its attitude. From a range of parameters that are usually of interest in aerospace and aeronautic applications, the flight angular objectives that were chosen are:
– the angle-of-attack α;
– the side-slip angle β;
– the aerodynamic roll angle rate $\dot{\mu}$, that can be converted into a roll angle ϕ commanded value.

Some works that justify the choice of these control parameters include [HG70, HG79]. Without any loss of generality, the angle-of-attack α can be chosen as a control objective. In the aeronautic industry, this angular objective is used to conceive stall protection laws for airplanes. In aerospace applications, the angle-of-attack becomes a control objective of the utmost importance since it helps protect the low temperature insulation of reentry vehicles from over heating. Other control problems, where the load factor is usually the control objective, can rely on the angle-of-attack controller design. As a matter of fact, because the load factor n_z can be expressed as a function of the angle of attack as $n_z = f(\alpha)$, the controller design keeps the same structure.

The flight controller design is based on the dynamic behavior of these objectives. Therefore, a mathematical model allowing to explicitly represent the evolution of α, β and ϕ in time is required. Appendix A.3 shows how to derive these dynamic expressions from the general equations of Flight Mechanics and by using the relations between the different frames of reference used to model the motion of the reentry vehicle.

For attitude control, it is common practice to assume that the longitudinal dynamics of the air vehicle are decoupled from the lateral dynamics. The control problem of both the longitudinal and lateral dynamics can then be treated separately. Let us retake the dynamic equations (A.51), (A.52), (A.53) and (A.54) concerning the control objectives and develop their vector representations to obtain literal expressions highlighting the predominant terms for control design.

3.3.1 Modelling the longitudinal objective dynamics

The objective for the longitudinal dynamics is to modulate the angle-of-attack α which is directly coupled to the pitch rate q.

Let us recall from the definition in Appendix A.3, the differential equation describing the dynamic behavior of the angle-of-attack α:

$$\cos \beta \, \dot{\alpha} \;\; = \;\; \vec{\mathbf{\Omega}} \cdot \vec{\mathbf{y}}_a + \frac{\vec{\mathbf{\Gamma}} \cdot \vec{\mathbf{z}}_a}{V_a}$$

By making explicit the components of the vectors in the body frame of reference, one gets:

$$\cos \beta \, \dot{\alpha} = \begin{bmatrix} p \\ q \\ r \end{bmatrix} \cdot \begin{bmatrix} -\sin \beta \cos \alpha \\ \cos \beta \\ -\sin \beta \sin \alpha \end{bmatrix} + \frac{1}{V_a} \left(\begin{bmatrix} a_x \\ a_y \\ a_z \end{bmatrix} + g \begin{bmatrix} -\sin \theta \\ \sin \phi \cos \theta \\ \cos \phi \cos \theta \end{bmatrix} \right) \cdot \begin{bmatrix} -\sin \alpha \\ 0 \\ \cos \alpha \end{bmatrix} \tag{3.11}$$

assuming that the IMU is located at the center of gravity of the vehicle.

Remark 3.1 *In a realistic scenario, the IMU is located at a point P different from the vehicle center of gravity G such that $\overrightarrow{\mathbf{GP}} = \begin{bmatrix} \lambda_x & \lambda_y & \lambda_z \end{bmatrix}^T$. Then, the acceleration $\vec{\mathbf{\Gamma}}$ due to all forces other that the force of gravity, can be associated to the acceleration $\vec{\mathbf{\Gamma}}_m$ measured by the IMU using the relation:*

$$\begin{bmatrix} a_x \\ a_y \\ a_z \end{bmatrix} = \begin{bmatrix} a_{x_m} \\ a_{y_m} \\ a_{z_m} \end{bmatrix} - (\lambda_x p + \lambda_y q + \lambda_z r) \begin{bmatrix} p \\ q \\ r \end{bmatrix} + (p^2 + q^2 + r^2) \begin{bmatrix} \lambda_x \\ \lambda_y \\ \lambda_z \end{bmatrix} - \begin{bmatrix} \dot{p} \\ \dot{q} \\ \dot{r} \end{bmatrix} \wedge \begin{bmatrix} \lambda_x \\ \lambda_y \\ \lambda_z \end{bmatrix} \tag{3.12}$$

given that $\;\vec{\mathbf{\Gamma}} = \vec{\mathbf{\Gamma}}_m + \vec{\mathbf{\Omega}} \wedge (\vec{\mathbf{\Omega}} \wedge \overrightarrow{\mathbf{PG}}) + \dot{\vec{\mathbf{\Omega}}} \wedge \overrightarrow{\mathbf{PG}}$.

Finally, expressing the scalar products of equation (3.11) leads to an angle-of-attack dynamics equation such as:

$$\begin{aligned} \cos \beta \, \dot{\alpha} \;&= q \cos \beta - \sin \beta \, (p \cos \alpha + r \sin \alpha) + \\ & \frac{1}{V_a} [a_z \cos \alpha - a_x \sin \alpha + g(\cos \alpha \cos \phi \cos \theta + \sin \alpha \sin \theta)] \end{aligned} \tag{3.13}$$

Remark 3.2 *The proposed modelling of the angle-of-attack objective becomes rather interesting since the expression of forces, which make intervene the thrust components along with additional coefficients such as C_z and C_x, for example, are all indirectly included in the acceleration measurements a_{x_m}, a_{y_m} and a_{z_m} provided by the IMU. Also, thanks to these available measurements, the NLC-based control laws that will be computed no longer depend on the instant value of the parameter mass m, which is hard to approximate in aerospace applications.*

The input δ_m of the dynamic model affects this angular objective α mainly through its action on the dynamics of the pitch rate q. The differential equation of the pitch rate dynamics is obtained

directly from the fundamental equation of moments (see Appendix A.1). By developing the vector equation

$$\mathbf{I}\dot{\vec{\Omega}} = \vec{\mathbf{M}}_{a_A} + \vec{\mathbf{F}}_a \wedge \overrightarrow{\mathbf{AG}} - \vec{\Omega} \wedge \mathbf{I}\vec{\Omega}$$

one gets:

$$\begin{bmatrix} I_{xx} & -I_{xy} & -I_{xz} \\ -I_{xy} & I_{yy} & -I_{yz} \\ -I_{xz} & -I_{yz} & I_{zz} \end{bmatrix} \begin{bmatrix} \dot{p} \\ \dot{q} \\ \dot{r} \end{bmatrix} = \begin{bmatrix} L \\ M \\ N \end{bmatrix} - \begin{bmatrix} X \\ Y \\ Z \end{bmatrix} \wedge \begin{bmatrix} dg_x \\ dg_y \\ dg_z \end{bmatrix} - \begin{bmatrix} p \\ q \\ r \end{bmatrix} \wedge \begin{bmatrix} I_{xx} & -I_{xy} & -I_{xz} \\ -I_{xy} & I_{yy} & -I_{yz} \\ -I_{xz} & -I_{yz} & I_{zz} \end{bmatrix} \begin{bmatrix} p \\ q \\ r \end{bmatrix} \quad (3.14)$$

Remark 3.3 *In some cases, the products of inertia I_{xy}, I_{xz} and I_{yz} are small and can be neglected from the control design model. The inertia products in the diagonal of the matrix $\mathbf{I}$ are preponderant.*

After developing and extracting the equation of the pitch axis y in (3.14), considering the remark above, it comes that:

$$I_{yy}\dot{q} = M - Z dg_x + X dg_z + (I_{zz} - I_{xx})pr \quad (3.15)$$

By further development, considering the aerodynamic model as introduced in Appendix 3.2, the pitch rate dynamics can be formulated as a function of the input δ_m. Consider the following approximation of the aerodynamic moment M

$$M \approx \bar{q}\, S_r\, l_r \left[C_{m_0}(\alpha, \mathcal{M}) + C_{m_q}(\alpha, \mathcal{M}) \frac{l_r}{V_a}\, q + C_{m_{\delta_m}}(\alpha, \mathcal{M})\delta_m \right] \quad (3.16)$$

With the simplification implied in Remark 3.3, the pitch rate dynamics can now be expressed in terms of q and the input δ_m as:

$$\begin{aligned} I_{yy}\dot{q} &= \bar{q}\, S_r\, l_r \left[C_{m_0}(\alpha, \mathcal{M}) + C_{m_q}(\alpha, \mathcal{M}) \frac{l_r}{V_a}\, q \right] + \bar{q}\, S_r\, l_r\, C_{m_{\delta_m}}(\alpha, \mathcal{M})\delta_m + \\ &\quad X\, dg_z - Z\, dg_x + (I_{zz} - I_{xx})pr \end{aligned} \quad (3.17)$$

3.3.2 Modelling the lateral objective dynamics

When it comes to the lateral control objectives, the focus is set on the side-slip angle β and the roll angle ϕ. As explained in Appendix A.3, the roll dynamics is contained in the Euler angles derivative and can be written as:

$$\dot{\phi} = p + \tan\theta(\cos\phi\, r + \sin\phi\, q) \quad (3.18)$$

The side-slip angle dynamics is obtained as shown also in Appendix A.3. In this case, by making explicit the body frame components of the vector equation

$$\dot{\beta} = -\vec{\Omega} \cdot \vec{\mathbf{z}}_a + \frac{\vec{\Gamma} \cdot \vec{\mathbf{y}}_a}{V_a}$$

one gets the expression:

$$\dot{\beta} = - \begin{bmatrix} p \\ q \\ r \end{bmatrix} \cdot \begin{bmatrix} -\sin\alpha \\ 0 \\ \cos\alpha \end{bmatrix} + \frac{1}{V_a} \left(\begin{bmatrix} a_x \\ a_y \\ a_z \end{bmatrix} + g \begin{bmatrix} -\sin\theta \\ \sin\phi\cos\theta \\ \cos\phi\cos\theta \end{bmatrix} \right) \cdot \begin{bmatrix} -\sin\beta\cos\alpha \\ \cos\beta \\ -\sin\beta\sin\alpha \end{bmatrix} \quad (3.19)$$

where Remark 3.1 should be considered. Finally, by further developing the previous equation, it comes that

$$
\begin{aligned}
\dot{\beta} =\ & p \sin \alpha - r \cos \alpha + \frac{1}{V_a} \left(a_y \cos \beta - a_x \cos \alpha \sin \beta - a_z \sin \alpha \sin \beta \right) + \\
& \frac{g}{V_a} \left(\cos \alpha \, \sin \theta \sin \beta + \sin \phi \, \cos \theta \cos \beta - \sin \alpha \, \sin \theta \, \cos \phi \sin \beta \right)
\end{aligned}
\tag{3.20}
$$

Notice also that Remark 3.2 made on the angle-of-attack dynamics, holds as well for the side-slip angle dynamics.

Clearly, both lateral objectives are coupled to the roll rate p and the yaw rate r. The inputs δ_l and δ_n affecting the lateral model impact the objectives mainly through these angular rates p and r, whose dynamic equations can be extracted from the roll axis x and the yaw axis z in (3.14), where

$$
I_{xx}\dot{p} - I_{xz}\dot{r} = L - Ydg_z + Zdg_y + \left[(I_{yy} - I_{zz})r + I_{xz}p \right] q
\tag{3.21}
$$

and

$$
I_{zz}\dot{r} - I_{xz}\dot{p} = N - Ydg_x + Xdg_y + \left[(I_{xx} - I_{yy})p + I_{xz}r \right] q
\tag{3.22}
$$

In fact, these dynamic equations are functions of the rates p and r and of the deflections δ_l and δ_n. Consider the following approximations of the roll moment L and the yaw moment N

$$
L \approx \bar{q}\, S_r\, l_r \left[C_{l_\beta}\beta + C_{l_p} \frac{l_r}{V_a} p + C_{l_r} \frac{l_r}{V_a} r + C_{l_{\delta_l}}\delta_l + C_{l_{\delta_n}}\delta_n \right]
\tag{3.23}
$$

$$
N \approx \bar{q}\, S_r\, l_r \left[C_{n_\beta}\beta + C_{n_p} \frac{l_r}{V_a} p + C_{n_r} \frac{l_r}{V_a} r + C_{n_{\delta_l}}\delta_l + C_{n_{\delta_n}}\delta_n \right]
\tag{3.24}
$$

It is reminded that all aerodynamic coefficients C_l, C_n and C_y are a function of the angle-of-attack α and the Mach number $\mathcal{M}$.

By neglecting the product of inertia I_{xz} as explained in Remark 3.3 and by assembling equations (3.23)-(3.24) with (3.21)-(3.22), the angular rate dynamic equations become

$$
\begin{aligned}
I_{xx}\dot{p} =\ & \bar{q}\, S_r\, l_r \left[C_{l_\beta}(\alpha, \mathcal{M})\beta + C_{l_p}(\alpha, \mathcal{M})\frac{l_r}{V_a} p + C_{l_r}(\alpha, \mathcal{M})\frac{l_r}{V_a} r \right] + \\
& \bar{q}\, S_r\, l_r \left[C_{l_{\delta_l}}(\alpha, \mathcal{M})\delta_l + C_{l_{\delta_n}}(\alpha, \mathcal{M})\delta_n \right] + Zdg_y - Ydg_z + \\
& (I_{yy} - I_{zz})r\, q
\end{aligned}
\tag{3.25}
$$

and

$$
\begin{aligned}
I_{zz}\dot{r} =\ & \bar{q}\, S_r\, l_r \left[C_{n_\beta}(\alpha, \mathcal{M})\beta + C_{n_p}(\alpha, \mathcal{M})\frac{l_r}{V_a} as\, p + C_{n_r}(\alpha, \mathcal{M})\frac{l_r}{V_a} r \right] + \\
& \bar{q}\, S_r\, l_r \left[C_{n_{\delta_l}}(\alpha, \mathcal{M})\delta_l + C_{n_{\delta_n}}(\alpha, \mathcal{M})\delta_n \right] + Xdg_y - Ydg_x + \\
& (I_{xx} - I_{yy})p\, q
\end{aligned}
\tag{3.26}
$$

3.4   Main sources of disturbance

Any given air vehicle is subject to a set of uncertain phenomenon that one needs to consider in order to validate the flight-control laws that will be computed. These phenomenon can be modelled as additive or multiplicative uncertainties Δ acting over the air vehicle nominal representation.

All additive uncertainties are expressed as a bounded range around a nominal value of a given parameter and are measured in same units as the parameter, while multiplicative uncertainties are expressed as a percentage of a nominal value of a given parameter. Numerical simulation values of these uncertainties can be found in Appendix D.

The main model disturbance sources that were taken into consideration are described below.
– Variation of the atmosphere density ($\Delta\rho$) as a function of the altitude h, modelled as a multiplicative uncertainty.
– Wind. The wind is decomposed into static wind ($\vec{\mathbf{V}}_{sw}$) and turbulent wind ($\vec{\mathbf{V}}_{tw}$). The wind modelling is detailed in Appendix D.1.2.
– Aerodynamic coefficient modelling errors (ΔC_{m0}, $\Delta C_{m\delta_m}$, $\Delta C_{m\delta_{bf}}$, ΔC_x, ΔC_z, $\Delta C_{l\delta_l}$, $\Delta C_{n\delta_l}$, $\Delta C_{l\delta_n}$, $\Delta C_{n\delta_n}$). Some of these are modelled as additive uncertainties and other as multiplicative uncertainties as detailed in Appendix D.2.3.
– Centring and inertia modelling error (Δdg_x, Δdg_y, Δdg_z) as additive uncertainties.
– IMU measurement errors. The direct measurements of the IMU, which are the translational accelerations $\vec{\mathbf{\Gamma}}_m$ and the rotation rates $\vec{\mathbf{\Omega}}_m$, are subject to deterministic and random phenomenon such as: biases, scale factors and random walks. The IMU direct measurements were modelled by the following formulas:

$$
\begin{aligned}
\vec{\mathbf{\Gamma}}_m &= \vec{\mathbf{\Gamma}}\,\mathrm{sf}_\Gamma(t) + \vec{\mathbf{w}}_\Gamma(t) + \vec{\mathbf{b}}_{m_\Gamma} & (3.27) \\
\vec{\mathbf{\Omega}}_m &= \vec{\mathbf{\Omega}}\,\mathrm{sf}_\Omega(t) + \vec{\mathbf{w}}_\Omega(t) + \vec{\mathbf{b}}_{m_\Omega} & (3.28)
\end{aligned}
$$

where the white noise vectors $\vec{\mathbf{w}}(t)$ represent a normally distributed random walk phenomena of standard deviation σ, and the vectors $\vec{\mathbf{b}}_m$ represent the measurement bias. The scale factors $\mathrm{sf}(t)$

$$
\begin{aligned}
\mathrm{sf}_\Gamma(t) &= (1 + w_\Gamma(t) + b_{m_\Gamma}) & (3.29) \\
\mathrm{sf}_\Omega(t) &= (1 + w_\Omega(t) + b_{m_\Omega}) & (3.30)
\end{aligned}
$$

are composed of a bias b_m affected by a white noise $w(t)$.

These disturbed measurements $\vec{\mathbf{\Gamma}}_m$ and $\vec{\mathbf{\Omega}}_m$ are then numerically integrated by the IMU to compute, as an output, the ground position vector $\vec{\mathbf{r}}_g$ (containing the component altitude h) and ground speed $\vec{\mathbf{V}}_g$, as well as the body attitude angles (ϕ, θ, ψ) and rotation rate vector $\vec{\mathbf{\Omega}}$ of components (p, q, r). The IMU output measurements are then made available for the flight control law. Depending on the control design objectives, this results in the introduction of uncertainties in the control-loop ($\Delta\phi$, $\Delta\theta$, $\Delta\psi$, Δp, Δq, Δr, Δh).

In fast flight regimes, the probe of the anemometric unit charged of measuring the airspeed of the reentry vehicle is retracted to protect it from overheating. Since the speed measurement made by the IMU is basically the ground speed $\vec{\mathbf{V}}_g$, in presence of wind, additional uncertainties should be considered for the computation of the airspeed and aerodynamic angular parameters (ΔV_a, $\Delta\alpha$, $\Delta\beta$).

ONERA
THE FRENCH AEROSPACE LAB

isae
Institut Supérieur de l'Aéronautique et de l'Espace

– Anemometer measurement errors ($\Delta\alpha$, $\Delta\beta$, ΔV_a) modelled as additive uncertainties.

The measurement errors considered may induce further errors on the calculation of diverse parameters that may need to be available for the Control system such as:
– The air density as a function of the altitude $\rho(h)$ in an exponential atmosphere model: $\Delta\tilde{\rho}$;
– Mach number $\mathcal{M}(V_a, h)$ as a function of the airspeed and altitude: $\Delta\mathcal{M}$.

Concluding comments

In this chapter, the main modelling aspects of air vehicles and common control objectives were presented, based on the fundamental equations of motion used in Flight Mechanics.

First, a general dynamic state model was presented, based on the fundamental equations of forces and moments which describe the dynamics of the translational and angular speed. The dynamics of the inertial position and attitude of the vehicle are also part of this 6-degree-of-freedom model which can be eventually completed by the dynamic equation of mass.

After introducing general models of air vehicle aerodynamics and actuators, the control objectives corresponding to the angle-of-attack α, the side-slip angle β and the roll angle ϕ, along with the dynamics of p, q and r, were derived as part of the longitudinal and lateral dynamics.

Finally, the main sources of disturbance which should be considered in simulation of air vehicles to introduce more realistic scenarios, were enlisted.

In the next chapter, the control objective models will be used to compute NLC-based control laws. Both approaches, the standard NDI design with PI control and the generalized NLC-$\mathcal{H}_\infty$ control design, will be employed to conceive attitude controllers for general air vehicles.

Chapter 4

Description of Nonlinear Compensation-based control design procedures

Introduction

As mentioned in Chapter 1, the NDI method is a particular case of nonlinear compensation, where the system nonlinearities are punctually eliminated by using the "system inverse" in a fixed inner loop structure. Unfortunately, this standard approach is not well adapted for some classes of nonlinear processes, including systems with input saturations. Although some efforts have been made to extend NDI for systems with input constraints using anti-windup control [YPY08, HTM+10], staying in a nonlinear context still remains a challenging task.

In contrast to standard NDI, the generalized NLC framework proposed in Chapter 2 allows to remain in a linear context, thus enabling a systematic implementation of robust controller design techniques, including anti-windup schemes, for a large class of nonlinear systems. This framework endows more flexibility to the compensation of a system nonlinearities while assuring certain levels of performance and restricting the size of the control signals. As it will be further explained, the control design of most aerospace applications fall within the modelling approach of our NLC framework.

The main objective of this chapter is to describe both, the design procedure of a standard NDI control law for attitude control of an air vehicle, and the design procedure under our generalized NLC framework.

First, in Section 4.1, baseline NDI control laws with PI correction are applied to the longitudinal and lateral control objectives following the time-scaling approach described in Chapter 1.

After having developed the standard NDI approach, Section 4.2 introduces the design-oriented models of the longitudinal and lateral dynamics of an air vehicle for robust control synthesis

within our NLC framework. This is achieved by using the general design guidelines proposed in Chapter 2.

Finally, by considering a complete air vehicle model accounting for input saturations, the design-oriented model for enhancing the nominal robust controllers with the use of anti-windup devices is presented in Section 4.3.

Throughout this chapter, consider the following assumptions:

Assumption 4.1 *For attitude control, the longitudinal and lateral dynamics of the air vehicle can be decoupled under the hypothesis that lateral dynamics is at a steady state while the longitudinal dynamics evolve and vice-versa,*

Assumption 4.2 *The angular rate dynamics of the air vehicle evolve sufficiently faster than the angular objectives in a time-scale basis, thus allowing the decoupling of both dynamics under the hypothesis that the slow dynamics is constant during the evolution of the fast dynamics, and that the fast dynamics is steady during the evolution of the slow dynamics.*

Assumption 4.3 *Measurements of the controlled output z and state x of the air vehicle are all available for controller design along with the vector of varying parameters Θ. Even though most state parameters are usually measurable thorugh the IMU, anemometric unit, GPS, etc, if these measurements are not readily available, a state reconstruction filter must be used to estimate these parameters.*

4.1 NDI-PI baseline controller design

To show how the standard NDI method can be applied to the objective dynamics for attitude control of our application, let us begin by making a more particular assumption in relation to the actuator dynamics. It is temporarily assumed that:

Assumption 4.4 *The air vehicle control surfaces are governed by actuator dynamics that can be idealized. This dynamics are sufficiently fast and have unlimited magnitude and rate capacities.*

The NDI control design procedure for the longitudinal and lateral angular objectives will be developed next.

4.1.1 Longitudinal case

Let us begin by recalling the longitudinal angular objective model described in Section 3.3.1 where the angle-of-attack is coupled to the pitch rate dynamics.

$$
\Sigma_{long} : \begin{cases}
\cos\beta\,\dot\alpha = & q\cos\beta - \sin\beta\,(p\cos\alpha + r\sin\alpha) + \\
& \dfrac{1}{V_a}[a_z\cos\alpha - a_x\sin\alpha + g(\cos\alpha\cos\phi\cos\theta + \sin\alpha\sin\theta)] \\
I_{yy}\dot q = & \bar q\,S_r\,l_r\left[C_{m_0}(\alpha,\mathcal M) + C_{m_q}(\alpha,\mathcal M)\dfrac{l_r}{V_a}\,q\right] + \bar q\,S_r\,l_r\,C_{m_{\delta_m}}(\alpha,\mathcal M)\,\delta_m + \\
& X\,dg_z - Z\,dg_x + (I_{zz} - I_{xx})p\,r
\end{cases}
\tag{4.1}
$$

Consider now Assumption 4.2, meaning that the pitch rate dynamics $\dot{q}$ is significantly faster than the angle-of-attack dynamics $\dot{\alpha}$. This assumption allows us treat the longitudinal angular objective model as two sub-systems: one containing the fast dynamics (the pitch rate q in this case) affected by the global model input δ_m, and the other containing the slow dynamics (angle-of-attack α) with the fast state q as the sub-system input.

The two sub-systems of the longitudinal model along with its angular objective z, can be re-written under a standard nonlinear formulation as:

$$\dot{\alpha} \;=\; Z_\alpha + q \tag{4.2}$$

$$\dot{q} \;=\; M_q + g_q\,\delta_m \tag{4.3}$$

$$z \;=\; C_{long}\,x \tag{4.4}$$

where

$$
\begin{aligned}
z &= \alpha \\
x &= \begin{bmatrix} \alpha & q \end{bmatrix}^T \\
\Theta &= \begin{bmatrix} p & r & a_x & a_z & \theta & \phi & \beta & \bar{q} & X & Z & V_a & \mathcal{M} \end{bmatrix}^T
\end{aligned}
$$

$$
\begin{aligned}
Z_\alpha(x,\Theta) &= -\tan\beta\,(p\cos\alpha + r\sin\alpha) + \\
&\qquad \frac{1}{V_a\cos\beta}[a_z\,\cos\alpha - a_x\,\sin\alpha + g(\cos\alpha\,\cos\phi\,\cos\theta + \sin\alpha\,\sin\theta)] \\[4pt]
M_q(x,\Theta) &= \frac{\bar{q}\,S_r\,l_r}{I_{yy}}\left[C_{m_0}(\alpha,\mathcal{M}) + C_{m_q}(\alpha,\mathcal{M})\frac{l_r}{V_a}\,q\right] + \frac{1}{I_{yy}}(X\,dg_z - Z\,dg_x) + \\
&\qquad \frac{1}{I_{yy}}[(I_{zz} - I_{xx})p\,r] \\[4pt]
g_q(x,\Theta) &= \frac{1}{I_{yy}}\bar{q}\,S_r\,l_r\,C_{m_{\delta_m}}(\alpha,\mathcal{M}) \\[4pt]
C_{long} &= \begin{bmatrix} 1 & 0 \end{bmatrix}
\end{aligned}
$$

An NDI controller design for this set is applied in two steps and can be formulated as follows:

Step 1 *Find the expression of the control input δ_m that inverts the fast dynamics in (4.2) and define a linear controller capable to enforce the convergence of the pitch rate q towards its commanded value q_c while following first-order dynamics.*

The control signal needed to invert the pitch rate dynamics, shown graphically on Figure 4.1, is defined by the NDI controller

$$\delta_m = g_q^{-1}\left[-M_q + \tilde{u}_q(q_c, q)\right] \tag{4.5}$$

The first-order dynamics can be imposed through the new input $\tilde{u}_q$ with a linear controller. A proportional controller can be used to this effect by defining $\tilde{u}_q$ such as:

$$\tilde{u}_q(q_c, q) = \frac{1}{\tau_q}(q_c - q) \tag{4.6}$$

where q_c is the commanded value that will be required to invert the slow dynamics as will be shown in the next step. Clearly, by replacing (4.5) in equation (4.3), considering (4.6), it follows that

$$\dot{q} = \frac{1}{\tau_q}(q_c - q) \tag{4.7}$$

Over a period of time determined by the value of the chosen time constant τ_q, the pitch rate q converges towards its commanded value q_c following first-order dynamics, *i.e.*, $q = q_c$.
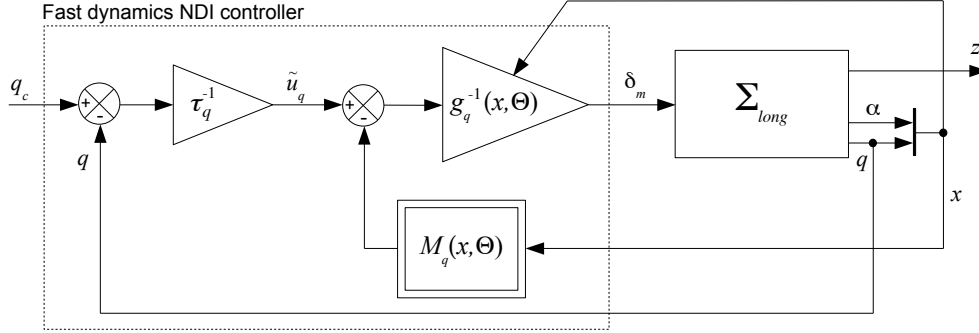

Figure 4.1: Longitudinal fast dynamics inversion via standard approach.

Step 2 *Find the commanded value of the pitch rate q_c that inverts the slow dynamics in (4.3) and define a linear controller that enforces the convergence of the angle-of-attack objective $z = \alpha$ towards its commanded value $z_c = \alpha_c$ while following second-order dynamics.*

In the same manner as shown for the fast dynamics, and given that after a small time $q = q_c$, the NDI controller required to invert the angle-of-attack dynamics is such as:

$$q_c = -Z_\alpha + \tilde{u}_\alpha(\alpha_c, \alpha) \tag{4.8}$$

Desired dynamics is enforced through the new input $\tilde{u}_\alpha$. In this case, second-order dynamics can be obtained with a PI controller with respective proportional and integral gains k_P and k_I as:

$$\tilde{u}_\alpha(\alpha_c, \alpha) = k_P(\alpha_c - \alpha) + k_I \int (\alpha_c - \alpha) \tag{4.9}$$

where α_c is the commanded value of the angular objective. By replacing (4.8) in (4.2) given (4.9), the angular objective dynamics become

$$\dot{\alpha} = k_P(\alpha_c - \alpha) + k_I \int (\alpha_c - \alpha) \tag{4.10}$$

When equation (4.10) is written in the frequency domain using the Laplace transform, it follows that:

$$\frac{\alpha}{\alpha_c} = \frac{k_P\,s + k_I}{s^2 + k_P\,s + k_I}$$

Second-order dynamics is enforced for the convergence of the angular objective $z = \alpha$ towards its commanded value $z_c = \alpha_c$ by posing $k_P = 2\,\xi_\alpha\,\omega_{c_\alpha}$ and $k_I = \omega_{c_\alpha}^2$, where ξ_α denotes the damping coefficient and ω_{c_α} denotes the cut-off frequency of such second-order dynamics.

Notice that a stable zero is introduced by this PI control structure, which may induce some additional overshoot on the closed-loop. This slight setback can be countered by filtering the setpoint signal α_c with a first-order filter of time constant τ_F and state α_F. In fact, filtering the setpoint signal usually improves the closed-loop performance. By introducing a pole at the same frequency of that of the stable zero, the overshoot generated by the PI controller structure is reduced. Consider the setpoint filter

$$F_{long}(s): \; \alpha_F = \frac{1}{\tau_F\,s + 1}\alpha_c, \qquad \tau_F = \frac{k_P}{k_I} \tag{4.11}$$

Then, the closed loop control objective becomes

$$\frac{\alpha}{\alpha_c} = \frac{k_I(k_P\,s + k_I)}{(s^2 + k_P\,s + k_I)(k_P\,s + k_I)}$$
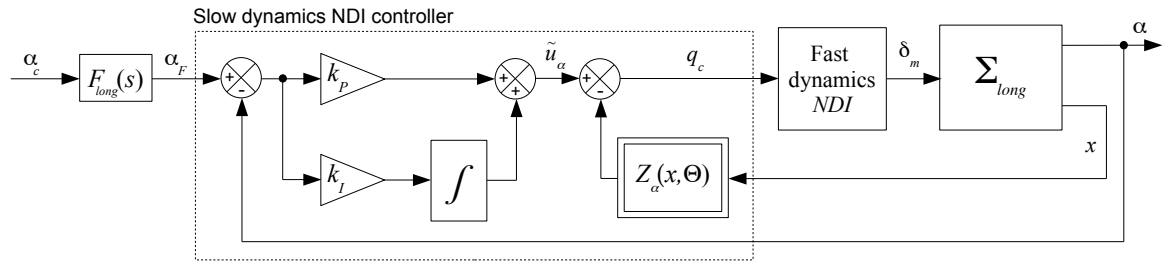
Figure 4.2: NDI-PI controller structure for the longitudinal model.

The expression of the NDI controller with proportional-integral correction (NDI-PI) for the longitudinal angular objective, depicted on Figure 4.2, is obtained by assembling equations (4.5) and (4.8) as:

$$\delta_m = g_q^{-1}\left[-M_q + \frac{1}{\tau_q}\left(-Z_\alpha + k_P(\alpha_F - \alpha) + k_I\int(\alpha_F - \alpha) - q\right)\right] \tag{4.12}$$

A simpler expression of the controller can be generated by creating a measurement vector $\tilde{y}$ regrouping: the setpoint filter state α_F, the integral of the error signal $\varepsilon_\alpha = (\alpha_F - \alpha)$ and the longitudinal model state $x = \begin{bmatrix} \alpha & q \end{bmatrix}^T$; along with a controller exogenous input vector w regrouping the nonlinear functions Z_α and M_q. The expression of this NDI-PI solution can be written as:

$$\delta_m = g_q^{-1}(K\,\tilde{y} + H\,w) \tag{4.13}$$

where

$$K = \begin{bmatrix} \dfrac{k_P}{\tau_q} & \dfrac{k_I}{\tau_q} & \dfrac{-1}{\tau_q} \end{bmatrix} \tag{4.14}$$

$$H = \begin{bmatrix} \dfrac{-1}{\tau_q} & -1 \end{bmatrix} \tag{4.15}$$

given the previously described vectors

$$\tilde{y} = \begin{bmatrix} \varepsilon_\alpha & \int \varepsilon_\alpha & q \end{bmatrix}^T \tag{4.16}$$

$$w = \begin{bmatrix} Z_\alpha & M_q \end{bmatrix}^T \tag{4.17}$$

A clear separation between the outer-loop and inner-loop controller gains can be easily identified under this simpler form. The static gain vector K regulates the outer-loop linear dynamics while the inner-loop static gain vector H eliminates the longitudinal model nonlinear dynamics.

4.1.2 Lateral case

Now, let us recollect the lateral angular objective model described in Section 3.3.2 where the side-slip angle and roll are coupled to the yaw rate and roll rate dynamics.

$$\Sigma_{lat} : \begin{cases} \dot{\beta} = p \sin\alpha - r \cos\alpha + \dfrac{1}{V_a}(a_y \cos\beta - a_x \cos\alpha \sin\beta - a_z \sin\alpha \sin\beta) + \\ \qquad \dfrac{g}{V_a}(\cos\alpha \sin\theta \sin\beta + \sin\phi \cos\theta \cos\beta - \sin\alpha \sin\theta \cos\phi \sin\beta) \\ \dot{\phi} = p + \tan\theta(\cos\phi\, r + \sin\phi\, q) \\ I_{xx}\dot{p} = \bar{q}S_r l_r \left[C_{l_\beta}(\alpha, \mathcal{M})\beta + C_{l_p}(\alpha, \mathcal{M})\dfrac{l_r}{V_a}p + C_{l_r}(\alpha, \mathcal{M})\dfrac{l_r}{V_a}r \right] + \\ \qquad \bar{q}\, S_r\, l_r \left[C_{l_{\delta_l}}(\alpha, \mathcal{M})\delta_l + C_{l_{\delta_n}}(\alpha, \mathcal{M})\delta_n \right] + Zdg_y - Ydg_z + (I_{yy} - I_{zz})r\, q \\ I_{zz}\dot{r} = \bar{q}S_r l_r \left[C_{n_\beta}(\alpha, \mathcal{M})\beta + C_{n_p}(\alpha, \mathcal{M})\dfrac{l_r}{V_a}p + C_{n_r}(\alpha, \mathcal{M})\dfrac{l_r}{V_a}r \right] + \\ \qquad \bar{q}\, S_r\, l_r \left[C_{n_{\delta_l}}(\alpha, \mathcal{M})\delta_l + C_{n_{\delta_n}}(\alpha, \mathcal{M})\delta_n \right] + \\ \qquad Xdg_y - Ydg_x + (I_{xx} - I_{yy})p\, q \end{cases} \tag{4.18}$$

Consider again Assumption 4.2. In this case, the yaw rate and the roll rate dynamics are faster when compared to the side-slip and roll angle dynamics. The lateral angular objective model can be represented as two sub-systems: one containing the fast dynamics $\dot{p}$ and $\dot{r}$ affected by the global model inputs δ_l and δ_n, and another containing the slow dynamics $\dot{\beta}$ and $\dot{\phi}$ with the fast states p and r as the sub-system input.

The two subsystems of the lateral model along with its angular objective z, can be re-written under a standard nonlinear formulation as:

$$\begin{bmatrix} \dot{\beta} \\ \dot{\phi} \end{bmatrix} = \begin{bmatrix} Y_\beta \\ X_\phi \end{bmatrix} + G_1 \begin{bmatrix} p \\ r \end{bmatrix} \tag{4.19}$$

$$\begin{bmatrix} \dot{p} \\ \dot{r} \end{bmatrix} = \begin{bmatrix} L_p \\ N_r \end{bmatrix} + G_2 \begin{bmatrix} \delta_l \\ \delta_n \end{bmatrix} \tag{4.20}$$

$$z = C_{lat}\, x \tag{4.21}$$

where

$$z = \begin{bmatrix} \beta & \phi \end{bmatrix}^T$$
$$x = \begin{bmatrix} \beta & \phi & p & r \end{bmatrix}^T$$
$$\Theta = \begin{bmatrix} q & a_x & a_y & a_z & \theta & \alpha & \bar{q} & X & Y & Z & V_a & \mathcal{M} \end{bmatrix}^T$$

$$Y_\beta(x,\Theta) = \frac{1}{V_a}\left(a_y\,\cos\beta - a_x\,\cos\alpha\sin\beta - a_z\,\sin\alpha\sin\beta\right) +$$
$$\frac{g}{V_a}\left(\cos\alpha\,\sin\theta\sin\beta + \sin\phi\,\cos\theta\cos\beta - \sin\alpha\,\sin\theta\cos\phi\sin\beta\right)$$

$$X_\phi(x,\Theta) = \tan\theta(\cos\phi\,r + \sin\phi\,q)$$

$$L_p(x,\Theta) = \frac{\bar{q}\,S_r\,l_r}{I_{xx}}\left[C_{l_\beta}(\alpha,\mathcal{M})\beta + C_{l_p}(\alpha,\mathcal{M})\frac{l_r}{V_a}\,p + C_{l_r}(\alpha,\mathcal{M})\frac{l_r}{V_a}\,r\right] +$$
$$\frac{1}{I_{xx}}[Zdg_y - Ydg_z + (I_{yy}-I_{zz})r\,q]$$

$$N_r(x,\Theta) = \frac{\bar{q}\,S_r\,l_r}{I_{zz}}\left[C_{n_\beta}(\alpha,\mathcal{M})\beta + C_{n_p}(\alpha,\mathcal{M})\frac{l_r}{V_a}\,p + C_{n_r}(\alpha,\mathcal{M})\frac{l_r}{V_a}\,r\right] +$$
$$\frac{1}{I_{zz}}[Xdg_y - Ydg_x + (I_{xx}-I_{yy})p\,q]$$

$$G_1(x,\Theta) = \begin{bmatrix} \sin\alpha & -\cos\alpha \\ 1 & 0 \end{bmatrix}$$

$$G_2(x,\Theta) = \begin{bmatrix} \dfrac{\bar{q}\,S_r\,l_r}{I_{xx}}C_{l_{\delta_l}}(\alpha,\mathcal{M}) & \dfrac{\bar{q}\,S_r\,l_r}{I_{xx}}C_{l_{\delta_n}}(\alpha,\mathcal{M}) \\ \dfrac{\bar{q}\,S_r l_r}{I_{zz}}C_{n_{\delta_l}}(\alpha,\mathcal{M}) & \dfrac{\bar{q}\,S_r l_r}{I_{zz}}C_{n_{\delta_n}}(\alpha,\mathcal{M}) \end{bmatrix}$$

$$C_{lat} = \begin{bmatrix} 1 & 0 & 0 & 0 \\ 0 & 1 & 0 & 0 \end{bmatrix}$$

Remark 4.5 *The choice of adding to the function $X_\phi(x,\Theta)$ the term $\tan\theta\cos\phi\,\mathbf{r}$, which contains explicitly a combination of the slow sub-system input $\mathbf{r}$, has been made. This term could alternatively be included inside the matrix $G_1(x,\Theta)$.*

By choosing to include this term as part of the function $X_\phi(x,\Theta)$ it is implicitly intended to eliminate as much as possible the coupling between the angular objective ϕ and the yaw rate r which may become relevant for $\theta \neq (0,\pi)$. Then, from Assumption 4.1, the matrix $G_1(x,\Theta)$ can be considered as constant or rather slow varying.

After writing the MIMO lateral model with the standard nonlinear formulation with two time-scales, the NDI controller design for this set is also applied in two steps and can be formulated as follows:

Step 1 *Find the expression of the lateral input $u = \begin{bmatrix} \delta_l & \delta_n \end{bmatrix}^T$ that inverts the fast dynamics in (4.19) and define a linear controller capable of enforcing the convergence of the angular rates p and r towards commanded values p_c and r_c while following first-order dynamics.*

The NDI controller, shown on Figure 4.3, required to eliminate the angular rate nonlinear dynamics is defined by:

$$\begin{bmatrix} \delta_l \\ \delta_n \end{bmatrix} = G_2^{-1}\left(-\begin{bmatrix} L_p \\ N_r \end{bmatrix} + \begin{bmatrix} \tilde{u}_p(p_c,p) \\ \tilde{u}_r(r_c,r) \end{bmatrix} \right) \tag{4.22}$$

The first-order dynamics can be imposed through the new input $\tilde{u} = \begin{bmatrix} \tilde{u}_p & \tilde{u}_r \end{bmatrix}^T$ with a linear controller. As proposed for the fast longitudinal dynamics, a proportional controller can be used

to this effect by defining $\tilde{u} = \begin{bmatrix} \tilde{u}_p & \tilde{u}_r \end{bmatrix}^T$ such as:

$$\begin{bmatrix} \tilde{u}_p(p_c, p) \\ \tilde{u}_r(r_c, r) \end{bmatrix} = T \begin{bmatrix} (p_c - p) \\ (r_c - r) \end{bmatrix} \tag{4.23}$$

where p_c and r_c are the commanded values required to invert the slow dynamics and the constant matrix T is

$$T = diag(\tau_p^{-1}, \tau_r^{-1}) \tag{4.24}$$

When the NDI controller (4.22) is applied to the fast dynamics (4.20), considering the linear controller (4.23), it follows that

$$\begin{bmatrix} \dot{p} \\ \dot{r} \end{bmatrix} = T \begin{bmatrix} (p_c - p) \\ (r_c - r) \end{bmatrix} \tag{4.25}$$

Clearly, over a period of time determined by the value of the chosen time constants τ_p and τ_r, the angular rates p and r converge towards the commanded values p_c and r_c following first-order dynamics.
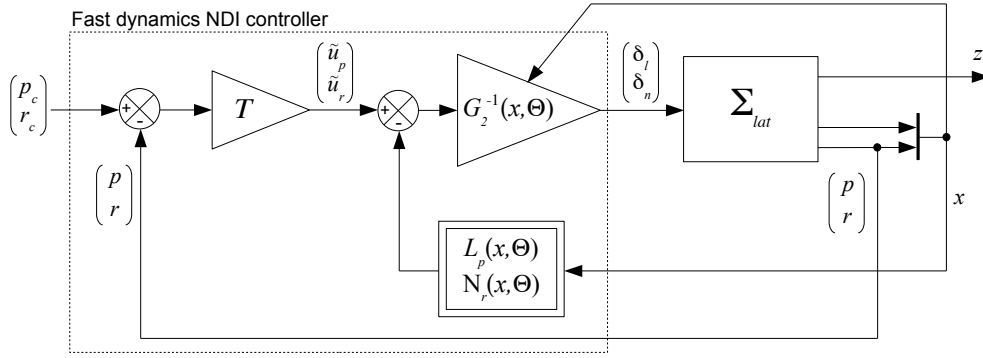
Figure 4.3: Lateral fast dynamics inversion via standard approach.

Step 2 *Find the commanded value of the angular rates p_c and r_c that invert the slow dynamics in (4.20) and define a linear controller that enforces the convergence of the lateral angular objective $z = \begin{bmatrix} \beta & \phi \end{bmatrix}^T$ towards the target $z_c = \begin{bmatrix} \beta_c & \phi_c \end{bmatrix}^T$ while following second-order dynamics.*

Considering that the angular rates p and r converge towards their commanded values p_c and r_c, and that the slow dynamics have the angular rates as their model inputs, the NDI controller required to eliminate the angular objective dynamics is defined as:

$$\begin{bmatrix} p_c \\ r_c \end{bmatrix} = G_1^{-1} \left(- \begin{bmatrix} Y_\beta \\ X_\phi \end{bmatrix} + \begin{bmatrix} \tilde{u}_\beta(\beta_c, \beta) \\ \tilde{u}_\phi(\phi_c, \phi) \end{bmatrix} \right) \tag{4.26}$$

Desired dynamics is enforced through the new inputs $\tilde{u}_\beta$ and $\tilde{u}_\phi$. In this case, second-order dynamics can be obtained with a PI controller with respective proportional and integral gains K_P and K_I as:

$$\begin{bmatrix} \tilde{u}_\beta(\beta_c, \beta) \\ \tilde{u}_\phi(\phi_c, \phi) \end{bmatrix} = K_P \begin{bmatrix} (\beta_c - \beta) \\ (\phi_c - \phi) \end{bmatrix} + K_I \begin{bmatrix} \int (\beta_c - \beta) \\ \int (\phi_c - \phi) \end{bmatrix} \tag{4.27}$$

where β_c and ϕ_c are the angular objective commanded values and the constant matrices K_P and K_I are defined by:

$$K_P = \begin{bmatrix} k_{P_\beta} & 0 \\ 0 & k_{P_\phi} \end{bmatrix} \tag{4.28}$$

$$K_I = \begin{bmatrix} k_{I_\beta} & 0 \\ 0 & k_{I_\phi} \end{bmatrix} \tag{4.29}$$

By applying the nonlinear controller (4.26) to the subsystem (4.19), given the linear control law (4.27), the angular objective dynamics become

$$\begin{bmatrix} \dot{\beta} \\ \dot{\phi} \end{bmatrix} = K_P \begin{bmatrix} (\beta_c - \beta) \\ (\phi_c - \phi) \end{bmatrix} + K_I \begin{bmatrix} \int (\beta_c - \beta) \\ \int (\phi_c - \phi) \end{bmatrix} \tag{4.30}$$

As described in the case of the longitudinal objectives, second-order dynamics is fixed by choosing

$$k_{P_\beta} = 2\,\xi_\beta\,\omega_{c_\beta}, \qquad k_{I_\beta} = \omega_{c_\beta}^2$$
$$k_{P_\phi} = 2\,\xi_\phi\,\omega_{c_\phi}, \qquad k_{I_\phi} = \omega_{c_\phi}^2$$

where ξ_i are the damping coefficients and ω_{c_i} are the cut-off frequencies of such second-order dynamics. To improve the performance of the closed-loop, given that the PI structure introduces a stable zero on the linear dynamics of β and ϕ, consider the setpoint filter

$$F_{lat}(s) : \begin{bmatrix} \beta_F \\ \phi_F \end{bmatrix} = \begin{bmatrix} \dfrac{1}{\frac{k_{P_\beta}}{k_{I_\beta}}\,s + 1} & 0 \\ 0 & \dfrac{1}{\frac{k_{P_\phi}}{k_{I_\phi}}\,s + 1} \end{bmatrix} \begin{bmatrix} \beta_c \\ \phi_c \end{bmatrix} \tag{4.31}$$

The expression of the NDI-PI controller for the lateral angular objectives, illustrated on Figure 4.4, is obtained by assembling equations (4.22) and (4.26) as:

$$\begin{bmatrix} \delta_l \\ \delta_n \end{bmatrix} = G_2^{-1} \left[-\begin{bmatrix} L_p \\ N_r \end{bmatrix} + T \left\{ G_1^{-1} \left(-\begin{bmatrix} Y_\beta \\ X_\phi \end{bmatrix} + K_P \begin{bmatrix} \varepsilon_\beta \\ \varepsilon_\phi \end{bmatrix} + K_I \begin{bmatrix} \int \varepsilon_\beta \\ \int \varepsilon_\phi \end{bmatrix} \right) - \begin{bmatrix} p \\ r \end{bmatrix} \right\} \right] \tag{4.32}$$

where

$$\varepsilon_\beta = (\beta_F - \beta) \tag{4.33}$$
$$\varepsilon_\phi = (\phi_F - \phi) \tag{4.34}$$
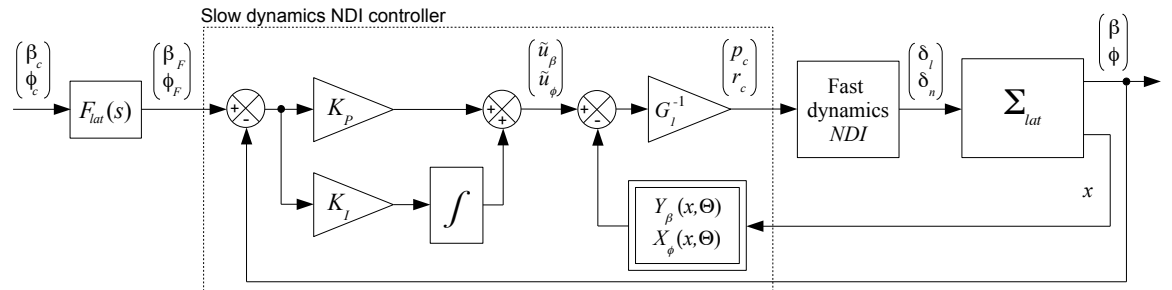
Figure 4.4: NDI-PI controller structure for the lateral model.

To obtain a more compact expression of this controller, a measurement vector $\tilde{y}$ can be proposed by regrouping: the setpoint filter states β_F and ϕ_F, the integral of the error signals ε_β and ε_ϕ, and the longitudinal model state $x = \begin{bmatrix} \beta & \phi & p & r \end{bmatrix}^T$; along with a controller exogenous input vector w regrouping the nonlinear functions Y_β, X_ϕ, L_p and N_r. The expression of this NDI-PI solution can be written as:

$$\begin{bmatrix} \delta_l \\ \delta_n \end{bmatrix} = G_2^{-1}(K\,\tilde{y} + H\,w) \tag{4.35}$$

where

$$K = \begin{bmatrix} \tilde{T}\,K_P & \tilde{T}\,K_I & -T \end{bmatrix} \tag{4.36}$$

$$H = \begin{bmatrix} -\tilde{T} & -I \end{bmatrix} \tag{4.37}$$

considering that

$$\tilde{T} = T\,G_1^{-1} \tag{4.38}$$

and given the previously described vectors

$$\tilde{y} = \begin{bmatrix} \varepsilon_\beta & \varepsilon_\phi & \int \varepsilon_\beta & \int \varepsilon_\phi & p & r \end{bmatrix}^T \tag{4.39}$$

$$w = \begin{bmatrix} Y_\beta & X_\phi & L_p & N_r \end{bmatrix}^T \tag{4.40}$$

Under this simplified expression, the static gain matrix K regulates the outer-loop linear dynamics while the inner-loop static gain matrix H is charged of eliminating the lateral model nonlinear dynamics.

4.2 Multi-channel NLC-$\mathcal{H}_\infty$ design reformulations

The reformulation of the standard NDI approach to our NLC framework introduced in Section 2.2, will be now explained for the attitude control objectives of an air vehicle. Multi-channel design-oriented models will be deduced for the longitudinal and lateral dynamics considering an actuator model.

For the design procedure of nominal robust controllers, let us temporarily consider the following assumption:

Assumption 4.6 *The actuator dynamics of the air vehicle control surfaces can be closely modelled by a first-order system and this dynamics has unlimited magnitude and rate capacities.*

4.2.1 Longitudinal design-oriented model

Now, let us demonstrate how a NLC-$\mathcal{H}_\infty$ controller $K_{long}(s)$ can be designed to follow a second-order reference model $R_{long}(s)$ while rejecting the system nonlinearities contained in the longitudinal model.

In the context of the formulation proposed in Chapter 2, the nonlinear dynamics of both, the angle-of-attack α and of the pitch rate q are now considered as *measured disturbances $w(x,\Theta)$* that

can be exploited for controller synthesis. The longitudinal model represented in equation (4.1) can be represented by the compact expression

$$\Sigma_{long} : \begin{cases} \dot{\alpha} &=& w_\alpha + q \\ \dot{q} &=& w_q + \lambda_q\,\delta_m \end{cases}$$

where, taken from the model in Section 4.1.1,

$$\begin{array}{rcl} w_\alpha &=& Z_\alpha(x,\Theta) \\ w_q &=& M_q(x,\Theta) \\ \lambda_q &=& g_q(x,\Theta) \end{array}$$

As explained in Section 2.1, in order to reduce the size of the signals entering the controller via the exogenous inputs, one should extract as much linear information from these measured disturbances $w(x,\Theta)$ as possible.

By fixing the flight conditions of the varying parameter vector Θ, linear approximations of the measured disturbances $w(x,\Theta)$ can be obtained straight from classic modelling in linear flight control about the trimmed conditions $(\bar{\alpha}, \bar{\delta}_m)$ such as:

$$\hat{w}_\alpha = z_\alpha\,\tilde{\alpha} \tag{4.41}$$

$$\hat{w}_q = m_\alpha\,\tilde{\alpha} + m_q\,q \tag{4.42}$$

with $\tilde{\alpha} = \alpha - \bar{\alpha}$. These approximations can now be included as part of the longitudinal model linear dynamics by subtracting them from $w(x,\Theta)$, thus helping reduce the size of the measured disturbances to be rejected by the controller.

$$\hat{f}_\alpha = w_\alpha - z_\alpha\,\tilde{\alpha} \tag{4.43}$$

$$\hat{f}_q = w_q - m_\alpha\,\tilde{\alpha} - m_q\,q \tag{4.44}$$

Using the above approximations, the longitudinal model along with the angular objective z can be expressed with the generalized NLC framework proposed in Section 2.2, under the nonlinear form

$$\Sigma_{long}(s) : \begin{cases} \dot{\tilde{x}} &=& \begin{bmatrix} z_\alpha & 1 \\ m_\alpha & m_q \end{bmatrix} \tilde{x} + B_1 \begin{bmatrix} f_\alpha \\ f_q \end{bmatrix} + B_2\,\lambda_q\,\delta_m \\ \\ z &=& \begin{bmatrix} 1 & 0 \end{bmatrix} \tilde{x} \end{cases} \tag{4.45}$$

with

$$\tilde{x} = \begin{bmatrix} \tilde{\alpha} & q \end{bmatrix}^T$$

$$B_1 = \begin{bmatrix} 1 & 0 \\ 0 & 1 \end{bmatrix}, \qquad B_2 = \begin{bmatrix} 0 \\ 1 \end{bmatrix}$$

$$f_\alpha = \hat{f}_\alpha + w_{f_\alpha}, \qquad f_q = \hat{f}_q + w_{f_q}$$

Remark 4.7 *Even though the time-scaling separation assumption is still implicitly considered, the system is no longer separated into two sub-systems since the controller synthesis will be done in one single step through an $\mathcal{H}_\infty$ optimization approach.*

Now, retake the simplification described in Section 2.3, where the scaled inputs $\tilde{u} = \Lambda(x, \Theta)u$ and $\tilde{u}_c = \Lambda(x, \Theta)u_c$ are used in the multi-channel design-oriented model and its respective standard form. Then,

$$\tilde{\delta}_m = \lambda_q\, \delta_m, \qquad \tilde{\delta}_{m_c} = \lambda_q\, \delta_{m_c} \tag{4.46}$$

Based on the actuator dynamics defined in Appendix D.2.2 for the control surfaces δ_{real}, consider the following first-order actuator model for controller design:

$$\Sigma_A(s): \ \dot{\tilde{\delta}}_m = \frac{1}{\tau_a}(\tilde{\delta}_{m_c} - \tilde{\delta}_m) \tag{4.47}$$

To help improve the performance of the controller vis-a-vis the overshoot in the time response of the closed-loop system, the design-oriented model can include the setpoint filtered signal α_F considered for the standard NDI design. Then, the filter $F_{long}(s)$ introduced in equation (4.11) can be kept as part of the control system structure.

Once these considerations concerning the actuator model and filtered setpoint signal have been made, the multi-channel reformulation of our NLC approach can be represented by the control design scheme of Figure 4.5. From this figure, the control law that can ensure the reference model tracking while rejecting the system nonlinearities along with any modelling errors can be expressed as:

$$\delta_{m_c} = \lambda_q^{-1}\, K_{long}(s)\, \tilde{y} \tag{4.48}$$

with $\ \tilde{y} = \begin{bmatrix} \hat{f}_\alpha & \hat{f}_q & \alpha_c & \tilde{\alpha} & q \end{bmatrix}^T$.
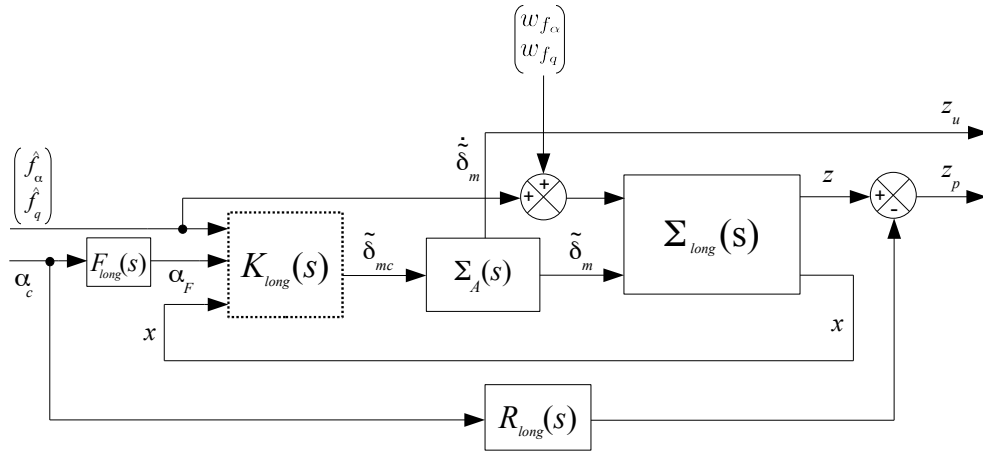
Figure 4.5: Multi-channel $\mathcal{H}_\infty$ design-oriented model I for longitudinal dynamics.

To avoid the use of weighting filters $W(s)$ to ensure the tracking of the target α_c, an artificial signal containing an integral term of the tracking error $\varepsilon_\alpha = \alpha_F - \tilde{\alpha}$ can be created and added as part of the input vector $\tilde{y}$ of the NLC-$\mathcal{H}_\infty$ controller $K_{long}(s)$.

As mentioned in Section 2.3 (see page 51), to better exploit the extra degrees-of-freedom offered by higher-order robust controllers one should try to make available as much information possible

about the system to the controller. Therefore, let us propose a new input vector $\tilde{y}$ for $K_{long}(s)$ including the following signals:

$$\tilde{y} = \begin{bmatrix} \hat{f}_\alpha & \hat{f}_q & \int \varepsilon_\alpha & \alpha_F & \alpha_c & \tilde{\alpha} & q \end{bmatrix}^T \tag{4.49}$$

The resulting multi-channel $\mathcal{H}_\infty$ design-oriented model for nonlinear compensation is depicted on Figure 4.6.
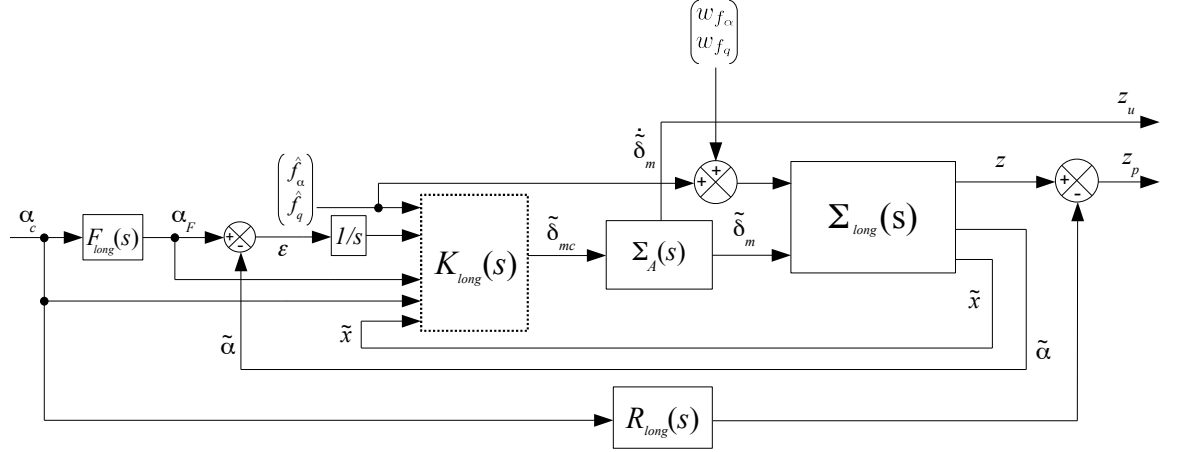
Figure 4.6: Multi-channel $\mathcal{H}_\infty$ design-oriented model II for longitudinal dynamics.

The respective standard form, which will be used for controller synthesis, is represents by the block diagram of Figure 4.7
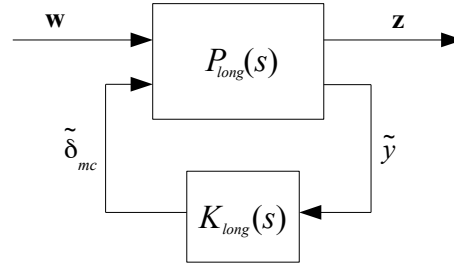
Figure 4.7: Standard form of the multi-channel $\mathcal{H}_\infty$ design for longitudinal dynamics.

where
– $\mathbf{w} = \begin{bmatrix} w_{f_\alpha} & w_{f_q} & \hat{f}_\alpha & \hat{f}_q & \alpha_c \end{bmatrix}^T$ is the exogenous input vector;
– $\mathbf{z} = \begin{bmatrix} z_u & z_p \end{bmatrix}^T$ is the weighted output vector.

4.2.2 Lateral design-oriented model

Now, an NLC-$\mathcal{H}_\infty$ controller $K_{lat}(s)$ will be designed to follow a second-order reference model $R_{lat}(s)$ while rejecting the system nonlinearities contained in the lateral model of an air vehicle. In

this case, the reference model contains the desired dynamics of both, the side-slip angle objective β and of the roll objective ϕ.

The nonlinear dynamics of the lateral model are now considered measured disturbances $w(x, \Theta)$ that can be exploited for controller synthesis, according to our NLC framework. The lateral model presented in equation (4.18) can then be represented by the compact expression

$$\Sigma_{lat} : \quad \begin{bmatrix} \dot{\beta} \\ \dot{\phi} \\ p \\ r \end{bmatrix} = \begin{bmatrix} w_\beta \\ w_\phi \\ w_p \\ w_r \end{bmatrix} + \begin{bmatrix} G & \mathbf{0} \\ \mathbf{0} & \Lambda \end{bmatrix} \begin{bmatrix} p \\ r \\ \delta_l \\ \delta_n \end{bmatrix}$$

where, taken from the lateral standard model in Section 4.1.2,

$$\begin{array}{ll} w_\beta = Y_\beta(x, \Theta), & w_\phi = X_\phi(x, \Theta) \\ w_p = L_p(x, \Theta), & w_r = N_r(x, \Theta) \\ G = G_1(x, \Theta), & \Lambda = G_2(x, \Theta) \end{array}$$

In order to minimize the size of the measured disturbances, let us extract linear approximations that are standard in modelling for linear flight control. By fixing specific flight conditions of the varying parameter vector Θ, linear approximations of $w(x, \Theta)$ can be modelled as:

$$\hat{w}_\beta = y_\beta\,\beta \tag{4.50}$$

$$\hat{w}_p = l_\beta\,\beta + l_p\,p + l_r\,r \tag{4.51}$$

$$\hat{w}_r = n_\beta\,\beta + n_p\,p + n_r\,r \tag{4.52}$$

As a matter of fact, the dynamics equation of the roll ϕ does not present any suitable linear terms that could be use in this case. The above approximations of the measured disturbances can now be associated to the linear dynamics of the lateral model by subtracting them from $w(x, \Theta)$, thus helping reduce the size of the measured disturbances to be rejected by the controller.

$$\hat{f}_\beta = w_\beta - y_\beta\,\beta \tag{4.53}$$

$$\hat{f}_p = w_p - l_\beta\,\beta - l_p\,p - l_r\,r \tag{4.54}$$

$$\hat{f}_r = w_r - n_\beta\,\beta - n_p\,p - n_r\,r \tag{4.55}$$

$$\tag{4.56}$$

Using the above approximations, the re-modelled lateral dynamics, along with its control objective z, can be expressed using our generalized linear oriented framework under the nonlinear form

$$\Sigma_{lat}(s) : \begin{cases} \dot{x} = \begin{bmatrix} y_\beta & 0 & \sin\alpha & -\cos\alpha \\ 0 & 0 & 1 & 0 \\ l_\beta & 0 & l_p & l_r \\ n_\beta & 0 & n_p & n_r \end{bmatrix} x + B_1 \begin{bmatrix} f_\beta \\ f_\phi \\ f_p \\ f_r \end{bmatrix} + B_2\,\Lambda \begin{bmatrix} \delta_l \\ \delta_n \end{bmatrix} \\[3em] z = \begin{bmatrix} 1 & 0 & 0 & 0 \\ 0 & 1 & 0 & 0 \end{bmatrix} x \end{cases} \tag{4.57}$$

with

$$x = \begin{bmatrix} \beta & \phi & p & r \end{bmatrix}^T$$

$$B_1 = \begin{bmatrix} 1 & 0 & 0 & 0 \\ 0 & 1 & 0 & 0 \\ 0 & 0 & 1 & 0 \\ 0 & 0 & 0 & 1 \end{bmatrix}, \qquad B_2 = \begin{bmatrix} 0 & 0 \\ 0 & 0 \\ 1 & 0 \\ 0 & 1 \end{bmatrix}$$

$$f_\beta = \hat{f}_\beta + w_{f_\beta}, \qquad f_\phi = \hat{f}_\phi + w_{f_\phi}$$

$$f_p = \hat{f}_p + w_{f_p}, \qquad f_r = \hat{f}_r + w_{f_r}$$

Notice that also in the lateral case, the time-scaling separation assumption is implicitly considered but the system is not separated into two sub-systems since the controller synthesis will be done in one single step through an $\mathcal{H}_\infty$ optimization approach.

For controller synthesis using our multi-channel design-oriented model, the following simplification of the input controls is retained:

$$\begin{bmatrix} \tilde{\delta}_l \\ \tilde{\delta}_n \end{bmatrix} = \Lambda \begin{bmatrix} \delta_l \\ \delta_n \end{bmatrix}, \qquad \begin{bmatrix} \tilde{\delta}_{l_c} \\ \tilde{\delta}_{n_c} \end{bmatrix} = \Lambda \begin{bmatrix} \delta_{l_c} \\ \delta_{n_c} \end{bmatrix} \tag{4.58}$$

Consider the following first-order actuator model associated to the scaled controls defined above for controller design:

$$\Sigma_A(s): \quad \dot{\tilde{\delta}} = \tau_a^{-1}(\tilde{\delta}_c - \tilde{\delta}) \tag{4.59}$$

with

$$\tilde{\delta} = \begin{bmatrix} \tilde{\delta}_l & \tilde{\delta}_n \end{bmatrix}^T, \qquad \tilde{\delta}_c = \begin{bmatrix} \tilde{\delta}_{l_c} & \tilde{\delta}_{n_c} \end{bmatrix}^T$$

and

$$\tau_a = diag(\tau_{a_l}, \tau_{a_n})$$

To add as much information possible to the controller, consider the setpoint filter $F_{lat}(s)$ presented in (4.31) to help improve the controller performance and the artificial signals containing the integral of the tracking errors $\varepsilon_\beta = \beta_F - \beta$ and $\varepsilon_\phi = \phi_F - \phi$ that will ensure the convergence of the angular objective z to the target z_c, as part of the input vector $\tilde{y}$.

After having made the pertinent considerations on the actuator model and the controller input vector $\tilde{y}$, the resulting multi-channel $\mathcal{H}_\infty$ design-oriented model for nonlinear compensation is illustrated on Figure 4.8.

The control law that ensures a reference model tracking while rejecting the lateral model nonlinearities along with any modelling errors can be expressed as:

$$\begin{bmatrix} \delta_{l_c} \\ \delta_{n_c} \end{bmatrix} = \Lambda^{-1} \, K_{lat}(s) \, \tilde{y} \tag{4.60}$$

with

$$\tilde{y} = \begin{bmatrix} \hat{f}_\beta & \hat{f}_\phi & \hat{f}_p & \hat{f}_r & \int \varepsilon_\beta & \int \varepsilon_\phi & \beta_F & \phi_F & \beta_c & \phi_c & \beta & \phi & p & r \end{bmatrix}^T \tag{4.61}$$
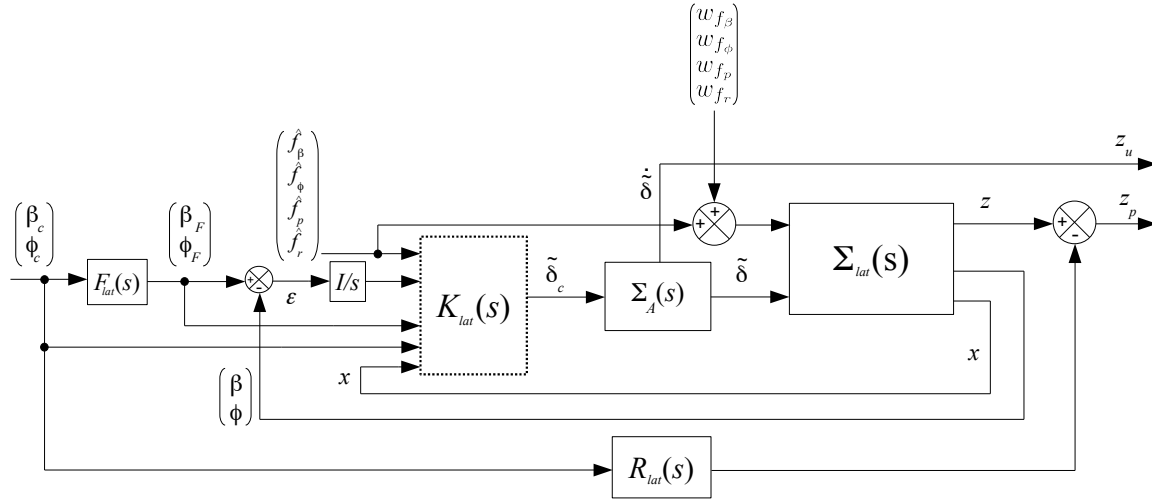
Figure 4.8: Multi-channel $\mathcal{H}_\infty$ design-oriented model for lateral dynamics.

It is now only a matter of proposing the right the weighting filters $W(s)$ that will shape the frequency domain characteristics of the exogenous inputs and the weighted outputs.

Once the weighting filters have been defined according to the performance requirements and integrated to the design-oriented model, the associated standard form that will be used for controller synthesis is represents by the block diagram of Figure 4.9.
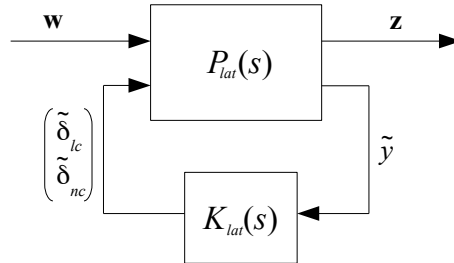
Figure 4.9: Standard form of the multi-channel $\mathcal{H}_\infty$ design for lateral dynamics.

where
– $\mathbf{w} = \begin{bmatrix} w_{f_\beta} & w_{f_\phi} & w_{f_p} & w_{f_r} & \hat{f}_\beta & \hat{f}_\phi & \hat{f}_p & \hat{f}_r & \beta_c & \phi_c \end{bmatrix}^T$ is the exogenous input vector;
– $\mathbf{z} = \begin{bmatrix} z_u & z_p \end{bmatrix}^T$ is the weighted output vector.

4.3 Anti-windup enhancement

As previously discussed, the anti-windup control loop is charged of enlarging the stability domain of the closed loop in presence of input saturation. The controller $J(s)$ is therefore restrained to assuring stability constraints that can be formulated also through the small gain theorem. The

resulting design-oriented model will be presented in a general from which can be applied to both, the longitudinal and lateral nominal controllers K previously obtained.

Strong assumptions have been made concerning the actuator models. In the standard NDI design procedure, the actuator dynamics are basically neglected through assumption 4.4 since they cannot be accounted for directly in controller synthesis.

An improved controller synthesis scheme is presented by our generalized NLC framework, where the actuator dynamics form part of the design-oriented model, thus allowing for a less restrictive assumption. A fist order dynamic model of the actuator was used considering the scaled signals

$$\tilde{\delta} = \Lambda \delta, \qquad \tilde{\delta}_c = \Lambda \, \delta_c$$

In this section, the particular assumption 4.6 concerning the limits of the actuator dynamics can be discarded. A realistic actuator model accounting for first-order dynamics along with rate and magnitude saturations can now considered.

As explained in Section 2.4.1 (see page 2.4.1), let us use a control limiter structure over $K(s)$. Since the more restrictive constraints correspond to the rate limitations of the actuators, a *rate limiter* is added to the nominal controller $K(s)$.

Consider a first-order rate limiter that ensures the nominal unconstrained behavior of the actuators δ_{real}. Using the operator $sat(\cdot)$, this structure of maximum scaled rate $\tilde{L} = \Lambda \, L$ can be expressed as:

$$\Sigma_{RL}: \qquad \dot{\tilde{\delta}}_{c_L} = sat_{\tilde{L}}\left(\frac{1}{\tau_L}(\tilde{\delta}_c - \tilde{\delta}_{c_L})\right) \tag{4.62}$$

where $\tilde{\delta}_c$ is the unconstrained control signal and $\tau_L = diag(\tau_{L_1}, \ldots, \tau_{L_m})$ is the time constant of the rate limiter. To avoid interactions with the actuator dynamics, thus guaranteeing its nominal behavior, the rate limiter dynamics should be chosen sufficiently faster than the actuator dynamics $\tau_L << \tau_a$.

The saturation included in the rate limiter can be used to generate the input of the anti-windup controller by following the design-oriented model depicted on Figure 4.10.

The measurements of the error ε and its integral, used for the synthesis of the nominal controller, are now included as part of the internal structure of $K(s)$. The nominal control law structure is now augmented by the anti-windup controller to help enhance the closed-loop stability domain. By expressing $K(s)$ using the state-space equation

$$K(s): \left\{ \begin{array}{rcl} \dot{x}_K & = & A_K \, x_K + B_K \, \tilde{y} \\ \tilde{\delta}_c & = & C_K \, x_K \end{array} \right.$$

under the Direct Linear Anti-windup strategy illustrated on Figure 4.10 (see page 100), the structure of the augmented controller becomes

$$K_a(s): \left\{ \begin{array}{rcl} \dot{x}_K & = & A_K \, x_K + B_K \, \tilde{y} + v_1 \\ \tilde{\delta}_c & = & C_K \, x_K \end{array} \right. \tag{4.63}$$

Given the anti-windup controller

$$\begin{bmatrix} v_1 \\ v_2 \end{bmatrix} = J(s) \, u_{AW} \tag{4.64}$$

the enhanced robust control law takes the form:

$$\delta_c = \Lambda^{-1}(x,\Theta)\ K_a(s)\ \tilde{y} + v_2 \tag{4.65}$$

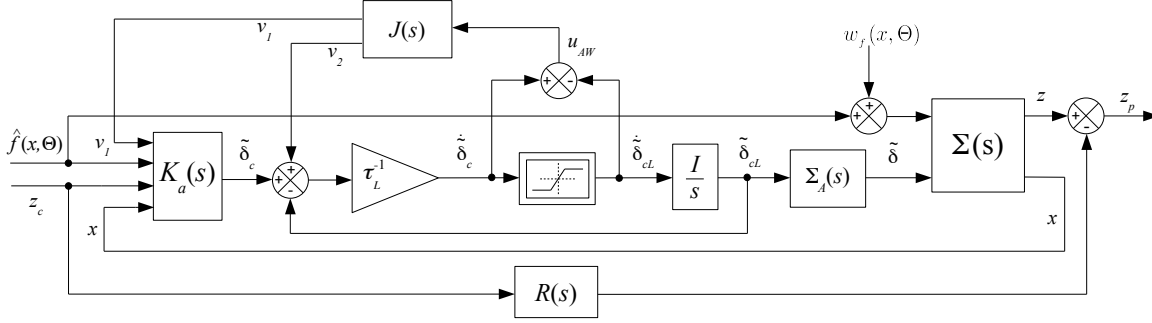with $\tilde{y} = \begin{bmatrix} v_1 & \hat{f}(x,\Theta) & z_c & x \end{bmatrix}^T$.

Figure 4.10: Anti-windup control scheme with rate limiter.

The anti-windup controller input u_{AW} can be expressed as a measurement of the rate-limited control signal $\dot{\tilde{\delta}}_{c_L}$ disturbed by a dead-zone operator $\varphi(\cdot)$. From this consideration about u_{AW}, it comes that

$$\dot{\tilde{\delta}}_{c_L} = \dot{\tilde{\delta}}_c - u_{AW} \tag{4.66}$$

Besides increasing the stability of the closed-loop, an additional objective can be included to reduce the impact of the nonlinear disturbance w_φ on z. This can be achieved by creating the exogenous output z_s as shown on the figure above.

The resulting design-oriented model for anti-windup synthesis with controller rate limiter is illustrated on Figure 4.11.
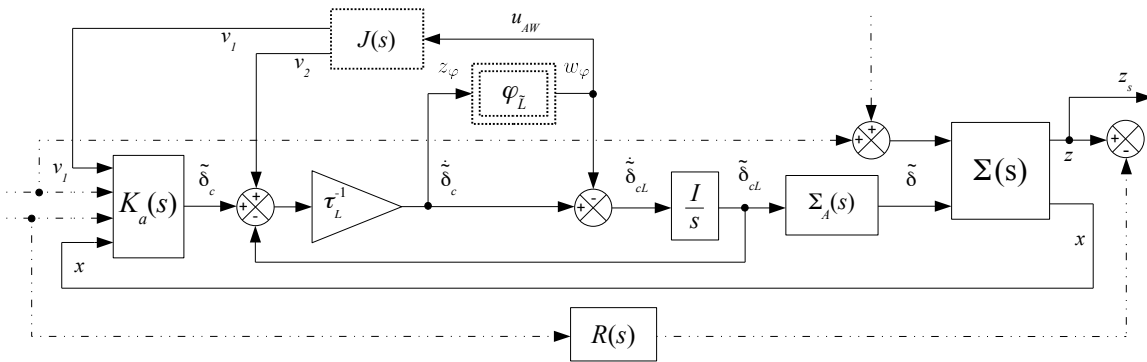
Figure 4.11: Flight control design-oriented scheme with rate limiter and anti-windup correction.

The anti-windup controller $J(s)$ can now be computed through the optimization process described in Section 2.4.2 (see page 59).

Concluding comments

In this chapter, the design procedure of standard NDI laws and generalized NLC controllers for attitude control of an air vehicle were detailed. For clarity of the design procedures, the longitudinal and lateral control objectives were treated separately.

First, the double loop controller structure of baseline NDI design with PI control was presented. In this case, the time-scaling approach was used as part of the control objective modelling. It was also shown how second order stable dynamics can be imposed on the closed loop via the PI controller of the outer loop.

In contrast to the baseline NDI design, in the generalized framework, the control objectives are not required to be modelled as two cascade interconnected sub-systems. Even though the time-scaling assumption is still implicitly considered, the generalized NLC controller can be designed using the model of the control objectives as a whole. Also, the desired dynamics to be imposed on the systems can take the form of higher-order dynamics through a reference model $R(s)$.

Finally, an anti-windup control scheme designed to enhance the generalized nominal NLC controllers was also presented.

Once the design of these generic control laws for the longitudinal and lateral control objectives of air vehicles have been described, in the next chapter, the case of an atmospheric reentry control problem will be addressed.

Chapter 5

An atmospheric reentry control problem

Introduction

Control design for atmospheric reentry vehicles remains a challenging task. Typically, because the flight domain is extremely large, nonlinear and time-varying aspects induce nontrivial issues. Moreover, the flying qualities required in atmospheric reentry missions demand high levels of performance.

In this context, the attitude Control System of a reentry vehicle plays a key role. In early reentry, the attitude protects the vehicle from overheating as the pressure builds up against the *thermal protection system*. Then, the attitude of the vehicle regulates its deceleration as it flies (or glides) down to a landing site safely.

It is in this type of applications that NLC-based approaches show to be powerful design techniques. Several examples of standard NDI implementations to this control problem can be found in the literature [Jou92, IGVW02, DN02, GV03, LRDY07, MCV09].

The main objective of this chapter is to apply the previously described flight control design methodology to an atmospheric reentry vehicle at different points of a possible trajectory.

First, in Section 5.1, a brief introduction to the physical context of an atmospheric reentry mission and the on-board means of a space vehicle to accomplish it is presented.

Then, Section 5.2 contains a general description of the reentry vehicle aerodynamic controls (or control surfaces) governed by the on-board Control System. These controls ultimately allow the vehicle to realize the commanded attitude positions required for the reentry mission while inside the atmosphere.

Finally, the computation and implementation procedures of the final control laws resulting from both approaches are detailed in Section 5.3. After having defined the performance requirements

that the control laws should ensure, the controller designs presented in the previous chapter are computed using desired dynamics which respond to those performance specifications.

Once the flight controllers are synthesized, a robustness and stability analysis will be conducted in the longitudinal case. Further validation of the method is provided by means of a 6 degrees-of-freedom Flight Mechanics simulation using the aerodynamic model of a reentry vehicle. Simulation results of independent manoeuvres for the longitudinal and lateral dynamics are then displayed. A thorough comparison between the baseline NDI controller and the NLC-$\mathcal{H}_\infty$ controller obtained via our generalized framework is also presented.

5.1 Atmospheric reentry physical context

Reentry vehicles are compact and rigid air vehicles that suffer large parameter variations throughout their flight domain. There are two main types of reentry vehicles that have been historically used for manned space exploration: space capsules and delta-wing spacecrafts. On the one hand, space capsules have a simpler aerodynamic profile, [1] without any wings, but with good heat dissipation capacities. On the other hand, delta-wing shaped spacecrafts are re-usable, they have better adapted lift/drag characteristics and more complex aerodynamics.

For this thesis work, a delta-wing reentry vehicle type was considered for simulation, specially due to the nonlinear characteristics involved in the different phases of the mission.

5.1.1 On the mission of a reentry vehicle

The atmospheric reentry mission comprises a wide range of scientific fields such as Space Mechanics, Flight Mechanics, Aerodynamics, Thermodynamics, Trajectography, amongst others, thus making it a very complex application. In the context of a lifting body, the purpose of such mission is to decelerate the gliding flight of the vehicle while directing it to a runway for its landing on Earth. Typically the mission starts with the vehicle at a low orbit around the Earth (between 400 km and 450 km from the Earth's surface) and it continues by re-entering the vehicle into the Earth's atmosphere. The path to follow throughout the reentry is very precise and does not give much margin for error. The consequences of a bad trajectory planning and tracking include:
– bounce the vehicle on the higher layers of atmosphere when the entry angle is too shallow,
– incinerate the vehicle with the heat shock wave produced by the compression of the air layers when the entry angle is too steep or
– land the vehicle in an unanticipated region.

The typical reentry mission of a delta-wing spacecraft can characterized by four main phases [HG79, VF03, VF05, Fal09]:

1. **Descent Orbit phase**. It begins with a manoeuvre made using the thrusters to reduce the vehicle orbital speed allowing it to fall back smoothly to the Earth. The vehicle descends from the initial orbit until contact with the atmosphere, taken conventionally at 120 km of altitude.

---

1. Space capsules are commonly designed as a spherical section with a blunted cone attached, providing good aerodynamic stability.

Using the thrusters, the attitude of the vehicle is positioned in such a way to direct the thermal protection system [2] facing the atmosphere at a very precise angle-of-attack (usually between 30° and 40° depending on the vehicle design).

A good manoeuvre precision is required at this phase to prevent the vehicle from bouncing off the upper layers of the atmosphere or to disintegrate by thermal heating. In fact, a hot sonic boom is produced around the vehicle as it compresses air molecules while entering the atmosphere.

2. **Hypersonic phase**. It begins at 120 km altitude with a flight speed of about $\mathcal{M} \approx 25$ (airspeed $V_a \approx 27000$ km/h).

   The attitude of the vehicle is maintained by steering thrusters early in this phase but as the dynamic pressure rises around the vehicle, it begins a gradual transition from spacecraft to aircraft enabling the use of the vehicle control surfaces.

   The main objective of this phase is to target a predefined point in terms of down-range, cross-range, speed and altitude to begin with the energy dissipation phase known as the Terminal Area Energy Management (TAEM).

3. **Energy Dissipation phase or TAEM**. This phase starts when the speed of the vehicle decreases conventionally to $\mathcal{M} = 2$. During this phase, the vehicle performs 'S' manoeuvres or banking turns to dissipate the remaining kinetic energy until it reaches a predefined point in terms of altitude, speed and the distance to the runway position called NEP (nominal exit point).

   The NEP is reached when the vehicle is aligned with the runway after following a circular profile defined as the Horizontal Alignment Cylinder (HAC) and starts dropping its altitude.

4. **Approach and Landing phase**. Once aligned with the runway, the vehicle begins a steep approach. This approach is fixed for different vehicles on the order of $\gamma = -16.5°$ to $\gamma = -15°$. Finally, a rounding manoeuvre is performed following a parabolic trajectory thus reducing significantly the speed and angle of decent before posing the landing gear on the runway. The angle of descent of this last manoeuvre, commonly $\gamma \leq -1.5°$, chosen in order to facilitate touchdown. However, as this value is far from the approach angle, it can only be maintained for a short time.

5.1.2 Automatic on-board systems: Guidance, Navigation and Control

To accomplish its mission, the reentry vehicle is equipped with 3 main systems. These systems are interconnected with a given architecture allowing the vehicle to determine its desired trajectory path, its actual point on the trajectory and how to enforce the desired trajectory path with specific performance requirements.

1. The Navigation system is in charge of determining the instantaneous speed, position and attitude of the vehicle. The measurement of the vehicle state is usually done using redundant systems to improve accuracy and avoid isolated system failure.

---

2. The thermal protection system (TPS) of a delta-wing spacecraft is usually based on carbon materials and silica ceramics capable of absorbing large amounts of heat without increasing much their temperature. These materials can withstand temperatures of over $1600°C$ during this phase and can be re-used.

The Inertial Measurement Unit (IMU) is the most common sensor used to determine the reentry vehicle state. This unit uses accelerometers which can measure acceleration in all axis and gyroscopes to determine the rotation rate. From this basic measurements, the IMU provides by integration a measure of the position and attitude.

As IMU measurements have a tendency to drift from the actual values due deterministic and random phenomenon, error correction can be provided by telemetry, GPS, radar, optical celestial navigation and other navigation aids via communication systems when outside of the blackout part of the reentry trajectory. Kalman filters provide a practical approach to combining navigation data from multiple sensors to resolve the current state of a vehicle.

2. The Guidance system uses the information made available by the Navigation system to compute the desired trajectory path in terms of specific parameters that can be physically controlled by the vehicle via its actuators.

   In the context of atmospheric reentry, the Guidance system uses a pre-defined entry corridor to define the trajectory based on two profiles: the altitude vs. speed profile and the attack angle vs. speed profile. By substituting the altitude by the drag acceleration, it can be proved that the trajectory is completely determined by these two profiles, from which the aerodynamic bank-angle commands that the vehicle must follow are generated [HG79]. To maintain or recover the nominal path targeted, corrections to the drag acceleration profile are done on-line mainly by determining the remaining nominal distance and the actual distance to the landing site.

3. Finally, the Control system is responsible of tracking the Guidance system commands to keep the vehicle on the desired trajectory while assuring the global system stability and performance. It uses the measurements from the IMU and the commands of the Guidance system to generate control signals to activate the different actuators (either aerodynamic control surfaces or thrusters) of the vehicle as required. **This thesis is focused on the design of such control laws that build this last system**.

For many reasons, control design for reentry vehicles still remains a challenging task. Typically, because the flight domain is extremely large, nonlinear and time-varying aspects induce non-trivial issues for guaranteeing the system stability and performance.

5.2   From control surfaces to forces and moments

The type of reentry vehicle considered for this thesis work, uses a combination of control surfaces to direct the airflow around the vehicle. Changes in the airflow direction produces moments about the vehicle center of gravity and ultimately have an effect on different parameters for attitude control. At the same time, these control surfaces are activated by means of actuators.

Modelling the interactions between these as the input of the reentry vehicle dynamic model is of great importance. Let us elaborate on some key points from a system modelling perspective.

5.2.1 Generating aerodynamic forces and moments

Depending on the vehicle design, a number of control surfaces are available to control its motion. The deflection of this control surfaces is denoted δ. The control system of the reentry vehicle is in charge of generating suitable signals or deflection commands δ for these control surfaces in order to modulate specific parameters of the vehicle.

For example, to modulate the lift force, the vehicle has to produce a pitch moment M to induce changes on the angle-of-attack α. To achieve this effect, most delta-wing shaped vehicles have two symmetrically placed control surfaces on the back-end called elevons. The deflection of these surfaces is denoted by δ_{re} for the right elevon, and δ_{le} for the left elevon.

Elevons are also used to generate roll moment L, which means that the elevator and aileron effects of a traditional aircraft are concentrated all together in these control surfaces.

In addition to the elevons, a body flap is integrated for trimming or to create extra pitch moment at some specific flight conditions. The body flap is denoted δ_{bf}.

To modulate the lateral force, a yaw moment N is needed to induce changes on the side-slip angle β. The type of vehicles considered commonly dispose of two vertical wing flaps or winglets. The deflection of the winglets is denoted δ_{rw} for the right winglet, and δ_{lw} for the left winglet. Although, they are mainly used to produce yaw, these winglets can also be used to produce a small amount of pitch moment if necessary.

It may be added that the reentry vehicle also disposes of air-brake surfaces but these are not useful for attitude control.

From the control surface display, one can create the independent control signals δ_l, δ_m and δ_n that represent the global effects of the control surfaces on each body axis. As seen in Section 3.2, these pseudo-controls are typically used to compute aerodynamic models and allow to distribute or allocate the control signals onto each real control surface. The general expression of such allocation for the described control surfaces can be written as:

$$\delta_{real} = \mathcal{G}\,\delta_{pseudo} \tag{5.1}$$

where

$$\delta_{real} = \begin{bmatrix} \delta_{le} & \delta_{re} & \delta_{bf} & \delta_{lw} & \delta_{rw} \end{bmatrix}^T \tag{5.2}$$

$$\delta_{pseudo} = \begin{bmatrix} \delta_l & \delta_m & \delta_n \end{bmatrix}^T \tag{5.3}$$

The term $\mathcal{G}$ can be considered as a constant matrix that distributes the independent control signals δ_{pseudo} to the actual control surfaces δ_{real} with specific weighting values, or it can be considered as time function usually dependent on the state $\mathcal{G}(t, x)$ for dynamic allocation.

5.2.2 Choosing an allocation strategy

Any allocation strategy to compute $\mathcal{G}$ can be seen as an optimization of the control surface efficiency. In fact, it is intended to obtain the maximum efficiency from the control surfaces at the

lowest deflection by combination of all the surfaces. Specific choices for allocation of efforts on the control surfaces of a reentry vehicle are based on the geometry of the vehicle and the placement of the control surfaces.

The allocation of δ_l and δ_m onto the real control surfaces δ_{re}, δ_{le} and δ_{bf} can be separated into: a decoupling strategy of the longitudinal effects and the roll lateral effects, and an *a priori* optimized function.

In the case of the elevons, a simple mechanical mixer strategy is commonly used. The latter allows to decouple the effects of these control surfaces on the axis x and y of the reentry vehicle. The symmetric deflection δ_m of the elevons has an effect longitudinal motion (on the y axis), whereas their anti-symmetric deflection δ_l affects the roll lateral motion (on the x axis). Then,

$$
\begin{array}{rcl}
\delta_{le} & = & \delta_m - \delta_l \\
\delta_{re} & = & \delta_m + \delta_l
\end{array}
\tag{5.4}
$$

The body flap δ_{bf} can be used as a trim tab to ease the efforts of the elevons at different operating points. Generally, δ_{bf} is a function of the pitch axis control δ_m and other system parameters Θ or states x such as

$$
\delta_{bf} = f_{\delta_{bf}}(\delta_m, \Theta, x)
\tag{5.5}
$$

The function $f_{\delta_{bf}}$ can be defined, for example, in the form of a data table as a function of the Mach number $\mathcal{M}$, the control signal δ_m and other parameters.

Finally, the allocation of the winglets is mainly determined by the vehicle geometry and the placement of the winglets with respect to the center of gravity. The choice for the allocation is commonly a constant relation with the control δ_n. This can be expressed in general as:

$$
\begin{array}{rcl}
\delta_{lw} & = & f_{\delta_{lw}}(\delta_n) \\
\delta_{rw} & = & f_{\delta_{rw}}(\delta_n)
\end{array}
\tag{5.6}
$$

An allocation example of the winglet control surfaces can be found in Appendix D.2.2.

Different allocation strategies can also be used depending on the control requirements to comply with. More sophisticated allocation methods can be employed to, for example: optimize the total distribution of efforts on all control surfaces [ODB06], or to minimize all control surface activity and thus preventing premature actuator saturation [Zac09].

Such allocation strategies are supposed to be determined *a priori* before synthesis of the following flight control laws.

5.3   Implementation of control laws and results

To develop how the implementation of the baseline NDI controllers and the generalized NLC controllers takes place, it is first necessary to establish the performance specifications of the control objectives that the control laws should comply with. To have a clear view of the specifications, which are usually defined in the frequency domain, it is practical to set these requirements as time

domain characteristics such as: rise time t_r, settling time t_s and maximum overshoot to a step response.

Once the performance specifications have been set and analysed, the controller computation process will be described. First, different values of the NDI-PI controller will be computed based on the same desired dynamics by adjusting the tuning parameters.

Then, starting from one of these NDI-PI controllers, a set of robust controllers will be computed using our generalized NLC framework which accounts for actuator dynamics. As some results become unsatisfactory in presence of magnitude and rate saturations of the actuators, anti-windup controllers will be synthesized to enhance the stability of the nominal NLC-$\mathcal{H}_\infty$ controllers previously computed.

The implementation of the nonlinear control laws to the reentry vehicle will be done at different flight conditions representative of the mission flight domain. This set of flight conditions is contained in Table 5.1 and defined mainly by the altitude h and Mach number $\mathcal{M}$, for which the trim conditions $\bar{\alpha}$ and $\bar{\delta}_m$ of the reentry vehicle nominal model are computed.

	Flight point				**Trim values**	
nº	h (m)	$\mathcal{M}$	$\bar{q}$ (Pa)	γ (º)	$\bar{\alpha}$ (º)	$\bar{\delta}_m$ (º)
1	68 500	20	1 639	-0.3	33	2.08
2	54 500	11	3 615	-0.5	33	1.86
3	48 000	8	4 379	-1.5	28	5.43
4	38 000	5	6 395	-2.5	24	5.78
5	25 000	2.5	10 986	-5	16	1.78
6	10 000	0.8	11 843	-10	10	-4.89
7	5 000	0.6	13 613	-15	7	-7.59
8	0	0.3	6 383	-16	10	-5.99

Table 5.1: Flight points considered in simulation with associated trimmed flight conditions.

To highlight the benefits of our NLC framework, a comparison of the obtained simulation results with both solutions will be developed for the reentry vehicle attitude control problem considering modelling errors. In order to simplify the reading of this section, a selection of relevant flight points will be made which helps emphasise the attributes of both, the NDI controllers and the generalized NLC controllers. A more extensive compilation of the simulation results, using the computed controllers at all considered flight points, can be found in Appendix E (see page 263).

Finally, simulation results of the closed-loop system under external environmental factors like static wind gusts and turbulent wind will be presented to validate the proposed methodology.

Let us now detail the controller computation procedure by first considering the longitudinal dynamics of the reentry vehicle.

5.3.1 Longitudinal axis

Recall that the control objective of the longitudinal dynamics is the angle-of-attack α, which is a parameter of the utmost importance in the atmospheric reentry of a space vehicle. As previously mentioned, the performance requirements have to be set and analysed first.

The performance specifications of the time response on the angle-of-attack α can be regrouped in a bounded normalized area as will be detailed next.

5.3.1.1 Performance specification on angle-of-attack

Consider the normalized bounded region on Figure 5.1 as an example of the attitude control performance specification for the angle-of-attack α in an atmospheric reentry mission.

The lower bounds of this performance specification accounts for the rise time t_r and the settling time t_s as a function of the Mach number $\mathcal{M}$, while the upper bound fixes the maximum overshoot of the time response. The static regime accuracy of the angle-of-attack α is also enclosed by both, upper and lower bounds. Two main characteristics can be pointed-out from this specification.
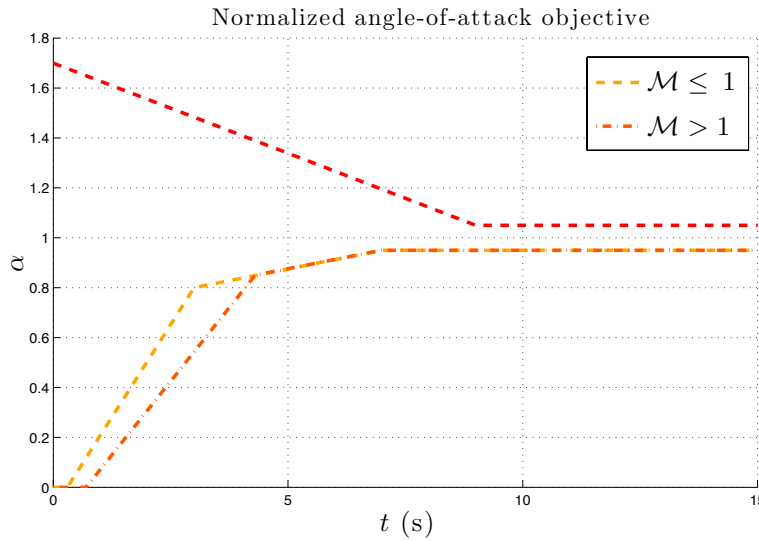
Figure 5.1: Performance specification on the angle-of-attack α.

The first remark that can be made is that at higher Mach numbers, the lower bound is less restrictive than that at lower Mach numbers. This is explained directly from the reentry mission altitude vs. speed profile where the vehicle has higher speeds at higher altitudes and lower speeds at lower altitudes.

Since the dynamic pressure $\bar{q}$ is lower at higher altitudes, the attitude dynamics are slower, whereas these dynamics are faster at lower altitudes where the atmosphere is denser and the dynamic pressure greater. As a result, a faster time response on the angle-of-attack α is expected at slower

Mach numbers than at higher Mach numbers.

The next remark that can be made about the performance specification bounds is that they allow for second-order dynamics or higher. In this case, second-order dynamics will be defined for the baseline NDI controller design as well as for the reference model $R_{long}(s)$ of our NLC framework. Clearly, to stay within the boundaries, a reduced range of desired dynamics can be chosen.

To guide the choice of the desired dynamics to comply with the performance specifications, consider the following:
– To avoid having excessive overshoot, the desired dynamics must be well damped. A damping coefficient $\xi_\alpha \geq 0.7$ should be chosen to this effect, thus remaining below the upper bound of Figure 5.1.
– The rise time t_r and settling time t_s are mainly affected by the cut-off frequency ω_{c_α} of the desired dynamics. In this case, it can be deduced by observation that the settling time is of about $t_s \approx 6.5\,s$ and it is the same for both lower bounds ($\mathcal{M} \leq 1$ and $\mathcal{M} > 1$).
As for the rise time, for the yellow bound it can be deduced that $t_r \approx 0.3°/s$, while for orange bound one can estimate $t_r \approx 0.23°/s$. Then, $\omega_{c_\alpha}|_{\mathcal{M} \leq 1} > \omega_{c_\alpha}|_{\mathcal{M} > 1}$.

After having defined the control requirements and characteristics of the dynamic behavior to be followed by the closed-loop system, the computation of control laws will be detailed next.

5.3.1.2 Fixing the NDI-PI controller parameters

Let us now present the control laws obtained using the standard NDI controller design procedure for the longitudinal dynamics of the reentry vehicle. Based on the general control law design detailed in Section 4.1.1 (see page 84), consider the NDI-PI solution expressed in equation (4.13) as:

$$\delta_{m_c} = g_q^{-1}(K\,\tilde{y} + H\,w) \tag{5.7}$$

where

$$K = \begin{bmatrix} \dfrac{k_P}{\tau_q} & \dfrac{k_I}{\tau_q} & \dfrac{-1}{\tau_q} \end{bmatrix} \tag{5.8}$$

$$H = \begin{bmatrix} \dfrac{-1}{\tau_q} & -1 \end{bmatrix} \tag{5.9}$$

and

$$\tilde{y} = \begin{bmatrix} \varepsilon_\alpha & \int \varepsilon_\alpha & q \end{bmatrix}^T \tag{5.10}$$

$$w = \begin{bmatrix} Z_\alpha & M_q \end{bmatrix}^T \tag{5.11}$$

The nonlinear function $g_q^{-1}(x, \Theta)$ is estimated on-line while the gains K and H contain controller parameters that should be fixed based on the control requirements. The vectors $\tilde{y}$ and w are the controller input signals corresponding to system measurements and nonlinear function estimations.

It is now only a matter of choosing the value of the parameters k_P, k_I and τ_q to obtain the final controller expression to be implemented. The values of the static gains k_P and k_I are directly linked to the desired dynamics of the angle-of-attack α to be imposed on the closed-loop system

via the outer loop. From these constants, the value of the setpoint filter $F_{long}(s)$ time constant τ_F is obtained.

A first example of the possible desired dynamics that can be established for the control objective α, along with its associated controller parameters, is presented on Table 5.2.

	Desired dynamics #1		Parameter values		
$\mathcal{M}$	ω_{c_α} (rad/s)	ξ_α	k_P	k_I	τ_F
> 1	0.95	0.7	1.33	0.903	1.47
≤ 1	1.5	0.7	2.10	2.250	0.94

Table 5.2: Choice #1 of the controller parameters defining the desired dynamics for α.

Since the parameters k_P and k_I are fixed to comply with the performance specifications, the truly adjustable controller parameter that allows to improve the closed-loop performance for specific desired dynamics is τ_q. As a matter of fact, the only theoretical restriction that τ_q should abide by is that the value of its inverse τ_q^{-1} must remain sufficiently greater than the fixed cut-off frequency ω_{c_α}, thus respecting the time-scaling assumption.

As the desired dynamics are established as a function of the Mach number, the obtained controller can be considered as a self-scheduled solution which can be easily implemented thanks to the fact that it is composed of static gains. A first choice of τ_q and the resulting NDI controller gains is presented on Table 5.3.

	NDI-PI controller #1		
$\mathcal{M}$	τ_q (s)	K	H
> 1	0.5	$\begin{bmatrix} 2.66 & 1.805 & -2 \end{bmatrix}$	$\begin{bmatrix} -2 & -1 \end{bmatrix}$
≤ 1	0.25	$\begin{bmatrix} 8.4 & 9.000 & -4 \end{bmatrix}$	$\begin{bmatrix} -4 & -1 \end{bmatrix}$

Table 5.3: Definition of the NDI-PI controller #1.

Better results can be obtained by changing the value of the tuning parameter. In general, it will be proved that reducing the value of τ_q tends to improve the closed-loop performance, translated as a better tracking of the set-point and desired dynamics. Still, as the fast subsystem interacts with the actuator dynamics, reducing the value of τ_q also results in an under-damped fast sub-system that creates larger and faster oscillations of the control signal δ_{m_c}, which could lead to premature actuator attrition and even worse, to stability issues in presence of input saturations.

Consider a second NDI controller such as the one presented on Table 5.4, where the values of the tuning parameter have been reduced.

$\mathcal{M}$	τ_q (s)	**NDI-PI controller #2** K	H
> 1	0.25	$\begin{bmatrix} 5.32 & 3.610 & -4 \end{bmatrix}$	$\begin{bmatrix} -4 & -1 \end{bmatrix}$
≤ 1	0.1	$\begin{bmatrix} 21 & 22.50 & -10 \end{bmatrix}$	$\begin{bmatrix} -10 & -1 \end{bmatrix}$

Table 5.4: Definition of the NDI-PI controller #2.

Hoping to improve the tracking of the desired dynamics, one can keep reducing the value of the tuning parameter. Take, for example, the third NDI controller presented on Table 5.5 where lower values of τ_q have been considered.

$\mathcal{M}$	τ_q (s)	**NDI-PI controller #3** K	H
> 1	0.05	$\begin{bmatrix} 13.30 & 9.025 & -10 \end{bmatrix}$	$\begin{bmatrix} -10 & -1 \end{bmatrix}$
≤ 1	0.1	$\begin{bmatrix} 42.00 & 45.00 & -20 \end{bmatrix}$	$\begin{bmatrix} -20 & -1 \end{bmatrix}$

Table 5.5: Definition of the NDI-PI controller #3.

As the tuning parameter τ_q keeps being reduced, it will come to a point where very little or no performance improvement will be perceived, while the control signal will increase its magnitude and start to oscillate.

In presence of input saturations, the reentry vehicle may be destabilized at some points of the flight domain. Specifically in the hypersonic regime, simulation results will show that the three NDI-PI controllers computed above exhibit difficulties to maintain the stability of flight point n°1. Still, one can preserve the stability of this flight point by "relaxing" the choice of the desired dynamics and computing the NDI controller n°4 presented on Table 5.7.

Desired dynamics #2		**Parameter values**		
ω_{c_α} (rad/s)	ξ_α	k_P	k_I	τ_F
0.7	0.7	0.98	0.49	2

Table 5.6: Choice #2 of the controller parameters defining the desired dynamics for α.

τ_q (s)	**NDI-PI controller #4** K	H
0.25	$\begin{bmatrix} 3.92 & 1.96 & -4 \end{bmatrix}$	$\begin{bmatrix} -4 & -1 \end{bmatrix}$

Table 5.7: Definition of the NDI-PI controller #4.

Finally, let us propose a fifth NDI-PI controller obtained from the desired dynamics presented on Table 5.8 and that are capable of covering the whole flight envelop. The choice of the tuning parameter τ_q and the final controller gains are given on Table 5.9.

ONERA
THE FRENCH AEROSPACE LAB

ISAE
Institut Supérieur de l'Aéronautique et de l'Espace

Desired dynamics #3		Parameter values		
ω_{c_α} (rad/s)	ξ_α	k_P	k_I	τ_F
1.2	0.7	1.68	1.44	1.16

Table 5.8: Choice #3 of the controller parameters defining the desired dynamics for α.

NDI-PI controller #5		
τ_q (s)	K	H
0.1	$\begin{bmatrix} 16.8 & 14.4 & -10 \end{bmatrix}$	$\begin{bmatrix} -10 & -1 \end{bmatrix}$

Table 5.9: Definition of the NDI-PI controller #5.

Based on this controller, a solution with improved robust performance can be obtained via our generalized NLC framework.

5.3.1.3 Computation of NLC-$\mathcal{H}_\infty$ robust controllers

The method allowing to obtain generalized NLC-$\mathcal{H}_\infty$ controllers for the longitudinal dynamics of the reentry vehicle will now be described. In fact, the frequency domain response of the baseline NDI solution can be exploited to begin shaping the robust controller synthesis.

First, let us recall the reformulated longitudinal dynamics model under the form (4.45) presented on page 93, which reads:

$$\Sigma_{long}(s) : \begin{cases} \dot{\tilde{x}} &=& A\,\tilde{x} + B_1 \begin{bmatrix} f_\alpha \\ f_q \end{bmatrix} + B_2\,\lambda_q\,\delta_m \\ \\ z &=& \begin{bmatrix} 1 & 0 \end{bmatrix}\tilde{x} \end{cases} \tag{5.12}$$

where

$$\tilde{x} = \begin{bmatrix} \tilde{\alpha} & q \end{bmatrix}^T$$

$$\tilde{\alpha} = \alpha - \bar{\alpha}, \qquad A = \begin{bmatrix} z_\alpha & 1 \\ m_\alpha & m_q \end{bmatrix}$$

$$B_1 = \begin{bmatrix} 1 & 0 \\ 0 & 1 \end{bmatrix}, \qquad B_2 = \begin{bmatrix} 0 \\ 1 \end{bmatrix}$$

$$f_\alpha = \hat{f}_\alpha + w_{f_\alpha}, \qquad f_q = \hat{f}_q + w_{f_q} \tag{5.13}$$

The matrix A is chosen so that the norm of the functions f_α and f_q is reduced for most operating conditions. In this case, based on the linearization about the trim conditions $(\bar{\alpha}, \bar{\delta}_m)$, the different matrices A and eigenvalues associated to the flight points in Table 5.1 were calculated. These eigenvalues correspond to the modes of the anlge-of-attack and pitch rate. The flight point considered the closest to the "center" of the flight domain, from a pole location point of view, was then selected. This corresponds approximately to a mean value of the linear coefficients covering the flight domain.
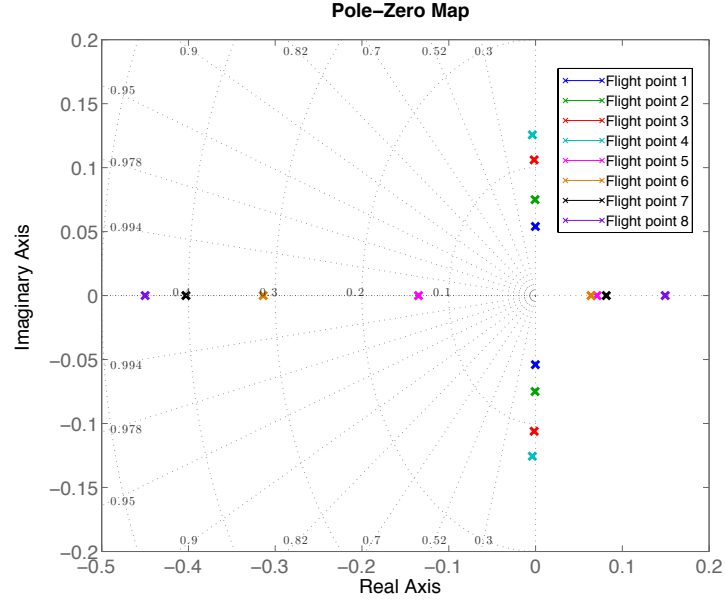
Figure 5.2: Longitudinal open-loop poles of the flight domain considered for simulation.

From the map of poles presented on Figure 5.2, flight point n°5 can be considered to have the best eigenvalues corresponding to the criteria described above. For this flight point, the following matrix can be deduced:

$$A = \begin{bmatrix} -0.001574 & 1 \\ 0.009643 & -0.06239 \end{bmatrix} \tag{5.14}$$

Now, the NDI-PI controller can be used to begin tuning the weighting functions for the synthesis of the generalized robust compensator. Using the longitudinal model representation based on flight point n°5 and by closing the control loop using the baseline NDI control law (4.13), one can generate the preliminary analysis model presented on Figure 5.3. Notice that the latter retakes the reference model tracking structure to generate a performance measurement z_p, and the measurement of the actuator rate z_u, which are used in the multi-channel design-oriented model.
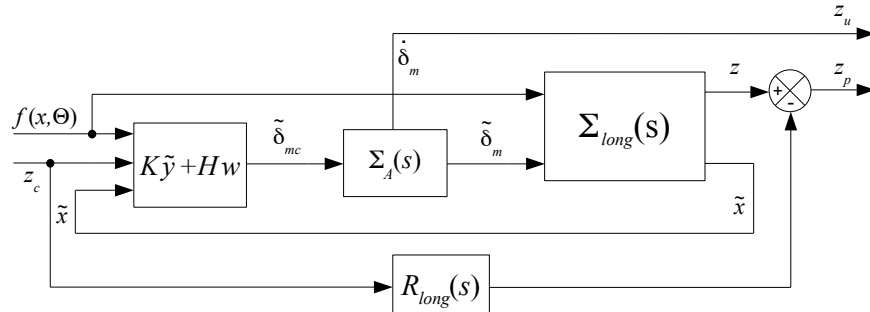
Figure 5.3: Preliminary analysis model for the longitudinal baseline NDI controller.

Consider the NDI-PI controller #5 contained in Table 5.9. The second-order dynamics of the reference model $R_{long}(s)$, which is presented in Table 5.8, can be expressed as:

$$R_{long}(s) = \frac{\omega_{c_\alpha}^2}{s^2 + 2\,\xi_\alpha\,\omega_{c_\alpha}\,s + \omega_{c_\alpha}^2} \qquad (5.15)$$

with $\omega_{c_\alpha} = 1.2$ rad/s and $\xi_\alpha = 0.7$. Using the analysis model proposed on Figure 5.3, the singular value plots of the transfers $\mathcal{T}_{\mathbf{w}\to z_p}$ and $\mathcal{T}_{\mathbf{w}\to z_u}$, where $\mathbf{w} = \begin{bmatrix} z_c & f_\alpha & f_q \end{bmatrix}^T$, are depicted on Figure 5.4.
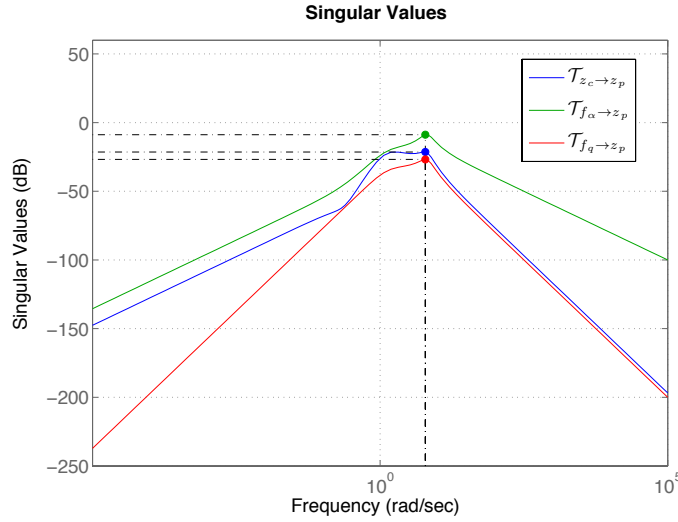
(a) Performance transfer
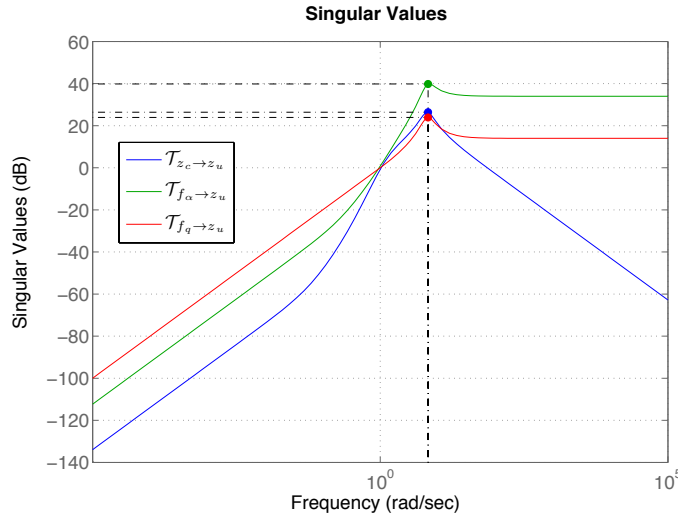
(b) Actuator rate transfer

Figure 5.4: Singular value analysis of the closed-loop with NDI-PI controller #5.

From the singular value curves depicted above, one gets that the peak gains of the performance transfer $\mathcal{T}_{\mathbf{w} \to z_p}$ and the actuator rate transfer $\mathcal{T}_{\mathbf{w} \to z_u}$ are

$$\sigma_{z_p} = 0.379 = -8.4 \, dB, \quad \text{and} \quad \sigma_{z_u} = 102.145 = 40.2 \, dB \tag{5.16}$$

The frequency domain response of the transfer $\mathcal{T}_{\mathbf{w} \to z_p}$ can be used to obtain a starter idea of the required performance characteristics for the robust controller synthesis. The weighting function of the exogenous output z_p can be designed by defining a lead filter that wraps all the singular value curves as shown on Figure 5.5. This filter corresponds to the inverse of the weighting function $W_p(s)$ that should be used for loop-shaping the controller synthesis problem.

This intermediate step between standard NDI design and robust nonlinear compensation is of great help to reduce the time consuming process of designing appropriate weighting functions $W(s)$ to loop-shape the optimization problem.Then, the proposed weighting functions provide only a starting point of the tuning procedure. Obtaining a controller with improved robustness results with respect to the baseline NDI solution may require further adjustments of $W(s)$.
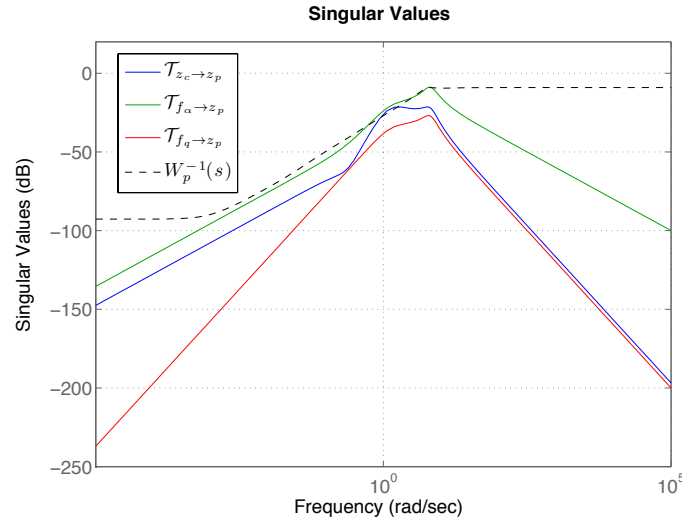
Figure 5.5: Defining a weighting function $W_p(s)$ using the NDI-PI controller #5.

A first weighting function $W_p(s)$, whose inverse $W_p^{-1}(s)$ is depicted on Figure 5.5, was obtained using the graphic tool *magshape* of MATLAB in the form of a sixth-order lag filter such as:

$$W_p(s) = \frac{s^6 + 12.8\,s^5 + 85.3\,s^4 + 366.4\,s^3 + 654.4\,s^2 + 262.3\,s + 12.7}{0.35\,s^6 + 2.8\,s^5 + 15.8\,s^4 + 27.5\,s^3 + 8.9\,s^2 + 0.3\,s + 0.0003} \tag{5.17}$$

Remark 5.1 *With full-order $\mathcal{H}_\infty$ techniques, the use of high-order weighting functions $W(s)$ becomes a concern because it increases the order of the design-oriented model. As a consequence, the order of the controller is also increased and computational issues become non-trivial. Since the synthesis technique that will be used allows to fix the structure and the order of the robust controller, this restriction on the order of the design-oriented model can be discarded.*

For the actuator rate measurement z_u a dynamic weighting function $W_u(s)$ will not be employed. Instead, a static gain g_{z_u} can be used accordingly to increase or reduce the magnitude of the actuator rate signal considered for the optimization process. Generally, when $g_{z_u} > 1$ is used, the actuator rate is considered to be large, then, the optimization process produces a controller that tends to attenuate the actuator activity. This has a direct impact on the achievable performance which, in this case, is reduced.

When $g_{z_u} < 1$ is considered, the opposite effect is produced and the actuator activity is favored thus attaining better performance levels. A unit gain $g_{z_u} = 1$ will be used hereafter.

Based on the cut-off frequency ω_{c_α} chosen for the reference model dynamics and following the criteria defined in Section 2.3 (see page 54), two lag filters $W_{f_\alpha}(s)$ and $W_{f_q}(s)$ can be proposed for the measured disturbances $\hat{f}(x, \Theta)$ as:

$$W_{f_\alpha}(s) = \frac{0.01}{s + 1.5}, \quad \text{and} \quad W_{f_q}(s) = \frac{0.1}{s + 1.5} \tag{5.18}$$

Once the longitudinal model has been established and that the weighting functions $W(s)$ have been selected, it is now only a matter of choosing a suitable controller structure for synthesis. Actually, if a PI structure is chosen for the robust controller $K(s)$, one can reproduce the baseline NDI solution following this methodology as explained in [HJB11], thus exposing the generalizing character of our NLC framework.

In this case, a state-space structure of higher-order will be used to introduce several degrees-of-freedom to the controller $K_{long}(s)$. More specifically, a fifth-order controller structure will be retained.

For controller synthesis, consider the multi-channel design-oriented model presented on Figure 4.6 of page 95. The generalized NLC-$\mathcal{H}_\infty$ controller $K_{long}(s)$ can be computed via the MATLAB function *hinfstruct*. The latter implements the structured $\mathcal{H}_\infty$ synthesis technique presented in [AN06], based on nonsmooth optimization.

By merging the fifth-order dynamics of the computed controller $K_{long}(s)$ with those of the setpoint filter $F_{long}(s)$ and the error ε_α integral, one gets an augmented compensator structure of state $x_K \in \mathbb{R}^7$. It can be expressed under the form:

$$\begin{bmatrix} \dot{x}_K \\ \delta_{m_c} \end{bmatrix} = K_{long} \begin{bmatrix} x_K \\ \tilde{y} \end{bmatrix} \tag{5.19}$$

where

$$\tilde{y} = \begin{bmatrix} \alpha_c & \hat{f}_\alpha & \hat{f}_q & \alpha & q \end{bmatrix}^T \tag{5.20}$$

Using the reference model (5.15) along with the weighting functions (5.17) and (5.18), the first computed NLC-$\mathcal{H}_\infty$ controller is:

ONERA
THE FRENCH AEROSPACE LAB

ISAE
Institut Supérieur de l'Aéronautique et de l'Espace

$$K_{long} = \begin{bmatrix} -0.85 & 0 & 0 & 0 & 0 & 0 & 0 & 1 & 0 & 0 & 0 & 0 \\ 0.85 & 0 & 0 & 0 & 0 & 0 & 0 & 0 & 0 & 0 & -1 & 0 \\ 2.9 & 1.5 & -5.8 & -0.2 & 0 & 0 & 0 & 1.2 & 0.35 & 0.4 & 3.1 & 1.1 \\ 15 & -1.5 & -18 & -4.8 & -18 & 0 & 0 & -13 & 4.1 & 10.3 & 15.1 & -3.4 \\ 14.8 & -19 & 0 & -0.4 & 0.2 & -16 & 0 & 4.2 & -0.1 & -0.7 & -7.5 & -4.1 \\ 15.5 & -9.9 & 0 & 0 & 4.2 & -18 & -0.3 & 2.1 & -2.2 & -0.8 & -18 & -5.7 \\ 6.04 & 4.9 & 0 & 0 & 0 & 2.35 & -1.7 & 16.2 & 0.74 & -0.4 & 6.7 & 9.4 \\ \hline 9.61 & -13 & 13.4 & -0.2 & 0.8 & -17 & 0.2 & 0.9 & -2.2 & -1.1 & -31.2 & -13 \end{bmatrix}$$

Table 5.10: Definition of the NLC-$\mathcal{H}_\infty$ controller #1.
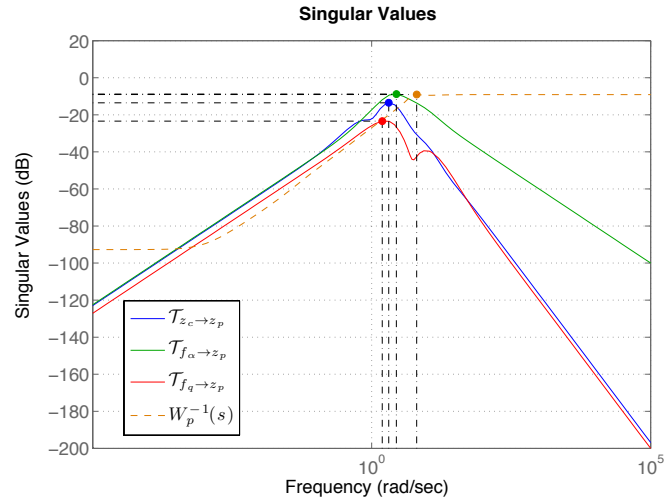
(a) Performance transfer
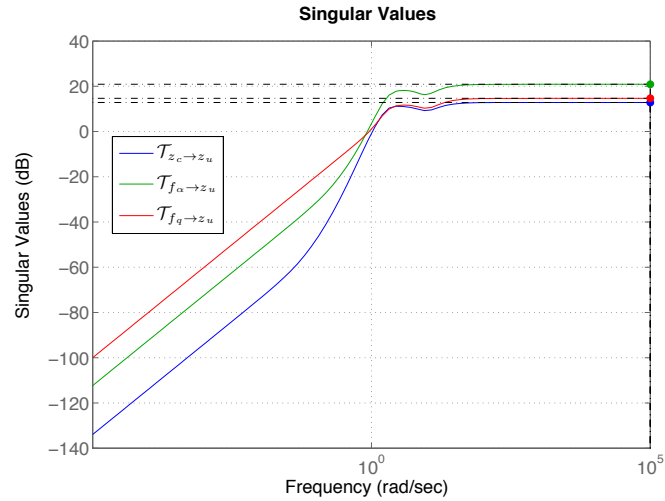
(b) Actuator rate transfer

Figure 5.6: Preliminary analysis of the closed-loop with the NLC-$\mathcal{H}_\infty$ controller #1.

ONERA
THE FRENCH AEROSPACE LAB

ISAE
Institut Supérieur de l'Aéronautique et de l'Espace

A preliminary singular value analysis of the closed-loop with the NLC-$\mathcal{H}_\infty$ controller #1 produces the curves presented on Figure 5.6. From these singular value plots, one gets that the peak gains of the performance transfer $\mathcal{T}_{\mathbf{w} \to z_p}$ and the actuator rate transfer $\mathcal{T}_{\mathbf{w} \to z_u}$ become:

$$\sigma_{z_p} = 0.418 = -7.5\,dB, \quad \text{and} \quad \sigma_{z_u} = 13.076 = 22.3\,dB \tag{5.21}$$

Clearly, the peak gain σ_{z_u} has been successfully reduced when compared to that of the NDI-PI controller #5 presented in (5.16). Still, σ_{z_p} remains slightly greater than the peak gain of the performance transfer obtained by the NDI controller. This means that the performance level attained by the latter, is better than the one obtained by the NLC-$\mathcal{H}_\infty$ controller #1.

To achieve a better results, the $\mathcal{H}_\infty$ norm associated with the performance transfer can be reduced by adjusting the weighting function $W_p(s)$ tuning. In order for the optimization process to produce a controller capable of reducing this particular transfer, one should generally proceed to increase the static gain of this weighting function. By tuning $W_p(s)$ this way, it is considered that the performance measurement z_p is large at low frequencies, thus the optimization process tends to generate a controller that will act stronger to minimize the $\mathcal{H}_\infty$ norm of this transfer.

Consider now the following forth-order weighting function $W_p(s)$ that keeps the cut-off frequency characteristics of the previous function (5.17), but for which the static gain has been increased:

$$W_p(s) = \frac{s^4 + 8.6\,s^3 + 37.7\,s^2 + 92.5\,s + 71.5}{0.1\,s^4 + 0.57\,s^3 + 1.8\,s^2 + 1.5\,s + 0.002} \tag{5.22}$$

Using once more the reference model (5.15) along with the newly adjusted weighting function (5.22) and the previously defined functions (5.18), the second NLC-$\mathcal{H}_\infty$ controller obtained is:

$$K_{long} = \left[\begin{array}{ccccccc|ccccc}
-0.85 & 0 & 0 & 0 & 0 & 0 & 0 & 1 & 0 & 0 & 0 & 0 \\
0.85 & 0 & 0 & 0 & 0 & 0 & 0 & 0 & 0 & 0 & -1 & 0 \\
248 & -105 & -6.6 & 10.1 & 0 & 0 & 0 & -20 & -36 & -5.8 & -65 & -23 \\
-98 & 36.3 & 4.02 & -11 & -10 & 0 & 0 & -7.2 & -3.2 & -1.7 & 179 & 3.9 \\
83.1 & 139 & 0 & 3.7 & -8.8 & -5.1 & 0 & -30 & 15 & 2 & -10 & 3.7 \\
64.5 & -183 & 0 & 0 & -3.4 & -4.3 & 4.6 & 81 & -22 & -5.2 & 38 & -13 \\
32.4 & -74 & 0 & 0 & 0 & -1.5 & 2.02 & 87 & -6 & -3 & -42 & -11 \\
\hline
253.4 & -37.4 & -3.3 & 12.2 & -4.6 & -9.1 & 4.2 & 1.7 & -6.8 & -1.7 & -115 & -16.3
\end{array}\right]$$

Table 5.11: Definition of the NLC-$\mathcal{H}_\infty$ controller #2.

The preliminary singular value analysis of the closed-loop with the NLC-$\mathcal{H}_\infty$ controller #2 produces the curves presented on Figure 5.7. From these singular value plots, one gets that the peak gains of the performance transfer $\mathcal{T}_{\mathbf{w} \to z_p}$ and the actuator rate transfer $\mathcal{T}_{\mathbf{w} \to z_u}$ become:

$$\sigma_{z_p} = 0.291 = -10.7\,dB, \quad \text{and} \quad \sigma_{z_u} = 35.952 = 31.1\,dB \tag{5.23}$$

In this case, the peak gain σ_{z_p} attains a lower level than that of the NDI-PI controller #5 presented in (5.16). Yet, this reduction of the $\mathcal{H}_\infty$ norm on the performance transfer comes at a cost. Clearly, the peak gain σ_{z_u} has increased its value, even though it still remains lower than that obtained by the NDI-PI controller #5.

A trade-off raised by the loop-shaping approach, between the closed-loop performance and control signal activity becomes evident. One cannot reduce the activity of the actuators, thus protecting them from attrition and from reaching prematurely their saturation limits, while expecting the highest levels of performance at the same time.
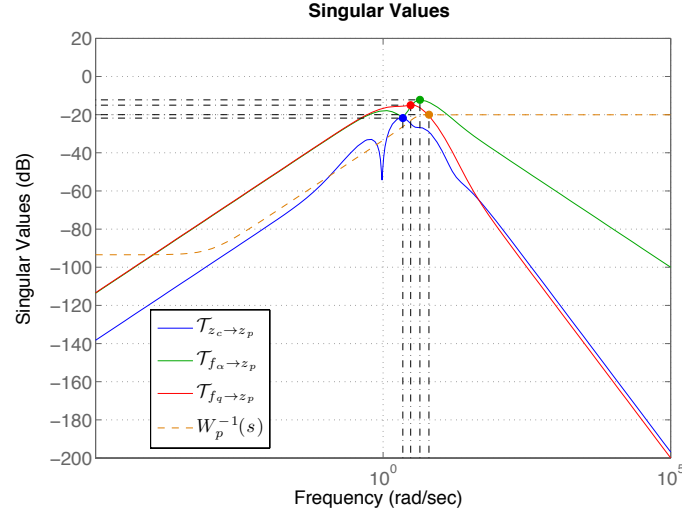
(a) Performance transfer
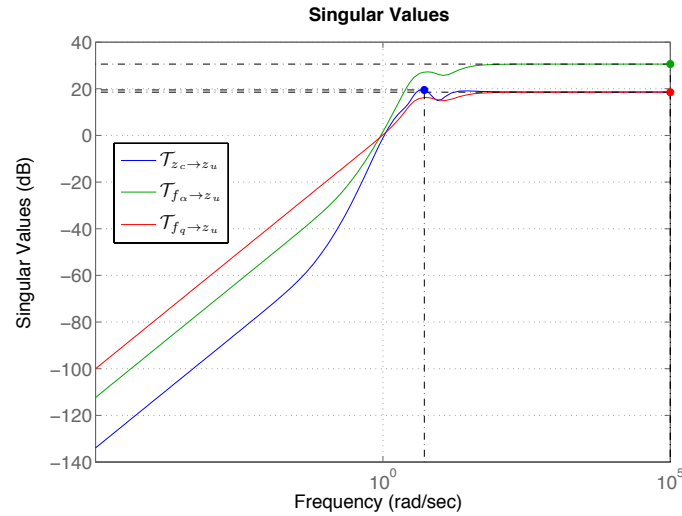
(b) Actuator rate transfer

Figure 5.7: Preliminary analysis of the closed-loop with the NLC-$\mathcal{H}_\infty$ controller #2.

Finally, when actuator limits are considered, the stability of some flight points in the hypersonic regime is lost when using either the NDI-PI controller #5 or any of the two NLC-$\mathcal{H}_\infty$ controllers that have been computed above. This will be proved with simulation results. In fact, the NDI-PI controller is incapable of preserving the stability of flight points n°1, n°2 and n°3. The NLC-$\mathcal{H}_\infty$

controller #2 is unable to maintain the stability of flight points n°1 and n°2, whereas the NLC-$\mathcal{H}_\infty$ controller #1 is only incapable of preserving the stability of flight point n°1.

From one point of view, this shows that the NLC framework proposed obtains better robustness properties than an equivalent NDI-PI controller. Still, this solution remains insufficient for stabilizing the whole flight envelop considered for this thesis work. Therefore, an anti-windup device can be employed to enlarge the closed-loop stability domain under input saturations.

Consider, for example, the seventh-order nominal NLC-$\mathcal{H}_\infty$ controller #2 contained in Table 5.11. Under the rate limited Direct Linear Anti-windup strategy illustrated on Figure 4.10 of page 100, consider that $v_2 = 0$ and $v_1 = v$. Given the first-order anti-windup controller

$$\begin{bmatrix} \dot{x}_J \\ \hline v \end{bmatrix} = J_{long} \begin{bmatrix} x_J \\ \hline u_{AW} \end{bmatrix} \tag{5.24}$$

where $v \in \mathbb{R}^7$ and $u_{AW} \in \mathbb{R}$, the enhanced NLC-$\mathcal{H}_\infty$ controller takes the form:

$$\begin{bmatrix} \dot{x}_K \\ \hline \delta_{m_c} \end{bmatrix} = K_{a_{long}} \begin{bmatrix} x_K \\ v \\ \tilde{y} \end{bmatrix} \tag{5.25}$$

with $\tilde{y} = \begin{bmatrix} \alpha_c & \hat{f}_\alpha & \hat{f}_q & \alpha & q \end{bmatrix}^T$.

Referring to the design-oriented model of Figure 4.11 presented on page 100, the exogenous output z_s can be weighted using the same filters as in the nominal NLC-$\mathcal{H}_\infty$ controller synthesis $W_s(s) = W_p(s)$. Consider the weighting function (5.17) for the exogenous output z_s and its inverse for the exogenous input w_φ. The anti-windup device J_{long} is computed once again via the MATLAB function *hinfstruct* and one gets the following controller:

$$J_{long} = \begin{bmatrix} -1.954 & 0.3077 \\ \hline -1.965 & -0.6037 \\ 0.5254 & 0.6714 \\ -68.28 & -251.8 \\ 4.647 & -128.5 \\ -14.06 & 39.01 \\ -10.19 & -148.2 \\ 5.032 & -60.65 \end{bmatrix}$$

Table 5.12: Definition of the anti-windup device for NCL-$\mathcal{H}_\infty$ controller #2.

This anti-windup device completes the robust nonlinear compensation strategy proposed for the longitudinal dynamics.

5.3.1.4   Robustness assessment

Before assessing the stability of the computed control laws, let us propose the following numbering code that will help identify each NDI-PI and NLC-$\mathcal{H}_\infty$ controller:

Control Law	nº	Type	Desired Dynamics	Controller
	1	NDI-PI #1	Table 5.2	Table 5.3
	2	NDI-PI #2	Table 5.2	Table 5.4
$\delta_{m_c} = g_q^{-1}(K\,\tilde{y} + Hw)$	**3**	NDI-PI #3	Table 5.2	Table 5.5
	4	NDI-PI #4	Table 5.6	Table 5.7
	5	NDI-PI #5	Table 5.8	Table 5.9
$\delta_{m_c} = \lambda_q^{-1}\,K_{long}(s)\,\tilde{y}$	**6**	NLC-$\mathcal{H}_\infty$ #1	Table 5.8	Table 5.10
	7	NLC-$\mathcal{H}_\infty$ #2	Table 5.8	Table 5.11
$\delta_{m_c} = \lambda_q^{-1}\,K_{a_{long}}(s)\begin{bmatrix} v \\ \tilde{y} \end{bmatrix}$ $v = J_{long}(s)\,u_{AW}$	**8**	NLC-$\mathcal{H}_\infty$ #2 + AW	Table 5.8	Table 5.12

Table 5.13: Compilation of computed controllers for the longitudinal axis.

Using the LFT closed-loop modelling proposed in Section 2.5, the basic approach invoking the small gain theorem and the refined approach based scaled bounded real lemma are employed. As an example, the choice of the equilibrium point about which the small variations of the state will be analysed corresponds to the trim conditions of flight point n°5.

To expose some characteristics of the stability test that will be used, first, the NDI-PI and the NLC-$\mathcal{H}_\infty$ controllers are analysed discarding the presence of input saturations and modelling errors in the Δ blocks. The following $\mathcal{H}_\infty$ norms were obtained from this stability tests:

Controller		$\mathcal{H}_\infty$ norm γ	
Type	**nº**	**Basic approach**	**Scaled BRL**
	1	3.354	1.4448
	2	3.011	0.8319
NDI-PI	**3**	3.7557	0.74212
	4	1.5793	0.67314
	5	2.4997	0.68959
NLC-$\mathcal{H}_\infty$	**6**	1.9565	1.1670
	7	1.6563	0.70548
NLC-$\mathcal{H}_\infty$+AW	**8**	1.5972	0.65582

Table 5.14: Stability analysis results with nonlinearities.

As expected, the scaled BRL approach yields less restrictive results. In this case, the Lipschitz constants of the system nonlinearities can attain a maximum value defined by the inverse of γ before destabilizing the system.

Now, let us include in the stability tests modelling errors as uncertainties on the previously considered nonlinearities. The Δ block now includes nonlinear operators and real time-varying uncertainties.

Controller		$\mathcal{H}_\infty$ norm γ	
Type	**n$^\text{o}$**	**Basic approach**	**Scaled BRL**
NDI-PI	**1**	4.8105	2.2373
	2	4.312	1.3890
	3	5.3513	1.2197
	4	2.3841	1.4841
	5	3.6036	1.2174
NLC-$\mathcal{H}_\infty$	**6**	2.1613	1.2707
	7	1.9422	0.82788
NLC-$\mathcal{H}_\infty$+AW	**8**	1.9296	0.82122

Table 5.15: Stability analysis results with modelling errors and nonlinearities.

By comparing the results contained in Tables 5.14 and 5.15, it can be observed that the values of γ are greater when the modelling errors are accounted for. Finally, let us consider the saturation operator in the Δ block. The stability tests yield the following results:

Controller		$\mathcal{H}_\infty$ norm γ	
Type	**n$^\text{o}$**	**Basic approach**	**Scaled BRL**
NDI-PI	**1**	583.1	2.6642
	2	1421.3	1.9933
	3	2832	2.4492
	4	583.1	1.9196
	5	1421.3	1.7469
NLC-$\mathcal{H}_\infty$	**6**	348.41	1.6398
	7	987.75	1.5587
NLC-$\mathcal{H}_\infty$+AW	**8**	987.75	1.4124

Table 5.16: Stability analysis results with modelling errors, nonlinearities and saturations.

It is now clear that by adding more operators to the block Δ, these stability analysis tests produce greater values of γ. In fact this can be expected since the proposed stability tests become rather conservative as more crossed transfers are added to the analysis. Some of these transfers lack of a real physical interpretation, thus making these stability tests conservative.

In particular, the results contained in Table 5.16 demonstrate how the small gain theorem based test obtains excessively large values of γ. Then, this test provides a very small characterization of the stability domain meaning that only very small variations from the equilibrium point are admissible.

In contrast, the scaled BRL based test is able to keep the values γ rather small and very close together as more operators are added to the Δ block. Still, the stability domain characterization is smaller when modelling errors, nonlinearities and saturations are accounted for. This can be attributed to the conservatism of the test.

From the results presented above using the two stability tests, the flight control law that yields the largest characterization of the stability domain corresponds to the NLC-$\mathcal{H}_\infty$+AW solution. In an interesting manner, the effects of the anti-windup device on stability can be observed in all cases since lower values of γ are obtained.

5.3.1.5 Simulation results

Let us now present the simulation results obtained using the different controllers that have been computed using the standard NDI procedure and the generalized NLC framework.

A disturbed aerodynamic model that considers the modelling errors presented in Section 3.4 and that are detailed in Appendix D.2.3 (see page 261), is used in simulation. The latter differs from the nominal model employed to estimate the nonlinear measured disturbances used by the NDI-PI controllers and the NLC-$\mathcal{H}_\infty$ controllers. Also, the Flight Mechanics simulator accounts for measurement disturbances including: measurement noise, scale factors and biases.

In a first instance, the different computed controllers will be tested discarding the external environmental factors such as static wind gusts and turbulent wind effects. This will allow a clearer comparison between the simulation results. In a second instance, once a final solution capable of controlling the reentry vehicle throughout the whole flight envelop is exhibited, these environmental factors will be added to validate the control law under a more realistic scenario.

For this longitudinal simulation case, the lateral dynamics are kept at a steady state by fixing the values of the rotation rates $p = r \equiv 0$ in our six degrees-of-freedom nonlinear Flight Mechanics simulator. The Mach number $\mathcal{M}$ and the altitude h are also kept constant during the simulation given that the Control System is being tested independently at different flight points of a possible reentry trajectory. The longitudinal dynamics of the reentry vehicle are then simulated with a step setpoint signal α_c such that

Step	$\mathcal{M} > 4$	$\mathcal{M} < 4$
$\alpha_{\mathbf{c}}$	$3°$	$5°$

Table 5.17: Magnitude of the step α_c used for simulation as a function of $\mathcal{M}$.

To present the simulation results, two kind of figures are used to show the curves that characterize the evolution of the most relevant parameters.

The first kind of figure is used for simulations considering an actuator model with unlimited rate and magnitude. This type of simulation will help contrast the different computed controllers before exhibiting the effects of input saturations. The figures used include graphs of: the control objective α, the pitch rate q and the control input δ_m. Consider the following precisions:
– In the control objective graph there are three curves corresponding to: a reference angle-of-attack signal α_r (purple dotted line), the simulation angle-of-attack α (orange line) and the measured angle-of-attack α_m (blue line). The simulation angle-of-attack is the actual α as perceived by the reentry vehicle.
  The reference signal α_r is in fact an artificially generated signal out of the control loop whose only use is to show how the simulation angle-of-attack α should ideally evolve given the fixed desired dynamics.

The measured angle-of-attack α_m is obtained by: a simulation inertial measurement unit when the Mach number is $\mathcal{M} > 2.5$, and by a simulation anemometric unit when the Mach number is $\mathcal{M} \leq 2.5$. The performance objective is also presented on this graph as a fine dotted red line.
– Next, the pitch rate q graph contains two curves corresponding to the simulation pitch rate q (orange line) and the measured pitch rate q_m (blue line). The simulation pitch rate is the actual q as perceived by the reentry vehicle, whereas the measured pitch rate q_m is the signal provided by the simulation IMU.
– Finally, the third graph depicts two curves corresponding to the commanded control signal δ_{m_c} (orange line) and the elevon signal δ_{el} (blue line). The commanded control δ_{m_c} is the actual signal generated by the controllers and that is fed to the reentry vehicle actuator model after allocation.
The elevon signal δ_{el} is generated from the measurements of the real actuator states and coincides with the average value of the elevons deflection δ_{le} and δ_{re}, as defined by the allocation strategy presented in Section 5.2.2 (page 107).

The second kind of figures is used when the saturated actuator model is used for simulation. In this case, besides presenting the graphs of the control objective α, the pitch rate q and the control input δ_m, two more graphs are included corresponding to: the rate of the elevon actuators $\dot{\delta}_{el}$ and the rate of the body-flap actuator $\dot{\delta}_{bf}$. The limit and dynamics description of the elevon and body-flap actuators used in simulation is presented in Appendix D.2.2 (see page 259). Consider the following precisions:
– In the case of the control input graph, the two curves depicted now correspond to the commanded signal δ_{m_c} (orange line) produced by the controller and to the real deflection of the elevon actuators δ_{el_r} (blue line).
– In the cases of the elevon actuator rate $\dot{\delta}_{el}$ and the body-flap actuator rate $\dot{\delta}_{bf}$, two curves are illustrated on these graphs: the signal of the actuator rate $\dot{\delta}$ (orange line) due to the commanded control signal δ_{m_c} and the real signal of the actuator rate $\dot{\delta}_r$ (blue line).

The controller numbering used in the following corresponds to that proposed in the compilation presented on Table 5.13.

Remark 5.2 *To allow the reader of this thesis work a better comparison of the simulation results obtained by the different computed controllers, the graphs of a same flight point will be presented on the same page or on side by side pages.*

Comparing simulation results of NDI-PI controllers n°1 and n°3. Consider these two NDI-PI controllers contained in Tables 5.3 and 5.5. As an example, let us consider flight points n°5 and n°6. In this case, the simulation results of flight point n°5 are presented on Figures 5.14 and 5.15 of page 136, while the simulation results of flight point n°6 are presented on figures 5.22 and 5.23 of page 142.

In the first and second graphs of each figure, it can be observed that the measured curves α_m and q_m overlap with the simulation curves α and q, meaning that the measurement disturbances of the IMU have little impact on the closed loop. It can also be observed that the tracking of the setpoint generates no static error thanks to the integral term in the NDI controller structure. Yet, the tracking of the desired dynamics in both cases is not very accurate during the transitory regime. The performance objective is satisfied in both cases.

It becomes clear that as the value of the tuning parameter τ_q is reduced (from controller n°1 to controller n°3), an improvement of the closed-loop performance is obtained. This translates in general as a better tracking of the desired dynamics represented by the reference signal α_r.

However, specially in the case of flight point n°6, the control signal δ_{m_c} increases its magnitude and begins to present undesired oscillations when using NDI controller n°3.

Then, better suited values of the tuning parameter τ_q that respond to the trade-off of obtaining a good level of performance while keeping the magnitude and oscillations of the control signal δ_{m_c} low should be retained. This is the case of the NDI-PI controller n°2.

NDI-PI controller simulation results with a saturated actuator model. To show the impact of input saturations on the closed-loop, the saturated actuator models of the elevons and body-flap is now employed.

Consider the NDI-PI controller n°2 presented on Table 5.4. The simulation results of flight points n°5 and n°6 are depicted on Figures 5.16 and 5.24 of pages 137 and 143 respectively. The impact of the input saturations on these flight points is barely noticeable since only the actuator rate of the body-flap saturates and very slightly. Both cases comply with the performance objective.

Still, in other points of the hypersonic regime, the saturation effects are more evident (see Appendix E.1.1 on pages 265-272 for simulation results over the complete flight envelop). As a matter of fact, flight point n°1 is destabilized due to a more severe effect of the actuator rate saturations as illustrated on Figure 5.8 of page 130.

To preserve the stability of this flight point considering the saturated actuator, a possible solution is to change the desired dynamics and use the NDI controller n°4 presented on Table 5.7. Simulation results of flight point n°1 using this controller are shown on Figure 5.9 of page 131. Clearly, the time response is stable although the angle-of-attack α curves come closer to the lower bound of the performance objective.

Comparing simulation results of NLC-$\mathcal{H}_\infty$ controllers n°6 and n°7. Now, let us compare the two NLC-$\mathcal{H}_\infty$ controllers presented on Tables 5.10 and 5.11.

Consider once more flight points n°5 and n°6. The simulation results of flight point n°5 using the NLC-$\mathcal{H}_\infty$ controllers are found on Figures 5.18 and 5.19 of page 139, while the simulation results of flight point n°6 are found on Figures 5.26 and 5.27 of page 145.

Clearly, in the two flight points considered, both compensators satisfy with the control requirements and achieve very good levels of performance. As exposed during the computation process, the NLC-$\mathcal{H}_\infty$ controller n°7 achieves a lower $\mathcal{H}_\infty$ norm of the performance transfer, which leads to a very close tracking of the desired dynamics. This becomes more evident in the case of flight point n°6.

The magnitude of the control signal δ_{m_c} stays low and does not produce any oscillations. As expected, this magnitude is lower when using NLC-$\mathcal{H}_\infty$ controller n°6. The performance is slightly deteriorated with respect to that obtained when using NLC-$\mathcal{H}_\infty$ controller n°7.

Comparing simulation results of an equivalent NDI-PI controller and NLC-$\mathcal{H}_\infty$ controller with a saturated actuator model. Consider the NDI-PI controller n°5 contained in Table 5.9, which was computed using the same desired dynamics as the robust compensator n°7. This dynamics, common to both solutions, is contained in Table 5.8.

Flight points n°5 and n°6 are used again to help contrast the simulation results obtained by the two different controller design approaches for same desired dynamics. This time, the saturated actuator model is considered.

The results of flight point n°5 are shown on Figures 5.17 and 5.20 of pages 138 and 140, while the results of flight point n°6 are found on Figures 5.25 and 5.28 of page 144 and 146.

Even though both solutions prove to be satisfactory at these flight points, a better performance level is achieved by the NLC-$\mathcal{H}_\infty$ controller n°7. The control signal δ_{m_c} produced by the NLC-$\mathcal{H}_\infty$ controller n°7 shows to be less active and slightly lower in magnitude compared to that generated by the NDI-PI controller n°5.

Furthermore, flight points n°1, n°2 and n°3 controlled by the NDI controller n°5 are destabilized due to the input saturations as shown on Appendix E.1.1 (see pages 273-275).

When using the NLC-$\mathcal{H}_\infty$ controller n°7, only flight points n°1 and n°2 are destabilized under the saturated actuator model as illustrated on Figures 5.10 and 5.12 of pages 132 and 134. To maintain the stability of these flight points, an anti-windup device that augments this NLC-$\mathcal{H}_\infty$ controller can be used to actively control the saturated system, thus enlarging the stability domain of the closed-loop.

Simulation results of the enhanced anti-windup controller. Finally, consider controller n°8 composed of the anti-windup device presented on Table 5.12, that enhances the nominal NLC-$\mathcal{H}_\infty$ controller n°7.

The simulation results of this complete robust solution can be found on Figure 5.11 of page 133 for flight point n°1, and on Figure 5.13 of page 135 for flight point n°2. Very satisfactory results are obtained under the saturated actuator model.

As can be expected, the enlargement of the stability domain of the closed-loop is followed by an increase of the control signal δ_{m_c} activity and by a slight deterioration of the performance level. However, the evolution of the angle-of-attack α curves stays within the performance objective and the primary objective of preserving the closed-loop stability is successfully achieved. The reentry vehicle is controlled throughout the whole flight envelop while satisfying the performance requirements established for the control objective α.

Finally, simulation results at flight points n°5 and n°6 are shown on Figures 5.21 and 5.29 of pages 141 and 147 considering a more realistic scenario with a static wind gust and wind turbulence, following the profile described in Appendix D.1.2 (see page 256). It should be kept in mind that the moderate wind turbulence profile considered for simulation starts at an altitude of 20km.

Simulation results of the whole flight domain with the NLC controller n°8 under the effects of wind can be found in Appendix E.1.3 (see pages 305-312).
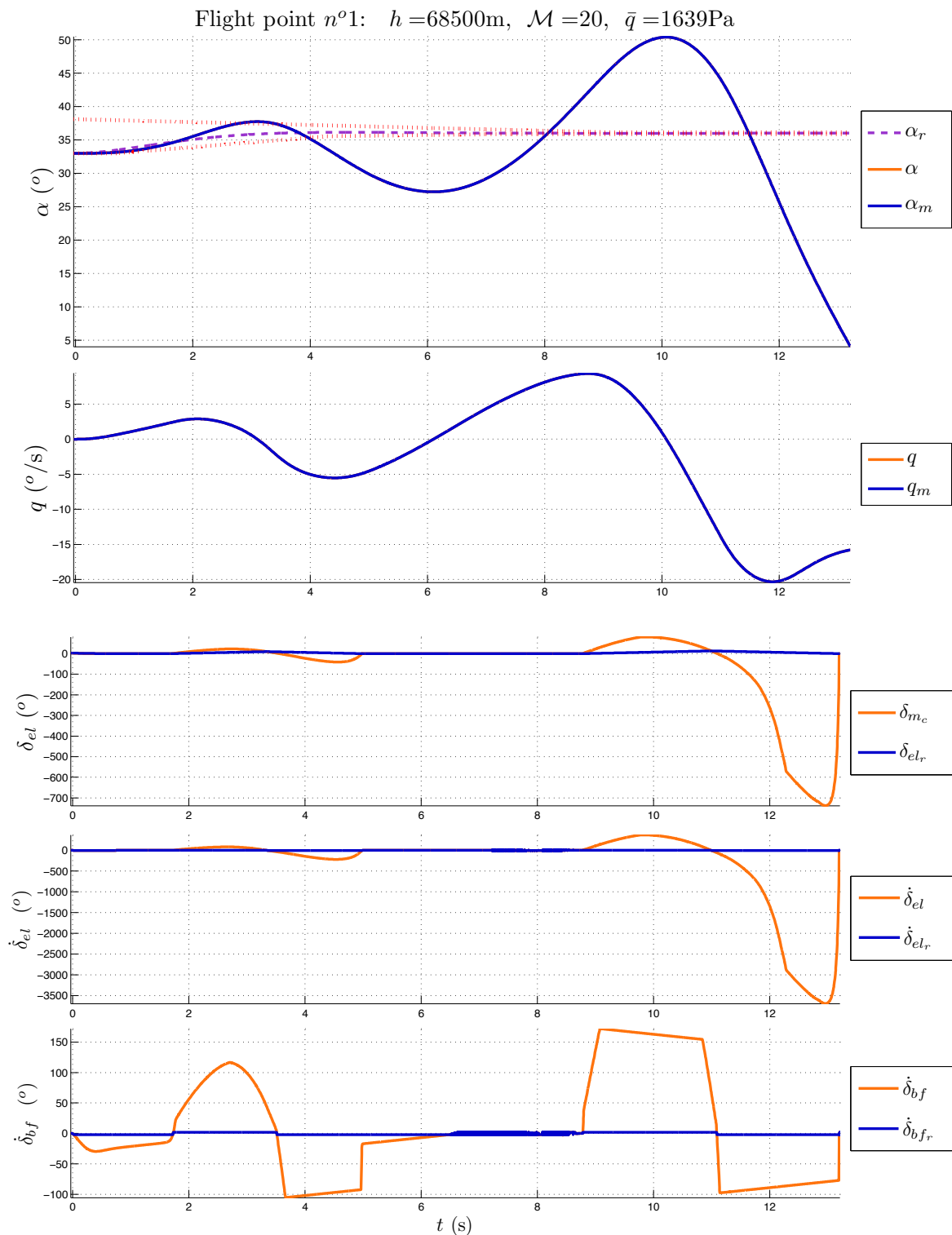
Figure 5.8: Simulation with saturated actuator and controller **n°2**.
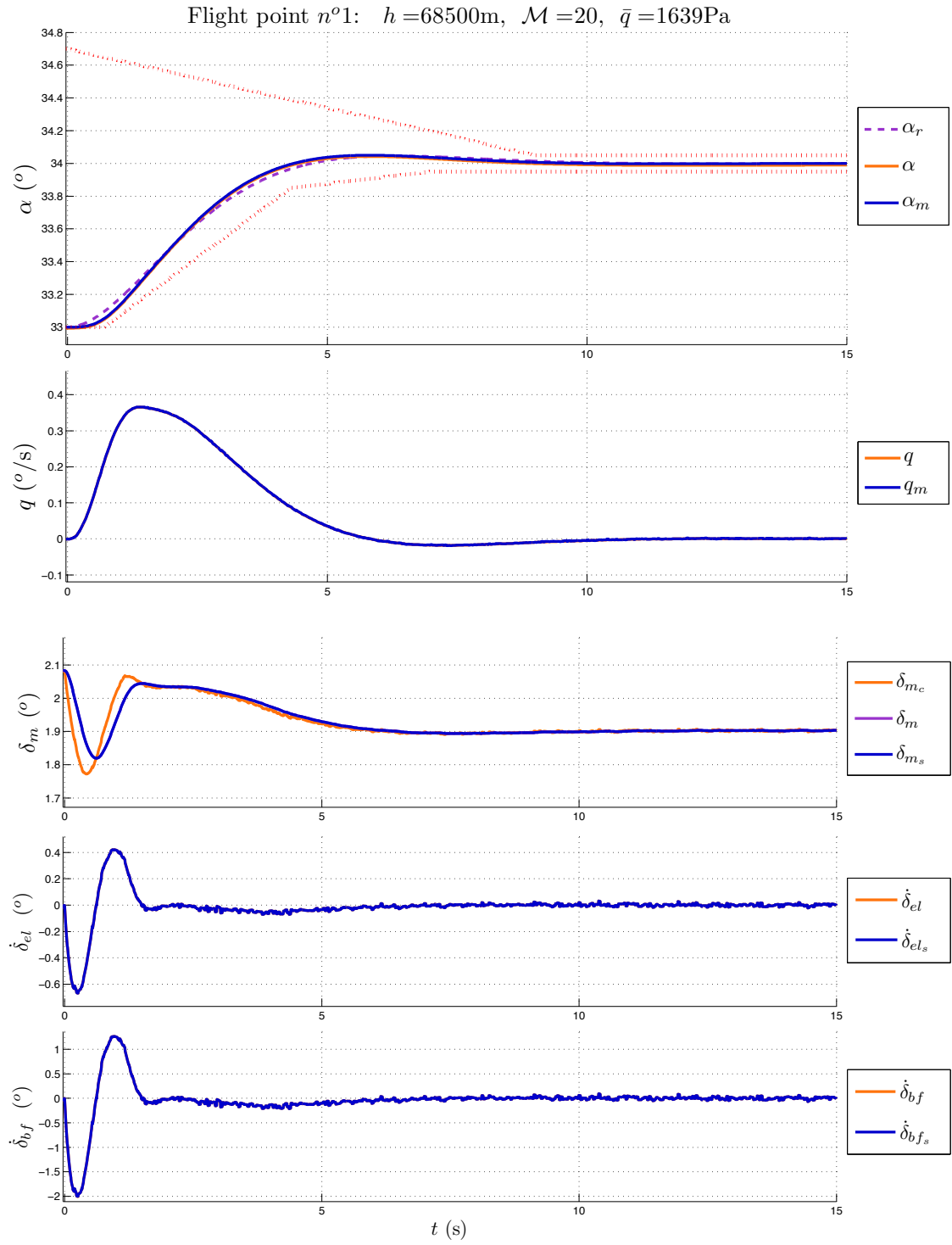
Figure 5.9: Simulation with saturated actuator and controller **n°4**.
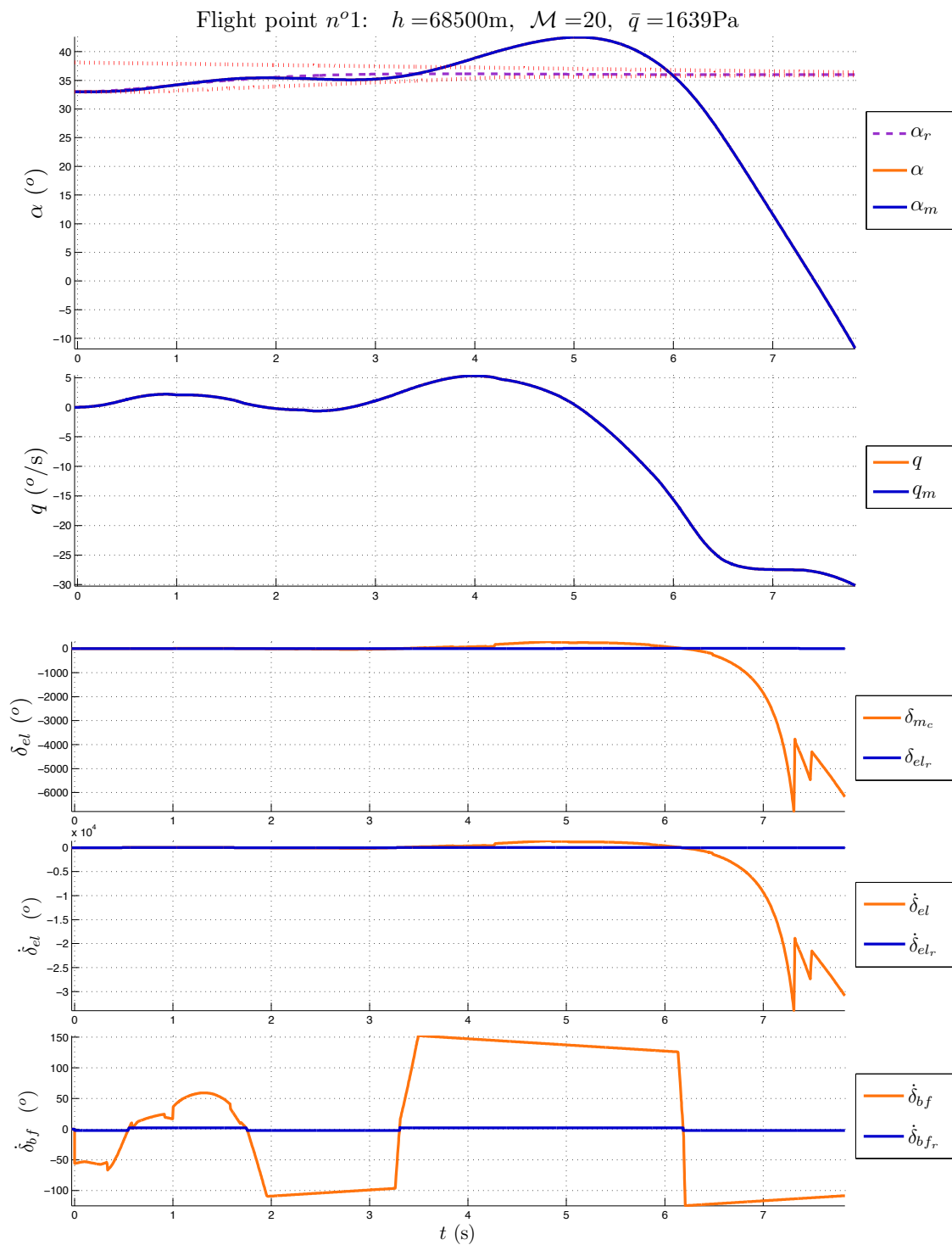
Figure 5.10: Simulation with saturated actuator and controller **n°7**.
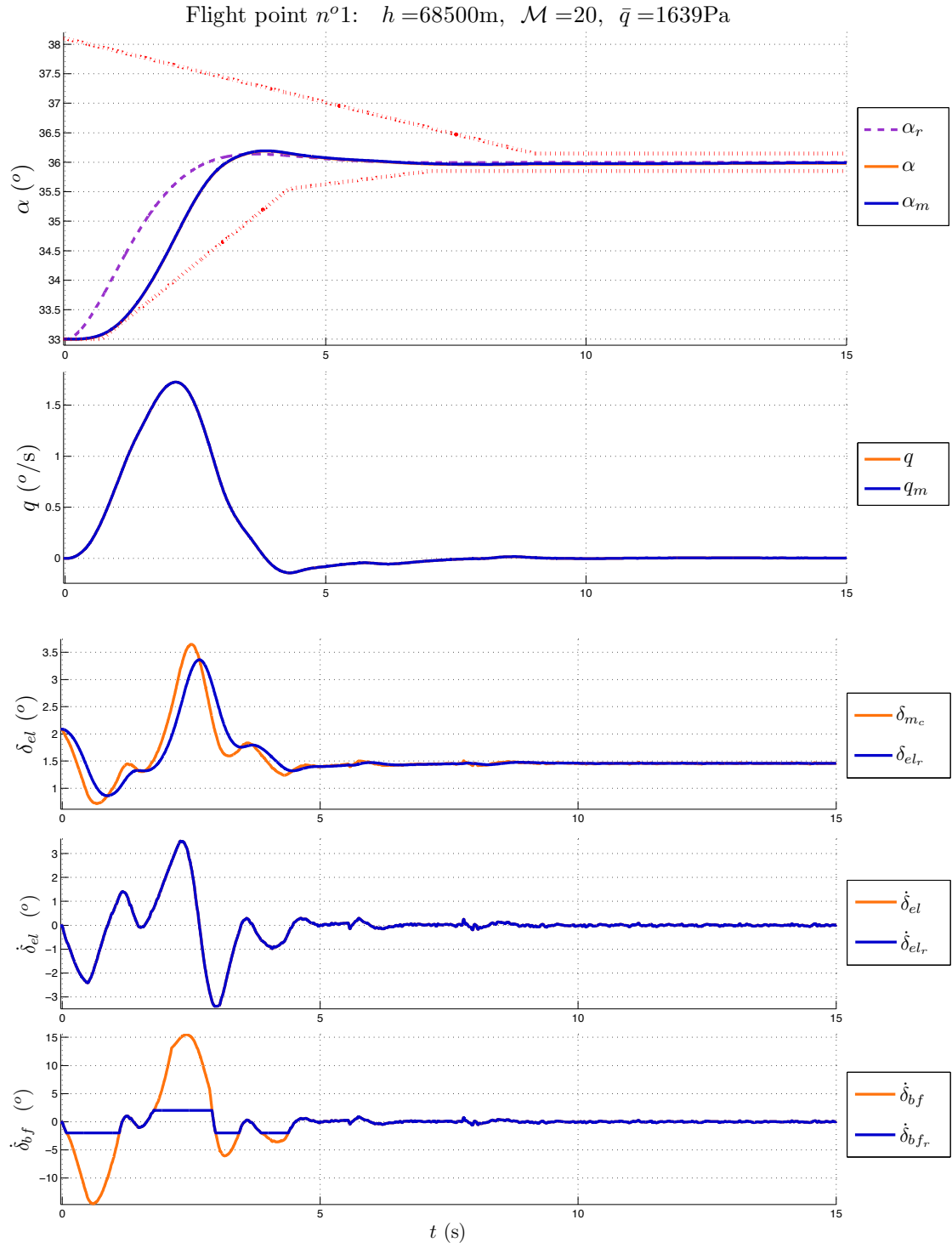
Figure 5.11: Simulation with saturated actuator and controller **nº8**.
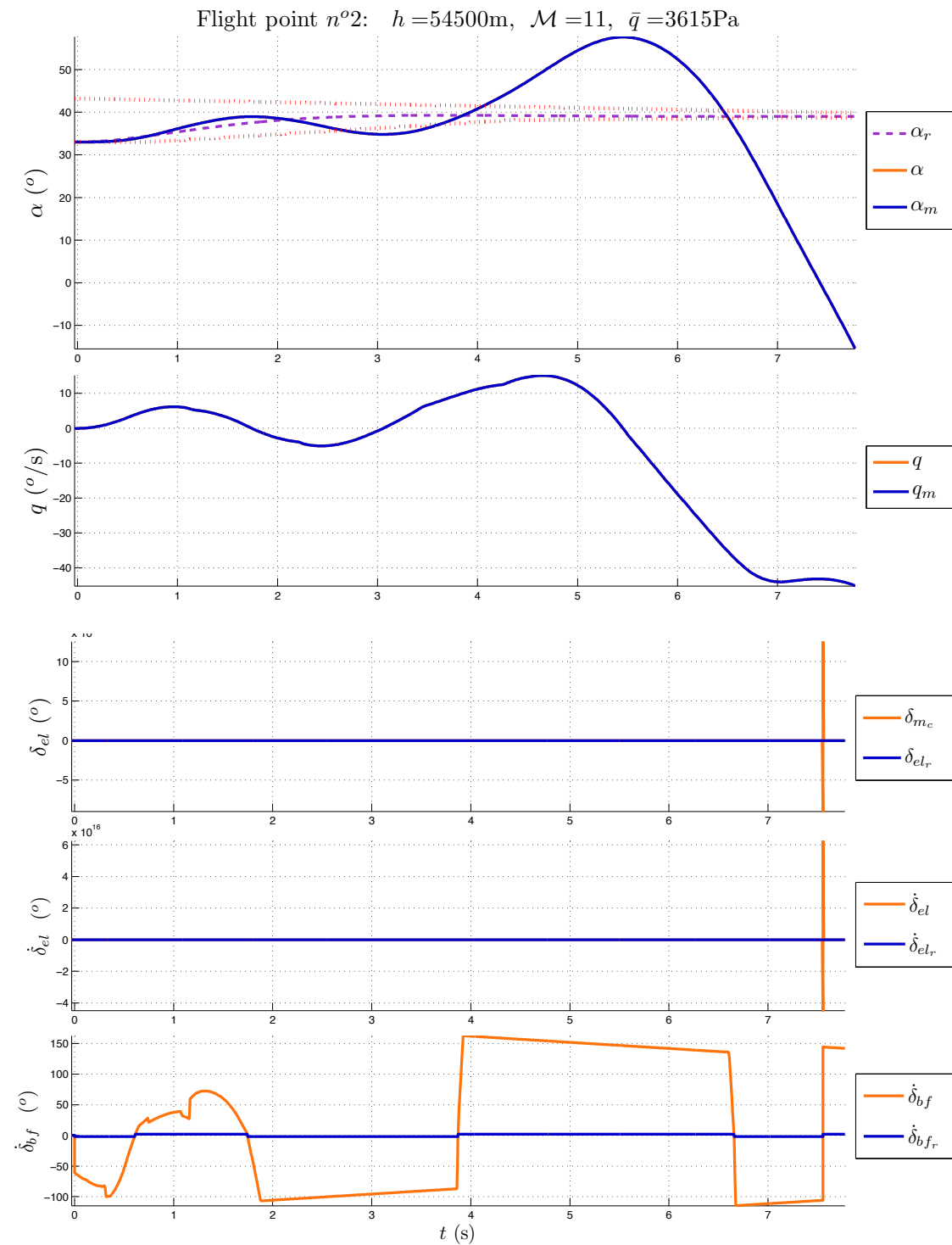
Figure 5.12: Simulation with saturated actuator and controller **n°7**.
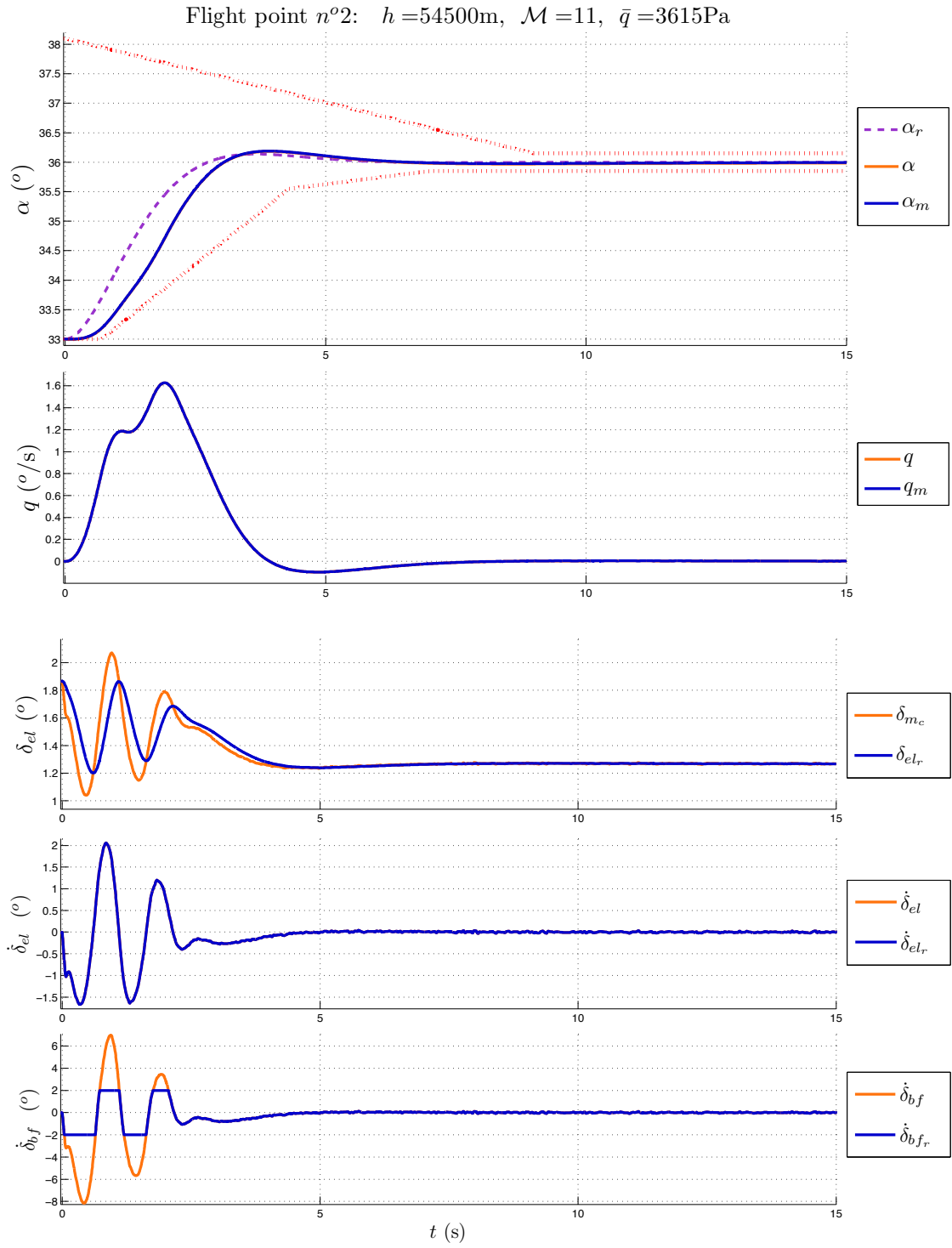
Figure 5.13: Simulation with saturated actuator and controller **nº8**.
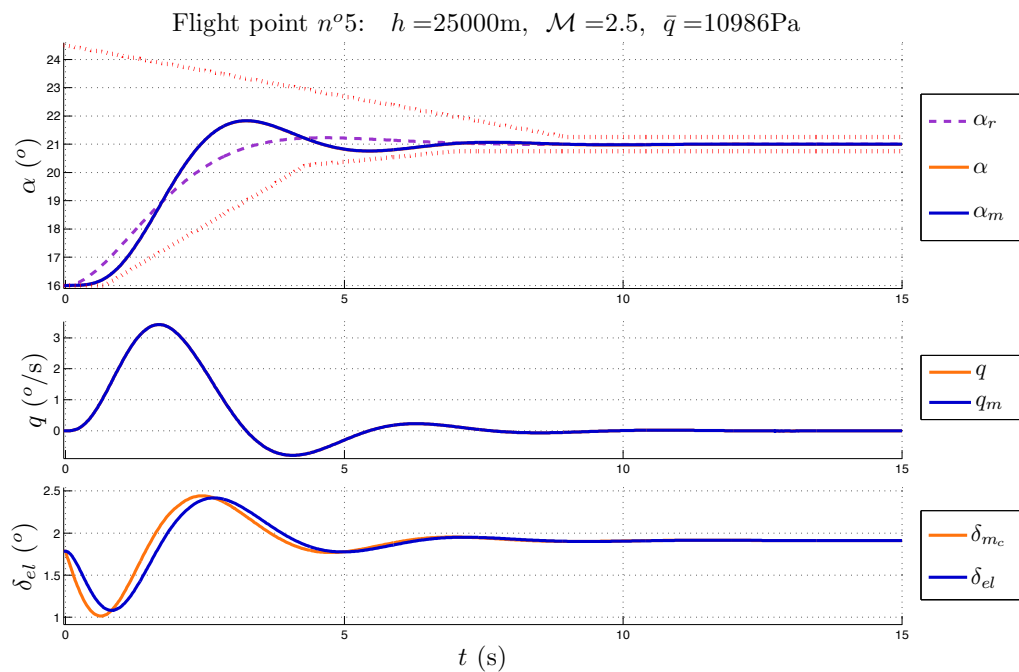
Figure 5.14: Simulation at $\mathcal{M} > 1$ with unsaturated actuator and controller **nº1**.
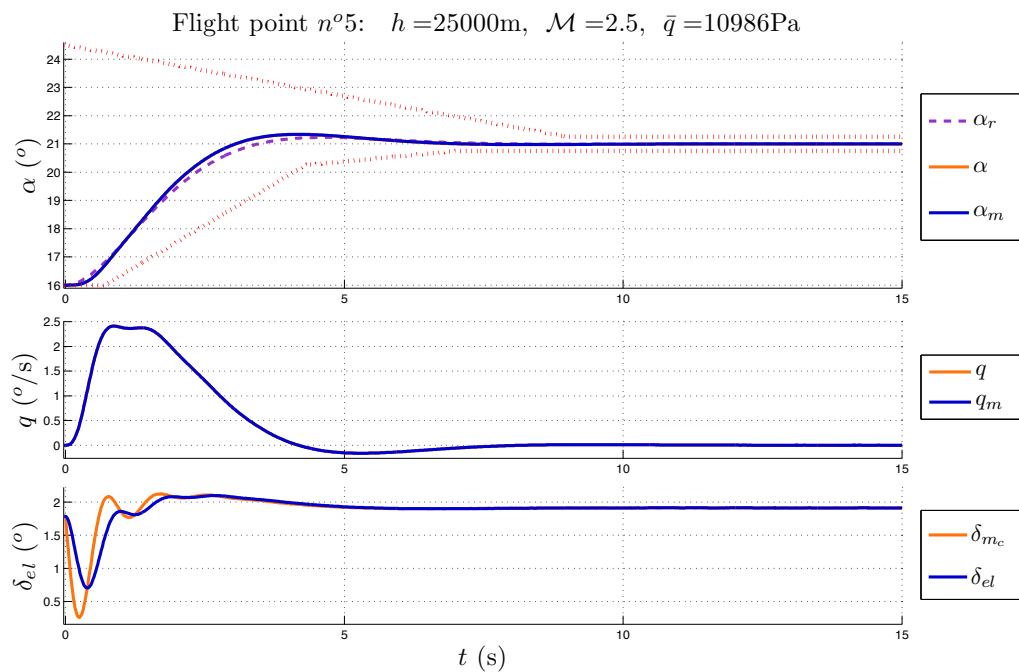
Figure 5.15: Simulation at $\mathcal{M} > 1$ with unsaturated actuator and controller **nº3**.

Figure 5.16: Simulation at $\mathcal{M} > 1$ with saturated actuator and controller **n°2**.
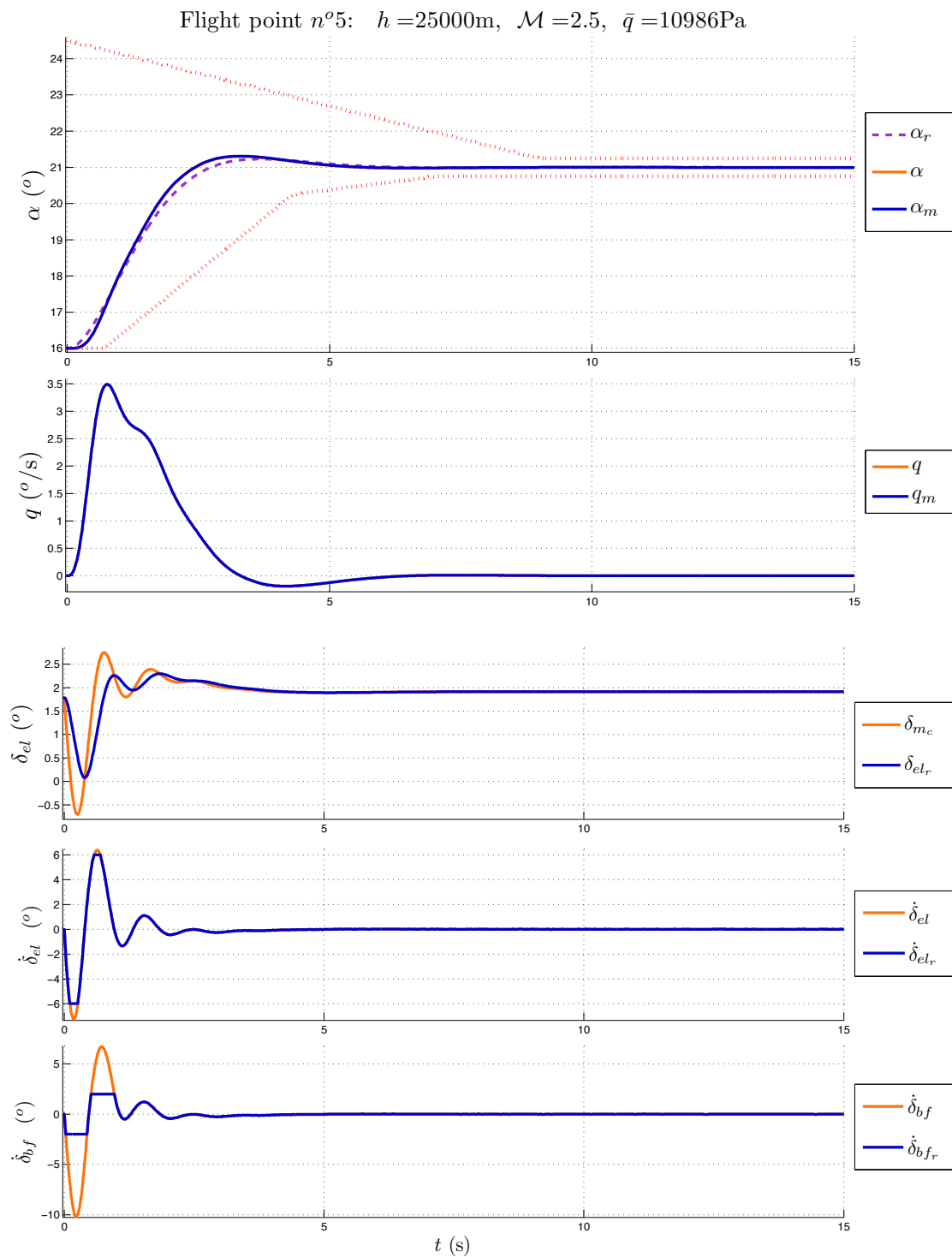
Figure 5.17: Simulation at $\mathcal{M} > 1$ with saturated actuator and controller **n°5**.
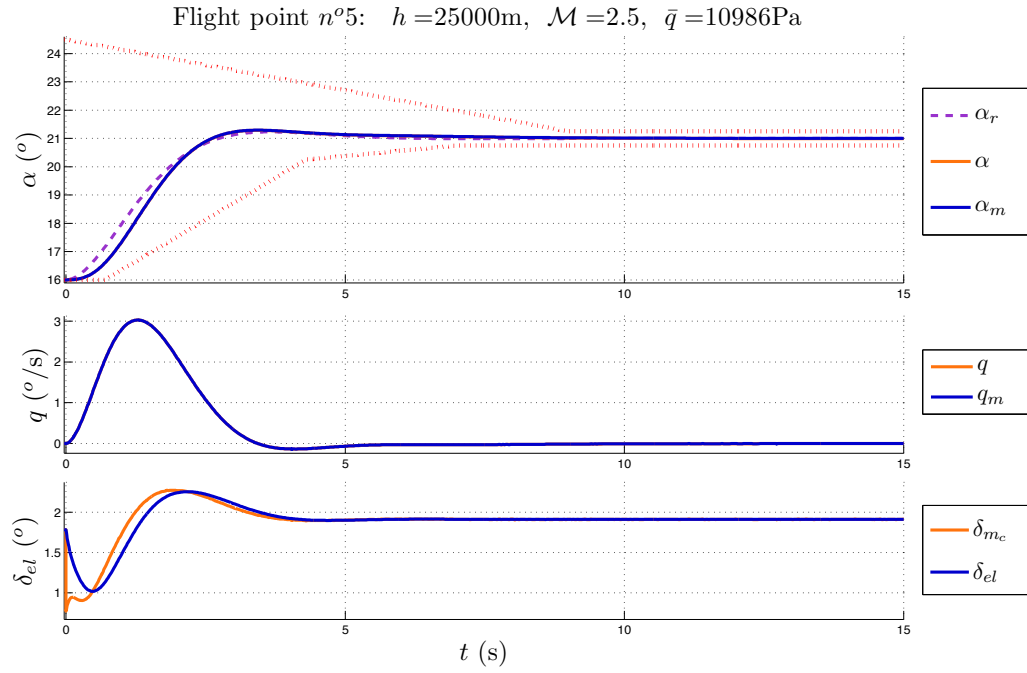
Figure 5.18: Simulation at $\mathcal{M} > 1$ with unsaturated actuator and controller **n°6**.
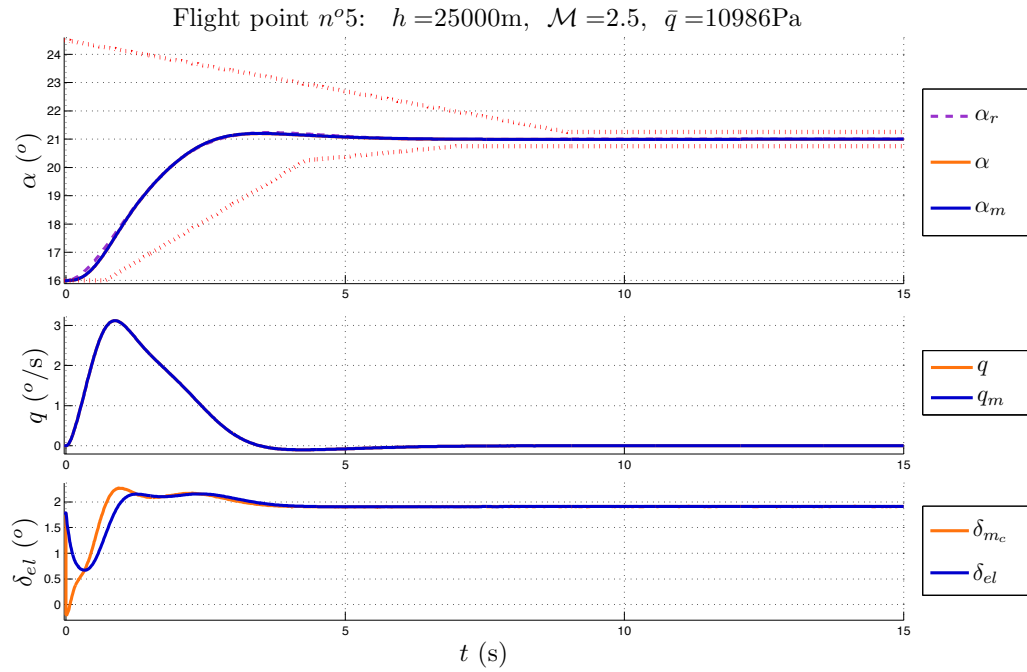
Figure 5.19: Simulation at $\mathcal{M} > 1$ with unsaturated actuator and controller **n°7**.
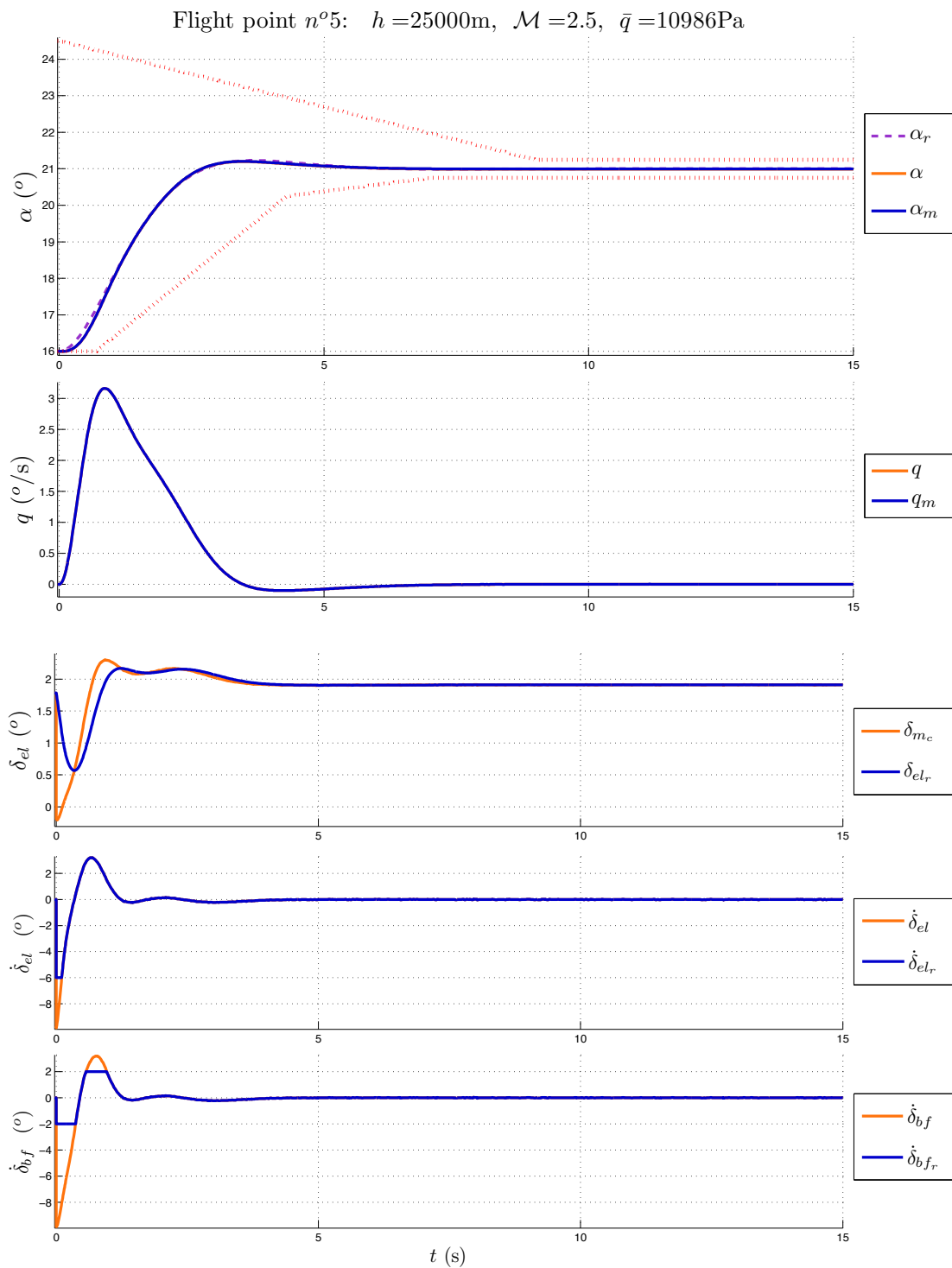
Figure 5.20: Simulation at $\mathcal{M} > 1$ with saturated actuator and controller **n°7**.
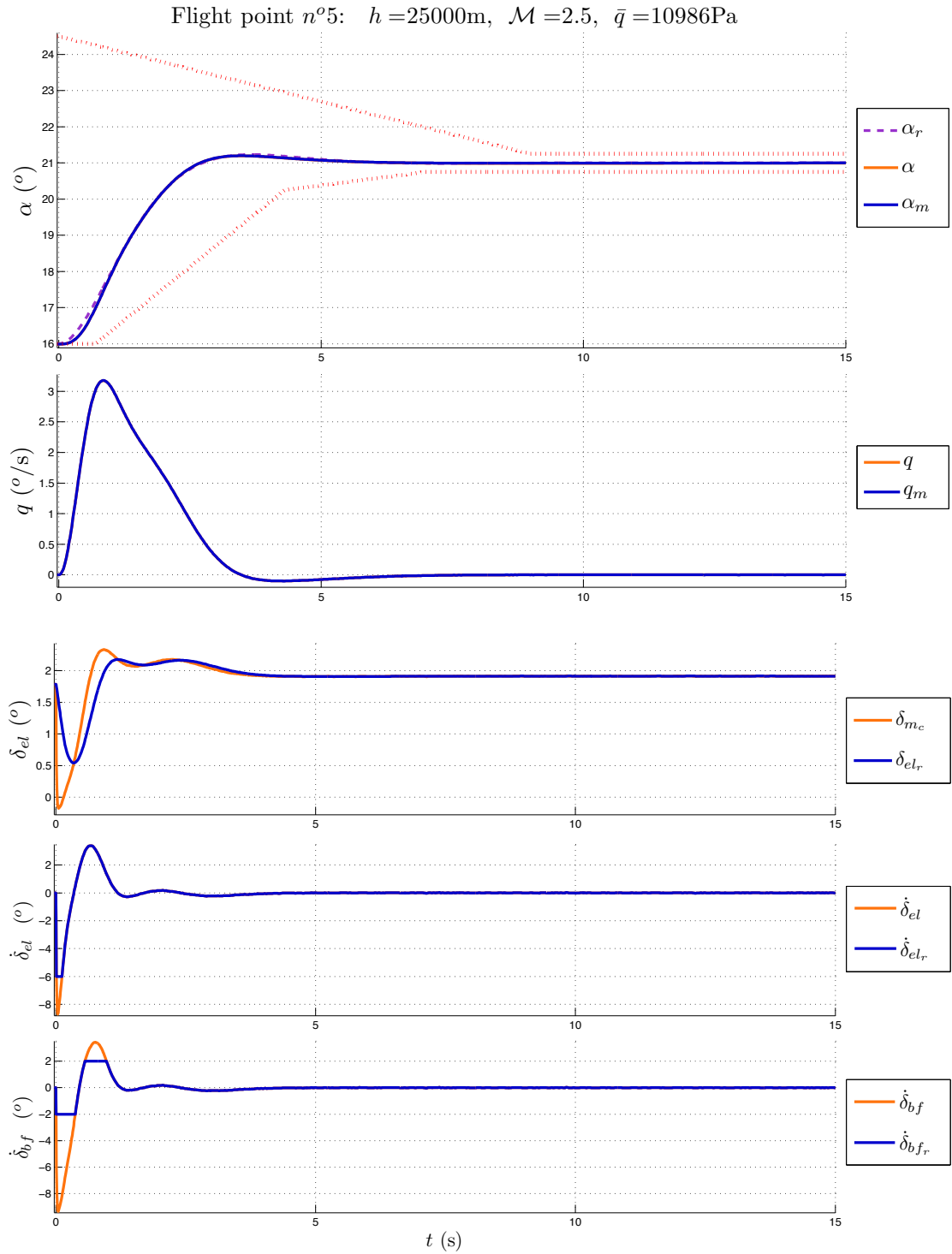
Figure 5.21: Simulation with wind disturbances, saturated actuator and controller **nº8**.
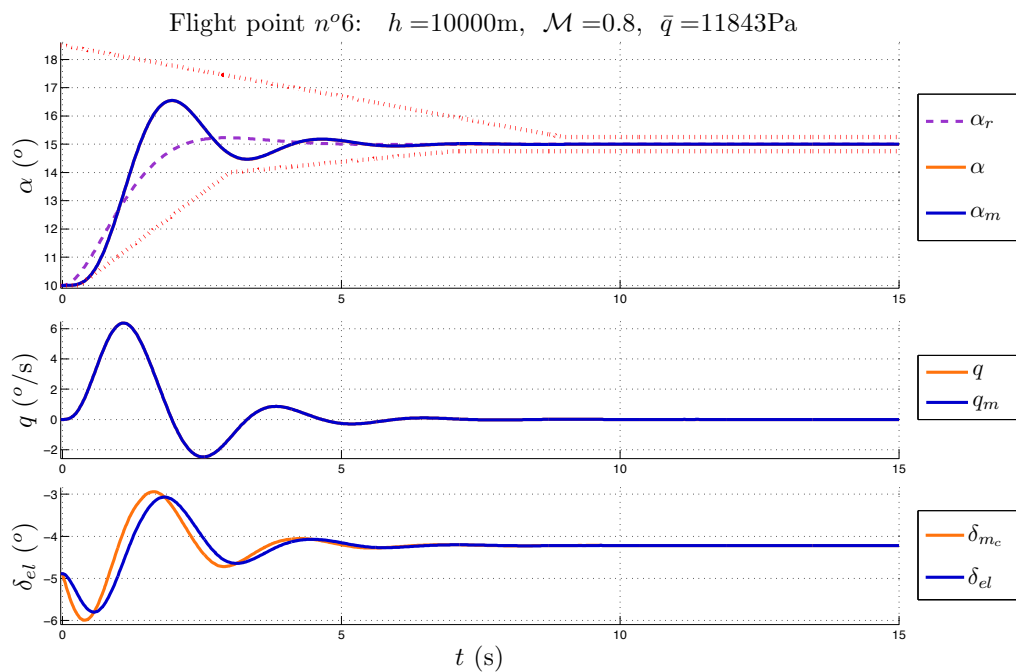
Figure 5.22: Simulation at $\mathcal{M} < 1$ with unsaturated actuator and controller **n°1**.
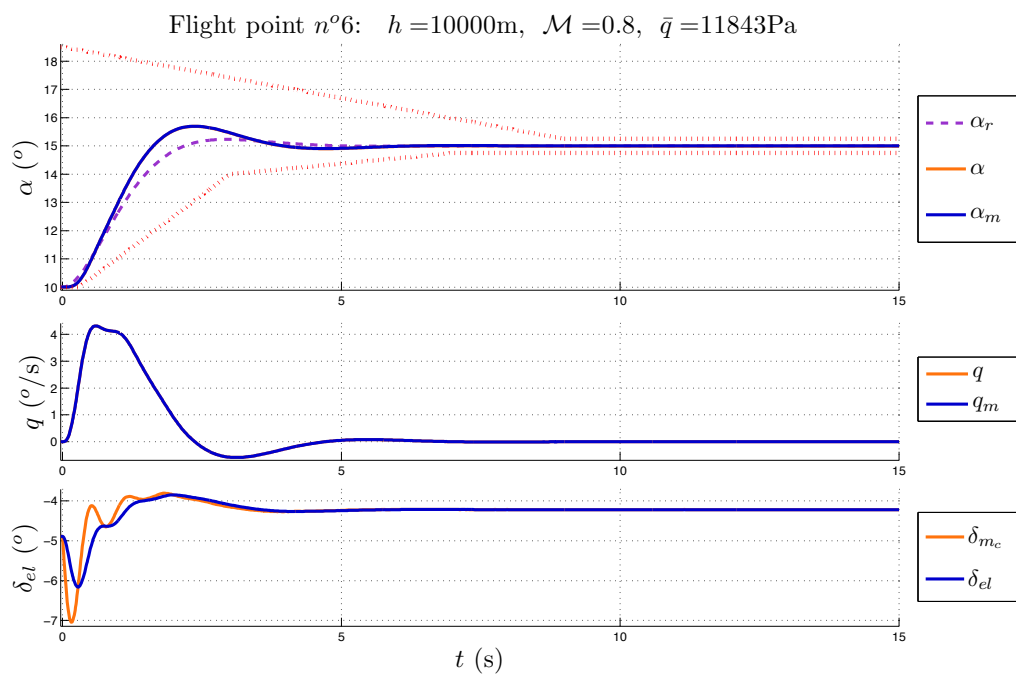
Figure 5.23: Simulation at $\mathcal{M} < 1$ with unsaturated actuator and controller **n°3**.

Flight point n^o6: $h = 10000$m, $\mathcal{M} = 0.8$, $\bar{q} = 11843$Pa
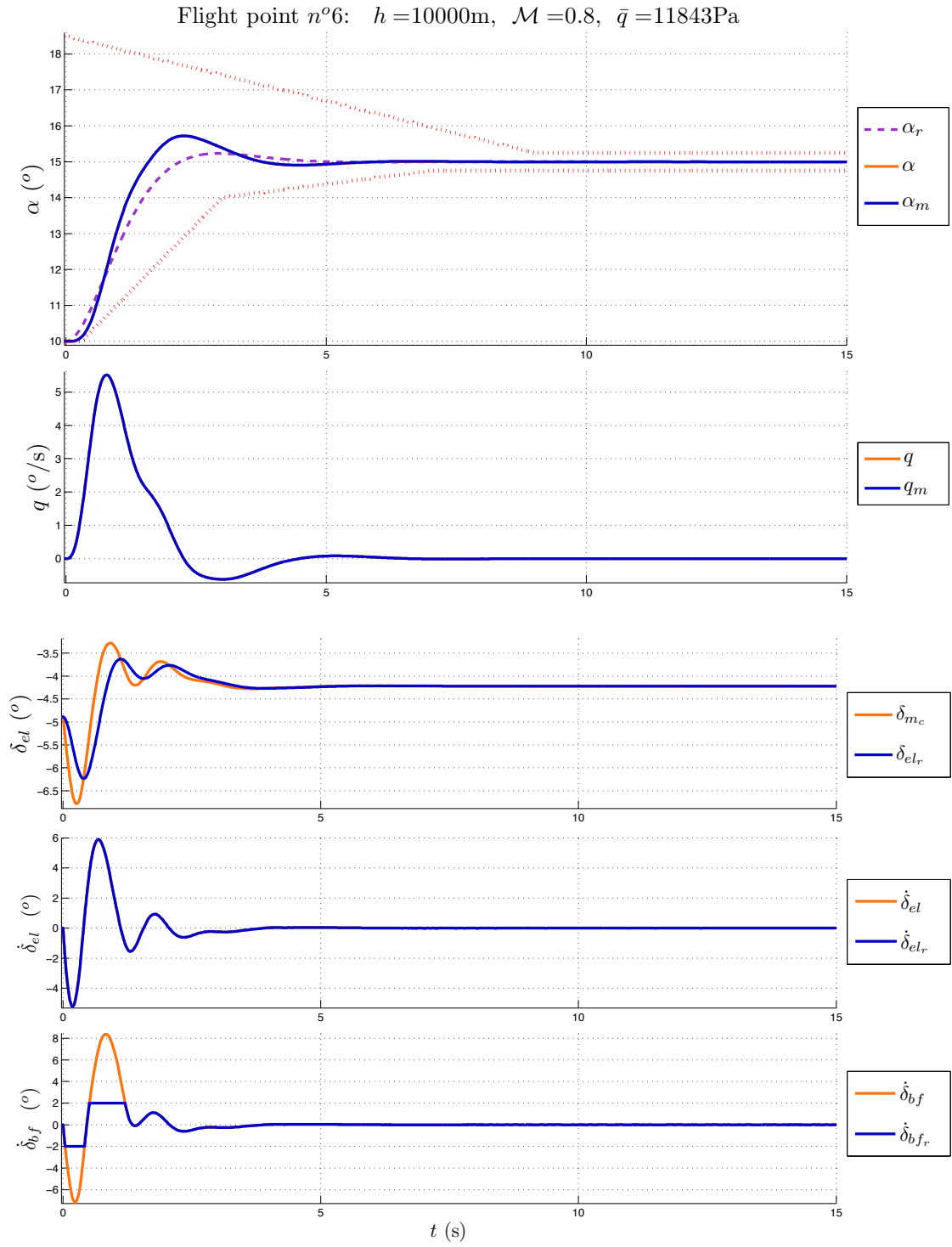
Figure 5.24: Simulation at $\mathcal{M} < 1$ with saturated actuator and controller **n°2**.
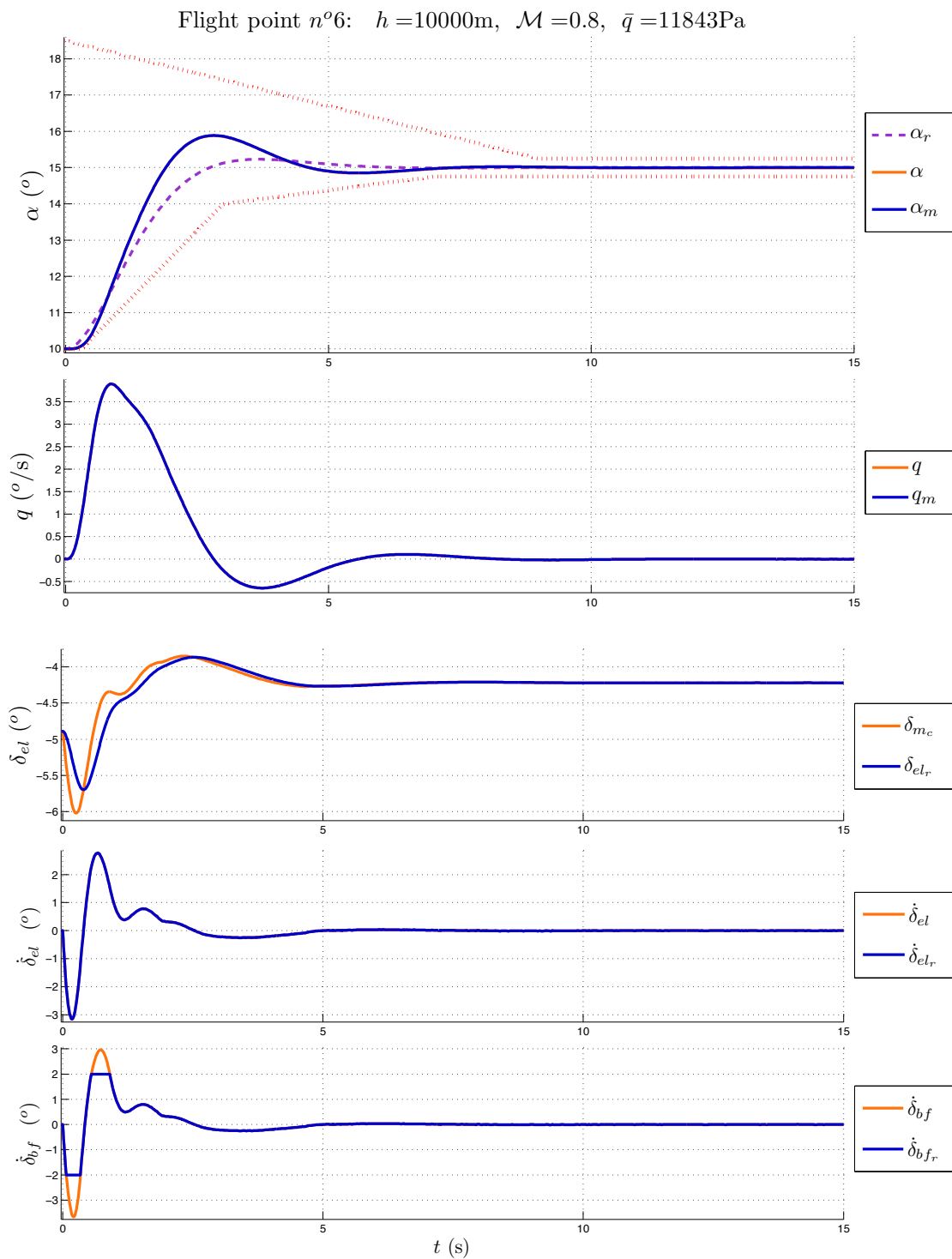
Figure 5.25: Simulation at $\mathcal{M} < 1$ with saturated actuator and controller **n°5**.
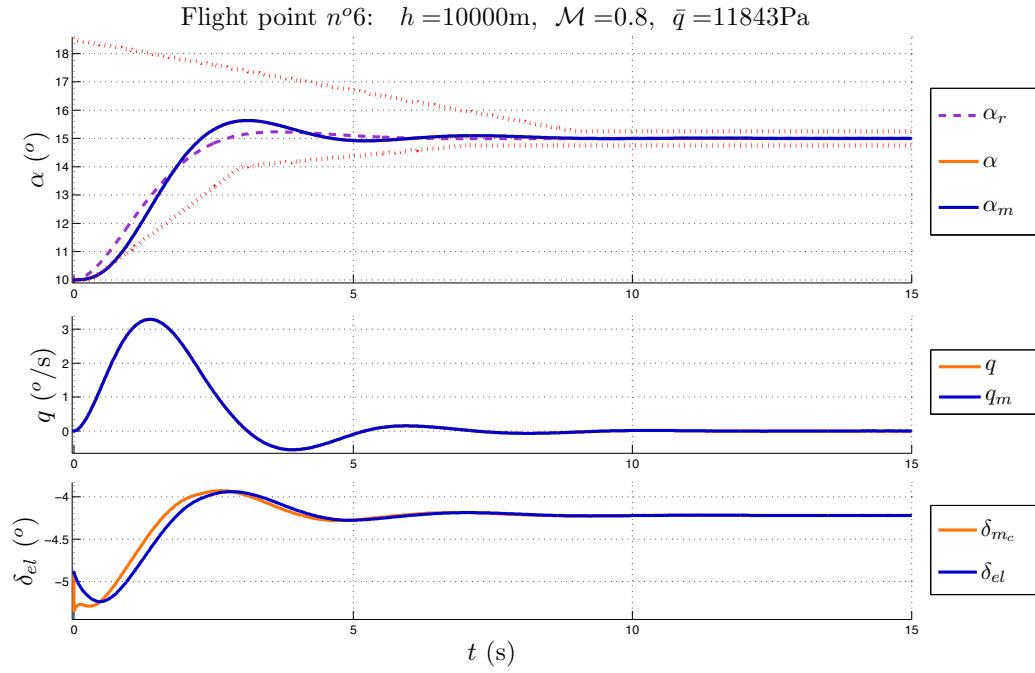
Figure 5.26: Simulation at $\mathcal{M} < 1$ with unsaturated actuator and controller **n°6**.
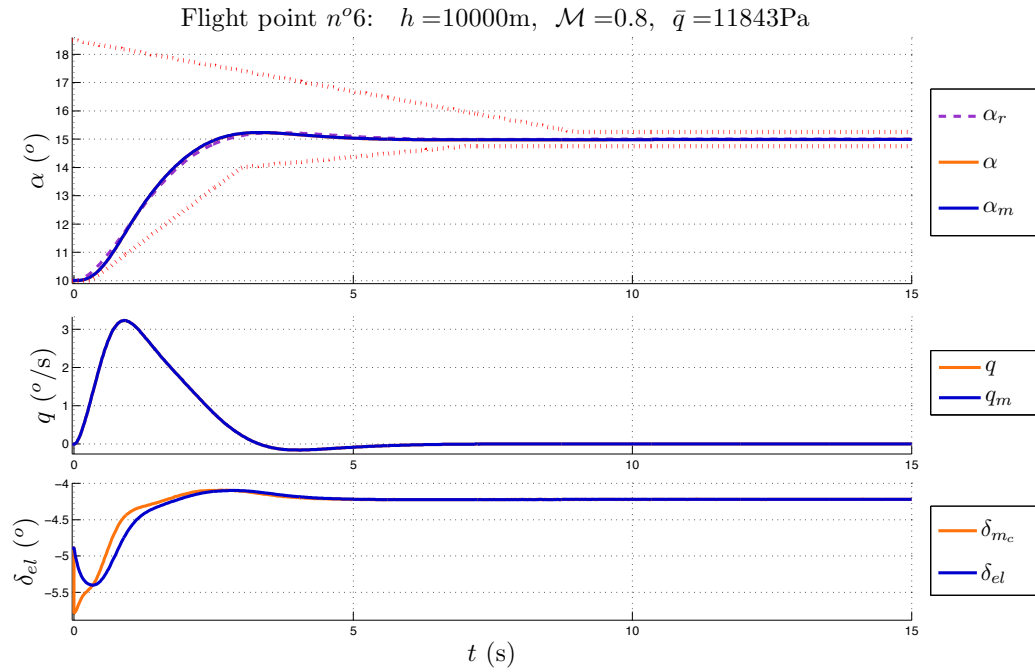
Figure 5.27: Simulation at $\mathcal{M} < 1$ with unsaturated actuator and controller **n°7**.
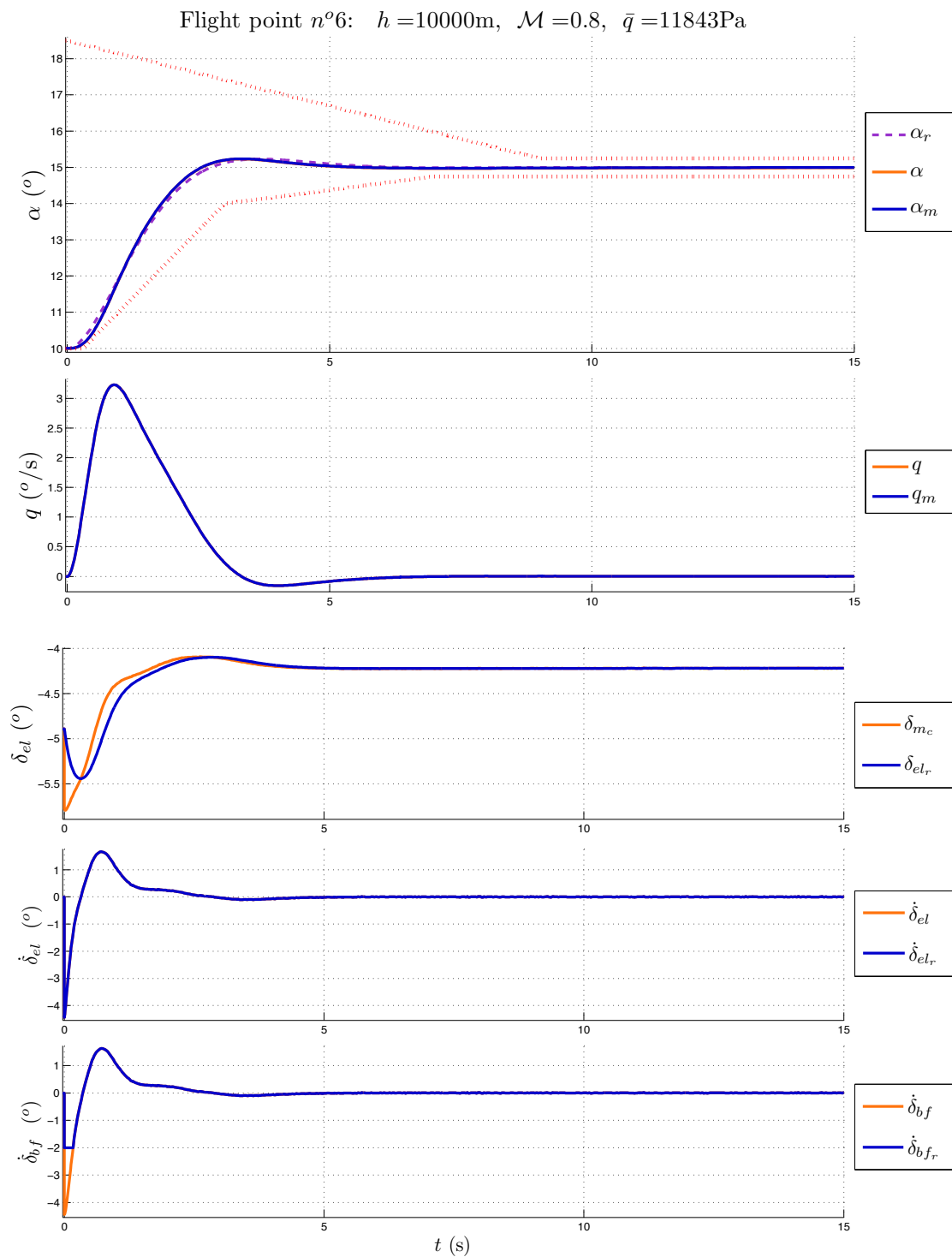
Figure 5.28: Simulation at $\mathcal{M} < 1$ with saturated actuator and controller **n⁰7**.
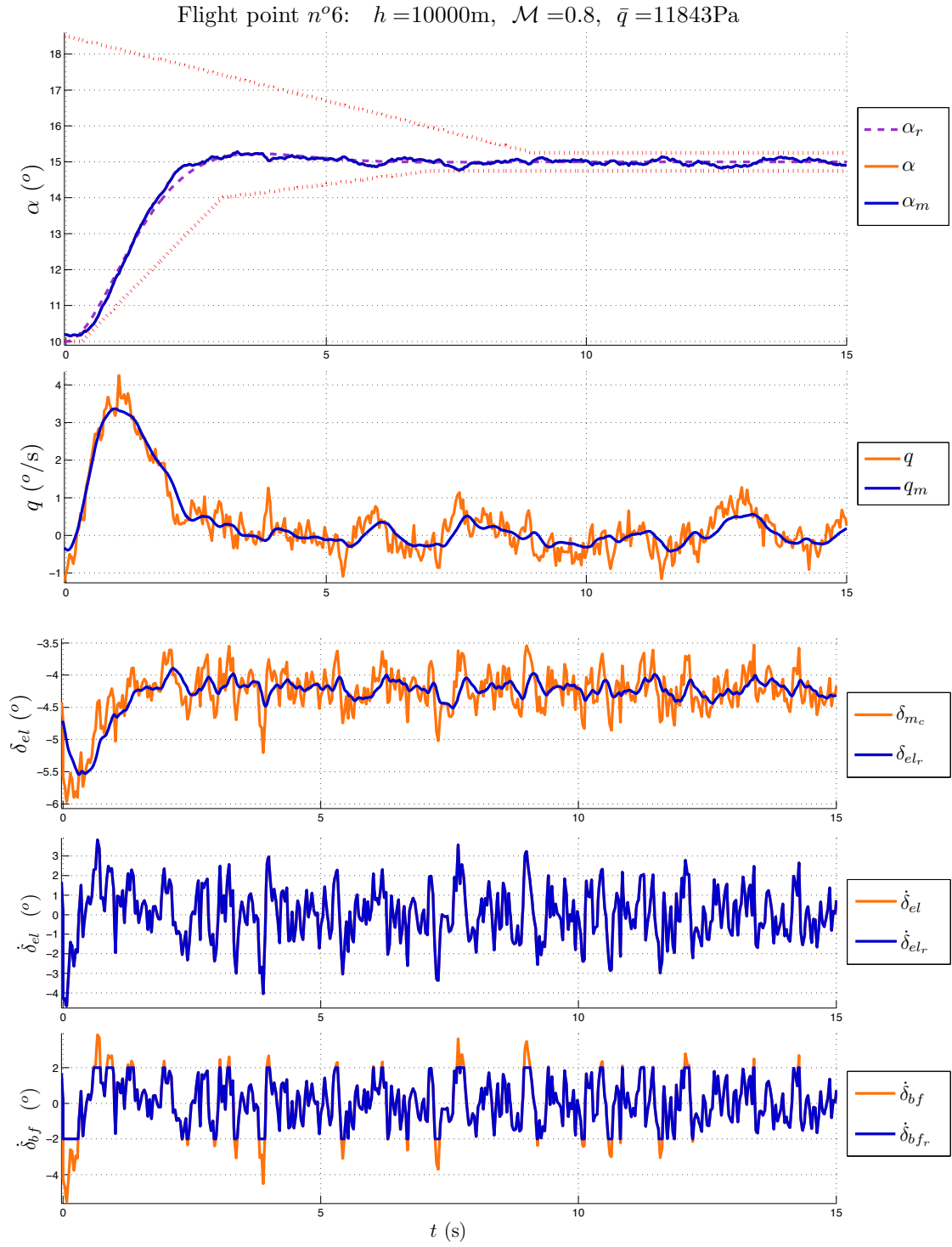
Figure 5.29: Simulation with wind disturbances, saturated actuator and controller **n°8**.

5.3.2 Lateral axis

The control objectives on the lateral dynamics are the side-slip angle β and the roll angle ϕ. In this specifications example, the performance requirements are actually set on the roll angle rate $\dot{\phi}$ rather than on the roll angle ϕ.

Throughout a reentry mission, side-slip angle objective is kept close to zero, while the specifications on the time response of the roll angle rate $\dot{\phi}$ can be regrouped in a bounded normalized area as will be explained next.

5.3.2.1 Performance objective on side-slip and roll angle rate

Let us now present the performance objectives that the control problem of the lateral dynamics of the reentry vehicle should comply with.

– The side-slip angle β is to be kept around 0° and must verify in all cases: $|\beta(t)| < 2°$;
– The constraints on roll angle rate $\dot{\phi}$ are defined by the normalized bounded regions as functions of the Mach number on Figure 5.30.
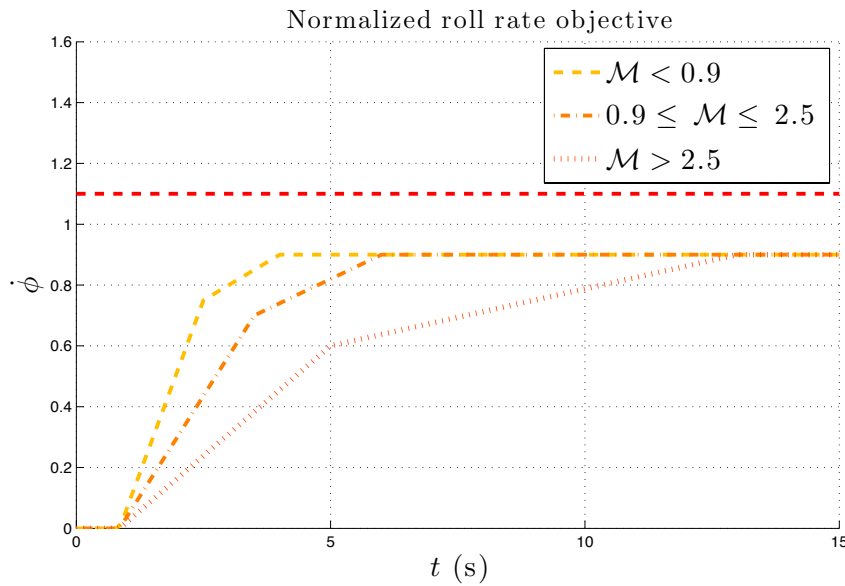
Figure 5.30: Performance specification on the roll angle rate $\dot{\phi}$.

Clearly, at higher Mach numbers, the lower bounds are less restrictive than that at lower Mach numbers. A faster time response on the roll angle rate $\dot{\phi}$ is then expected at slower Mach numbers than at higher Mach numbers.

Then, the bounds of this performance specification hardly admit any overshoot. Then, the roll angle rate should preferably follow first-order dynamics, although they will be indirectly imposed

by the roll rate p desired dynamics. Yet, to be consistent with the control designs of Chapter 4 for the lateral control objectives, second-order dynamics will be defined for the roll angle ϕ through the baseline NDI controller design as well as through the reference model $R_{lat}(s)$ of our NLC framework.

In this case, to guide the choice of the desired dynamics which will allow to satisfy the performance specifications, the settling time t_s and rise time t_r are affected by the time constants τ_i and the cut-off frequencies ω_{c_i}. It can be deduced by observation that the settling time is of about $t_s \approx 3.5\,s$ for $\mathcal{M} < 0.9$, $t_s \approx 5.5\,s$ for $0.9 \leq \mathcal{M} \leq 2.5$ and $t_s \approx 12.5\,s$ for $\mathcal{M} > 2.5$. As for the rise time, it can be estimated that for $\mathcal{M} < 0.9$ a minimum t_r of approximately $0.45°/s$ should be satisfied; for $0.9 \leq \mathcal{M} \leq 2.5$, $t_r \approx 0.25°/s$; and for $\mathcal{M} > 2.5$, $t_r \approx 0.15°/s$.

5.3.2.2   Controller synthesis process

Let us now present the control law obtained via the standard NDI controller design procedure for the lateral dynamics of the reentry vehicle. Based on the general control law design detailed in Section 4.1.2 (see page 88), consider the NDI-PI solution expressed in equation (5.26) as:

$$\begin{bmatrix} \delta_l \\ \delta_n \end{bmatrix} = G_2^{-1}(K\,\tilde{y} + H\,w) \tag{5.26}$$

where

$$K = \begin{bmatrix} \tilde{T}\,K_P & \tilde{T}\,K_I & -T \end{bmatrix} \tag{5.27}$$

$$H = \begin{bmatrix} -\tilde{T} & -I \end{bmatrix} \tag{5.28}$$

with

$$\tilde{T} = T\,G_1^{-1} \tag{5.29}$$

and given the vectors

$$\tilde{y} = \begin{bmatrix} \varepsilon_\beta & \varepsilon_\phi & \int \varepsilon_\beta & \int \varepsilon_\phi & p & r \end{bmatrix}^T \tag{5.30}$$

$$w = \begin{bmatrix} Y_\beta & X_\phi & L_p & N_r \end{bmatrix}^T \tag{5.31}$$

Recall that the control efficiency inverse $G_2^{-1}(x, \Theta)$ is estimated on-line while the gains K and H contain controller parameters which respond to the performance specifications. The vectors $\tilde{y}$ and w are the controller input signals corresponding to system measurements and nonlinear function estimations.

The static gain values k_P and k_I contained in the matrices K_P, K_I are directly linked to the desired dynamics of the side-slip angle β and the roll angle ϕ to be imposed on the closed-loop system. From these constants, the time constants of the setpoint filters in $F_{lat}(s)$ are obtained such as $\tau_{F_i} = k_{P_i}/k_{I_i}$.

An example of the possible desired dynamics that can be established for the control objectives, along with its associated controller parameters, is presented on Table 5.18.

$\mathcal{M}$	Desired dynamics			Parameter values			
	ω_{c_β} (rad/s)	ω_{c_ϕ} (rad/s)	ξ_i	k_{P_β}	k_{I_β}	k_{P_ϕ}	k_{I_ϕ}
> 2.5	1.00	0.65	1.0	2.00	1.00	1.30	0.42
$[0.9, 2.5]$	1.5	1.0	0.8	2.40	2.25	1.60	1.00
< 0.9	2.0	1.2	0.8	2.62	4.00	1.92	1.44

Table 5.18: Controller parameters defining the desired dynamics for the lateral control objectives.

The final lateral flight controller is computed by defining the matrix $\tilde{T}$, which contains the value of time constants τ_p and τ_r. These are the controller main adjustable parameters. It should be reminded that the choice of these adjustable parameters needs to verify the time scaling hypothesis made for the controller design.

Since the guidelines and outcomes of the choice of τ_i have been cleared out in the longitudinal case, consider a single example which leads to the following Mach number-scheduled controller:

$\mathcal{M}$	NDI-PI controller #6														
	Tuning		Controller Gains												
	τ_p (s)	τ_r (s)	K						H						
> 2.5	0.30	0.15	$\begin{bmatrix} 0 & 4.3 & 0 & 1.4 & -3.3 & 0 \\ -15.9 & 5.6 & -7.9 & 1.8 & 0 & -6.7 \end{bmatrix}$						$\begin{bmatrix} 0 & -3.3 & -1 & 0 \\ 7.9 & -4.3 & 0 & -1 \end{bmatrix}$					
$[0.9, 2.5]$	0.20	0.10	$\begin{bmatrix} 0 & 8 & 0 & 5 & -5 & 0 \\ -24.9 & 4.6 & -23.4 & 2.8 & 0 & -10 \end{bmatrix}$						$\begin{bmatrix} 0 & -5 & -1 & 0 \\ 10.4 & -2.8 & 0 & -1 \end{bmatrix}$					
< 0.9	0.10	0.05	$\begin{bmatrix} 0 & 19.2 & 0 & 14.4 & -10 & 0 \\ -64.9 & 6.7 & -81.2 & 5.1 & 0 & -20 \end{bmatrix}$						$\begin{bmatrix} 0 & -10 & -1 & 0 \\ 20.3 & -3.5 & 0 & -1 \end{bmatrix}$					

Table 5.19: Definition of the NDI-PI controller #6.

Next, the method allowing to obtain generalized NLC-$\mathcal{H}_\infty$ controllers for the lateral dynamics of the reentry vehicle is employed. Given that the difference between the expected dynamics at higher and lower Mach numbers is significant in the lateral case, two robust controller will be computed: one for the high hypersonic regime ($\mathcal{M} > 2.5$), and another one for the lower hypersonic, transonic and subsonic regimes ($\mathcal{M} \leq 2.5$).

The synthesis procedure presented for the longitudinal case, where the frequency domain response of the baseline NDI solution is exploited to begin shaping the robust controller synthesis is used.

First, let us retake the reformulated lateral dynamics model under the form (4.57) presented on

page 96, which reads:

$$\Sigma_{lat}(s) : \begin{cases} \dot{x} &= Ax + B_1 \begin{bmatrix} f_\beta \\ f_\phi \\ f_p \\ f_r \end{bmatrix} + B_2 \Lambda \begin{bmatrix} \delta_l \\ \delta_n \end{bmatrix} \\[2em] z &= \begin{bmatrix} 1 & 0 & 0 & 0 \\ 0 & 1 & 0 & 0 \end{bmatrix} x \end{cases} \tag{5.32}$$

with

$$x = \begin{bmatrix} \beta & \phi & p & r \end{bmatrix}^T, \qquad A = \begin{bmatrix} y_\beta & 0 & \sin\alpha & -\cos\alpha \\ 0 & 0 & 1 & 0 \\ l_\beta & 0 & l_p & l_r \\ n_\beta & 0 & n_p & n_r \end{bmatrix}$$

$$B_1 = \begin{bmatrix} 1 & 0 & 0 & 0 \\ 0 & 1 & 0 & 0 \\ 0 & 0 & 1 & 0 \\ 0 & 0 & 0 & 1 \end{bmatrix}, \qquad B_2 = \begin{bmatrix} 0 & 0 \\ 0 & 0 \\ 1 & 0 \\ 0 & 1 \end{bmatrix}$$

$$f_\beta = \hat{f}_\beta + w_{f_\beta}, \qquad f_\phi = \hat{f}_\phi + w_{f_\phi}$$

$$f_p = \hat{f}_p + w_{f_p}, \qquad f_r = \hat{f}_r + w_{f_r}$$

Recall that the A matrix is chosen so that the norms of the functions f_β, f_ϕ, f_p and f_r are reduced for most operating conditions. The flight points considered the closest to the "center" of the flight domain, from a pole location point of view, are selected. From the map of poles presented on Figure 5.31, flight point n°8 seems to be the best operating conditions which correspond to this criteria at lower Mach numbers, while flight point n°1 responds to the criteria at higher Mach numbers.

The following matrices are deduced:

$$A_1 = \begin{bmatrix} -0.000016 & 0.001345 & 0.5446 & -0.8387 \\ 0 & 0 & 1 & 0.6494 \\ -0.003554 & 0 & -0.04241 & -0.05504 \\ 0.009815 & 0 & 0.07721 & 0.06083 \end{bmatrix} \tag{5.33}$$

$$A_8 = \begin{bmatrix} -0.002112 & 0.09435 & 0.1736 & -0.9848 \\ 0 & 0 & 1 & 0.1763 \\ -0.02659 & 0 & -0.2988 & 0.3691 \\ -0.005022 & 0 & 0.1823 & -0.638 \end{bmatrix} \tag{5.34}$$

where the index 1 and 8 correspond to the flight points.

ONERA
THE FRENCH AEROSPACE LAB

isae
Institut Supérieur de l'Aéronautique et de l'Espace
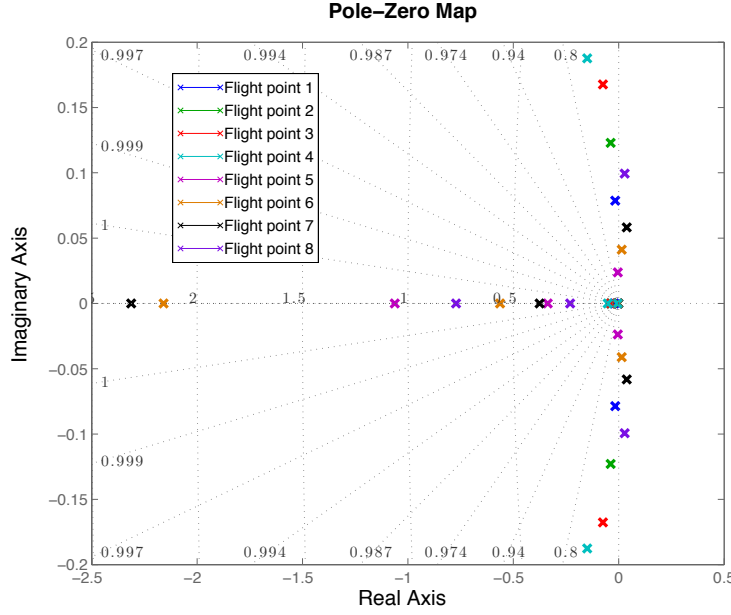
Figure 5.31: Lateral open-loop poles of the flight domain considered for simulation.

First, let us present the computation of the controller which will control the lateral dynamics of the reentry vehicle for $\mathcal{M} \leq 2.5$. For controller synthesis, consider the multi-channel design-oriented model presented on Figure 4.8 of page 98.

A preliminary singular value analysis of the NDI-PI solution contained in Table 5.19, specifically for $\mathcal{M} < 0.9$, is used. Consider the general analysis model presented on Figure 5.32. One gets that the peak gains of the performance transfers $\mathcal{T}_{\mathbf{w} \to z_p}$ and the actuator rate transfers $\mathcal{T}_{\mathbf{w} \to z_u}$ are

$$
\begin{aligned}
\sigma_{z_\beta} = 0.552 = -5.2\,dB, && \sigma_{z_{\delta_l}} = 111.515 = 40.9\,dB \\
\sigma_{z_\phi} = 0.424 = -7.5\,dB, && \sigma_{z_{\delta_n}} = 492.685 = 53.8\,dB
\end{aligned}
\tag{5.35}
$$

considering that $\mathbf{w} = \begin{bmatrix} \beta_c & \phi_c & f_\beta & f_\phi & f_p & f_r \end{bmatrix}^T$, $z_p = \begin{bmatrix} z_\beta & z_\phi \end{bmatrix}^T$ and $z_u = \begin{bmatrix} z_{\delta_l} & z_{\delta_n} \end{bmatrix}^T$.

From the singular value analysis and after a few trial-and-error tunings, the following weighting functions are retained for loop-shaping the design-oriented model presented on Figure 4.8:

$$
W_{p_\beta} = \frac{s^6 + 22.97\,s^5 + 200.2\,s^4 + 1185\,s^3 + 1516\,s^2 + 342.3\,s + 6.705}{0.2059\,s^6 + 2.997\,s^5 + 16.11\,s^4 + 13.41\,s^3 + 1.709\,s^2 + 0.02276\,s + 0.00002}
\tag{5.36}
$$

$$
W_{p_\phi} = \frac{s^5 + 7.742\,s^4 + 36.2\,s^3 + 84.43\,s^2 + 39.98\,s + 1.941}{0.05578\,s^5 + 0.2789\,s^4 + 1.078\,s^3 + 0.8219\,s^2 + 0.08158\,s + 0.00008}
\tag{5.37}
$$

The weighted outputs z_u corresponding to the actuator rate transfers are weighted by constant values $g_{z_i} = 1$.
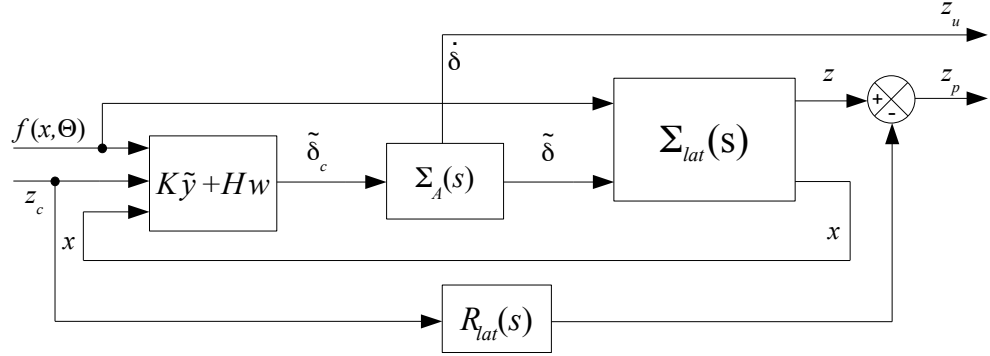
Figure 5.32: Preliminary analysis model for the lateral baseline NDI controller.

The reference models in $R_{lat}(s)$ contain the desired dynamics of β and ϕ described in Table 5.18 for $\mathcal{M} < 0.9$. These desired dynamics are defined as second-order according to the transfer function

$$R_{lat_i}(s) = \frac{\omega_{c_i}^2}{s^2 + 2\,\xi_i\,\omega_{c_i}\,s + \omega_{c_i}^2} \tag{5.38}$$

The generalized NLC-$\mathcal{H}_\infty$ controller $K_{lat}(s)$ can now be computed via the MATLAB function *hinfstruct* which implements the structured $\mathcal{H}_\infty$ synthesis technique. A fifth-order state-space controller structure was chosen for this controller.

By merging the fifth-order dynamics of the computed controller $K_{lat}(s)$ with those of the setpoint filter $F_{lat}(s)$ and the error integrals ε_β and ε_ϕ, one gets an augmented compensator structure of state $x_K \in \mathbb{R}^9$. It can be expressed under the form:

$$\left[\begin{array}{c} \dot{x}_K \\ \hline \delta_{l_c} \\ \delta_{n_c} \end{array}\right] = K_{lat} \left[\begin{array}{c} x_K \\ \hline \tilde{y} \end{array}\right] \tag{5.39}$$

where

$$\tilde{y} = \begin{bmatrix} \beta_c & \phi_c & \hat{f}_\beta & \hat{f}_\phi & \hat{f}_p & \hat{f}_r & \beta & \phi & p & r \end{bmatrix}^T \tag{5.40}$$

Using the reference model (5.38) along with the weighting functions (5.48), the lateral NLC-$\mathcal{H}_\infty$ controller is:

$$K_{lat} = \left[\begin{array}{c|c} A_K & B_K \\ \hline C_K & D_K \end{array}\right] \tag{5.41}$$

where the values of A_K, B_K, C_K and D_K are defined in the following table:

ONERA
THE FRENCH AEROSPACE LAB

isae
Institut Supérieur de l'Aéronautique et de l'Espace

$$A_K = \begin{bmatrix} -0.75 & 0 & 0 & 0 & 0 & 0 & 0 & 0 & 0 \\ 0 & -0.75 & 0 & 0 & 0 & 0 & 0 & 0 & 0 \\ 0.75 & 0 & 0 & 0 & 0 & 0 & 0 & 0 & 0 \\ 0 & 0.75 & 0 & 0 & 0 & 0 & 0 & 0 & 0 \\ -92.5 & -66.1 & 75.3 & 121 & -15.1 & -1.5 & 0 & 0 & 0 \\ 5.2 & -29.5 & 52.6 & 45.1 & 23.7 & -20.2 & 4.6 & 0 & 0 \\ 32.7 & -44.3 & 7.03 & -26 & 0 & 5.3 & -2.8 & 0.13 & 0 \\ -1.7 & 652 & 20 & -78.6 & 0 & 0 & 13.6 & -1.6 & -3.1 \\ -55.4 & 7.1 & -26.4 & -109 & 0 & 0 & 0 & -1.2 & -12.7 \end{bmatrix} \quad (5.42)$$

$$B_K = \begin{bmatrix} 1 & 0 & 0 & 0 & 0 & 0 & 0 & 0 & 0 & 0 \\ 0 & 1 & 0 & 0 & 0 & 0 & 0 & 0 & 0 & 0 \\ 0 & 0 & 0 & 0 & 0 & 0 & -1 & 0 & 0 & 0 \\ 0 & 0 & 0 & 0 & 0 & 0 & 0 & -1 & 0 & 0 \\ -5.1 & -3.3 & -2.5 & -2.5 & -0.61 & 0.4 & -26 & -28 & -2.2 & 8.1 \\ -5.5 & 0.6 & -5.8 & 4.1 & 1.7 & 1.7 & -21 & 51.9 & 22.2 & -6.9 \\ 3.8 & 20.6 & -2.8 & 3.9 & 1.1 & 3.5 & 17 & 20.2 & -5.4 & -16 \\ 325 & -375 & 80.7 & -32 & 0.1 & -27 & -151 & -27 & -76 & 72.2 \\ -39 & 51.8 & -10 & 4.4 & 0.2 & 4.1 & 13.1 & 19.2 & 8.3 & -7 \end{bmatrix} \quad (5.43)$$

$$C_K = \begin{bmatrix} -136. & 35.4 & 35.9 & 22 & -38.2 & 19.2 & -3.9 & -0.9 & -9.1 \\ 155 & -115 & -30.5 & 119 & -0.2 & 9.2 & -5.2 & 2.4 & 22.1 \end{bmatrix} \quad (5.44)$$

$$D_K = \begin{bmatrix} 0.4 & 1.9 & -0.5 & -5.4 & -1.8 & -0.2 & -23 & -98 & -33 & 16.9 \\ -1.6 & -0.7 & 5.5 & -0.8 & -0.01 & -1.4 & 51 & -23 & -10 & -13 \end{bmatrix} \quad (5.45)$$

Table 5.20: Definition of the NLC-$\mathcal{H}_\infty$ controller #3.

When the singular value analysis scheme is used, generating a closed-loop with the controller presented above, the following peak gain values are obtained:

$$\begin{aligned} \sigma_{z_\beta} &= 0.595 = -4.5\,dB, & \sigma_{z_{\delta_l}} &= 30.539 = 29.7\,dB \\ \sigma_{z_\phi} &= 0.483 = -6.3\,dB, & \sigma_{z_{\delta_n}} &= 30.463 = 29.6\,dB \end{aligned} \quad (5.46)$$

By comparing this results with those contained in (5.35), it can be observed that even though the performance measurements obtained by both solutions are basically the same, there is an important reduction on the peak gains of the actuator rate transfers.

Now, let us present the computation of the NLC-$\mathcal{H}_\infty$ for the lateral dynamics of the reentry vehicle for $\mathcal{M} > 2.5$. Let us begin with the singular value analysis of the NDI-PI solution contained in Table 5.19, which is done using the gains defined for $\mathcal{M} > 2.5$. In this case, the peak gains of the performance transfers $\mathcal{T}_{\mathbf{w} \to z_p}$ and the actuator rate transfers $\mathcal{T}_{\mathbf{w} \to z_u}$ are

$$\begin{aligned} \sigma_{z_\beta} &= 0.621 = -4.1\,dB, & \sigma_{z_{\delta_l}} &= 26.338 = 28.4\,dB \\ \sigma_{z_\phi} &= 0.932 = -0.6\,dB, & \sigma_{z_{\delta_n}} &= 112.441 = 41\,dB \end{aligned} \quad (5.47)$$

From these results, the following weighting functions are obtained for loop-shaping the design-oriented model:

$$W_{p_\beta} = \frac{s^6 + 82.4\,s^5 + 473.9\,s^4 + 1491\,s^3 + 1866\,s^2 + 690\,s + 29.79}{0.05548\,s^6 + 4.323\,s^5 + 12.62\,s^4 + 15.29\,s^3 + 4.405\,s^2 + 0.1126\,s + 0.0001} \tag{5.48}$$

$$W_{p_\phi} = \frac{s^6 + 8.894\,s^5 + 28.81\,s^4 + 42.98\,s^3 + 33.54\,s^2 + 14.38\,s + 0.757}{0.0986\,s^6 + 0.7815\,s^5 + 2.037\,s^4 + 1.902\,s^3 + 0.497\,s^2 + 0.008076\,s + 0.00007} \tag{5.49}$$

Once more, the weighted outputs z_u are weighted by constant values $g_{z_i} = 1$. The desired dynamics of β and ϕ, contained in the reference models $R_{lat}(s)$, correspond to those defined in Table 5.18 for $\mathcal{M} > 2.5$.

As in the previous case, a fifth-order state-space controller structure was chosen for this controller. Merged with the setpoint filters in $F_{lat}(s)$ and the error integrals ε_β and ε_ϕ, the final augmented compensator structure has its state such that $x_K \in \mathbb{R}^9$.

By merging the fifth-order dynamics of the computed controller $K_{lat}(s)$ with those of the setpoint filter $F_{lat}(s)$ and the error integrals ε_β and ε_ϕ, one gets an augmented compensator structure of state $x_K \in \mathbb{R}^9$. The lateral NLC-$\mathcal{H}_\infty$ flight controller for $\mathcal{M} > 2.5$ is:

$$K_{lat} = \left[\begin{array}{c|c} A_K & B_K \\ \hline C_K & D_K \end{array} \right] \tag{5.50}$$

where

$$A_K = \begin{bmatrix} -0.32 & 0 & 0 & 0 & 0 & 0 & 0 & 0 & 0 \\ 0 & -0.32 & 0 & 0 & 0 & 0 & 0 & 0 & 0 \\ 0.32 & 0 & 0 & 0 & 0 & 0 & 0 & 0 & 0 \\ 0 & 0.32 & 0 & 0 & 0 & 0 & 0 & 0 & 0 \\ 2.9 & 8.2 & 31.4 & -18.5 & -16.3 & -0.9 & 0 & 0 & 0 \\ -36.5 & -50.4 & -18.1 & -1.8 & -0.9 & -2.4 & -9.1 & 0 & 0 \\ 10.1 & -30.9 & -27.1 & -62.5 & 0 & -4 & -20.6 & 10.2 & 0 \\ -7.8 & -26 & 13.8 & 3.3 & 0 & 0 & 0.15 & -4.1 & 0.3 \\ 78.6 & 73.6 & 26 & -25.6 & 0 & 0 & 0 & 8.6 & -0.7 \end{bmatrix} \tag{5.51}$$

$$B_K = \begin{bmatrix} 1 & 0 & 0 & 0 & 0 & 0 & 0 & 0 & 0 & 0 \\ 0 & 1 & 0 & 0 & 0 & 0 & 0 & 0 & 0 & 0 \\ 0 & 0 & 0 & 0 & 0 & 0 & -1 & 0 & 0 & 0 \\ 0 & 0 & 0 & 0 & 0 & 0 & 0 & -1 & 0 & 0 \\ -11.9 & -2.9 & 7.8 & 4.2 & 3.4 & -0.9 & 28 & 25 & 14 & -4.2 \\ 188 & 38 & -32 & -8.9 & -5.9 & -2.7 & 31 & 56 & 37 & -13 \\ -19 & -10 & -3.4 & -4.1 & -0.8 & -2.5 & 70 & 26 & 23 & -17 \\ 29 & -3.8 & -27 & -10 & -4.5 & -3.5 & 36 & 56 & 27 & -4.1 \\ -274 & -57 & 60 & 17 & 10 & 4.8 & -67 & -118 & -54 & 9.6 \end{bmatrix} \tag{5.52}$$

$$C_K = \begin{bmatrix} 11.8 & -10.7 & -12.6 & 17.3 & 19.1 & -0.8 & -6.9 & 4.3 & -0.4 \\ 31.5 & -56.6 & -22.5 & -47.7 & 14.1 & -9.9 & -38.6 & 20.8 & -2.4 \end{bmatrix} \tag{5.53}$$

$$D_K = \begin{bmatrix} 0.6 & 1.3 & -3 & -3.3 & -3.8 & 1.4 & -33.6 & -45.3 & -20.7 & 0.6 \\ -0.7 & 0.6 & 5.2 & -2.4 & -2.1 & -0.6 & 92.3 & -27.7 & 11.8 & -33.6 \end{bmatrix} \tag{5.54}$$

Table 5.21: Definition of the NLC-$\mathcal{H}_\infty$ controller #4.

Applying the singular value analysis to the closed-loop systems with the NLC-$\mathcal{H}_\infty$ computed above, the following peak gain values are obtained:

$$\begin{aligned} \sigma_{z_\beta} &= 0.591 = -4.6\,dB, & \sigma_{z_{\delta_l}} &= 31.313 = 29.9\,dB \\ \sigma_{z_\phi} &= 0.791 = -2.1\,dB, & \sigma_{z_{\delta_n}} &= 31.315 = 29.9\,dB \end{aligned} \tag{5.55}$$

By comparing this results with those contained in (5.47), it is clear that the performance transfers have been improved since the values of σ_{z_p} become smaller under the action of this NLC-$\mathcal{H}_\infty$ controller. As for the actuator rate transfers, even though the peak gain $\sigma_{z_{\delta_l}}$ presents an increase, a significant reduction on the gain $\sigma_{z_{\delta_n}}$ can be clearly identified.

Finally, as it will be shown in simulation, some points may be destabilized when input constraints are accounted for. In both cases, the NDI-PI solution and the NLC-$\mathcal{H}_\infty$ controller, flight point n°1 is destabilized due to the severe effects of saturations. Then, let us propose a complete solution using an anti-windup device.

In particular, the elevons rate limits generate the destabilizing effects when the roll manoeuvre is done at flight point n°1. Then, the rate limiter structure proposed for the longitudinal case is retained for the control input δ_l.

Consider the ninth-order nominal NLC-$\mathcal{H}_\infty$ controller #4 contained in Table 5.21. Using the rate limited Direct Linear Anti-windup strategy illustrated on Figure 4.10 of page 100, consider that $v_2 = 0$ and $v_1 = v$. Given the first-order anti-windup controller

$$\begin{bmatrix} \dot{x}_J \\ \hline v \end{bmatrix} = J_{lat} \begin{bmatrix} x_J \\ \hline u_{AW} \end{bmatrix} \tag{5.56}$$

where $v \in \mathbb{R}^9$ and $u_{AW} \in \mathbb{R}$, the enhanced lateral NLC-$\mathcal{H}_\infty$ controller takes the form:

$$\begin{bmatrix} \dot{x}_K \\ \hline \delta_{l_c} \\ \delta_{n_c} \end{bmatrix} = K_{a_{lat}} \begin{bmatrix} x_K \\ \hline v \\ \tilde{y} \end{bmatrix} \tag{5.57}$$

Referring to the design-oriented model of Figure 4.11 (see page 100), adapted for this lateral particular case, the anti-windup device J_{lat} is computed using once more the function *hinfstruct*. The following first-order anti-windup device is obtained:

$$J_{lat} = \begin{bmatrix} -6.814 & -2.967 \\ \hline -3.269 & -1.592 \\ -0.4469 & -0.2394 \\ -2.76 & -1.033 \\ -0.1131 & -0.004452 \\ 12.64 & 4.442 \\ 4.926 & 6.157 \\ 8.098 & 10.83 \\ 8.734 & 5.242 \\ 19.3 & 7.968 \end{bmatrix}$$

Table 5.22: Definition of the anti-windup device for NCL-$\mathcal{H}_\infty$ controller #4.

This anti-windup device completes the robust nonlinear compensation strategy proposed for the lateral dynamics.

5.3.2.3 Simulation results

Next, the simulation results obtained using the different controllers that have been computed above, are presented considering a disturbed aerodynamic model of the reentry vehicle. Also, the Flight Mechanics simulator employed accounts for measurement disturbances including: measurement noise, scale factors and biases. All results presented in this section will also consider saturated actuator models. It is reminded that a complete compilation of simulation results including all flight points of the domain studied are contained in Appendix E.

As treated in the longitudinal case, to allow a clearer comparison between the simulation results, external environmental factors such as static wind gusts and turbulent wind effects will be temporarily discarded. Once a final solution capable of controlling the reentry vehicle throughout the whole flight envelop is exhibited, these environmental factors will be added to recreate a more realistic scenario.

For the lateral simulation case, the longitudinal dynamics are kept at a steady state by fixing the flight point trim values and by keeping the value of the pitch rate at $q \equiv 0$.

The lateral dynamics of the reentry vehicle are then simulated with a ramp function on the commanded value ϕ_c. The ramp function generates an artificial step manoeuvre on the roll angle rate $\dot{\phi}$. This manoeuvre will be held at $6°/s$ and the simulation will cover a range on the roll angle of $\phi = 0°$ to at least $\phi = 70°$.

The commanded signal on the side-slip angle will be defined as $\beta_c \equiv 0°$ for all cases.

The figures containing the graphs that characterize the evolution of the most relevant lateral parameters in simulation include the following:
– The first graph contains two curves corresponding to: the simulation roll angle rate $\dot{\phi}$ (orange line), the measured roll angle rate $\dot{\phi}_m$ (blue line). In addition to these curves, this graph includes the upper and lower boundaries (red fine dotted lines) defined by the normalized performance objectives presented in Section 5.3.2.1. The simulation roll angle rate is the actual $\dot{\phi}$ as perceived

by the reentry vehicle while $\dot{\phi}_m$ is an artificially created measurement within the IMU which serves as a reference.

– The second graph includes three curves: The reference roll angle ϕ_r (purple dotted line), the simulation roll angle ϕ (orange line) and the measured roll angle ϕ_m (blue line). The reference curve ϕ_r is generated using the desired dynamics to be imposed by the controllers. The simulation curve is the actual roll angle as seen by the vehicle. The measurement curve is directly obtained via the simulation IMU.

– The third graph depicts two curves corresponding to the simulation side-slip angle β (orange line) and to the measured side-slip angle β_m (blue line). The measured side-slip angle β_m is obtained by: a simulation inertial measurement unit when the Mach number is $\mathcal{M} > 2.5$, and by a simulation anemometric unit when the Mach number is $\mathcal{M} \leq 2.5$.

– The forth graph includes the evolution of the angular rates of the lateral dynamics: the simulation roll rate p (orange line), the measured roll rate p_m (blue line), the yaw rate r (violet line) and the measured yaw rate (green line). Again, the simulation values correspond to the actual angular rates while the measured values correspond to the simulation IMU measurements.

– The fifth graph presents the actuator signals associated with: the right elevon δ_{re} (orange line), the left elevon δ_{le} (blue line), the right winglet δ_{rw} (violet dotted line) and the left winglet δ_{lw} (green dotted line). These curves represent the actual evolution of the actuators attached to the corresponding control surfaces.

– Finally, the sixth graph contains the elevon rate signals, which help visualize the saturation levels of these actuators. There are four curves presented in this graph: the demanded right elevon rate $\dot{\delta}_{re}$ (orange line), the demanded left elevon rate $\dot{\delta}_{le}$ (blue line), the realized right elevon rate $\dot{\delta}_{re_r}$ (violet dotted line) and the realized left elevon rate $\dot{\delta}_{le_r}$ (green dotted line).

To discuss the simulation results, let us compare the controllers computed on the previous section at the high hypersonic regime on the one hand, and at the low hypersonic, transonic and subsonic regimes on the other.

Comparing simulation results of NDI-PI controller #6 and NLC-$\mathcal{H}_\infty$ controller #3 at $\mathcal{M} \leq 2.5$. Consider the NDI-PI controller matrices for $\mathcal{M} \leq 2.5$ contained in Table 5.19 and the NLC-$\mathcal{H}_\infty$ controller in Table 5.20. As an example, let us consider once more flight points n°5 and n°6. In this case, the simulation results of flight point n°5 are presented on Figures 5.40 and 5.41 of pages 167 and 168, while the simulation results of flight point n°6 are presented on figures 5.43 and 5.44 of pages 170 and 171.

Both controllers present satisfactory time responses which abide by the performance specifications defined for $\dot{\phi}$ and β. Yet, improvements in the performance of the reentry vehicle can be easily perceived in the case of NLC-$\mathcal{H}_\infty$ controller #3 with respect to the baseline solution. The tracking of the reference signal ϕ_r shows virtually no static error while the curves of β and β_m remain closer to 0° (easily seen on flight point n°6) using the NLC-$\mathcal{H}_\infty$ controller.

The control signals generated in both cases are very close in size and oscillating activity. Still, with a closer look, the size of the control signals generated by the NLC-$\mathcal{H}_\infty$ controller #3 seems to be slightly lower and smoother. Looking at the elevons rate $\dot{\delta}_{el}$ graph, the control rate signal demanded by the NLC-$\mathcal{H}_\infty$ controller is smaller with respect to that of the baseline NDI-PI solution, which induces less damaging saturation effects.

Comparing simulation results of NDI-PI controller #6 and NLC-$\mathcal{H}_\infty$ controller #4 at $\mathcal{M} > 2.5$. Now, consider the NDI-PI controller matrices for $\mathcal{M} > 2.5$ of Table 5.19 and

the NLC-$\mathcal{H}_\infty$ controller in Table 5.21. Flight points n°2 and n°3 will be retained to discuss the results obtained in the hypersonic regime. Simulation results of flight point n°2 are presented on Figures 5.36 and 5.37 of pages 163 and 164, while the simulation results of flight point n°3 are presented on figures 5.38 and 5.39 of pages 165 and 166.

In the hypersonic regime, both flight controllers give a satisfactory solution to the lateral control problem of the reentry vehicle. The performance achieved by the NLC-$\mathcal{H}_\infty$ solution still remains better, specially in terms of the tracking of the reference roll angle ϕ_r. The regulation of β towards $0°$ using both controllers remains quite similar at flight point n°2. In flight point n°3, the β curve remains closer to $0°$ with the NLC-$\mathcal{H}_\infty$ controller. For same desired dynamics, the NLC-$\mathcal{H}_\infty$ solution produces almost no static error in the tracking of ϕ_r.

In contrast to the previous comparison, the control signals generated by the NDI-PI controller seem to be slightly lower in size to those generated by the NLC-$\mathcal{H}_\infty$ controller. This fact can be more clearly seen in the elevon rate $\dot{\delta}_{el}$ graph. Yet, the generated control signals remain very similar in both cases.

Next, let us consider flight point n°1. Simulation results using both, NDI-PI controller #6 and NLC-$\mathcal{H}_\infty$ controller #4, are contained in Figures 5.33 and 5.34 of pages 160 and 161. Clearly, the closed-loop is destabilized due to the severe effects of the input saturations in both cases.

Now, the anti-windup device presented in Table 5.22, which enhances NLC-$\mathcal{H}_\infty$ controller #4, will be employed. Simulation results are presented on Figure 5.35, page 162. The closed-loop shows a stable response in spite of input saturations even though a performance deterioration can be perceived. As can be expected, the enlargement of the stability domain is accompanied by an increase of the control signals size and activity. Yet, the curves of $\dot{\phi}$ and β verify the performance objectives while preserving the stability of the closed-loop which is the primary objective.

Finally, simulation results with this complete robust solution at flight points n°5 and n°6 are shown on Figures 5.42 and 5.42 of pages 169 and 169. A more realistic scenario is considered with a static wind gust and turbulence, following the profile described in Appendix D.1.2 (see page 256). It should be kept in mind that the moderate wind turbulence profile starts at an altitude of 20km.

At high numbers of Mach ($\mathcal{M} > 2.5$) while in the presence of lateral wind and turbulence, the simulation β is offset by more than $2°$ (see other simulation results in Section E.2.3 of Appendix E). This effect is mainly due to the fact that the anemometric probe is protected at these speeds, thus incapable of measuring and giving feedback on this offset. Therefore, all wind speed related parameters, such as β, are estimated by the IMU without any direct information on $\vec{\mathbf{V}}_w$. Yet, the simulation β always shows a tendency to come closer to its commanded value $\beta_c = 0°$ under the effects of the robust controller.

The lateral performance objectives are satisfied by the complete robust solution proposed through the whole flight domain.
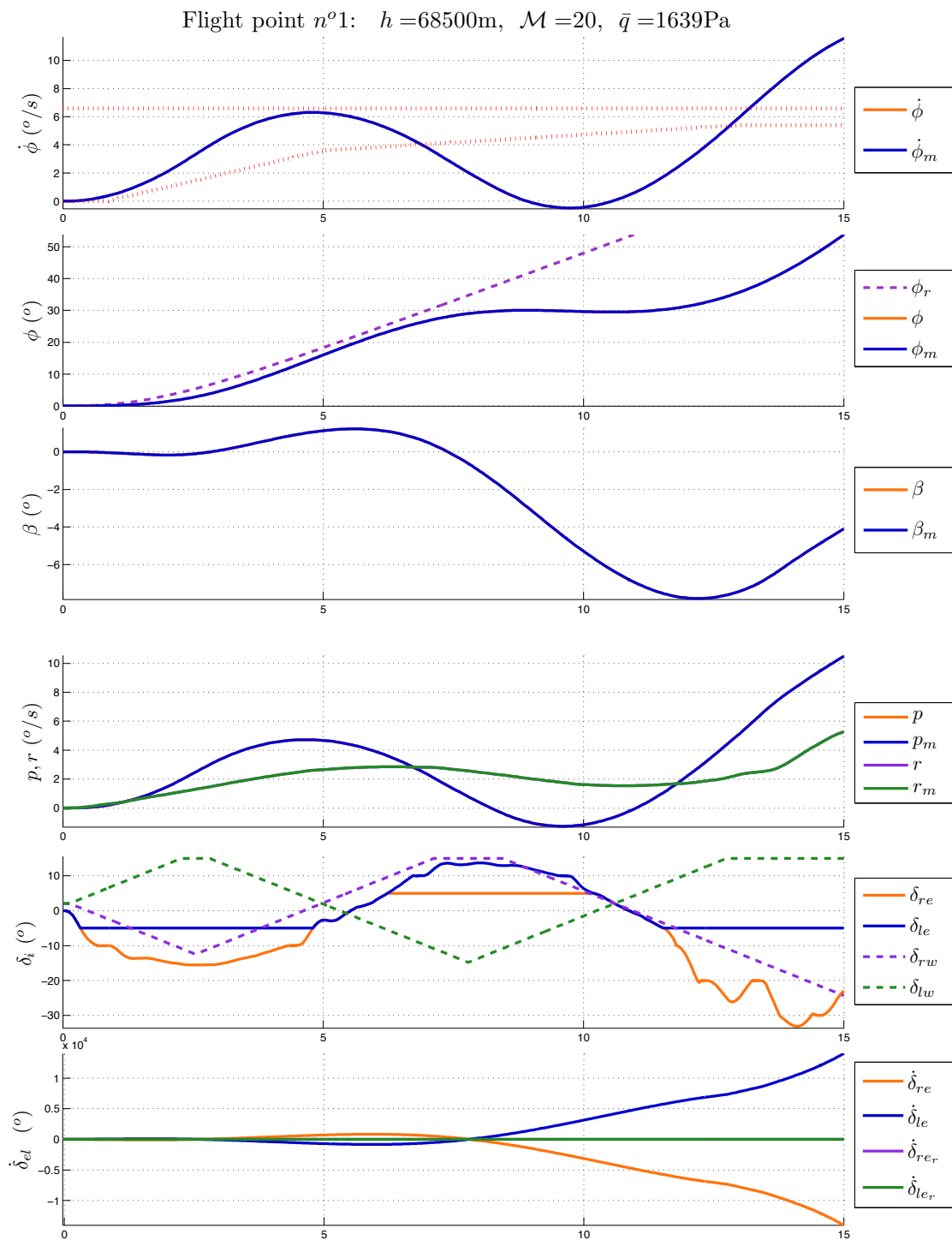
Figure 5.33: Simulation with saturated actuator and NDI-PI controller #6.
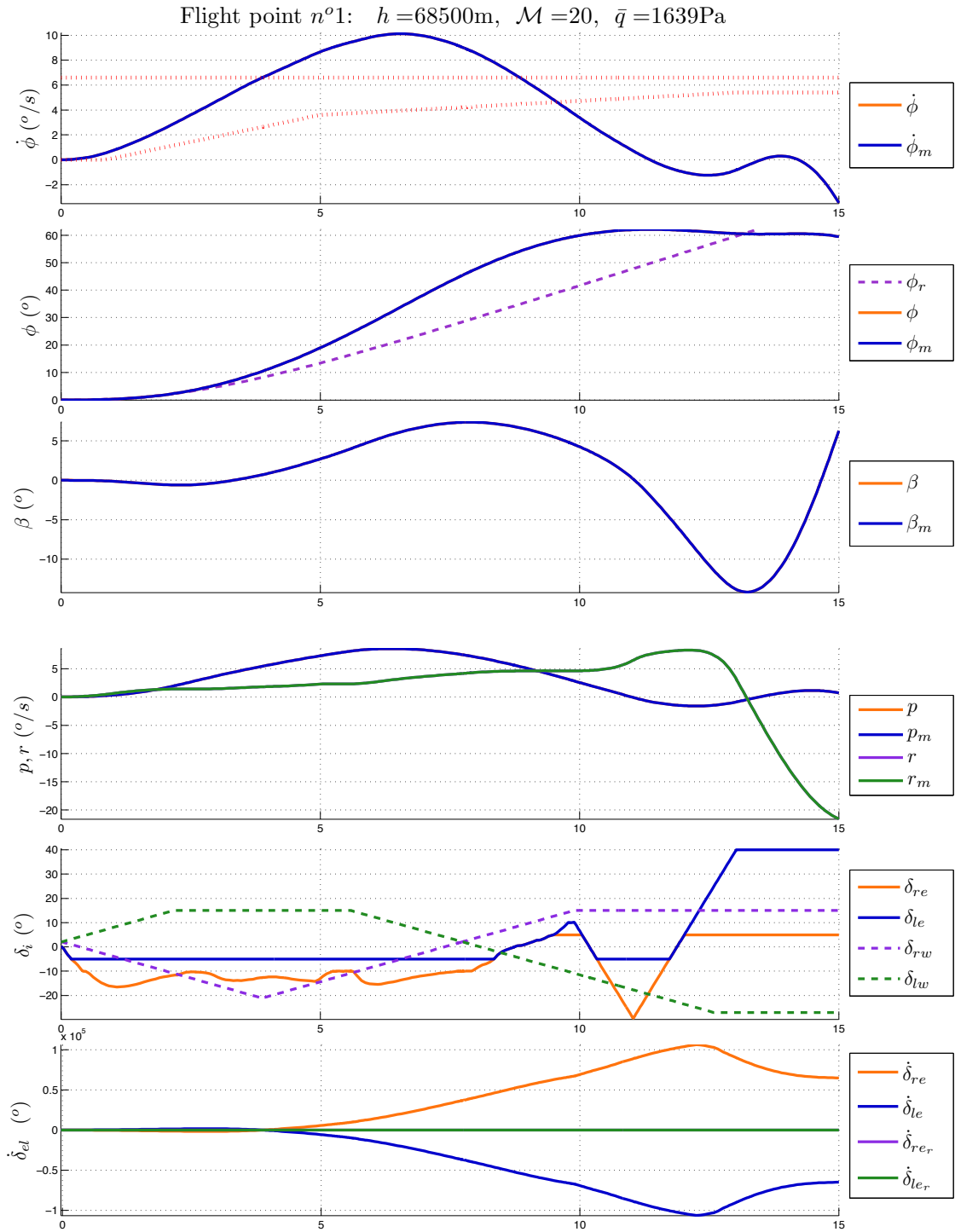
Figure 5.34: Simulation with saturated actuator and NLC-$\mathcal{H}_\infty$ controller #4.
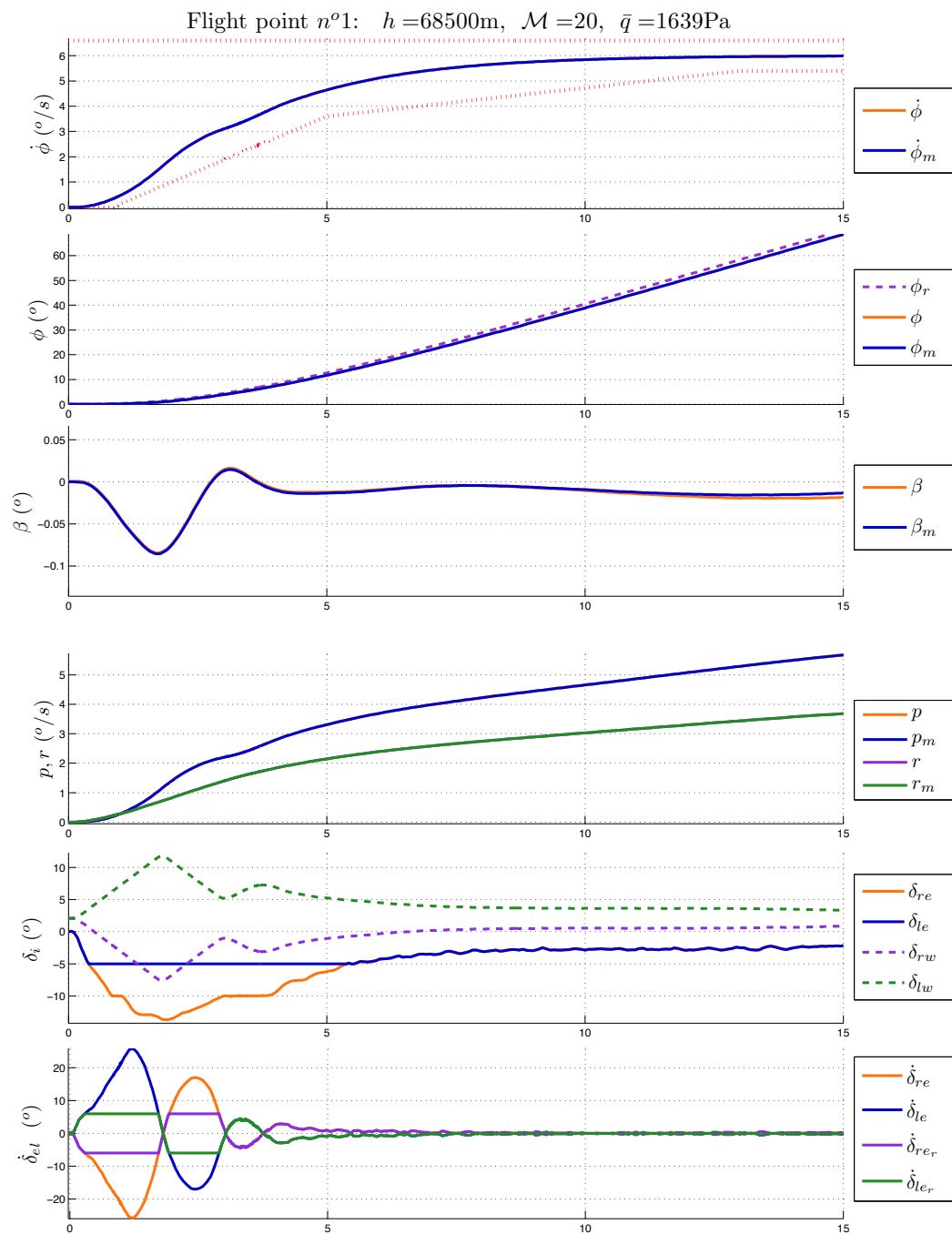
Figure 5.35: Simulation with saturated actuator and NLC-$\mathcal{H}_\infty$ controller #4+AW.
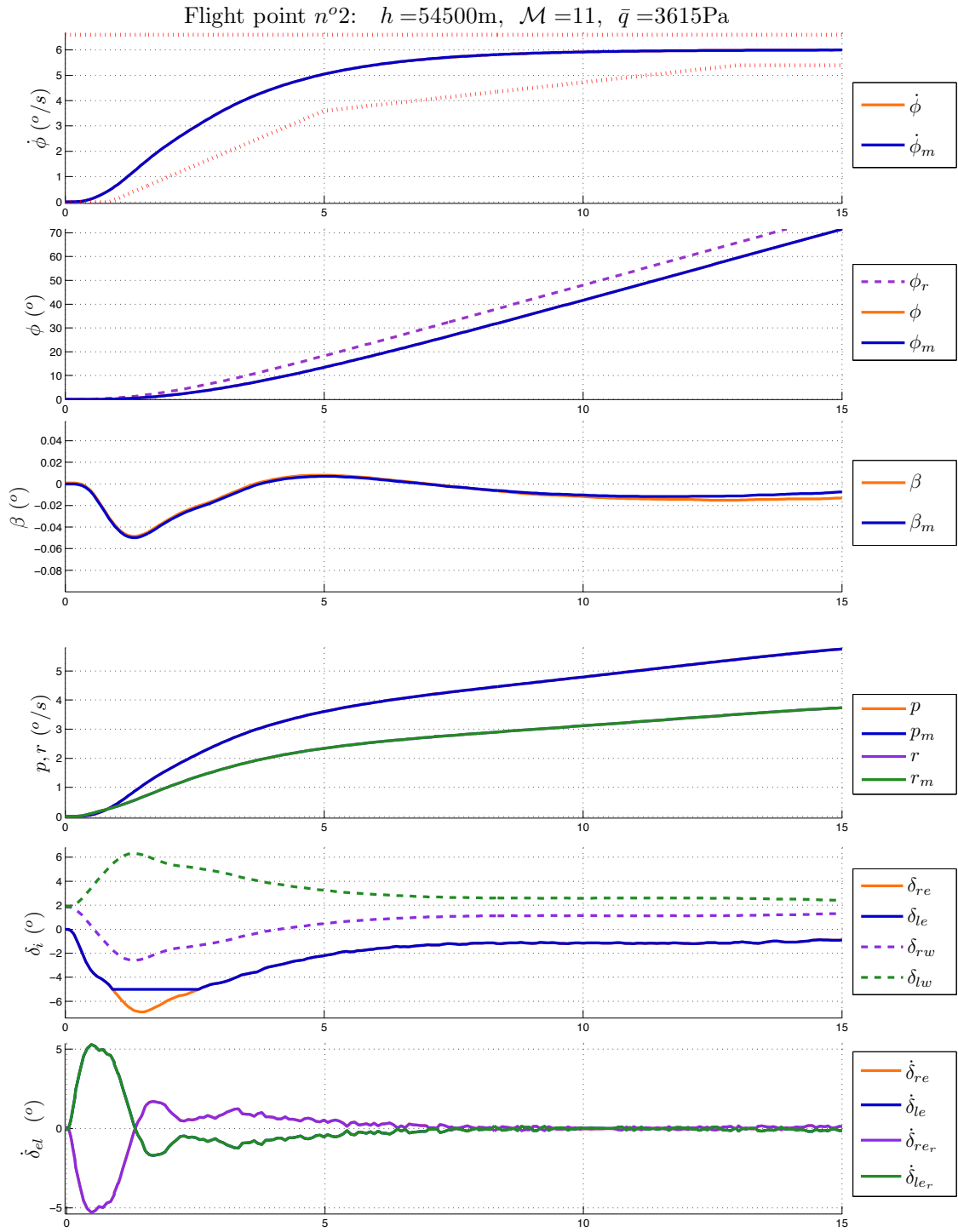
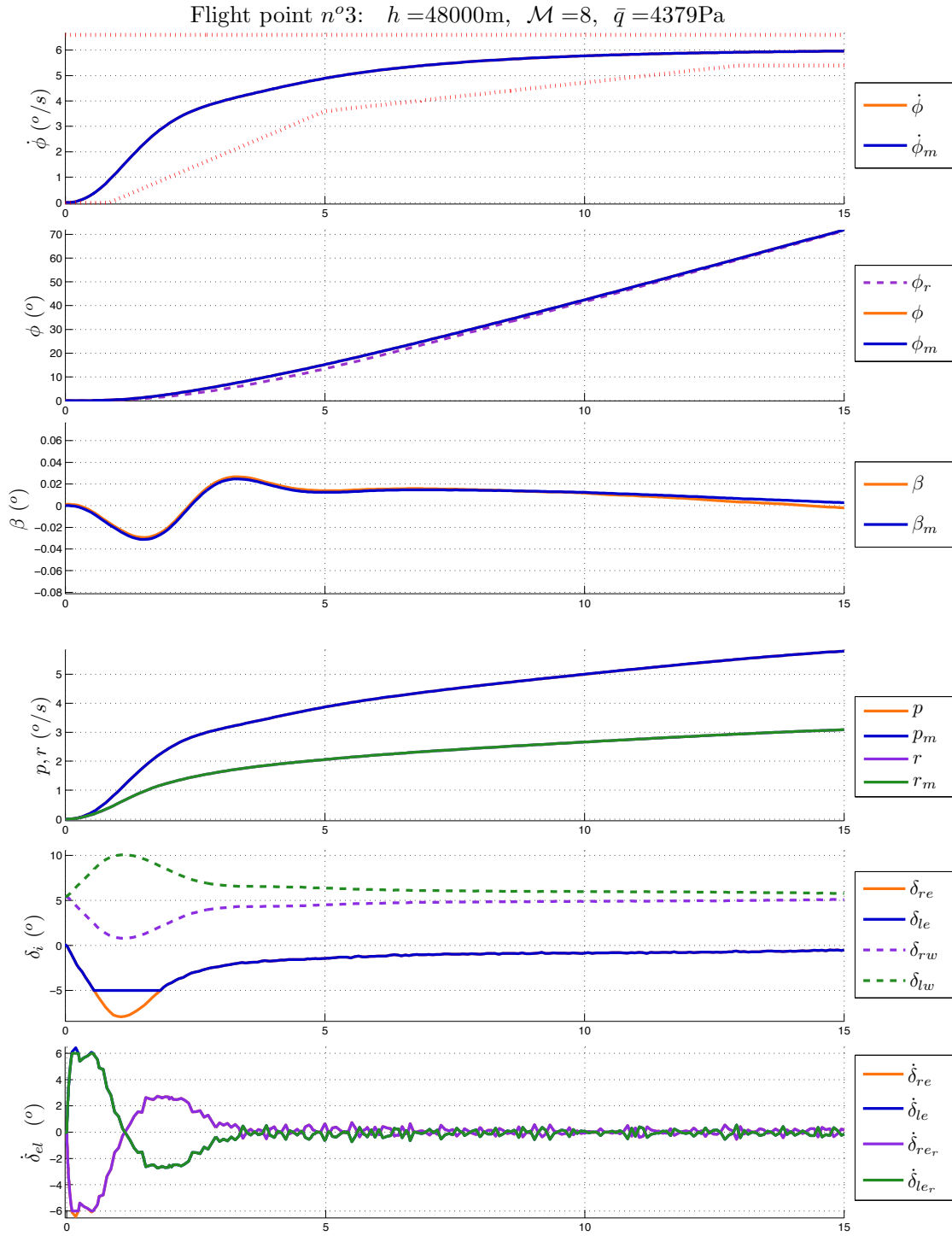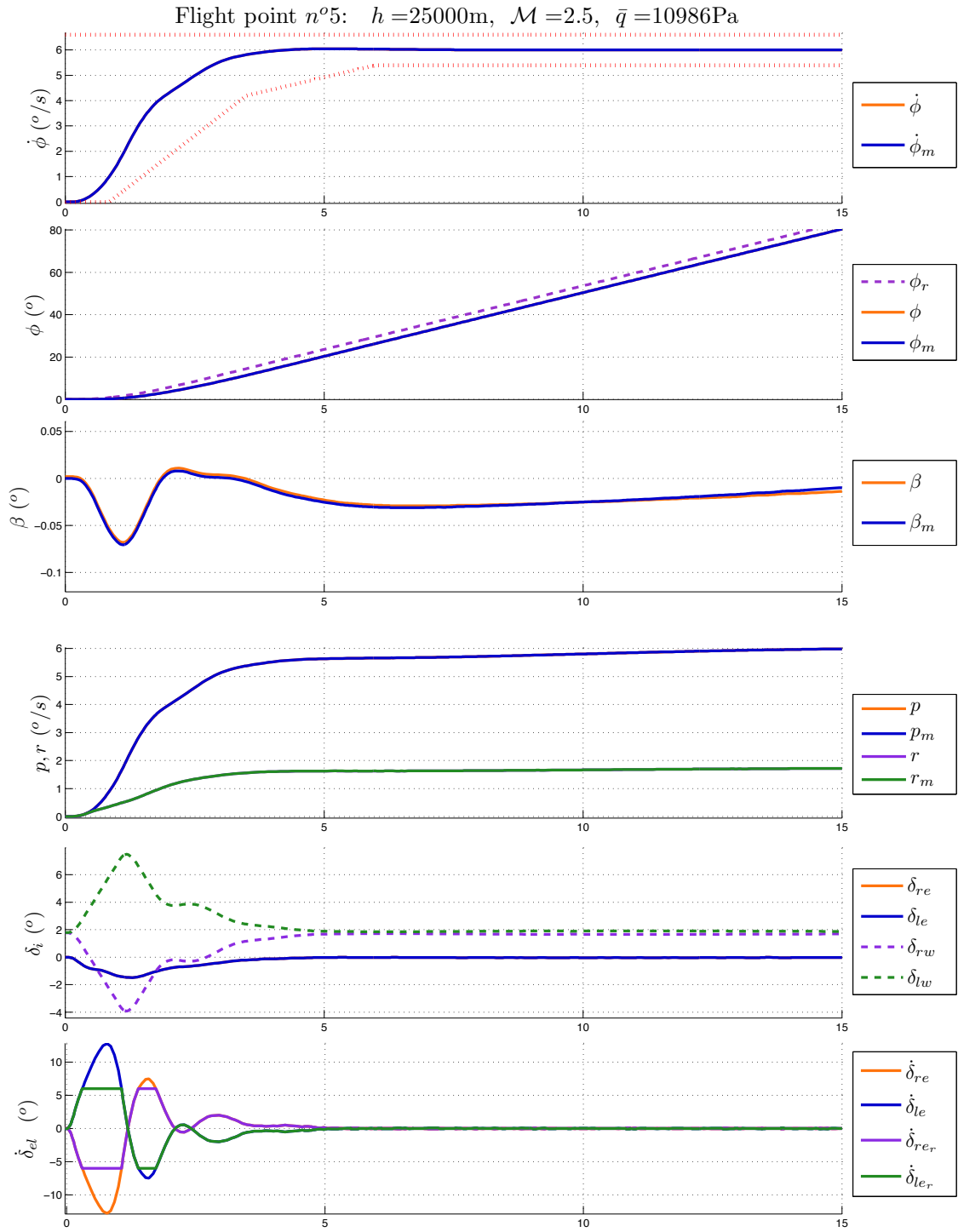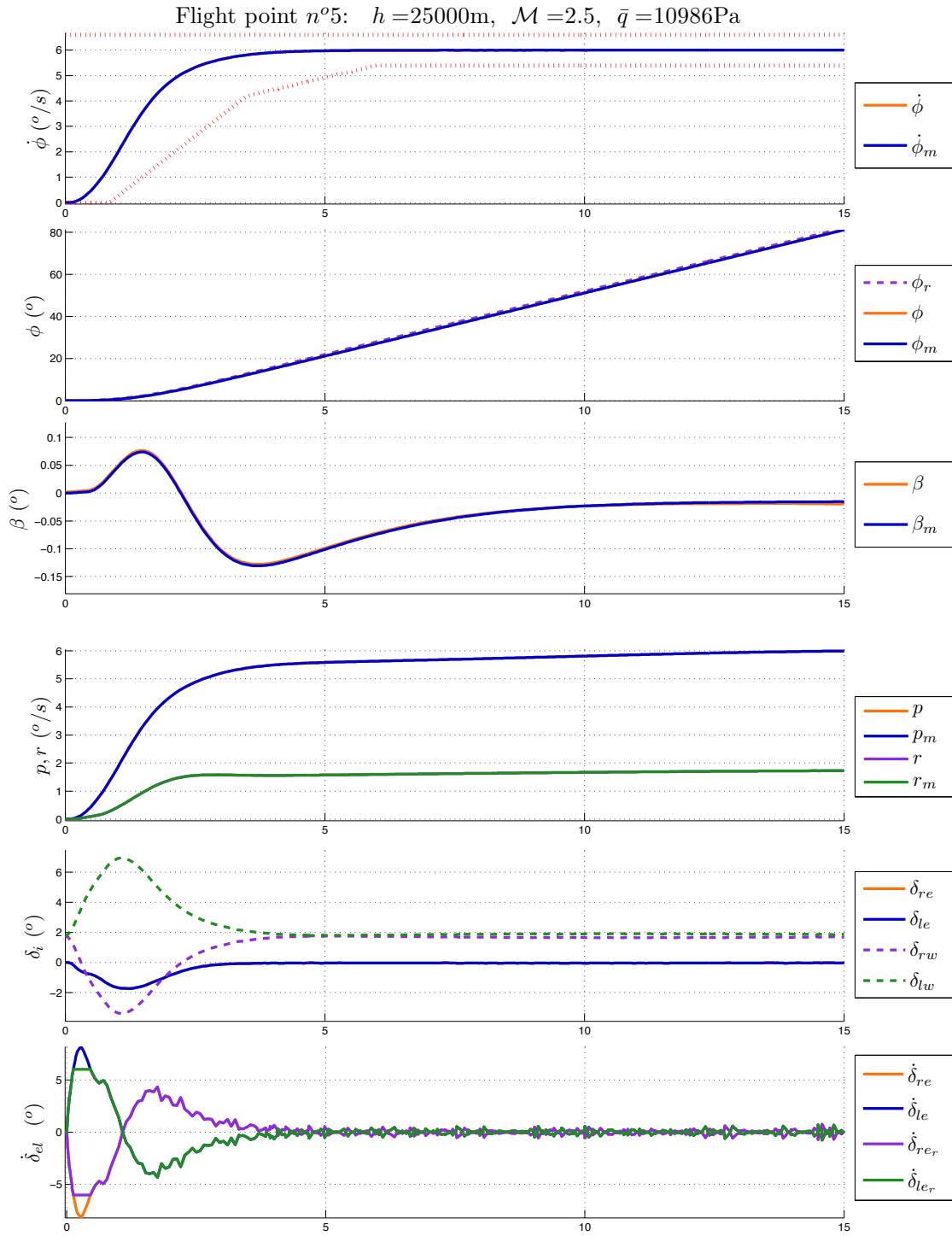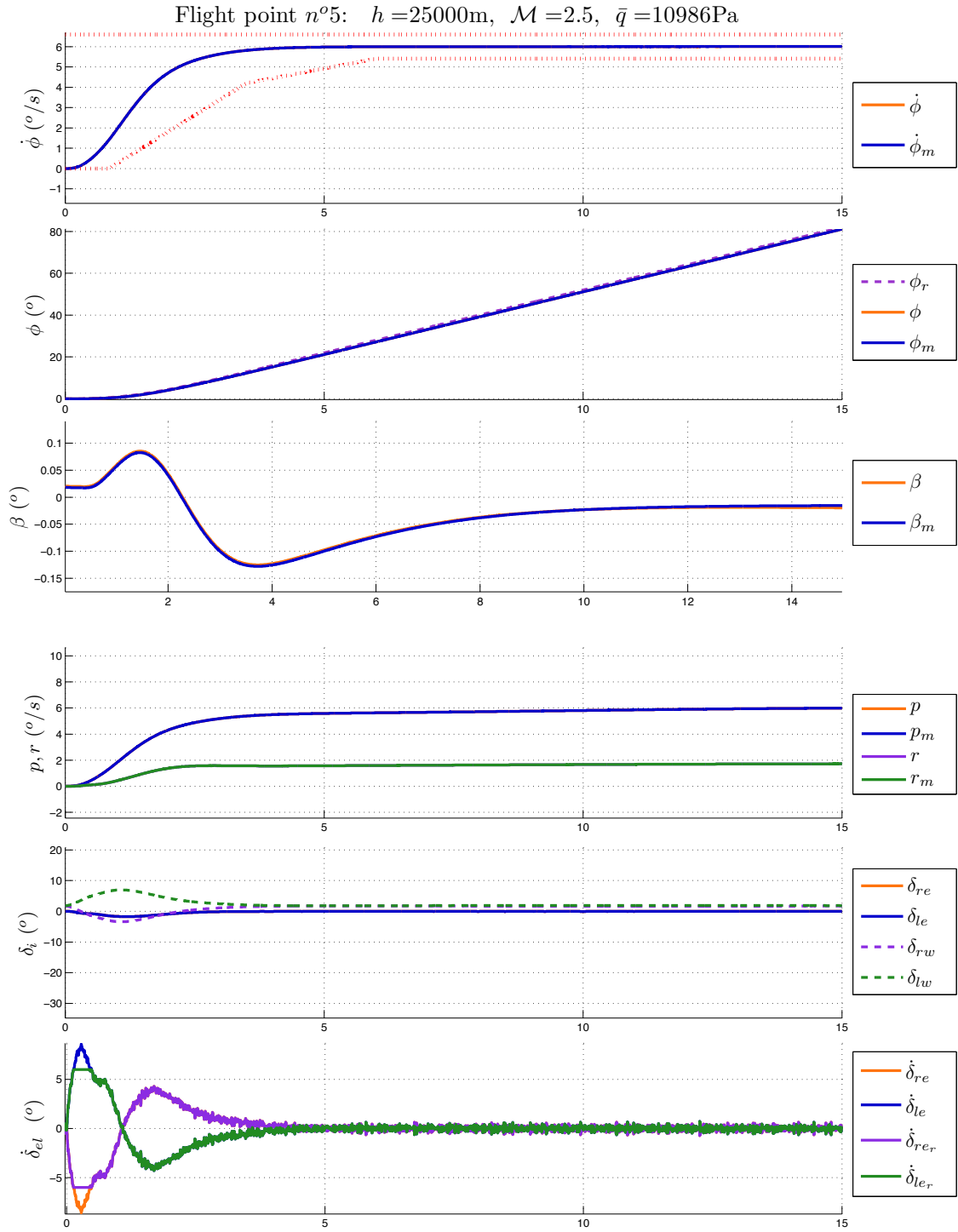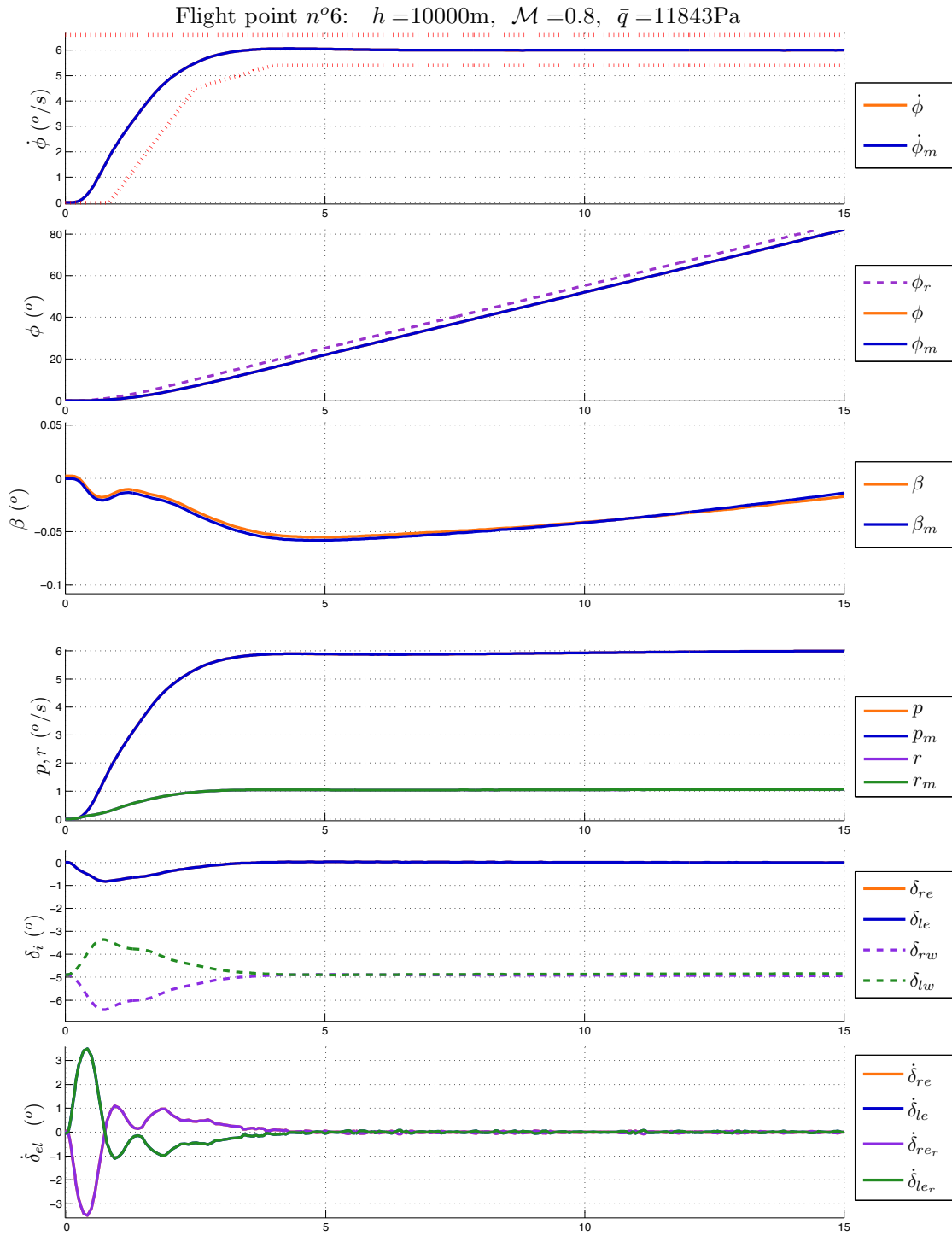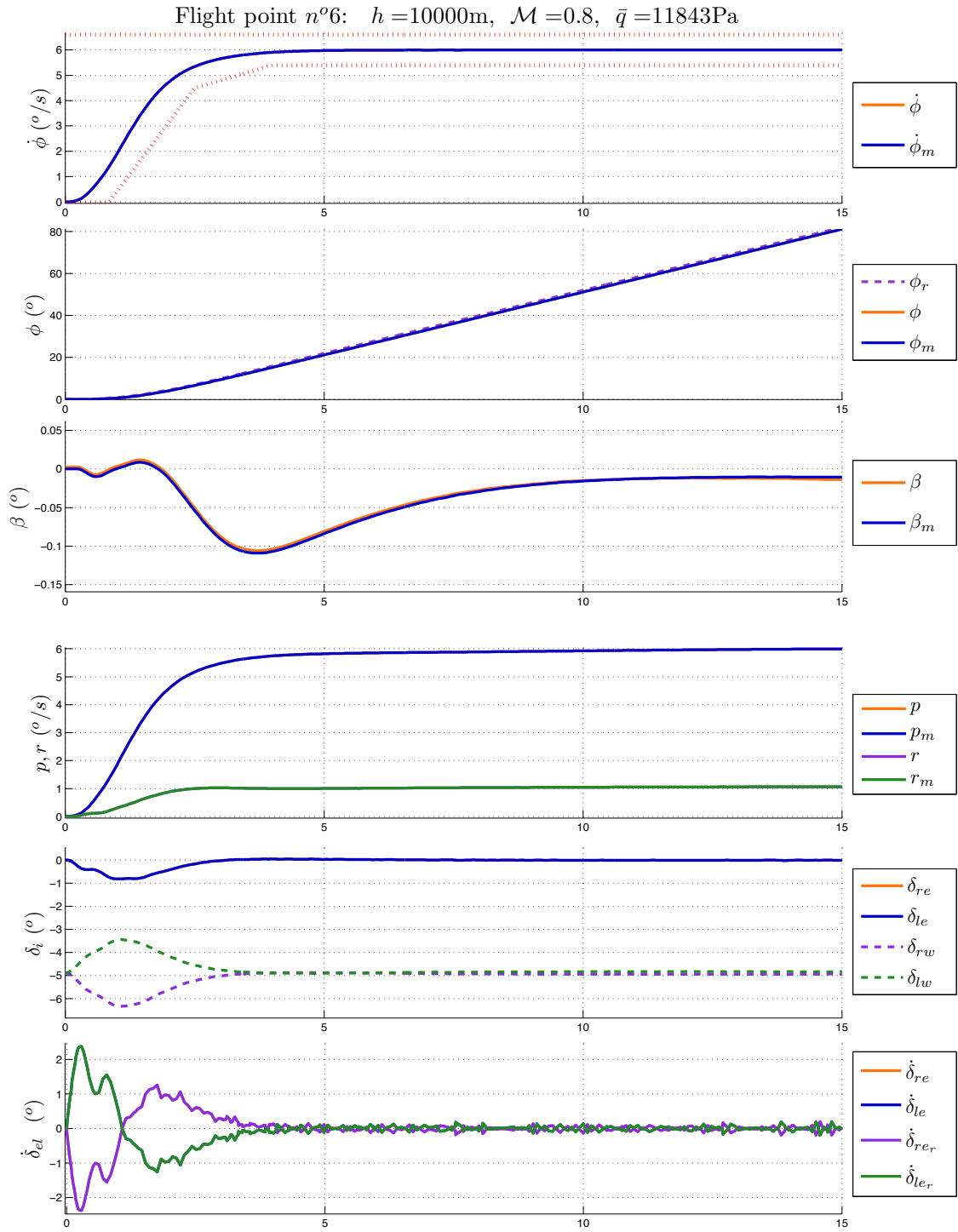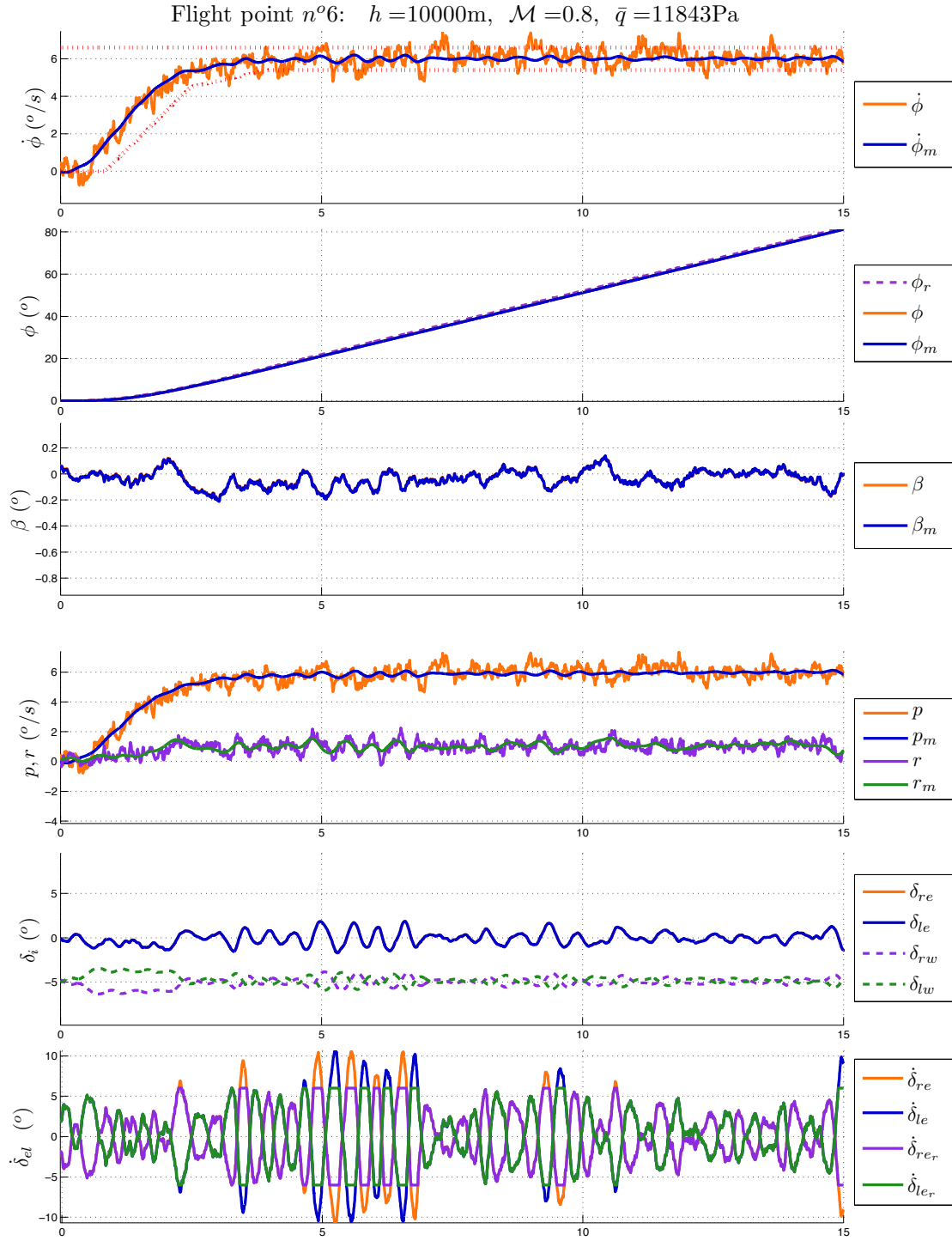Figure 5.36: Simulation with saturated actuator and NDI-PI controller #6.
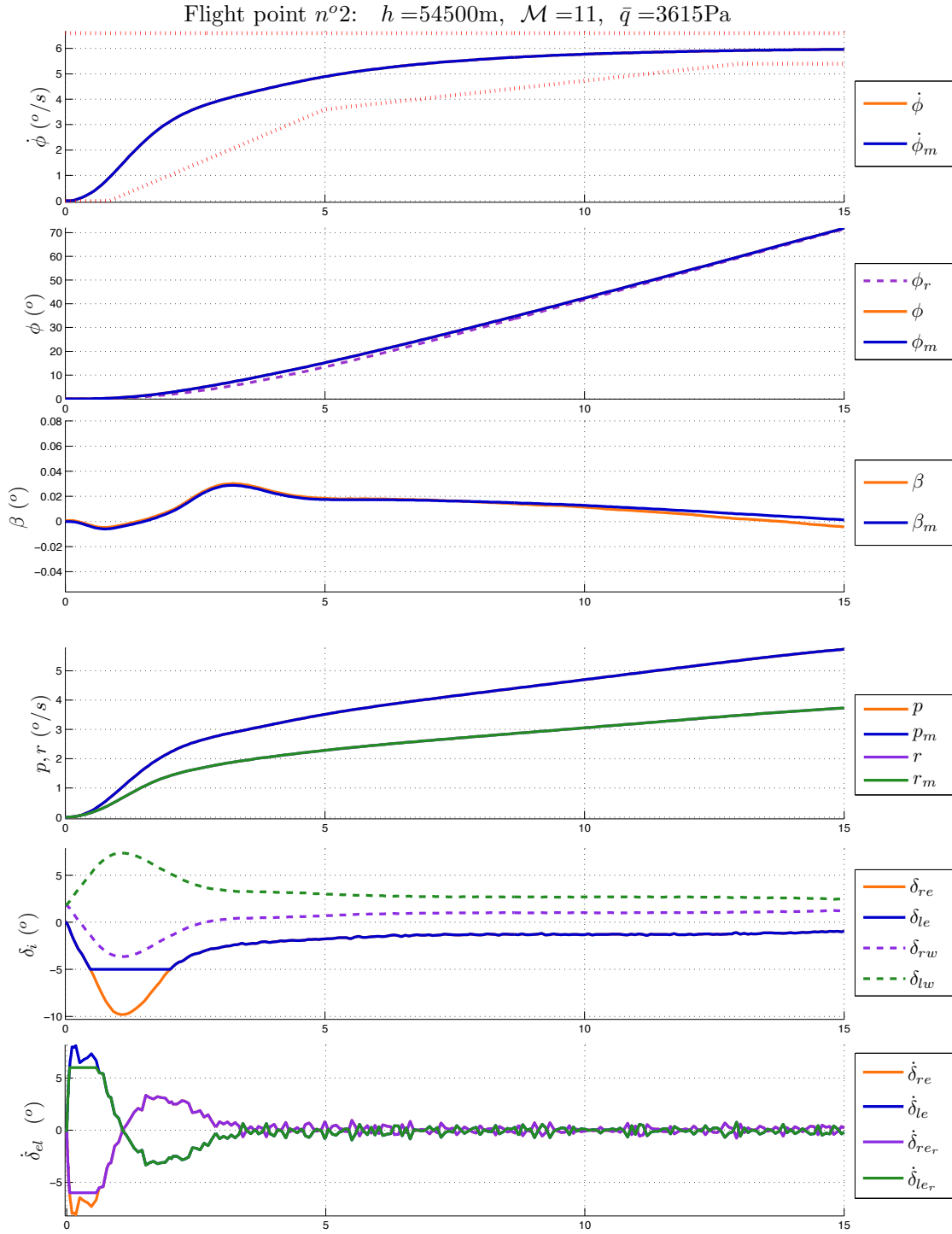
Figure 5.37: Simulation with saturated actuator and NLC-$\mathcal{H}_\infty$ controller #4.
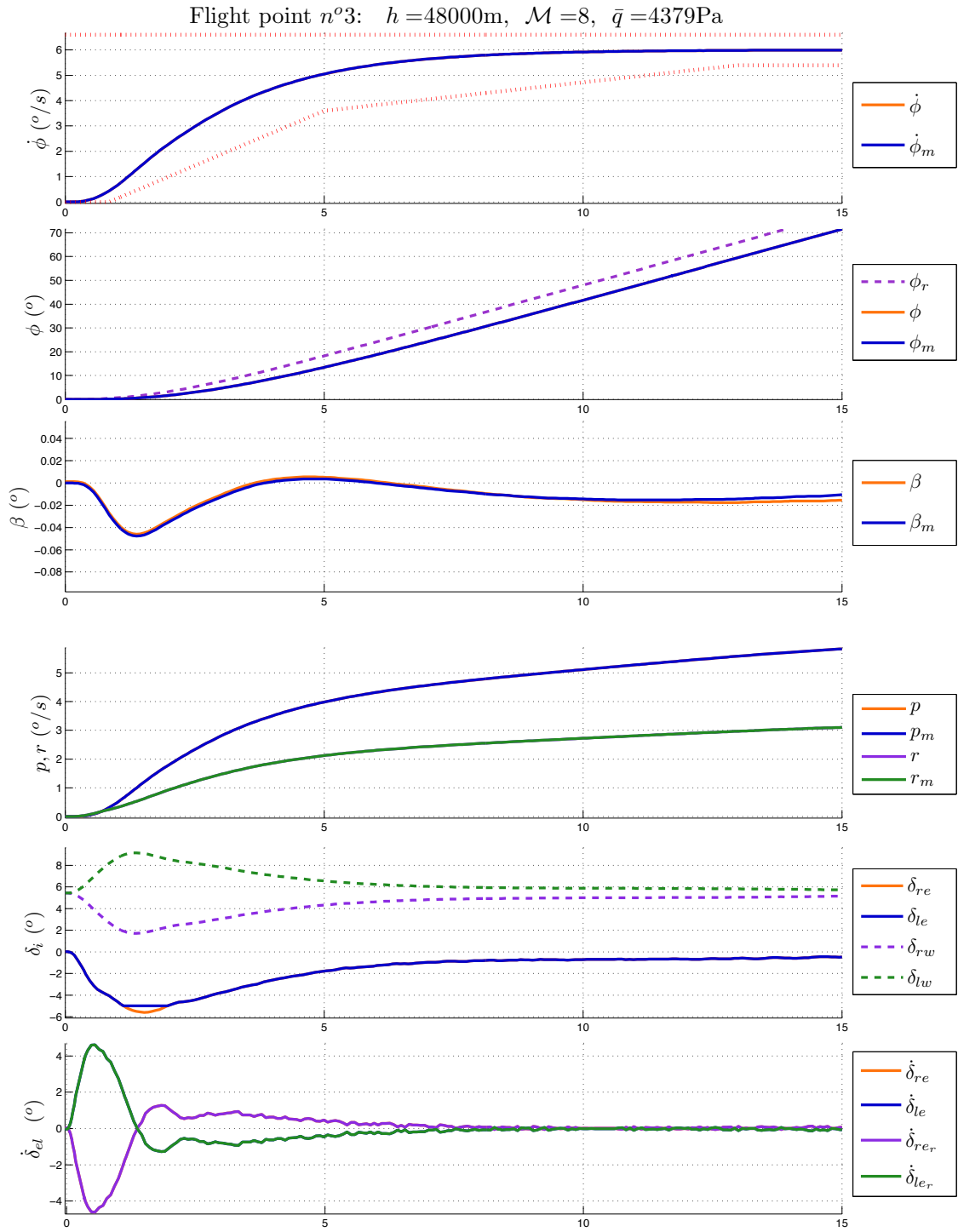
Figure 5.38: Simulation with saturated actuator and NDI-PI controller #6.

Figure 5.39: Simulation with saturated actuator and NLC-$\mathcal{H}_\infty$ controller #4.

Figure 5.40: Simulation with saturated actuator and NDI-PI controller #6.

Figure 5.41: Simulation with saturated actuator and NLC-$\mathcal{H}_\infty$ controller #3.

Figure 5.42: Simulation with wind and saturated actuator and NLC-$\mathcal{H}_\infty$ controller #4+AW.

Figure 5.43: Simulation with saturated actuator and NDI-PI controller #6.

Figure 5.44: Simulation with saturated actuator and NLC-$\mathcal{H}_\infty$ controller #3.

Figure 5.45: Simulation with wind and saturated actuator and NLC-$\mathcal{H}_\infty$ controller #3.

Concluding comments

In this chapter, the attitude control design methodology described in Chapter 4 were implemented on an atmospheric reentry vehicle at different points of a possible mission trajectory.

First, an introduction to the physical context of atmospheric reentry missions was given. Also, a general description of the reentry vehicle control surfaces display and how it allows to produce changes in the attitude of the vehicle was presented.

Then, the computation and implementation procedures of the control laws resulting from the design procedures of both approaches were detailed. Based on the performance requirements that the control laws should ensure, the controller designs were computed using appropriate desired dynamics. In the case of the NDI-PI solution, as desired dynamics are fixed, the only remaining adjustable parameter is τ_q. This parameter was adjusted to different values to show its effect on the closed-loop behavior.

In contrast, the generalized NLC framework uses different tuning parameters such as the weighting functions and the reference model $R(s)$ containing the desired dynamics. An initial tuning of the weighting functions that allow to loop-shape the controller synthesis problem was obtained from the standard NDI-PI solution. Using a simple performance analysis scheme, a singular value analysis of the NDI-PI solution allowed to get an idea of the weighting functions frequency domain characteristics. In fact, by following this procedure, the standard NDI-PI solution can be reproduced using the generalized NLC framework as explained in [HJB11]. By adjusting the tuning of the weighting functions, the trade-off between better performance and smaller control signals was managed.

Then, a robustness and stability test was presented in the case of the longitudinal controllers computes using both, the standard NDI procedure with PI control and the generalized NLC framework. It was concluded that the best stability characterization is that obtained by the NLC-$\mathcal{H}_\infty$+AW solution. Yet, it was shown that as more operators are added to the Δ block of the closed-loop analysis model, the stability tests employed tend to generate more conservative results.

Finally, the computed controllers were tested using a 6 degrees-of-freedom fully nonlinear Flight Mechanics simulator. On the one hand, the standard NDI-PI solution proved to be a sufficient solution when input constraints are discarded. When the tuning parameters τ_i is reduced, the performance of the vehicle improved, although increasingly oscillating control signals of larger size were produced.

In the longitudinal case, for example, a single tuning of the NDI-PI controller, corresponding to controller n°5, was able to satisfy the performance requirements through the whole set of flight points considered of a possible reentry trajectory. Yet, as physical limits of the control surface actuators are considered, some of these flight points were destabilized due to the effects of saturation.

On the other hand, the generalized NLC-$\mathcal{H}_\infty$ controllers proved to get significantly better performance than the NDI-PI solution, while handling better the size and activity of the control signals generated thanks to the multi-channel design approach. As input constraints are considered in the synthesis process using our generalized framework, the NLC-$\mathcal{H}_\infty$+AW controller was able to satisfy the performance requirements through the whole set of flight points even under the worst

case scenarios considering static wind gusts and turbulence. A complete solution was found for both, the lateral and longitudinal dynamics of this reentry vehicle example using the Generalized Nonlinear Compensation Framework proposed.

These highlights of the obtained results using nonlinear compensation for the attitude control of a reentry vehicle conclude the works of this thesis.

Conclusion

Thesis conclusions and contributions

The works presented in this thesis introduce a new methodology devoted to nonlinear compensation of systems with uncertainties, varying parameters and input saturations in a unified framework.

After having introduced some theoretical preliminaries on the well-known Nonlinear Dynamic Inversion (NDI) control design, it was concluded that this technique is basically a compensation approach. It can only be directly applied to a limited set of nonlinear systems. The central limitations inherent to the technique were exposed along with some standard remedies.

The main contributions of the thesis concern the development of a Generalized Nonlinear Compensation (NLC) Framework. Parting from the insight of NDI design, and inspired by linear robust control design, the proposed framework allows the systematic computation of robust controllers for a large class of nonlinear systems affected by uncertainties, varying parameters and input saturations. This framework also proved to endow a greater flexibility to controller design than the standard NDI approaches.

First, a refined NDI-based control law approach was proposed to better balance efforts between the inner and outer loops of the standard NDI controller structure. In a very straightforward way, this approach led to the generalized NLC framework by considering the nonlinear dynamics of a system as "measured disturbances". Then, the nonlinear compensation problem can be reformulated as a disturbance rejection problem, which is common in Linear Control. With this reformulation, the proposed structure of the NLC control law proved to generalize the standard NDI controller structure.

In order to enable the use of robust control techniques to solve the nonlinear compensation problem, a particular nonlinear representation that stresses the linear interactions between the state variables and the system nonlinear dynamics was proposed. Some general guidelines were also presented to derive this representation.

Multi-channel design-oriented models were then established to solve the nonlinear compensation problem via $\mathcal{H}_\infty$ optimization strategies using a reference model structure. These design-oriented models can include anti-windup devices to alleviate the effects of input saturations in the closed-loop, thus enlarging the stability domain.

A helpful procedure for the controller synthesis phase, which serves as an aid for tuning the weighting functions of the multi-channel design-oriented models, was proposed. Interestingly, baseline NDI controllers can be reproduced by the generalized NLC framework using this procedure.

Finally, a well-adapted LFT representation of the resulting closed-loop was proposed for robustness and stability analysis.

The last three chapters of the thesis were dedicated to the implementation of the generalized NLC framework to the flight controller design of air vehicles (including aircraft, space launchers and spacecrafts). In particular, NLC-based controllers were designed and computed for the attitude control of a reentry vehicle. These controllers were further tested in a 6 degrees-of-freedom Flight Mechanics simulator.

The main modelling aspects of air vehicles were introduced. After a general description of the fundamental equations of motion used in Flight Mechanics, the proposed modelling of the control objectives resulted very interesting since it allows an easier implementation of the NLC-based control laws.

Then, the method proposed for computing NLC-$\mathcal{H}_\infty$ controllers was presented in detail along with a standard NDI approach using PI control. Both control designs are based on the models of the control objectives.

Finally, the control design methodology was applied to an atmospheric reentry vehicle at different points of a possible trajectory. The flight domain covered include the hypersonic ($\mathcal{M} = 20$ to $\mathcal{M} = 2.5$), transonic ($\mathcal{M} = 0.8$) and subsonic ($\mathcal{M} = 0.6$ to $\mathcal{M} = 0.3$) phases of a possible reentry trajectory. The altitude range considered goes from $68500\,m$ to $0\,m$, while the speed domain covered goes from approximately $6000\,m/s$ to $100\,m/s$. Therefore, a wide domain of low and high dynamic pressures $\bar{q}$ was also covered.

In simulation, manoeuvres on α were performed to cover a wide domain from high angles-of-attack ($36°$) to low incidence ($7°$). On the lateral case, the side-slip angle β was kept close to $0^c irc$ as part of the reentry mission profile. The roll angle ϕ was tested in a range of $0°$ to around $80°$ with manoeuvres on the roll angle rate $\dot{\phi}$ of $6°/s$.

A thorough comparison between the two approaches was presented based on synthesis procedures, robustness analysis and simulation results. It was concluded that the greater flexibility of the generalized NLC framework allows to obtain significantly better performance and stability than standard NDI controllers, while handling better the size and activity of the control signals generated thanks to the multi-channel design approach proposed and to the use of standard anti-windup control schemes.

Future Work

Further studies on the Generalized Nonlinear Compensation Framework proposed in this contribution can be of interest. Some of them will be exposed next.

In this thesis, only the case of rigid air vehicles was considered. Then, the case of air vehicles with flexible modes is yet to be assessed for designing flight controllers under the NLC framework. A

concern arises as the NLC controller might be such that the flexible modes of an air vehicle become resonant. One way to overcome this problem could be to limit or cut-off some frequencies of the NLC controller bandwidth to avoid exciting the flexible modes. A more sophisticated solution could use the available information on these modes in the synthesis process to actively control them.

Even though the NLC framework was used to design and compute flight control laws of air vehicles, other uses can be foreseen for this method within aerospace applications. Such is the case of the synthesis of Guidance Systems. Also, one could think of using this generalized framework for controller design with fault detection strategies using $\mathcal{H}_\infty$ observers, which can be designed simultaneously with the proposed approach.

The method proposed for controller synthesis within our NLC framework is based on a structured $\mathcal{H}_\infty$ optimization process. Still, other robust controller synthesis strategies and anti-windup schemes can be foreseen depending on the available information about the nonlinear system. These alternative strategies are yet to be explored in more detail to generate, for example, polytopic or high-fidelity system representations for synthesis of self-scheduled LPV controllers.

Last but not least, basic and rather conservative approaches were used to characterize the stability domain attained by NLC controllers. Using the LFT modelling of the nonlinear closed-loop proposed, refined performance and stability analysis tests can be explored considering a better compromise between the accuracy of the results and the computational burden foregone for its estimation. Such tests can be based on Integral Quadratic Constraints (IQC) or on Lyapunov functions for time-varying and parameter-varying systems.

RÉSUMÉ ÉTENDU

Cadre de travail généralisé de compensation non-linéaire robuste

Application à la rentrée atmosphérique.

Introduction

Ce travail de thèse est consacré à l'extension de l'Inversion Dynamique non-linéaire (NDI-Nonlinear Dynamic Inversion) pour un ensemble plus grand de systèmes non-linéaires, tout en garantissant des conditions de stabilité suffisantes.

Après la formalisation mathématique de la "linéarisation par retour d'état" dans les années 80 [IKGGM81], la NDI a été étudiée dans le cas de diverses applications, y compris en aéronautique et en aérospatiale [Har91, Jou92, RBG95, RBG96, SK98, IGVW02, Pap03, GV03, Lav05, Kol05, LRDY07]. La NDI permet de calculer des lois de contrôle capables de linéariser et de découpler un modèle non-linéaire à tout point de fonctionnement de son enveloppe d'état. Cependant cette méthode est intrinsèquement non-robuste aux erreurs de modélisation et aux saturations en entrée. En outre, dans un contexte non-linéaire, l'obtention d'une garantie quantifiable du domaine de stabilité atteint reste à l'heure actuelle complexe. C'est l'ensemble de ces paramètres qui a motivé la rédaction de cette thèse.

Dans les applications aérospatiales, la plus grande partie des approches linéaires pour la conception de lois de pilotage ont, en général, du mal à donner une réponse satisfaisante au problème de contrôle, à moins d'utiliser des gains auto-séquencés. Dans cette contribution, pour éviter les difficultés soulevées par les approches utilisant des gains auto-séquencés (absence de garantie entre les points d'interpolation, procédure de réglage longue...), une autre méthode, inspirée par la NDI, est ensuite proposée.

Contrairement aux approches classiques de la NDI, notre méthodologie peut être considérée comme un cadre de compensation non-linéaire généralisé qui permet d'intégrer les incertitudes et les saturations en entrée dans le processus de conception. En utilisant des stratégies de contrôle anti-windup, la loi de pilotage peut être calculée grâce à un simple processus multi-canaux ou par un simple processus en deux phases. La première, grâce aux avancements récents des techniques d'optimisation non-lisse, consiste à optimiser un correcteur structuré $\mathcal{H}_\infty$, puis dans une deuxième phase, une stratégie anti-windup est utilisée pour améliorer les propriétés du correcteur en dépit des contraintes sur l'entrée du système.

Dans ce cadre de travail généralisé des transformations linéaires fractionnaires (LFT - Linear Fractional Transformations) de la boucle fermée non-linéaire peuvent être facilement déduites pour l'analyse de la stabilité robuste utilisant des outils habituellement dédiés aux systèmes linéaires incertains. La méthode proposée est testée pour le pilotage d'un véhicule de rentrée atmosphérique de type aile delta lors de ses phases hypersonique, transsonique et subsonique. Pour cette thèse, un simulateur du vol incluant divers facteurs externes ainsi que des erreurs de modélisation a été développé sous Simulink.

Un cadre de travail généralisé inspiré de la NDI

R.1 Introduction aux techniques d'Inversion Dynamique Non-linéaire

Dans ce chapitre, la méthode de synthèse par inversion dynamique non-linéaire est présentée. L'objectif principal est de présenter les bases de la technique, tout en soulignant certains aspects qui nous ont amenés à développer une méthode plus générale inspirée de la NDI.

R.1.1 Systèmes carrés et affines

Le cas des systèmes carrés affines est intéressant car il permet de visualiser avec simplicité le principe de la méthode NDI classique. Le modèle Σ représente un tel système :

$$\Sigma : \qquad \dot{x} = f(x) + G(x)\, u \tag{R.1}$$

où
– $x \in \mathbb{R}^n$ est le vecteur d'état ;
– $u \in \mathbb{R}^m$ est l'entrée, avec $n = m$;
– $f(x) \in \mathbb{R}^n$ et $G(x) \in \mathbb{R}^{m \times m}$ sont des fonctions non-linéaires lisses ;

Assumption R.1 *La matrice $G(x) \in \mathbb{R}^{m \times m}$ est inversible.*

Principe général

La NDI permet de linéariser et de découpler un système non-linéaire par retour d'état. L'idée de base est de construire une loi de commande $u(x)$ dite "interne" en utilisant explicitement les fonctions $f(x)$ and $G(x)$ afin d'éliminer les dynamiques non-linéaires du système. Ensuite, on peut créer une boucle externe chargée de stabiliser le système et lui conférer une dynamique désirée.

Assumption R.2 *Le vecteur d'état x est disponible pour la conception de la loi de pilotage.*

La conception de la loi de pilotage se fait en deux étapes :

Step 1 *Prenons le système carré et affine (R.1). Trouver l'expression de la loi de commande $u(x)$ tel que les dynamiques non-linéaires $f(x)$ et $G(x)$ soient compensées :*

$$u(x) = G^{-1}(x)[-f(x) + \tilde{u}] \tag{R.2}$$

En boucle fermée, le système résultant $\tilde{\Sigma}$ peut s'écrire, avec un léger abus de notation, ainsi :

$$\tilde{\Sigma} : \quad \dot{x} = \tilde{u}(x_c, x) \tag{R.3}$$

$$x = \tilde{\Sigma}(s) \, \tilde{u}(x_c, x), \quad \text{with} \quad \tilde{\Sigma}(s) = \frac{I}{s}$$

Le système est réduit à un ensemble d'intégrateurs purs.

Des dynamiques linéaires peuvent alors être imposées via un signal d'entrée auxiliaire $\tilde{u}(x_c, x) \in \mathbb{R}^n$.

Step 2 *Construire une boucle externe capable d'imposer une dynamique linéaire et stable à la boucle fermée, telle :*

$$\tilde{u}(x_c, x) = C(s) \begin{bmatrix} x_c \\ x \end{bmatrix} \tag{R.4}$$

La loi de commande finale obtenue par NDI classique s'écrit :

$$u(x) = G^{-1}(x) \left(-f(x) + C(s) \begin{bmatrix} x_c \\ x \end{bmatrix} \right) \tag{R.5}$$

Il est clair que la méthode NDI classique est en effet une technique de compensation non-linéaire.

Limites de la méthode

À ce niveau, des hypothèse très restrictives ont été considérées. L'hypothèse R.2 suppose que l'on est capable de mesurer le vecteur d'état et de reproduire exactement les fonctions $f(x)$ et $G(x)$.

Les processus dans la vie réelle sont soumis à des limitations physiques. Dans un scénario plus réaliste :
– le modèle Σ est une représentation simplifiée d'un processus réel et son environnement ;
– la mesure du vecteur d'état pourrait ne pas être accessible ou être entachée de bruits et divers phénomènes ;
– les entrées de la plus grande partie de systèmes ont des actionneurs avec limitations physiques et dynamiques.

La plus grande limitation de la méthode NDI classique est que la compensation exacte des non-linéarités du système requière :
– un accès à la mesure du vecteur d'état x ;
– une bonne modélisation du phénomène physique à commander, notamment en terme des fonctions $f(x)$ et $G(x)$;
– des actionneurs avec des bandes passantes très larges afin d'être capables de réaliser les signaux de commande produits par le correcteur NDI.

Solutions classiques

La rejection de perturbations est un problème bien connu de commande linéaire. La structure de commande proportionnelle-intégrale (PI) est très pratique pour ce type de problèmes due à ses caractéristiques de robustesse. Le correcteur PI assure l'erreur statique nulle et une bonne rejection de perturbations.

Cette structure est définie ainsi :

$$\tilde{u}(x_c, x) = K_P\, \varepsilon + K_I \int \varepsilon \, dt \tag{R.6}$$

avec

$$\begin{array}{rcl} K_P & = & diag(k_{P_1},\ k_{P_2},\ \ldots,\ k_{P_n}) \\ K_I & = & diag(k_{I_1},\ k_{I_2},\ \ldots,\ k_{I_n}) \end{array}$$

La valeur du correcteur PI est unique pour des dynamiques désirées fixes. Le réglage des gains K_P and K_I produit une seule dynamique désirée possible.

Techniques de *robustification* avancées

Il existe deux types d'approches permetantes d'améliorer les capacités de la NDI par rapport aux erreurs d'inversion : la commande adaptative ou la commande robuste. Cette thèse se focalise sur les approches de commande robuste même s'il existe un lien fort avec des approches adaptatives indirectes.

Des structures plus complexes que la structure PI peuvent être envisagées en considérant des correcteurs d'ordre plus importants, ce qui tend à ajouter des degrés de liberté dans le problème de synthèse.

Avec la structure PI, la commande $\mathcal{H}_\infty$ est devenue très répandue pour le problème de rejet de perturbations.
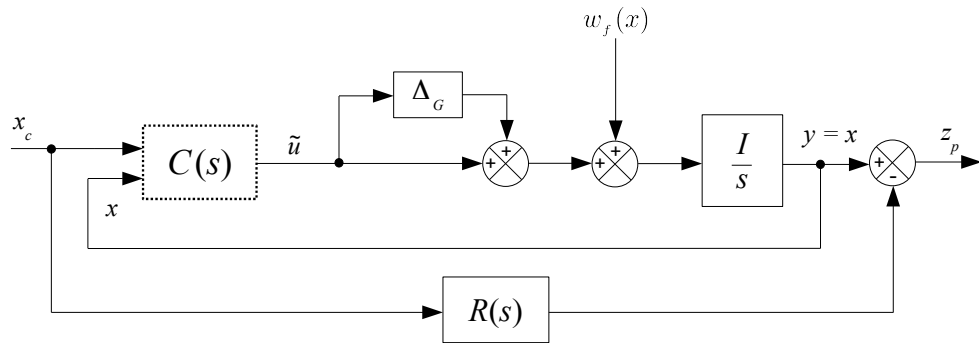
FIGURE R.46 – Schéma de design $\mathcal{H}_\infty$ du système $\tilde{\Sigma}$.

Ce schéma général de synthèse peut être mis sous forme standard tel que représenté sur la Figure R.47. La forme standard est une LFT qui est très utile pour la synthèse de correcteurs où :

- $P(s)$ est l'interconnexion linéaire qui définit le problème de synthèse. Dans notre contexte, elle contient les dynamiques de $\tilde{\Sigma}(s)$, $R(s)$ et $W(s)$;
- $\mathbf{w}$ est un vecteur regroupant toutes les entrées exogènes, y compris le signal x_c et des perturbations tel que w_f ;
- $\mathbf{z}$ est un vecteur regroupant toutes les sorties pondérées.
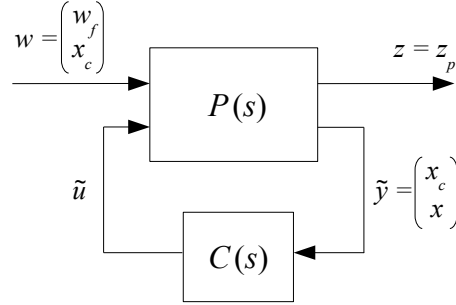
FIGURE R.47 – Forme standard utilisée pour la synthèse de correcteurs $\mathcal{H}_\infty$.

Pour calculer le correcteur robuste $C(s)$, il suffit de résoudre le problème d'optimisation suivant :

$$\min_{C(s)} \gamma \,/\, ||\mathcal{F}_l(P(s), C(s))||_\infty < 1 \tag{R.7}$$

Remark R.3 *Dans les approches robustes, pour une dynamique désirée décrite dans le modèle de référence $R(s)$ une gamme large de correcteurs $C(s)$ peuvent être obtenus. Ces approches présentent plus de flexibilité que les solutions classiques.*

R.1.2 Sur la commande des systèmes avec saturations en entrée

Jusqu'à présent, nous avons négligé les limitations physiques présentes au niveau des actionneurs. Ces dernières sont pourtant systématiquement présents et malheureusement très gênantes quand il s'agit de saturations d'amplitude ou de vitesse sur les signaux de commande.

Représentation et effets des saturations en entrée

Dans un grand nombre d'applications, la dynamiques des actionneurs peut être approximée correctement par un modèle du premier ordre tel que :
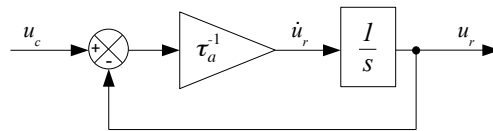
FIGURE R.48 – Un modèle général d'actionneur du premier ordre.

$$\Sigma_A(s) = \frac{1}{\tau_a\, s + 1} \tag{R.8}$$

où τ_a est la constante de temps de l'actionneur.

La commande u_c générée par le correcteur et le signal de sortie de l'actionneur u_r peuvent présenter des écarts transitoires, voir pire, quand l'actionneur sature. Le modèle tenant compte des saturations en position et en vitesse est représenté sur la figure suivante :
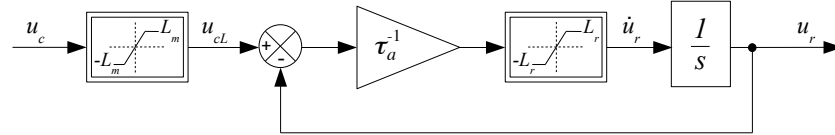
FIGURE R.49 – Modèle d'actionneur saturé pour la synthèse de correcteurs.

Strategie anti-windup

L'approche de commande anti-windup a été développée pour une large classe de systèmes tels que : des systèmes LTI [ZT02, WL04, GdST05], des représentations LFT [FB07], et plus particulière dans le contexte aérospatial [BT09, Boa10].

Le principe de base de la commande anti-windup est d'élargir le domaine de stabilité d'un système en boucle fermée en corrigeant le comportement du correcteur nominal quand une saturation est détectée. Une stratégie classique est la commande *Direct Linear Anti-windup* (DLAW) qui modifie la loi de commande de la façon suivante :
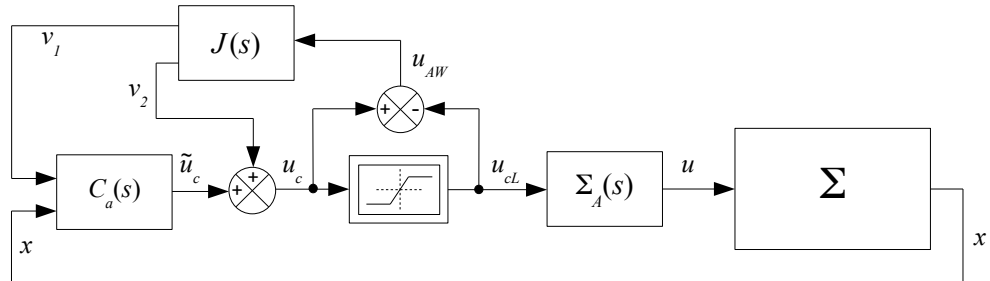
FIGURE R.50 – Schéma de synthèse DLAW.

où
– $C_a(s)$ est le correcteur robuste augmenté par le dispositif anti-windup ;
– $u_{AW} \in \mathbb{R}^m$ est l'entrée du correcteur anti-windup, définie comme : $u_{AW} = u_c - u_{c_L}$;
– $v_1 \in \mathbb{R}^{n_C}$ est le signal anti-windup qui renforce le correcteur $C(s)$;
– $v_2 \in \mathbb{R}^m$ est le signal anti-windup qui modifie la commande $\tilde{u}_c$.

Typiquement, le calcul du correcteur anti-windup correspond a une étape finale une fois conçu un correcteur nominal $C(s)$. Des nouvelles méthodes fondées sur l'optimisation non-lisse, permettent de calculer le correcteur $C_a(s)$ et le correcteur $J(s)$ de manière simultanée [BA11].

R.2 Vers un cadre de travail généralisé de compensation non-linéaire

Dans la présentation de la méthode NDI, le principe de base a été clarifié : les dynamiques non-linéaires sont compensées à travers la boucle interne. Pour ce faire, la boucle interne utilise l'inverse du système. Pour linéariser un système : *Est-ce qu'il est vraiment nécessaire d'utiliser une structure fixe qui se sert de termes non-linéaires pour reproduire l'inverse d'un système dans le correcteur ?*

L'objectif principal de ce chapitre est de présenter une reformulation de la méthode classique NDI, qui peut être considérée comme un cadre de travail généralisé de Compensation Non-linéaire (NLC) qui permet l'utilisation systématique des outils de synthèse robuste.

R.2.1 Raffinement des lois de commande linéarisantes

D'après la procédure de conception décrite dans le cadre de la NDI classique, on s'aperçoit qu'il existe un déséquilibre entre l'effort de la commande dans la boucle interne et de boucle externe. Afin de mieux équilibrer les signaux de commande entre les boucles, on propose de reformuler la fonction $f(x)$ de la manière suivante :

$$f(x) = A(\Theta)\,x + \tilde{f}(x) \tag{R.9}$$

La matrice A est déterminée de manière à minimiser la norme du terme résiduel $\tilde{f}(x)$. Par conséquent, après avoir appliqué la boucle interne au modèle reformulé, le système linéarisé devient :

$$\tilde{\Sigma}: \qquad \dot{x} = A(\Theta)\,x + \tilde{u} \tag{R.10}$$

Ce système permet l'utilisation de techniques de commande LPV pour la conception de la boucle externe du correcteur NDI.

R.2.2 Un cadre de travail linéaire

Ce cadre de travail linéaire que l'on propose ici, permet de généraliser la méthode classique d'inversion dynamique non-linéaire. Il utilise une représentation particulière qui s'adapte à un grand nombre d'applications dans le domaines aéronautiques et spatiaux.

$$\begin{cases} \dot{x} &= A(\Theta)\,x + B_1\,f(x,\Theta) + B_2\,\Lambda(x,\Theta)\,u \\ z &= Cx \end{cases} \tag{R.11}$$

avec
– le vecteur d'état $x \in \mathbb{R}^n$;
– le vecteur de paramètres variants $\Theta \in \mathbb{R}^q$;
– la fonction dépendante de l'état et des paramètres variants $f(x,\Theta) \in \mathbb{R}^{m_1}$;
– le vecteur de commandes $u \in \mathbb{R}^{m_2}$;
– la matrice d'efficacitée $\Lambda(x,\Theta) \in \mathbb{R}^{m_2 \times m_2}$;
– la variable commandée $z \in \mathbb{R}^p$.

Assumption R.4 *La matrice d'efficacité* $\Lambda(x, \Theta)$ *est inversible.*

Assumption R.5 *Le vecteur d'état x et les paramètres variants Θ sont disponibles à la conception de la loi de pilotage.*

Sous la représentation (R.11), le système présente une structure particulière composée de :
– une matrice $A(\Theta) \in \mathbb{R}^{n \times n}$;
– deux matrices en entrée $B_1 \in \mathbb{R}^{n \times m_1}$ and $B_2 \in \mathbb{R}^{n \times m_2}$;
– une matrice de variables commandées $C \in \mathbb{R}^{p \times n}$.

Avec un léger abus de notation, on peut montrer plus clairement la nature linéaire de ce type de représentation :

$$z = \Sigma(s) \begin{bmatrix} f \\ \Lambda\, u \end{bmatrix} \tag{R.12}$$

avec

$$\Sigma(s) = C \ (sI - A(\Theta))^{-1} \begin{bmatrix} B_1 & B_2 \end{bmatrix} \tag{R.13}$$

À la différence d'autres perturbations en entrée, le vecteur $f(x, \Theta)$ contient des fonctions qui sont mesurables. C'est pour quoi on utilise ici le terme *perturbations mesurées*.

Inspirée de la NDI, où les dynamiques non-linéaires sont inclus dans une structure fixe du correcteur pour les compenser, la rejection de perturbations mesurées $f(x, \Theta)$ peut être atteint en rendant disponible l'information sur ces non-linéarités à la loi de commande.

Les perturbations mesurées peuvent s'exprimer comme :

$$f(x, \Theta) = \hat{f}(x, \Theta) + w_f \tag{R.14}$$

Enfin, le critère de performance peut être établi dans la boucle fermée au moyen d'un modèle de référence $R(s)$. Un schéma général de ce modèle de synthèse est présenté sur la Figure R.51.
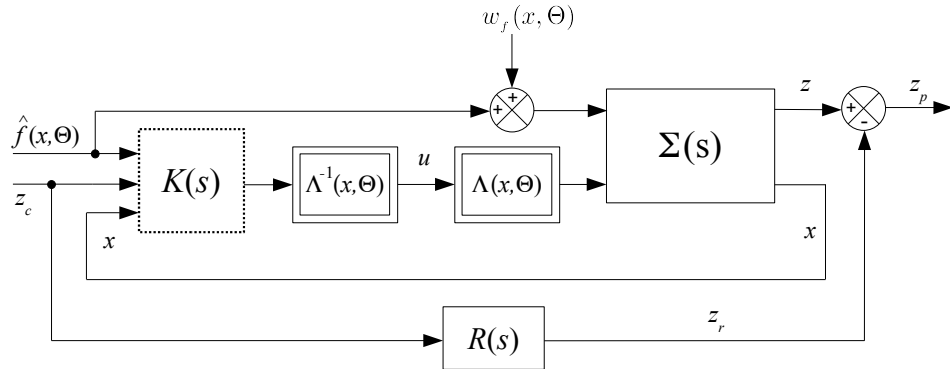
FIGURE R.51 – Schéma de synthèse générale robuste pour la compensation non-linéaire.

Le but du modèle de synthèse est de trouver le meilleur correcteur $K(s)$, tel que la loi de commande

$$u(x, \Theta) = \Lambda^{-1}(x, \Theta) \ K(s) \begin{bmatrix} \hat{f}(x, \Theta) \\ z_c \\ x \end{bmatrix} \tag{R.15}$$

puisse minimiser l'écart entre la variable commandée z et le modèle de référence z_r en dépit des perturbations mesurées $\hat{f}(x, \Theta)$ et erreurs de modélisation w_f.

Le cadre de travail linéaire permet plus de flexibilité au processus de synthèse du correcteur $K(s)$ étant donné que plus d'informations sur le système peuvent être rendus disponible au processus de calcul. Une forme standard est obtenue facilement à partir de ce schéma multi-canaux de synthèse, où :
– $\mathbf{w} = \begin{bmatrix} w_f & \hat{f} & z_c \end{bmatrix}^T$ est le vecteur des entrées exogènes ;
– $\mathbf{z} = \begin{bmatrix} z_u & z_p \end{bmatrix}^T$ est le vecteur de sorties pondérées ;
– $\tilde{y} = \begin{bmatrix} \hat{f} & z_c & x & \tilde{u} \end{bmatrix}^T$ est le vecteur d'entrées du correcteur.
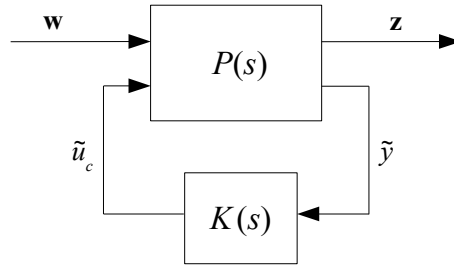
FIGURE R.52 – Forme standard du schéma de synthèse.

Le correcteur $K(s)$ est calculé via l'optimisation $\mathcal{H}_\infty$ du problème suivant :

$$\min_{K(s)} ||\mathcal{F}_l(P(s), K(s))||_\infty \tag{R.16}$$

Selon les fonctions de pondération $W(s)$ utilisées, le correcteur robuste obtenu produit les effets suivants :
– Plus $\mathcal{T}_{z_c \to z_p}$ est petit, meilleur est le suivi de modèle de référence $R(s)$;
– Plus $\mathcal{T}_{\hat{f} \to z_p}$ sont petits, plus grand sera le domaine de fonctionnement ;
– Plus $\mathcal{T}_{w_f \to z_p}$ est petit, plus faible sera l'impacte des erreurs de modélisation ;
– Plus $\mathcal{T}_{\mathbf{w} \to z_u}$ sont petits, plus faible sera la commande u.

Ensuite, ce cadre de travail permet de renforcer la stabilité de la boucle fermée au moyen des dispositifs anti-windup. Par exemple, le schéma de la Figure R.53 présente un schéma de synthèse avec la structure DLAW.
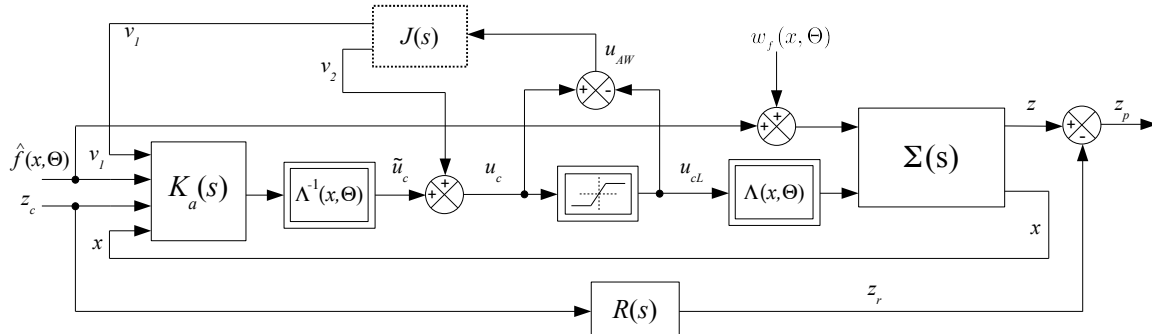
FIGURE R.53 – Renforcement anti-windup pour la compensation non-linéaire.

L'expression de la loi de commande augmentée par le dispositif anti-windup devient :

$$u_c(x,\Theta) = \Lambda^{-1}(x,\Theta)\ K_a(s) \begin{bmatrix} v_1 \\ \hat{f}(x,\Theta) \\ z_c \\ x \end{bmatrix} + v_2 \tag{R.17}$$

avec

$$\begin{bmatrix} v_1 \\ v_2 \end{bmatrix} = J(s)\, u_{AW} \tag{R.18}$$

Le but de ce nouveau schéma de synthèse est de trouver un correcteur $J(s)$ capable d'élargir le domaine de stabilité de la boucle fermée en dépit de saturations et de dynamiques des actionneurs.

Notons que la loi de commande NDI classique peut être considérée comme un cas particulier d'un problème de compensation non-linéaire plus général. La loi de commande NDI classique :

$$u_c(x,\Theta) = \Lambda^{-1}(x,\Theta)\ \left(-\hat{f}(x,\Theta) + C(s) \begin{bmatrix} z_c \\ x \end{bmatrix} \right)$$

peut s'exprimer sous la forme :

$$K_a(s) = \begin{bmatrix} \mathbf{0} & -I & C(s) \end{bmatrix}, \qquad v_2 = \mathbf{0}$$

Pour la synthèse du correcteur anti-windup, on considère l'hypothèse suivante :

Assumption R.6 *Il existe un scalaire positif k_φ tel que $\forall\ z_\varphi \in \mathbb{R}^m$*

$$||w_\varphi|| = ||\varphi(z_\varphi)|| \le k_\varphi\, ||z_\varphi|| \tag{R.19}$$
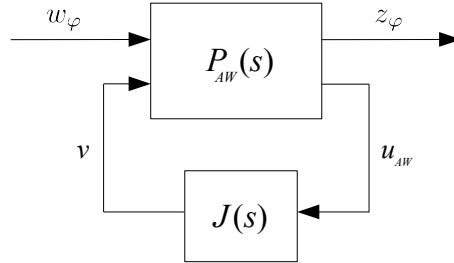
FIGURE R.54 – Forme standard pour la synthèse anti-windup.

À partir de la forme standard représentée dans la Figure R.54, le correcteur anti-windup est obtenu comme la solution du problème d'optimisation suivant :

$$\hat{J}(s) = \underset{J(s)}{\mathrm{Argmin}}\, ||\mathcal{F}_l(P_{AW}(s), J(s))||_\infty \tag{R.20}$$

Il est clair que plus petite est la norme $\mathcal{H}_\infty$ obtenue, moins restrictive sera l'hypothèse R.6.

Des techniques récentes, permettent de faire simultanément la synthèse du correcteur robuste et du correcteur anti-windup [MTK09, BA11].

R.2.3 Analyse de stabilité et robustesse

Pour l'analyse de stabilité, il est nécessaire de représenter la boucle fermée non-linéaire, tout en laissant une partition $M(s)$ en interconnexion linéaire avec des blocs contenant des incertitudes ou des non-linéarités. Le formalisme LFT est bien adapté pour ce type de modélisation.

En introduisant un par un les blocs contenant les dynamiques non-linéaires et contenant des incertitudes, on peut générer une représentation LFT de la boucle fermé non-linéaire. Cette modélisation représente les petites variations du système par rapport à un point d'équilibre $\tilde{x} = x - \bar{x}$.

Le schéma de la Figure R.55 représente la boucle fermée d'un système non-linéaire, à paramètres variants et qui est soumis à des incertitudes et à des saturations en entrée.
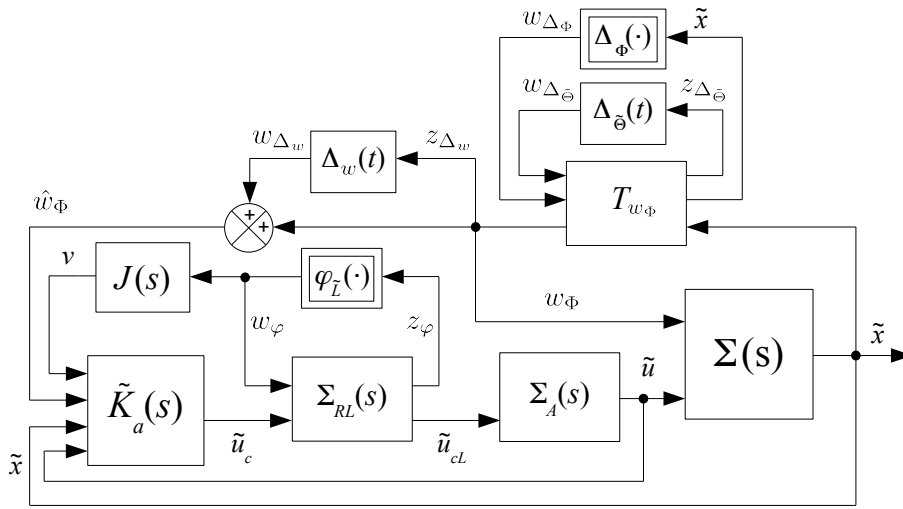
FIGURE R.55 – Schéma de la boucle fermée non-linéaire avec incertitudes paramétriques.
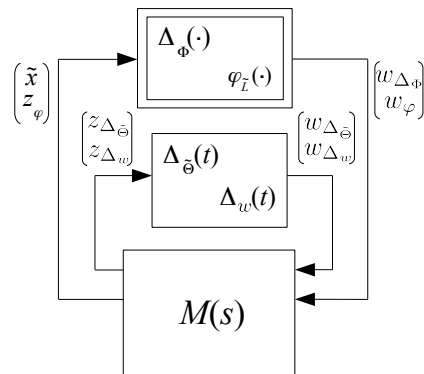
FIGURE R.56 – Représentation LFT du modèle d'analyse.

À partir du modèle d'analyse, différents outils d'analyse LPV peuvent être considérés dans le but de calculer le domaine de stabilité le plus large possible. Pour ce faire, il existe diverses méthodes

soumises à un compromis fondamental : plus la méthode d'analyse est précise, plus est la charge numérique à résoudre par les tests de stabilité.

Application : véhicules volants

R.3   Modélisation de la Mécanique du Vol et des objectifs de commande

Les lois fondamentales du mouvement de la Mécanique classique s'appliquent à tout corps de manière générale. Ce principe reste valable pour les véhicules volants tels que les avions, les lanceurs de satellites et les véhicules aérospatiaux comme les véhicules de rentrée atmosphérique. Les équations fondamentales de la Mécanique du Vol [Etk95, Boi98, Taq09] décrivent la dynamique des véhicules en vol quel que soit leur profil aérodynamique.

L'objectif central de ce chapitre est de présenter les aspects importants de la modélisation d'un véhicule en vol. En particulier, on présente la modélisation des objectifs de commande qui servent à la synthèse de lois de pilotage non-linéaires.

R.3.1   Un modèle d'état général (à 6 degrés de liberté)

Le modèle dynamique capable de décrire le mouvement d'un véhicule en vol est obtenu à partir des équations générales de la Mécanique du Vol. Un tel modèle dynamique sous forme de représentation d'état peut s'exprimer en général sous la forme :

$$\left\{ \begin{array}{rcl} \dot{\vec{\mathbf{x}}} & = & \vec{\mathbf{f}}(t, \vec{\mathbf{x}}(t), \vec{\mathbf{c}}(t), \vec{\mathbf{u}}(t)) \\ \vec{\mathbf{y}}(t) & = & \vec{\mathbf{g}}(t, \vec{\mathbf{x}}(t), \vec{\mathbf{c}}(t), \vec{\mathbf{u}}(t)) \end{array} \right. \tag{R.21}$$

avec le vecteur d'état $\vec{\mathbf{x}}(t) \in \mathbb{R}^n$, le vecteur d'entrées $\vec{\mathbf{u}}(t) \in \mathbb{R}^m$, le vecteur de de mesures en sortie $\vec{\mathbf{y}}(t) \in \mathbb{R}^p$, le vecteur de paramètres constants ou variants dans le temps $\vec{\mathbf{c}}(t) \in \mathbb{R}^q$, et les champs vectoriels contenant la dynamique du système $\vec{\mathbf{f}}$ et $\vec{\mathbf{g}}$.

Quand on modélise le mouvement avec les 6 degrés de liberté d'un véhicule en vol, on se focalise sur la valeur instantanée de la position, l'attitude, la vitesse de translation et de rotation, ainsi que de la masse :

$$\vec{\mathbf{x}}(t) = \begin{bmatrix} \vec{\mathbf{r}}(t) & \vec{\mathbf{V}}(t) & \mathbf{q}(t) & \vec{\mathbf{\Omega}}(t) & m(t) \end{bmatrix}^T \tag{R.22}$$

avec le vecteur position $\vec{\mathbf{r}}$, le vecteur vitesse $\vec{\mathbf{V}}$, le quaternion d'attitude $\mathbf{q}$, la vitesse angulaire $\vec{\mathbf{\Omega}}$ et la masse du véhicule m.

Les entrées $\vec{\mathbf{u}}(t)$ qui affectent la dynamique du système sont principalement le braquage des gouvernes aérodynamiques et la propulsion des moteurs à gaz.

Les sorties $\vec{\mathbf{y}}(t)$ représentent les mesures obtenues à partir d'instruments à bord tels que la centrale à inertie (IMU), la centrale anémométrique, les systèmes de positionnement global (GPS), *etc.*

L'équation (R.23) contient un modèle général du mouvement à 6 degrés de liberté d'un véhicule en vol :

$$\begin{cases} \dot{\vec{\mathbf{r}}} & = & \vec{\mathbf{V}} \\ m\dot{\vec{\mathbf{V}}} & = & m\vec{\mathbf{\Gamma}} = \sum \vec{\mathbf{F}} \\ \dot{\mathbf{q}}_i & = & \frac{1}{2}\mathbf{q}_i \otimes \vec{\mathbf{\Omega}} \\ \mathbf{I}\dot{\vec{\mathbf{\Omega}}} & = & \sum \vec{\mathbf{M}}_G - \vec{\mathbf{\Omega}} \wedge \mathbf{I}\vec{\mathbf{\Omega}} \end{cases} \tag{R.23}$$

avec
– $\vec{\mathbf{r}} = (\overrightarrow{\mathbf{OG}})_{/R_i}$: vecteur position inertielle, de l'origine du corps attracteur O vers le centre de gravité du véhicule G ;
– $\vec{\mathbf{V}} = \vec{\mathbf{V}}_g - \vec{\mathbf{\Omega}}_E \wedge \vec{\mathbf{r}}$: vecteur vitesse inertielle ;
– $\vec{\mathbf{V}}_g = \vec{\mathbf{V}}_a - \vec{\mathbf{V}}_w$: vecteur vitesse sol ;
– $\vec{\mathbf{\Gamma}}$: vecteur d'accélération inertielle ;
– $\mathbf{q}_i$: quaternion d'attitude inertielle ;
– $\vec{\mathbf{\Omega}} = \vec{\mathbf{\Omega}}_i - \vec{\mathbf{\Omega}}_o - \vec{\mathbf{\Omega}}_E$: vecteur vitesse angulaire ;
– $\vec{\mathbf{\Omega}}_o$: vecteur vitesse angulaire local ;
– $\vec{\mathbf{\Omega}}_E$: vecteur vitesse angulaire de la Terre ;
– $\sum \vec{\mathbf{F}} = \vec{\mathbf{F}}_a + \vec{\mathbf{F}}_p + m\vec{\mathbf{g}}$: somme de forces aérodynamiques, de propulsion et de gravitation ;
– $\sum \vec{\mathbf{M}}_G = \vec{\mathbf{M}}_{a_G} + \vec{\mathbf{M}}_{p_G}$: somme de moments aérodynamiques et de propulsion ;
– $\otimes$: multiplication non-commutative des quaternions.

R.3.2 Modèles aérodynamiques

Le modèle aérodynamique décrit les forces et les moments s'exerçant sur le véhicule en vol. Ce modèle comporte de coefficients qui affectent directement les équations de forces et moments comme le montre l'équation (R.24).

Les coefficients aérodynamiques sont liés à la géométrie et à l'écoulement autour du véhicule. La formulation générale des forces et moments aérodynamiques autour d'un point de référence A peut s'exprimer ainsi :

$$\begin{aligned} \vec{\mathbf{M}}_{a_A} & = & \bar{q}S_r \begin{bmatrix} l_r C_l \\ b_r C_m \\ l_r C_n \end{bmatrix} = \begin{bmatrix} L \\ M \\ N \end{bmatrix} \\ \\ \vec{\mathbf{F}}_a & = & \bar{q}S_r \begin{bmatrix} C_x \\ C_y \\ C_z \end{bmatrix} = \begin{bmatrix} X \\ Y \\ Z \end{bmatrix} \end{aligned} \tag{R.24}$$

avec
– S_r : surface de référence ;
– l_r : longueur de référence latérale ;
– b_r : longueur de référence longitudinale ;
– $\bar{q} = \frac{1}{2}\rho V_a^2$: pression dynamique ;

– ρ : masse volumique instantanée de l'atmosphère ;
– C_l : coefficient aérodynamique de roulis ;
– C_m : coefficient aérodynamique de tangage ;
– C_n : coefficient aérodynamique de lacet ;
– C_x : coefficient aérodynamique de traînée ;
– C_y : coefficient aérodynamique de force latérale ;
– C_z : coefficient aérodynamique de poussée.

En général, on définit trois signaux de commande δ_l, δ_m et δ_n qui agissent de manière indépendante sur les moments L, M and N.

Les effets des coefficients aérodynamiques sont généralement considérés comme additifs. De ce fait, ces coefficients peuvent se décomposer de la manière suivante :

$$
\begin{bmatrix} C_l \\ C_m \\ C_n \end{bmatrix} = \begin{bmatrix} C_{l_\beta}(\alpha,\mathcal{M})\beta + C_{l_p}(\alpha,\mathcal{M})\tilde{p} + C_{l_r}(\alpha,\mathcal{M})\tilde{r} + C_{l_{\delta_l}}(\alpha,\mathcal{M},\delta_l) + C_{l_{\delta_n}}(\alpha,\mathcal{M},\delta_n) \\ C_{m_0}(\alpha,\mathcal{M}) + C_{m_q}(\alpha,\mathcal{M})\tilde{q} + C_{m_{\delta_m}}(\alpha,\mathcal{M},\delta_m) \\ C_{n_\beta}(\alpha,\mathcal{M})\beta + C_{n_p}(\alpha,\mathcal{M})\tilde{p} + C_{n_r}(\alpha,\mathcal{M})\tilde{r} + C_{n_{\delta_l}}(\alpha,\mathcal{M},\delta_l) + C_{n_{\delta_n}}(\alpha,\mathcal{M},\delta_n) \end{bmatrix}
$$
$$
\begin{bmatrix} C_{x_a} \\ C_{y_a} \\ C_{z_a} \end{bmatrix} = \begin{bmatrix} C_{x_0}(\alpha,\mathcal{M}) + C_{x_{\delta_m}}(\alpha,\mathcal{M},\delta_m) \\ C_{y_\beta}(\alpha,\mathcal{M})\beta + C_{y_{\delta_l}}(\alpha,\mathcal{M},\delta_l) + C_{y_{\delta_n}}(\alpha,\mathcal{M},\delta_n) \\ C_{z_0}(\alpha,\mathcal{M}) + C_{z_{\delta_m}}(\alpha,\mathcal{M},\delta_m) \end{bmatrix} \tag{R.25}
$$

ainsi que $\tilde{p} = \dfrac{l_r}{V_a}p$, $\tilde{q} = \dfrac{b_r}{V_a}q$ et $\tilde{r} = \dfrac{l_r}{V_a}r$.

Les paramètres α, $\mathcal{M}$ et β correspondent à l'angle d'attaque, le nombre du Mach et à l'angle de dérapage. Les coefficients C_{x_a}, C_{y_a}, et C_{z_a} sont exprimés en axes aérodynamiques. Ces coefficients peuvent être aussi exprimés en axes du véhicule en utilisant les expressions suivantes :

$$
\begin{aligned}
C_x &= -(C_{x_a}\cos\alpha\cos\beta - C_{y_a}\cos\alpha\sin\beta - C_{z_a}\sin\alpha) & \text{(R.26)} \\
C_y &= C_{x_a}\sin\beta + C_{y_a}\cos\beta & \text{(R.27)} \\
C_z &= -(C_{x_a}\sin\alpha\cos\beta - C_{y_a}\sin\alpha\sin\beta + C_{z_a}\cos\alpha) & \text{(R.28)}
\end{aligned}
$$

Ensuite, on présente la modélisation des objectifs de commande.

R.3.3 Objectifs de commande

L'objectif principal du système de pilotage d'un véhicule en vol, est le contrôle de son attitude. De l'ensemble des paramètres qui sont généralement intéressants pour le pilotage dans des applications en aéronautique et en aérospatial, les objectifs angulaires qui ont été retenus pour cette étude sont : l'incidence α, l'angle de dérapage β et le roulis ϕ.

Pour le pilotage d'attitude d'un véhicule, les dynamiques latérales et longitudinales peuvent être considérées comme découplées. On peut donc traiter le pilotage d'attitude de ces deux dynamiques de manière séparée.

L'objectif de la dynamique longitudinale est de moduler l'incidence α qui est directement liée à la dynamique de la vitesse angulaire de tangage q. L'équation dynamique de l'incidence est de façon tout à fait général :

$$
\cos\beta\,\dot{\alpha} = \vec{\boldsymbol{\Omega}}\cdot\vec{\mathbf{y}}_a + \frac{\vec{\boldsymbol{\Gamma}}\cdot\vec{\mathbf{z}}_a}{V_a} \tag{R.29}
$$

En développant les produits de cette équation vectorielle, on obtient la relation dynamique suivante :

$$
\begin{aligned}
\cos\beta\,\dot\alpha \;=\; & q\cos\beta - \sin\beta\,(p\cos\alpha + r\sin\alpha)+ \\
& \frac{1}{V_a}[a_z\cos\alpha - a_x\sin\alpha + g(\cos\alpha\,\cos\phi\,\cos\theta + \sin\alpha\,\sin\theta)]
\end{aligned}
\tag{R.30}
$$

Remark R.7 *La modélisation proposée pour l'objectif incidence α devient intéressante car on s'affranchit alors de l'expression de forces grâce aux mesures d'accélération a_{x_m}, a_{y_m} et a_{z_m} fournies par la centrale à inertie. Grâce à ces mesures, l'expression dynamique de l'incidence ne dépend pas explicitement de la masse m, ce qui est très intéressant puisque ce paramètre est habituellement mal connu.*

La commande δ_m affecte l'objective α principalement à travers la dynamique de la vitesse de tangage q. L'équation dynamique de la vitesse de tangage est obtenue à partir de l'expression fondamentale de moments :

$$
\mathbf{I}\dot{\vec{\boldsymbol\Omega}} = \vec{\mathbf{M}}_{a_A} + \vec{\mathbf{F}}_a \wedge \overrightarrow{\mathbf{AG}} - \vec{\boldsymbol\Omega} \wedge \mathbf{I}\vec{\boldsymbol\Omega}
\tag{R.31}
$$

Remark R.8 *Dans certains cas, les produits d'inertie I_{xy}, I_{xz} et I_{yz} sont assez petits et peuvent être négligés. Les composants prépondérant dans la matrice d'inertie $\mathbf{I}$ se trouvent sur sa diagonale.*

En considérant la simplification dans la Remarque R.8, la dynamique de la vitesse de tangage peut s'exprimer en fonction de la commande δ_m tel que :

$$
\begin{aligned}
I_{yy}\dot q \;=\; & \bar q\,S_r\,l_r\left[C_{m_0}(\alpha,\mathcal{M}) + C_{m_q}(\alpha,\mathcal{M})\frac{l_r}{V_a}\,q\right] + \bar q\,S_r\,l_r\,C_{m_{\delta_m}}(\alpha,\mathcal{M})\delta_m+ \\
& X\,dg_z - Z\,dg_x + (I_{zz} - I_{xx})p\,r
\end{aligned}
\tag{R.32}
$$

Dans le cas de la dynamique latérale, le système de pilotage se focalise sur la modulation de l'angle de dérapage β et l'angle de roulis ϕ. La dynamique de l'angle de roulis est contenue dans les expressions de la dérivée des angles d'Euler tel que :

$$
\dot\phi = p + \tan\theta(\cos\phi\,r + \sin\phi\,q)
\tag{R.33}
$$

L'expression de la dynamique de β peut être obtenue en développant l'expression vectorielle suivante :

$$
\dot\beta \;=\; -\vec{\boldsymbol\Omega}\cdot\vec{\mathbf{z}}_a + \frac{\vec{\boldsymbol\Gamma}\cdot\vec{\mathbf{y}}_a}{V_a}
\tag{R.34}
$$

Il en résulte que :

$$
\begin{aligned}
\dot\beta \;=\; & p\sin\alpha - r\cos\alpha + \frac{1}{V_a}\left(a_y\cos\beta - a_x\cos\alpha\sin\beta - a_z\sin\alpha\sin\beta\right)+ \\
& \frac{g}{V_a}\left(\cos\alpha\,\sin\theta\sin\beta + \sin\phi\,\cos\theta\cos\beta - \sin\alpha\,\sin\theta\,\cos\phi\sin\beta\right)
\end{aligned}
\tag{R.35}
$$

On peut souligner que la Remarque R.7 reste également valide aussi pour la modélisation de l'objectif angulaire β.

Les dynamiques de l'angle de dérapage et du roulis sont clairement liées à la vitesse de roulis p et à la vitesse de lacet r. Les commandes δ_l et δ_n qui interviennent dans le modèle latéral impactent les objectifs angulaires à travers les vitesses angulaires p et r. En négligeant le produit inertiel I_{xz}, tel qu'il est précisé dans la Remarque R.8, les expressions dynamiques des vitesses angulaires dévient :

$$
\begin{aligned}
I_{xx}\dot{p} = {} & \bar{q}\,S_r\,l_r \left[C_{l_\beta}(\alpha,\mathcal{M})\beta + C_{l_p}(\alpha,\mathcal{M})\frac{l_r}{V_a}\,p + C_{l_r}(\alpha,\mathcal{M})\frac{l_r}{V_a}\,r \right] + \\
& \bar{q}\,S_r\,l_r \left[C_{l_{\delta_l}}(\alpha,\mathcal{M})\delta_l + C_{l_{\delta_n}}(\alpha,\mathcal{M})\delta_n \right] + Zdg_y - Ydg_z + \\
& (I_{yy} - I_{zz})r\,q
\end{aligned}
\tag{R.36}
$$

et

$$
\begin{aligned}
I_{zz}\dot{r} = {} & \bar{q}\,S_r\,l_r \left[C_{n_\beta}(\alpha,\mathcal{M})\beta + C_{n_p}(\alpha,\mathcal{M})\frac{l_r}{V_a}\,as\,p + C_{n_r}(\alpha,\mathcal{M})\frac{l_r}{V_a}\,r \right] + \\
& \bar{q}\,S_r\,l_r \left[C_{n_{\delta_l}}(\alpha,\mathcal{M})\delta_l + C_{n_{\delta_n}}(\alpha,\mathcal{M})\delta_n \right] + Xdg_y - Ydg_x + \\
& (I_{xx} - I_{yy})p\,q
\end{aligned}
\tag{R.37}
$$

R.3.4 Principales sources de perturbation

Un véhicule en vol quelconque est soumis à un ensemble de phénomènes que l'on doit considérer afin de valider les lois de pilotage obtenues. Ces phénomènes peuvent être modelés par des incertitudes Δ additives ou multiplicatives, qui agissent sur la représentation nominale du véhicule.

Les principales sources de perturbation considérées en simulation sont les suivantes :
– Variations de la masse volumique de l'atmosphère ($\Delta\rho$) en fonction de l'altitude h.
– Vent. Le vent se décompose en vent statique ($\vec{\mathbf{V}}_{sw}$) et turbulence ($\vec{\mathbf{V}}_{tw}$).
– Erreurs de modélisation des coefficients aérodynamiques (ΔC_{m0}, $\Delta C_{m\delta_m}$, $\Delta C_{m\delta_{bf}}$, ΔC_x, ΔC_z, $\Delta C_{l\delta_l}$, $\Delta C_{n\delta_l}$, $\Delta C_{l\delta_n}$, $\Delta C_{n\delta_n}$).
– Erreurs de modélisation du centrage et moment d'inertie (Δdg_x, Δdg_y, Δdg_z).
– Erreurs de mesure de la centrale à inertie. Les mesures de la centrale, qui correspondent aux accélérations en translation $\vec{\mathbf{\Gamma}}_m$ et la vitesse de rotation angulaire $\vec{\mathbf{\Omega}}_m$, sont soumis à des phénomènes déterministes et stochastiques tels que : biais, facteurs d'échelle et marches au hasard.
– Erreurs de mesure de la centrale anémométrique ($\Delta\alpha$, $\Delta\beta$, ΔV_a) en dessous de Mach 2.5.

Les erreurs de mesure que l'on considère peuvent entraîner des erreurs supplémentaires dans divers paramètres qui pourraient intervenir dans la loi de pilotage tels que :
– La masse volumique de l'atmosphère en fonction de l'altitude $\rho(h)$: $\Delta\tilde{\rho}$;
– Le nombre du Mach $\mathcal{M}(V_a, h)$ en fonction de la vitesse et l'altitude : $\Delta\mathcal{M}$.

Dans ce chapitre, ce sont les aspects de modélisation et les objectifs de commande pour un véhicule volant qui sont traités. Tout d'abord, à partir des équations fondamentales utilisées dans la Mécanique du Vol, un modèle général avec 6 degrés de liberté du véhicule a été présenté. Puis, la modélisation aérodynamique et des actionneurs d'un véhicule quelconque ont été abordés. Les expressions dynamiques des objectifs angulaires pour le pilotage d'attitude d'un véhicule quelconque ont été obtenus. Enfin, les sources principales de perturbation que l'on doit considérer en simulation ont été énumérées.

R.4 Conception des lois de commande par Compensation Non-linéaire

L'objectif principal de ce chapitre est de présenter et d'exposer les diverses contraintes dans les processus de conception des lois de pilotage en utilisant la méthode NDI classique ainsi qu'en utilisant le cadre de travail généralisé NLC. On retiendra les hypothèses suivantes au long de ce chapitre :

Assumption R.9 *Pour la synthèse des lois de pilotage, les dynamiques latérales et longitudinales peuvent être découplées sous l'hypothèse que la dynamique latérale reste en équilibre durant l'évolution de la dynamique longitudinale et vice-versa.*

Assumption R.10 *La dynamique des vitesses angulaires évolue, de manière suffisante, plus rapidement que celle des objectifs angulaires en fonction d'une échelle de temps. Les dynamiques lentes et les dynamiques rapides peuvent donc être découplées.*

Assumption R.11 *Les mesures des sorties commandées z et de l'état du véhicule sont accessibles par la loi de pilotage ainsi que par la mesure du vecteur de paramètres lentement variants Θ.*

R.4.1 Compensation classique NDI-PI

Dans le cas de la méthode NDI classique, on gardera temporairement l'hypothèse suivante :

Assumption R.12 *La dynamique des actionneurs liée aux gouvernes aérodynamiques n'est pas soumise à des saturations et, elle est suffisamment rapide pour réaliser n'importe quel signal de commande.*

En utilisant l'approche de séparation par échelles de temps multiples, les deux sous-systèmes du modèle longitudinal avec sortie commandée z peut-être exprimé ainsi :

$$\dot{\alpha} = Z_\alpha + q \tag{R.38}$$
$$\dot{q} = M_q + g_q\, \delta_m \tag{R.39}$$
$$z = C_{long}\, x \tag{R.40}$$

avec

$$z = \alpha$$
$$x = \begin{bmatrix} \alpha & q \end{bmatrix}^T$$
$$\Theta = \begin{bmatrix} p & r & a_x & a_z & \theta & \phi & \beta & \bar{q} & X & Z & V_a & \mathcal{M} \end{bmatrix}^T$$

$$Z_\alpha(x,\Theta) = -\tan\beta\,(p\cos\alpha + r\sin\alpha) +$$
$$\frac{1}{V_a\cos\beta}[a_z\,\cos\alpha - a_x\,\sin\alpha + g(\cos\alpha\,\cos\phi\,\cos\theta + \sin\alpha\,\sin\theta)]$$

$$M_q(x,\Theta) = \frac{\bar{q}\,S_r\,l_r}{I_{yy}}\left[C_{m_0}(\alpha,\mathcal{M}) + C_{m_q}(\alpha,\mathcal{M})\frac{l_r}{V_a}\,q\right] + \frac{1}{I_{yy}}(X\,dg_z - Z\,dg_x) +$$
$$\frac{1}{I_{yy}}\,[(I_{zz} - I_{xx})p\,r]$$

$$g_q(x,\Theta) = \frac{1}{I_{yy}}\bar{q}\,S_r\,l_r\,C_{m_{\delta_m}}(\alpha,\mathcal{M})$$

$$C_{long} = \begin{bmatrix} 1 & 0 \end{bmatrix}$$

La conception de la loi de pilotage NDI-PI s'effectue en deux étapes :

Step 1 *Trouver l'expression de la commande δ_m qui inverse la dynamique rapide dans (R.38) et définir une commande linéaire capable de stabiliser la boucle rapide en suivant une dynamique du premier ordre.*

Step 2 *Trouver la valeur commandée de la vitesse de tangage q_c nécessaire pour inverser les dynamiques rapides (R.39) et définir un correcteur linéaire capable d'imposer une dynamique de deuxième ordre à la convergence de l'objectif commandé vers son signal de consigne $z_c = \alpha_c$.*

En considérant un signal de consigne α_c filtré par une fonction du premier ordre α_F, l'expression finale du correcteur NDI avec compensation PI (NDI-PI) est tel que :

$$\delta_m = g_q^{-1}\left[-M_q + \frac{1}{\tau_q}\left(-Z_\alpha + k_P(\alpha_F - \alpha) + k_I \int (\alpha_F - \alpha) - q\right)\right] \tag{R.41}$$

avec

$$k_P = 2\,\xi_\alpha\,\omega_{c_\alpha} \qquad k_I = \omega_{c_\alpha}^2 \tag{R.42}$$

De manière plus concise, cette loi de commande peut s'écrire ainsi :

$$\delta_m = g_q^{-1}(K\,\tilde{y} + H\,w) \tag{R.43}$$

avec

$$K = \begin{bmatrix} \dfrac{k_P}{\tau_q} & \dfrac{k_I}{\tau_q} & \dfrac{-1}{\tau_q} \end{bmatrix} \tag{R.44}$$

$$H = \begin{bmatrix} \dfrac{-1}{\tau_q} & -1 \end{bmatrix} \tag{R.45}$$

et en considérant les vecteurs suivants :

$$\tilde{y} = \begin{bmatrix} \varepsilon_\alpha & \int \varepsilon_\alpha & q \end{bmatrix}^T \tag{R.46}$$

$$w = \begin{bmatrix} Z_\alpha & M_q \end{bmatrix}^T \tag{R.47}$$

Sous cette formulation, on s'aperçoit que le gain statique K est chargé d'asservir la boucle externe tandis que le gain statique H permet d'éliminer les non-linéarités du modèle longitudinal.

Dans le cas du modèle latéral que l'on utilise pour le processus de conception, le système peut s'écrire en deux sous-systèmes de la manière suivante :

$$\begin{bmatrix} \dot{\beta} \\ \dot{\phi} \end{bmatrix} = \begin{bmatrix} Y_\beta \\ X_\phi \end{bmatrix} + G_1 \begin{bmatrix} p \\ r \end{bmatrix} \tag{R.48}$$

$$\begin{bmatrix} \dot{p} \\ \dot{r} \end{bmatrix} = \begin{bmatrix} L_p \\ N_r \end{bmatrix} + G_2 \begin{bmatrix} \delta_l \\ \delta_n \end{bmatrix} \tag{R.49}$$

$$z = C_{lat}\,x \tag{R.50}$$

ONERA
THE FRENCH AEROSPACE LAB

ISaE
Institut Supérieur de l'Aéronautique et de l'Espace

avec

$$z = \begin{bmatrix} \beta & \phi \end{bmatrix}^T$$
$$x = \begin{bmatrix} \beta & \phi & p & r \end{bmatrix}^T$$
$$\Theta = \begin{bmatrix} q & a_x & a_y & a_z & \theta & \alpha & \bar{q} & X & Y & Z & V_a & \mathcal{M} \end{bmatrix}^T$$

$$Y_\beta(x,\Theta) = \frac{1}{V_a} \left(a_y \cos\beta - a_x \cos\alpha \sin\beta - a_z \sin\alpha \sin\beta \right) +$$
$$\frac{g}{V_a} \left(\cos\alpha \sin\theta \sin\beta + \sin\phi \cos\theta \cos\beta - \sin\alpha \sin\theta \cos\phi \sin\beta \right)$$

$$X_\phi(x,\Theta) = \tan\theta(\cos\phi\, r + \sin\phi\, q)$$

$$L_p(x,\Theta) = \frac{\bar{q}\, S_r\, l_r}{I_{xx}} \left[C_{l_\beta}(\alpha,\mathcal{M})\beta + C_{l_p}(\alpha,\mathcal{M})\frac{l_r}{V_a} p + C_{l_r}(\alpha,\mathcal{M})\frac{l_r}{V_a} r \right] +$$
$$\frac{1}{I_{xx}}[Z dg_y - Y dg_z + (I_{yy} - I_{zz})r\, q]$$

$$N_r(x,\Theta) = \frac{\bar{q}\, S_r\, l_r}{I_{zz}} \left[C_{n_\beta}(\alpha,\mathcal{M})\beta + C_{n_p}(\alpha,\mathcal{M})\frac{l_r}{V_a} p + C_{n_r}(\alpha,\mathcal{M})\frac{l_r}{V_a} r \right] +$$
$$\frac{1}{I_{zz}}[X dg_y - Y dg_x + (I_{xx} - I_{yy})p\, q]$$

$$G_1(x,\Theta) = \begin{bmatrix} \sin\alpha & -\cos\alpha \\ 1 & 0 \end{bmatrix}$$

$$G_2(x,\Theta) = \begin{bmatrix} \dfrac{\bar{q}\, S_r\, l_r}{I_{xx}} C_{l_{\delta_l}}(\alpha,\mathcal{M}) & \dfrac{\bar{q}\, S_r\, l_r}{I_{xx}} C_{l_{\delta_n}}(\alpha,\mathcal{M}) \\ \dfrac{\bar{q}\, S_r\, l_r}{I_{zz}} C_{n_{\delta_l}}(\alpha,\mathcal{M}) & \dfrac{\bar{q}\, S_r\, l_r}{I_{zz}} C_{n_{\delta_n}}(\alpha,\mathcal{M}) \end{bmatrix}$$

$$C_{lat} = \begin{bmatrix} 1 & 0 & 0 & 0 \\ 0 & 1 & 0 & 0 \end{bmatrix}$$

Puis, en suivant les deux étapes décrites pour le cas longitudinal, on obtient l'expression du correcteur NDI-PI :

$$\begin{bmatrix} \delta_l \\ \delta_n \end{bmatrix} = G_2^{-1}\left[-\begin{bmatrix} L_p \\ N_r \end{bmatrix} + T\left\{ G_1^{-1}\left(-\begin{bmatrix} Y_\beta \\ X_\phi \end{bmatrix} + K_P \begin{bmatrix} \varepsilon_\beta \\ \varepsilon_\phi \end{bmatrix} + K_I \begin{bmatrix} \int \varepsilon_\beta \\ \int \varepsilon_\phi \end{bmatrix} \right) - \begin{bmatrix} p \\ r \end{bmatrix} \right\} \right] \tag{R.51}$$

avec

$$T = diag(\tau_p^{-1}, \tau_r^{-1}) \tag{R.52}$$

$$K_P = \begin{bmatrix} k_{P_\beta} & 0 \\ 0 & k_{P_\phi} \end{bmatrix} \qquad K_I = \begin{bmatrix} k_{I_\beta} & 0 \\ 0 & k_{I_\phi} \end{bmatrix} \tag{R.53}$$

$$k_{P_i} = 2\,\xi_i\,\omega_{c_i} \qquad k_{I_i} = \omega_{c_i}^2 \tag{R.54}$$

$$\varepsilon_\beta = (\beta_F - \beta) \qquad \varepsilon_\phi = (\phi_F - \phi) \tag{R.55}$$

Une expression plus concise peut être aussi formulée pour la loi NDI du modèle latéral sous la forme :

$$\begin{bmatrix} \delta_l \\ \delta_n \end{bmatrix} = G_2^{-1}(K\,\tilde{y} + H\,w) \tag{R.56}$$

avec

$$K \quad = \quad \begin{bmatrix} \tilde{T} \, K_P & \tilde{T} \, K_I & -T \end{bmatrix} \tag{R.57}$$

$$H \quad = \quad \begin{bmatrix} -\tilde{T} & -I \end{bmatrix} \tag{R.58}$$

en considérant que :

$$\tilde{T} = T \, G_1^{-1} \tag{R.59}$$

et étant donnés les vecteurs suivants :

$$\tilde{y} \quad = \quad \begin{bmatrix} \varepsilon_\beta & \varepsilon_\phi & \int \varepsilon_\beta & \int \varepsilon_\phi & p & r \end{bmatrix}^T \tag{R.60}$$

$$w \quad = \quad \begin{bmatrix} Y_\beta & X_\phi & L_p & N_r \end{bmatrix}^T \tag{R.61}$$

R.4.2 Reformulation sous le cadre généralisé de compensation non-linéaire

Pour le processus de conception dans le cadre de travail NLC, on considère l'hypothèse suivante :

Assumption R.13 *La dynamique des actionneurs liés aux gouvernes aérodynamiques suit une fonction de premier ordre comme décrit dans la Section **??**. On considère que l'actionneur n'est pas soumis à des saturations.*

Dans le contexte du cadre de travail généralisé proposé dans le Chapitre R.2, les non-linéarités du système sont considérées comme des *perturbations mesurées* w_i que l'on exploite pour la conception de la loi de commande. De telle sorte que, le modèle longitudinal puisse être écrit sous la forme :

$$\Sigma_{long} : \begin{cases} \dot{\alpha} & = & w_\alpha + q \\ \dot{q} & = & w_q + \lambda_q \, \delta_m \end{cases}$$

avec

$$w_\alpha = Z_\alpha(x, \Theta), \quad w_q = M_q(x, \Theta), \quad \lambda_q = g_q(x, \Theta) \tag{R.62}$$

En considérant les relations :

$$\hat{w}_\alpha = z_\alpha \, \tilde{\alpha}, \qquad \hat{w}_q = m_\alpha \, \tilde{\alpha} + m_q \, q \tag{R.63}$$

avec $\tilde{\alpha} = \alpha - \bar{\alpha}$, les approximations suivantes permettent de réduire la norme des signaux f_α et f_q :

$$\hat{f}_\alpha = w_\alpha - z_\alpha \, \tilde{\alpha}, \qquad \hat{f}_q = w_q - m_\alpha \, \tilde{\alpha} - m_q \, q \tag{R.64}$$

Le modèle longitudinal est facilement écrit sous la forme (R.11) proposée dans le cadre généralisé NLC. On obtient que :

$$\Sigma_{long}(s) : \begin{cases} \dot{\tilde{x}} & = & \begin{bmatrix} z_\alpha & 1 \\ m_\alpha & m_q \end{bmatrix} \tilde{x} + B_1 \begin{bmatrix} f_\alpha \\ f_q \end{bmatrix} + B_2 \, \lambda_q \, \delta_m \\ \\ z & = & \begin{bmatrix} 1 & 0 \end{bmatrix} \tilde{x} \end{cases} \tag{R.65}$$

avec

$$\tilde{x} = \begin{bmatrix} \tilde{\alpha} & q \end{bmatrix}^T$$

$$B_1 = \begin{bmatrix} 1 & 0 \\ 0 & 1 \end{bmatrix}, \qquad B_2 = \begin{bmatrix} 0 \\ 1 \end{bmatrix}$$

$$f_\alpha = \hat{f}_\alpha + w_{f_\alpha}, \qquad f_q = \hat{f}_q + w_{f_q}$$

Ensuite, on considère le modèle de l'actionneur suivant :

$$\Sigma_A(s): \ \dot{\tilde{\delta}}_m = \frac{1}{\tau_a}(\tilde{\delta}_{m_c} - \tilde{\delta}_m) \tag{R.66}$$

avec

$$\tilde{\delta}_m = \lambda_q\, \delta_m, \qquad \tilde{\delta}_{m_c} = \lambda_q\, \delta_{m_c} \tag{R.67}$$

Le schéma de synthèse permettant de calculer le correcteur NLC-$\mathcal{H}_\infty$ est présenté dans la Figure R.57. La loi de commande NLC du modèle longitudinal prend la forme :

$$\delta_{m_c} = \lambda_q^{-1}\ K_{long}(s)\ \tilde{y} \tag{R.68}$$

avec

$$\tilde{y} = \begin{bmatrix} \hat{f}_\alpha & \hat{f}_q & \int \varepsilon_\alpha & \alpha_F & \alpha_c & \tilde{\alpha} & q \end{bmatrix}^T \tag{R.69}$$
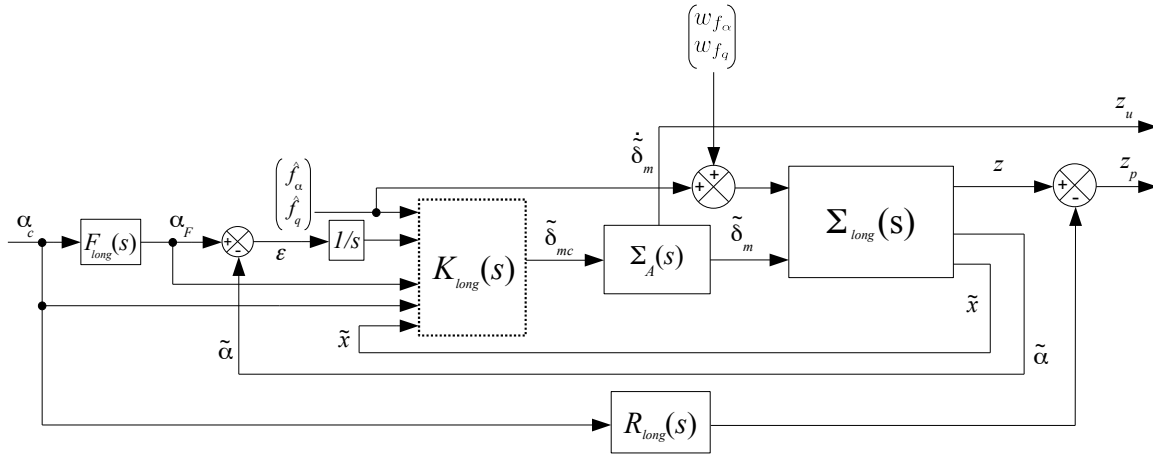
FIGURE R.57 – Modèle de synthèse multi-canaux pour la dynamique longitudinale.

Une fois définie la valeur des filtres de pondération, la forme standard correspondant au schéma de synthèse est facilement obtenu.

Dans le cas du modèle latéral, en suivant le même processus de modélisation que dans le cas longitudinal, on obtient la représentation suivante :

$$
\Sigma_{lat}(s) : \begin{cases} \dot{x} &= \begin{bmatrix} y_\beta & 0 & \sin\alpha & -\cos\alpha \\ 0 & 0 & 1 & 0 \\ l_\beta & 0 & l_p & l_r \\ n_\beta & 0 & n_p & n_r \end{bmatrix} x + B_1 \begin{bmatrix} f_\beta \\ f_\phi \\ f_p \\ f_r \end{bmatrix} + B_2\, \Lambda \begin{bmatrix} \delta_l \\ \delta_n \end{bmatrix} \\[1em] z &= \begin{bmatrix} 1 & 0 & 0 & 0 \\ 0 & 1 & 0 & 0 \end{bmatrix} x \end{cases}
\tag{R.70}
$$

avec

$$
x = \begin{bmatrix} \beta & \phi & p & r \end{bmatrix}^T
$$

$$
B_1 = \begin{bmatrix} 1 & 0 & 0 & 0 \\ 0 & 1 & 0 & 0 \\ 0 & 0 & 1 & 0 \\ 0 & 0 & 0 & 1 \end{bmatrix}, \qquad B_2 = \begin{bmatrix} 0 & 0 \\ 0 & 0 \\ 1 & 0 \\ 0 & 1 \end{bmatrix}
$$

$$
f_\beta = \hat{f}_\beta + w_{f_\beta}, \qquad f_\phi = \hat{f}_\phi + w_{f_\phi}
$$

$$
f_p = \hat{f}_p + w_{f_p}, \qquad f_r = \hat{f}_r + w_{f_r}
$$

Le schéma bloc de la Figure R.58 est utilisé pour la synthèse du correcteur NLC-$\mathcal{H}_\infty$ latéral qui est de la forme :

$$
\begin{bmatrix} \delta_{l_c} \\ \delta_{n_c} \end{bmatrix} = \Lambda^{-1} \, K_{lat}(s)\, \tilde{y}
\tag{R.71}
$$

avec

$$
\tilde{y} = \begin{bmatrix} \hat{f}_\beta & \hat{f}_\phi & \hat{f}_p & \hat{f}_r & \int\varepsilon_\beta & \int\varepsilon_\phi & \beta_F & \phi_F & \beta_c & \phi_c & \beta & \phi & p & r \end{bmatrix}^T
\tag{R.72}
$$
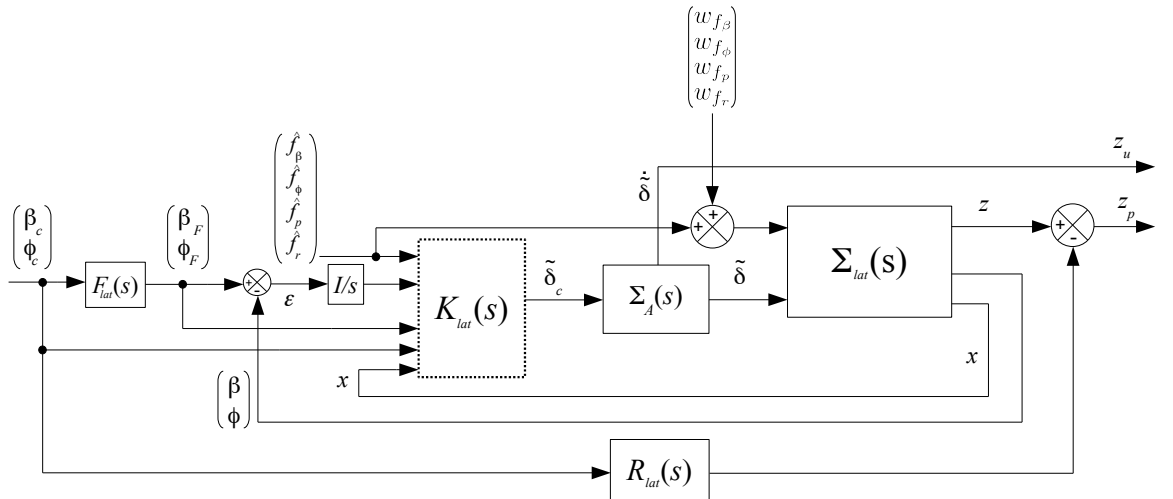
FIGURE R.58 – Modèle de synthèse multi-canaux pour la dynamique latérale.

R.4.3 Compensation Anti-windup

Dans ce cas, on considère un modèle d'actionneur tel que celui présenté dans la Section **??**. On introduit également aussi un *rate limiter* capable d'assurer le comportement nominal des actionneurs δ_{real}. Cette structure avec une vitesse d'évolution maximale de $\tilde{L} = \Lambda L$ peut s'exprimer ainsi :

$$\Sigma_{RL}: \qquad \dot{\tilde{\delta}}_{c_L} = sat_{\tilde{L}}\left(\frac{1}{\tau_L}(\tilde{\delta}_c - \tilde{\delta}_{c_L})\right) \tag{R.73}$$

La saturation qui apparait dans cette structure est utilisée pour générer le signal d'entrée du dispositif anti-windup selon le schéma de synthèse proposée dans la Figure R.59.

Le correcteur augmenté devient :

$$K_a(s): \left\{ \begin{array}{rcl} \dot{x}_K &=& A_K\,x_K + B_K\,\tilde{y} + v_1 \\ \tilde{\delta}_c &=& C_K\,x_K \end{array} \right. \tag{R.74}$$

Étant donné le correcteur anti-windup suivant :

$$\begin{bmatrix} v_1 \\ v_2 \end{bmatrix} = J(s)\,u_{AW} \tag{R.75}$$

la loi de compensation non-linéaire augmenté peut s'écrire ainsi :

$$\delta_c = \Lambda^{-1}(x,\Theta)\,K_a(s)\,\tilde{y} + v_2 \tag{R.76}$$

avec $\tilde{y} = \begin{bmatrix} v_1 & \hat{f}(x,\Theta) & z_c & x \end{bmatrix}^T$.
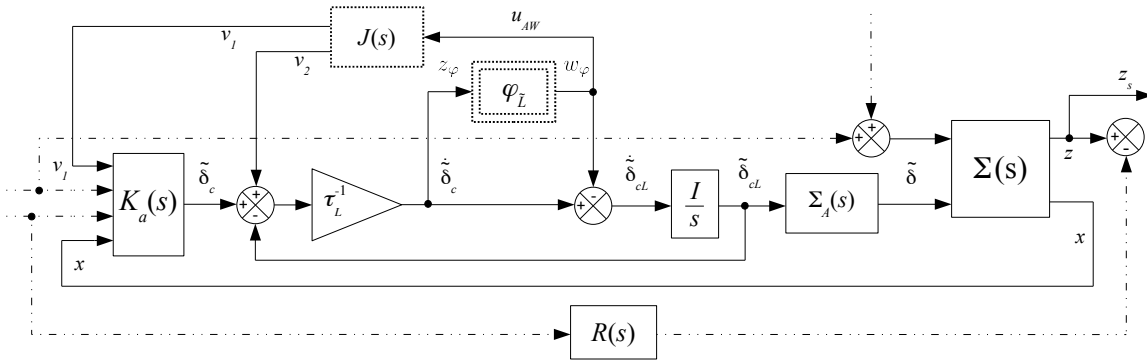
FIGURE R.59 – Schéma de synthèse avec rate-limiter et correction anti-windup.

Dans ce chapitre, les processus de conception de lois de pilotage, avec la méthode NDI classique et le cadre généralisé NLC, ont été abordés. Pour des raisons de simplicité et de clarté dans la présentation de ces processus, les dynamiques latérales et longitudinales ont été étudiés de manière indépendante.

R.5 Un problème de commande pour la rentrée atmosphérique

Le pilotage d'un véhicule de rentrée atmosphérique reste une tâche ardue à l'heure actuelle à cause de son large domaine de vol, des caractéristiques non-linéaires et des aspects variants dans le temps. Par ailleurs, une mission de rentrée atmosphérique requière un niveau de performance élevé.

L'objectif de ce chapitre est d'appliquer les lois de pilotage, obtenues dans le chapitre précédent, au modèle longitudinal d'un véhicule de rentrée atmosphérique. Les lois de pilotage sont testées à différents points de vol d'un exemple de trajectoire.

R.5.1 Contexte physique de la rentrée atmosphérique

Les véhicules de rentrée atmosphérique sont des véhicules volants compacts et rigides soumis à des variations paramétriques importantes tout au long de son domaine de vol. Pour cette thèse, un véhicule de type aile delta a été retenu.

Une mission de rentrée atmosphérique commence à partir d'une orbite basse de la Terre (environ 400 km de la surface de la Terre) et continue par la rentrée du véhicule dans l'atmosphère Terrestre. Une mission pour un véhicule de type aile delta est effectué en quatre phases principales [HG79, VF03, VF05, Fal09] :

1. **Déorbitation**. Elle commence avec une manœuvrer dans le but de réduire légèrement la vitesse orbitale du véhicule, ainsi, le véhicule commence à descendre vers la Terre. Le véhicule descend de son orbite jusqu'à l'entrée dans l'atmopshpère, considéré conventionnellement à 120 km d'altitude.

2. **Hypersonique**. Cette phase commence à $90km$ d'altitude avec un vitesse d'environ $\mathcal{M} \approx 25$ (airspeed $V_a \approx 27000\ km/h$). L'objectif principal, c'est de viser un point en fonction de divers paramètres afin de commencer la phase de dissipation d'énergie ou Terminal Area Energy Management (TAEM).

3. **Dissipation de l'énergie ou TAEM**. Elle commence conventionnellement quand la vitesse diminue autour de $\mathcal{M} = 2$. Durant cette phase, le véhicule peut réaliser des manœuvres en 'S' pour dissiper de l'énergie cinétique.

4. **Approach and Landing phase**. Une fois que le véhicule est aligné avec la piste d'atterrissage, le véhicule réalise une approche à forte pente. Enfin, il effectue une manœuvre en suivant une trajectoire qui permet de conserve une tangente avec une vitesse au dessus de la vitesse de décrochage et permettant de faire l'arrondi.

R.5.2 Implantation des lois de commande et résultats

Les lois de pilotage ont été testées sur différents points d'un exemple de trajectoire. Les points contenus dans le Tableau R.23, correspondent à des conditions de vol équilibré.

Flight point					Trim values	
n°	h (m)	$\mathcal{M}$	$\bar{q}$ (Pa)	γ (^{o})	$\bar{\alpha}$ (^{o})	$\bar{\delta}_m$ (^{o})
1	68 500	20	1 639	-0.3	33	2.08
2	54 500	11	3 615	-0.5	33	1.86
3	48 000	8	4 379	-1.5	28	5.43
4	38 000	5	6 395	-2.5	24	5.78
5	25 000	2.5	10 986	-5	16	1.78
6	10 000	0.8	11 843	-10	10	-4.89
7	5 000	0.6	13 613	-15	7	-7.59
8	0	0.3	6 383	-16	10	-5.99

TABLE R.23 – Points de vol considérés en simulation.

Après avoir défini les spécifications et caractéristiques désirées pour la dynamique de la boucle fermée, à partir du cahier de charges, on peut maintenant calculer les lois de pilotage.

Réglage du correcteur NDI-PI longitudinal

Rappelons la structure du correcteur NDI-PI pour le modèle longitudinal :

$$\delta_{m_c} = g_q^{-1}(K\,\tilde{y} + H\,w) \tag{R.77}$$

avec

$$K = \begin{bmatrix} \dfrac{k_P}{\tau_q} & \dfrac{k_I}{\tau_q} & \dfrac{-1}{\tau_q} \end{bmatrix}, \qquad H = \begin{bmatrix} \dfrac{-1}{\tau_q} & -1 \end{bmatrix} \tag{R.78}$$

Les gains k_P et k_I servent à fixer la dynamique désirée de la boucle fermée. En effet, le seul paramètre véritablement ajustable est la constante de temps τ_q. Plus on diminue sa valeur, plus la performance tend à améliorer et plus grande devient l'activité du signal de commande.

Le tableau R.25 contient les valeurs des gains du correcteur NDI-PI, calculée à partir du choix des paramètres de réglage suivant :

Dynamique désirée		Valeurs des paramètres		
ω_{c_α} (rad/s)	ξ_α	k_P	k_I	τ_F
1.2	0.7	1.68	1.44	1.16

TABLE R.24 – Paramètres du correcteur et dynamique désirée.

Loi de commande NDI-PI		
τ_q (s)	K	H
0.1	$\begin{bmatrix} 16.8 & 14.4 & -10 \end{bmatrix}$	$\begin{bmatrix} -10 & -1 \end{bmatrix}$

TABLE R.25 – Correcteur NDI-PI.

À partir de ce résultat, une solution améliorée peut être obtenue avec le cadre de travail généralisé du NLC.

Synthèse de correcteurs NLC-$\mathcal{H}_\infty$

Rappelons le modèle contenant la dynamique longitudinal qui a été reformulé sous la forme proposée dans le cadre généralisé NLC :

$$\Sigma_{long}(s) : \begin{cases} \dot{\tilde{x}} &=& A\,\tilde{x} + B_1 \begin{bmatrix} f_\alpha \\ f_q \end{bmatrix} + B_2\,\lambda_q\,\delta_m \\[2mm] z &=& \begin{bmatrix} 1 & 0 \end{bmatrix} \tilde{x} \end{cases} \tag{R.79}$$

avec

$$\tilde{x} = \begin{bmatrix} \tilde{\alpha} & q \end{bmatrix}^T$$

$$\tilde{\alpha} = \alpha - \bar{\alpha}, \qquad A = \begin{bmatrix} z_\alpha & 1 \\ m_\alpha & m_q \end{bmatrix}$$

$$B_1 = \begin{bmatrix} 1 & 0 \\ 0 & 1 \end{bmatrix}, \qquad B_2 = \begin{bmatrix} 0 \\ 1 \end{bmatrix}$$

$$f_\alpha = \hat{f}_\alpha + w_{f_\alpha}, \qquad f_q = \hat{f}_q + w_{f_q} \tag{R.80}$$

La valeur de la matrice A est choisie de manière à réduire la norme des signaux f_α et f_q pour la plus grande partie de conditions de vol. Selon le critère proposé, on considère la matrice suivante :

$$A = \begin{bmatrix} -0.001574 & 1 \\ 0.009643 & -0.06239 \end{bmatrix} \tag{R.81}$$

Pour commencer le réglage des filtres de pondération, on peut utiliser la loi de pilotage NDI-PI. Pour ce faire, il faut effectuer une analyse de valeurs singulières des transferts $\mathcal{T}_{\mathbf{w} \to z_u}$ et $\mathcal{T}_{\mathbf{w} \to z_p}$ de la boucle fermée entre le système non-linéaire et le correcteur NDI-PI. À partir de l'allure de la réponse obtenue, on peut définir un filtre passe haut capable de maîtriser les courbes des valeurs singulières. De telle sorte, l'inverse de ce filtre passe haut peut être utilisé comme réglage de référence pour les filtres de pondération. Ensuite, il suffit de trouver le réglage qui permet de minimiser l'objective de performance et d'activité dans la commande.

L'analyse de valeurs singulières réalisée au correcteur NDI-PI fournit les gains maximaux suivants :

$$\sigma_{z_p} = 0.379 = -8.4\,dB, \quad \text{and} \quad \sigma_{z_u} = 102.145 = 40.2\,dB \tag{R.82}$$

Après quelques essais, on obtiens le réglage suivant du filtre de pondération sur la sortie de performance $z_p = \alpha_r - \alpha$:

$$W_p(s) = \frac{s^4 + 8.6\,s^3 + 37.7\,s^2 + 92.5\,s + 71.5}{0.1\,s^4 + 0.57\,s^3 + 1.8\,s^2 + 1.5\,s + 0.002} \tag{R.83}$$

Puisqu'on utilise une méthode d'optimisation non-lisse pour le calcul des lois de commande, l'ordre des filtres de pondération ne pose pas de problème pour sa résolution. Par ailleurs, cette étape pas intermédiaire permet éventuellement de reproduire la solution NDI-PI [HJB11].

La loi de pilotage est de la forme :

$$\left[\frac{\dot{x}_K}{\delta_{m_c}}\right] = K_{long}\left[\frac{x_K}{\tilde{y}}\right] \tag{R.84}$$

avec

$$\tilde{y} = \begin{bmatrix} \alpha_c & \hat{f}_\alpha & \hat{f}_q & \alpha & q \end{bmatrix}^T \tag{R.85}$$

En utilisant le modèle de référence $R_{long}(s)$ ainsi que le filtre de pondération pour générer la forme standard permettant d'adresser le problème de synthèse, on obtient le correcteur suivant :

$$K_{long} = \left[\begin{array}{ccccccc|ccccc}
-0.85 & 0 & 0 & 0 & 0 & 0 & 0 & 1 & 0 & 0 & 0 & 0 \\
0.85 & 0 & 0 & 0 & 0 & 0 & 0 & 0 & 0 & 0 & -1 & 0 \\
248 & -105 & -6.6 & 10.1 & 0 & 0 & 0 & -20 & -36 & -5.8 & -65 & -23 \\
-98 & 36.3 & 4.02 & -11 & -10 & 0 & 0 & -7.2 & -3.2 & -1.7 & 179 & 3.9 \\
83.1 & 139 & 0 & 3.7 & -8.8 & -5.1 & 0 & -30 & 15 & 2 & -10 & 3.7 \\
64.5 & -183 & 0 & 0 & -3.4 & -4.3 & 4.6 & 81 & -22 & -5.2 & 38 & -13 \\
32.4 & -74 & 0 & 0 & 0 & -1.5 & 2.02 & 87 & -6 & -3 & -42 & -11 \\
\hline
253.4 & -37.4 & -3.3 & 12.2 & -4.6 & -9.1 & 4.2 & 1.7 & -6.8 & -1.7 & -115 & -16.3
\end{array}\right]$$

TABLE R.26 – Correcteur NLC-$\mathcal{H}_\infty$.

De la même manière que dans le cas du correcteur NDI-PI, l'analyse des valeurs singulières fournit les gains maximaux suivants :

$$\sigma_{z_p} = 0.291 = -10.7\,dB, \quad \text{et} \quad \sigma_{z_u} = 35.952 = 31.1\,dB \tag{R.86}$$

La valeur des gains σ_{z_u} et σ_{z_p} est plus petite ici que dans le cas du correcteur NDI-PI.

Enfin, on peut utiliser un dispositif anti-windup tel que celui détaillé auparavant. La structure du correcteur NLC-$\mathcal{H}_\infty$ est modifiée selon le schéma de synthèse de la Figure R.59, où :

$$\left[\frac{\dot{x}_J}{v}\right] = J_{long}\left[\frac{x_J}{u_{AW}}\right] \tag{R.87}$$

avec $v \in \mathbb{R}^7$ et $u_{AW} \in \mathbb{R}$. Le correcteur NLC-$\mathcal{H}_\infty$ renforcé par le dispositif anti-windup peut s'écrire ainsi :

$$\left[\frac{\dot{x}_K}{\delta_{m_c}}\right] = K_{a_{long}}\left[\begin{array}{c} x_K \\ v \\ \tilde{y} \end{array}\right] \tag{R.88}$$

avec $\tilde{y} = \begin{bmatrix} \alpha_c & \hat{f}_\alpha & \hat{f}_q & \alpha & q \end{bmatrix}^T$.

Ayant défini la forme standard pour la synthèse du correcteur anti-windup, on utilise à nouveau la synthèse par optimisation $\mathcal{H}_\infty$ non-lisse. On obtient le correcteur suivant :

$$
J_{long} = \left[
\begin{array}{c|c}
-1.954 & 0.3077 \\
\hline
-1.965 & -0.6037 \\
0.5254 & 0.6714 \\
-68.28 & -251.8 \\
4.647 & -128.5 \\
-14.06 & 39.01 \\
-10.19 & -148.2 \\
5.032 & -60.65
\end{array}
\right]
$$

TABLE R.27 – Correcteur NCL-$\mathcal{H}_\infty$ + AW.

Avec l'analyse de stabilité et robustesse, on devrait être capable de montrer que ce correcteur augmenté induit une marge de robustesse plus grande. Ainsi, ce correcteur anti-windup complète la stratégie de compensation non-linéaire pour le pilotage des dynamiques longitudinales du véhicule de rantrée atmosphérique.

Résultats de simulation

Par la suite, on présente les résultats de simulation obtenus avec les différents lois de pilotage calculées. Ces résultats de simulation sont représentés dans un graphique contenant les courbes associées aux cinq différents paramètres d'intérêt : l'incidence α, la vitesse de tangage q, le braquage des elevons δ_{el} et sa vitesse de variation $\dot{\delta}_{el}$, et la vitesse de variation du body flap $\dot{\delta}_{bf}$.

Comparaison de résultats de simulation entre solutions équivalentes NDI-PI et NLC-$\mathcal{H}_\infty$. Ces deux correcteurs ont été conçus en utilisant la même dynamique désirée contenue dans le Tableau R.24.

Le point de vol n°6 est utilisé pour comparer les résultats. D'un côté, on trouve la réponse temporelle à l'échelon du système en boucle fermée avec le correcteur NDI-PI dans la Figure R.62 (page 216). De l'autre côté, on trouve la réponse du véhicule asservie par le correcteur NLC-$\mathcal{H}_\infty$ dans la Figure R.63 (page 217).

Clairement, les deux correcteurs permettent d'obtenir des réponses temporelles satisfaisantes. Néanmoins, le correcteur NLC-$\mathcal{H}_\infty$ possède très clairement une meilleur performance par rapport au suivi du modèle de référence α_r. Dans le cas du correcteur NLC-$\mathcal{H}_\infty$, l'activité de la commande reste aussi inférieure à celle du correcteur NDI-PI.

Á cause des effets sévères des saturations dans la boucle fermée, aucun de ces deux correcteurs n'est capable de prévenir la déstabilisation du système au point de vol n°1.

Résultats de simulation avec le correcteur robuste renforcé. On teste maintenant le correcteur augmenté qui résulte de la synthèse anti-windup.

D'un côté, on trouve la réponse temporelle à l'échelon du système en boucle fermée avec le correcteur NLC-$\mathcal{H}_\infty$ dans la Figure R.60 (page 214). De l'autre côté, on trouve la réponse du véhicule asservie par le correcteur NLC-$\mathcal{H}_\infty$ + AW dans la Figure R.61 (page 215).

La réponse stable dans le cas du correcteur NLC-$\mathcal{H}_\infty$ + AW est évidente. Comme on l'attendait, le domaine de stabilité de la boucle fermée est élargi par le dispositif anti-windup. L'activité de la commande augmente durant le transitoire mais cela lui permet de satisfaire les contraintes temporelles du cahier de charges. En effet, le but principal de stabiliser la boucle tout au long du domaine de vol est atteint.

Dans ce chapitre, les lois de pilotage destinées à la commande d'attitude d'un véhicule de rentrée atmosphérique ont été calculées et testées en simulation. Le cadre généralisé NLC permet d'obtenir des meilleurs résultats de performance que la solution NDI classique.
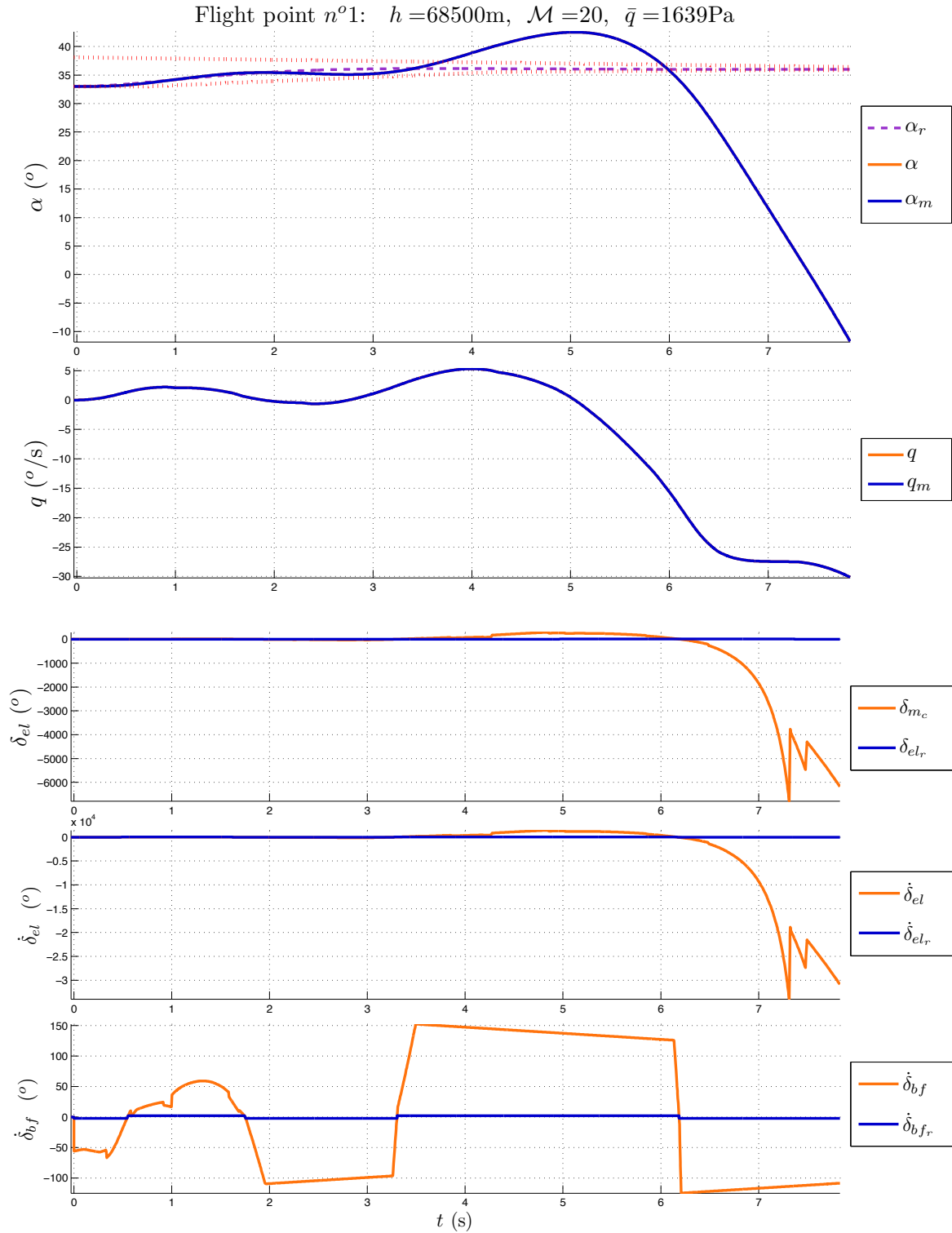
FIGURE R.60 – Simulation avec actionneurs saturés et loi de commande NLC-$\mathcal{H}_\infty$.
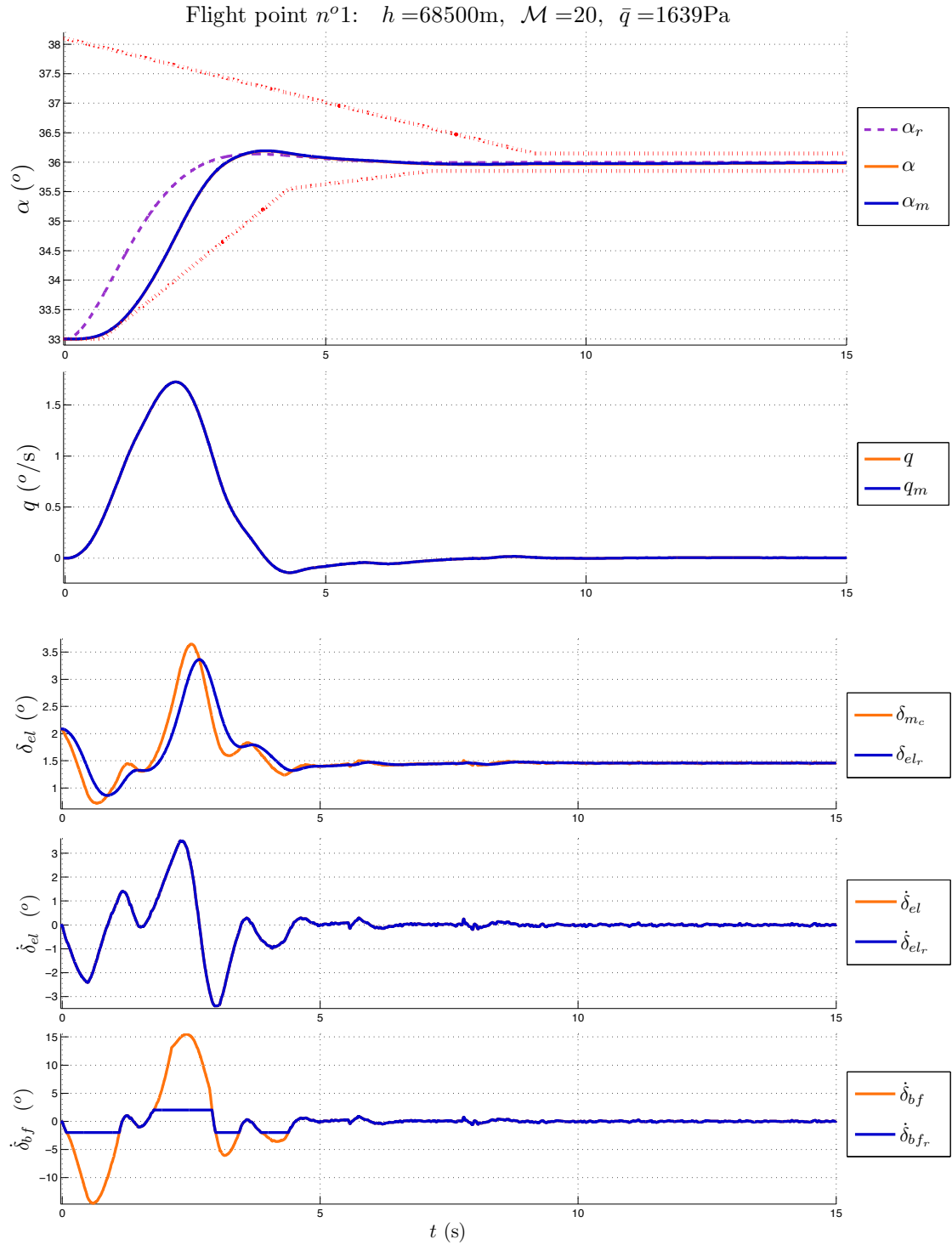
FIGURE R.61 – Simulation avec actionneurs saturés et loi de commande NLC-$\mathcal{H}_\infty$+AW.
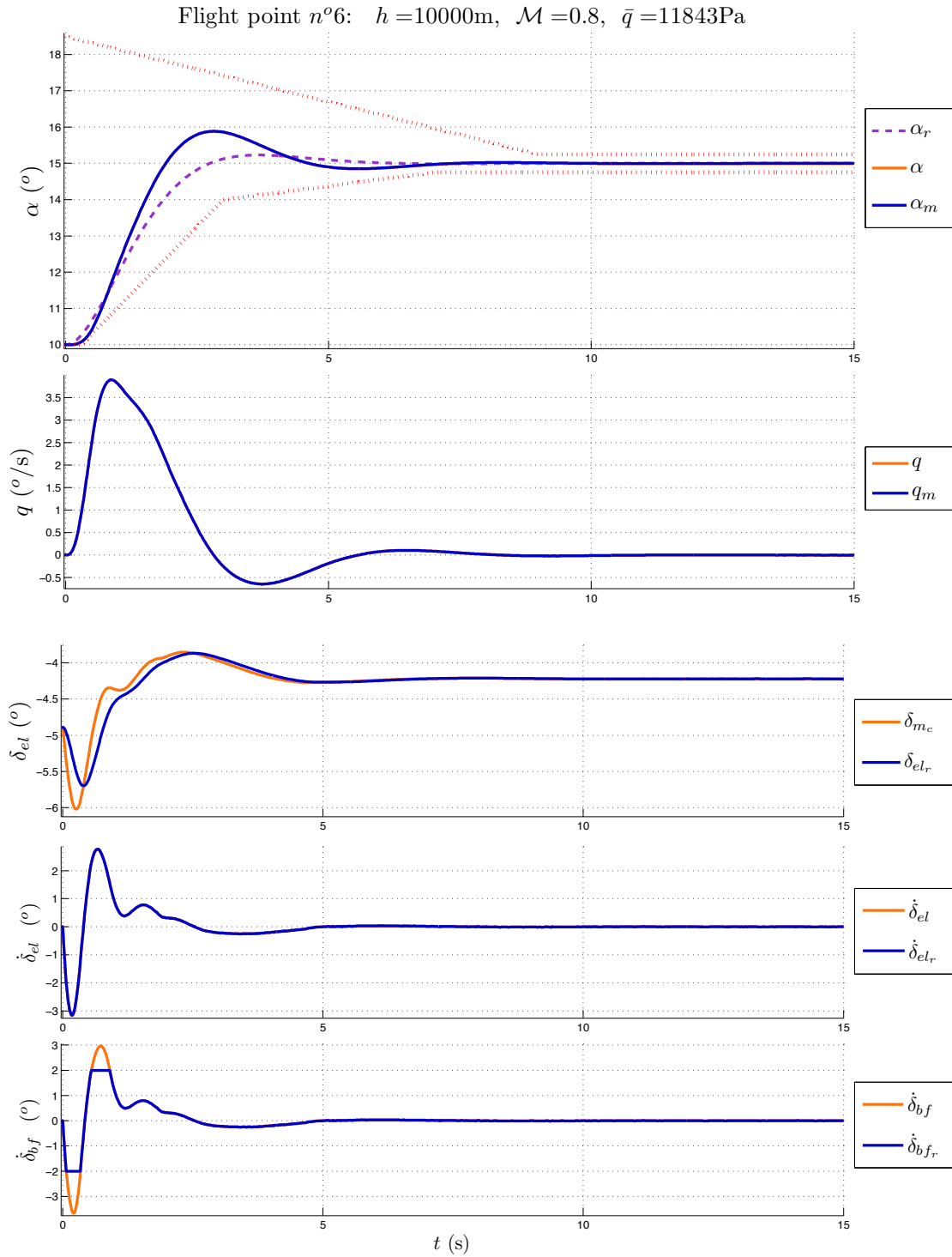
FIGURE R.62 – Simulation à $\mathcal{M} < 1$ avec actionneurs saturés et loi de commande NDI-PI.
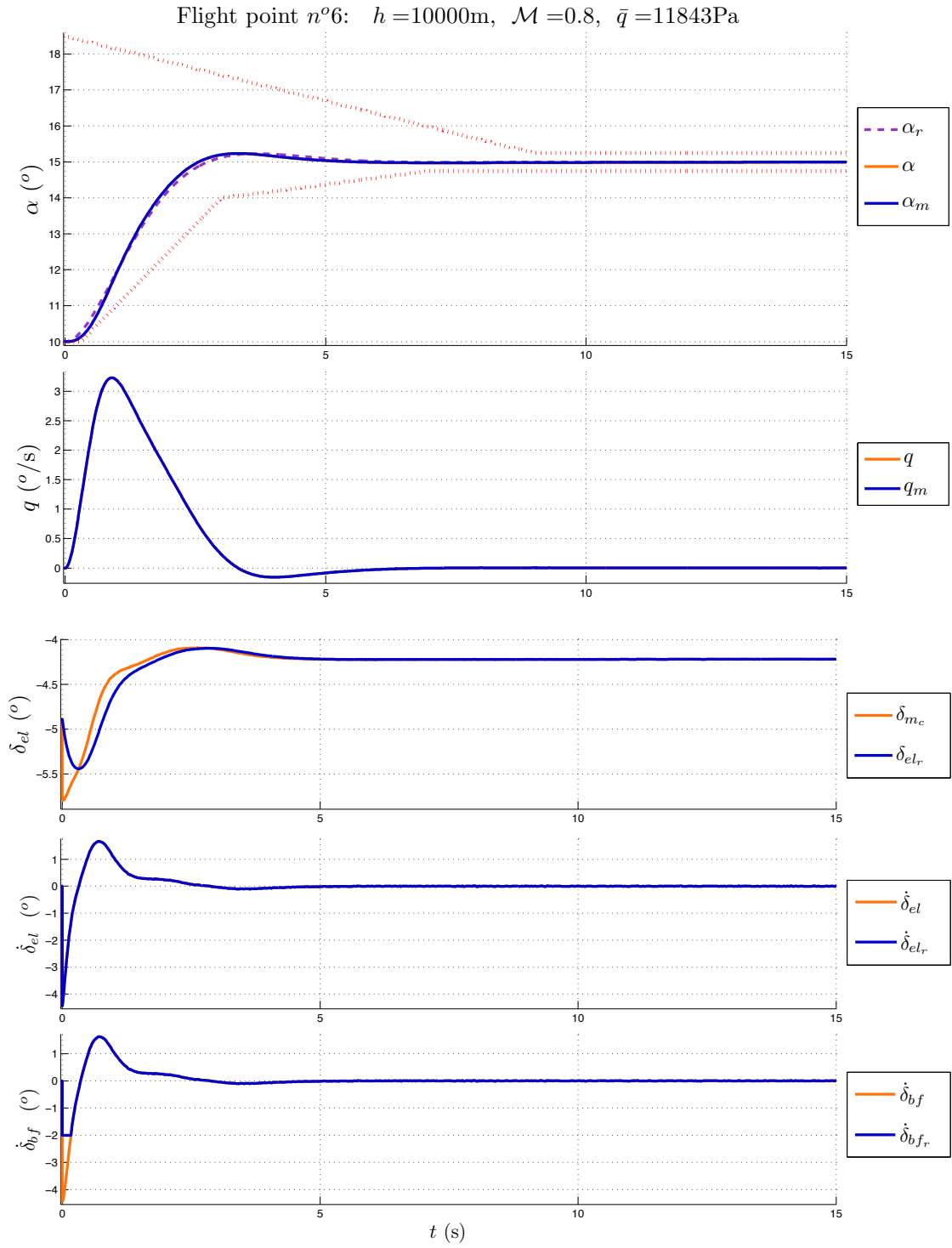
FIGURE R.63 – Simulation à $\mathcal{M} < 1$ avec actionneurs saturés et loi de commande NLC-$\mathcal{H}_\infty$.

Conclusion

Le travail présenté dans cette thèse, introduit une nouvelle méthodologie pour la compensation non-linéaire des systèmes incertains avec paramètres variants et saturations en entrée, dans un cadre de travail unifié.

Après avoir fait un préambule théorique sur l'inversion dynamique non-linéaire (NDI), nous avons conclu que cette technique est un cas particulier des compensations non-linéaires. Celle-ci ne peut être appliquée qu'à une gamme limitée de systèmes non-linéaires. Les principales limitations inhérentes à la technique ont été présentées avec des solutions classiques.

Les principales contributions de cette thèse, concernent le développement d'un cadre de travail généralisé pour la compensation non-linéaire (NLC). Partant des principes de base de la NDI et inspiré par les techniques de commandes robustes, le cadre de travail proposé permet le calcul systématique des correcteurs robustes pour une gamme plus large de systèmes non-linéaires. Ce cadre de travail a également démontré être plus flexible que les approches NDI classiques.

Tout d'abord, une approche permettant de mieux équilibrer l'effort entre la boucle externe et la boucle interne de la structure NDI classique a été proposée. d'une façon très directe, cette approche a mené à la généralisation du cadre de travail NLC, en considérant la dynamique non-linéaire du système comme une perturbation mesurée. Ainsi, le problème de synthèse a pu être reformulé comme un problème de rejet de perturbation. Avec cette reformulation, la structure du correcteur NLC, généralise la structure du correcteur NDI classique.

Dans le but de permettre l'utilisation de techniques de commande robuste et afin de résoudre les problèmes de compensation non-linéaire, une modélisation mettant en avant l'interaction linéaire entre les systèmes et les variables d'état, a été proposée. Des lignes directrices générales ont également été proposées afin de déduire cette représentation.

Des schémas de synthèse ont été établis pour résoudre les problèmes de compensation non-linéaire par le biais d'une stratégie d'optimisation $\mathcal{H}_\infty$, en utilisant une structure avec modèle de référence. Ces schémas de synthèse peuvent aussi inclure des dispositifs anti-windup afin de compenser les effets de saturation en entrée dans la boucle fermée.

Une procédure qui rend la phase de synthèse plus aisée a été proposée afin de faciliter la conception des filtres de pondération. De façon très intéressante, cette procédure permet de reproduire la solution NDI classique, dans le cadre de travail généralisé NLC.

Enfin, une représentation LFT de la boucle fermé résultante est proposée pour l'analyse de stabilité

et de robustesse.

Les trois derniers chapitres de cette thèse ont été dédiés à l'implantation du cadre généralisé NLC pour la synthèse des lois de pilotage destinée aux véhicules volants. En particulier, différentes lois de pilotage ont été calculées pour le pilotage de l'attitude d'un véhicule de rentrée atmosphérique. Ces lois de pilotage ont été testées dans un simulateur de vol à 6 degrés de liberté.

Les principaux aspects de modélisation pour des véhicules volants ont été introduits. Après une description générale des équations fondamentales du mouvement utilisé par la mécanique du vol, la modélisation proposée se révèle très intéressante puisq'elle facilite l'implantation des lois de pilotage par compensation non-linéaire.

Puis, le processus de synthèse des correcteurs NLC -$\mathcal{H}_\infty$ a été détaillé ainsi que celui des correcteurs NDI-PI.

Enfin, la méthode de synthèse a été appliquée à un véhicule de rentrée atmosphérique sur différents points d'un exemple de trajectoire. Le domaine de vol couvert comprend les régimes hypersoniques, transsoniques et subsoniques. La gamme d'altitudes prise en compte s'étend de $68500\,m$ à $0\,m$, tandis que la gamme de vitesses prise en compte, s'étend d'environs $6000\,m/s$ à $100\,m/s$. C'est pourquoi, un large domaine de pression dynamique a également été couvert.

En simulation, des manœuvres en α ont été réalisées afin de couvrir un large domaine d'incidence, allant d'environ $36°$ jusqu'à $7°$. Dans le cas latéral, la valeur de l'angle de dérapage β est maintenu autour de $0°$. L'angle de roulis ϕ a été testé dans une domaine allant de $0°$ jusqu'à environs $80°$ avec une rampe de $6°/s$.

Finalement, une comparaison approfondie entre la NDI classique et le cadre généralisé NLC a été présentée en fonction du processus de synthèse, de l'analyse de robustesse et des résultats de simulation. Il a été montré que le cadre généralisé NLC comporte plus de flexibilité et permet d'obtenir de meilleurs résultats de performance tout en gérant de façon plus satisfaisante la taille et l'activité du signal de commande.

Bibliography

[AB93]   R. Adams and S. Banda. Robust Flight Control Design Using Dynamic Inversion and Structured Singular Value Synthesis. *IEEE Transactions on Control Systems Technology*, 1(2), 1993.

[ACL05]   K.H. Ang, G. Chong, and Y. Li. PID Control System Analysis, Design and Technology. *IEEE Transactions on Control Systems Technology*, 13(4), 2005.

[AG95]   P. Apkarian and P. Gahinet. A Convex Characterization of Gain-Scheduled H_∞ Controllers. *IEEE Transactions on Automatic Control*, 40(5), 1995.

[AN06]   P. Apkarian and D. Noll. Nonsmooth H_∞ synthesis. *IEEE Transactions on Automatic Control*, 51(1), 2006.

[AR89]   K.J. Astrom and L. Rundqwist. Integrator windup and how to avoid it. *American Control Conference Proceedings, Pittsburgh, USA*, 1989.

[BA99]   J.M. Biannic and P. Apkarian. Missile autopilot design via a modified LPV synthesis technique. *Aerospace Science and Technology*, 3(3), 1999.

[BA11]   J.M. Biannic and P. Apkarian. Anti-windup design via nonsmooth multi-objective H_∞ optimisation. *American Control Conference Proceedings, San Francisco, USA*, 2011.

[BDG$^+$90] G. Balas, J.C. Doyle, K. Glover, A.K. Packard, and R. Smith. *μ-Analysis and synthesis toolbox: User's guide.* The mathworks Inc., 1990.

[BEE90]   D. Bugajski, D. Enns, and M. Elgersma. A dynamic inversion based control law with application to the high angle-of- attack research vehicle. *AIAA Guidance, Navigation and Control Conference Proceedings, Portland, USA*, 1990.

[BHLO06]   J.V. Burke, D. Henrion, A.S. Lewis, and M.L. Overton. Stabilization via nonsmooth nonconvex optimization. *IEEE Transactions on Automatic Control*, 51(11), 2006.

[Bia96]   J.M. Biannic. *Commande Robuste des Systèmes à Paramètres Variables: Applications en Aéronautique.* PhD thesis, Ecole Nationale Superieur de l'Aeronautique et de l'Espace, Toulouse, France, 1996.

[Boa10]   J. Boada. *Satellite control with saturating inputs.* PhD thesis, Université de Toulouse, Toulouse, France, 2010.

[Boi98]   J.-L. Boiffier. *The Dynamics of Flight: the Equations.* Chichester: Wiley, 1998.

[Bos10]   J.T. Bosworth. Success Stories in Control: Nonlinear Dynamic Inversion Control. http://naca.larc.nasa.gov/search.jsp?R=20110008197& qs=N%3D4294965662 %2B4294961016, June, 2010.

[Bro78]   R.W. Brockett. Feedback invariants for nonlinear systems. *IFAC Congress Proceedings, Helsinki, Finland*, 1978.

[BT09]   J.M. Biannic and S. Tarbouriech. Optimization and Implementation of Dynamic Anti-windup Compensators with Multiple Saturations in Flight Control Systems. *Control Engineering Practice*, 17(6), 2009.

[Che84]   C.T. Chen. *Linear System Theory and Design.* Oxford: Oxford University Press, 1984.

[CLM91]   B. Charlet, J. Lévine, and R. Marino. Sufficient Conditions for Dynamic State Feedback Linearisation. *SIAM Journal on Control and Optimisation*, 29(1), 1991.

[CR98]   A. Calise and R. Rysdyk. Nonlinear adaptive flight control using neural networks. *IEEE Control Systems*, 18(6), 1998.

[DAOM92]   F. Doyle, F. Allgöwer, S. Oliveira, and M. Morari. On Nonlinear Systems with Poorly Behaved Zero Dynamics. *American Control Conference Proceedings, Chicago, USA*, 1992.

[DGKF89]   J. Doyle, K. Glover, P. Khargonekar, and B. Francis. State-space Solutions to Standard H_2 and H_∞ Control Problems. *IEEE Transactions on Automatic Control*, 1989.

[DM85]   J. Descusse and C.H. Moog. Decoupling with dynamic compensation for strong invertible affine nonlinear systems. *International Journal of Control*, 42(6), 1985.

[DN02]   D. Doman and A. Ngo. Dynamic Inversion-Based Adaptive/Reconfigurable Control of the X-33 on Ascent. *Guidance, Control and Dynamics*, 25(2), 2002.

[Doy82]   J.C. Doyle. Analysis of feedback systems with structured uncertainties. *IEEE Control Theory and Applications Conference Proceedings, Minneapolis, USA*, 129(6), 1982.

[DSE87]   J. Doyle, R. Smith, and D. Enns. Control of plants with input saturation nonlinearities. *American Control Conference Proceedings, Minneapolis, USA*, 1987.

[Dum05]   B. Dumitrescu. Bounded Real Lemma for FIR MIMO systems. *IEEE Signal Processing Letters*, 12(7), 2005.

[EBHS94]   D. Enns, D. Bugajski, R. Hendrick, and G. Stein. Dynamic inversion: an evolving methodology for flight control design. *International Journal of Control*, 59(1), 1994.

[Etk95]   B. Etkin. *Dynamics of Flight: Stability and Control.* Toronto: John Wiley & Sons, 1995.

[Fal09]   A. Falcoz. *Contribution au Dévelopement de Stratégies de Diagnostic à Base de Modèles pour les Véhicules Spatiaux.* PhD thesis, Université Bordeaux I, Bordeaux, France, 2009.

[FB07]   G. Ferreres and J.M. Biannic. Convex design of a robust Anti-windup controller for an LFT model. *IEEE Transactions on Automatic Control*, 52(11), 2007.

[Fli85]   M. Fliess. A new approach to the noninteracting control problem in nonlinear system theory. *23rd IEEE Conference on Decision and Control Proceedings, Monticello, USA*, 1985.

[FLMR95]   M. Fliess, J. Lévine, P. Martin, and P. Rouchon. Flatness and defect of nonlinear systems : introduction theory and examples. *International Journal of Control*, 61(6), 1995.

[GA94]   P. Gahinet and P. Apkarian. A Linear Matrix Inequality Approach to H_∞ Control. *International Journal of Robust Nonlinear Control*, 3(3), 1994.

[GdST05]   J. Gomes da Silva and S. Tarbouriech. Antiwindup Design With Guaranteed Regions of Stability: An LMI-Based Approach. *IEEE Transactions on Automatic Control*, 50(1), 2005.

[GHMO09]   S. Gumusoy, D. Henrion, M. Millstone, and M.L. Overton. Multi-Objective Robust Control with HIFOO 2.0. *IFAC Symposium on Robust Control Design Proceedings, Haifa, Israel*, 2009.

[GMO08]   S. Gumusoy, M. Millstone, and M.L. Overton. H_∞ strong stabilization via HIFOO, a package for fixed-order controller design. *47th IEEE Conference on Decision and Control Proceedings, Cancun, Mexico*, 2008.

[GT91]   G. Gilbert and K.T. Tan. Linear systems with state and control constraints: The theory and application of maximal output admissible sets. *IEEE Transactions on Automatic Control*, 36(9), 1991.

[GV03]   J. Georgie and J. Valasek. Evaluation of Longitudinal Desired Dynamics for Dynamic-Inversion Controlled Generic Reentry Vehicles. *Journal of Guidance, Control and Dynamics*, 26(5), 2003.

[Ha88]   I.J. Ha. The standard decomposed system and noninteracting feedback control of nonlinear systems. *SIAM journal of control and optimization*, 26(5), 1988.

[Har91]   J.P. Harcaut. *Commande Nonlinear Appliquée au Pilotage d'un Engin.* PhD thesis, Ecole Nationale Superieur de l'Aeronautique et de l'Espace, Toulouse, France, 1991.

[Hel99]   A. Helmsersson. An IQC-based stability criterion for systems with slowly varying parameters. *14th IFAC Trienial World Congress Proceedings, Beijing, China*, 1999.

[HG70]   J.C. Harpold and C.A. Graves. Reentry targeting philosophy and flight results from APOLLO 10 and 11. *AIAA 8th Aerospace Sciences Meeting, New York, USA*, 70(28), 1970.

[HG79]   J.C. Harpold and C.A. Graves. Shuttle entry guidance. *The Journal of Astronautical Science*, 27(3), 1979.

[HJB11]   M. Hernandez, F. Jouhaud, and J.M. Biannic. Reentry flight-control design by a new dynamic inversion based approach. *3rd International ARA Days Conference Proceedings, Arcachon, France*, 2011.

[HKH87]   R. Hanus, M. Kinnaert, and J.-L. Henrotte. Conditioning technique, a general anti-windup and bumpless transfer method. *Automatica*, 23(6), 1987.

[HLS06]   N. Hovakimyan, E. Lavretsky, and A. Sasane. Adaptive Dynamic Inversion via Time-Scale Separation. *IEEE Conference on Decision and Control Proceedings, San Diego, USA*, 2006.

[HMA97]   H.J.C. Huijberts, C.H. Moog, and R. Andiarti. Generalized controlled invariance for nonlinear systems. *SIAM journal of control and optimization*, 35(3), 1997.

[Hor83]   I. Horowitz. A synthesis theory for a class of saturating systems. *International Journal of Control*, 38(1), 1983.

[HS90]   M. Henson and D. Seborg. Input-output linearization of general nonlinear processes. *AICheE Journal*, 36(11), 1990.

[HTM+10]   G. Herrmann, M. Turner, P. Menon, D. Bates, and I. Postlethwaite. Anti-windup synthesis for Nonlinear Dynamic Inversion control schemes. *International Journal of Robust and Nonlinear Control*, 20(13), 2010.

[IG88]   A. Isidori and J. Grizzle. Fixed modes and nonlinear noninteracting control with stability. *IEEE Transactions on Automatic Control*, 33(10), 1988.

[IGVW02]   D. Ito, J. Georgie, J. Valasek, and D. Ward. *Reentry Vehicle Flight Controls Design Guidelines: Dynamic Inversion.* PhD thesis, Texas A&M University, Texas, USA, 2002.

[IKGGM81]   A. Isidori, A.J. Krener, C. Gori-Giorgi, and S. Monaco. Nonlinear decoupling via feedback: a differential geometric approach. *IEEE Transactions on Automatic Control*, 26(2), 1981.

[IKGGM89] A. Isidori, A.J. Krener, C. Gori-Giorgi, and S. Monaco. Block noninteracting control with stability via static state feedback. *Mathematics of control, signals and systems*, 2(4), 1989.

[IMDL86] A. Isidori, C.H. Moog, and A. De Luca. A Sufficient condition for full linearization via dynamic state feedback. *25th IEEE Conference on Decision and Control Proceedings, Athens, Greece*, 1986.

[Isi85] A. Isidori. *Nonlinear Control Systems*. Berlin: Springer-Verlag, 1985.

[Jou92] F. Jouhaud. Nonlinear Attitude Control Law of a Space Plane. *IFAC Congress: Aerospace Control Proceedings, Munich, Germany*, 1992.

[Kha96] H.K. Khalil. *Nonlinear Systems*. New Jersey: Prentice Hall, 1996.

[Kol05] E. Kolesnikov. NDI based Flight Control Law Design. *AIAA Guidance, Navigation, and Control Conference and Exhibit*, 2005.

[Lav05] F. Lavergne. *Méthodologie de Synthèse de Lois de Commandes Non Linéaires et Robustes: Application au suivi de Trajectoire des Avions de Transport*. PhD thesis, Université Paul Sabatier, Toulouse, France, 2005.

[LRDY07] H. Lee, S. Reiman, C. Dillon, and H. Youssef. Robust Nonlinear Dynamic Inversion Control for a Hypersonic Cruise Vehicle. *AIAA Guidance, Navigation, and Control Conference and Exhibit Proceedings, South Carolina, USA*, 2007.

[Lé11] J. Lévine. On necessary and sufficient conditions for differential flatness. *Applicable Algebra in Engineering, Communication and Computing*, 22(1), 2011.

[Mag02] J.F. Magni. Presentation of the Linear Fractional Representation Toolbox (LFRT). *IEEE International Symposium on Computer Aided Control System Design Proceedings, Glasgow, Scotland*, 2002.

[Mar86] R. Marino. On the largest feedback linearizable subsystem. *Systems and Control Letters*, 6(5), 1986.

[Mat11a] Mathworks. MatLab R2011b, Aerospace Blockset - Dryden Wind Turbulence Model. http://www.mathworks.com/help/toolbox/aeroblks/drydenwindturbulencemodel continuous.html, September, 2011.

[Mat11b] Mathworks. MatLab R2011b, Robust Control Toolbox. http://www.mathworks.com/help/toolbox/robust/ref/hinfstruct.html, September, 2011.

[MCV09] V. Morio, F. Cazaurang, and P. Vernis. Flatness-based hypersonic reentry guidance of a lifting-body vehicle. *Control Engineering Practice*, 17(5), 2009.

[Meg09] A. Megretski. Dynamic Systems and Control Lecture. Notes (MIT), USA, Fall 2009.

[Mor09] V. Morio. *Contribution au développement d'une loi de guidage autonome par platitude. Application à une mission de rentrée atmosphérique*. PhD thesis, Université Bordeaux I, Bordeaux, France, 2009.

[MR97] A. Megretski and A. Rantzer. System analysis via integral quadratic constraints. *IEEE Transactions on Automatic Control*, 42(6), 1997.

[MT95] R. Marino and P. Tomei. *Nonlinear Control Design: Geometric, Adaptive and Robust*. Hertfordshire: Prentice Hall, 1995.

[MTK09] E. Mulder, P. Tiwari, and M. Kothare. Simultaneous linear and anti-windup controller synthesis using multiobjective convex optimisation. *Automatica*, 45(3), 2009.

[NS86] H. Nijmeijer and J.M. Schumacher. The regular local noninteracting control problem for nonlinear control systems. *SIAM journal of control and optimization*, 24(6), 1986.

[NT04] D. Nesic and A.R. Teel. Input-Output Stability Properties of Networked Control Systems. *IEEE Transactions on Automatic Control*, 2004.

[ODB06]   M. Oppenheimer, D.B. Doman, and M. Bolender. Control Allocation for Over-actuated Systems. *14th Mediterranean Conference: Control and Automation Proceedings, Ancona, Italy*, 2006.

[Oga02]   K. Ogata. *Modern Control Engineering*. New Jersey: Prentice Hall, 2002.

[Pap03]   C. Papageorgiou. *Robustness Analysis of Nonlinear Dynamic Inversion Control Laws for Flight Control Applications*. PhD thesis, University Of Cambridge, Cambridge, United Kingdom, 2003.

[Ple03]   G. Plett. Adaptive Inverse Control of Linear and Nonlinear Systems Using Dynamic Neural Networks. *IEEE Transactions on Neural Networks*, 14(2), 2003.

[Por70]   W.A. Porter. Diagonalization and inverses for nonlinear systems. *International Journal of Control*, 11(1), 1970.

[Ran96]   A. Rantzer. On the Kalman-Yakubovich-Popov Lemma. *Systems and Control Letters*, 28(1), 1996.

[RBG95]   J. Reiner, G. Balas, and L. Garrard. Robust Dynamic Inversion for Control of Highly Manoeuvrable Aircraft. *Journal of Guidance, Control and Dynamics*, 18(1), 1995.

[RBG96]   J. Reiner, G. Balas, and L. Garrard. Flight Control Design Using Robust Dynamic Inversion and Time-scale Separation. *Automatica*, 32(11), 1996.

[Roo07]   C. Roos. *Contribution à la commande des systèmes saturés en présence d'incertitudes et de variations paramétriques. Application au pilotage d'un avion au sol.* PhD thesis, Université de Toulouse, Toulouse, France, 2007.

[SDSX97]   P. Shi, C. De Souza, and L. Xie. Bounded Real Lemma for linear systems with finite discrete jumps. *International Journal of Control*, 66(1), 1997.

[SI89]   S. Sastry and A. Isidori. Adaptive Control of Linearizable Systems. *IEEE Transactions on Automatic Control*, 34(11), 1989.

[SK98]   C. Schumacher and P. Khargonekar. Stability Analysis of a Missile Control System with a Dynamic Inversion Controller. *American Control Conference Proceedings, Philadelphia, USA*, 1998.

[SL91]   J. Slotine and W. Li. *Applied Nonlinear Control*. New Jersey: Prentice Hall, 1991.

[SRS04]   H. Siria-Ramirez and Agrawal S.K. *Differentially flat systems*. New York: Marcel Dekker, 2004.

[SS01]   U. Shaked and V. Suplin. A new Bounded Real Lemma representation for the continuous-time case. *IEEE Transactions on Automatic Control*, 46(9), 2001.

[SYdS98]   U. Shaked, I. Yaesh, and C.I. de Souza. Bounded real criteria for linear time-delay systems. *IEEE Transactions on Automatic Control*, 43(7), 1998.

[SZ03]   S. Sam and J. Zhang. Neural-network Control of Nonaffine Nonlinear System With Zero Dynamics by State and Output Feedback. *IEEE Transactions on Neural Networks*, 14(4), 2003.

[Tan06]   M.D. Tandale. *Adaptive Dynamic Inversion Control of Nonlinear Systems subjected to Control Saturation Constraints*. PhD thesis, Texas A&M University, Texas, USA, 2006.

[Taq09]   G. Taquin. Flight Dynamics. Notes (ISAE-Supaero), France, Octobre 2009.

[TK11]   M. Turner and M. Kerr. $\mathcal{L}_2$ gain bounds for systems with sector bounded and slope restricted nonlinearities. *International Journal of Robust and Nonlinear Control*, 2011.

[VF03]   P. Vernis and E. Ferreira. Hypersonic Re-entry Guidance Application to ARES Experiment. *Proceedings AAAF*, 2003.

[VF05]   P. Vernis and E. Ferreira. On-Board Trajectory Planner for the TAEM Guidance of a Winged Body. *Proceedings AAAF*, 2005.

[Vid93]   M. Vidyasagar. *Nonlinear Systems Analysis*. New Jersey: Prentice Hall, 1993.

[WL04]   F. Wu and B. Lu. Anti-windup control design for exponentially unstable LTI systems with actuator saturation. *Systems & Control Letters*, 52(3-4), 2004.

[YCHL06]   A. Young, C. Cao, N. Hovakimyan, and E. Lavretsky. Control of a Nonaffine Double-Pendulum System via Dynamic Inversion and Time-Scale Separation. *American Control Conference Proceedings, Minneapolis, USA*, 2006.

[YPY08]   S. Yoon, J.K. Park, and T. Yoon. Dynamic anti-windup scheme for feedback linearizable nonlinear control systems with saturating inputs. *Automatica*, 44(12), 2008.

[Zac09]   L. Zaccarian. Dynamic Allocation for Input Redundant Control Systems. *Automatica*, 45(6), 2009.

[ZDK10]   H. Zhang, P. Dower, and C. Kellett. A bounded Real Lemma for nonlinear $\mathcal{L}_2$ gain. *IEEE Conference on Decision and Control Proceedings, Atlanta, USA*, 2010.

[ZT02]   L. Zaccarian and A.R. Teel. A common framework for Anti-windup, bumpless transfer and reliable designs. *Automatica*, 38(10), 2002.

[ZXS08]   G. Zhanga, Y. Xiab, and P. Shic. New Bounded Real Lemma for discrete-time singular systems. *Automatica*, 44(3), 2008.

Appendix A

Backgrounds on Flight Mechanics

A.1 Fundamental principle

Flight Mechanics is the discipline concerned with the study of the motion of air vehicles. It focuses on the combination of the two basic motions of an air vehicle: the displacement of a solid body and the rotation of the solid body about its center of gravity. All air vehicles are subject to this same basic principle of physics and thus their motion can be represented by the same basic kinematic equations.

The foundation of Flight Mechanics is centred on Newton's Second law of classical Mechanics. This law can be stated as:

The sum of all the exterior forces interacting with a solid body is equal to the time rate of change of its momentum in an inertial coordinate system. In the case of rotating bodies, the sum of all moments impressed to the solid body is equal to the time rate of change of its angular momentum.

First of all, an inertial coordinate system needs to be defined along with other support reference frames to describe the motion of an air vehicle. This will be treated in the next section. Then, an explicit listing of the aerodynamic and propulsion forces and moments acting over the air vehicle is required depending on the desired application. In some applications, propulsion systems are not considered for atmospheric flight which is the case of reentry vehicles.

From these basic principle, the following relations are established

$$\sum_i \vec{\mathbf{F}}_i \quad = \quad \frac{d(m\vec{\mathbf{V}})}{dt} \tag{A.1}$$

$$\sum_j \vec{\mathbf{M}}_{G_j} \quad = \quad \frac{d(\mathbf{I}\vec{\mathbf{\Omega}})}{dt} \tag{A.2}$$

with
– $\vec{\mathbf{F}}_i$ is the i-th external force interacting with a rigid air vehicle;

– $\vec{\mathbf{M}}_{G_j}$ is the j-th external moment impressed on a rigid air vehicle about its center of gravity G;
– m is the mass of the air vehicle;
– $\mathbf{I}$ is moment of inertia tensor of the air vehicle about G;
– $\vec{\mathbf{V}}$ is the inertial speed vector of the air vehicle;
– $\vec{\mathbf{\Omega}}$ is the angular speed vector of the air vehicle about G;
– t denotes the time. Any parameters topped by a dot or presided by the operator $\frac{d}{dt}$ indicate the time derivative of the parameter.

It is also worth noting that equations (A.3) and (A.4) account for mass m and mass distribution $\mathbf{I}$ variations on the air vehicle. The variation of mass is relevant in applications where the air vehicle consumes large amounts of fuel for propulsion or posses heavy sections that are detached in flight, which is the case of a space rocket for example. This is not usually the case of a reentry vehicle.

Also, the angular momentum $\mathbf{I}$ of any rigid body is constant when expressed in the frame of reference attached to the body (see sectionA.2.2). To avoid the use of more complex expressions due to variations of the angular momentum $\mathbf{I}$, the equation of moments will always be expressed in this non-inertial frame of reference carried by the air vehicle.

The translation and angular acceleration of the air vehicle can be expressed in terms of any moving reference frame. Consider an inertial frame $\mathcal{R}_i$ with origin O and a moving non-inertial frame $\mathcal{R}$ with origin Q and rotation Ω. Expressing the acceleration of the body center of gravity G as components parallel to the inertial axis of $\mathcal{R}_i$, the force and moments equations are described by (A.3) and (A.4). But when expressed in the non-inertial axis of $\mathcal{R}$, it is required to account for the *apparent* forces induced by the arbitrary motion of this frame of reference. The force and moments equations in the non-inertial frame become

$$m\left(\frac{d\vec{\mathbf{V}}_R}{dt}\right)_{/R} = \sum_i \vec{\mathbf{F}}_i + \vec{\mathbf{F}}_{co} + \vec{\mathbf{F}}_{ce} + \vec{\mathbf{F}}_{tr} \tag{A.3}$$

$$\mathbf{I}_{/R}\frac{d\vec{\mathbf{\Omega}}}{dt} = \sum_j \vec{\mathbf{M}}_{G_j} - \vec{\mathbf{\Omega}} \wedge \mathbf{I}_{/R}\vec{\mathbf{\Omega}} \tag{A.4}$$

with
– $\vec{\mathbf{r}}_R = (\overrightarrow{\mathbf{QG}})_{/R}$: relative position vector;
– $\vec{\mathbf{V}}_R = \left(\dfrac{d\vec{\mathbf{r}}_R}{dt}\right)_{/R}$: relative speed vector;
– $\vec{\mathbf{F}}_{co} = -2m\vec{\mathbf{\Omega}} \wedge \vec{\mathbf{V}}_R$: Coriolis apparent force;
– $\vec{\mathbf{F}}_{ce} = -m\vec{\mathbf{\Omega}} \wedge (\vec{\mathbf{\Omega}} \wedge \vec{\mathbf{r}}_R)$: centripetal apparent force;
– $\vec{\mathbf{F}}_{tr} = -m\left(\dfrac{d^2(\overrightarrow{\mathbf{OQ}})_{/R}}{dt^2}\right)_{/R} - m\dfrac{d\vec{\mathbf{\Omega}}}{dt} \wedge \vec{\mathbf{r}}_R$: transport apparent forces.

The sub-index $/R$ specifies that the vector components are expressed parallel to the non-inertial axis $\mathcal{R}$. For aerospace applications, the origin Q of the non-inertial frame is generally fixed at the center of gravity G.

A.2 Defining coordinate systems

To characterise the movement of an air vehicle with respect to another body, we first need to define fixed and independent coordinate systems. In the case of a reentry mission, the vehicle tries to

reach a specific landing point on Earth. While modelling the motion of such air vehicle, several coordinate systems or frames of reference are defined.

In this section, the following notation is used:
– $\mathcal{R}$: frame of reference;
– M : rotation matrix between two frames of reference;
– $\vec{\mathbf{r}} = (\overrightarrow{\mathbf{OG}})_{/R_i}$: inertial position vector;
– $\vec{\mathbf{V}}_a$, $\vec{\mathbf{V}}_w$: aerodynamic speed vector and wind speed vector ($\vec{\mathbf{V}}_a = \vec{\mathbf{V}} - \vec{\mathbf{V}}_w - \vec{\mathbf{\Omega}}_E \wedge \vec{\mathbf{r}}$);
– $\mathbf{q}$: attitude quaternion of the body frame relative to the local frame;
– $\vec{\mathbf{\Omega}}_o$: angular speed vector of the local frame rotation with respect to the inertial frame;
– $\vec{\mathbf{\Omega}}_E$: angular speed vector of the Earth about its z_i axis ($|\vec{\mathbf{\Omega}}_E| = 7.29212 \cdot 10^{-3}\,rad/s$);
– ϕ, θ, ψ : attitude Euler angles of roll, pitch and yaw respectively;
– μ, γ, χ : aerodynamic Euler angles;
– α, β : aerodynamic angle-of-attack and side-slip angle respectively;
– λ, λ_g : geocentric and geographic latitude respectively;
– L : geographic longitude;
– L_i : inertial longitude ($L_i = L + \Omega_T(t - t_0)$, t_0 is the instant of passage of the Greenwich meridian);
– R_{eq} : radius of the Earth at the equator ($R_eq = 6378.135\,km$);
– R_p : radius of the Earth at the poles ($R_p = 6356.611\,km$).

The main frames of reference used for this effect are presented next.

A.2.1 Definition of the inertial frame $\mathcal{R}_i$ and local frame $\mathcal{R}_o$

By definition, an inertial frame of reference is that in which the laws of physics apply to their simplest extent. For example, when a body without any force interactions is observed from an inertial frame, it is either at rest or in a state of uniform linear motion.

When studying the reentry of a space vehicle, generally, the origin of the inertial frame of reference is placed on the center of the Earth O, with fixed axes with respect to the stars. This frame of reference is based on the equatorial plane, with its x_i axis pointing in direction of the vernal point and with the z_i axis pointing towards the North Pole as depicted on Figure A.1. In other words, z_i is considered as the rotation axis of the Earth.

$$\mathcal{R}_i = (\vec{\mathbf{x}}_i, \vec{\mathbf{y}}_i, \vec{\mathbf{z}}_i) \tag{A.5}$$

To describe the movement of an air vehicle towards another body carrying the inertial frame, a local frame of reference fixed on the air vehicle is required. This local frame is mainly used to locate the vehicle position in relation to the body carrying the inertial frame.

The local frame of reference has its origin fixed at the vehicle center of gravity G and it is based on the position vector $\vec{\mathbf{r}}$ tying the center of the Earth to the vehicle center of gravity. The z_o axis is fixed downwards from the center of gravity of the vehicle towards a ground point in the Earth's surface. The x_o axis is fixed pointing North and the y_o axis is fixed pointing East.

$$\mathcal{R}_o = (\vec{\mathbf{x}}_o, \vec{\mathbf{y}}_o, \vec{\mathbf{z}}_o) \tag{A.6}$$
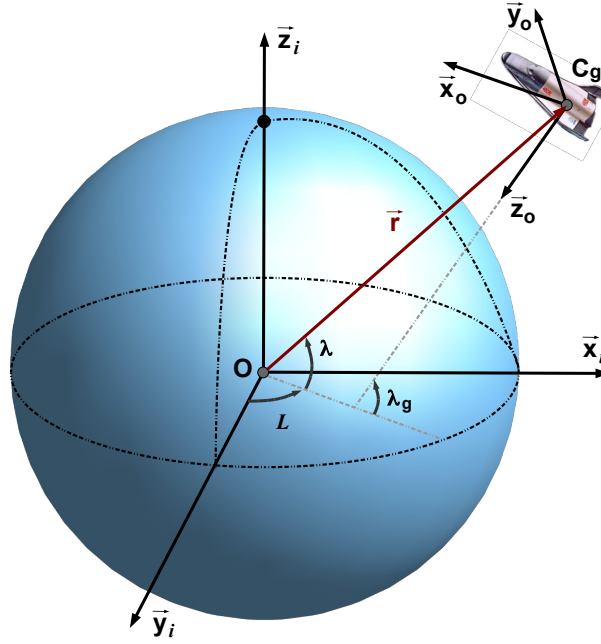
Figure A.1: Definition of the inertial frame $\mathcal{R}_i$ and the local frame $\mathcal{R}_o$.

In the figure above, to distinguish the geographic latitude λ_g from the geocentric latitude λ, the Earth is considered to be an oblate spheroid flattened at the poles. The difference between these two latitude measurements is usually very small, even though in the figure it appears to be significant.

A.2.2 Definition of the body frame $\mathcal{R}_b$ and aerodynamic frame $\mathcal{R}_a$

Both, the body reference frame and the aerodynamic frame, have their origin fixed at the air vehicle center of gravity G. They are mainly used to determine the attitude and rotation speed of the air vehicle with respect to the local frame $\mathcal{R}_o$ and with respect to the airspeed vector $\vec{\mathbf{V}}_a$.

The body frame is based on the air vehicle geometry, with its x_b axis directed towards the aft end and its z_b axis directed to the center of the Earth. This frame is useful for modelling the attitude of the air vehicle with respect to the local reference as illustrated on figure A.2.

$$\mathcal{R}_b = (\vec{\mathbf{x}}_b, \vec{\mathbf{y}}_b, \vec{\mathbf{z}}_b) \tag{A.7}$$
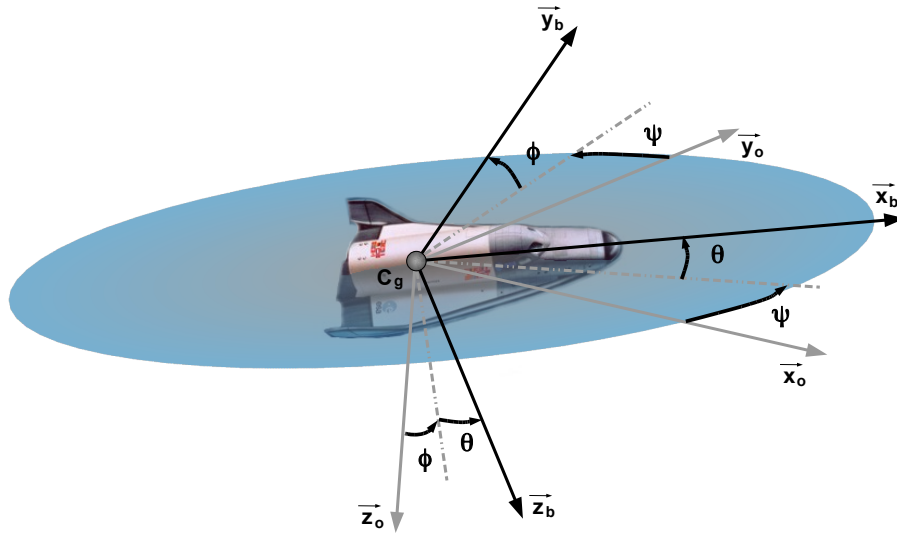
Figure A.2: Definition of the body frame $\mathcal{R}_b$ and its relation with the local frame $\mathcal{R}_b$.

And finally, the aerodynamic frame is based on the aerodynamic speed vector $\vec{\mathbf{V}}_a$ of the air vehicle, with its x_a axis over the speed vector and it z_a vector pointing in the direction of the Earth center. This frame is considered when modelling the air vehicle attitude with respect to the speed vector as shown on figure A.3.

$$\mathcal{R}_a = (\vec{\mathbf{x}}_a, \vec{\mathbf{y}}_a, \vec{\mathbf{z}}_a) \tag{A.8}$$
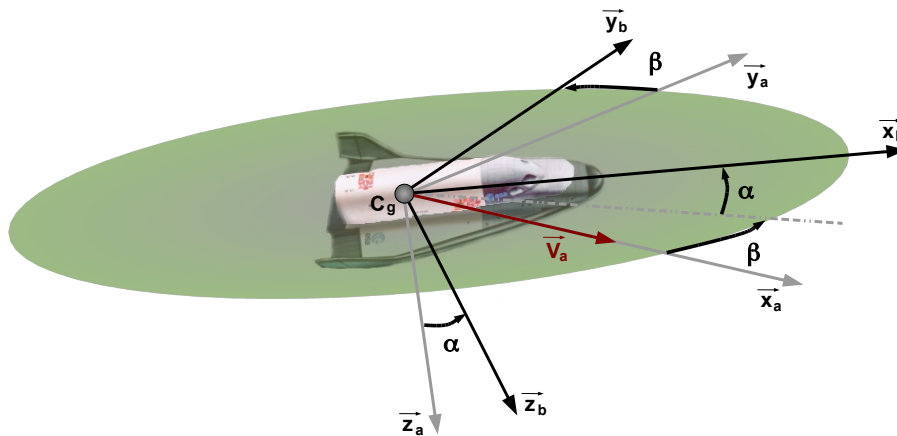
Figure A.3: Definition of the aerodynamic frame $\mathcal{R}_a$ and its relation with the body frame $\mathcal{R}_b$.

A.2.3 Relations between frames of reference

The natural relations between the different frames of reference is of the utmost for modelling the dynamics of the movement of an air vehicle. For some applications like an atmospheric reentry

mission, some predominant parameters defined in specific frames may need to be regulated and/or computed from other flight parameters defined in different frames.

Let us describe some key points of these relations for air vehicles modelling.

A.2.3.1   From local $\mathcal{R}_o$ to inertial frame $\mathcal{R}_i$

The inertial position vector $\vec{\mathbf{r}} = [x_i, y_i, z_i]$ ties the origin of the inertial frame $\mathcal{R}_i$ and that of the local frame $\mathcal{R}_o$ as depicted on figure A.1. This is the main relation for linking the movement of an air vehicle to its inertial frame. With the use of the geocentric latitude λ, the components of the position vector $\vec{\mathbf{r}}$ can be expressed as

$$x_i = |\vec{\mathbf{r}}| \cos \lambda \cos L \tag{A.9}$$
$$y_i = |\vec{\mathbf{r}}| \cos \lambda \sin L \tag{A.10}$$
$$z_i = |\vec{\mathbf{r}}| \sin \lambda \tag{A.11}$$

The construction of a rotation matrix can be done by linking the axis $\vec{\mathbf{z}}_l$ of the local frame $\mathcal{R}_o$ to a ground point in $\mathcal{R}_i$ from which the geographical latitude λ_g is measured. Considering the inertial longitude L_i, the base of $\mathcal{R}_o$ can be expressed as

$$\vec{\mathbf{x}}_o = \begin{bmatrix} -\sin \lambda_g \cos L_i \\ -\sin \lambda_g \sin L_i \\ \cos \lambda_g \end{bmatrix} \tag{A.12}$$

$$\vec{\mathbf{y}}_o = \begin{bmatrix} -\sin L_i \\ \cos L_i \\ 0 \end{bmatrix} \tag{A.13}$$

$$\vec{\mathbf{z}}_o = \begin{bmatrix} -\cos \lambda_g \cos L_i \\ -\cos \lambda_g \sin L_i \\ -\sin \lambda_g \end{bmatrix} \tag{A.14}$$

Then, the rotation matrix for expressing vectors from the local frame $\mathcal{R}_o$ to the inertial frame $\mathcal{R}_i$ comes from the concatenation of the expressions necessary to represent the base of $\mathcal{R}_o$ in terms of the geographic latitude and inertial longitude as

$$M_{io} = \begin{bmatrix} -\sin \lambda_g \cos L_i & -\sin \lambda_g \sin L_i & \cos \lambda_g \\ -\sin L_i & \cos L_i & 0 \\ -\cos \lambda_g \cos L_i & -\cos \lambda_g \sin L_i & -\sin \lambda_g \end{bmatrix} \tag{A.15}$$

Consider a vector

$$\vec{\mathbf{v}} = \begin{bmatrix} x_i \\ y_i \\ z_i \end{bmatrix} \text{ when defined in } \mathcal{R}_i, \text{ and } \vec{\mathbf{v}} = \begin{bmatrix} x_l \\ y_l \\ z_l \end{bmatrix} \text{ when defined in } \mathcal{R}_o.$$

Then, the following relation holds

$$\begin{bmatrix} x_i \\ y_i \\ z_i \end{bmatrix} = M_{io} \begin{bmatrix} x_l \\ y_l \\ z_l \end{bmatrix} \tag{A.16}$$

ONERA
THE FRENCH AEROSPACE LAB

ISae
Institut Supérieur de l'Aéronautique et de l'Espace

Now, let us express the components of the inertial speed vector as $\vec{\mathbf{V}} = [u, v, w]^T$. The angular speed due to the rotation of the local frame $\mathcal{R}_o$ with respect to the inertial frame $\mathcal{R}_i$ is obtained by:

$$\Omega_o = \begin{bmatrix} \cos \lambda_g \dot{L}_i \\ -\dot{\lambda}_g \\ -\sin \lambda_g \dot{L}_i \end{bmatrix} \tag{A.17}$$

with

$$\dot{L}_i = |\vec{\mathbf{\Omega}}_E| + \dot{L} = \frac{v\, x_i - u\, y_i}{x_i^2 + y_i^2} \tag{A.18}$$

$$\dot{\lambda}_g = \frac{R_p^2[w(x_i^2 + y_i^2) - z_i(u\, x_i + v\, y_i)]}{R_{eq}^2 \sqrt{x_i^2 + y_i^2} \left[\frac{R_p^4}{R_{eq}^4}(x_i^2 + y_i^2) + z_i^2 \right]} \tag{A.19}$$

A.2.3.2 From body $\mathcal{R}_b$ to local $\mathcal{R}_o$ and inertial frame $\mathcal{R}_i$

The relation between this two frames is useful for establishing the attitude of an air vehicle and its rotation speed.

The attitude of an air vehicle is determined by the displacement of the body frame $\mathcal{R}_b$ with respect to the local frame $\mathcal{R}_o$ and is defined as a triplet of angles known as the Euler angles. The Euler angles ϕ, θ and ψ are defined on Figure A.2 and they can be used to transform components of vectors defined in different frames.

Using the angular displacement between the two frames, to obtain the components of a vector parallel to the body frame $\mathcal{R}_b$ axis in the local frame $\mathcal{R}_o$, we use the rotation matrix (A.21) defined by the successive rotations (A.20).

$$
\begin{aligned}
R_1(\phi) &= \begin{bmatrix} 1 & 0 & 0 \\ 0 & \cos\phi & \sin\phi \\ 0 & -\sin\phi & \cos\phi \end{bmatrix} \\[2mm]
R_2(\theta) &= \begin{bmatrix} \cos\theta & 0 & -\sin\theta \\ 0 & 1 & 0 \\ \sin\theta & 0 & \cos\theta \end{bmatrix} \\[2mm]
R_3(\psi) &= \begin{bmatrix} \cos\psi & 0 & \sin\psi \\ -\sin\psi & \cos\psi & 0 \\ 0 & 0 & 1 \end{bmatrix} \\[2mm]
M_{ob} &= R_3(\psi) \cdot R_2(\theta) \cdot R_1(\phi)
\end{aligned}
\tag{A.20}
$$

$$M_{ob} = \begin{bmatrix} \cos\theta\cos\psi & \sin\phi\sin\theta\cos\psi - \cos\phi\sin\psi & \cos\phi\sin\theta\cos\psi + \sin\phi\sin\psi \\ \cos\theta\sin\psi & \sin\phi\sin\theta\sin\psi + \cos\phi\cos\psi & \cos\phi\sin\theta\sin\psi - \sin\phi\cos\psi \\ -\sin\theta & \sin\phi\cos\theta & \cos\phi\cos\theta \end{bmatrix} \tag{A.21}$$

Consider once more a vector

$$\vec{v} = \begin{bmatrix} x \\ y \\ z \end{bmatrix} \text{ when defined in } \mathcal{R}_b, \text{ and } \vec{v} = \begin{bmatrix} x_l \\ y_l \\ z_l \end{bmatrix} \text{ when defined in } \mathcal{R}_o.$$

Then, the following relation holds

$$\begin{bmatrix} x_l \\ y_l \\ z_l \end{bmatrix} = M_{ob} \begin{bmatrix} x \\ y \\ z \end{bmatrix} \tag{A.22}$$

Similarly, to transform a vector defined on the body frame $\mathcal{R}_b$ onto the inertial frame $\mathcal{R}_i$, we use the rotation matrix (A.23), where ϕ_i, θ_i and ψ_i are the inertial Euler angles.

$$M_{ib} = \begin{bmatrix} \cos\theta_i \cos\psi_i & \sin\phi_i \sin\theta_i \cos\psi_i - \cos\phi_i \sin\psi_i & \cos\phi_i \sin\theta_i \cos\psi_i + \sin\phi_i \sin\psi_i \\ \cos\theta_i \sin\psi_i & \sin\phi_i \sin\theta_i \sin\psi_i + \cos\phi_i \cos\psi_i & \cos\phi_i \sin\theta_i \sin\psi_i - \sin\phi_i \cos\psi_i \\ -\sin\theta_i & \sin\phi_i \cos\theta_i & \cos\phi_i \cos\theta_i \end{bmatrix} \tag{A.23}$$

The components of the angular speed due to the rotation of the air vehicle about its center of gravity is expressed in $\mathcal{R}_b$ as

$$\vec{\Omega} = \begin{bmatrix} p \\ q \\ r \end{bmatrix} \tag{A.24}$$

The change rate of the Euler angles, *i.e.*, the rotation speed between the two frames $\mathcal{R}_b$ and $\mathcal{R}_o$, can be expressed using the components of $\vec{\Omega}$ with the relation

$$\begin{bmatrix} \dot{\psi} \\ \dot{\theta} \\ \dot{\phi} \end{bmatrix} = \begin{bmatrix} \dfrac{1}{\cos\theta}(q\sin\phi + r\cos\phi) \\ q\cos\phi - r\sin\phi \\ p + \tan\theta(q\sin\phi + r\cos\phi) \end{bmatrix} \tag{A.25}$$

It is clear that in the time derivative equations of the Euler angles (A.25), a singularity is obtained for a value of $\theta = \pm\frac{\pi}{2}$. This singularity is purely mathematical. This is why it is common use to represent the attitude of an air vehicle with 4 dimensional vectors called quaternions. Quaternions are used to avoid mathematical calculation problems detached from the physical reality.

The quaternion $\mathbf{q}$ used to represent the attitude of the air vehicle as a function of the Euler angles is written as

$$\mathbf{q} = \begin{bmatrix} q_0 \\ q_1 \\ q_2 \\ q_3 \end{bmatrix} = \begin{bmatrix} \cos\frac{\psi}{2}\cos\frac{\theta}{2}\cos\frac{\phi}{2} + \sin\frac{\psi}{2}\sin\frac{\theta}{2}\sin\frac{\phi}{2} \\ \cos\frac{\psi}{2}\cos\frac{\theta}{2}\sin\frac{\phi}{2} - \sin\frac{\psi}{2}\sin\frac{\theta}{2}\cos\frac{\phi}{2} \\ \cos\frac{\psi}{2}\sin\frac{\theta}{2}\cos\frac{\phi}{2} + \sin\frac{\psi}{2}\cos\frac{\theta}{2}\sin\frac{\phi}{2} \\ \sin\frac{\psi}{2}\cos\frac{\theta}{2}\cos\frac{\phi}{2} - \cos\frac{\psi}{2}\sin\frac{\theta}{2}\sin\frac{\phi}{2} \end{bmatrix} \tag{A.26}$$

Then, the rotation matrix used to express vectors between the body and local frames is defined as follows:

$$M_{ob} = \begin{bmatrix} 2(q_0^2 + q_1^2) - 1 & 2(q_1 q_2 - q_0 q_3) & 2(q_1 q_3 + q_0 q_2) \\ 2(q_1 q_2 + q_0 q_3) & 2(q_0^2 + q_2^2) - 1 & 2(q_2 q_3 - q_0 q_1) \\ 2(q_1 q_3 - q_0 q_2) & 2(q_2 q_3 + q_0 q_1) & 2(q_0^2 + q_3^2) - 1 \end{bmatrix} \tag{A.27}$$

To obtain the rotation speed between the two frames $\mathcal{R}_b$ and $\mathcal{R}_o$ using quaternions, the variation rate defined by the time derivative of the attitude quaternion is

$$\dot{\mathbf{q}} = \frac{1}{2}\mathbf{q} \otimes \vec{\Omega} \tag{A.28}$$

where the symbol $\otimes$ represents the non commutative product of quaternions. Considering the component q_0 as a scalar s and the remaining three components $q_{1\dots3}$ as part of the vector $\vec{\mathbf{u}}$, the product of quaternions is defined as

$$\mathbf{q}_a \otimes \mathbf{q}_b = \begin{bmatrix} s_a \\ \vec{\mathbf{u}}_a \end{bmatrix} \otimes \begin{bmatrix} s_b \\ \vec{\mathbf{u}}_b \end{bmatrix} = \begin{bmatrix} s_a \; s_b - \vec{\mathbf{u}}_a \cdot \vec{\mathbf{u}}_b \\ s_a \; \vec{\mathbf{u}}_b + s_b \; \vec{\mathbf{u}}_a + \vec{\mathbf{u}}_a \wedge \vec{\mathbf{u}}_b \end{bmatrix} \tag{A.29}$$

Alternatively, to transform a vector defined on the body frame $\mathcal{R}_b$ to the inertial frame $\mathcal{R}_i$, the quaternion based rotation matrix (A.30) is used, where q_{0_i}, q_{1_i}, q_{2_i} and q_{3_i} are the components of the inertial quaternion $\mathbf{q}_i$ defined by the same expression as (A.26) but using the inertial Euler angles ϕ_i, θ_i and ψ_i

$$M_{ib} = \begin{bmatrix} 2(q_{0_i}^2 + q_{1_i}^2) - 1 & 2(q_{1_i} q_{2_i} - q_{0_i} q_{3_i}) & 2(q_{1_i} q_{3_i} + q_{0_i} q_{2_i}) \\ 2(q_{1_i} q_{2_i} + q_{0_i} q_{3_i}) & 2(q_{0_i}^2 + q_{2_i}^2) - 1 & 2(q_{2_i} q_{3_i} - q_{0_i} q_{1_i}) \\ 2(q_{1_i} q_{3_i} - q_{0_i} q_{2_i}) & 2(q_{2_i} q_{3_i} + q_{0_i} q_{1_i}) & 2(q_{0_i}^2 + q_{3_i}^2) - 1 \end{bmatrix} \tag{A.30}$$

A.2.3.3 From aerodynamic $\mathcal{R}_a$ to body $\mathcal{R}_b$ and local frame $\mathcal{R}_o$

Since the aerodynamic speed vector $\vec{\mathbf{V}}_a$ is probably the most important parameter for modelling the dynamics of any air vehicle, it is necessary to keep track of the attitude of the body with respect to $\vec{\mathbf{V}}_a$ and the attitude of $\vec{\mathbf{V}}_a$ with respect to the local frame.

The displacement of aerodynamic frame $\mathcal{R}_a$ carried by the speed vector $\vec{\mathbf{V}}_a$ with respect to the local frame $\mathcal{R}_o$ is defined by the aerodynamic Euler angles μ, γ and χ as shown on Figure A.4.
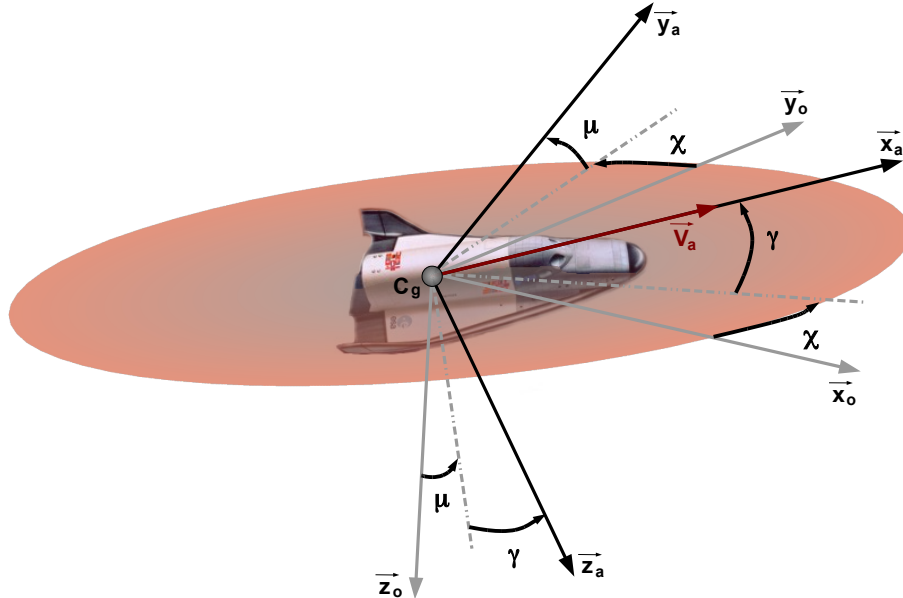
Figure A.4: Angles de Euler aérodynamiques entre les repères $\mathcal{R}_o$ et $\mathcal{R}_a$.

In the same way as described for the body frame, to express a vector defined on the aerodynamic frame $\mathcal{R}_a$ in the local frame $\mathcal{R}_o$, we use the equivalent rotation matrix (A.31).

$$M_{oa} = \begin{bmatrix} \cos\gamma\cos\chi & \sin\mu\sin\gamma\cos\chi - \cos\mu\sin\chi & \cos\mu\sin\gamma\cos\chi + \sin\mu\sin\chi \\ \cos\gamma\sin\chi & \sin\mu\sin\gamma\sin\chi + \cos\mu\cos\chi & \cos\mu\sin\gamma\sin\chi - \sin\mu\cos\chi \\ -\sin\gamma & \sin\mu\cos\gamma & \cos\mu\cos\gamma \end{bmatrix} \qquad (A.31)$$

Consider the vector

$$\vec{\mathbf{v}} = \begin{bmatrix} x_l \\ y_l \\ z_l \end{bmatrix} \text{ when defined in } \mathcal{R}_o, \text{ and } \vec{\mathbf{v}} = \begin{bmatrix} x_a \\ y_a \\ z_a \end{bmatrix} \text{ when defined in } \mathcal{R}_a.$$

Then, the following relation holds

$$\begin{bmatrix} x_l \\ y_l \\ z_l \end{bmatrix} = M_{oa} \begin{bmatrix} x_a \\ y_a \\ z_a \end{bmatrix} \qquad (A.32)$$

The displacement between the aerodynamic frame $\mathcal{R}_a$ and the body frame $\mathcal{R}_b$, as seen by the center of gravity of the air vehicle, produces two main angles that are very important for the creation of lift forces and yawing moments in flight. These angles are the angle-of-attack α and the side-slip angle β as defined on figure A.3.

With the angle-of-attack α and the side-slip angle β, the coordinate rotation established in (A.34) between the aerodynamic frame $\mathcal{R}_a$ and the body frame $\mathcal{R}_b$ can be defined by the successive rotations (A.33).

$$R_1(\alpha) = \begin{bmatrix} \cos\alpha & 0 & -\sin\alpha \\ 0 & 1 & 0 \\ \sin\alpha & 0 & \cos\alpha \end{bmatrix}$$

$$R_2(-\beta) = \begin{bmatrix} \cos\beta & -\sin\beta & 0 \\ \sin\beta & \cos\beta & 0 \\ 0 & 0 & 1 \end{bmatrix} \qquad (A.33)$$

$$M_{ba} = R_2(-\beta) \cdot R_1(\alpha)$$

$$M_{ba} = \begin{bmatrix} \cos\alpha\cos\beta & -\cos\alpha\sin\beta & -\sin\alpha \\ \sin\beta & \cos\beta & 0 \\ \sin\alpha\cos\beta & -\sin\alpha\sin\beta & \cos\alpha \end{bmatrix} \qquad (A.34)$$

Now, consider the vector

$$\vec{\mathbf{v}} = \begin{bmatrix} x \\ y \\ z \end{bmatrix} \text{ when defined in } \mathcal{R}_b, \text{ and } \vec{\mathbf{v}} = \begin{bmatrix} x_a \\ y_a \\ z_a \end{bmatrix} \text{ when defined in } \mathcal{R}_a.$$

Then, the following relation holds

$$\begin{bmatrix} x \\ y \\ z \end{bmatrix} = M_{ba} \begin{bmatrix} x_a \\ y_a \\ z_a \end{bmatrix} \qquad (A.35)$$

ONERA
THE FRENCH AEROSPACE LAB

Isae
Institut Supérieur de l'Aéronautique et de l'Espace

A.3 Deriving control objectives

All objectives for the automatic control system of an air vehicle can be obtained from the general equations described in Section A.1 and by using the relations between frames of reference described in Section A.2.3. For this thesis, the control objectives chosen are the angle-of-attack α, the side-slip angle β, and the roll angle ϕ. This section will show how the dynamic equations of these angular objectives were derived from the general equations of the movement of air vehicles.

Let us begin by expressing the base $(\vec{\mathbf{x}}_a, \vec{\mathbf{y}}_a, \vec{\mathbf{z}}_a)$ of the aerodynamic frame $\mathcal{R}_a$ in terms of the base $(\vec{\mathbf{x}}, \vec{\mathbf{y}}, \vec{\mathbf{z}})$ of the body frame $\mathcal{R}_b$, resulting in the set of equations presented below.

$$\vec{\mathbf{x}}_a = \cos\alpha\,\cos\beta\,\vec{\mathbf{x}} + \sin\beta\,\vec{\mathbf{y}} + \sin\alpha\,\cos\beta\,\vec{\mathbf{z}} = \frac{\vec{\mathbf{V}}_a}{V_a} \tag{A.36}$$

$$\vec{\mathbf{y}}_a = -\cos\alpha\,\sin\beta\,\vec{\mathbf{x}} + \cos\beta\,\vec{\mathbf{y}} + \sin\alpha\,\sin\beta\,\vec{\mathbf{z}} \tag{A.37}$$

$$\vec{\mathbf{z}}_a = -\sin\alpha\,\vec{\mathbf{x}} + \cos\alpha\,\vec{\mathbf{z}} \tag{A.38}$$

From figure A.3, one can then deduce the following expressions for the angle-of-attack α and the side-slip angle β

$$\tan\alpha = \frac{\vec{\mathbf{V}}_a \cdot \vec{\mathbf{z}}}{\vec{\mathbf{V}}_a \cdot \vec{\mathbf{x}}} \tag{A.39}$$

$$\tan\beta = \frac{\vec{\mathbf{V}}_a \cdot \vec{\mathbf{y}}}{\sqrt{(\vec{\mathbf{V}}_a \cdot \vec{\mathbf{x}})^2 + (\vec{\mathbf{V}}_a \cdot \vec{\mathbf{z}})^2}} \tag{A.40}$$

The aerodynamic speed vector $\vec{\mathbf{V}}_a$ is tied to the inertial speed vector $\vec{\mathbf{V}}$ by the relation:

$$\vec{\mathbf{V}} = \vec{\mathbf{V}}_a + \vec{\mathbf{V}}_w + \vec{\mathbf{V}}_E \tag{A.41}$$

where $\vec{\mathbf{V}}_E = \vec{\mathbf{\Omega}}_E \wedge \vec{\mathbf{r}}$ is the transport speed due to the rotation of the Earth.

The inertial rotation speed vector $\vec{\mathbf{\Omega}}_i$ can be decomposed into the following angular speeds:

$$\vec{\mathbf{\Omega}}_i = \vec{\mathbf{\Omega}} + \vec{\mathbf{\Omega}}_o + \vec{\mathbf{\Omega}}_E \tag{A.42}$$

The fundamental relation of the speed vector dynamics comes from the force equation. Let us retake this equation by explicitly expressing the acceleration as

$$\dot{\vec{\mathbf{V}}} = \frac{1}{m}\sum\vec{\mathbf{F}} = \vec{\mathbf{\Gamma}} = \vec{\mathbf{\Gamma}}_c + \vec{\mathbf{g}} \tag{A.43}$$

where $\vec{\mathbf{\Gamma}}$ is the acceleration resulting from all the forces interacting with the air vehicle. The acceleration vector $\vec{\mathbf{\Gamma}}$ can be decomposed as the acceleration due to gravity $\vec{\mathbf{g}}$ and the acceleration $\vec{\mathbf{\Gamma}}_c$ due to other forces and that is measurable by the accelerometers of the IMU.

Using the expression of the inertial speed (A.41), the last equation can be written as

$$\dot{\vec{\mathbf{V}}}_a + \dot{\vec{\mathbf{V}}}_w + \dot{\vec{\mathbf{V}}}_E = \vec{\mathbf{\Gamma}} \tag{A.44}$$

But since

$$\dot{\vec{V}}_E = \vec{\Omega}_E \wedge \vec{V} = \vec{\Omega}_E \wedge (\vec{V}_a + \vec{V}_w + \vec{V}_E) \tag{A.45}$$

then

$$\dot{\vec{V}}_a = \vec{\Gamma} - \vec{\Omega}_E \wedge \vec{V}_a - \dot{\vec{V}}_w - \vec{\Omega}_E \wedge \vec{V}_w - \vec{\Omega}_E \wedge (\vec{\Omega}_E \wedge \vec{r}) \tag{A.46}$$

Let us make the following simplifications:
- $\vec{\Omega}_E$ can be discarded since $|\vec{\Omega}_E| = 7.29212 \cdot 10^{-3} \, rad/s$ is too small compared to $\vec{\Omega}$;
- $\vec{\Omega}_o$ can be discarded since at most, a value $|\vec{\Omega}_o|_{max} = 1.163553 \cdot 10^{-3} \, rad/s$ is still too small compared to $\vec{\Omega}$;
- the term $\vec{\Omega}_E \wedge (\vec{\Omega}_E \wedge \vec{r})$ is integrated in the value of g, which is the standard value of the acceleration due to gravity on ground at 45° of latitude.

The time derivatives of the relations in (A.36) - (A.38) expressed in the aerodynamic frame of reference $\mathcal{R}_a$ can be written as

$$\dot{\vec{x}}_a = \dot{\beta} \, \vec{y}_a + \cos\beta \, \dot{\alpha} \, \vec{z}_a \tag{A.47}$$

$$\dot{\vec{y}}_a = -\dot{\beta} \, \vec{x}_a - \sin\beta \, \dot{\alpha} \, \vec{z}_a \tag{A.48}$$

$$\dot{\vec{z}}_a = \dot{\alpha} \, (\cos\beta \, \vec{x}_a - \sin\beta \, \vec{y}_a) \tag{A.49}$$

From (A.36) and (A.47), the airspeed vector time derivative can be expressed as

$$\dot{\vec{V}}_a = \dot{V}_a \, \vec{x}_a + V_a \, \dot{\vec{x}}_a = \dot{V}_a \, \vec{x}_a + V_a \, \dot{\beta} \, \vec{y}_a + V_a \, \cos\beta \, \dot{\alpha} \, \vec{z}_a \tag{A.50}$$

By extracting the components parallel to $\vec{z}_a$ and $\vec{y}_a$ of the time derivative of the airspeed vector, the dynamics of the angle-of-attack α and of the side-slip angle β can be written as

$$\cos\beta \, \dot{\alpha} = \vec{\Omega} \cdot \vec{y}_a + \frac{\vec{\Gamma} \cdot \vec{z}_a}{V_a} + \cos\beta \, q_w \tag{A.51}$$

$$\dot{\beta} = -\vec{\Omega} \cdot \vec{z}_a + \frac{\vec{\Gamma} \cdot \vec{y}_a}{V_a} + r_w \tag{A.52}$$

where q_w and r_w are angular speed components of the rotation between the aerodynamic frame of reference $\mathcal{R}_a$ and the local frame $\mathcal{R}_o$. These two components are defined as

$$q_w = -\frac{1}{\cos\beta \, V_a} \left(\dot{\vec{V}}_w + \vec{\Omega} \wedge \vec{V}_w \right) \cdot \vec{z}_a$$

$$r_w = -\frac{1}{V_a} \left(\dot{\vec{V}}_w + \vec{\Omega} \wedge \vec{V}_w \right) \cdot \vec{y}_a$$

When modelling control objectives, the wind speed vector $\vec{V}_w$ is considered as an exogenous disturbance, therefore q_w and r_w are usually discarded from the objectives model.

The dynamics of the roll ϕ is obtained directly by the classic relation for Euler angles derivative contained in equation (A.25), corresponding to

$$\dot{\phi} = p + \tan\theta(\sin\phi \, q + \cos\phi \, r) \tag{A.53}$$

Now, let us remind that the input u of the control model, corresponding mainly to control surfaces, is used to create moments around the air vehicle thus having a direct effect on the rotation rate

about the center of gravity G. And clearly, the dynamics of our angular objectives are functions of the body angular speed vector $\vec{\boldsymbol{\Omega}}$.

To control the angular objectives α, β, and ϕ, it is then necessary to include in the coupling between our objective dynamics (A.51) - (A.53) and the angular rate dynamics. Discarding the moments due to propulsion forces, the angular rate dynamics can be obtained straight from the equation of moments

$$\mathbf{I}\dot{\vec{\boldsymbol{\Omega}}} = \vec{\mathbf{M}}_{a_A} + \vec{\mathbf{F}}_a \wedge \overrightarrow{\mathbf{AG}} - \vec{\boldsymbol{\Omega}} \wedge \mathbf{I}\vec{\boldsymbol{\Omega}} \tag{A.54}$$

expressed parallel to the body frame axis.

Appendix B

Useful theorems and lemmas

B.1   On input-output stability (Small Gain Theorem)

To introduce the general notion of input-output stability, let us first introduce some notation which will be used to explain this concept [Vid93, NT04, Bia96]. Consider that μ is a measure in the sense of Lebesgue and that E is the space of functions f defined in $\mathbb{R}_+$, to values in $\mathbb{R}$, and that are Lebesgue measurable. A function $f \in E^n$ is essentially bounded if $\mu \neq 0$ is bounded over any interval in $\mathbb{R}_+$. Let us define the concept of $\mathcal{L}_q$ spaces first.

Definition B.1 ($\mathcal{L}_q$ space) *An $\mathcal{L}_q$ space is the metric space of functions f in E such that*

– $\displaystyle\int_0^\infty |f(t)|^q\, dt < \infty$ *for* $q < \infty$

– f *is essentially bounded for $q = \infty$, i.e.,* $\displaystyle\sup_{t\in\mathbb{R}_+} |f(t)| < \infty$.

An $\mathcal{L}_q$ space is constituted of all piecewise continuous functions

$$||f(t)||_q = \left(\int_0^\infty [|f_1(t)|^q + |f_2(t)|^q + \ldots + |f_p(t)|^q]\, dt \right)^{\frac{1}{q}} \tag{B.1}$$

where $|\cdot|$ represents the standard Euclidean norm and $||\cdot||_q$ is called a *norm function.*

Norm functions represent the formal idea of size of signals. The $\mathcal{L}_2$ norm, for example, is useful for problems where energy constraints are imposed while the $\mathcal{L}_\infty$ norm comes in handy for amplitude or bound constraints.

At this point, it is also needed to introduce the notion of *truncation operator* which is used to establish the input-output stability of a system.

Definition B.2 (Truncation operator) *Consider $u \in \mathcal{L}_q$. The truncation operator T of functions $\mathcal{L}_q \to \mathcal{L}_q$, is defined by*

$$\begin{cases} f_{\mathrm{T}}(t) & = & f(t) & \text{if } t \le \mathrm{T} \\ f_{\mathrm{T}}(t) & = & 0 & \text{if } t > \mathrm{T} \end{cases}$$

Taking into account the truncation operator of the function $f(t)$, the concept of $\mathcal{L}_q$ spaces can be extended as follows.

Definition B.3 (Extended $\mathcal{L}_q$ spaces) *The extension of the space $\mathcal{L}_q$, denoted $\mathcal{L}_{q,e}$, is defined as the space consisting of of all functions whose truncation belongs to $\mathcal{L}_q$. The space $\mathcal{L}_{q,e}$ is and extension of the space $\mathcal{L}_q$ because $\mathcal{L}_q \subset \mathcal{L}_{q,e}$*

After introducing some notation, now let us consider the autonomous nonlinear system

$$\begin{cases} \dot{x} & = & \mathrm{f}(x(t), u(t)) \\ y(t) & = & \mathrm{h}(x(t), u(t)) \end{cases} \tag{B.2}$$

with initial condition $x(t_0) = x_0$. It is assumed that the existence and uniqueness of solutions is verified. This means that given an initial condition x_0 and the input vector $u(t)$, only one output vector $y(t)$ can be determined. If the initial condition is at the origin and the input vector is set to zero, then

$$\begin{cases} \mathrm{f}(0,0) & = & 0 \\ \mathrm{h}(0,0) & = & 0 \end{cases} \tag{B.3}$$

It will also be assumed that the signals u and y belong to the spaces $\mathcal{L}_{q,e}^m$ and $\mathcal{L}_{q,e}^p$. Finally, an operator $H : \mathcal{L}_{q,e}^m \to \mathcal{L}_{q,e}^p$ is associated to system (B.2) as an input-output mapping, such as

$$y = H(u) \tag{B.4}$$

where H verifies the principle of causality or

$$\forall \, \mathrm{T} \ge 0, \ H(u)_{\mathrm{T}} = H(u_{\mathrm{T}})_{\mathrm{T}} \tag{B.5}$$

Causality means the past and present outputs $y(t)$ of the operator do not depend on future inputs $u(t)$. This principle also implies that the input can be determined by studying the output, which in terms means that the operator H is invertible [Che84]. Notice that the nature of the operator H is not specified, and therefore it may represent any type of process (whether autonomous, non-autonomous, time invariant, *etc.*).

We can now establish the definition of input-output stability in the sense of $\mathcal{L}_q$ spaces [Bia96].

Definition B.4 ($\mathcal{L}_q$ stability) *The operator H, or its associated system, is $\mathcal{L}_q$ stable if*
– $\forall \, u \in \mathcal{L}_{q,e}^m, \ H(u) \in \mathcal{L}_{q,e}^p$;
– there exists two constants γ and β such that $\forall \, u \in \mathcal{L}_{q,e}^m$ and $\forall \, \mathrm{T} > 0$

$$||(H(u))_{\mathrm{T}}||_q \le \gamma ||u_{\mathrm{T}}||_q + \beta \tag{B.6}$$

The constant γ represents the system gain and the smallest value of γ that satisfies the previous condition is called the $\mathcal{L}_q$ gain of the operator H. The term β is a residual term that vanishes

when the initial conditions are set at the origin $x_0 = 0$.

The $\mathcal{L}_2$ stability of a system is linked to the idea that an input signal $u(t)$ of finite energy should produce an output signal $y(t)$ of finite energy. This is not exactly the same notion as *bounded-input bounded-output* (BIBO) stability.

Definition B.5 (BIBO stability) *The general system (B.2) is BIBO stable if the output signal $y(t)$ remains bounded as long as the input signal $u(t)$ is bounded, this is, if the system is $\mathcal{L}_\infty$ stable.*

To analyse the input-output stability of a feedback control loop, the Small Gain Theorem states a basic requirement for the assessment of the $\mathcal{L}_q$ stability. Even though this theorem is not general as the Lyapunov method, it simplifies the analysis for systems with the interconnection scheme of figure B.1.
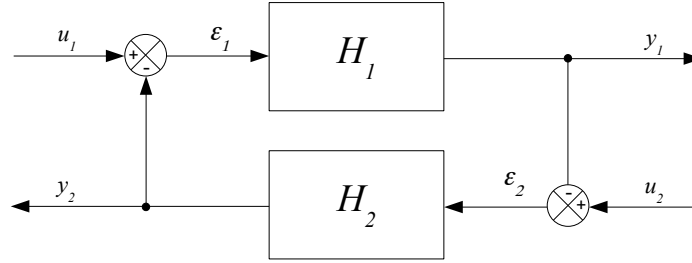
Figure B.1: Interconnection for small gain stability analysis.

Theorem B.6 (Small Gain) *Consider that the two operators H_1 and H_2 on figure B.1 are $\mathcal{L}_q$ stables and of respective $\mathcal{L}_q$ gains γ_1 and γ_2. If*

$$\gamma_1 \gamma_2 < 1$$

then $\forall\, u_1 \in \mathcal{L}_{q,e}^{m_1}$, $\forall\, u_2 \in \mathcal{L}_{q,e}^{m_2}$ and $\forall\, \mathrm{T} > 0$

$$||(\varepsilon_1)_\mathrm{T}|| \leq \frac{1}{1 - \gamma_1 \gamma_2} \left(||(u_1)_\mathrm{T}||_q + \gamma_1 ||(u_2)_\mathrm{T}||_q + \beta_2 + \gamma_2 \beta_1 \right)$$

$$||(\varepsilon_2)_\mathrm{T}|| \leq \frac{1}{1 - \gamma_1 \gamma_2} \left(||(u_2)_\mathrm{T}||_q + \gamma_2 ||(u_1)_\mathrm{T}||_q + \beta_1 + \gamma_1 \beta_2 \right)$$

Consequently, the closed loop is $\mathcal{L}_q$ stable from the inputs (u_1, u_2) to the outputs (y_1, y_2).

In practice, based on an $\mathcal{L}_2$ norm criteria, the following corollary becomes a more common application of the small gain theorem to linear control systems:

Corollary B.7 (Small Gain for LTI Systems with Unstructured Uncertainties) *Consider the closed-loop of Figure B.2, where $P(s)$ is a stable LTI system and the unstructured uncertainty $\Delta(\cdot)$ is an $\mathcal{L}_2$ operator which verifies the following condition:*

$$\forall\, u, \varepsilon \,\in \mathcal{L}_2,\; ||\Delta(\varepsilon) - \Delta(u)||_2 \leq \alpha ||\varepsilon - u||_2 \tag{B.7}$$

with $0 \leq \alpha \leq 1$, i.e., $\Delta(\cdot)$ is a contraction.

This closed-loop is internally stable for all $\Delta(\cdot)$ that verifies condition (B.7) if and only if:

$$||P(s)||_\infty < 1 \tag{B.8}$$

This result is preserved as the operator $\Delta(\cdot)$ belongs to the class of stable LTI systems bounded by $||\Delta(s)||_\infty < 1$.
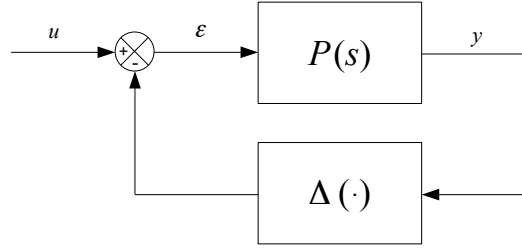
Figure B.2: Interconnection for small gain stability analysis of LTI systems.

B.2 On $\mathcal{H}_\infty$ norm and design tools (Bounded Real Lemma)

The $\mathcal{H}_\infty$ framework for robust control design has become of great importance in the last two decades. Indeed, the $\mathcal{H}_\infty$ norm is a rather convenient mathematical measure commonly used as a cost parameter in feedback optimisation problems.

Before giving the formal definition of this measurement, consider $H(s)$ the transfer function of an LTI system of input u and output y for which a state-space realisation is characterized by the quadruple (A, B, C, D). The system is stable if its associated matrix A is Hurwitz, *i.e.*, if all its eigenvalues have a negative definite real part.

The term $\mathcal{H}_\infty$ denotes the space of bounded functions $H(s)$ that are analytic in $(Re)(s) \geq 0$.

Definition B.8 ($\mathcal{H}_\infty$ norm) *The $\mathcal{H}_\infty$ norm of an LTI system is defined as the peak gain of the frequency response of its transfer function $H(s)$ over the imaginary axis:*

$$||H(s)||_\infty = \sup_{(Re)(s) \geq 0} \bar{\sigma}\left(H(s)\right) = \sup_{\omega \in \mathbb{R}} \bar{\sigma}\left(H(\omega j)\right) \tag{B.9}$$

where $\bar{\sigma}$ denotes the largest singular value of the frequency response.

A time-domain interpretation can be given to the $\mathcal{H}_\infty$ norm through the concept of $\mathcal{L}_2$ gain. From Definitions B.1, B.2 and B.4 the $\mathcal{L}_2$ gain can be defined as follows [Meg09]:

Definition B.9 ($\mathcal{L}_2$ gain) *Consider a stable system of input $u(t) \in \mathcal{L}_2$ and output $y(t) \in \mathcal{L}_2$. The $\mathcal{L}_2$ gain of such a system is the minimal gain $\gamma \geq 0$ on one side such that:*

$$\inf_{T \geq 0} \int_0^T (\gamma^2 |u(t)|^2 - |y(t)|^2)\, dt > -\infty \tag{B.10}$$

for all input-output pairs (u, y) over arbitrary finite time intervals.

From the definition above, it becomes clear why the $\mathcal{L}_2$ gain concept is of such relevance to robustness analysis. Still, for some classes of systems, the $\mathcal{L}_2$ gain can be difficult to calculate or even to estimate. Then, the importance of the $\mathcal{H}_\infty$ norm is largely due to the fact that, for stable LTI systems, the $\mathcal{H}_\infty$ norm is equal to the $\mathcal{L}_2$ gain of such systems.

Inspired from this interpretation and based on the concept of quadratic stability, which focuses on finding a quadratic Lyapunov function, the $\mathcal{H}_\infty$ norm computation problem can be transformed into a standard Linear Matrix Inequality (LMI) optimization problem. At the core of this idea, is Bounded Real Lemma (BRL).

Lemma B.10 (Bounded Real) *The gain of a stable LTI system represented by the state-space realisation (A, B, C, D) is bounded by $\gamma > 0$ if and only if there exist $X = X^T$ such that*

$$\begin{bmatrix} A^T X + X A^T & X B & C^T \\ B^T X & -\gamma I & D^T \\ C & D & -\gamma I \end{bmatrix} < 0 \tag{B.11}$$

with $X > 0$.

Originally, the BRL presented simple conditions under which any given system is contractive on the imaginary axis, which lead to a straightforward way of computing the $\mathcal{H}_\infty$ norm of such systems. Yet, this result proved to be much more flexible and interesting. It then became a relevant tool to prove that the existence of stabilizing feedback controllers was equivalent to the existence of solutions of specific LMI formulations through convex optimization.

Today, the BRL allows to establish conditions for a number of applications including: synthesis of H_∞ controllers, optimization of scalings, multipliers and integral quadratic constraints (IQC) in robustness analysis. Different adaptations of the BRL can be used for different classes of systems and representations in either continuous or discrete cases [ZDK10, ZXS08, Dum05, SDSX97, SYdS98, SS01].

Appendix C

Alternative synthesis and analysis tools

C.1 Simultaneous design of $K_a(s)$ and $J(s)$

Inspired by the schemes presented in [MTK09, BA11], a simultaneous synthesis of the linear controller $K_a(s)$ and the anti-windup device $J(s)$ can be foreseen.

In general, by computing the both controllers simultaneously, the conservatism of more conventional schemes can be reduced. This can be achieved by creating a structured multi-objective design model that will seek to:

– minimize a system performance criterion established as the error between the system $\Sigma(s)$ and a reference model $R(s)$,
– and preserve the closed-loop stability despite the effects of saturations.

Consider the actuator model presented in (2.18), the rate limiter model in (2.27) and the complete NLC control scheme presented on Figure C.1.

Figure C.1: Complete NLC control scheme.

From the control scheme presented above, the LFT representation of Figure C.2 can be easily derived, where

$$\mathbf{w} = \begin{bmatrix} z_c & \hat{f} & w_f \end{bmatrix}^T \quad \text{and} \quad \mathbf{z} = \begin{bmatrix} z_u & z_p \end{bmatrix}^T$$

Figure C.2: LFT representation of the complete NLC control scheme.

By removing the exogenous blocks of the LFT representation, a design-oriented model is obtained. The goal of such design-oriented model is to find the best controllers $K_a(s)$ and $J(s)$ which respond to the two control objectives previously stated.

Suitable weighting functions should be designed and added in this scheme to the exogenous weighted output vector $\mathbf{z}$ (and to the exogenous input vector $\mathbf{w}$ if required).

A standard form with its associated structured controller block $diag(J(s), K_a(s))$ can be easily derived. The latter is used for $\mathcal{H}_\infty$ controller synthesis and it is represented on Figure C.3.

Figure C.3: Standard form of the simultaneous $\mathcal{H}_\infty$ control design of $K_a(s)$ and $J(s)$.

Finally, from the small gain theorem, the stability of the closed-loop is guaranteed if condition (2.31) is verified. Moreover, the robust performance of the control loop is ensured if condition (2.19) is verified at the same time. As a result, both controllers $K_a(s)$ and $J(s)$ can be obtained as a solution of the following multi-channel $\mathcal{H}_\infty$ design problem:

$$\min_{J(s),K_a(s)} \gamma \Big/ \left\{ \begin{array}{l} ||\mathcal{F}_l(P_{nom}(s),K_a(s))||_\infty < \gamma \\ ||\mathcal{F}_l\left(P_{rob}(s),diag(J(s),K_a(s))\right)||_\infty < \gamma \end{array} \right. \tag{C.1}$$

where
– P_{nom} denotes the suitable linear interconnection of the transfer from the exogenous inputs $\mathbf{w}$ to the exogenous outputs $\mathbf{z}$, with $\varphi_{\tilde{L}} \equiv 0$;
– P_{rob} denotes the suitable linear interconnection of the transfer from the exogenous input w_φ to the exogenous output z_φ;

C.2 On IQC-based analysis

More precise results on the achieved robust stability of the closed-loop can be obtained using other analysis techniques. Some of these may also prove to be well-suited for the robustness analysis of the problem that has been proposed using the analysis model described in Section 2.5.1.

In the same context of input-output stability analysis, the IQC formalism presents a very interesting and complete framework allowing to obtain analysis results of lower conservatism. In fact, many robustness stability methods can be reformulated to fall within the IQC framework as exposed in the central contribution [MR97].

The basic principle of the IQC-based analysis is to replace a system nonlinearities, time-varying coefficients, parametric uncertainties and unmodelled dynamics by IQC characterizations. Then, the analysis model is immersed into a relaxed representation containing all possible solutions of the real system. This is done by defining multipliers Π that satisfy an integral quadratic condition denoted σ_Π. The analysis problem of the relaxed model is much easier and can be solved via convex optimization, which yields an upper bound of the $\mathcal{L}_2$ gain.

At the core of this framework, is the general interconnection of Figure C.4 which can be expressed as:

$$\left\{ \begin{array}{rcl} z & = & M(s)\,w \\ w & = & \Delta(z) \end{array} \right. \tag{C.2}$$

where $M(s)$ is a stable LTI system and the bounded operator $\Delta(\cdot) \in \mathcal{L}_2$ can contain nonlinearities, time-varying coefficients, parametric uncertainties and unmodelled dynamics. Then, the bounded operator $\Delta(\cdot)$ is said to satisfy the IQC σ_Π, defined by the multiplier Π, if $\forall\, w = \Delta(z)$ the following condition is verified:

$$\sigma_\Pi = \int_{-\infty}^{\infty} \begin{bmatrix} \hat{z}(j\omega) \\ \hat{w}(j\omega) \end{bmatrix}^* \Pi(j\omega) \begin{bmatrix} \hat{z}(j\omega) \\ \hat{w}(j\omega) \end{bmatrix} \geq 0 \tag{C.3}$$

where the symbol '$*$' denotes the conjugate transpose, $\hat{z}$ and $\hat{w}$ denote the Fourier transforms of the signals z and w, and the multiplier Π has the following general structure:

$$\Pi(j\omega) = \begin{bmatrix} \Pi_{11}(j\omega) & \Pi_{12}(j\omega) \\ \Pi_{12}(j\omega)^* & \Pi_{22}(j\omega) \end{bmatrix} \tag{C.4}$$
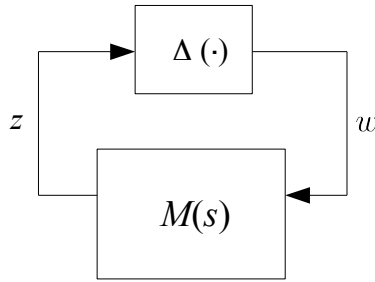
Figure C.4: Analysis interconnection of the IQC framework.

Considering that the quadruple (A_M, B_M, C_M, D_M) is a realization of the system $M(s)$, the stability of the interconnection depicted on Figure C.4 is guaranteed if:

$$\begin{bmatrix} M(j\omega) \\ I \end{bmatrix}^* \Pi(j\omega) \begin{bmatrix} M(j\omega) \\ I \end{bmatrix} < 0, \qquad \forall\, \omega \in \mathbb{R} \tag{C.5}$$

Interestingly, by application of the Kalman-Yakubovich-Popov Lemma [Ran96], it follows that the stability condition above is equivalent to verifying that there exists $X = X^T > 0$ such that:

$$\begin{bmatrix} A_M^T\, X + X\, A_M^T & X\, B_M \\ B_M^T\, X & \mathbf{0} \end{bmatrix} + \begin{bmatrix} Q & S \\ S^T & R \end{bmatrix} < 0 \tag{C.6}$$

where the symmetric matrices Q, S and R are part of the representations of the multiplier Π. Then, the stability analysis of the interconnection between $M(s)$ and $\Delta(\cdot)$ takes the form of a convex optimization problem defined by the LMI presented above.

A wide variety of multipliers Π can be proposed to characterize each particular operator contained in $\Delta(\cdot)$. An extensive list of multipliers that satisfy the IQC condition (C.3) can be found in [MR97].

Other refined characterizations of particular operators are a current subject of study. In fact, a useful feature of this framework is that by adding as many IQC satisfied by a same operator as possible, the method tends to reduce the conservatism of the results by considering all the IQC simultaneously. For example, a refined IQC formulation for systems with slowly varying parameters is proposed in [Hel99] based on the so called Swapping Lemma.

Also, an interesting formulation for computing the $\mathcal{L}_2$ gain of systems with bounded sector non-linearities and slope restrictions is presented in [TK11], founded on an IQC-based formulation of the Zames-Falb multiplier and the Popov multiplier. In this contribution, compared to the classic multipliers approach and the standard IQC framework, the conservatism of the results are reduced by adding two IQC characterizations satisfied by the bounded nonlinearity and by solving a set of LMI that result from the unified formulation.

On the downside, this technique may require large computational loads and longer times to run the analysis tests depending on the size of the characterizations contained in Π. It should be kept in mind that, from a computational point of view, it is difficult to obtain exact result to the robustness analysis problem, no matter what technique or framework is used. A trade-off between the conservatism of the analysis and computational burden or limits of the tests has to be considered.

In this thesis work, the IQC framework was not explored given the computational burden that it represents. Instead, the small gain theorem-based approaches will be preferred for robustness analysis.

Appendix D

Simulation parameters and values

This Appendix contains a detailed presentation of the numerical values of the simulation parameters that were used to test the Control System of the reentry vehicle model.

The simulation parameters are classified into two groups: the parameters linked to the flight conditions of the simulator, and the parameters associated to the reentry vehicle model. Different sources of disturbance affecting relevant parameters and their numerical values will also be introduced accordingly.

First, let us introduce the main simulation parameters linked to the Flight Mechanics simulator environment.

D.1 Flight conditions

The 6 degrees-of-freedom nonlinear Flight Mechanics simulator considers specific environmental conditions to which the reentry vehicle model is subject to. The following contains a brief description of such environmental conditions mainly determined by the atmospheric model, which may also consider the effects of diverse perturbations on the reentry vehicle.

D.1.1 Atmospheric model

The aerodynamic and propulsion model of any air vehicle has a direct dependency on the following atmospheric parameters:
– ρ: density;
– P: pressure;
– T: temperature;
– c_s: sound speed;

These parameters characterize standard atmospheric models such as the International Standard Atmosphere (ISA) model or the U.S. National Oceanic and Atmospheric Administration (NOAA) 1976 Committee on Extension to the Standard Atmosphere (COESA) model. The parameters

presented above are a function of the altitude h at which the air vehicle is located. More complex atmospheric models, such as the Committee on Space Research (COSPAR) International Reference Atmosphere (CIRA) model, use the geographic location and the month of the year to generate more accurate representations of the atmosphere at different altitudes.

In this work, the NOAA '76 COESA model was employed for simulation with the reentry vehicle model. The curves contained in the graphics of Figures D.1-D.4, present the atmospheric profile.
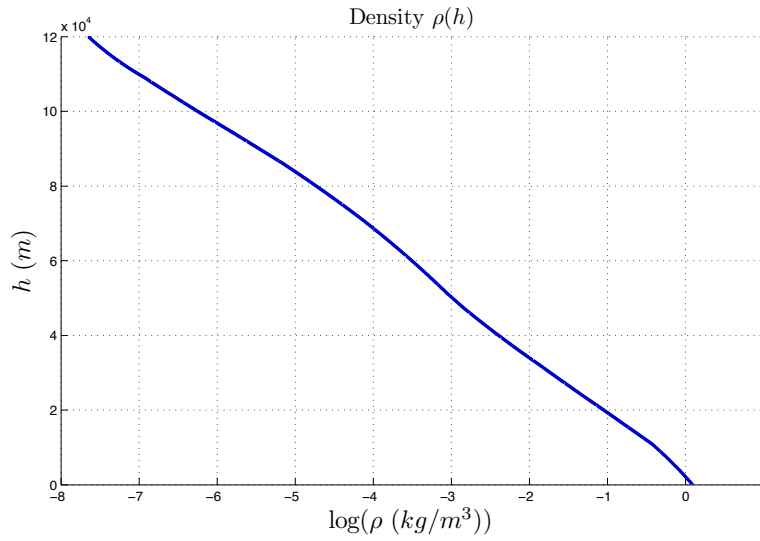
Figure D.1: Atmospheric density ρ as a function of the altitude h.
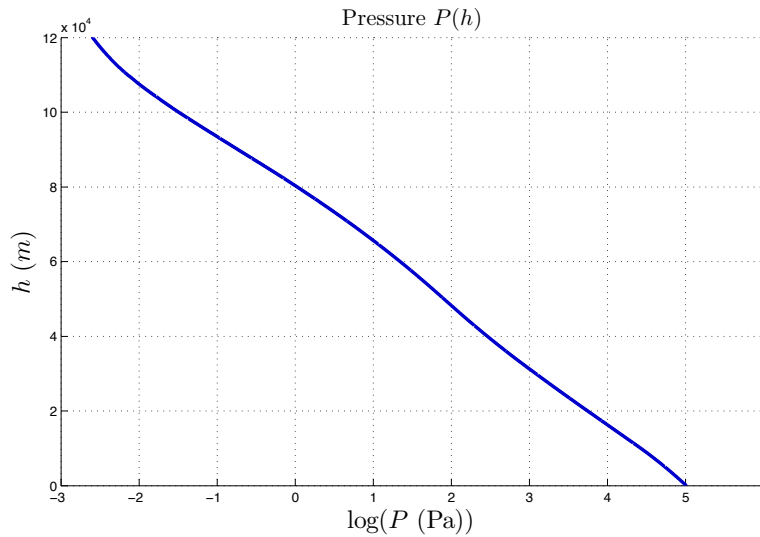
Figure D.2: Atmospheric pressure P as a function of the altitude h.
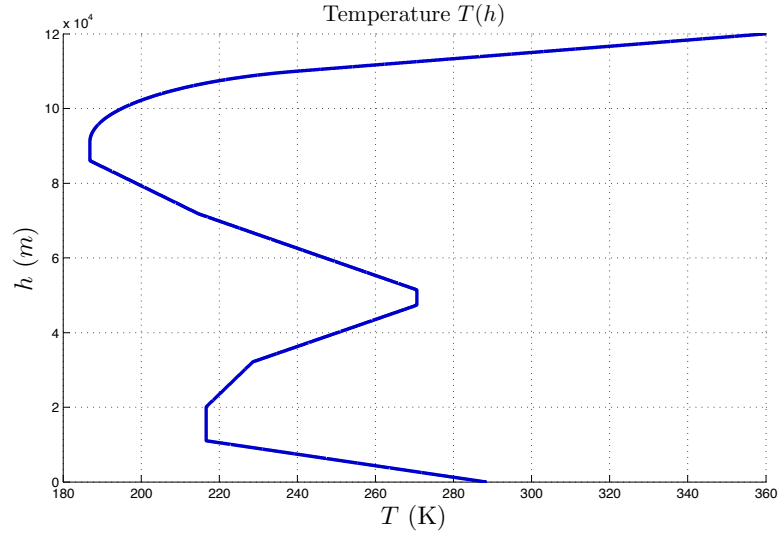
Figure D.3: Atmospheric Temperature T as a function of the altitude h.
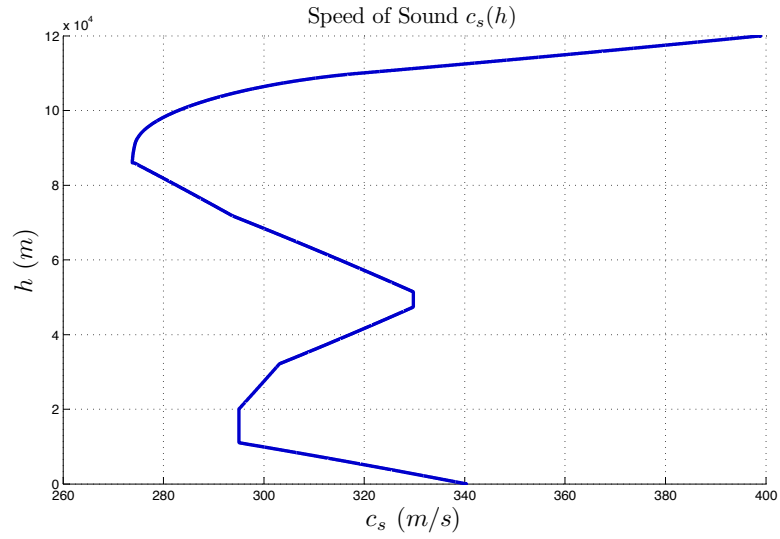
Figure D.4: Speed of sound c_s as a function of the altitude h.

The speed of sound is used to obtain the Mach number of a vehicle flying at an airspeed V_s such that:

$$\mathcal{M} = \frac{V_a}{c_s(h)} \tag{D.1}$$

Variations on the density ρ can be represented as a multiplicative uncertainty of the atmospheric model presented above as a function of the altitude h. The following values of this uncertainty were considered in simulation:

h (km)	25	45	60	80	90	120
$\mathbf{\Delta}\rho$	0	±11%	±14%	±12%	±16%	±8%

Table D.1: Atmospheric density variation $\Delta\rho$.

Inside the atmospheric environment, diverse phenomena takes place as a result of the interaction of air with different atmospheric characteristics. One such a phenomenon, caused mainly by a gradient of pressure, is the wind.

D.1.2 Wind as a source of disturbance

The wind is represented as a vector $\vec{\mathbf{V}}_w$ with a specific direction and speed. In this work, the wind is modelled as a static wind vector $\vec{\mathbf{V}}_{sw}$ affected by a turbulence vector $\vec{\mathbf{V}}_{tw}(t)$. This way, the effect of the wind can be added to the simulation by applying $\vec{\mathbf{V}}_w$ to the center of gravity of the reentry vehicle.

Other effects resulting from the wind speed variations on different points of the vehicle can be modelled by angular speeds due to the wind. For example, the components p_w, q_w and r_w can be added to the angular rates p, q and r.

The static wind vector $\vec{\mathbf{V}}_{sw}$ is modelled as an horizontal static wind defined by its magnitude as a function of the altitude and by the direction from which the wind comes. The static wind profile varies depending on the geographical zone.

The direction of $\vec{\mathbf{V}}_{sw}$ is usually West to East for reentry missions close to the equatorial region and it is measured with respect to the geographic North. In simulation with the reentry vehicle, the latter is considered to be random and the magnitude is considered to be a function only of the altitude h according to the following profile:

h (km)	0	5	10	27	50	60	75	80	115	120
$\mathbf{V_{sw}}$ (m/s)	15	25	35	62	190	190	150	150	200	200

Table D.2: Static wind V_{sw} profile as a function of the altitude h.

The wind turbulence $\vec{\mathbf{V}}_{tw}(t)$ is modelled by independent colored noises on the 3 vehicle axis with the respective longitudinal component u, lateral component v and vertical component w. The effects of the turbulence on the angular dynamics of the vehicle can be represented by 3 more colored noises through the variables p_w, q_w and r_w.

Each of these colored noises is characterized by a transfer function $H(s)$ between the wind turbulence and a white noise of standard deviation σ_i. For the angular speeds generated due to the wind turbulence, a reference length b_r, which corresponds usually to the wingspan or vehicle length, is used.

Consider the Dryden profile for wind turbulence [Mat11a], from which the following transfer functions $H(s)$ are obtained:

Speed	Angular speed
$H_u(s) = \sigma_u \sqrt{\frac{2\,\tau_u}{\pi}}\,\frac{1}{1+\tau_u\,s}$	$H_p(s) = \frac{\sigma_w}{V_a}\,\sqrt{\frac{0.8}{\tau_p^{\frac{1}{3}}\,\tau_w^{\frac{2}{3}}}}\,\frac{1}{1+\tau_p\,s}$
$H_v(s) = \sigma_v \sqrt{\frac{\tau_v}{\pi}}\,\frac{1+\sqrt{3}\,\tau_v\,s}{(1+\tau_v\,s)^2}$	$H_r(s) = \frac{s}{1+\tau_r\,s}\,\frac{H_v(s)}{V_a}$
$H_w(s) = \sigma_w \sqrt{\frac{\tau_w}{\pi}}\,\frac{1+\sqrt{3}\,\tau_w\,s}{(1+\tau_w\,s)^2}$	$H_q(s) = \frac{s}{1+\tau_q\,s}\,\frac{H_w(s)}{V_a}$

Table D.3: Transfer functions $H(s)$ defining the turbulence model.

In the transfer functions presented above, the time constants τ_i are expressed as a function of the correlation lengths L_i (not ot be confused with the inertial longitude L_i) and the air speed V_a such that

$$\tau_i = \frac{L_i}{V_a} \tag{D.2}$$

given

$$L_p = L_q = \frac{4\,b_r}{\pi} \quad \text{and} \quad L_r = \frac{3\,b_r}{\pi} \tag{D.3}$$

The other parameters in these transfer functions are mainly a function of the altitude. For example, considering the Dryden turbulence model, one gets that:
– for $0 < h \leq 300\ m$:

$$\sigma_w = 0.1\,V_{sw}$$
$$\sigma_u = \sigma_v = \frac{\sigma_w}{(0.177 + 0.000823\,h)^{0.4}}$$
$$L_w = h$$
$$L_u = L_v = \frac{h}{(0.177 + 0.000823\,h)^{1.2}}$$

– for $300\ m < h < 600\ m$, a linear interpolation is used.
– for $600\ m \leq h < 27000\ m$:

$$L_u = L_v = L_w = 533.4\ m$$

The values σ_u, σ_v and σ_w are interpolated from tables as a function of the altitude h and of the probability that the turbulence level is exceeded.
– for $h \geq 27000\ m$:

$$\sigma_i = \sigma_{0_i}\left(\frac{h}{h_0}\right)^{\kappa_{\sigma_i}}\ m/s$$
$$L_i = L_{0_i}\left(\frac{h}{h_0}\right)^{\kappa_{L_i}}\ m$$

where $\kappa_i \in \mathbb{R}$.

ONERA
THE FRENCH AEROSPACE LAB

isae
Institut Supérieur de l'Aéronautique et de l'Espace

For simulation, a moderate wind turbulence profile is considered, in which the RMS turbulence amplitude remains between 0 and 5 m/s with a 10^{-3} probability of exceedance starting at an altitude of about 20 km.

D.1.3 Flight operating points

The flight domain covered by a vehicle throughout a reentry mission is very large. To test the Control System of the reentry vehicle in simulation, different conditions within the flight domain can be chosen as fixed points of a possible mission trajectory. Let us recall the typical flight conditions presented in Section 5.3 of page 109, which were retained for simulation with the reentry vehicle model.

	Flight point				Trim values	
n°	h (m)	$\mathcal{M}$	$\bar{q}$ (Pa)	γ (^{o})	$\bar{\alpha}$ (^{o})	$\bar{\delta}_m$ (^{o})
1	68 500	20	1 639	-0.3	33	2.08
2	54 500	11	3 615	-0.5	33	1.86
3	48 000	8	4 379	-1.5	28	5.43
4	38 000	5	6 395	-2.5	24	5.78
5	25 000	2.5	10 986	-5	16	1.78
6	10 000	0.8	11 843	-10	10	-4.89
7	5 000	0.6	13 613	-15	7	-7.59
8	0	0.3	6 383	-16	10	-5.99

Table D.4: Recapitulation of flight points considered in simulation with associated trimmed flight conditions.

These points are completely defined as a function of the altitude h and the Mach number $\mathcal{M}$. The dynamic pressure $\bar{q}$ is then computes from these values, while the glide slope angle γ is mainly imposed by the Guidance System as a possible mission trajectory. Then, equilibrium conditions are used to fix the initial values of the simulator state vector and other flight parameters.

In general, an equilibrium state is sought such that the Euler derivatives, as well as the lateral angles ψ, ϕ, β, μ and lateral angular rates p, r are zero.

There are different ways of defining trim values of the longitudinal flight parameters can be foreseen. Two classical approaches are: the longitudinal moment equilibrium and the longitudinal load factor equilibrium. In particular, a moment equilibrium was used to compute the trim values of the angle-of-attack $\bar{\alpha}$ and the control signal $\bar{\delta}_m$ that renders $\dot{q} = 0$, given $q = 0$.

Because the grand majority of air vehicles are symmetric about the x axis, the trim values of the lateral attitude and angular speed are zero for zero deflection of the aerodynamic controls.

D.2 Vehicle characteristics

In the following, specific characteristics of the reentry vehicle model used in simulation are detailed. Numerical values are given for different relevant parameters of the vehicle, its actuators, and other on-board devices such as the IMU.

D.2.1 Physical and geometric characteristics

Let us now present the most relevant characteristics of the reentry vehicle. These cover the main physical and geometrical properties of the model used in simulation. Numerical values are not presented due to copyright restrictions on the simulation model. Consider the table presented below:

Parameter	Units
S_r: reference area	m^2
l_r: lateral reference length or wingspan	m
b_r: longitudinal reference length or chord	m
l: vehicle length	m
dg_x: x component of centring vector $\overrightarrow{\mathbf{AG}}$	m
dg_y: y component of centring vector $\overrightarrow{\mathbf{AG}}$	m
dg_z: z component of centring vector $\overrightarrow{\mathbf{AG}}$	m
m: vehicle mass	kg
I_{xx}: principal moment of inertia around axis x	$kg \cdot m^2$
I_{yy}: principal moment of inertia around axis y	$kg \cdot m^2$
I_{zz}: principal moment of inertia around axis z	$kg \cdot m^2$

Table D.5: Reentry vehicle physical and geometrical characteristics.

The order of grandeur of the lift-to-drag ratio of the simulation model is of about $L/D \approx 1.7$.

D.2.2 Actuators and physical limits

The control surfaces on any air vehicle are deflected by action of the actuators attached to them. These actuators are servomechanisms composed of mechanical and electric components whose physical response follow specific dynamics. As actuator dynamics is relevant to the controller design, these should always be considered when modelling an air vehicle.

In many cases, actuator dynamics of the control surfaces δ can be approximated in their nominal region either by a first or second-order transfer between the commanded deflection δ_c and the real surface deflection δ_r at any given time t. The second-order actuator model is characterized by the state equation:

$$\ddot{\delta}_r = \omega_a^2(\delta_c - \delta_r) - 2\xi_a\omega_a\dot{\delta}_r \tag{D.4}$$

where ω_a is the natural frequency of the actuator and ξ_a is the damping coefficient. The first-order actuator model, retained for this thesis work, can be expressed as:

$$\dot{\delta}_r = \frac{1}{\tau_a}(\delta_c - \delta_r) \tag{D.5}$$

where τ_a is the time constant, or period, of the actuator.

Besides the dynamics of the actuator physical response, it should also be considered that both, the electric and the mechanical components of any actuator have physical limits depending on their design. The two most common limits that should be accounted for correspond to: the range of action that can be attained by the actuator (magnitude limit) and the rate at which this range can be achieved (rate limit). These physical limits are in fact input saturations as described in Section 1.3 (see page 39).

Consider the maximum value $L_{\delta+}$ and the minimum value $L_{\delta-}$ for the deflection of the control surface achieved by the actuator, where

$$|L_{\delta+}| \neq |L_{\delta-}| \tag{D.6}$$

In the case of first-order actuator representation, to generate a valid control signal that lies within the magnitude saturation $L_{\delta-} \leq \delta_r \leq L_{\delta+}$ and the rate saturation $|\dot{\delta}_{r_s}| \leq L_{\dot{\delta}}$, the commanded value δ_c must verify that

$$\begin{array}{rcl} L_{\delta+} \leq & \delta_c & \leq L_{\delta+} \\ \delta_r - \tau_a L_{\dot{\delta}} \leq & \delta_c & \leq \delta_r + \tau_a L_{\dot{\delta}} \end{array} \tag{D.7}$$

Using the operator $sat(\cdot)$, the air vehicle actuator model (D.5) with anti-symmetric magnitude limits can be represented by the interconnection of Figure D.5, and expressed by the following state-space representation:

$$\Sigma_A : \left\{ \begin{array}{rcl} \dot{\delta}_{r_s} & = & sat_{L_{\dot{\delta}}}\left(\frac{1}{\tau_a}(\delta_c - \delta_{r_s})\right) \\ \delta_r & = & sat_{[L_{\delta+},L_{\delta-}]}(\delta_{r_s}) \end{array} \right. \tag{D.8}$$
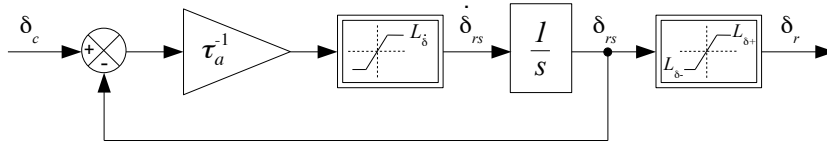
Figure D.5: An air vehicle first-order saturated actuator model.

It should be reminded that the pseudo commands, that contains the signals delivered by the Control System, are redistributed amongst the real aerodynamic control surfaces given the vectors

$$\delta_{pseudo} = \begin{bmatrix} \delta_l & \delta_m & \delta_n \end{bmatrix}^T \quad \text{and} \quad \delta_{real} = \begin{bmatrix} \delta_{re} & \delta_{le} & \delta_{bf} & \delta_{rw} & \delta_{lw} \end{bmatrix}^T \tag{D.9}$$

As presented in equation (5.4) of page 108, the allocation of δ_l and δ_m onto the real control surfaces δ_{re}, δ_{le} and δ_{bf} can be separated into: a simple mechanical mixer of δ_{re} and δ_{le} decoupling the longitudinal effects from the roll lateral effects, and an *a priori* optimized function $\delta_{bf}(\delta_m, \Theta, x)$.

As for the allocation of δ_n onto the winglets δ_{lw} and δ_{rw}, it is based mainly geometrical characteristics from which moments about the center of gravity of the vehicle are created. The following allocation functions for the winglets were considered in simulation:

$$\delta_{lw} = \max(L_{\delta_n-}, \delta_n) \tag{D.10}$$
$$\delta_{rw} = \min(L_{\delta_n+}, \delta_n) \tag{D.11}$$

where L_{δ_n-} and L_{δ_n+} are inward limits of the winglets that can be chosen as to maximize the control efficiency. In fact, the inward deflection of the winglets has less efficiency than the outward deflection. The effects of the boundary layer of the air flow on the winglets efficiency is considered in the aerodynamic model.

Finally, the table below contains an example of the saturation limits considered for the actuator models δ_{real}, which illustrate the order of grandeur of these physical limits:

Actuator	$\delta_{\mathbf{r}}$ (°)		$\mathbf{L}_{\dot{\delta}}$ (°/s)
	$\mathbf{L}_{\delta-}$	$\mathbf{L}_{\delta+}$	
δ_{le}, δ_{re}	-27	15	6
δ_{bf}	-27	15	2
δ_{lw}	-5	40	35
δ_{rw}	-40	5	35

Table D.6: Physical limits of the control surface actuators.

In the higher hypersonic regime of the reentry mission, in order to protect the elevons in hot flow and the winglets from the generated shock wave (generally for $\mathcal{M} > 20$), more restrictive deflection limitations should be considered, for example:

$$-24° \leq \delta_{re}, \delta_{le} \leq 12° \tag{D.12}$$
$$-12° \leq \delta_{rw}, \delta_{lw} \leq 12° \tag{D.13}$$

D.2.3 Vehicle related sources of disturbance

In simulation, different sources of disturbance associated with the reentry vehicle modelling were taken into account.

The following numerical values, which give an idea of the order of grandeur of these disturbances, were considered and correspond to:
– Aerodynamic coefficient modelling errors. These are represented as multiplicative or additive uncertainties depending on each case.

	$\mathbf{C_{m0}}$	$\mathbf{C_{m\delta_m}}$	$\mathbf{C_{m\delta_{bf}}}$	$\mathbf{C_x}$	$\mathbf{C_z}$	$\mathbf{C_{l\delta_l}}$	$\mathbf{C_{n\delta_l}}$	$\mathbf{C_{l\delta_n}}$	$\mathbf{C_{n\delta_n}}$
$\boldsymbol{\Delta}$	±0.0050	$\pm13.3\%$	$\pm13.3\%$	±0.033	±0.033	$\pm20\%$	$\pm20\%$	$\pm13.3\%$	$\pm13.3\%$

Table D.7: Aerodynamic coefficient modelling errors.

– Centring and inertia modelling error as an additive uncertainty: $\Delta y = \pm1\text{cm}$.
– IMU measurement errors. Considering that the white noise vectors $\vec{\mathbf{w}}(t)$ represent a normally distributed random walk of standard deviation σ, and that the vectors $\vec{\mathbf{b}}_m$ represent measurement bias in the following expressions

$$\vec{\boldsymbol{\Gamma}}_m \quad = \quad \vec{\boldsymbol{\Gamma}}(1 + w_\Gamma(t) + b_{m_\Gamma}) + \vec{\mathbf{w}}_\Gamma(t) + \vec{\mathbf{b}}_{m_\Gamma} \tag{D.14}$$

$$\vec{\boldsymbol{\Omega}}_m \quad = \quad \vec{\boldsymbol{\Omega}}(1 + w_\Omega(t) + b_{m_\Omega}) + \vec{\mathbf{w}}_\Omega(t) + \vec{\mathbf{b}}_{m_\Omega} \tag{D.15}$$

where:

	$\sigma_{\boldsymbol{\Gamma}}$ (m/s^2)	$\sigma_{\boldsymbol{\Omega}}$ (rad/s)	$\mathbf{b_{m_\Gamma}}$ (m/s^2)	$\mathbf{b_{m_\Omega}}$ (rad/s)
Value	1×10^{-5}	1×10^{-5}	1×10^{-5}	1×10^{-5}

Table D.8: IMU measurement error values.

– Anemometer unit measurement errors ($\Delta\alpha$, $\Delta\beta$, ΔV_a).

	α (°)	β (°)	$\mathbf{V_a}$ (Kts)
$\boldsymbol{\Delta}$	1	1	5

Table D.9: Anemometer unit measurement error values.

Appendix E

Compilation of simulation results

In this Appendix, simulation results of the control laws that were computed in Section 5.3, at all the flight operating points considered in Table D.4, are presented. Let us begin by making a recapitulation of the control laws computed.

Control Law	nº	Type	Desired Dynamics	Controller
$\delta_{m_c} = g_q^{-1}(K\,\tilde{y} + Hw)$	1	NDI-PI #1	Table 5.2	Table 5.3
	2	NDI-PI #2	Table 5.2	Table 5.4
	3	NDI-PI #3	Table 5.2	Table 5.5
	4	NDI-PI #4	Table 5.6	Table 5.7
	5	NDI-PI #5	Table 5.8	Table 5.9
$\delta_{m_c} = \lambda_q^{-1}\,K_{long}(s)\,\tilde{y}$	6	NLC-$\mathcal{H}_\infty$ #1	Table 5.8	Table 5.10
	7	NLC-$\mathcal{H}_\infty$ #2	Table 5.8	Table 5.11
$\delta_{m_c} = \lambda_q^{-1}\,\tilde{K}_{a_{long}}(s)\begin{bmatrix} v \\ \tilde{y} \end{bmatrix}$ $v = J_{long}(s)\,u_{AW}$	8	NLC-$\mathcal{H}_\infty$ #2 + AW	Table 5.8	Table 5.12
$\begin{bmatrix} \delta_{l_c} \\ \delta_{n_c} \end{bmatrix} = G_2^{-1}(K\,\tilde{y} + Hw)$	9	NDI-PI #6	Table 5.18	Table 5.19
$\begin{bmatrix} \delta_{l_c} \\ \delta_{n_c} \end{bmatrix} = \Lambda^{-1}\,K_{lat}(s)\,\tilde{y}$	10	NLC-$\mathcal{H}_\infty$ #3	Table 5.18	Table 5.20
	11	NLC-$\mathcal{H}_\infty$ #4	Table 5.18	Table 5.21
$\begin{bmatrix} \delta_{l_c} \\ \delta_{n_c} \end{bmatrix} = \Lambda^{-1}\,\tilde{K}_{a_{lat}}(s)\begin{bmatrix} v \\ \tilde{y} \end{bmatrix}$ $v = J_{lat}(s)\,u_{AW}$	12	NLC-$\mathcal{H}_\infty$ #4 + AW	Table 5.18	Table 5.22

Table E.1: Recapitulation of computed controllers.

By keeping only the most representative solutions computed using the standard NDI procedure and the generalized NLC framework, the table below contains an index of the simulation conditions

and results for the whole flight domain considered in this work.

Controller		Simulation conditions			Pages
nº	**Type**	**Model Uncertainty**	**Saturated Actuator**	**Wind Disturbance**	
2	NDI-PI #2	$\checkmark$	$\checkmark$	-	265 - 272
5	NDI-PI #5	$\checkmark$	$\checkmark$	-	273 - 280
6	NLC-$\mathcal{H}_\infty$ #1	$\checkmark$	$\checkmark$	-	281 - 288
7	NLC-$\mathcal{H}_\infty$ #2	$\checkmark$	$\checkmark$	-	289 - 296
8	NLC-$\mathcal{H}_\infty$ #2 + AW	$\checkmark$	$\checkmark$	-	297 - 304
8	NLC-$\mathcal{H}_\infty$ #2 + AW	$\checkmark$	$\checkmark$	$\checkmark$	305 - 312
9	NDI-PI #6	$\checkmark$	$\checkmark$	-	313 - 320
10	NLC-$\mathcal{H}_\infty$ #3	$\checkmark$	$\checkmark$	-	325 - 328
11	NLC-$\mathcal{H}_\infty$ #4	$\checkmark$	$\checkmark$	-	321 - 324
12	NLC-$\mathcal{H}_\infty$ #4 + AW	$\checkmark$	$\checkmark$	-	329 - 336
12	NLC-$\mathcal{H}_\infty$ #4 + AW	$\checkmark$	$\checkmark$	$\checkmark$	337 - 344

Table E.2: Index of simulation results.

The saturated actuator model used on each actual control surface δ_{real} of the reentry vehicle can be found in Appendix D.2.2, while the wind profile description is detailed in Appendix D.1.2.

E.1 Results on the longitudinal axis

E.1.1 NDI-PI controller simulation results
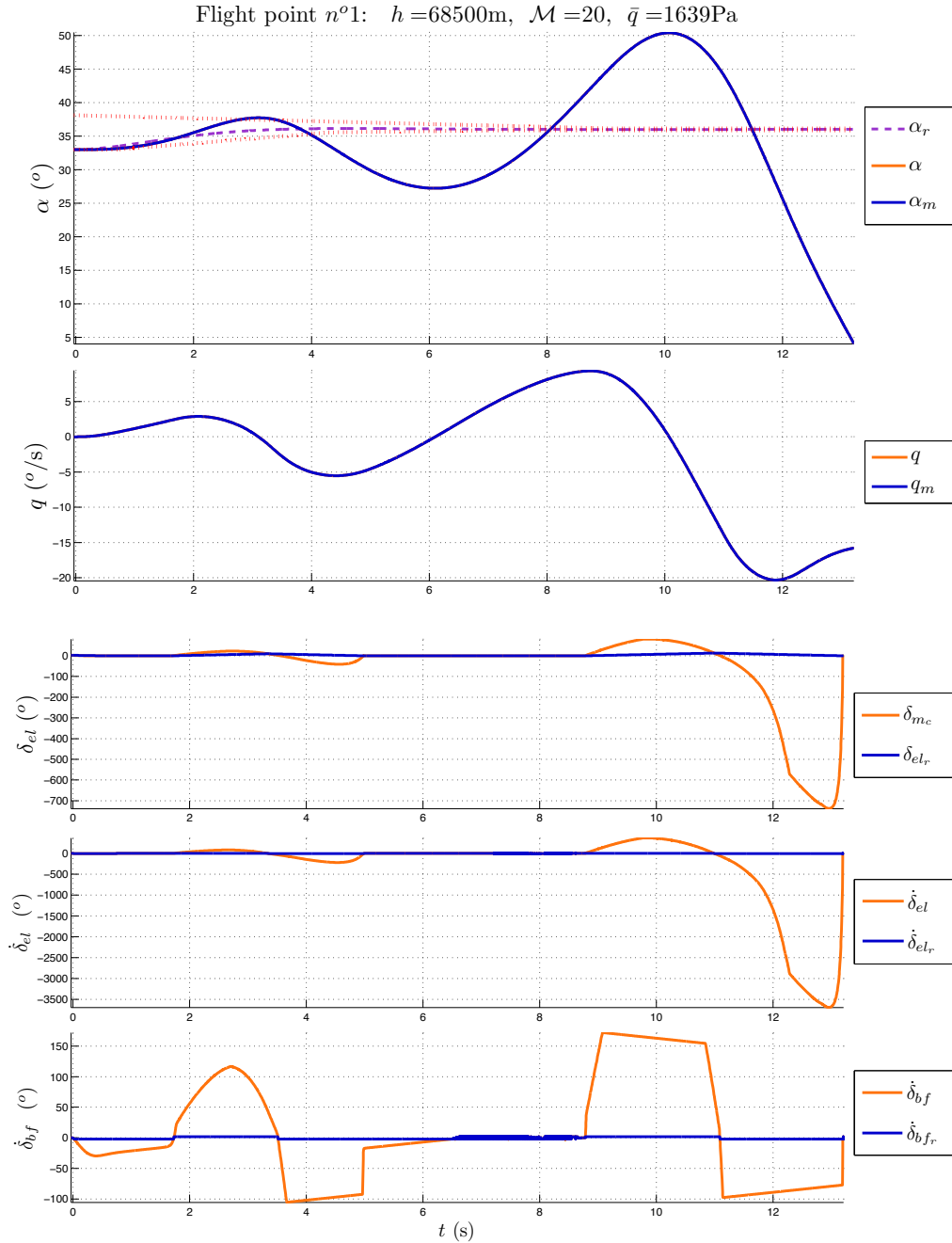
Figure E.1: Simulation with saturated actuator and controller **n°2**.
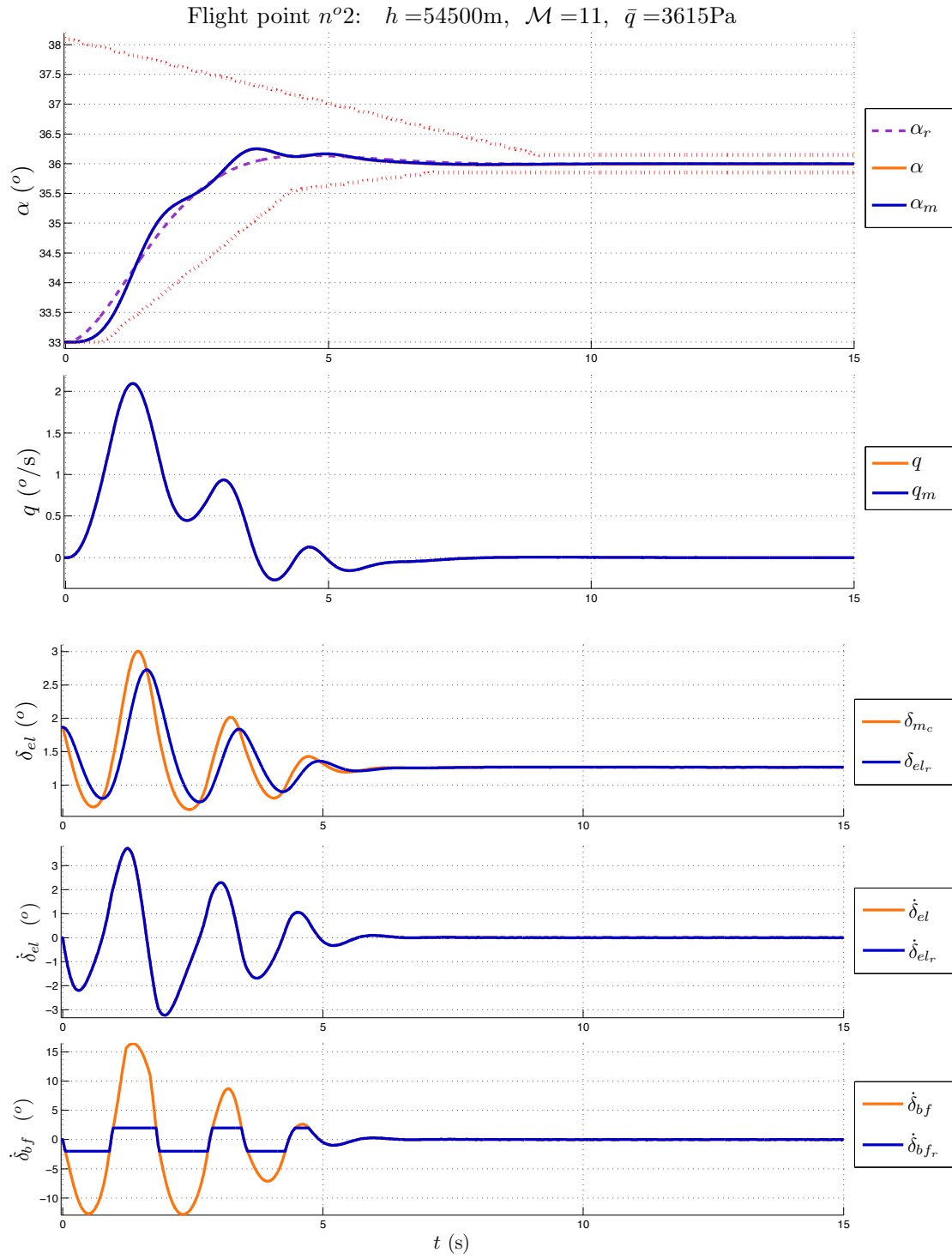
Figure E.2: Simulation with saturated actuator and controller **n°2**.
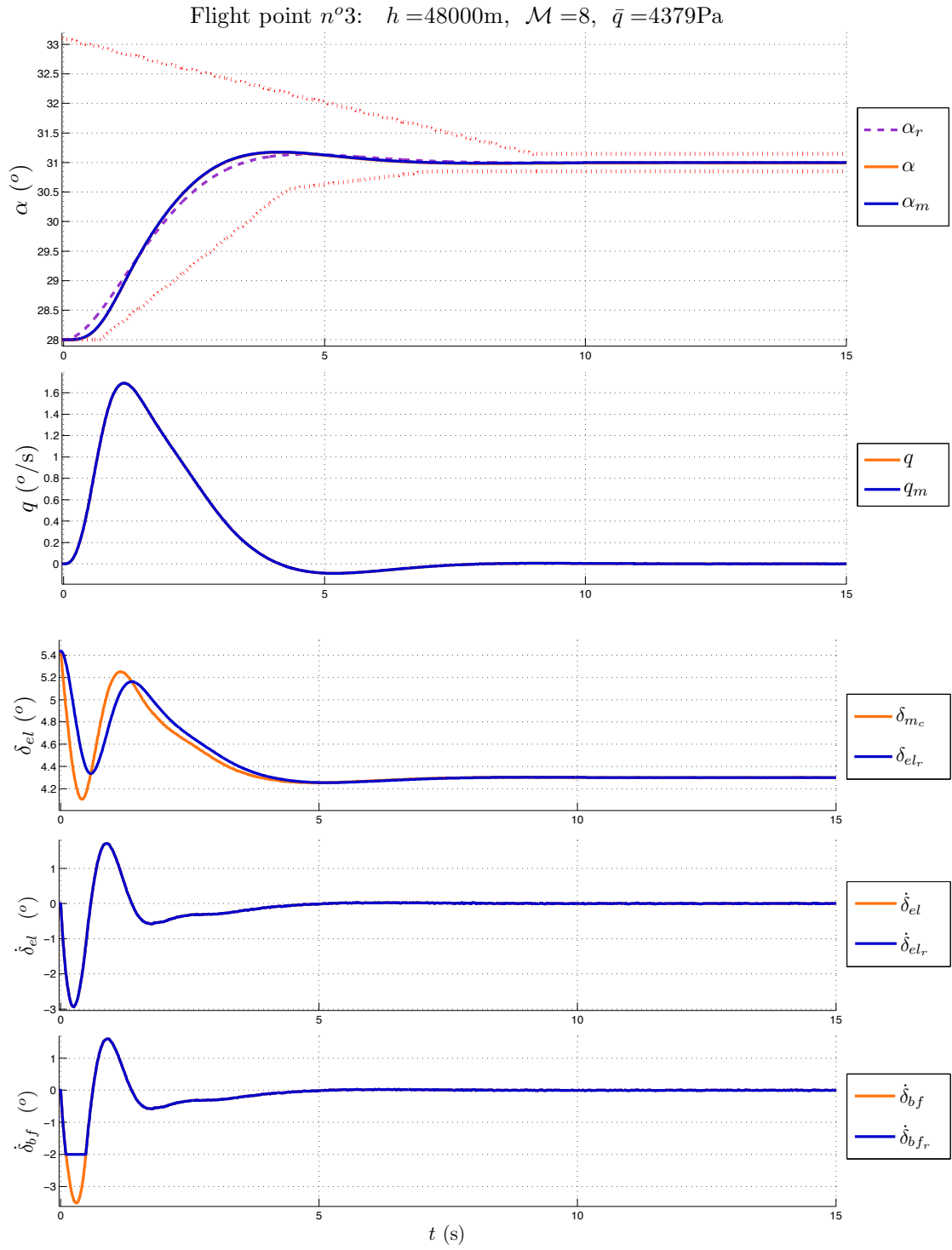
Figure E.3: Simulation with saturated actuator and controller **n°2**.
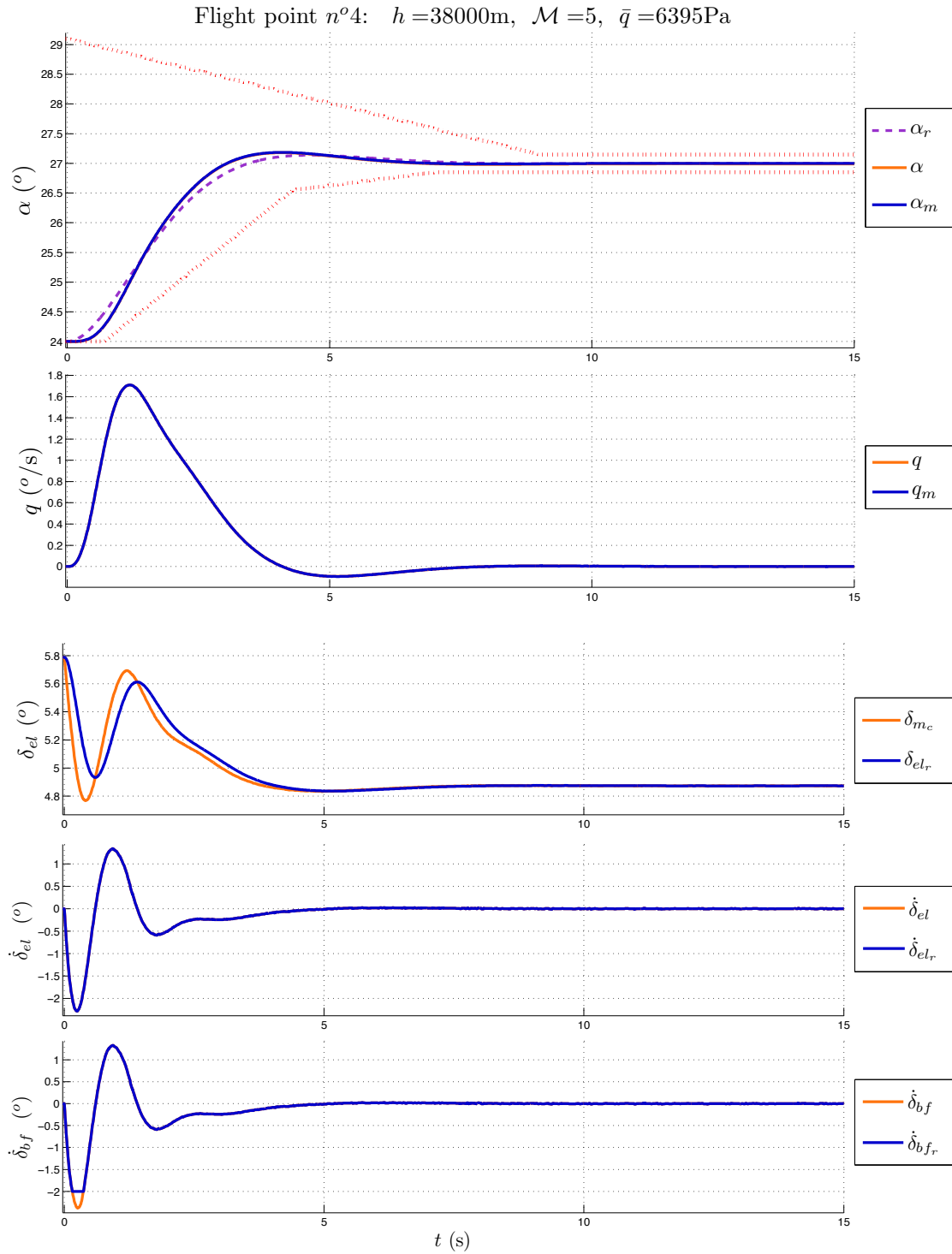
Figure E.4: Simulation with saturated actuator and controller **n°2**.
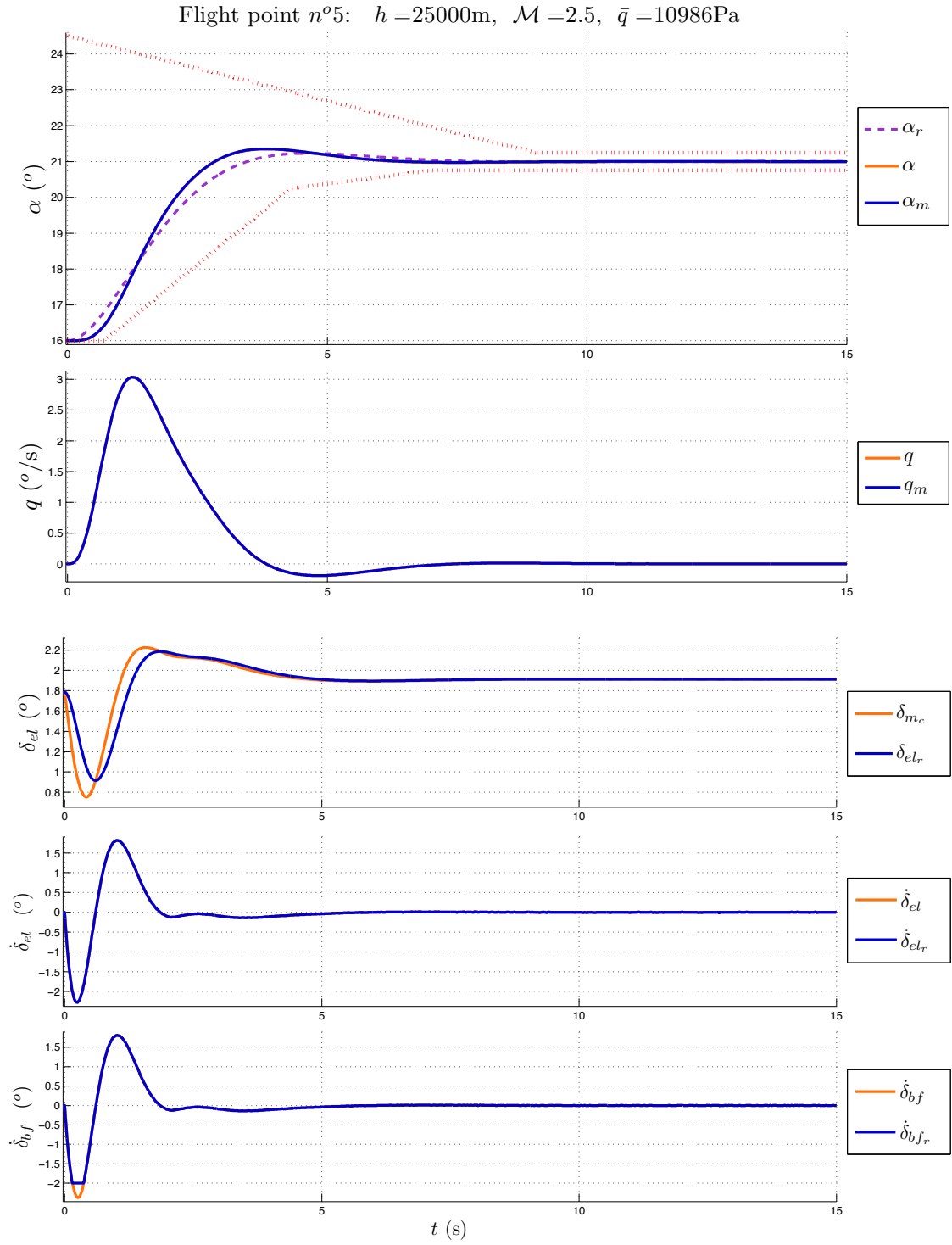
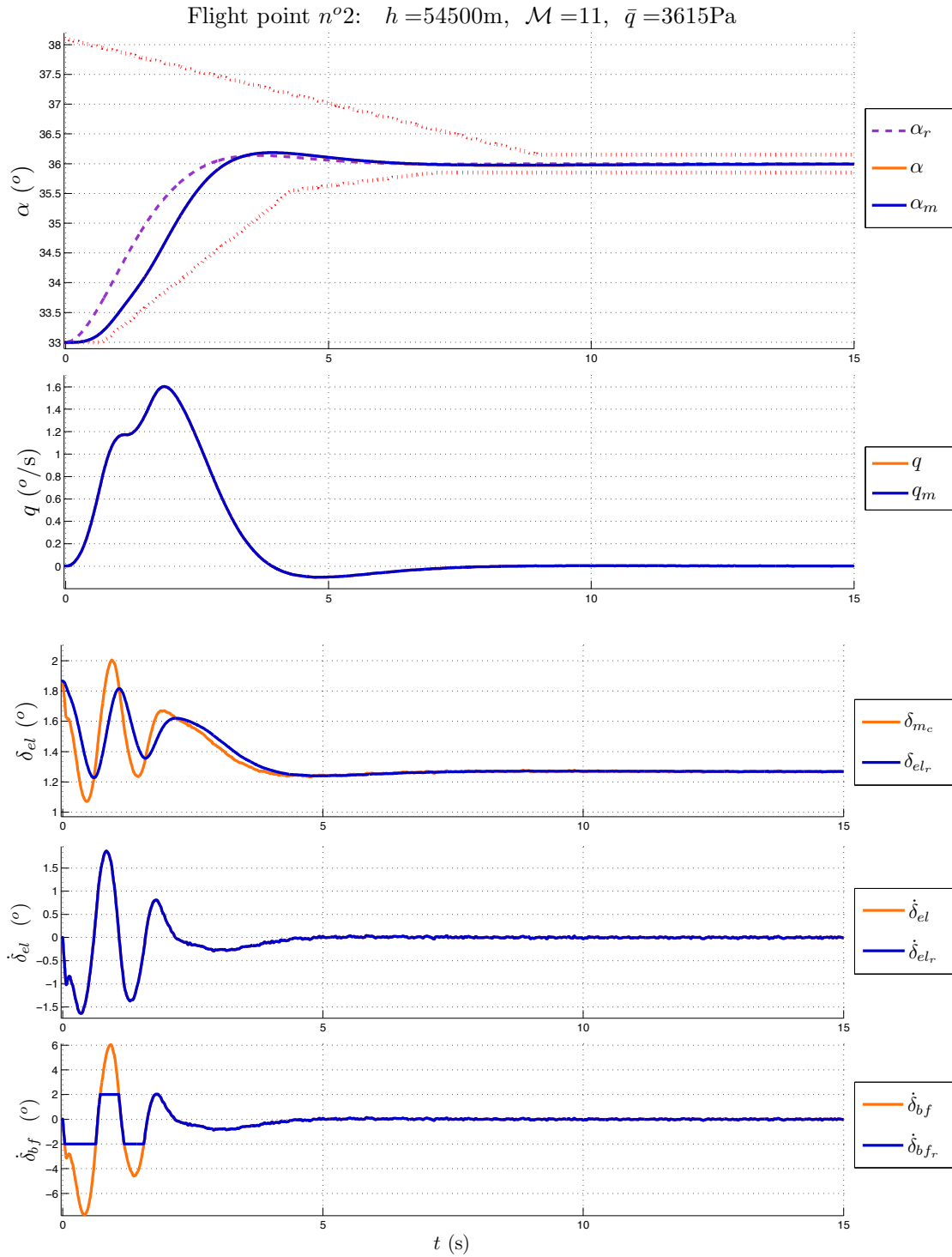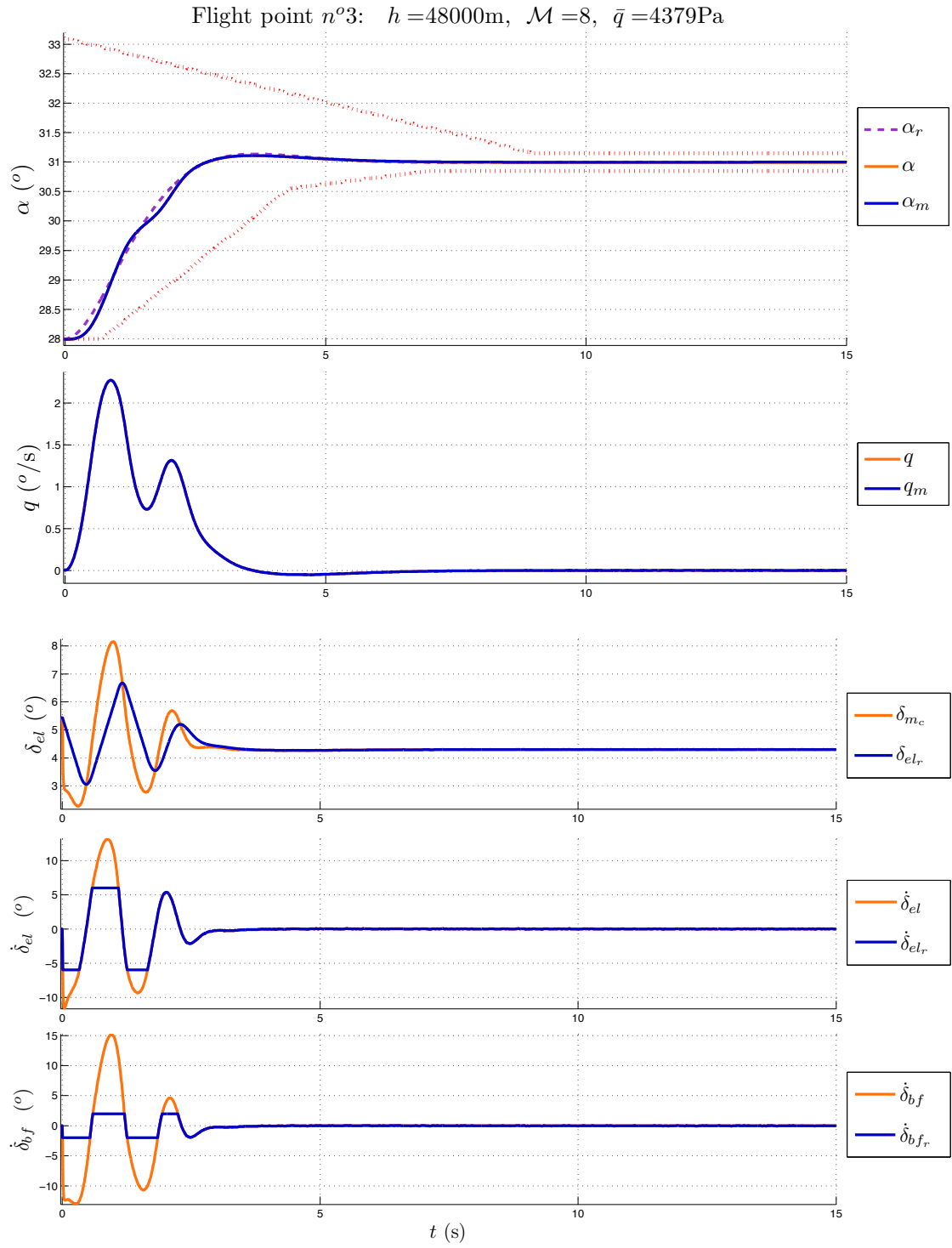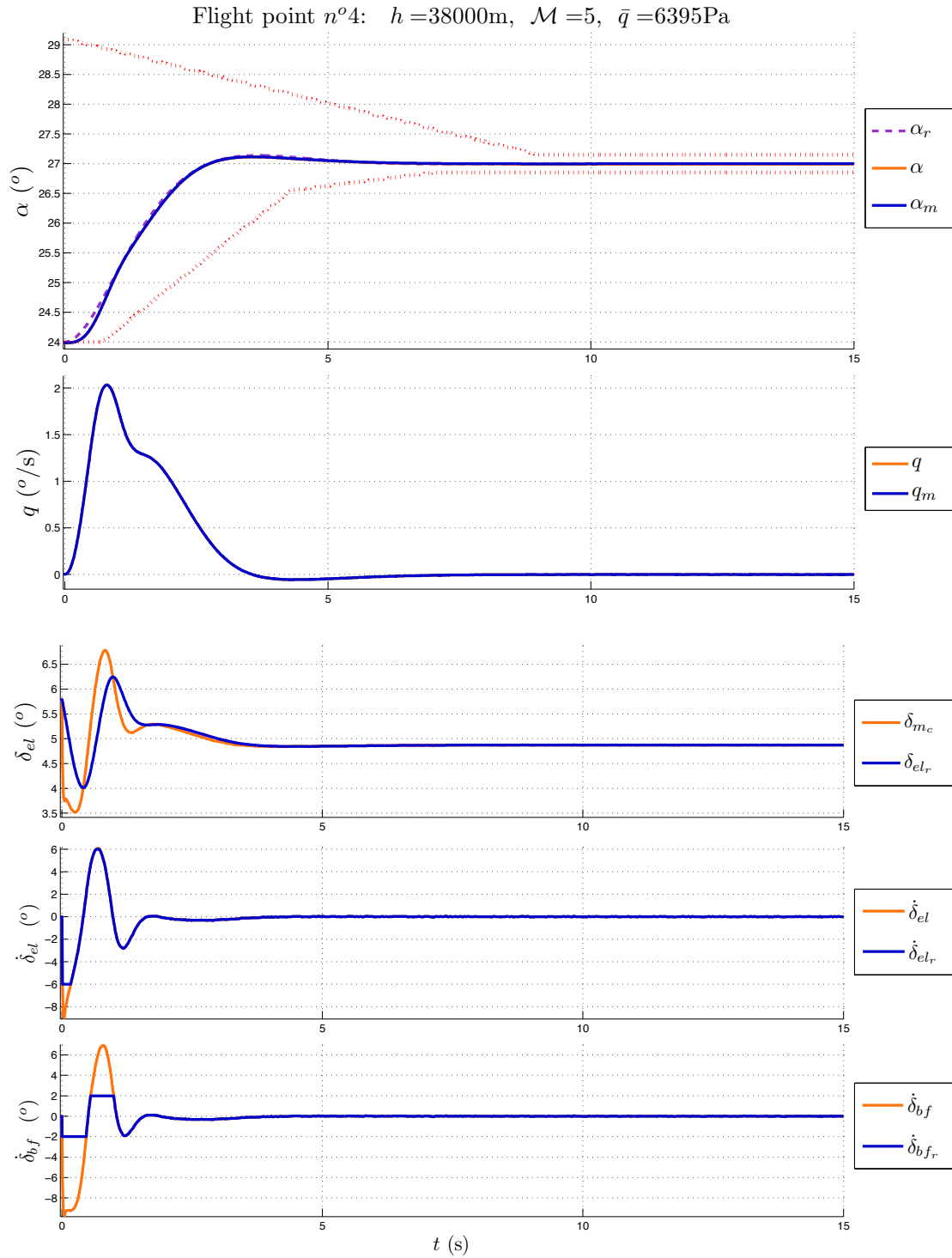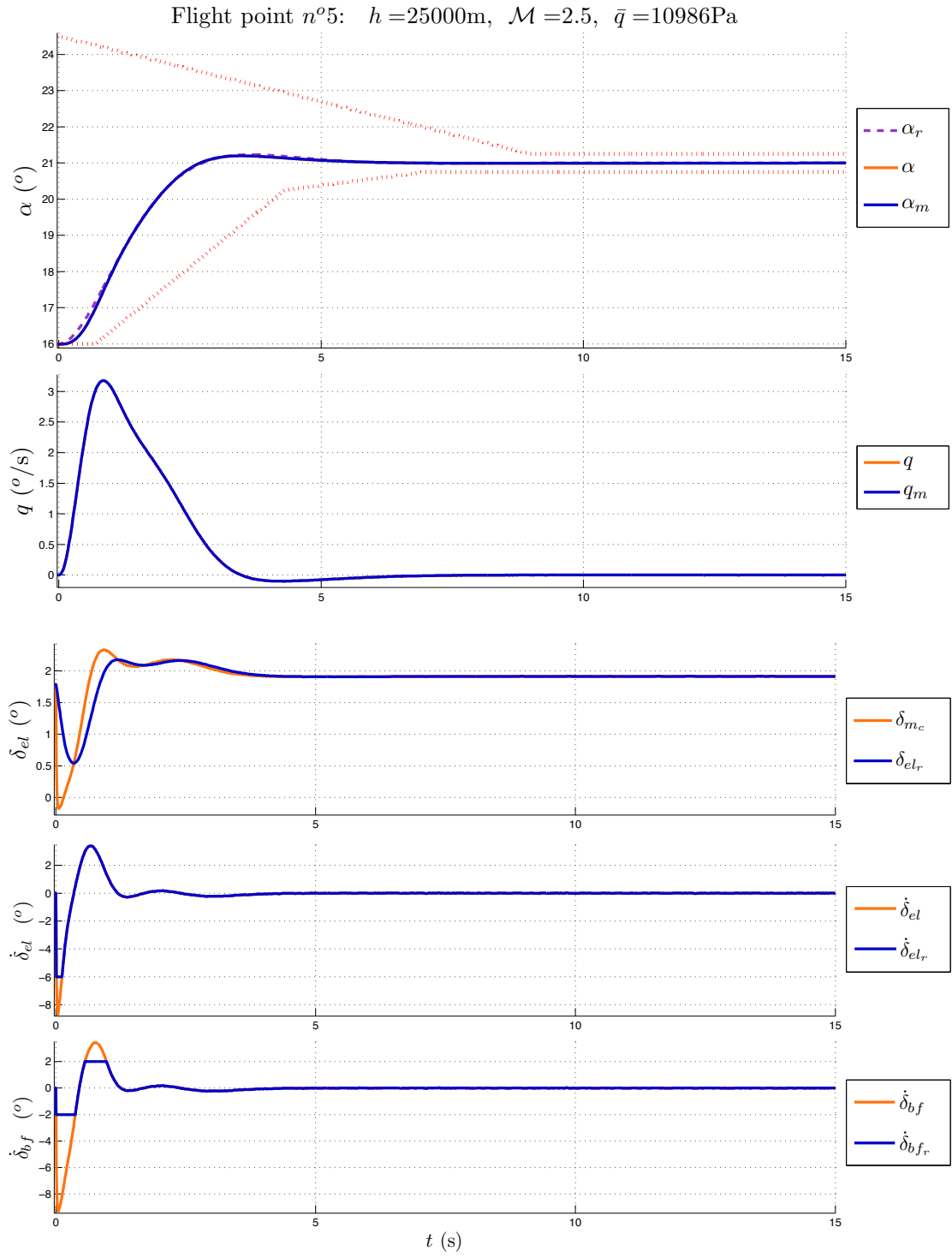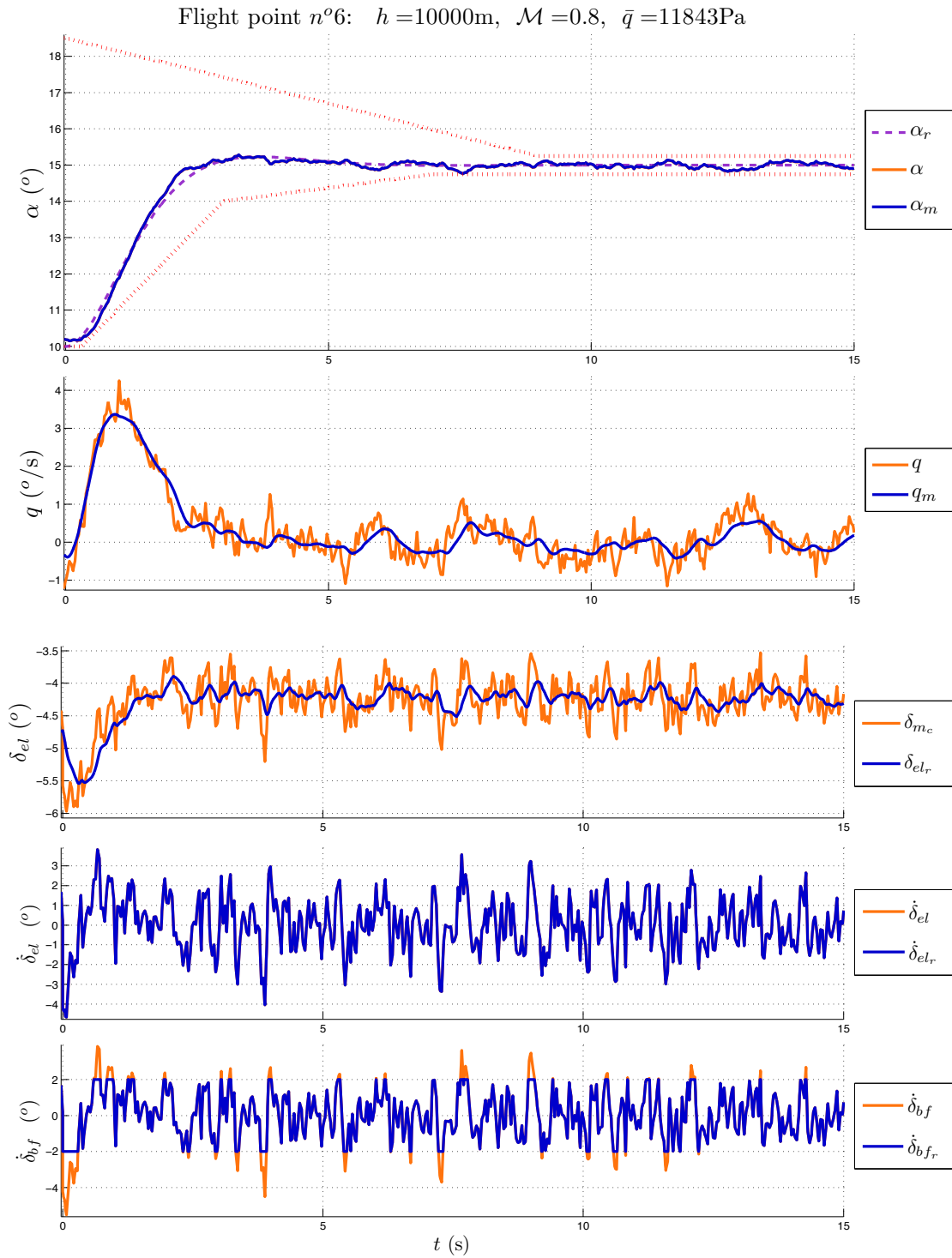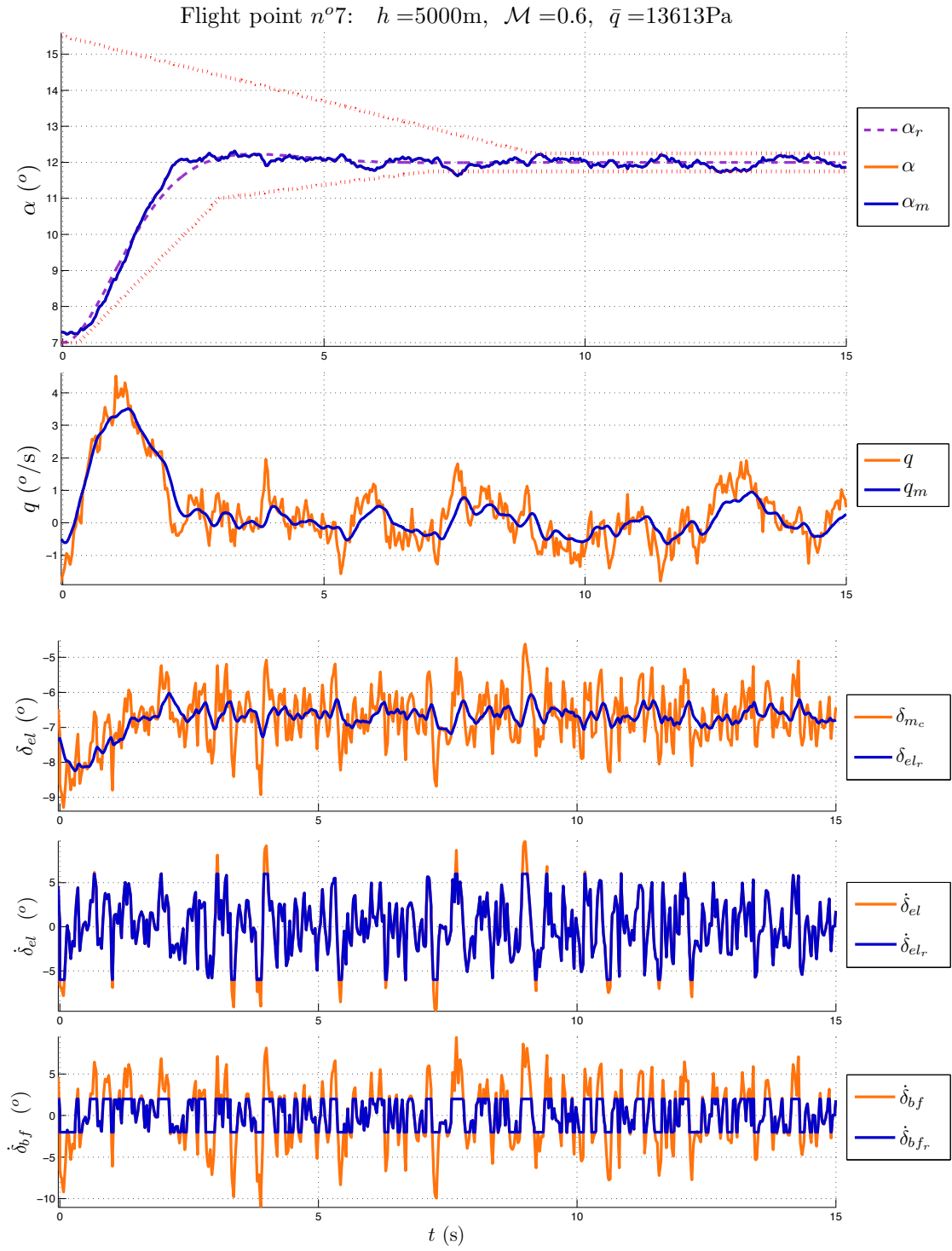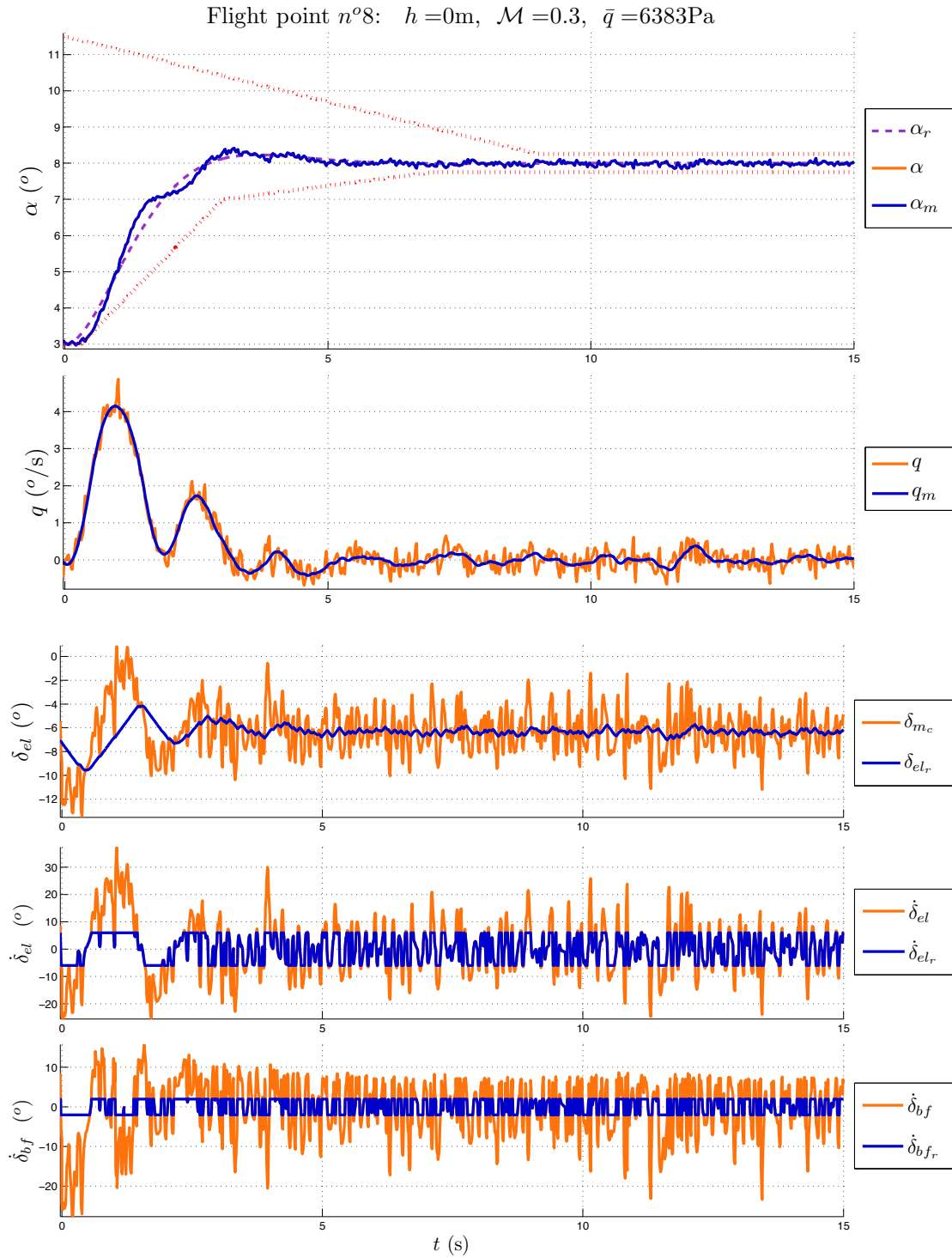Figure E.5: Simulation with saturated actuator and controller **n°2**.
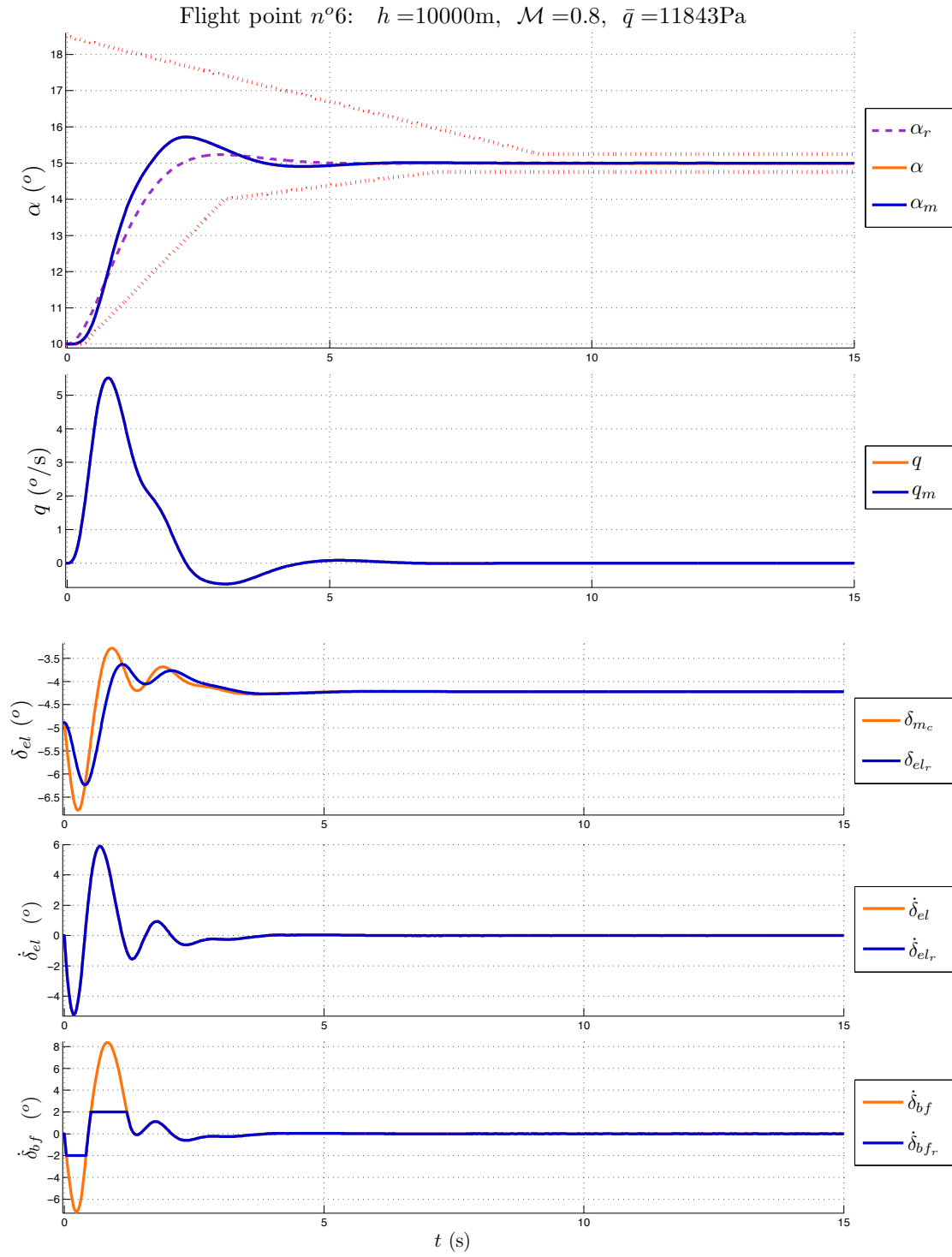
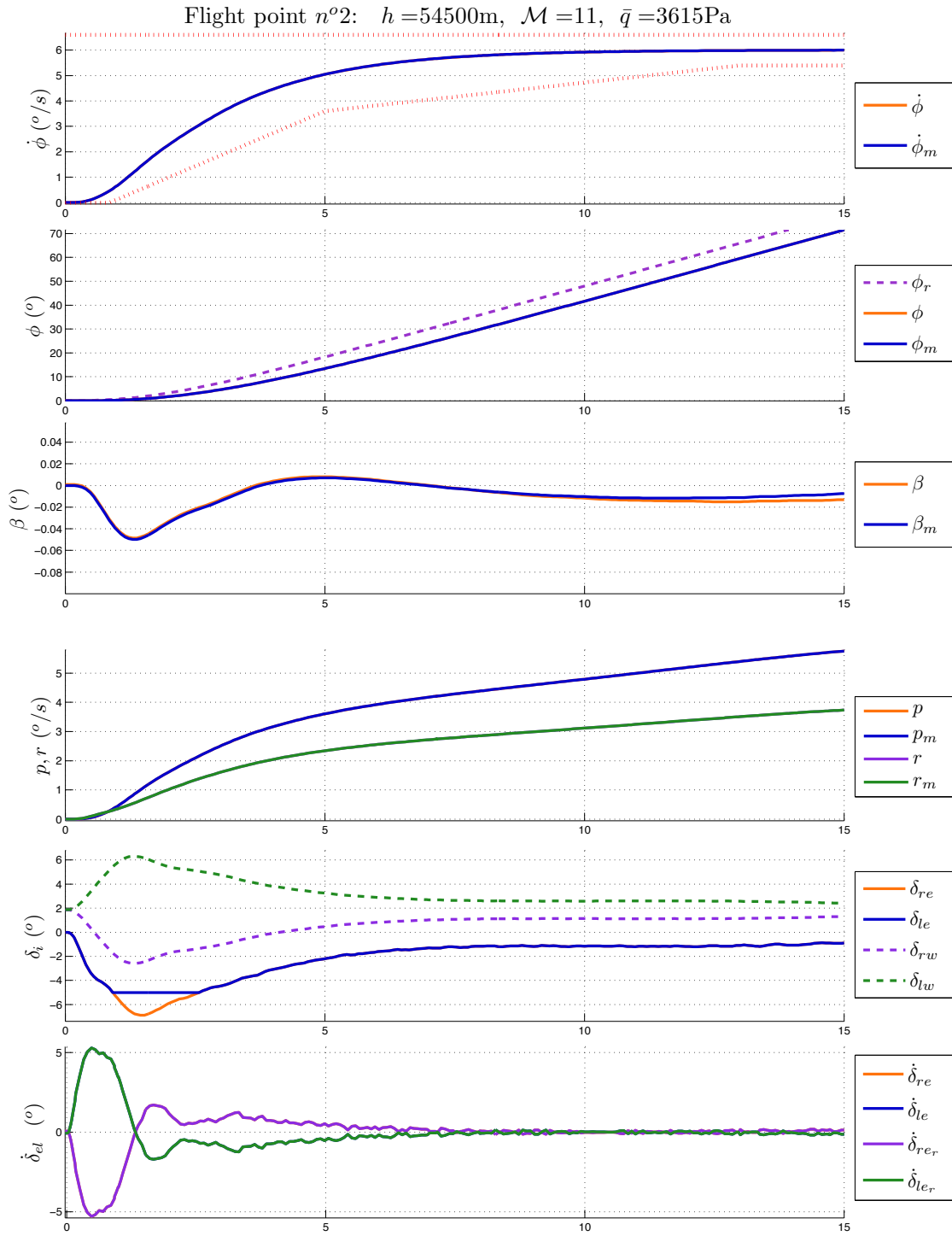Figure E.6: Simulation with saturated actuator and controller **nº2**.
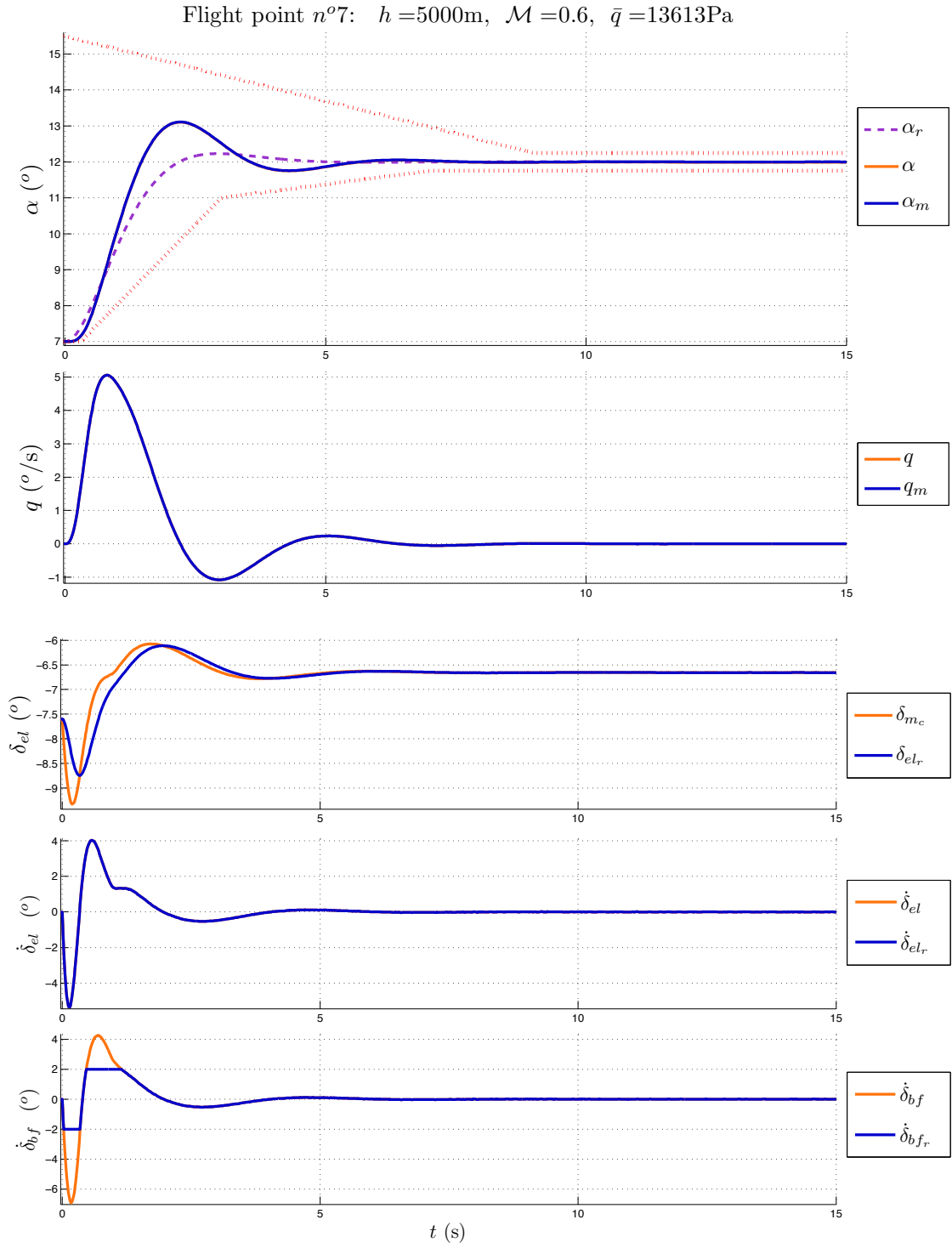
Figure E.7: Simulation with saturated actuator and controller **nº2**.

Flight point $n^o 8$: $\quad h = 0$m, $\quad \mathcal{M} = 0.3$, $\quad \bar{q} = 6383$Pa
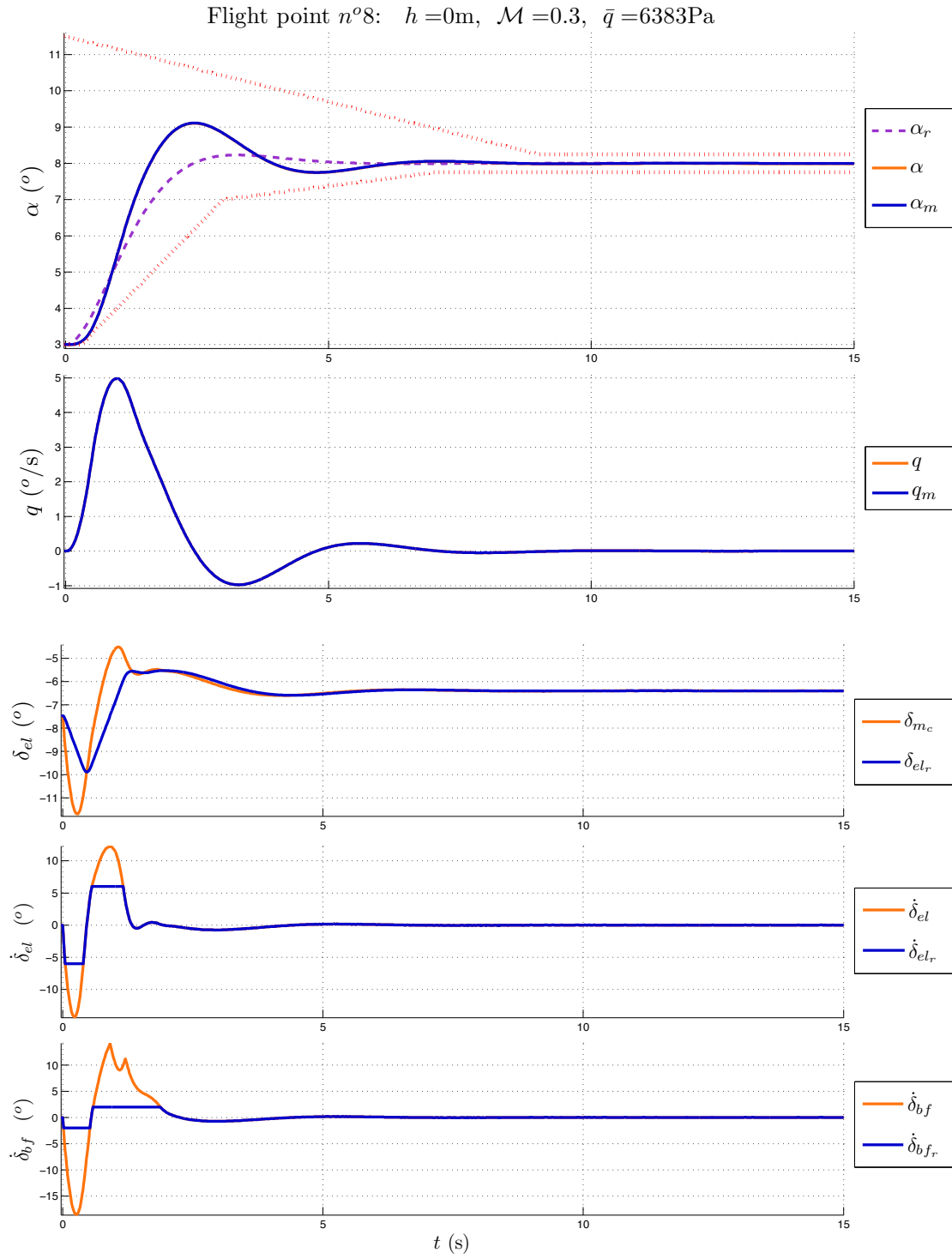
Figure E.8: Simulation with saturated actuator and controller **n°2**.
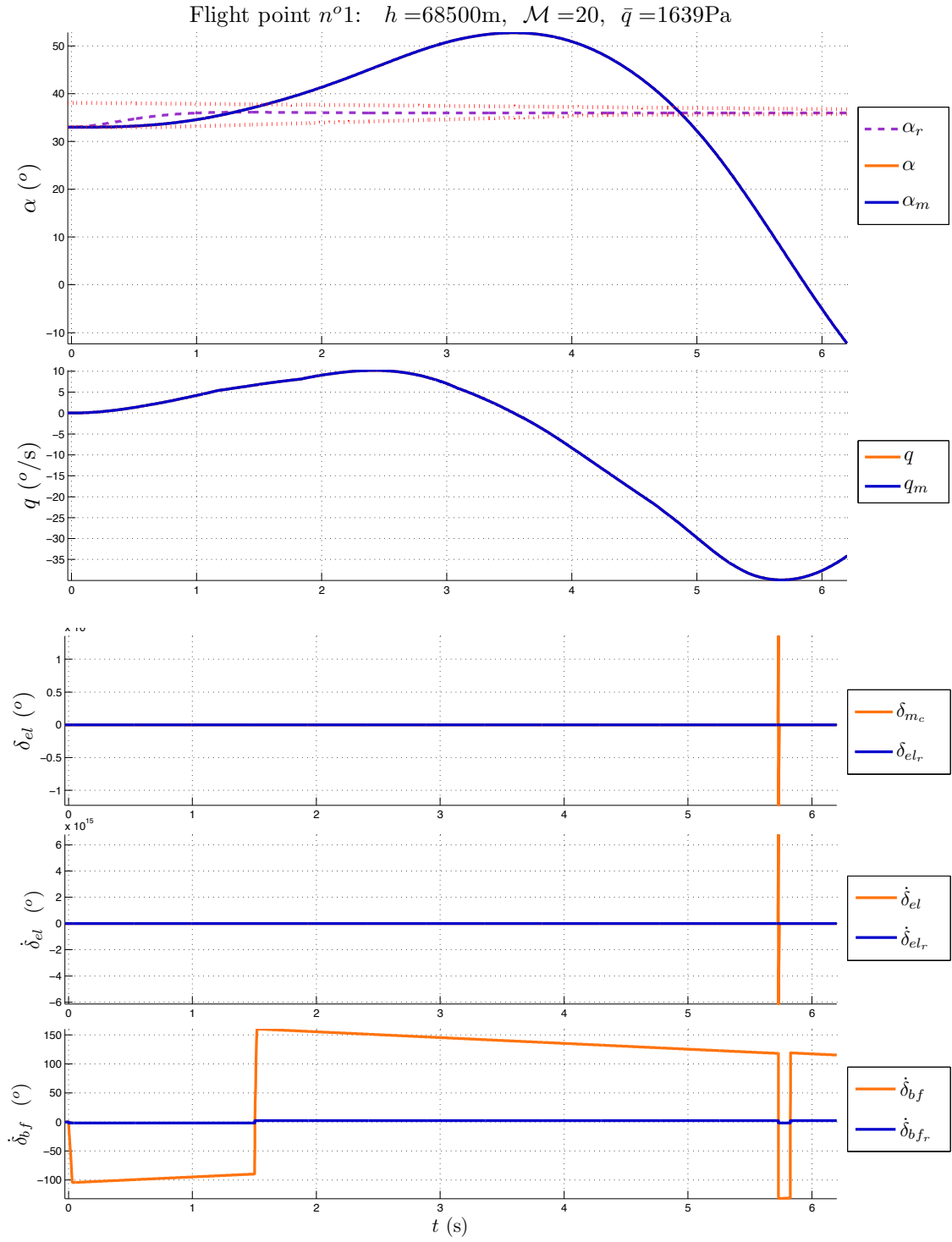
Figure E.9: Simulation with saturated actuator and controller **n°5**.
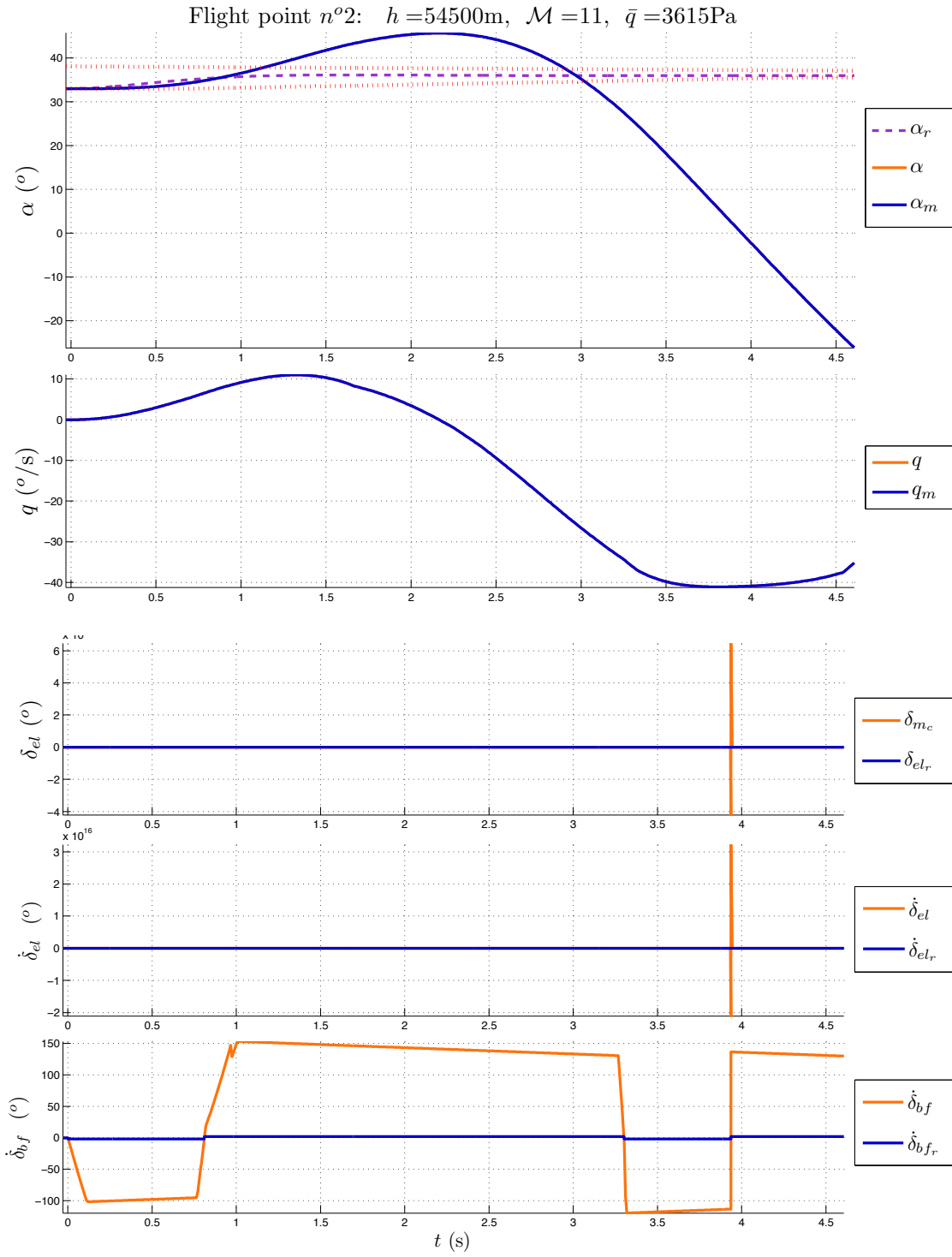
Figure E.10: Simulation with saturated actuator and controller **n°5**.
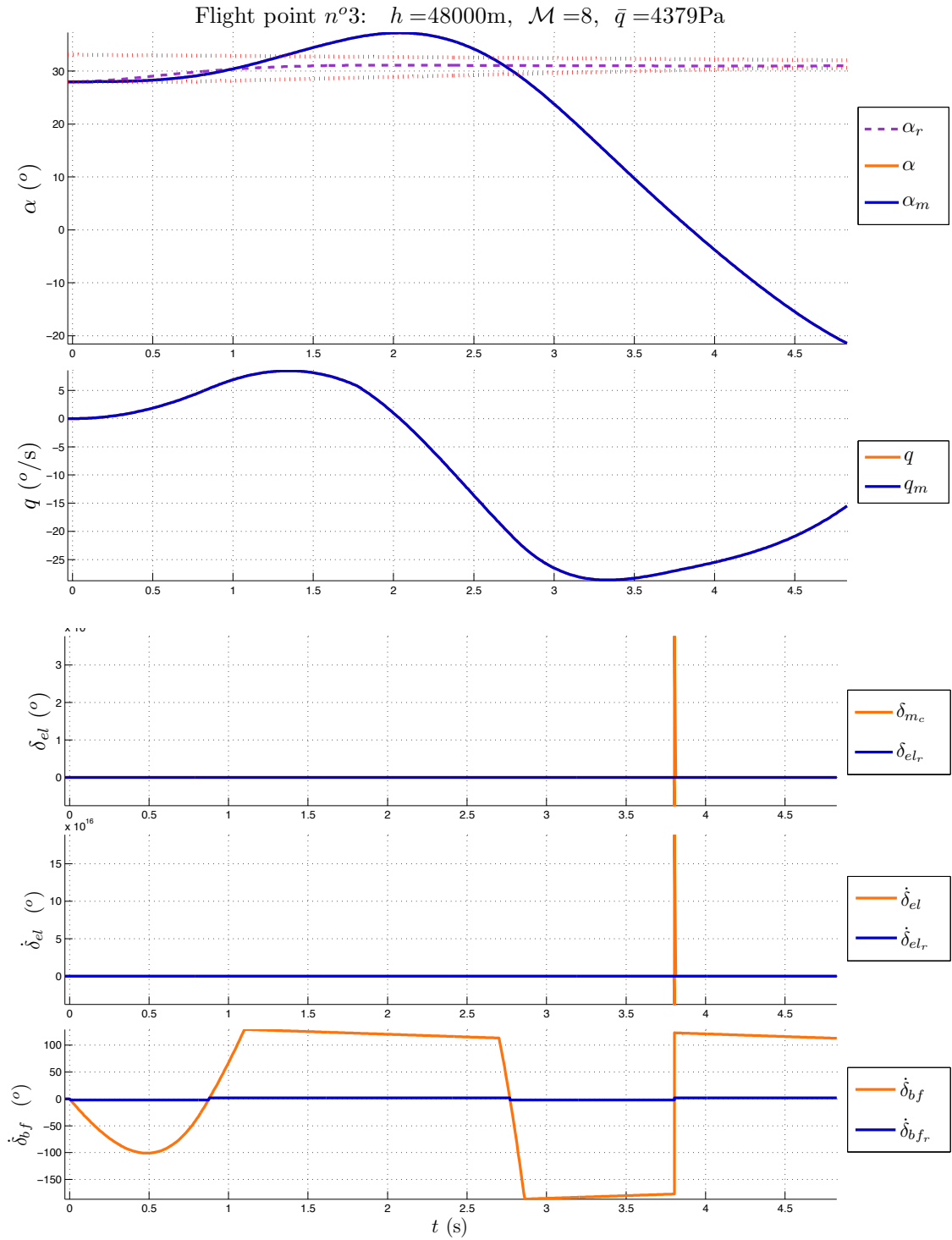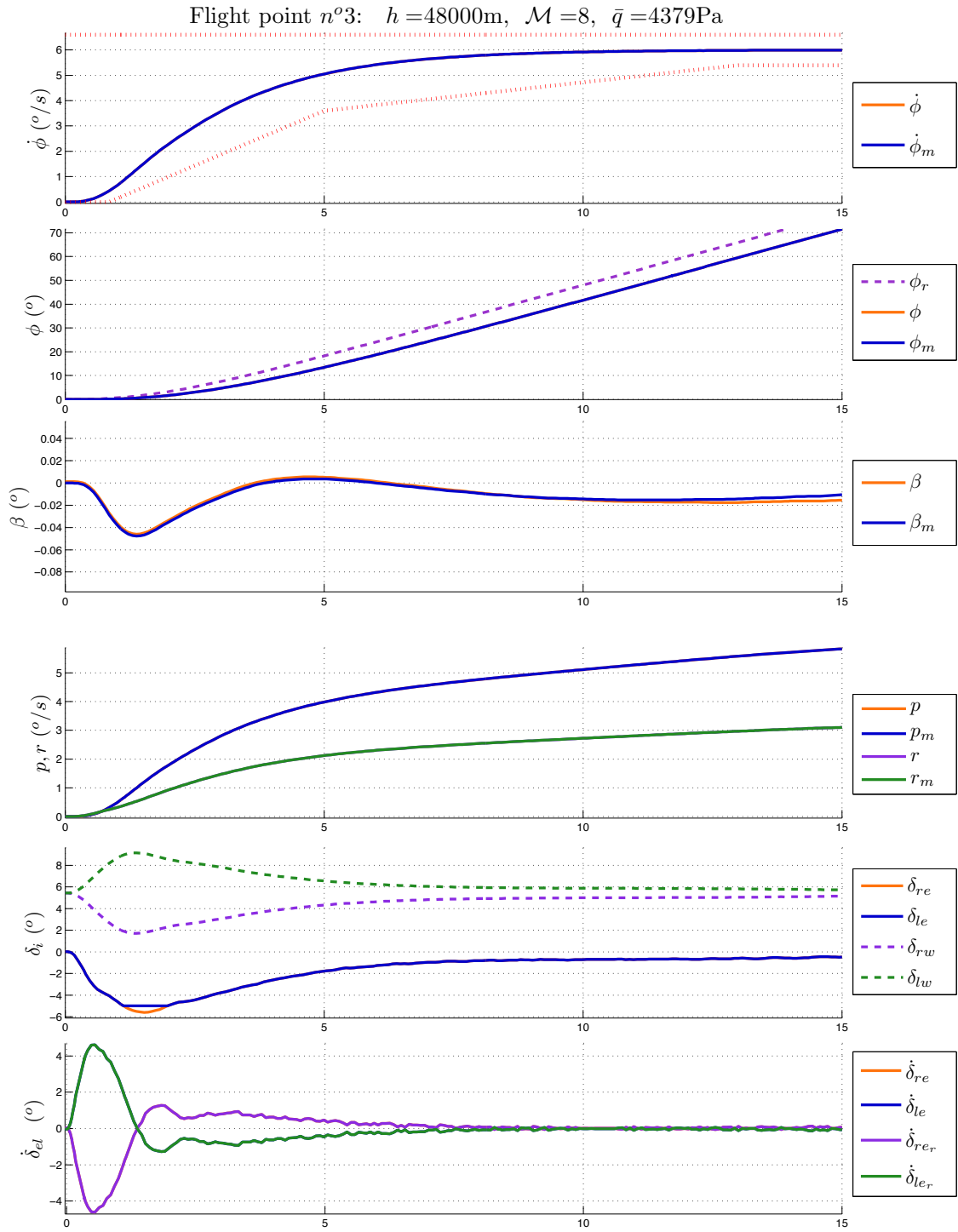
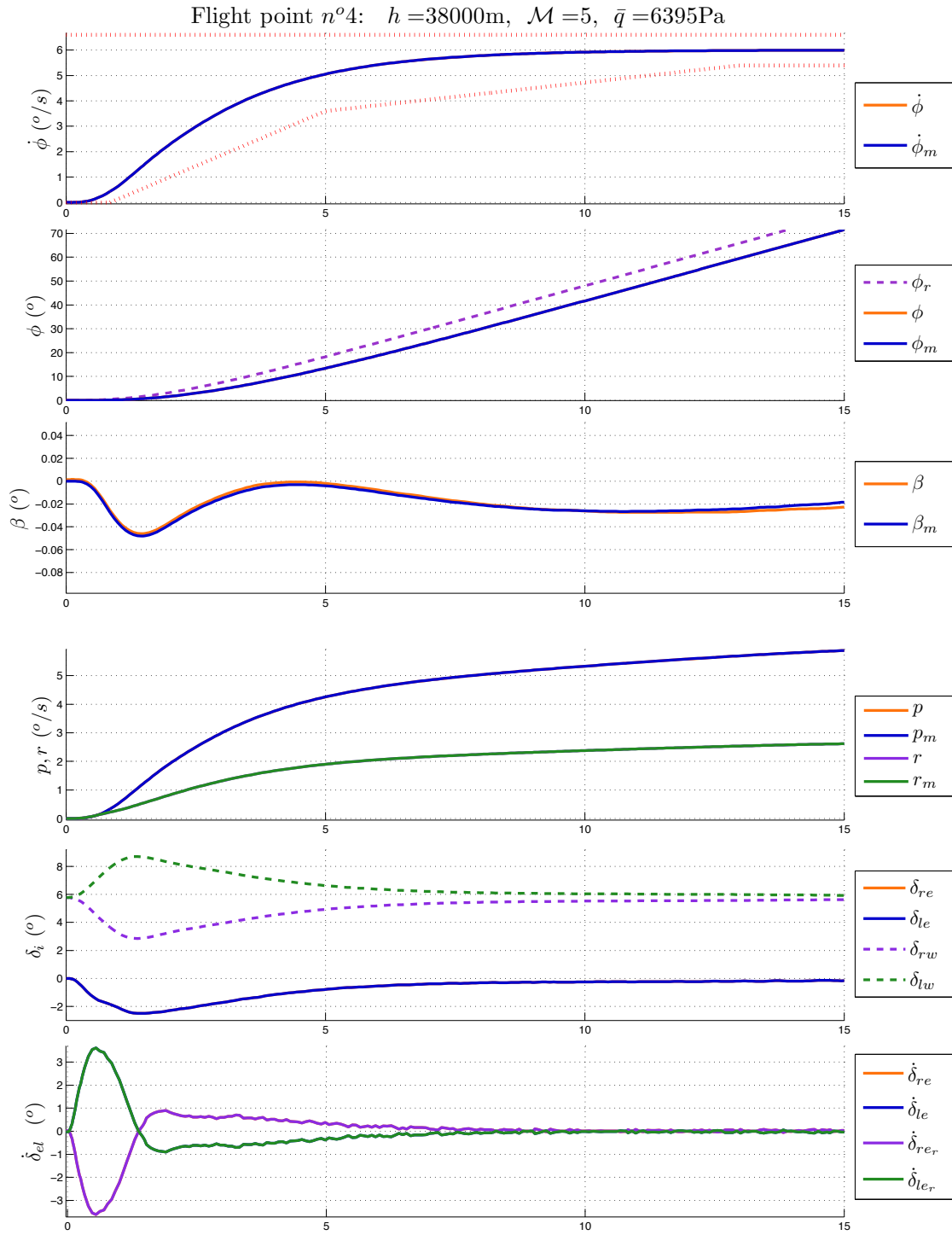Figure E.11: Simulation with saturated actuator and controller **nº5**.
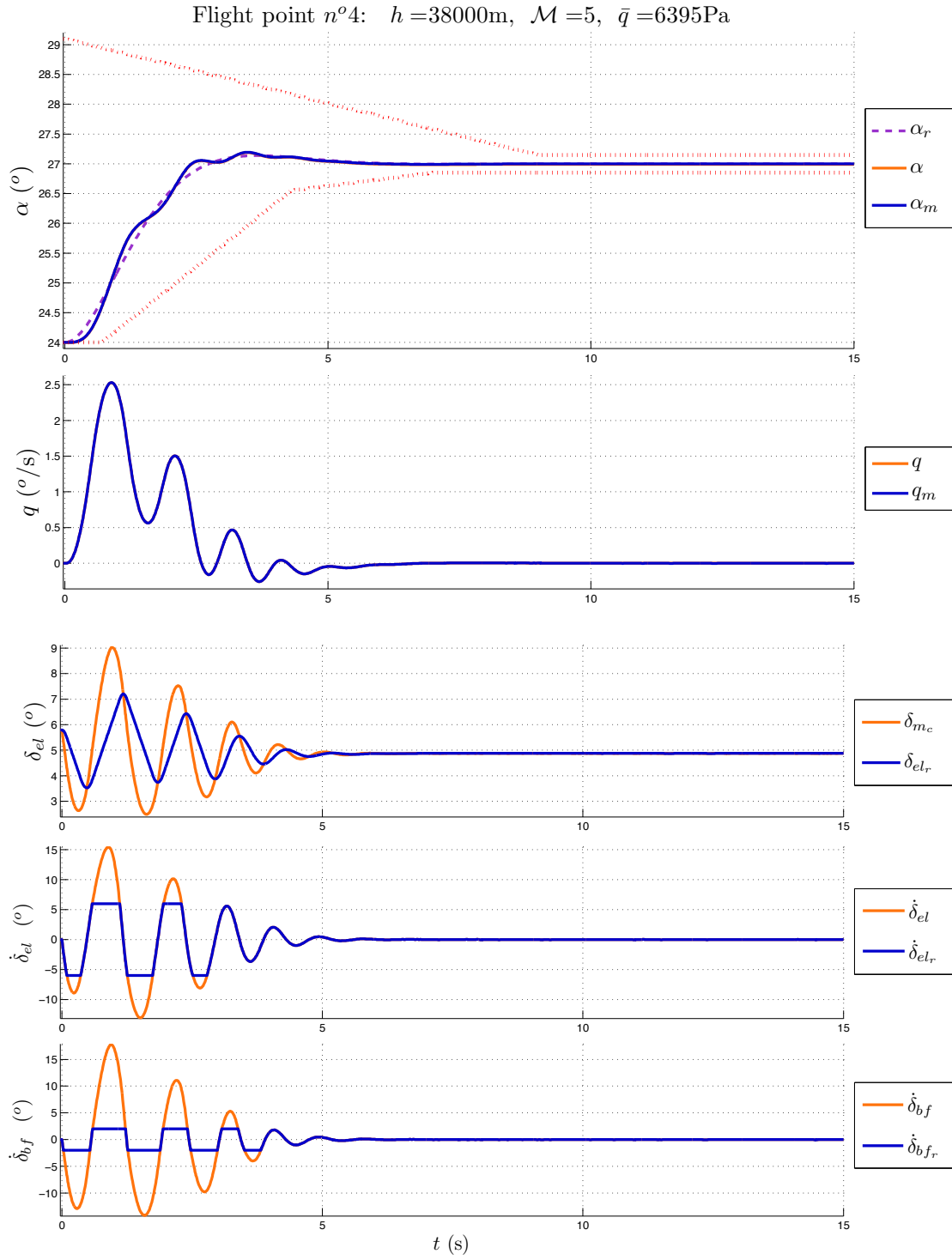
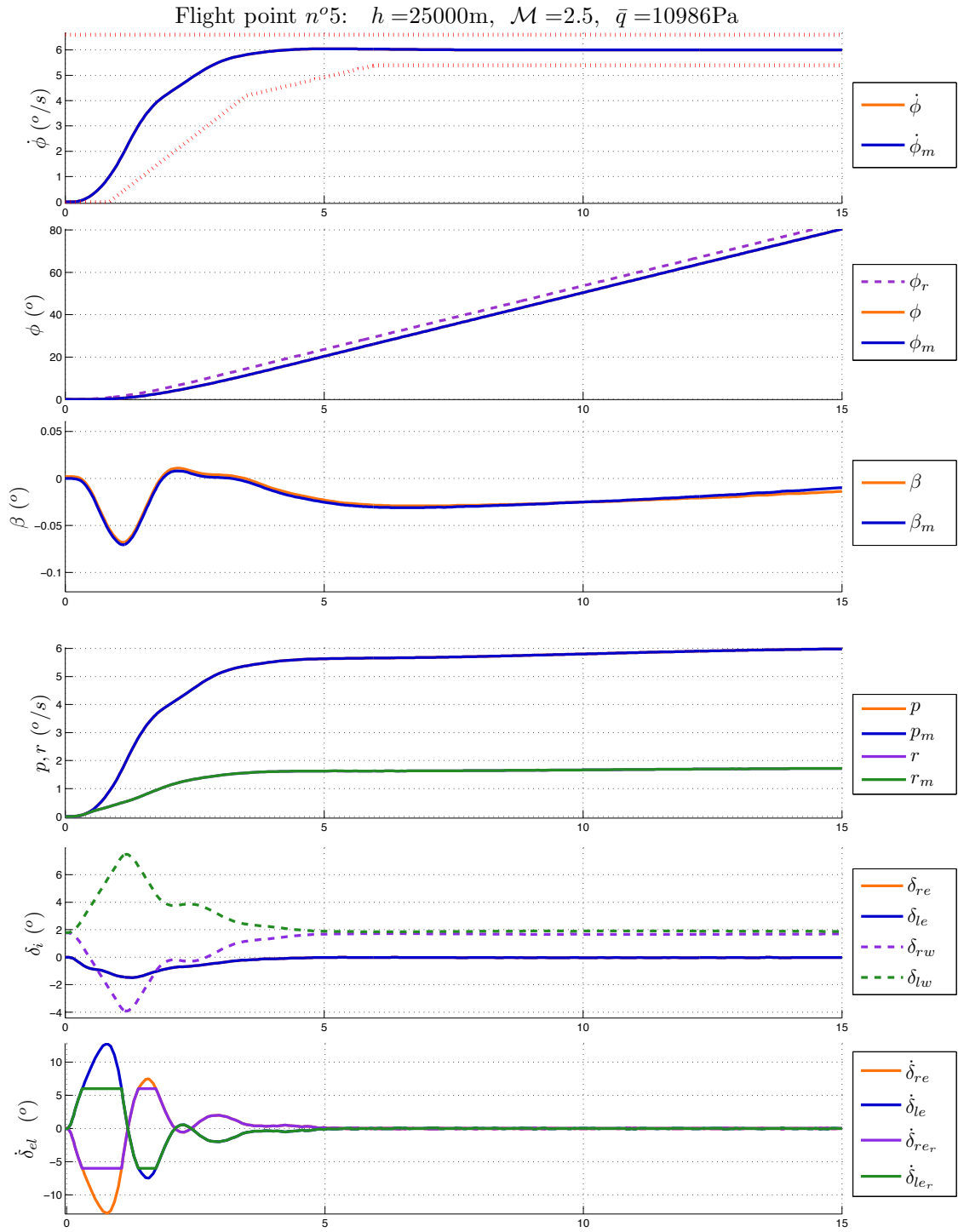Figure E.12: Simulation with saturated actuator and controller **nᵒ5**.
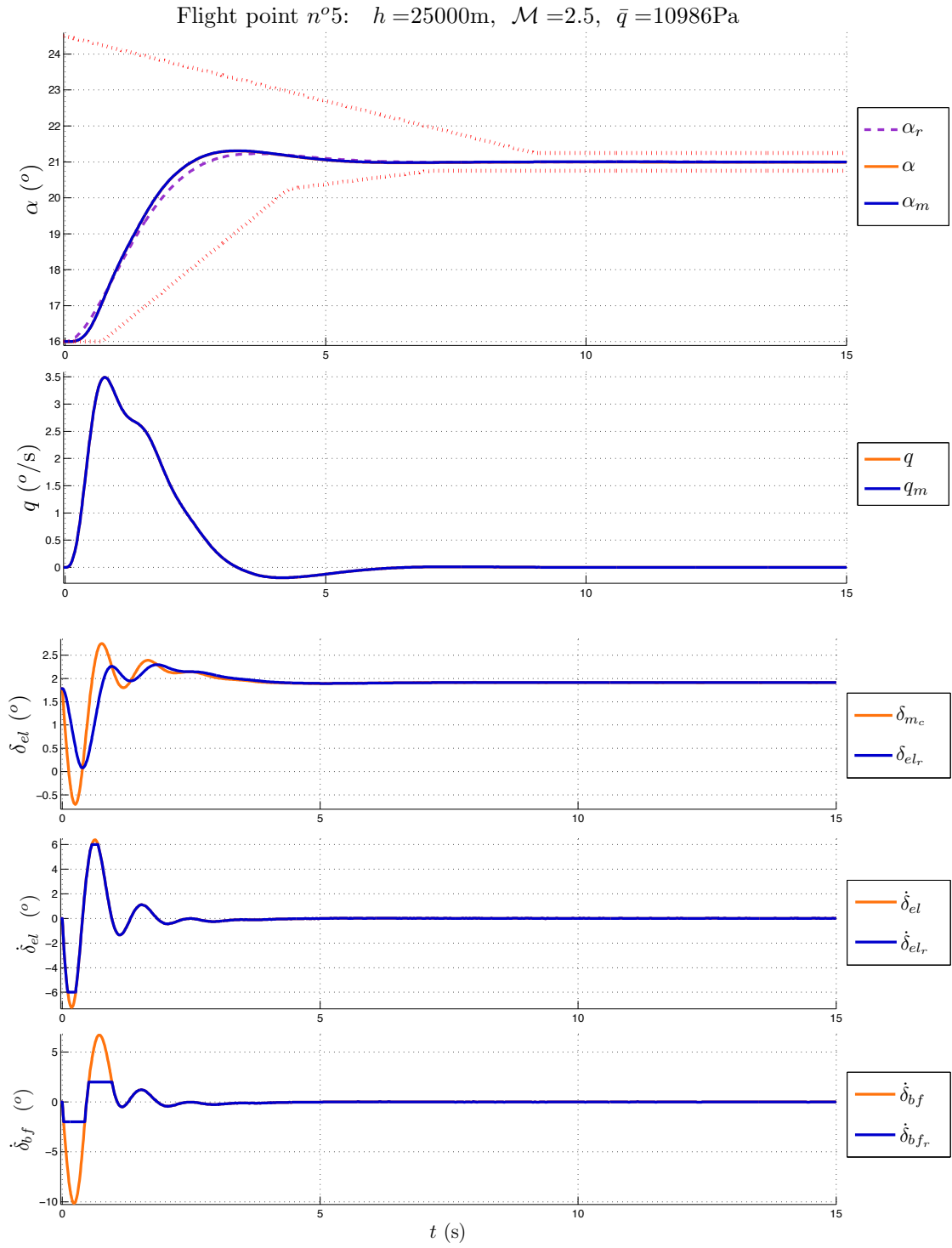
Figure E.13: Simulation with saturated actuator and controller **n°5**.
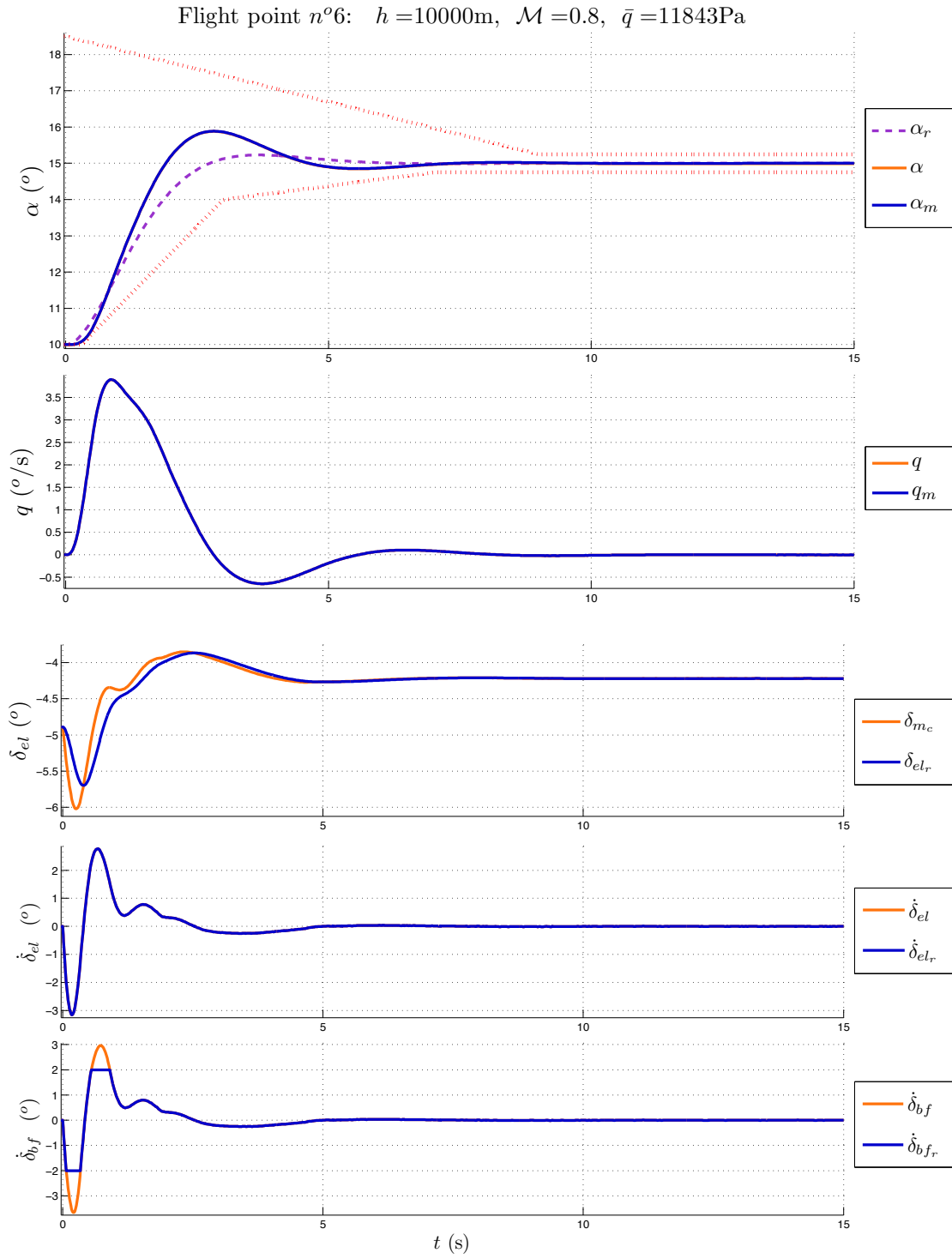
Figure E.14: Simulation with saturated actuator and controller **nº5**.
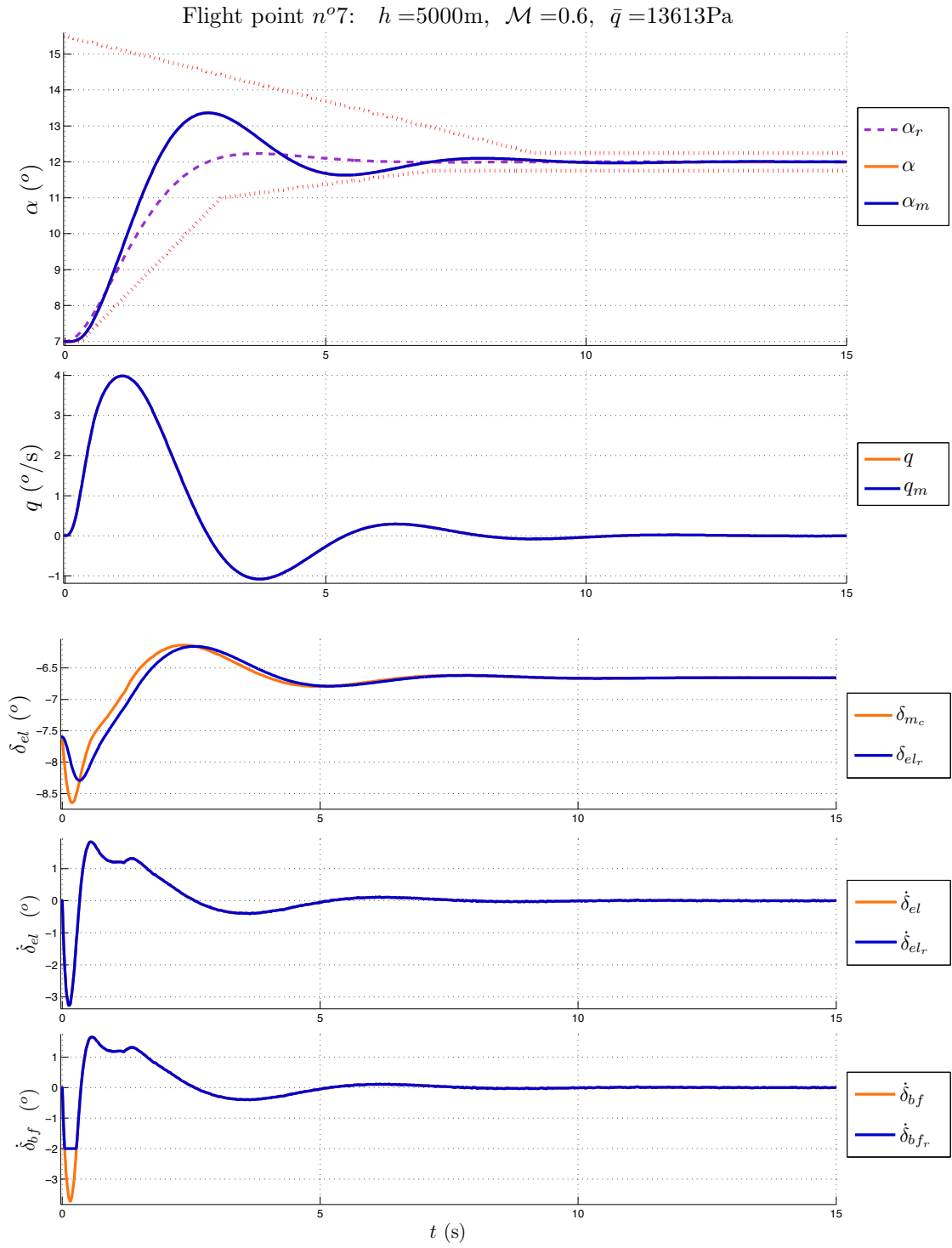
Figure E.15: Simulation with saturated actuator and controller **n⁰5**.
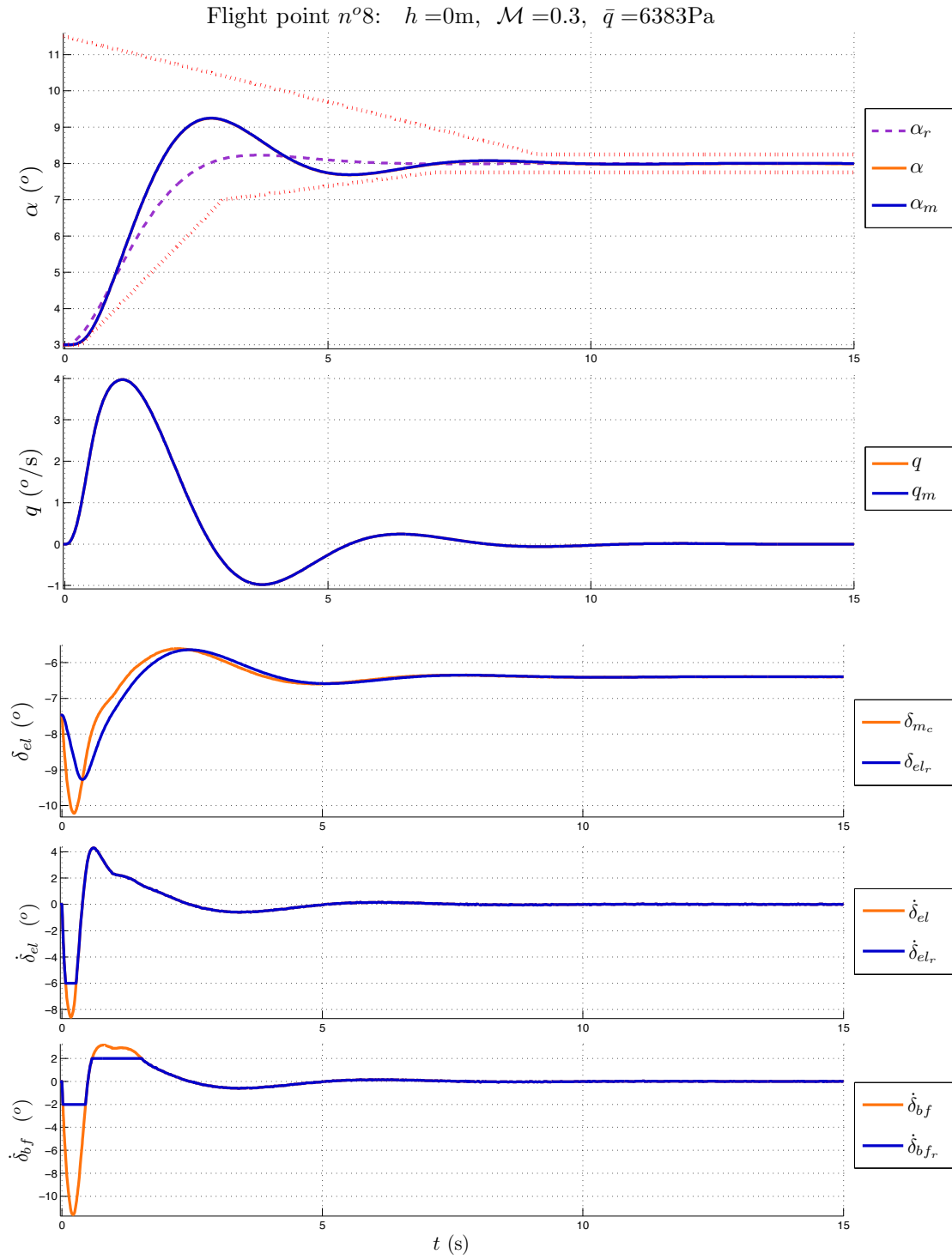
Figure E.16: Simulation with saturated actuator and controller **n°5**.

E.1.2 Robust nonlinear compensator simulation results
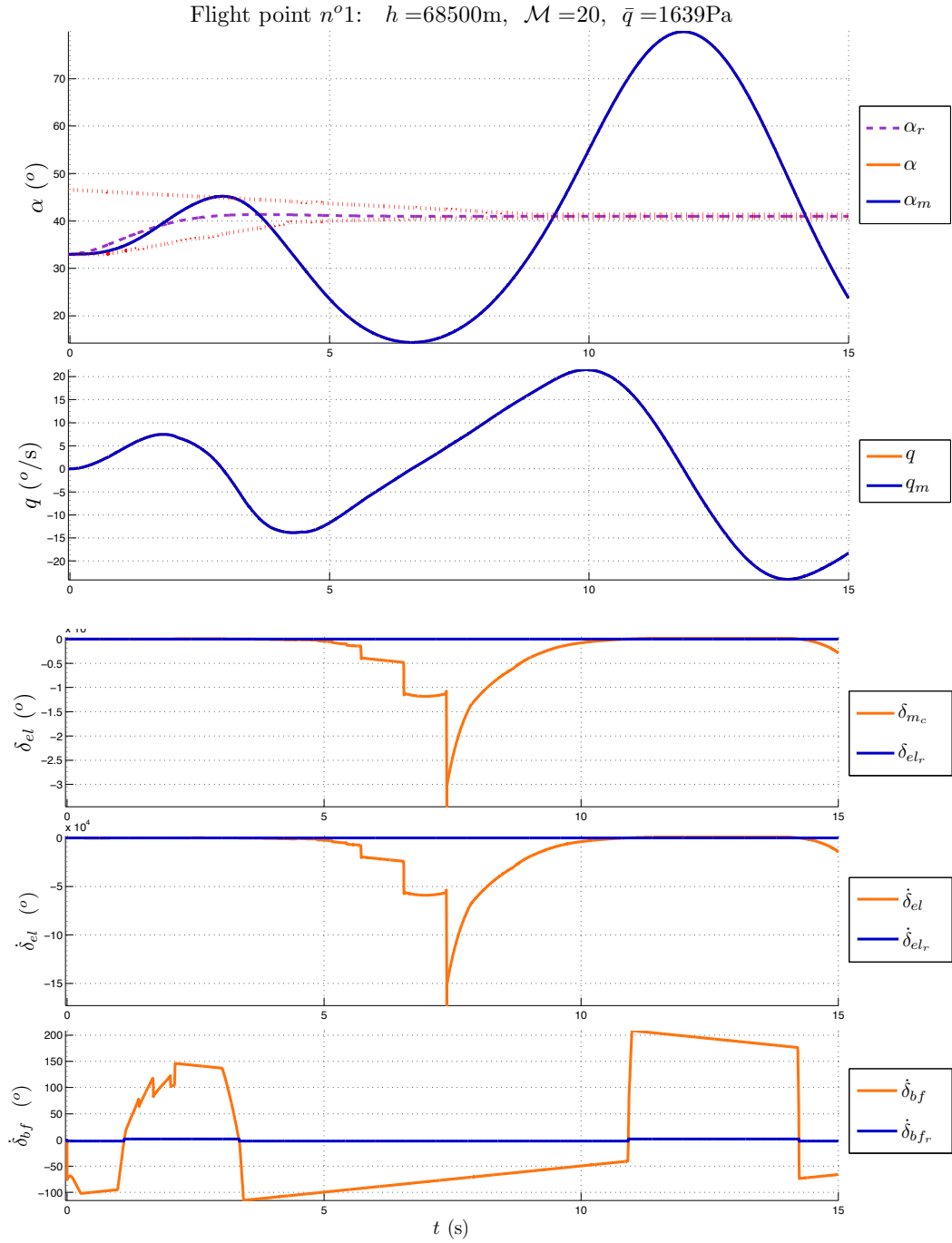
Figure E.17: Simulation with saturated actuator and controller **n°6**.

Flight point n^o2: $h = 54500$m, $\mathcal{M} = 11$, $\bar{q} = 3615$Pa
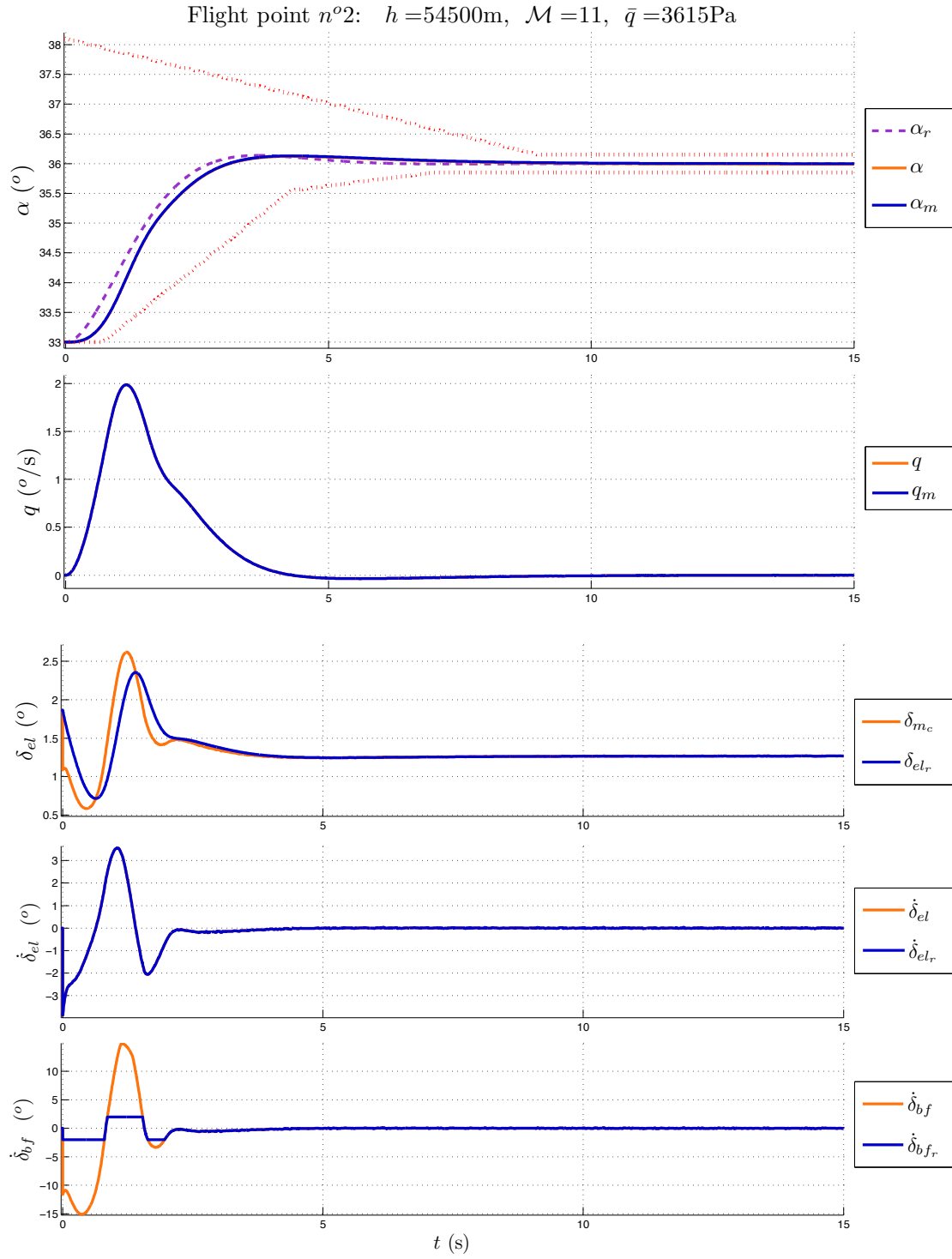
Figure E.18: Simulation with saturated actuator and controller **n°6**.
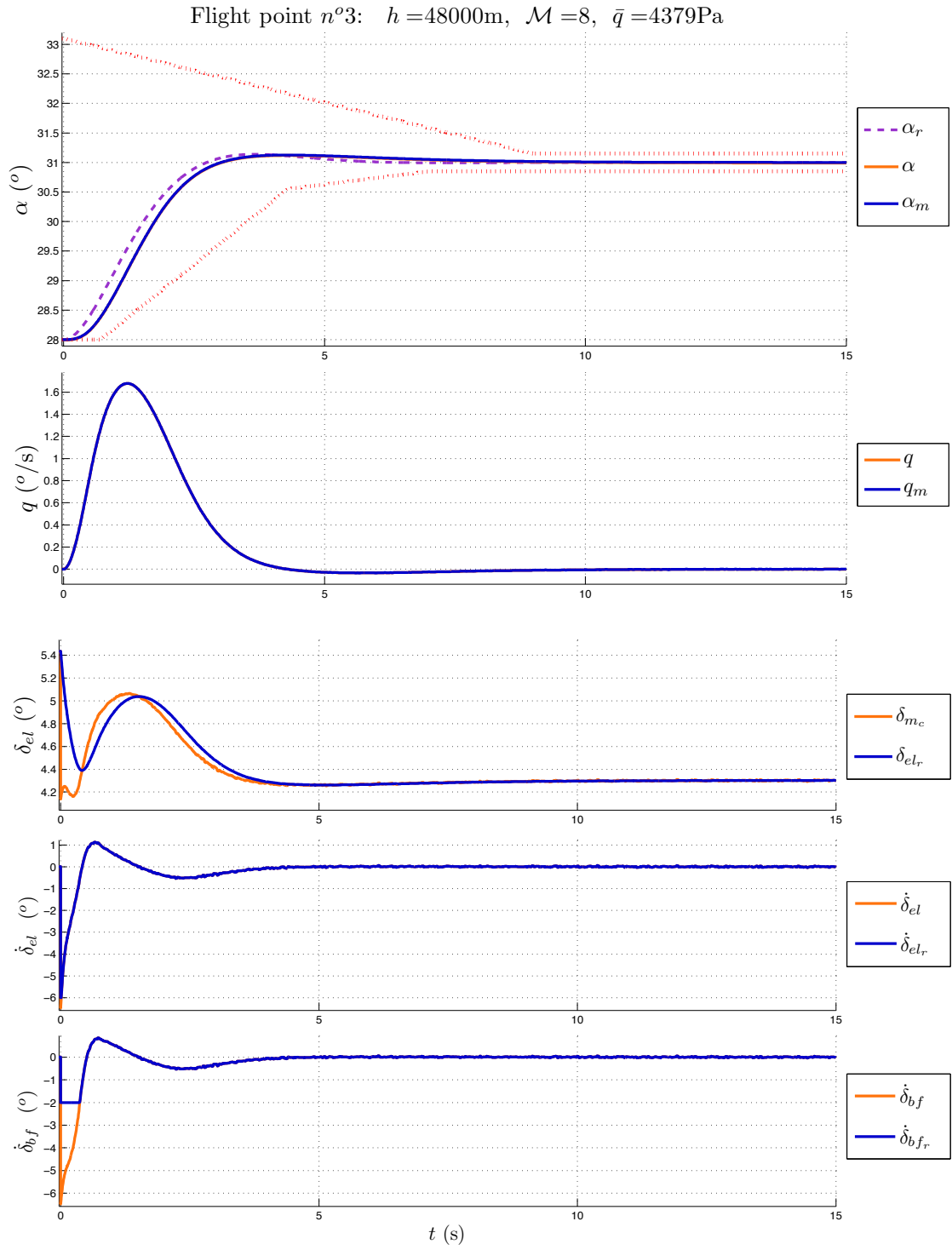
Figure E.19: Simulation with saturated actuator and controller **n°6**.
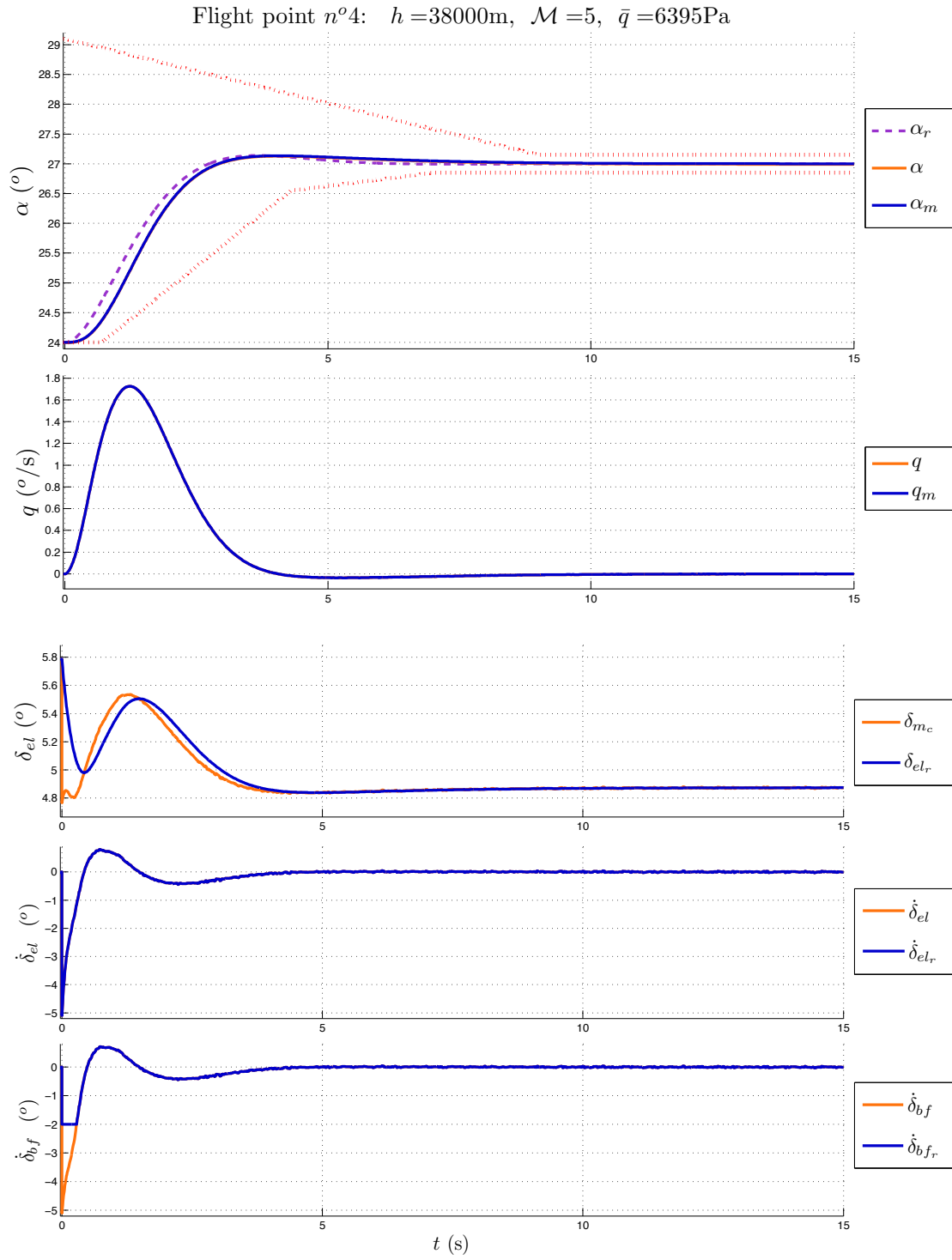
Figure E.20: Simulation with saturated actuator and controller **n°6**.
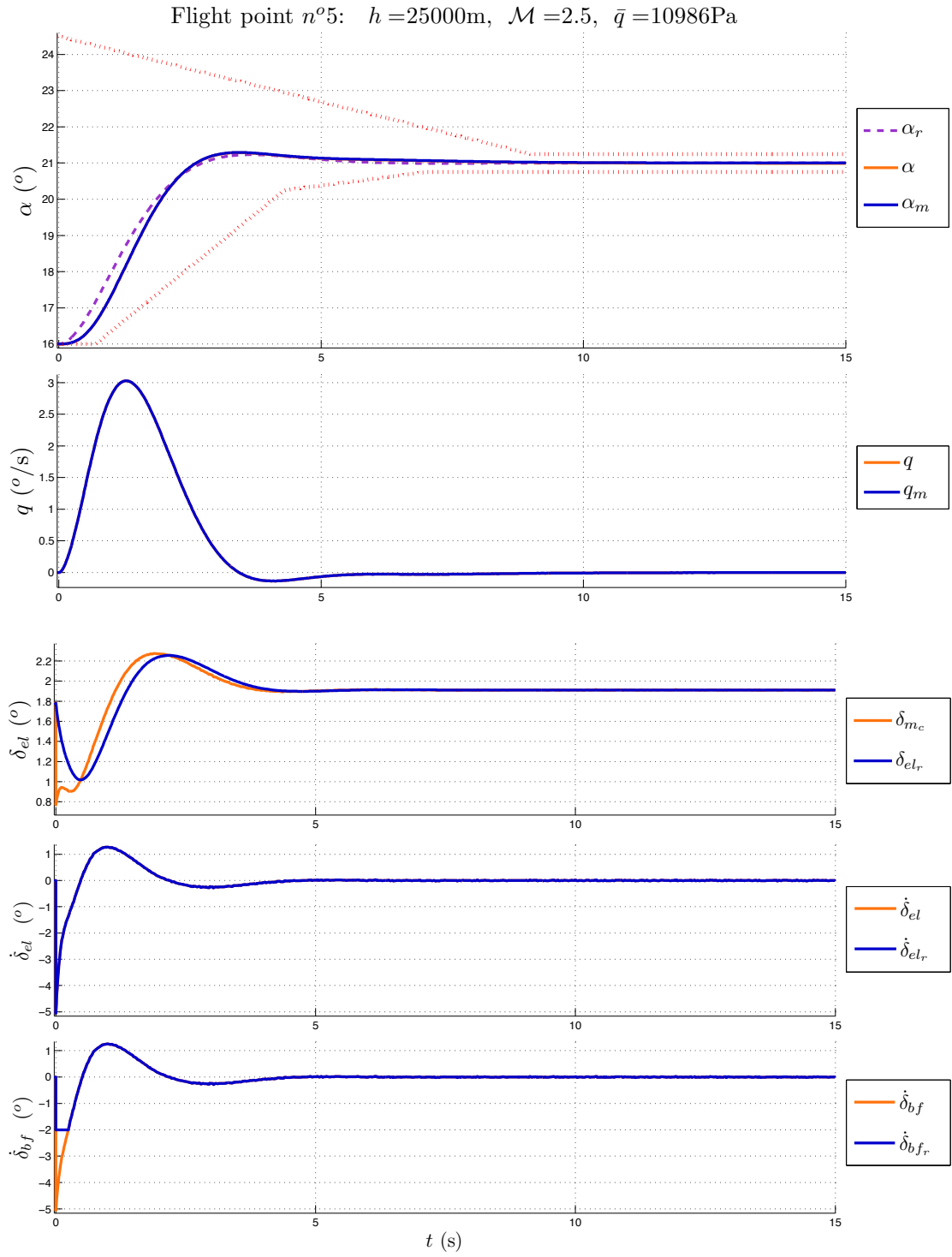
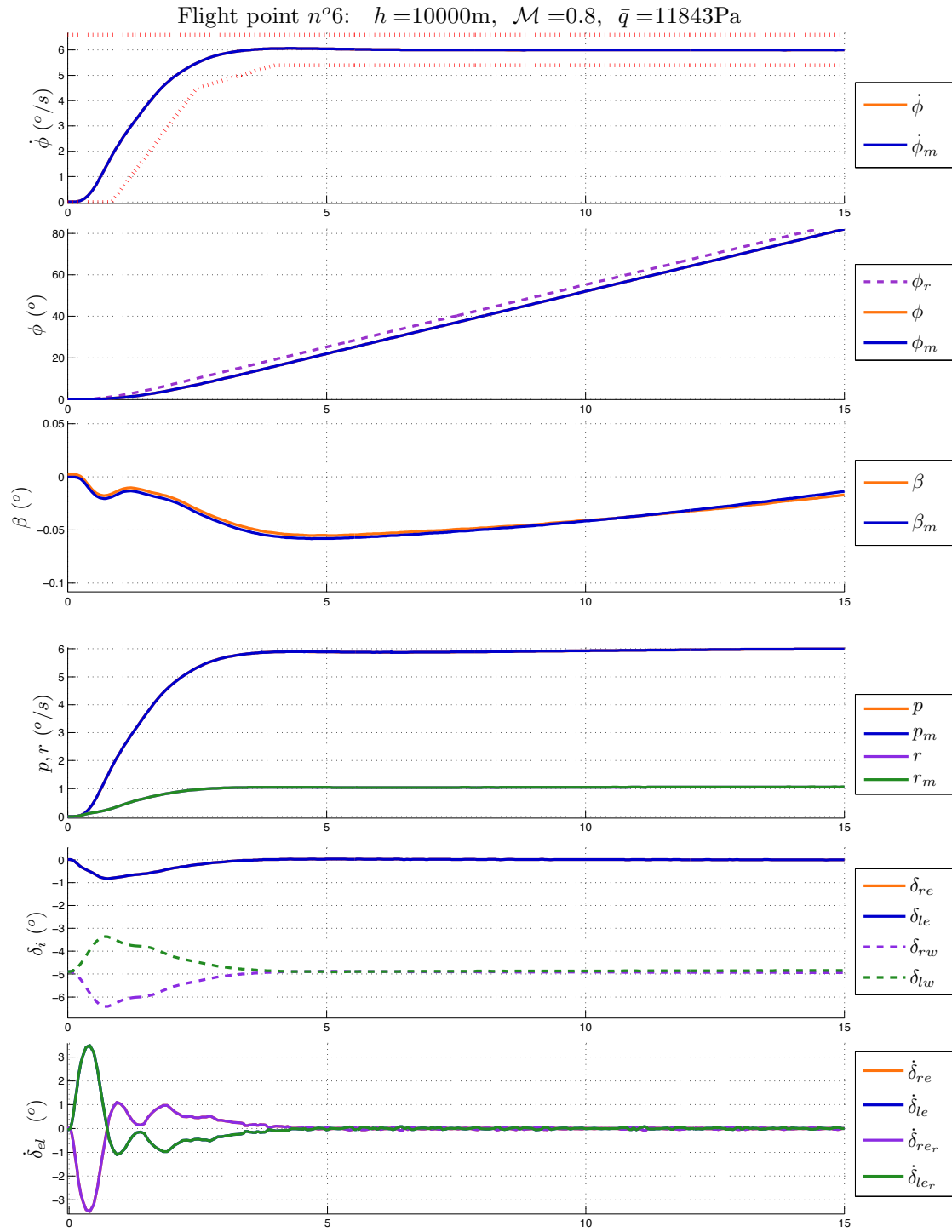Figure E.21: Simulation with saturated actuator and controller **n°6**.
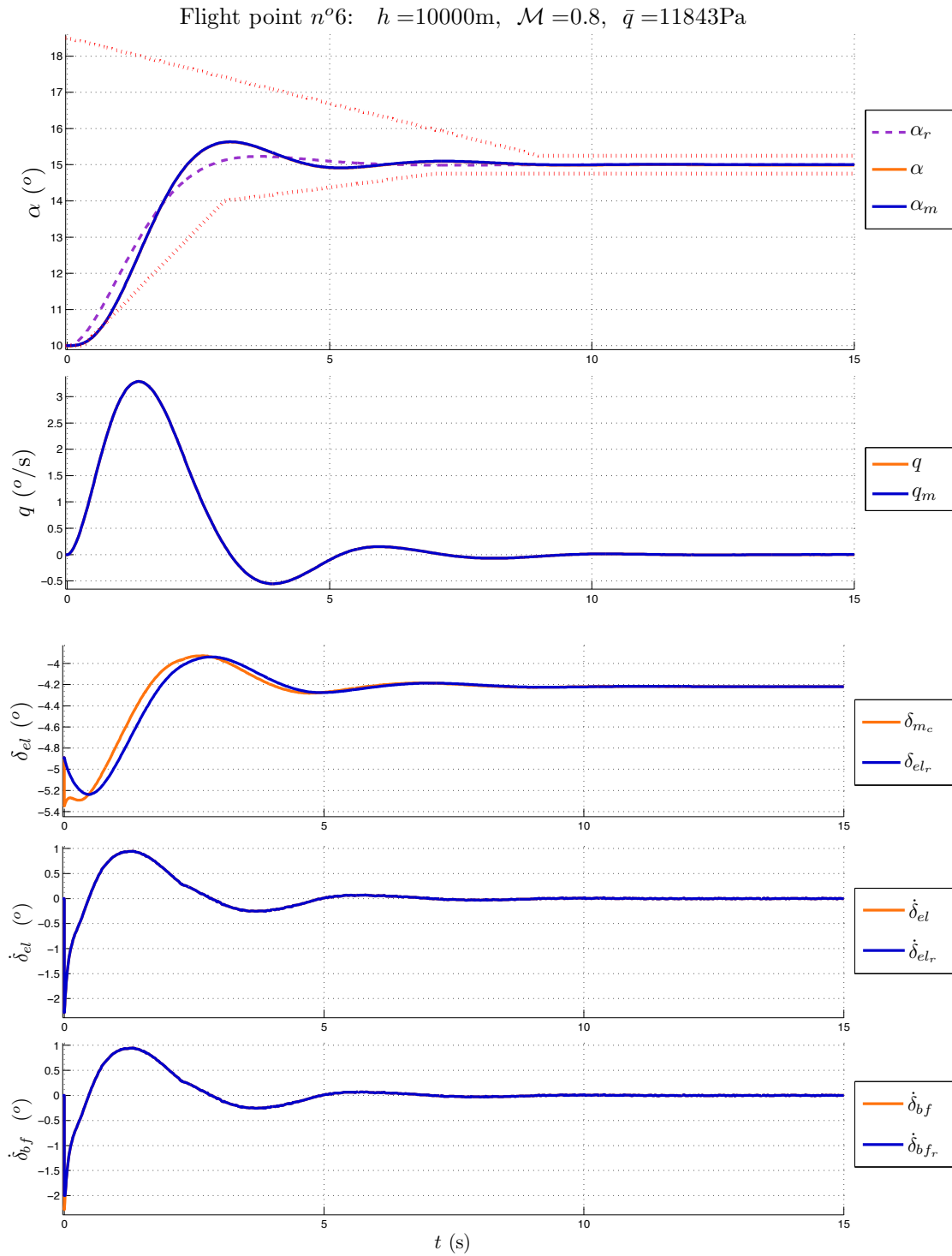
Figure E.22: Simulation with saturated actuator and controller **n⁰6**.
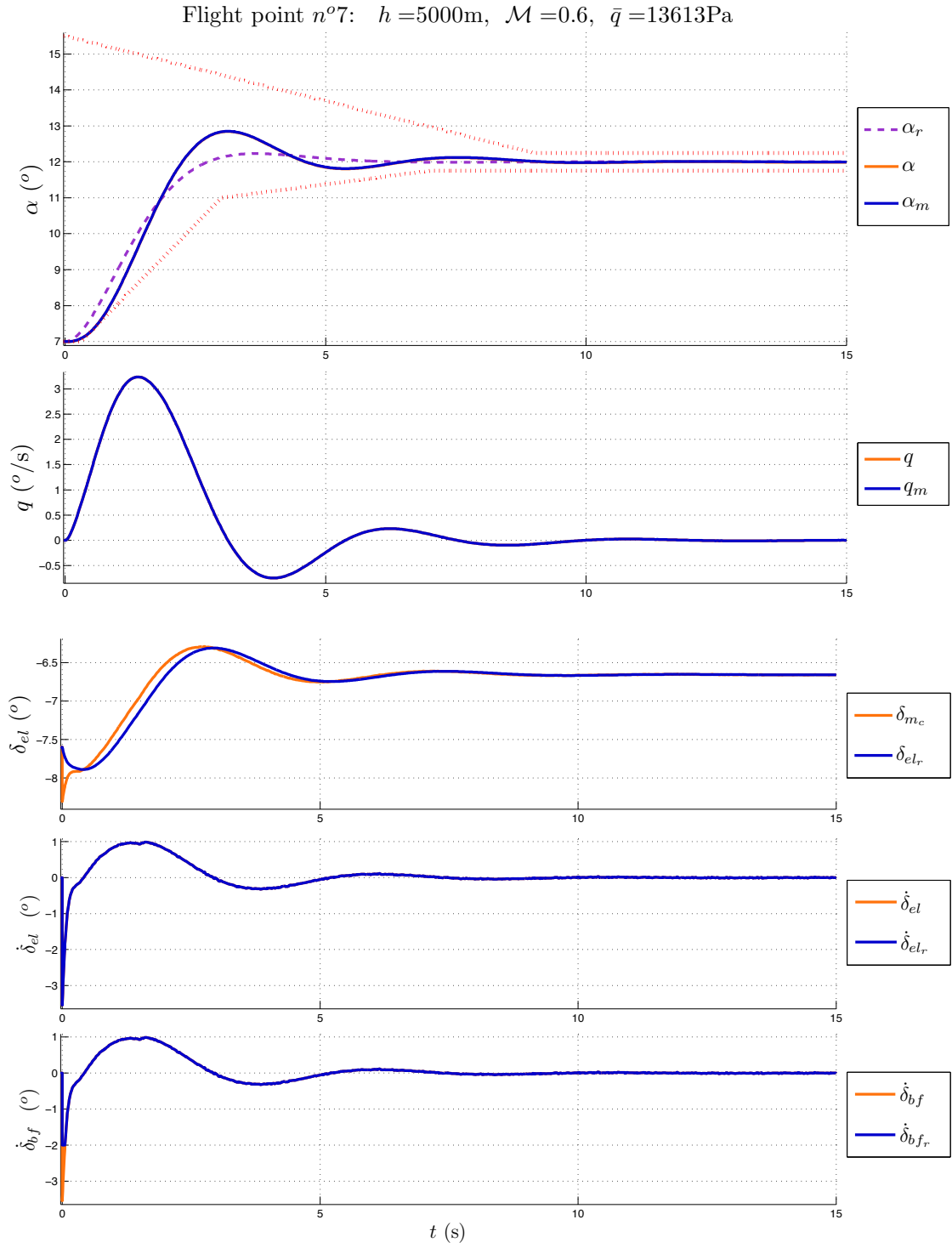
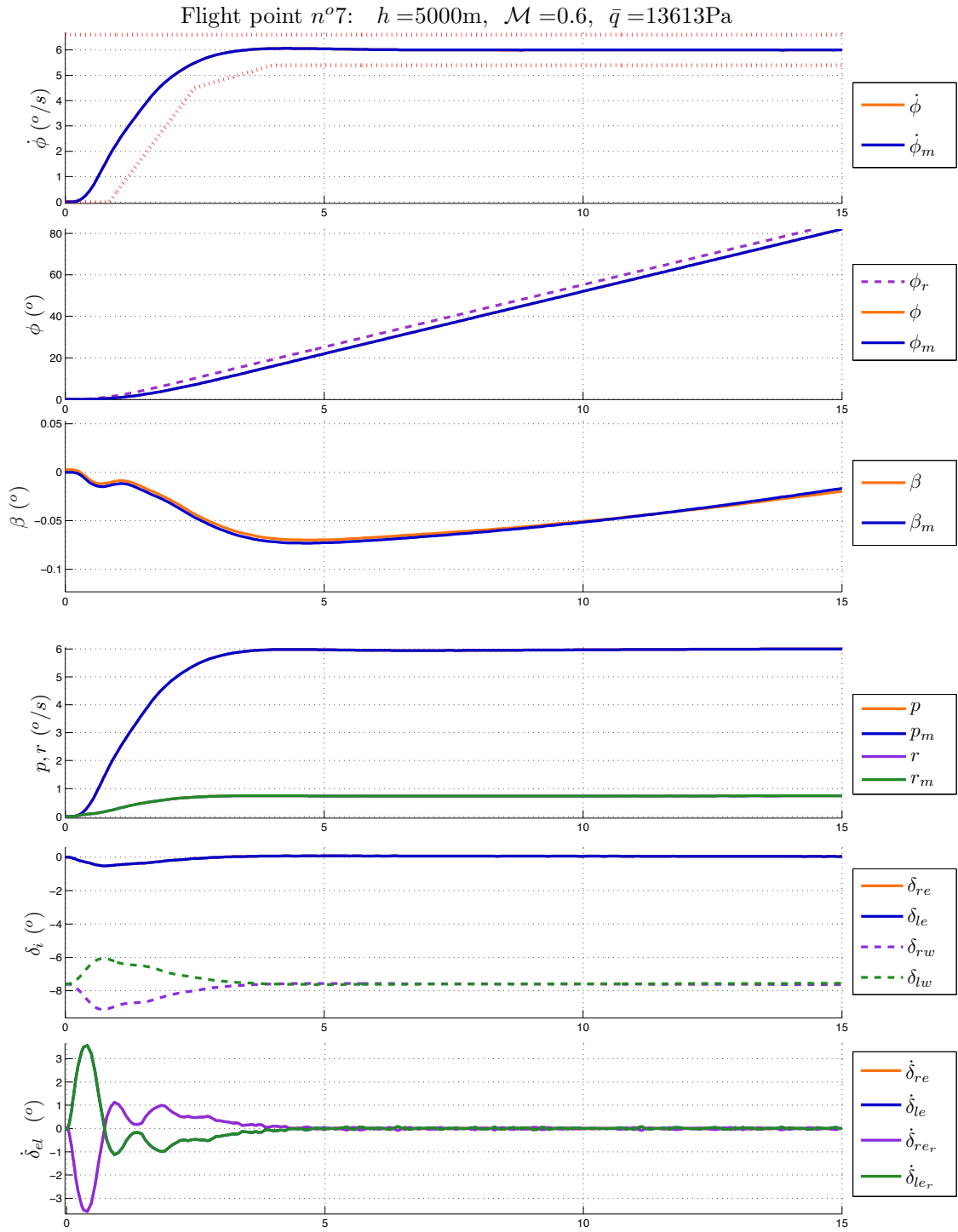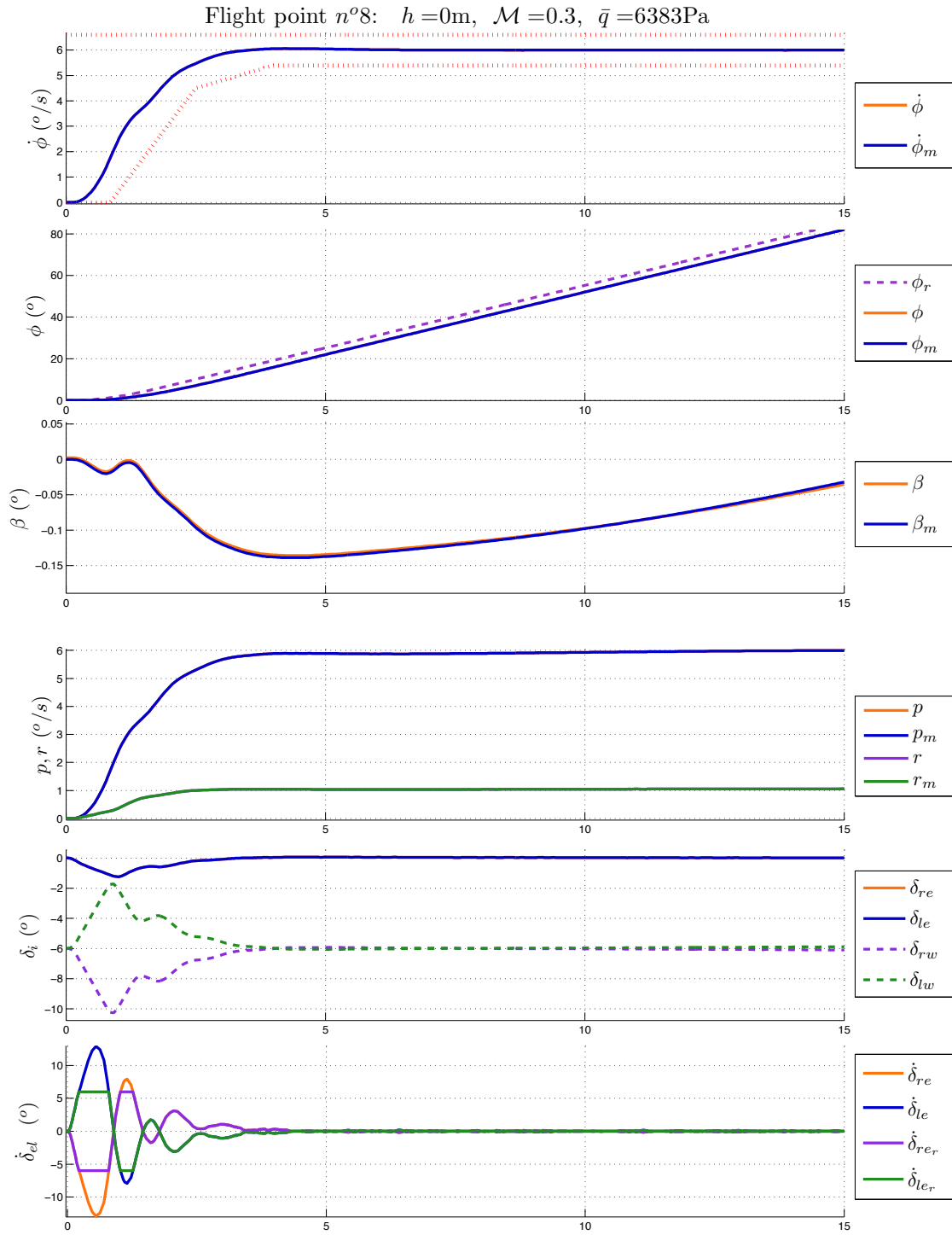Figure E.23: Simulation with saturated actuator and controller **n°6**.

Flight point n^o8: $h = 0$m, $\mathcal{M} = 0.3$, $\bar{q} = 6383$Pa
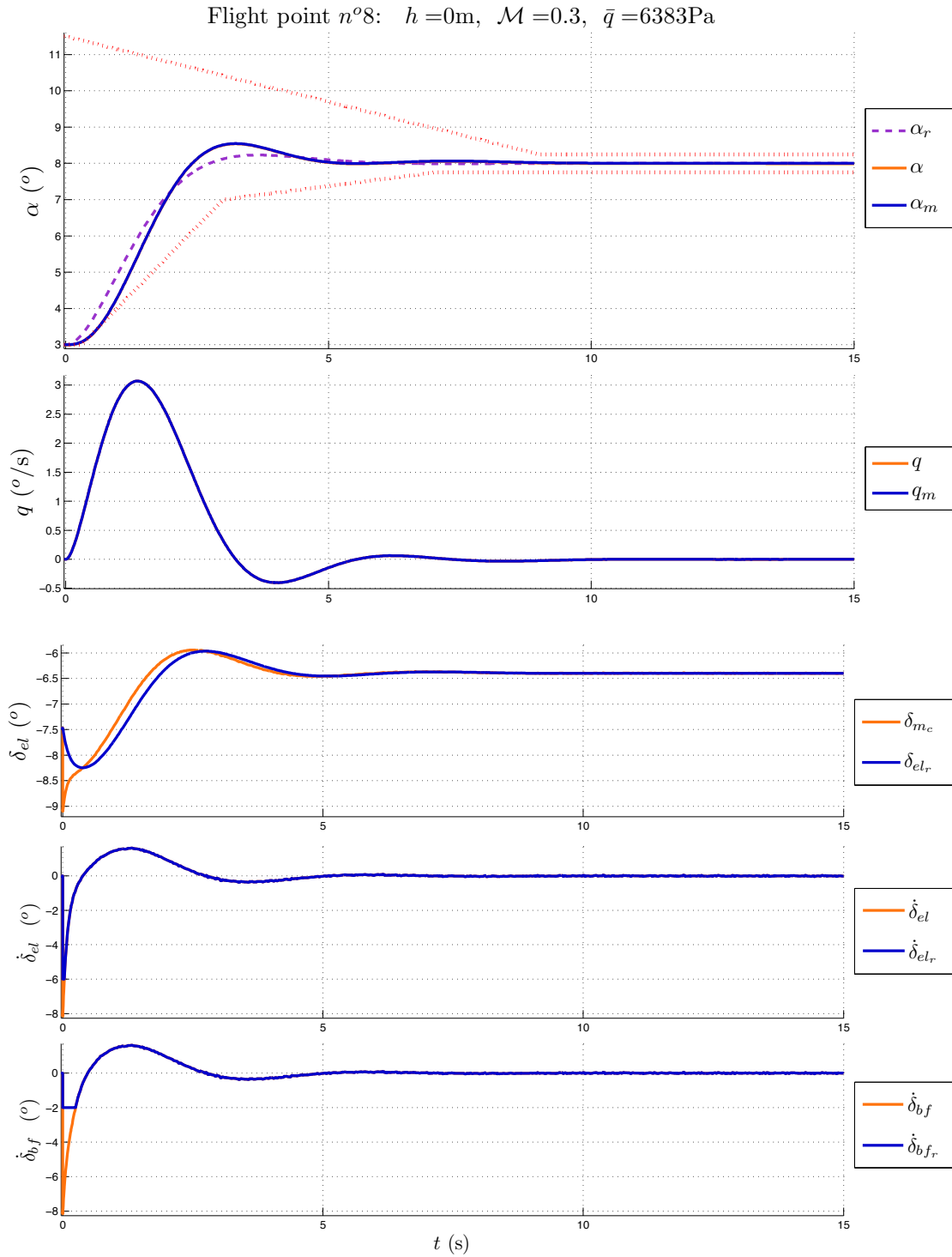
Figure E.24: Simulation with saturated actuator and controller **n°6**.
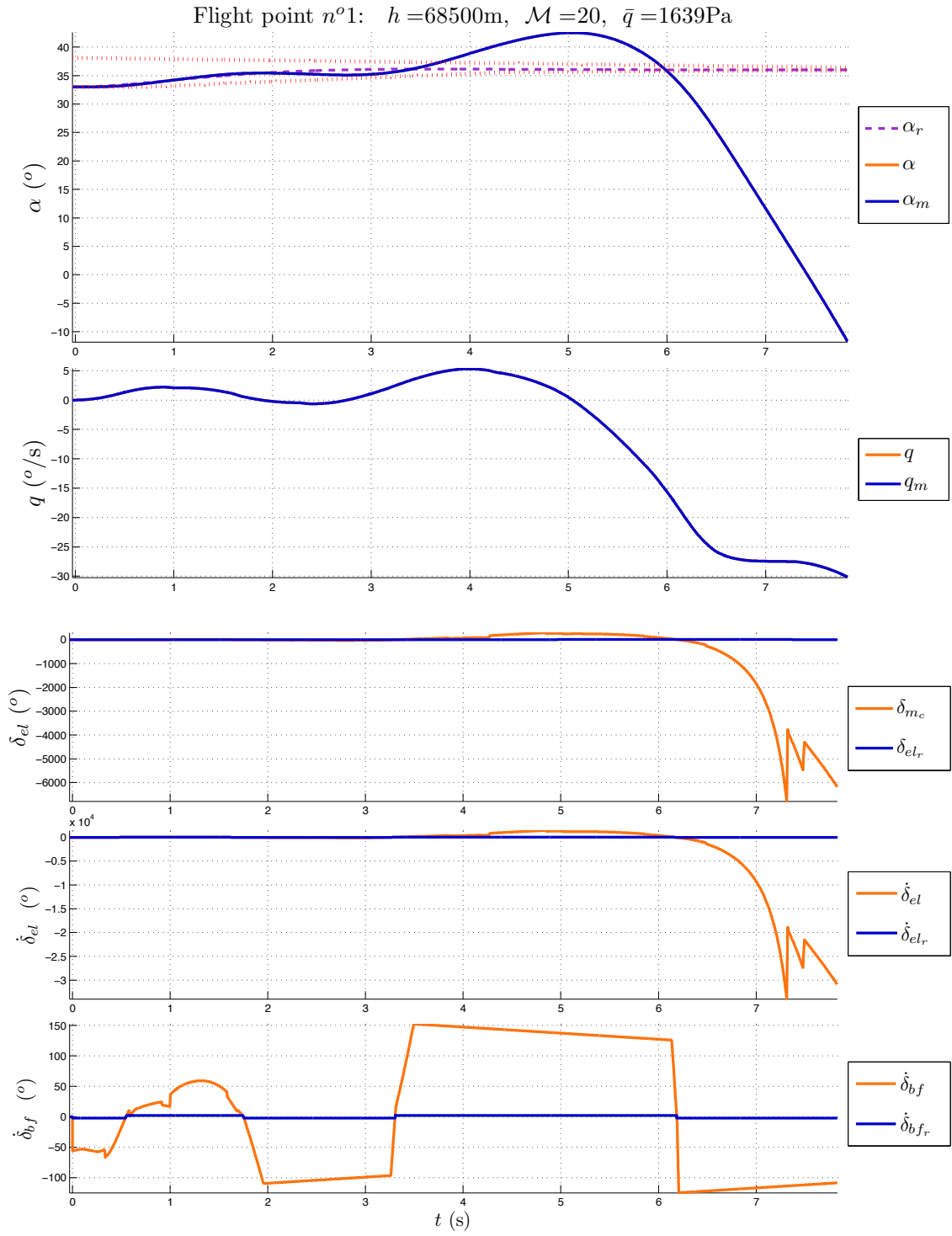
Figure E.25: Simulation with saturated actuator and controller **nº7**.
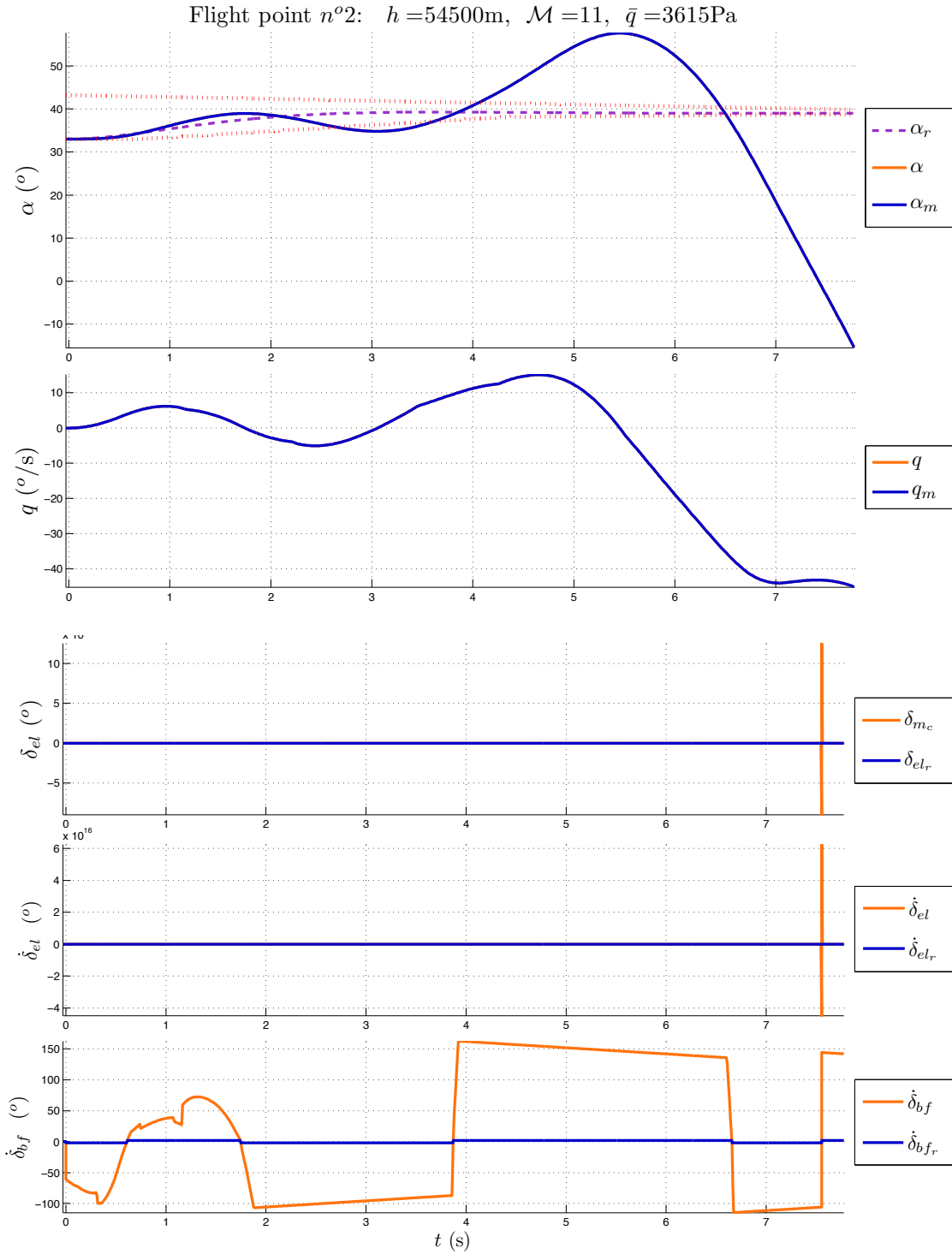
Figure E.26: Simulation with saturated actuator and controller **n°7**.
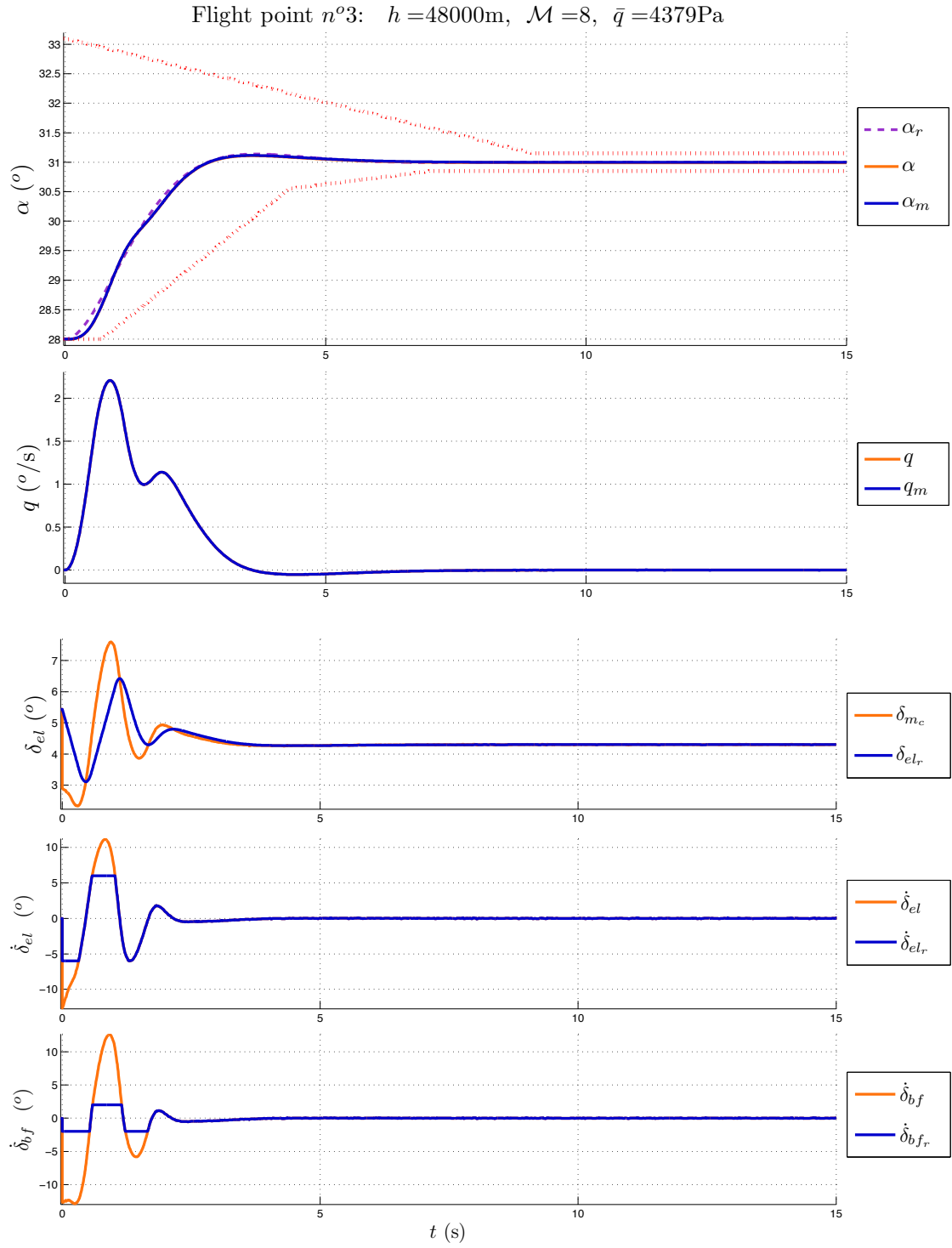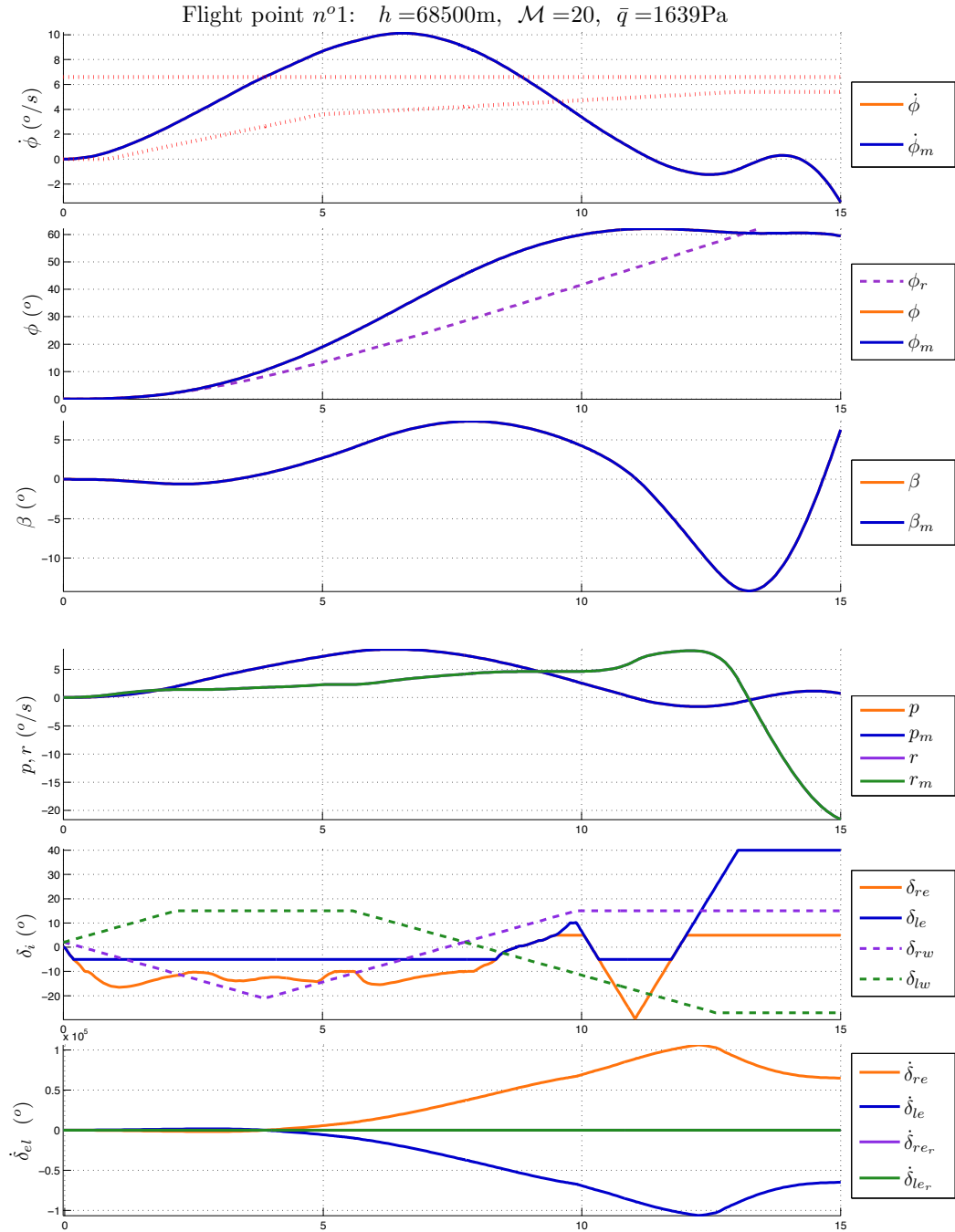
Figure E.27: Simulation with saturated actuator and controller **n°7**.
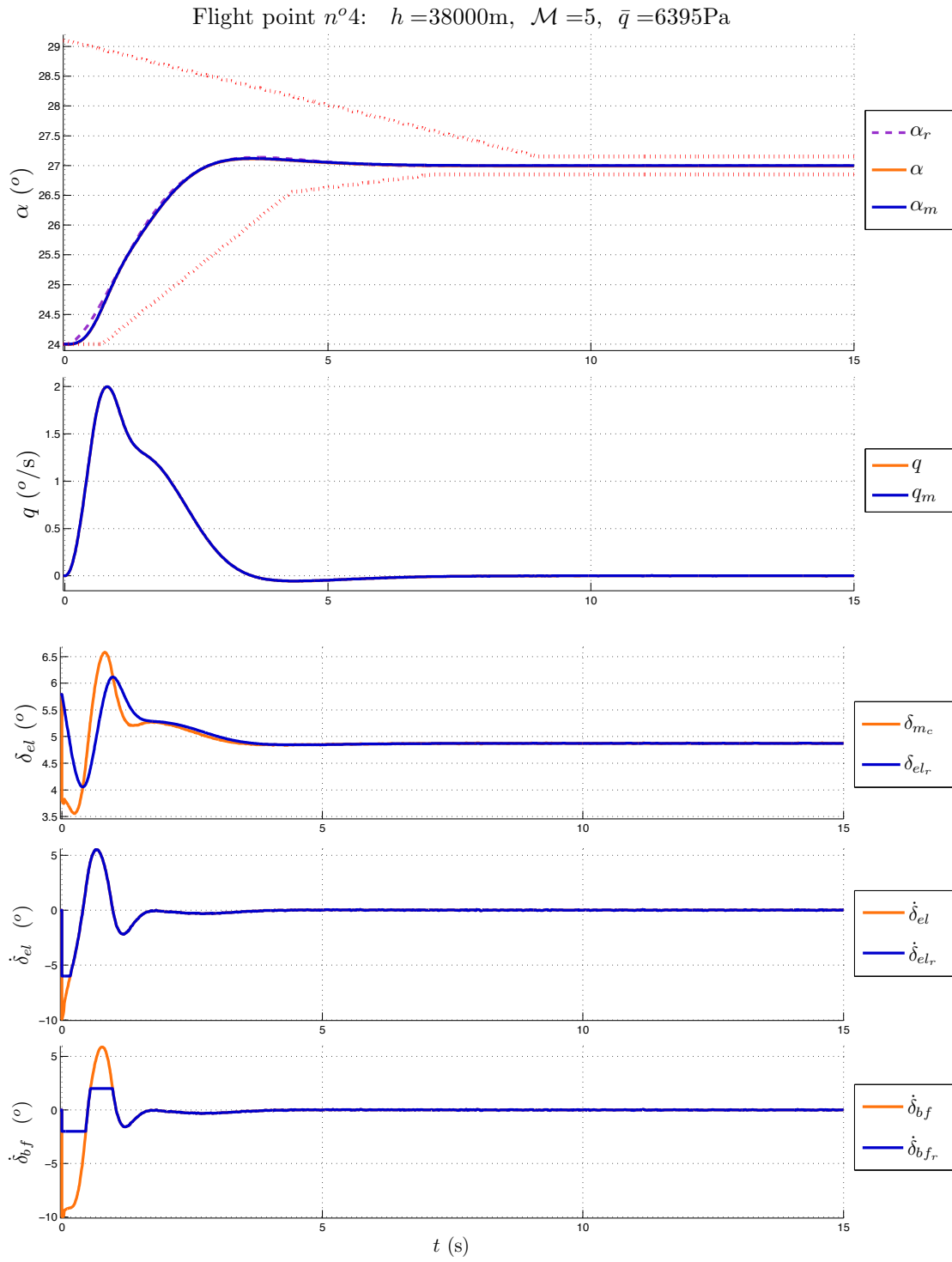
Figure E.28: Simulation with saturated actuator and controller **n°7**.
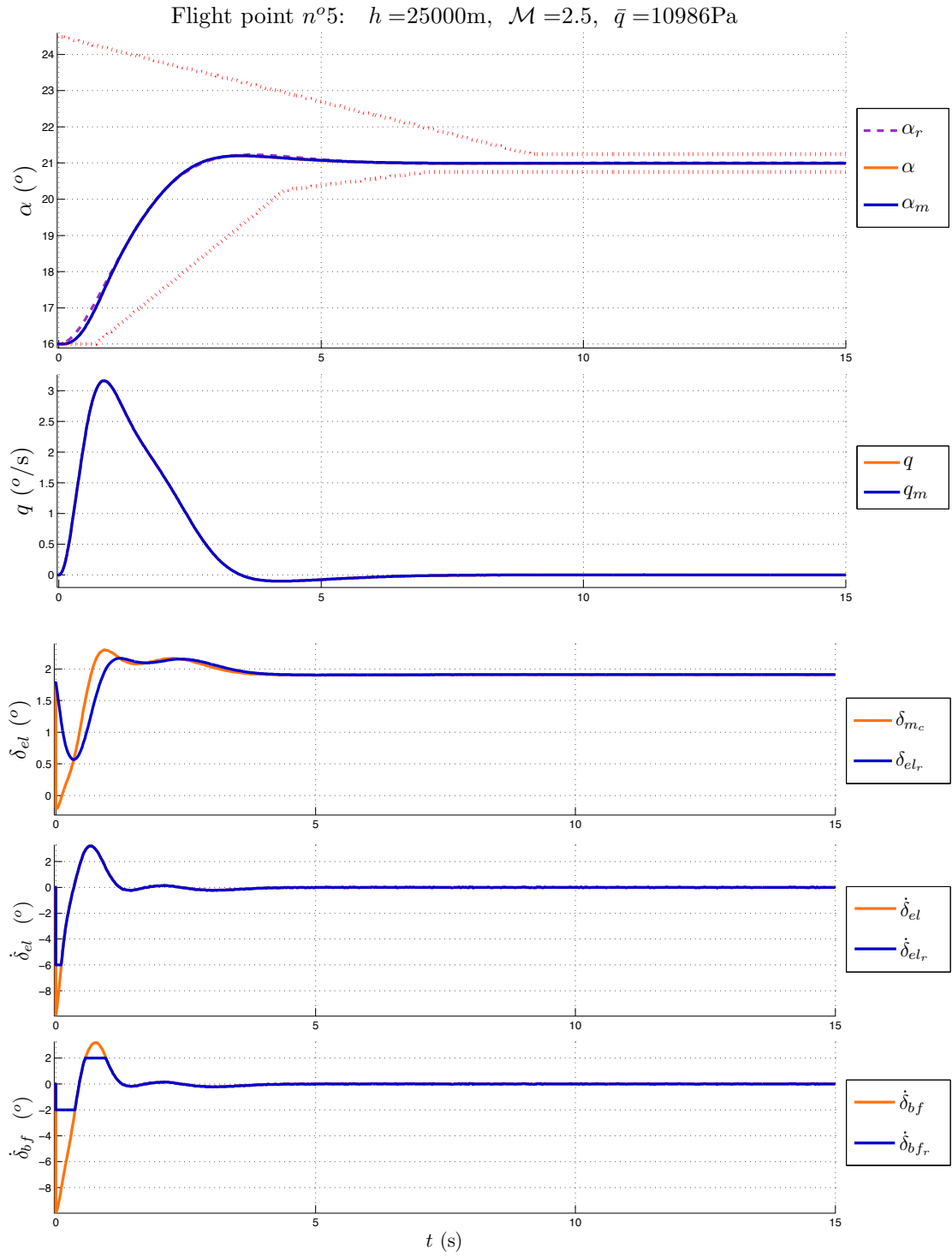
Figure E.29: Simulation with saturated actuator and controller **n°7**.
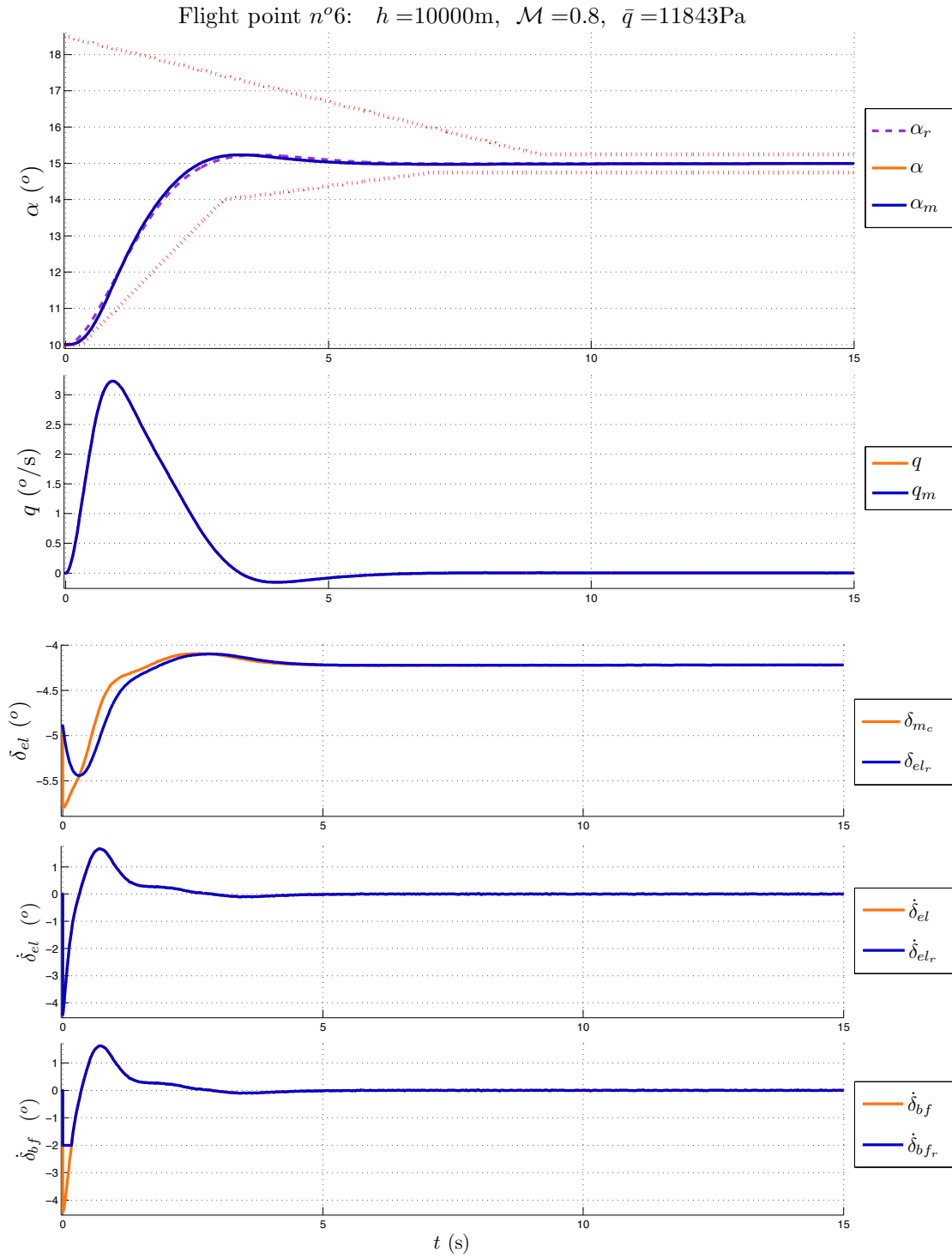
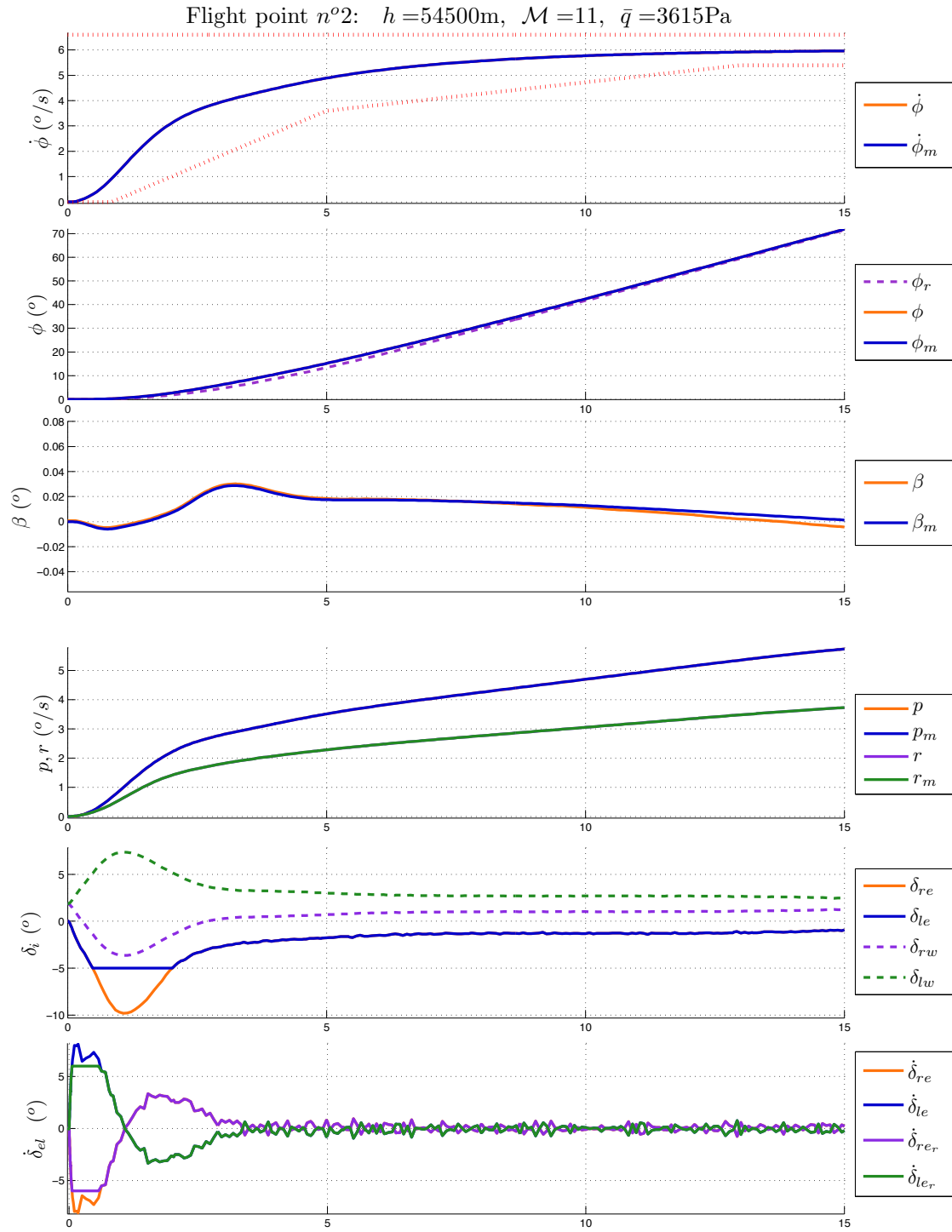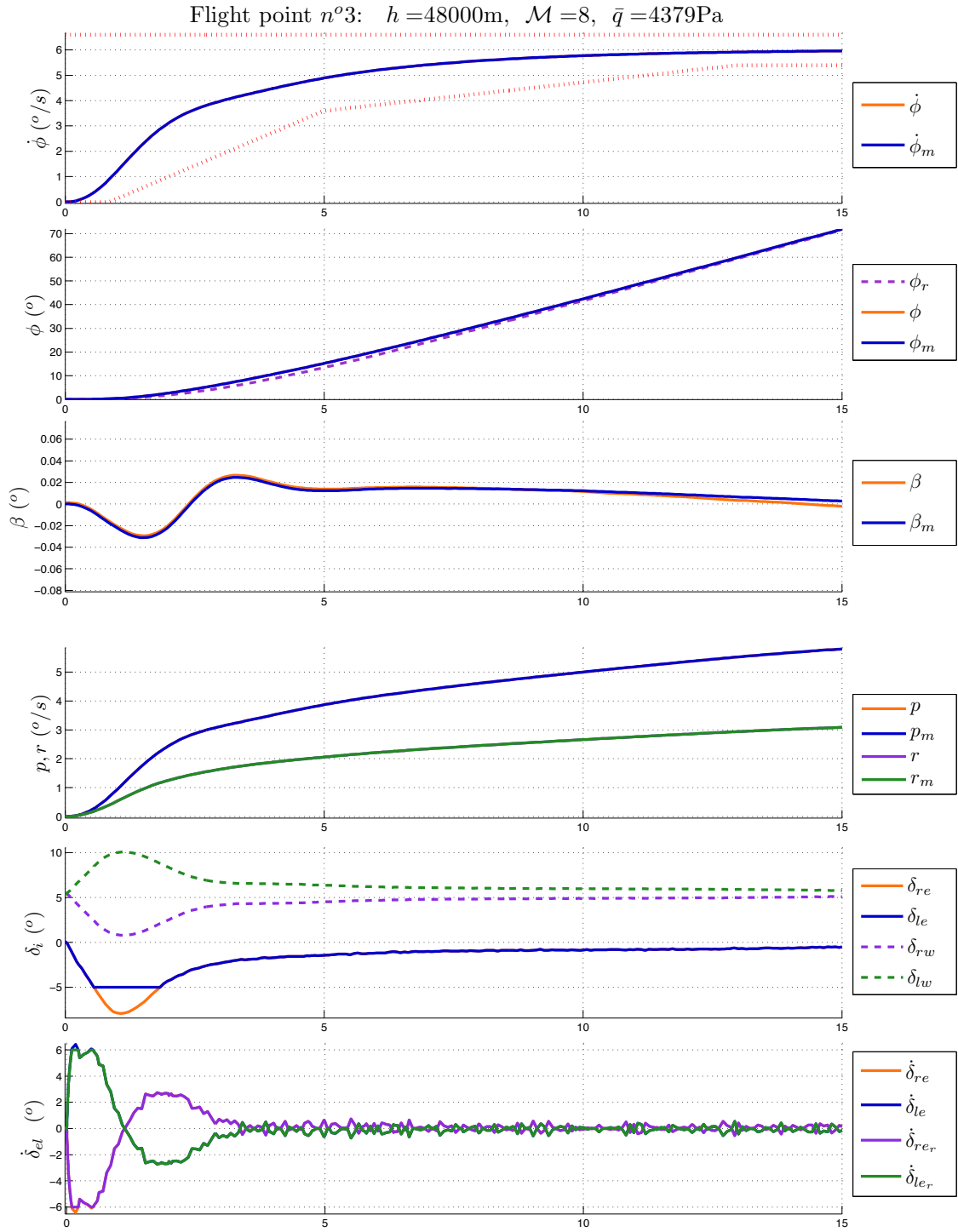Figure E.30: Simulation with saturated actuator and controller **nº7**.
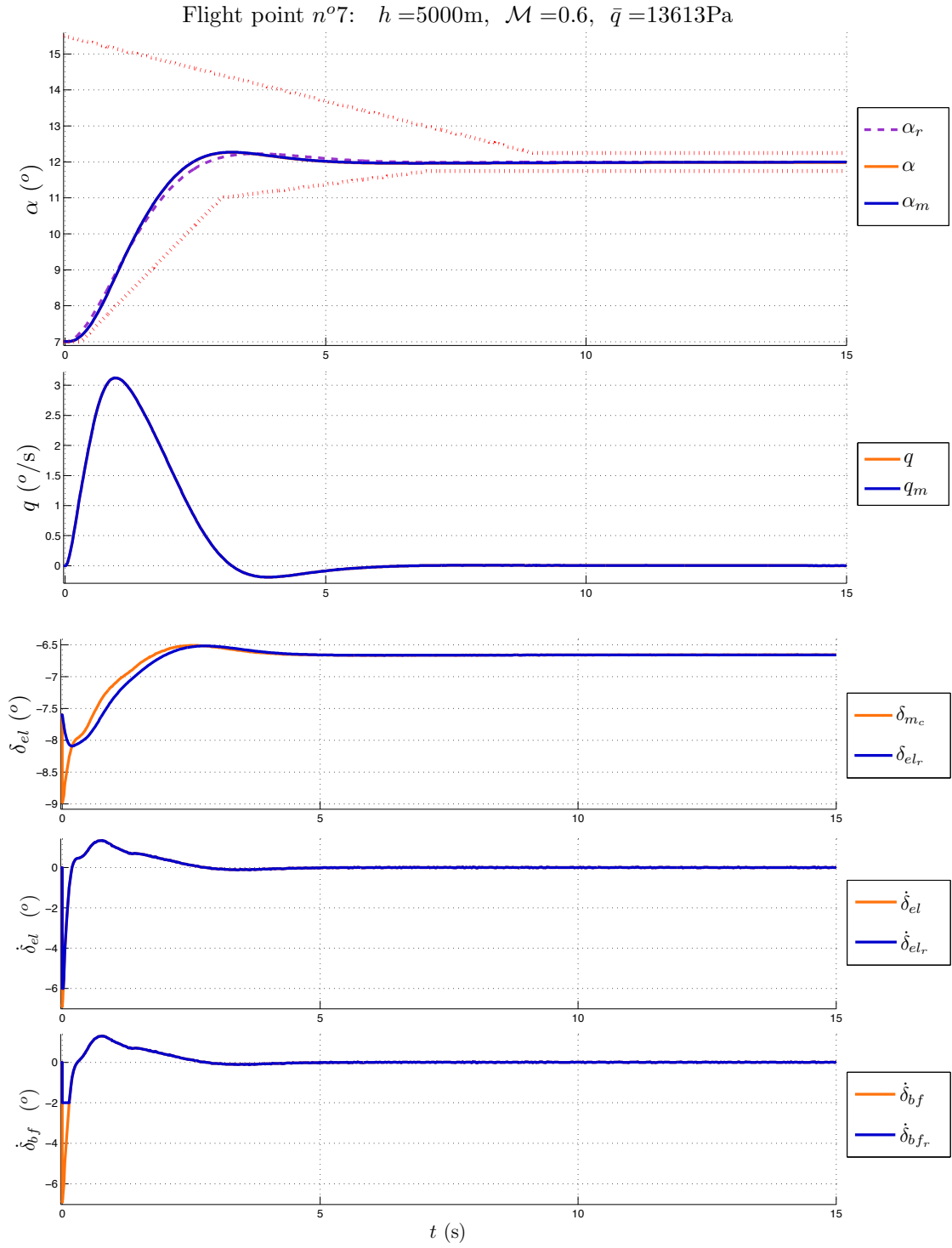
Figure E.31: Simulation with saturated actuator and controller **n°7**.
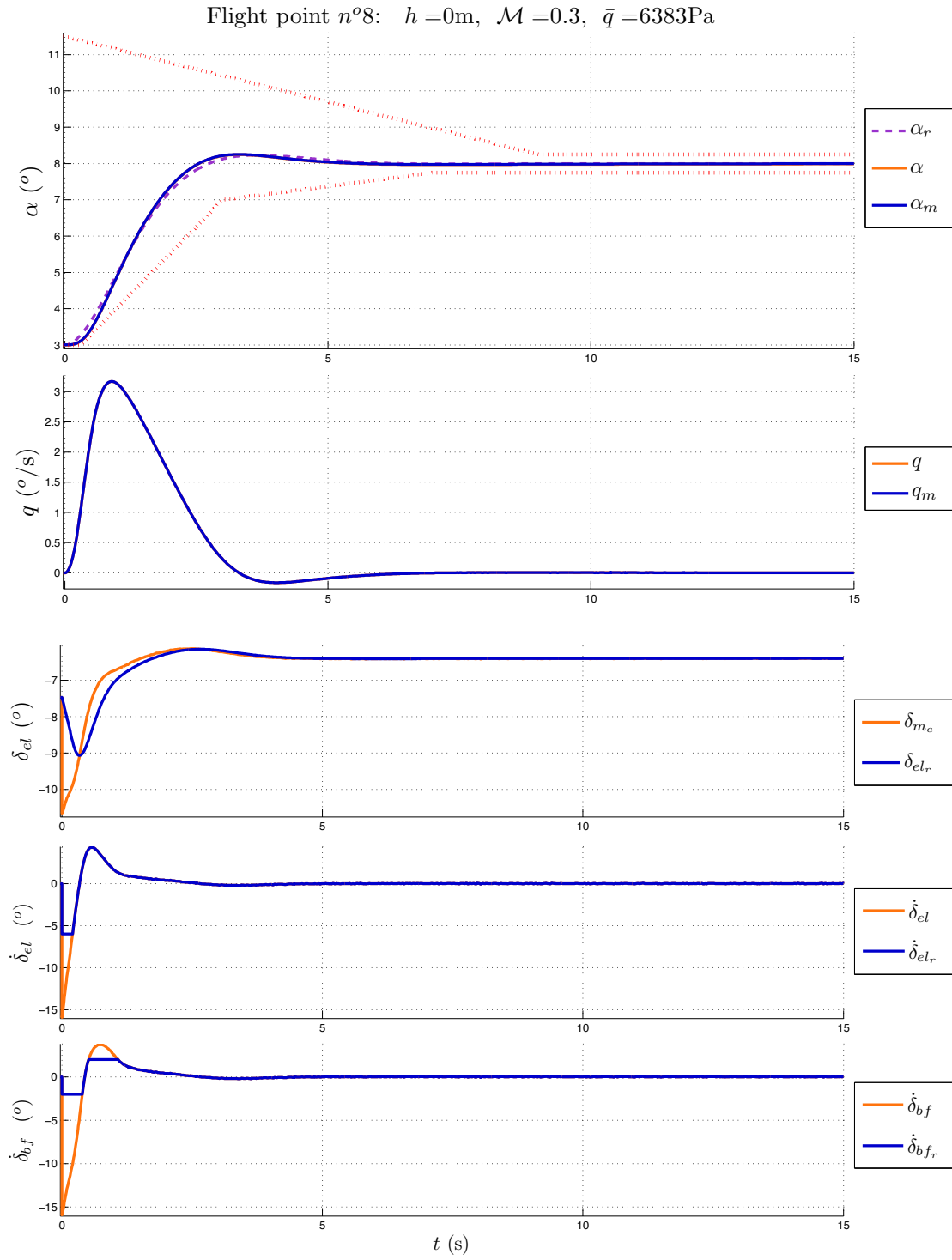
Figure E.32: Simulation with saturated actuator and controller **nº7**.

E.1.3 Anti-windup robust controller simulation results
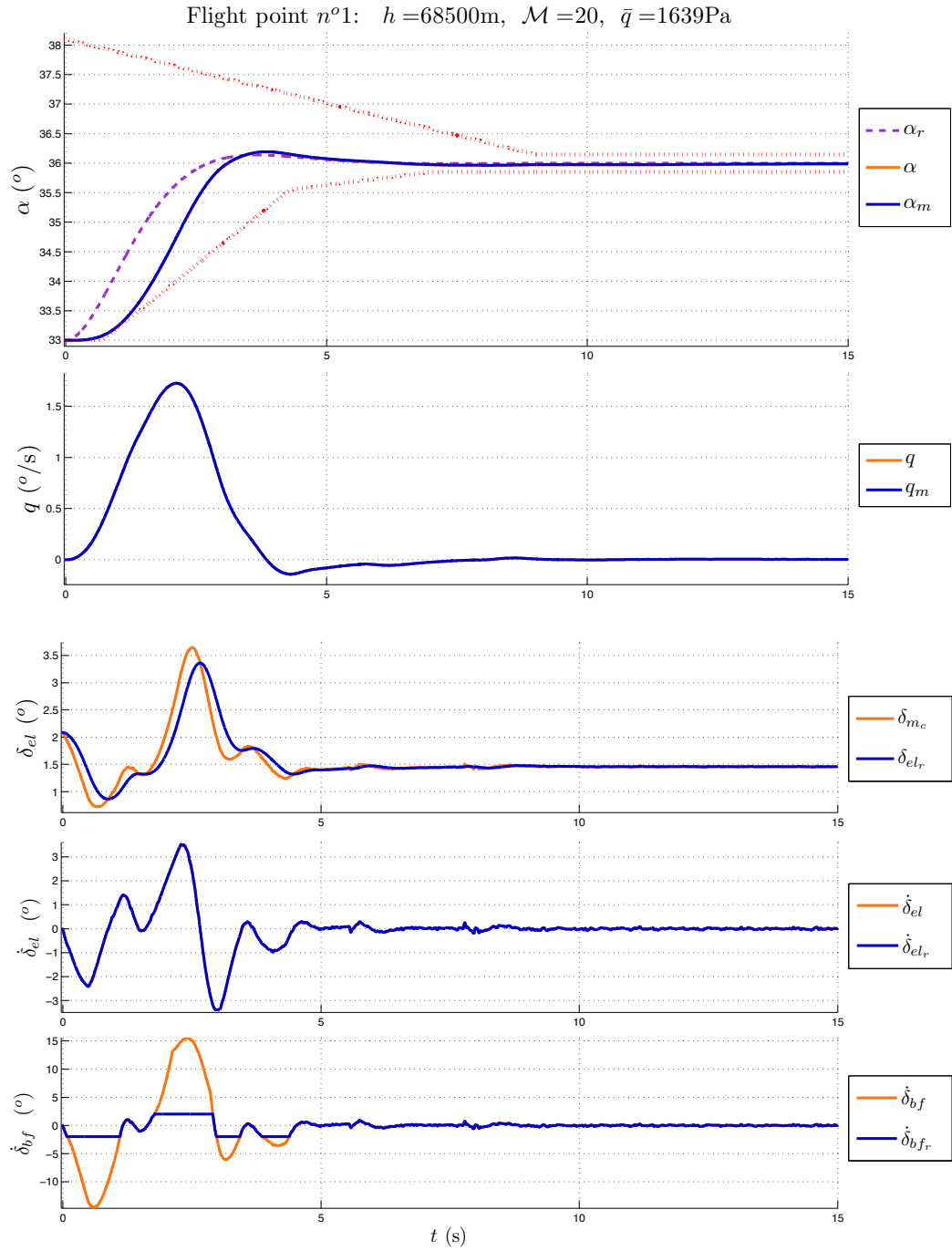
Figure E.33: Simulation with saturated actuator and controller **n°8**.
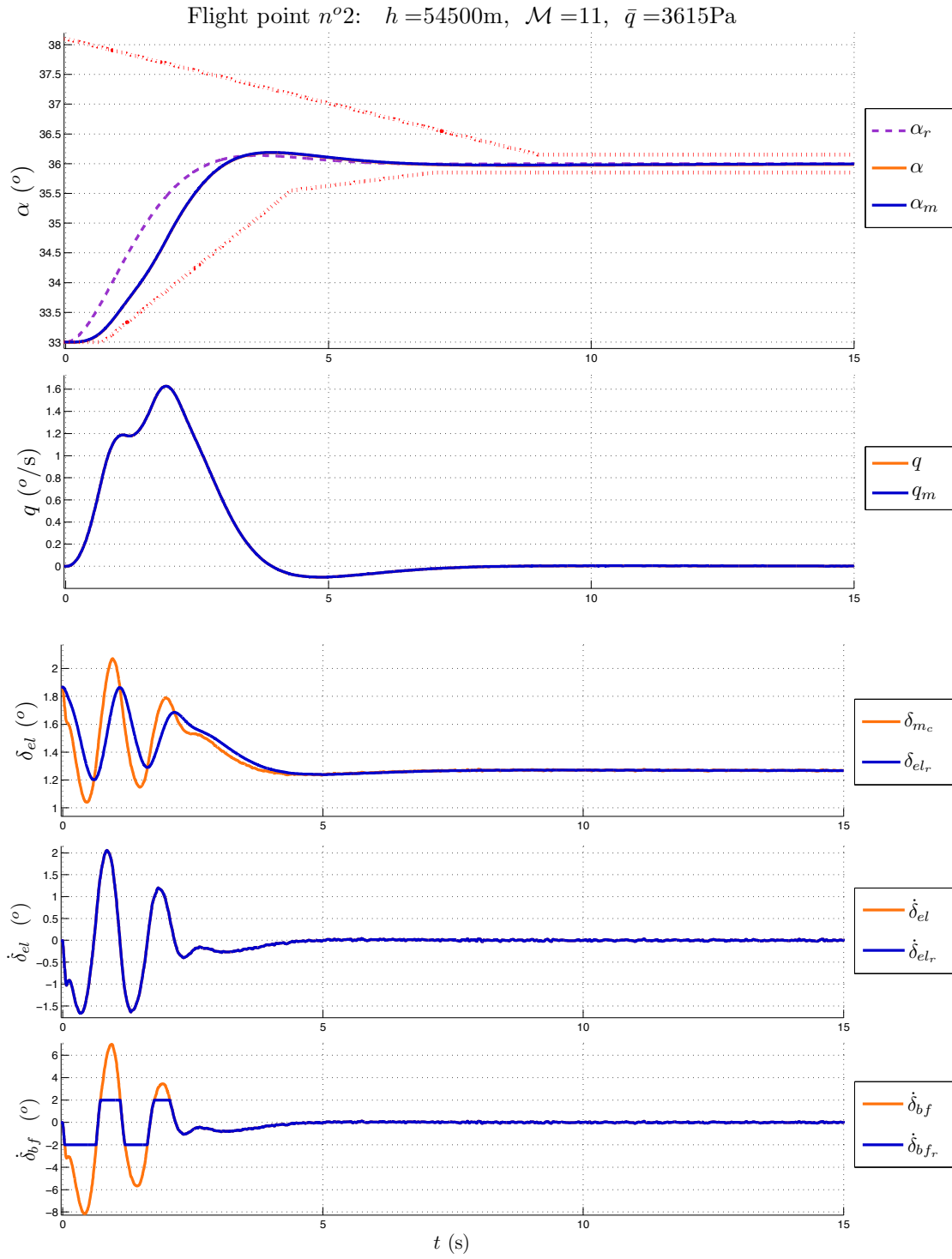
Figure E.34: Simulation with saturated actuator and controller **n°8**.
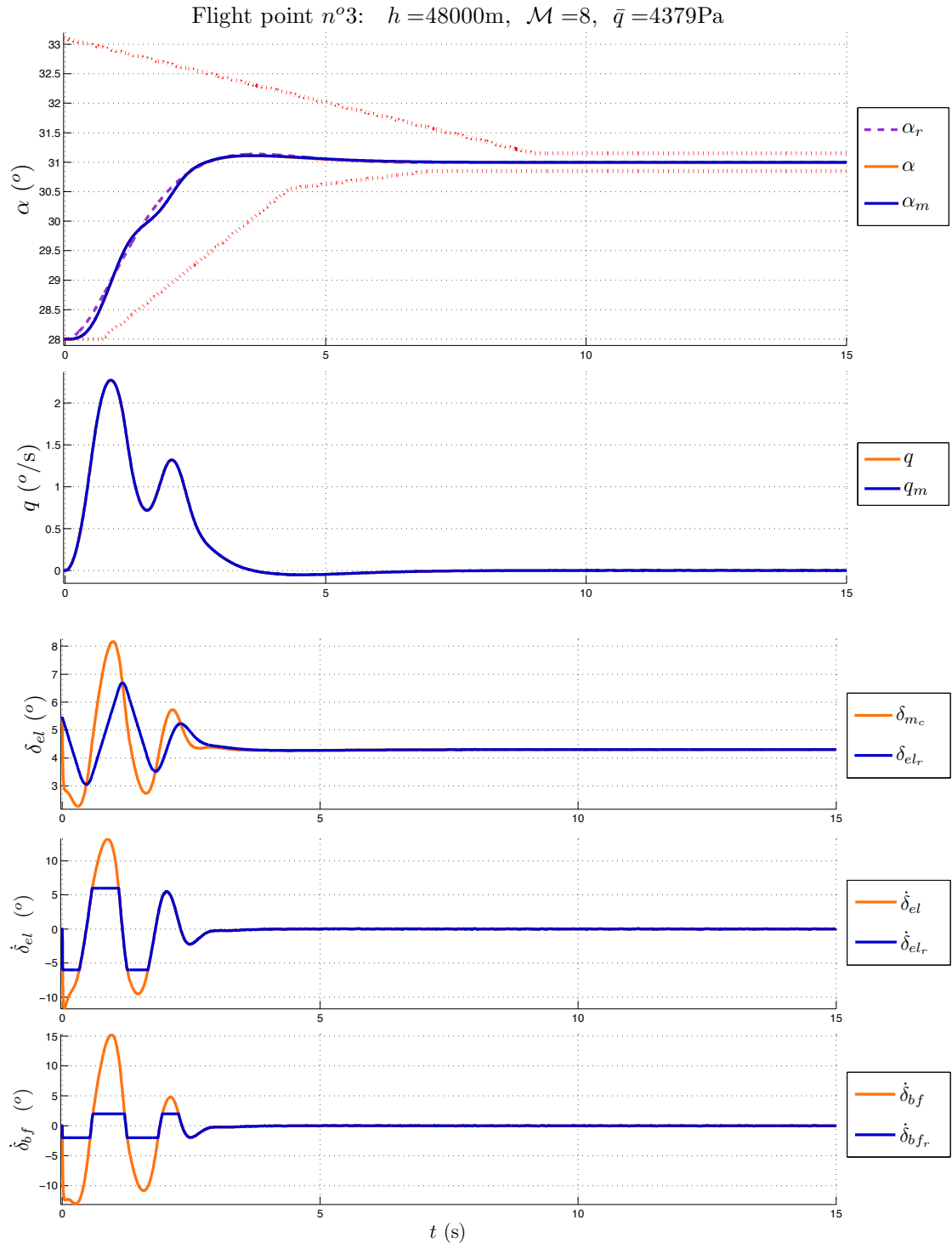
Figure E.35: Simulation with saturated actuator and controller **n°8**.
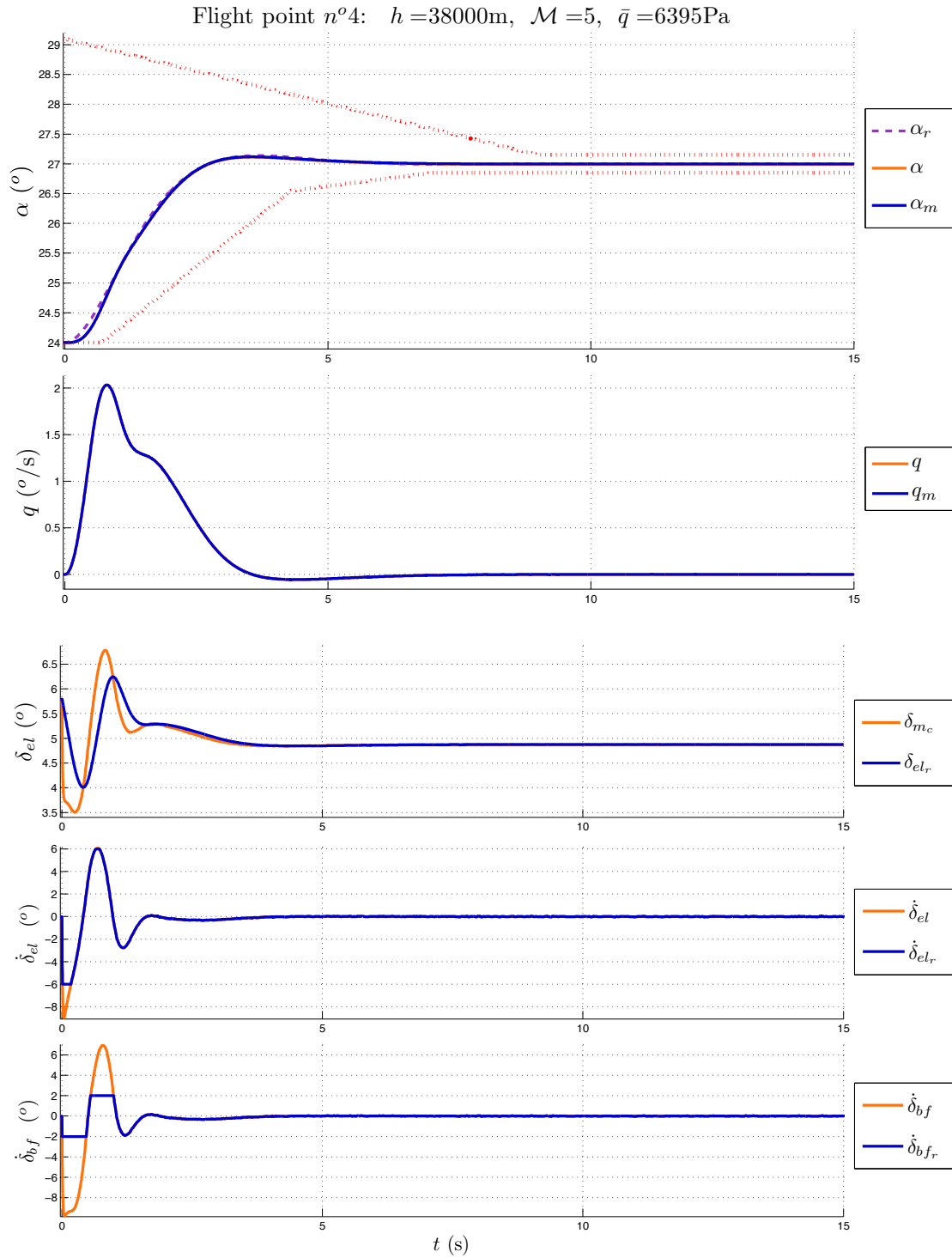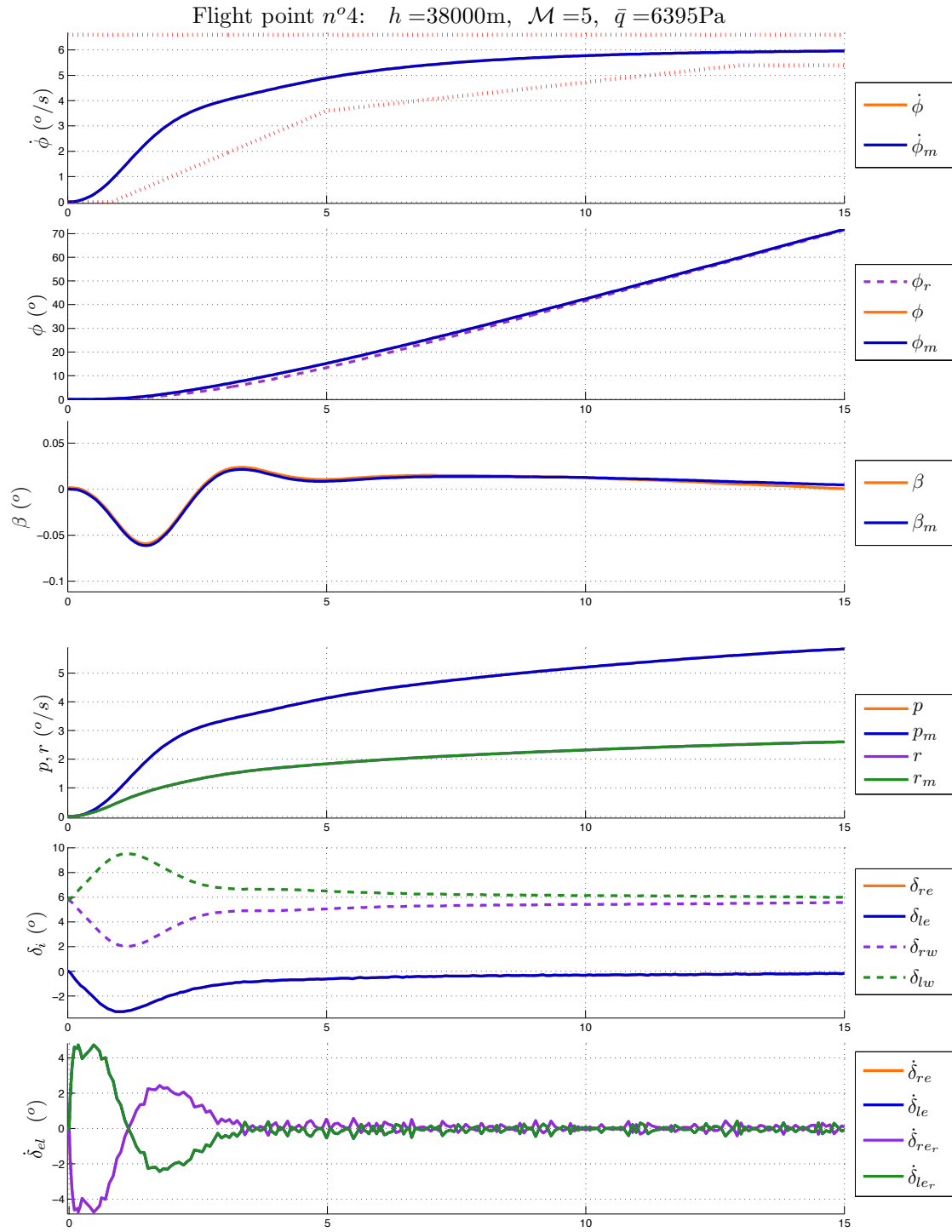
Figure E.36: Simulation with saturated actuator and controller **nº8**.
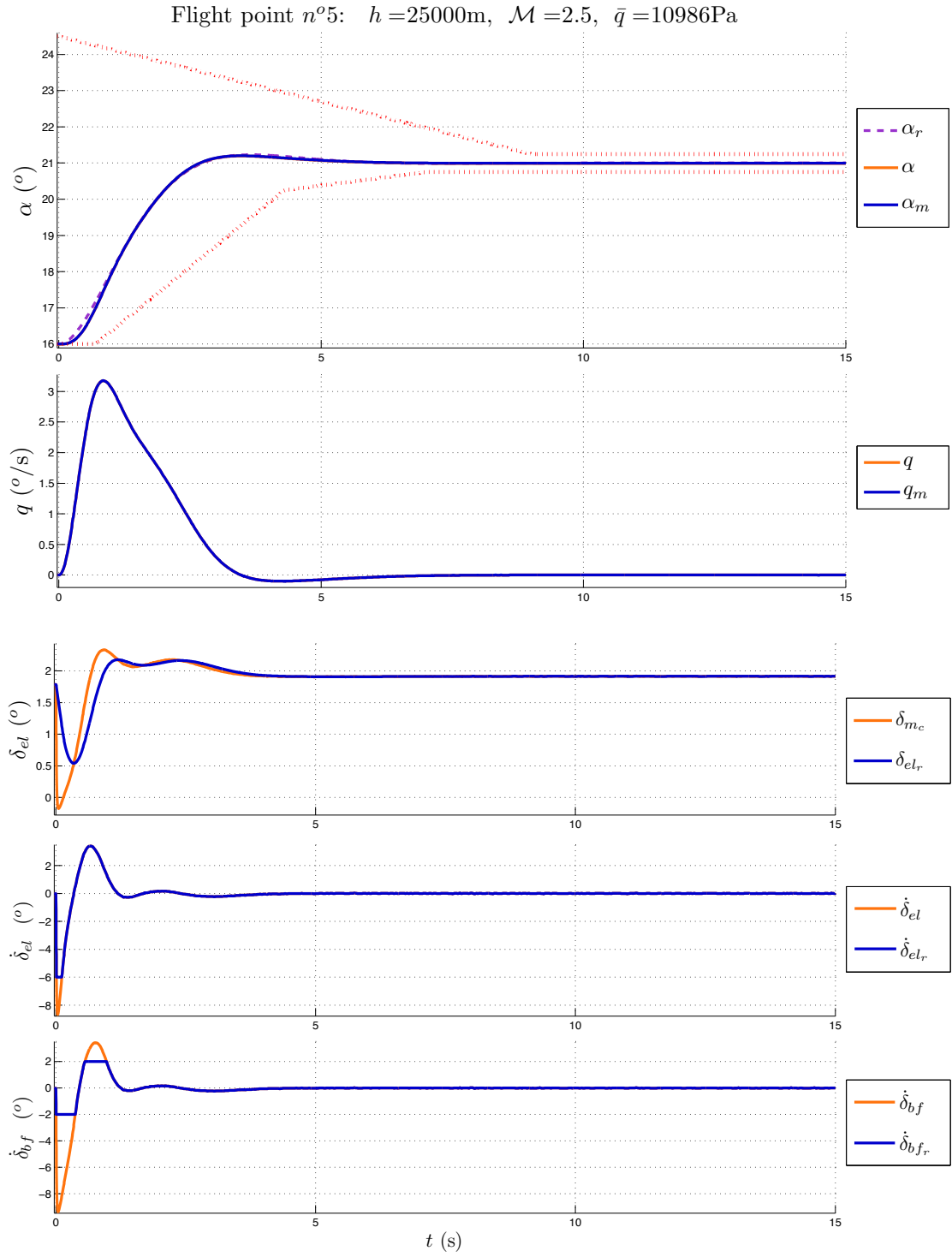
Figure E.37: Simulation with saturated actuator and controller **n°8**.
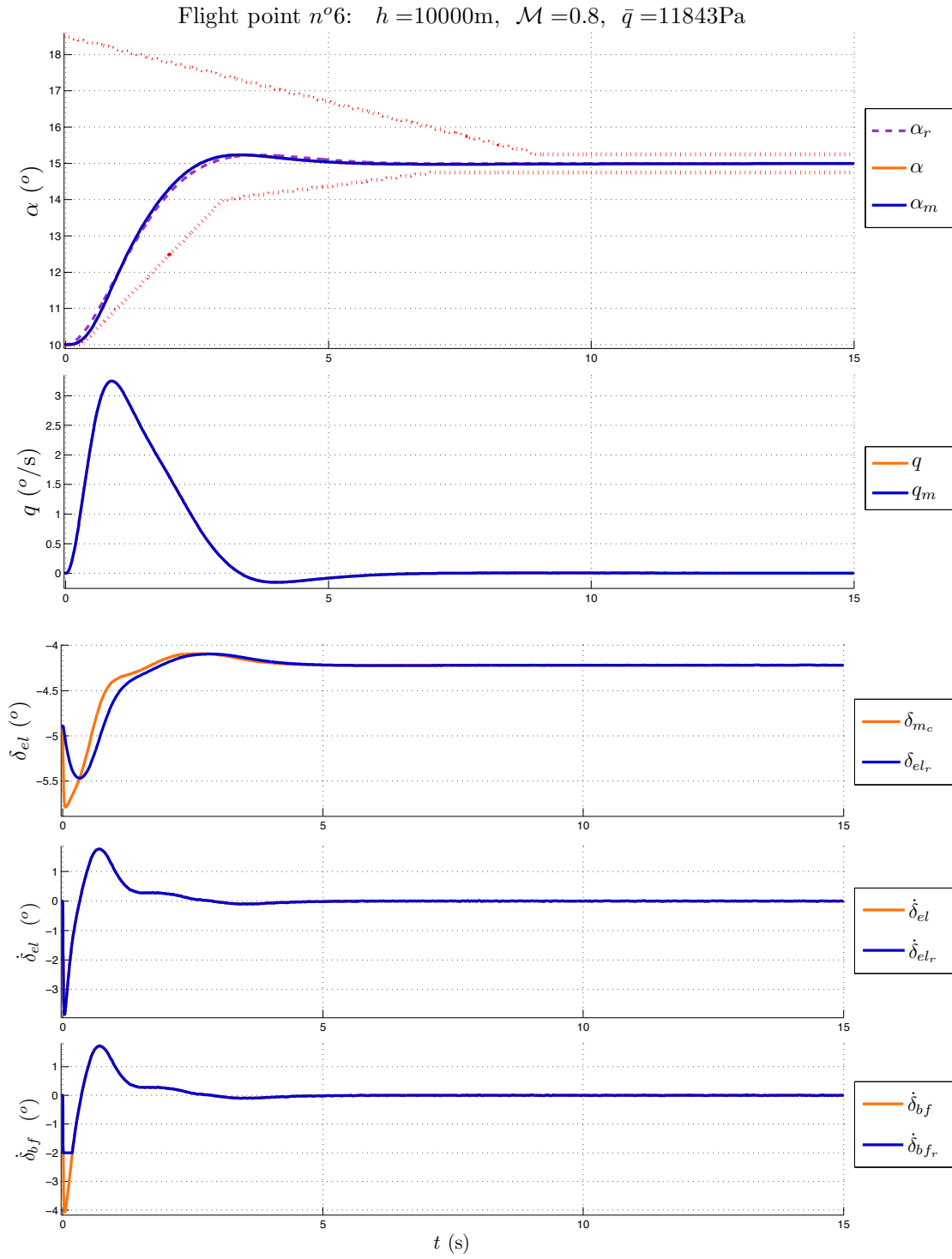
Figure E.38: Simulation with saturated actuator and controller **nº8**.
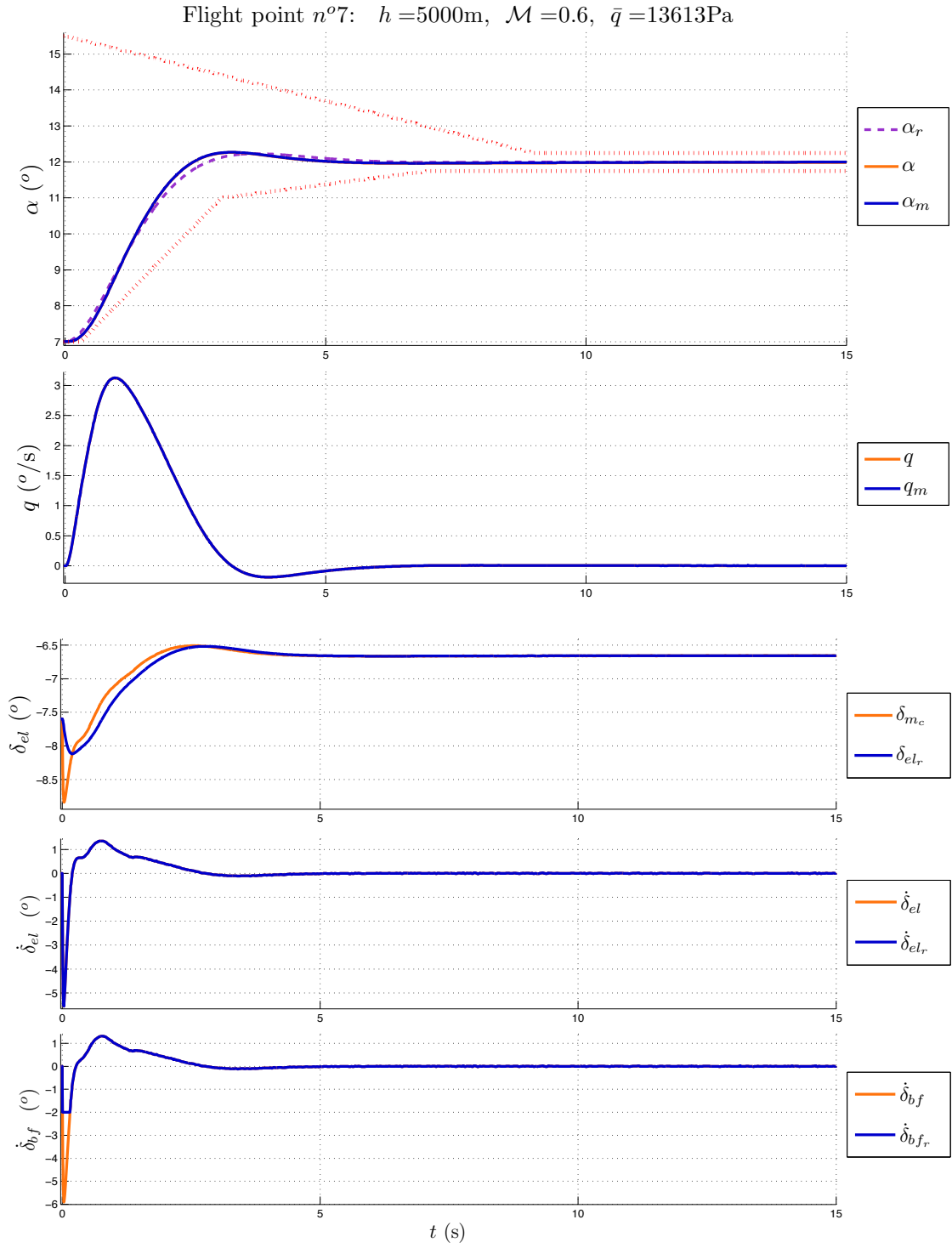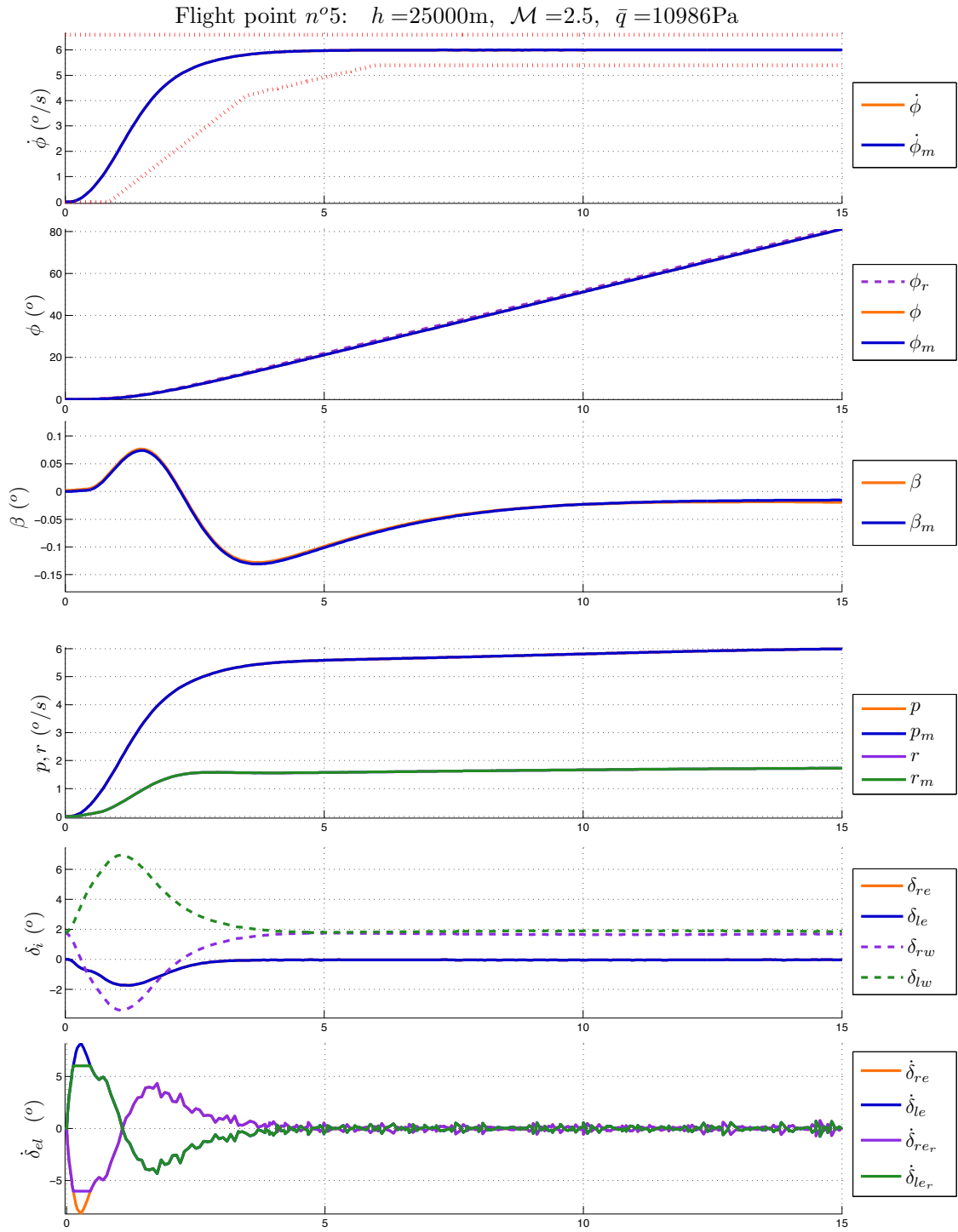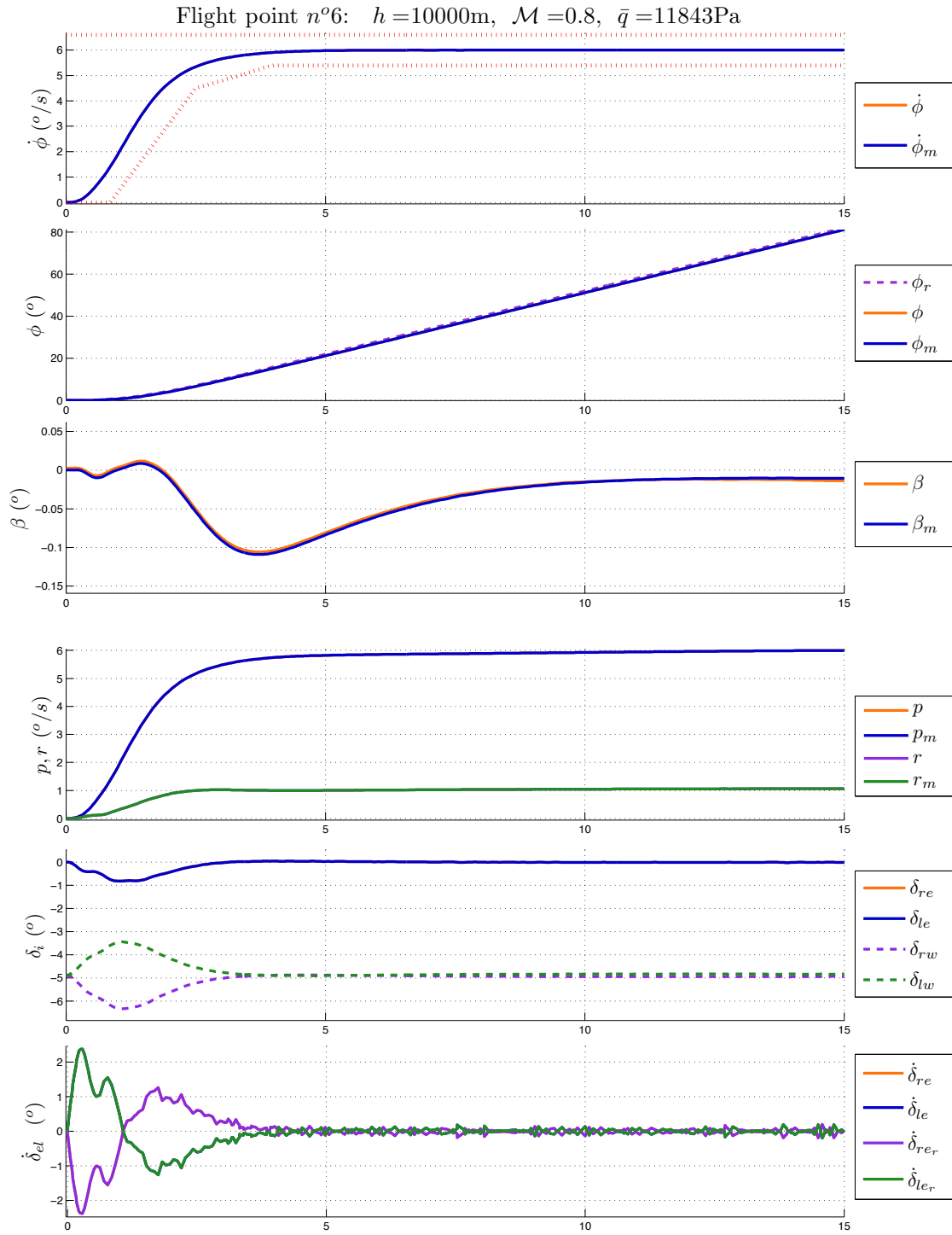
Figure E.39: Simulation with saturated actuator and controller **n°8**.
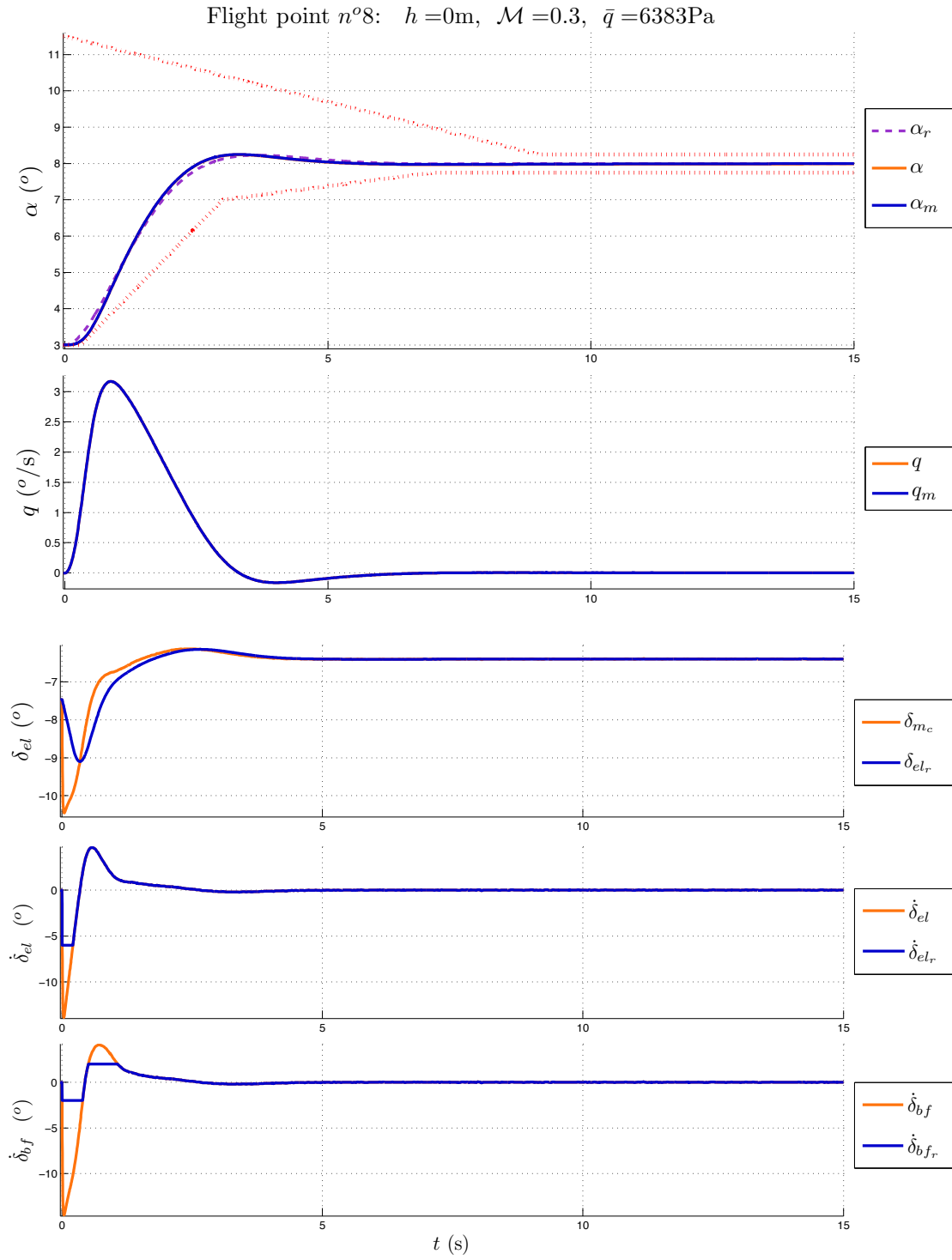
Figure E.40: Simulation with saturated actuator and controller **n⁰8**.
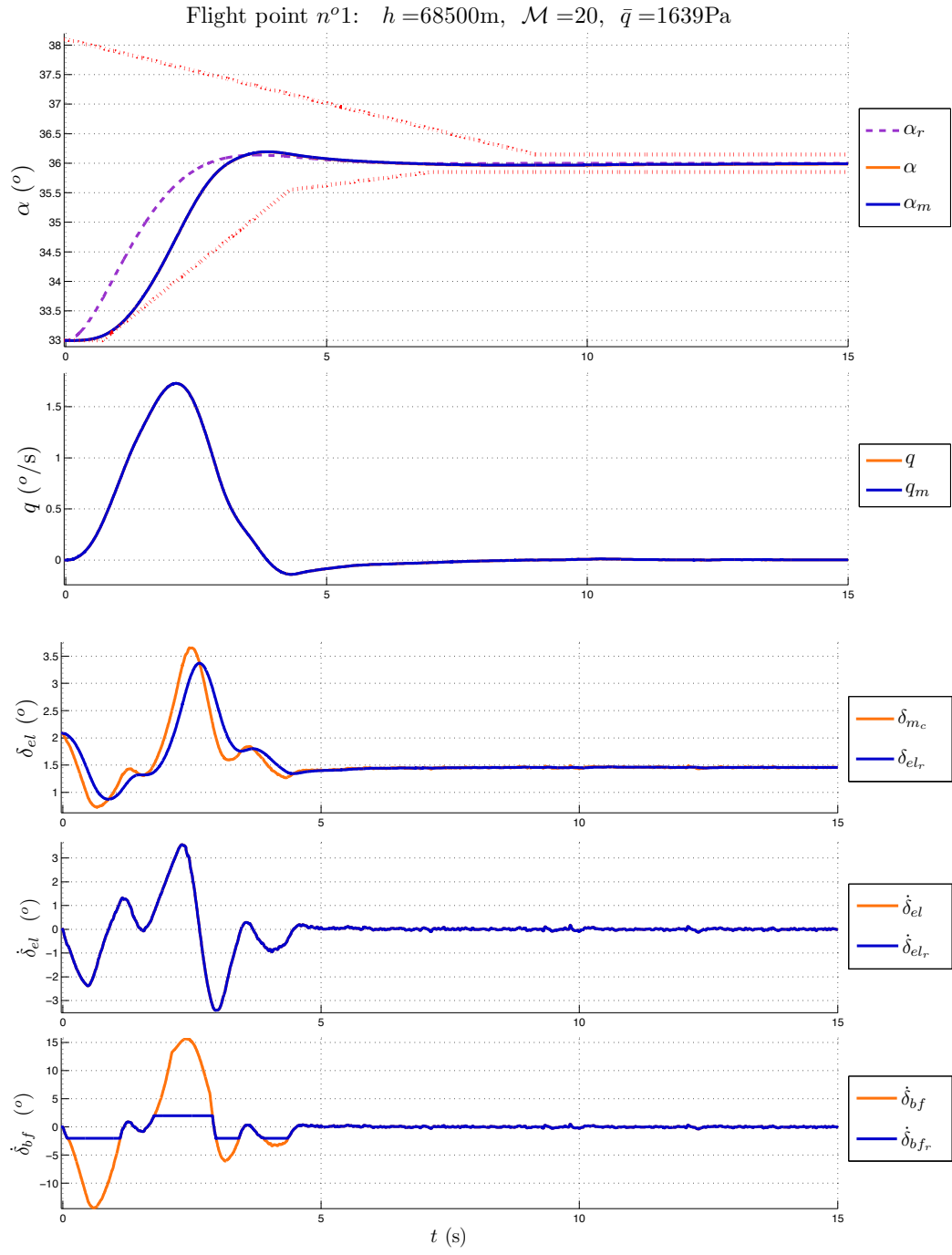
Figure E.41: Simulation with wind and saturated actuator and controller **n°8**.
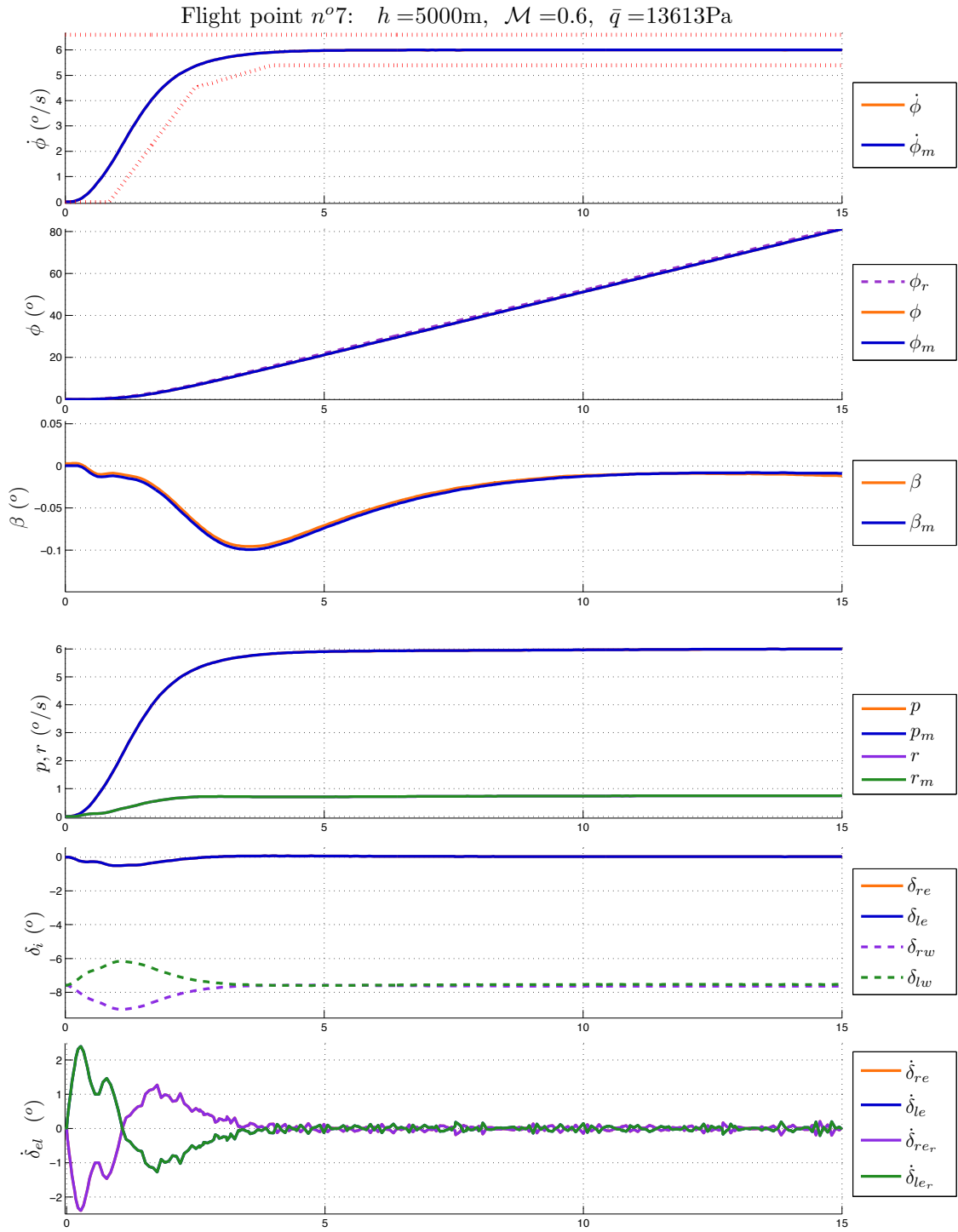
Figure E.42: Simulation with wind and saturated actuator and controller **n°8**.

Figure E.43: Simulation with wind and saturated actuator and controller **n°8**.

Figure E.44: Simulation with wind and saturated actuator and controller **n°8**.

Figure E.45: Simulation with wind and saturated actuator and controller **n°8**.

Figure E.46: Simulation with wind and saturated actuator and controller **n°8**.

Figure E.47: Simulation with wind and saturated actuator and controller **n°8**.

Figure E.48: Simulation with wind and saturated actuator and controller **nᵒ8**.

E.2 Results on the lateral axis

E.2.1 NDI-PI controller simulation results

Flight point n^o1: $h =68500$m, $\mathcal{M} =20$, $\bar{q} =1639$Pa
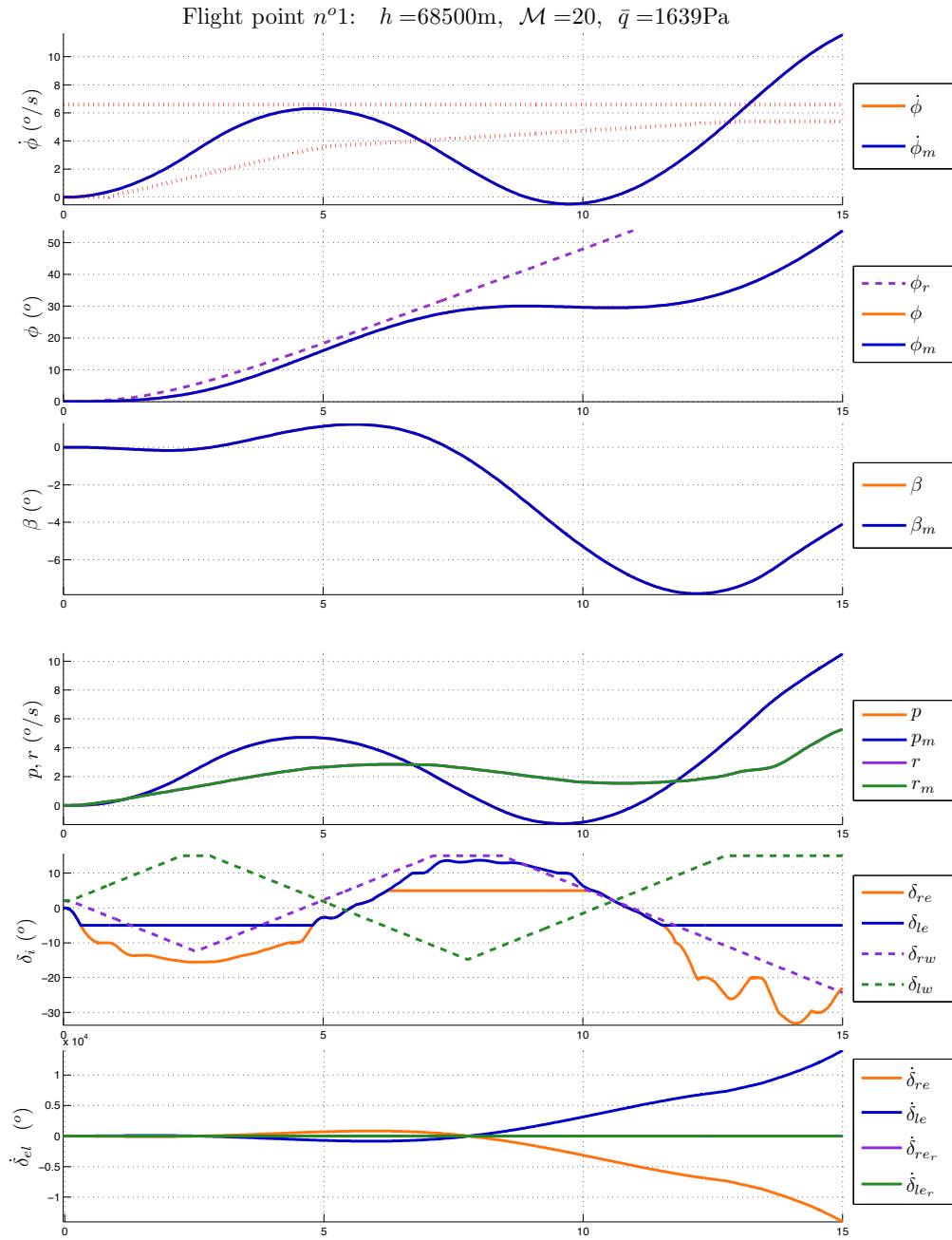
Figure E.49: Simulation with saturated actuator and controller **n°9**.
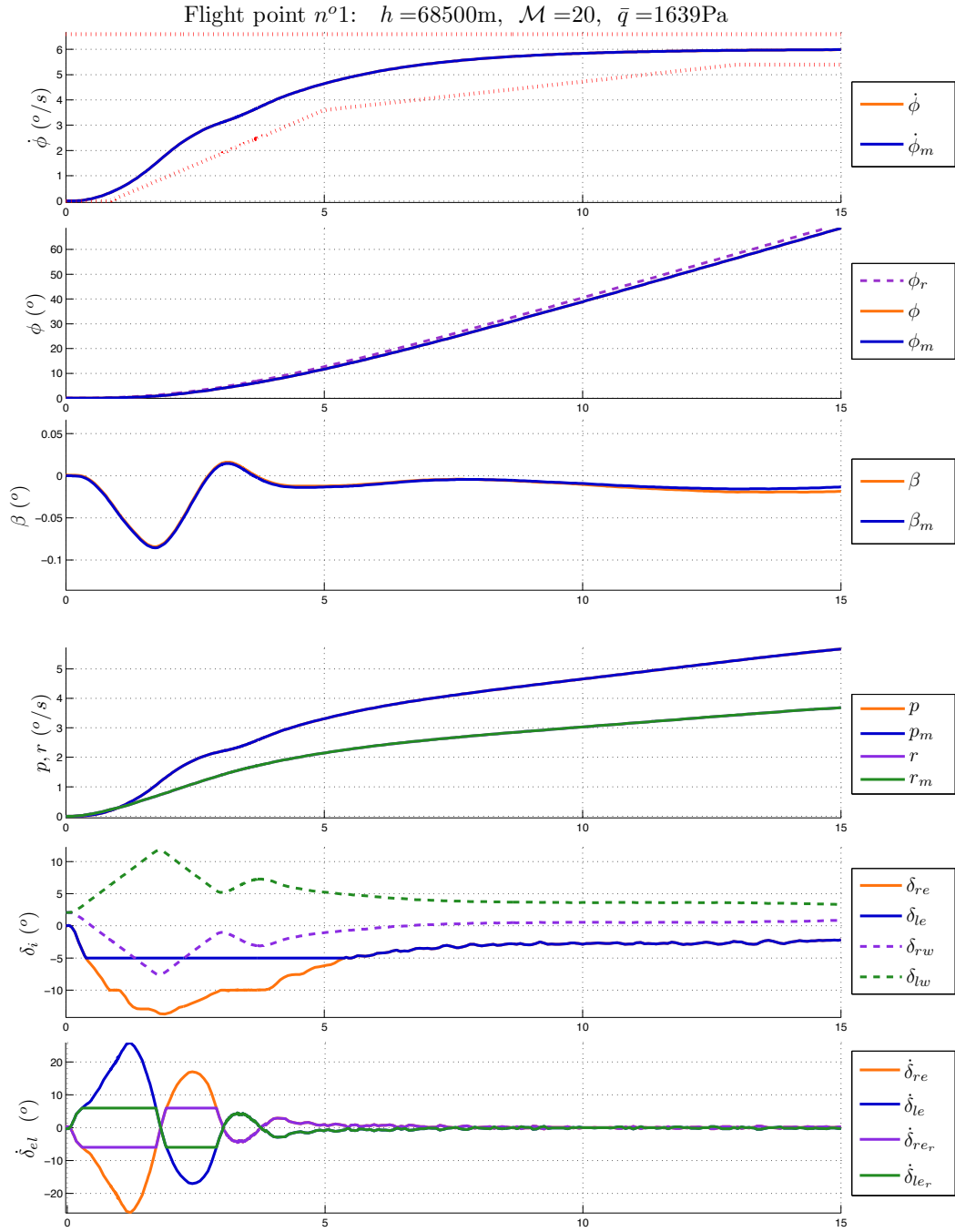
Figure E.50: Simulation with saturated actuator and controller **n°9**.

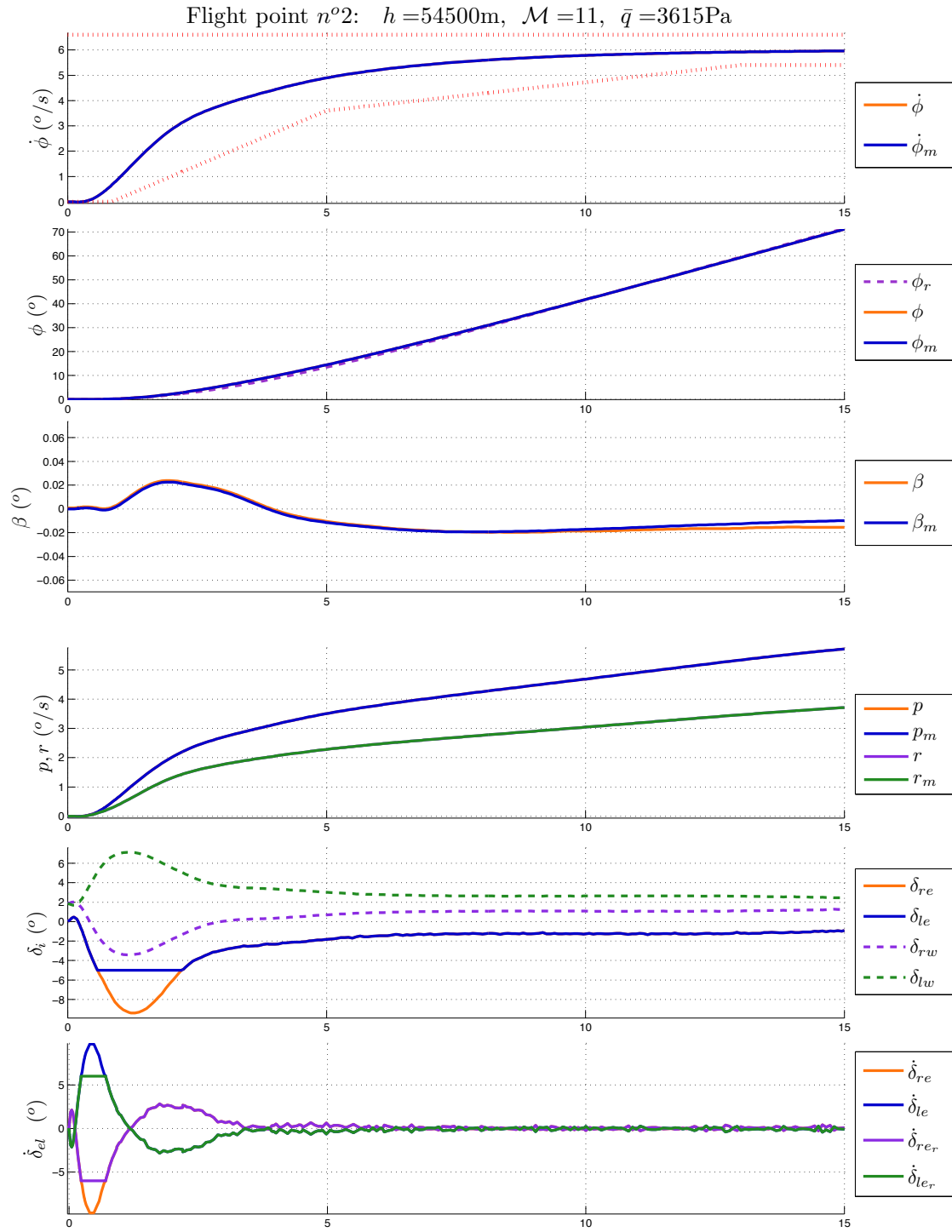Figure E.51: Simulation with saturated actuator and controller **n°9**.

Figure E.52: Simulation with saturated actuator and controller **n°9**.

Figure E.53: Simulation with saturated actuator and controller **n°9**.
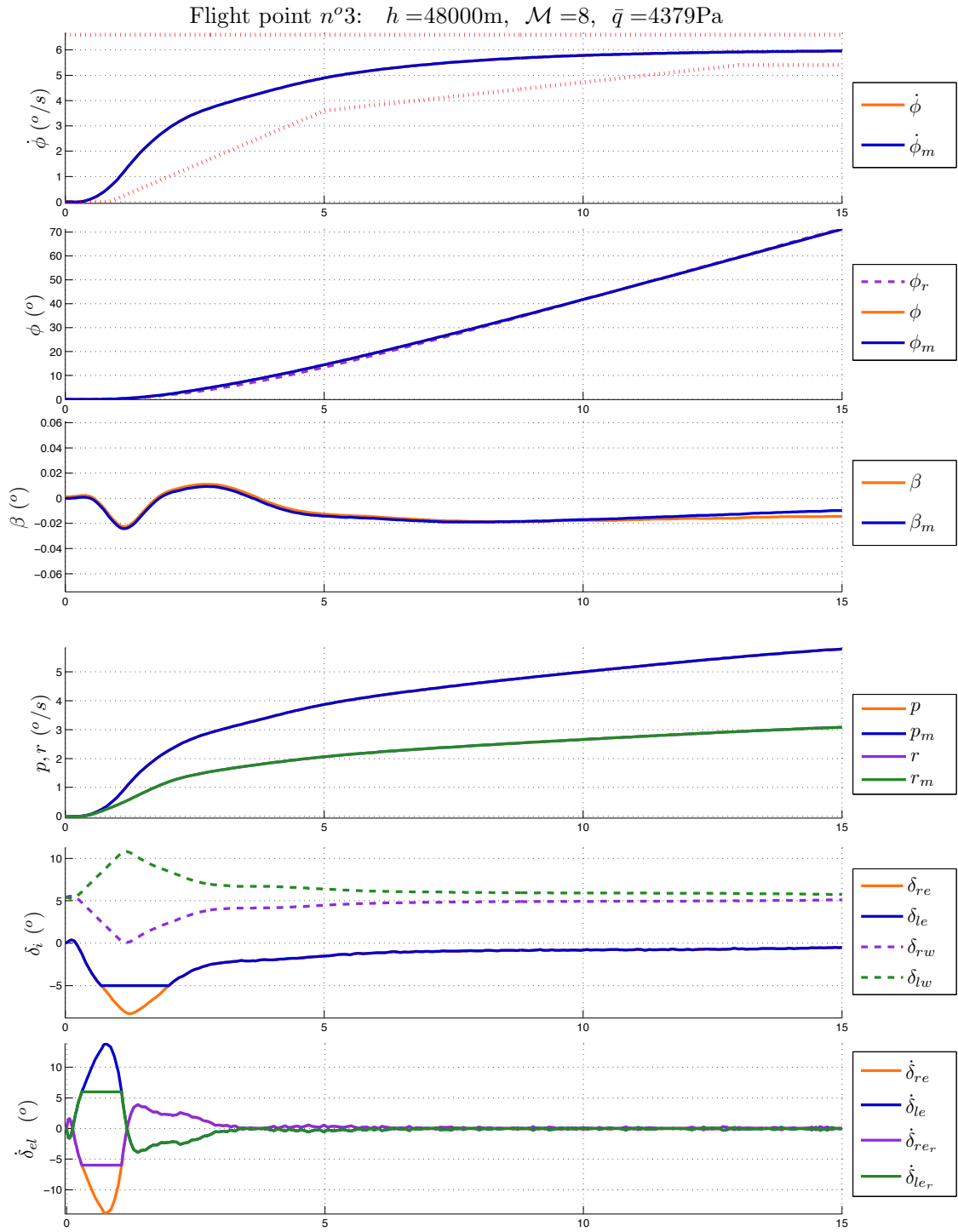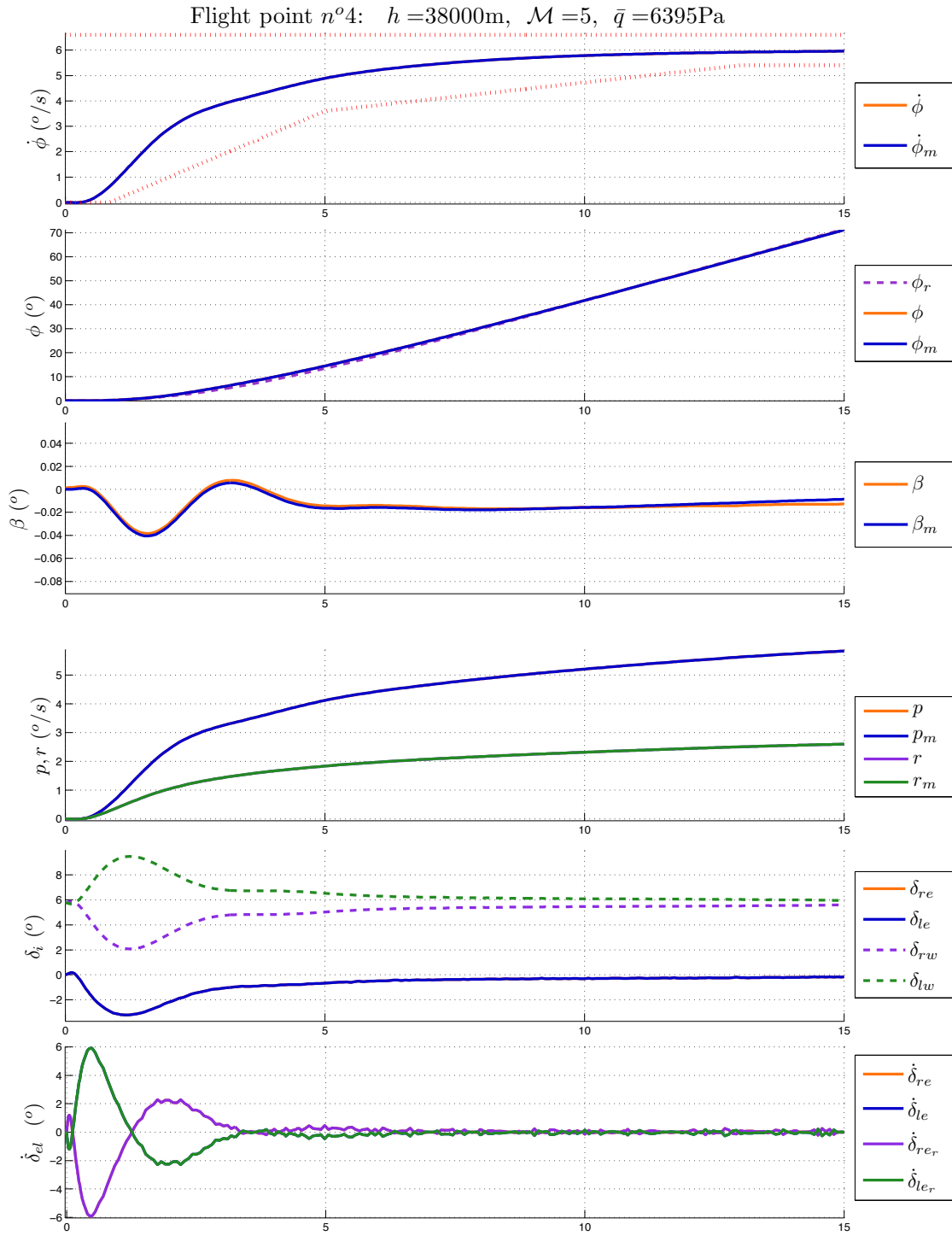
Figure E.54: Simulation with saturated actuator and controller **n°9**.

Figure E.55: Simulation with saturated actuator and controller **nº9**.

Figure E.56: Simulation with saturated actuator and controller **n°9**.

E.2.2 Robust nonlinear compensator simulation results

Figure E.57: Simulation with saturated actuator and controller **nᵒ11**.

Figure E.58: Simulation with saturated actuator and controller **nº11**.

Figure E.59: Simulation with saturated actuator and controller **nº11**.

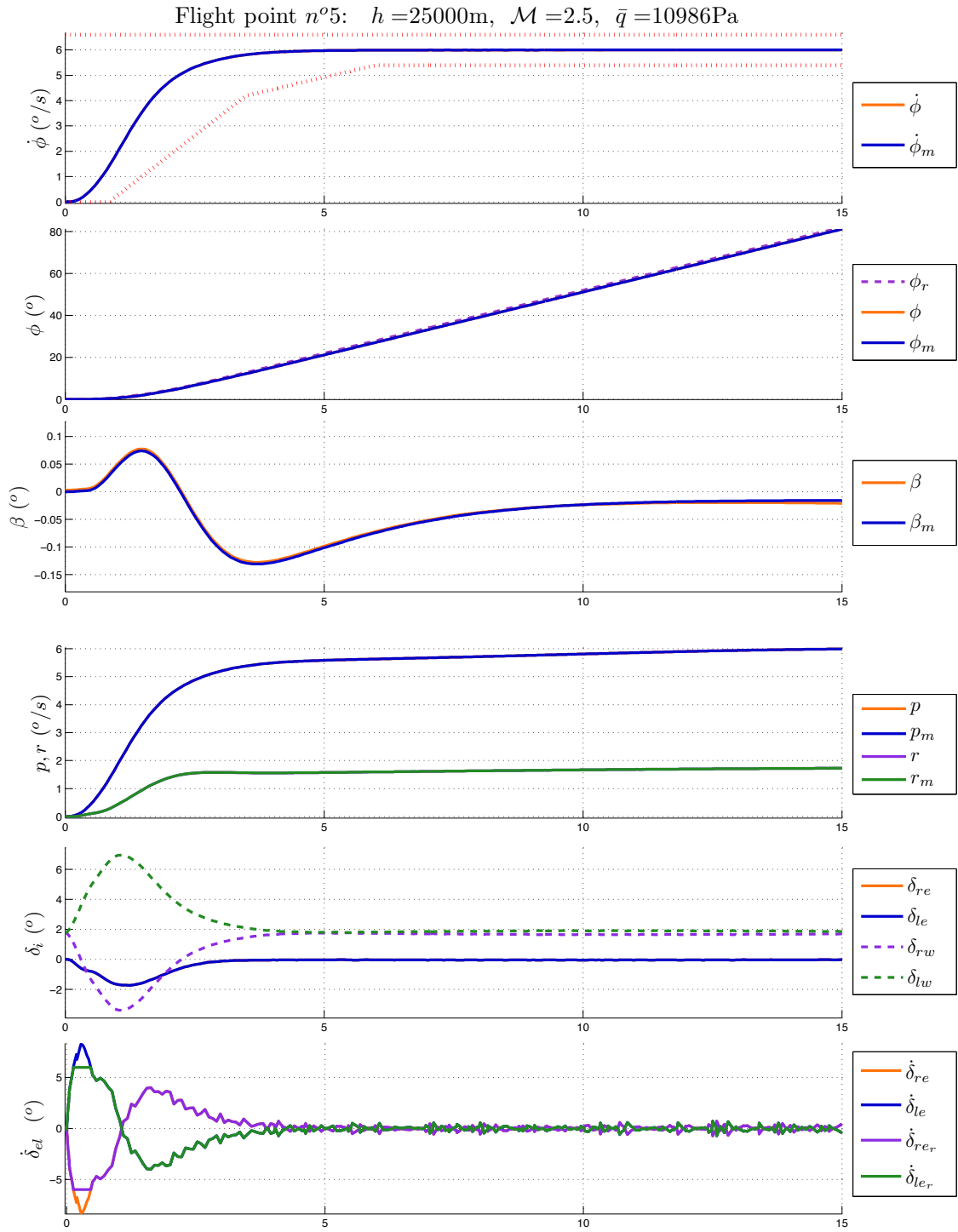Figure E.60: Simulation with saturated actuator and controller **n°11**.

Figure E.61: Simulation with saturated actuator and controller **nº10**.

Figure E.62: Simulation with saturated actuator and controller **n°10**.

Figure E.63: Simulation with saturated actuator and controller **n°10**.

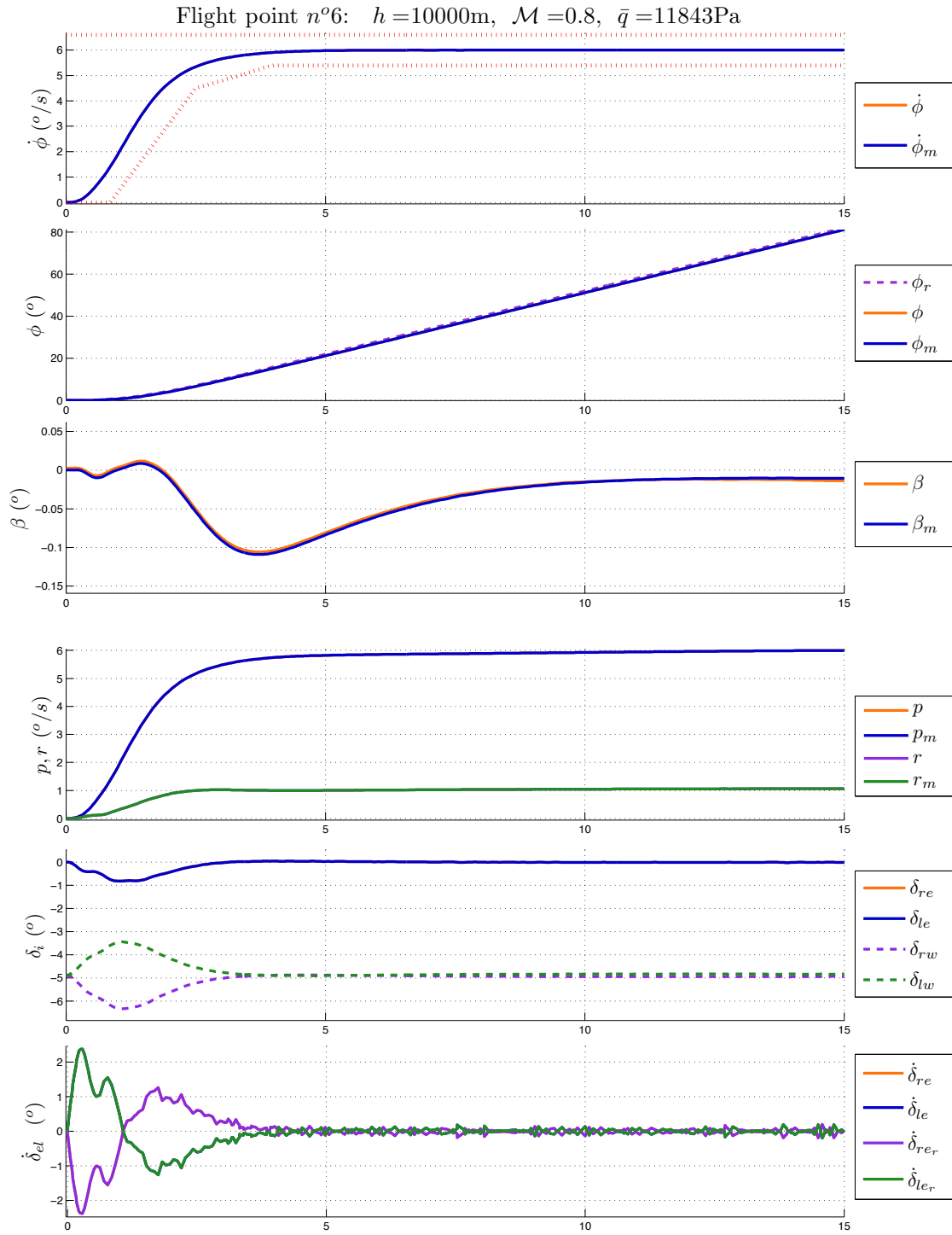Figure E.64: Simulation with saturated actuator and controller **n°10**.

E.2.3 Anti-windup robust controller simulation results

Figure E.65: Simulation with saturated actuator and controller **nº12**.

Figure E.66: Simulation with saturated actuator and controller **nº12**.

Figure E.67: Simulation with saturated actuator and controller **n°12**.

Figure E.68: Simulation with saturated actuator and controller **n°12**.

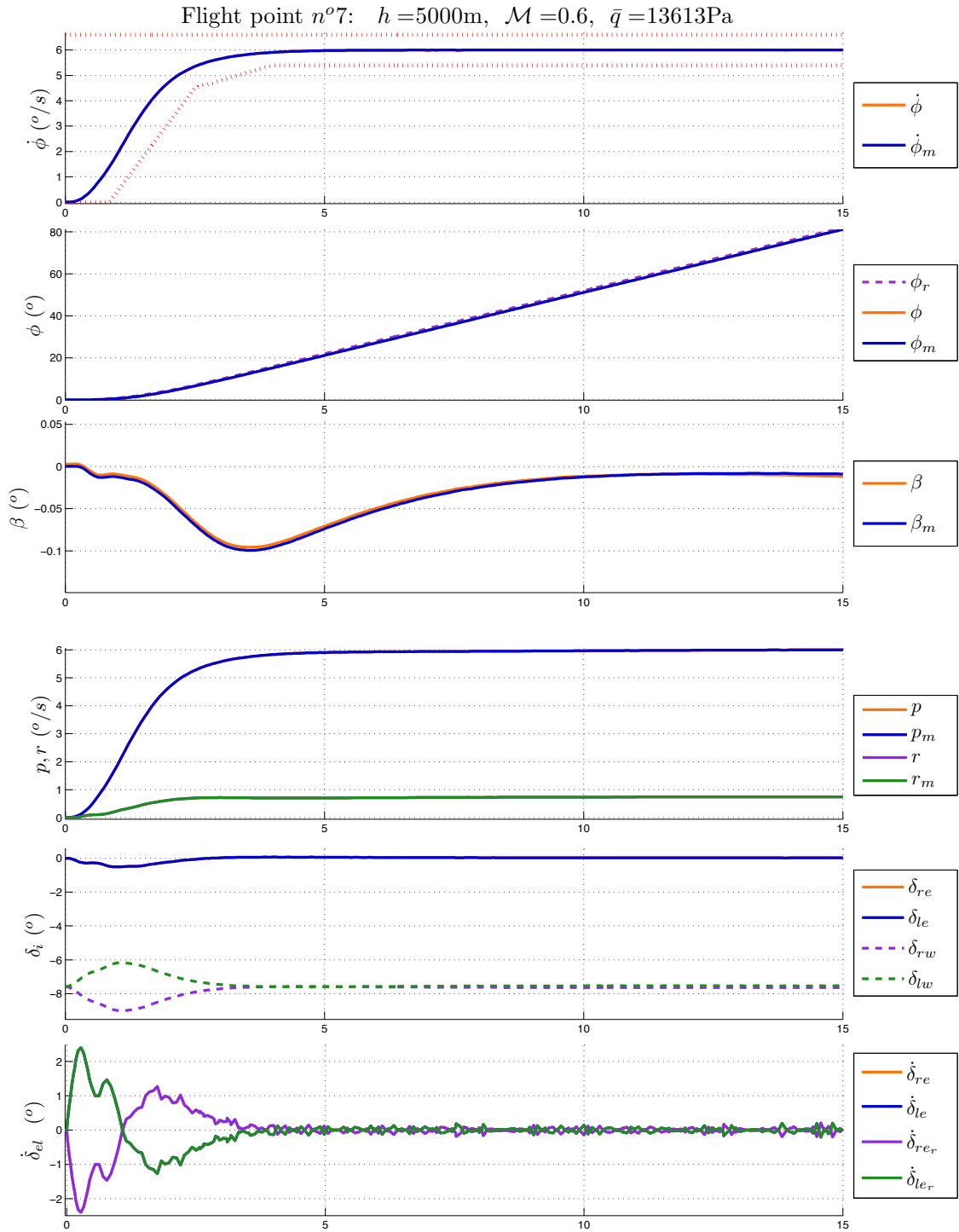Figure E.69: Simulation with saturated actuator and controller **n⁰10**.

Figure E.70: Simulation with saturated actuator and controller **nᵒ10**.

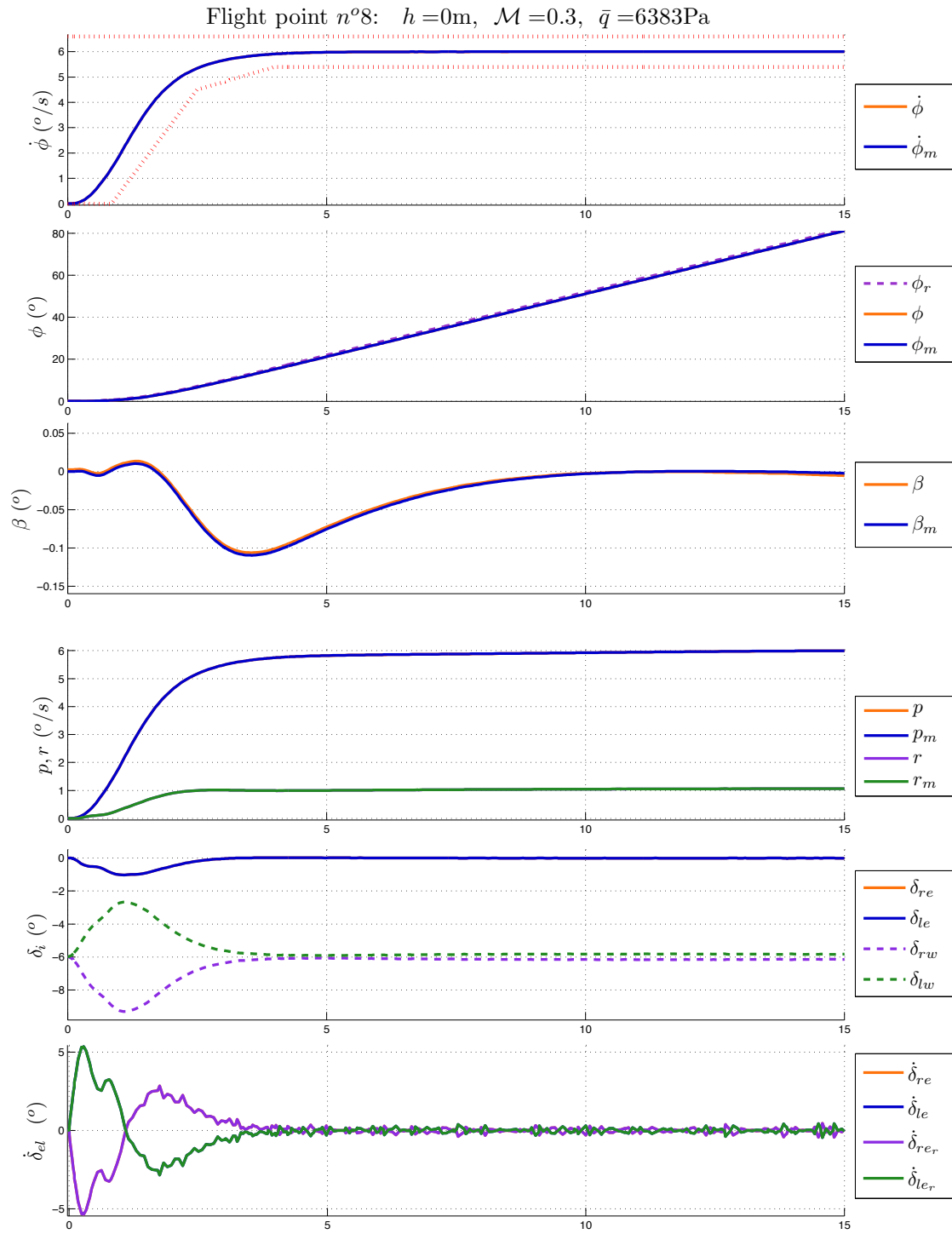Figure E.71: Simulation with saturated actuator and controller **n⁰10**.

Figure E.72: Simulation with saturated actuator and controller **n°10**.
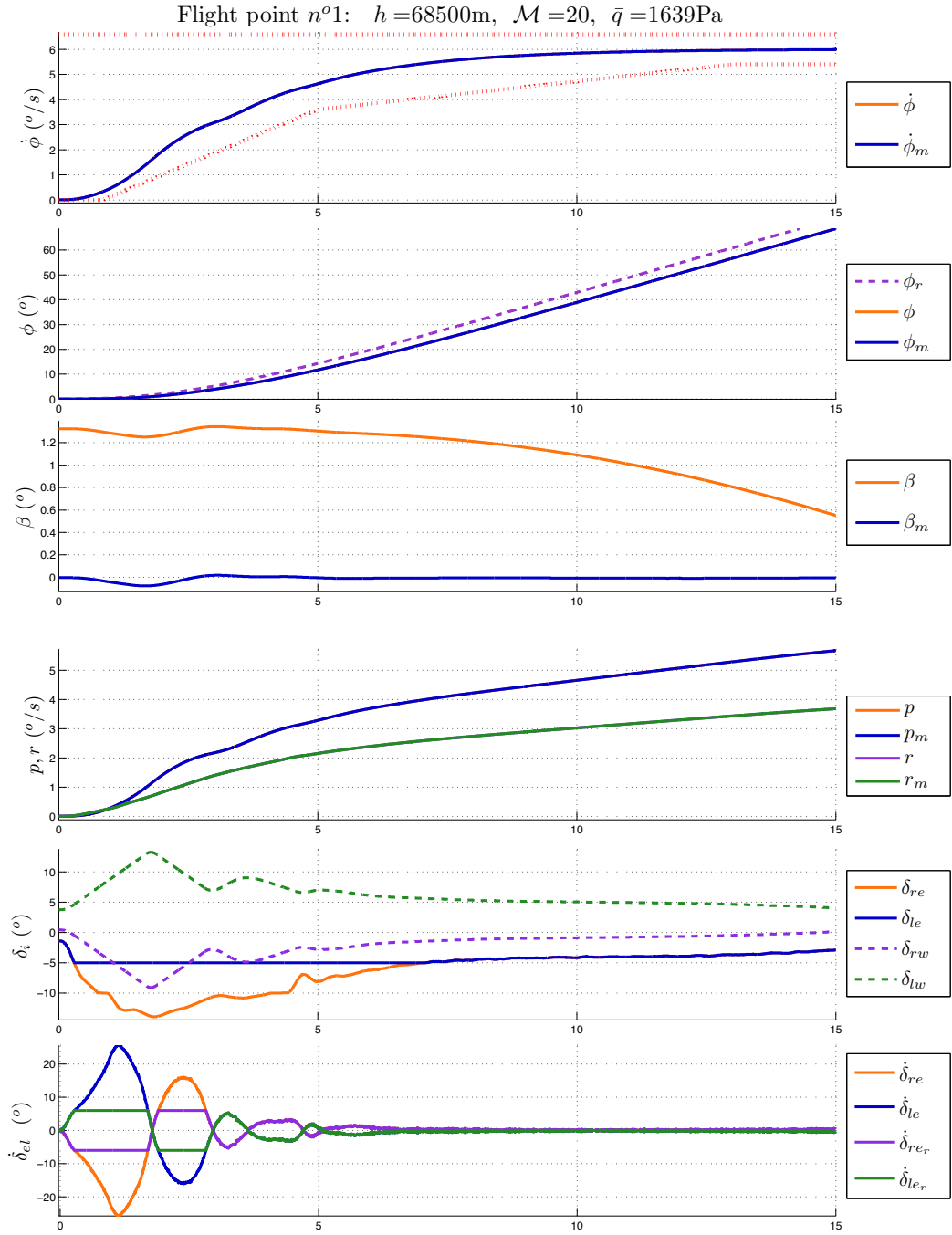
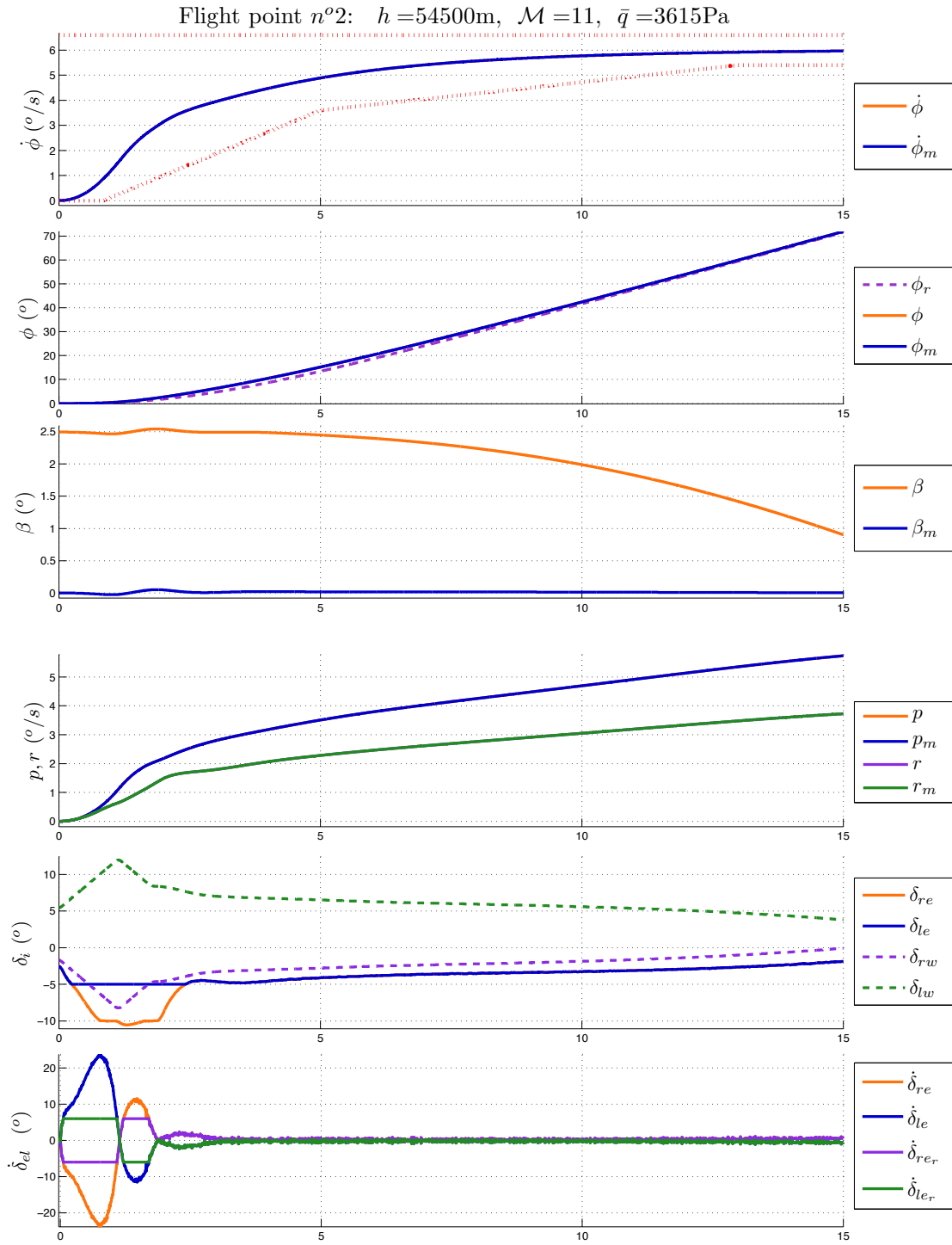Figure E.73: Simulation with wind and saturated actuator and controller **n⁰12**.
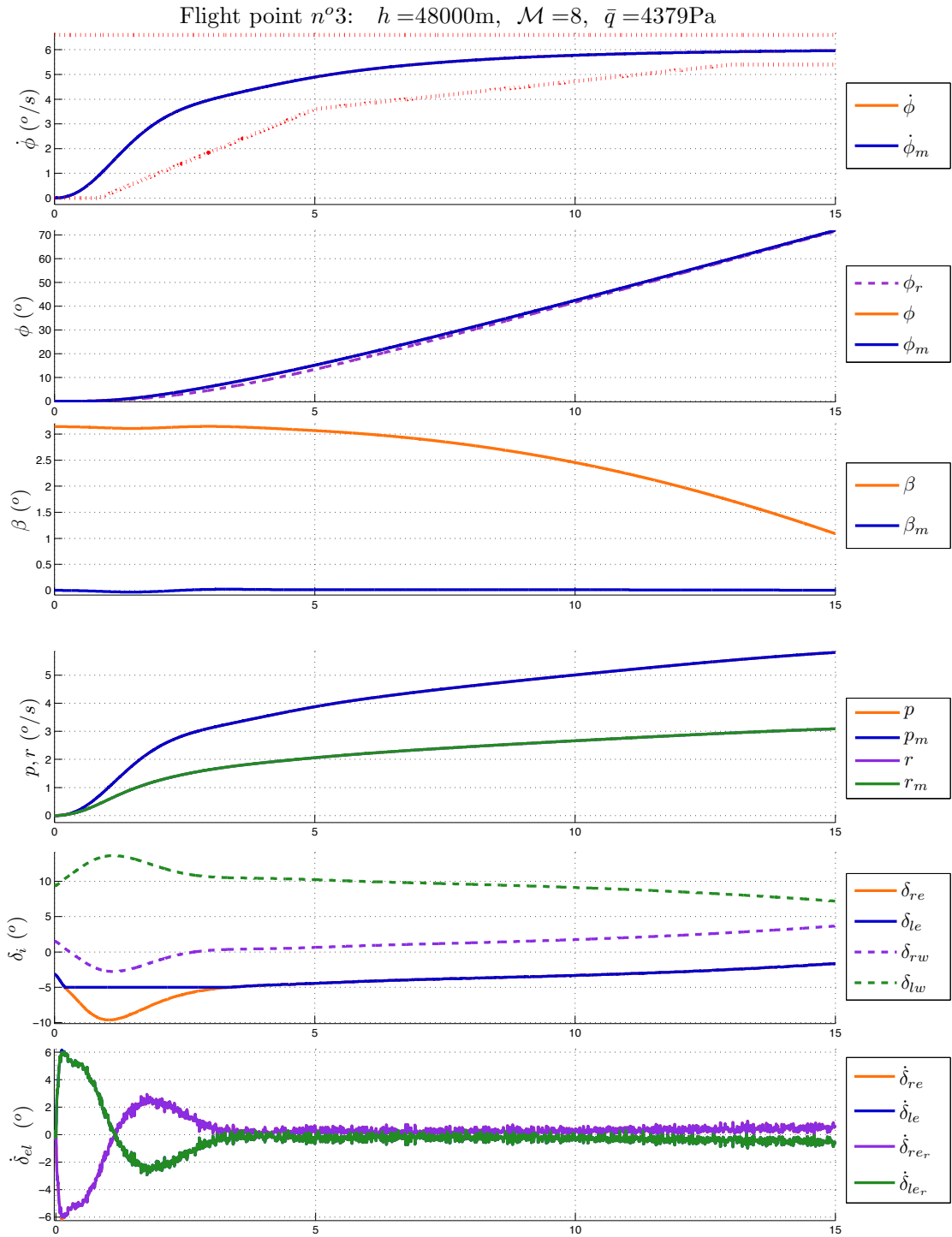
Figure E.74: Simulation with wind and saturated actuator and controller **n°12**.

Figure E.75: Simulation with wind and saturated actuator and controller **n°12**.

Figure E.76: Simulation with wind and saturated actuator and controller **nº12**.

Figure E.77: Simulation with wind and saturated actuator and controller **nᵒ10**.
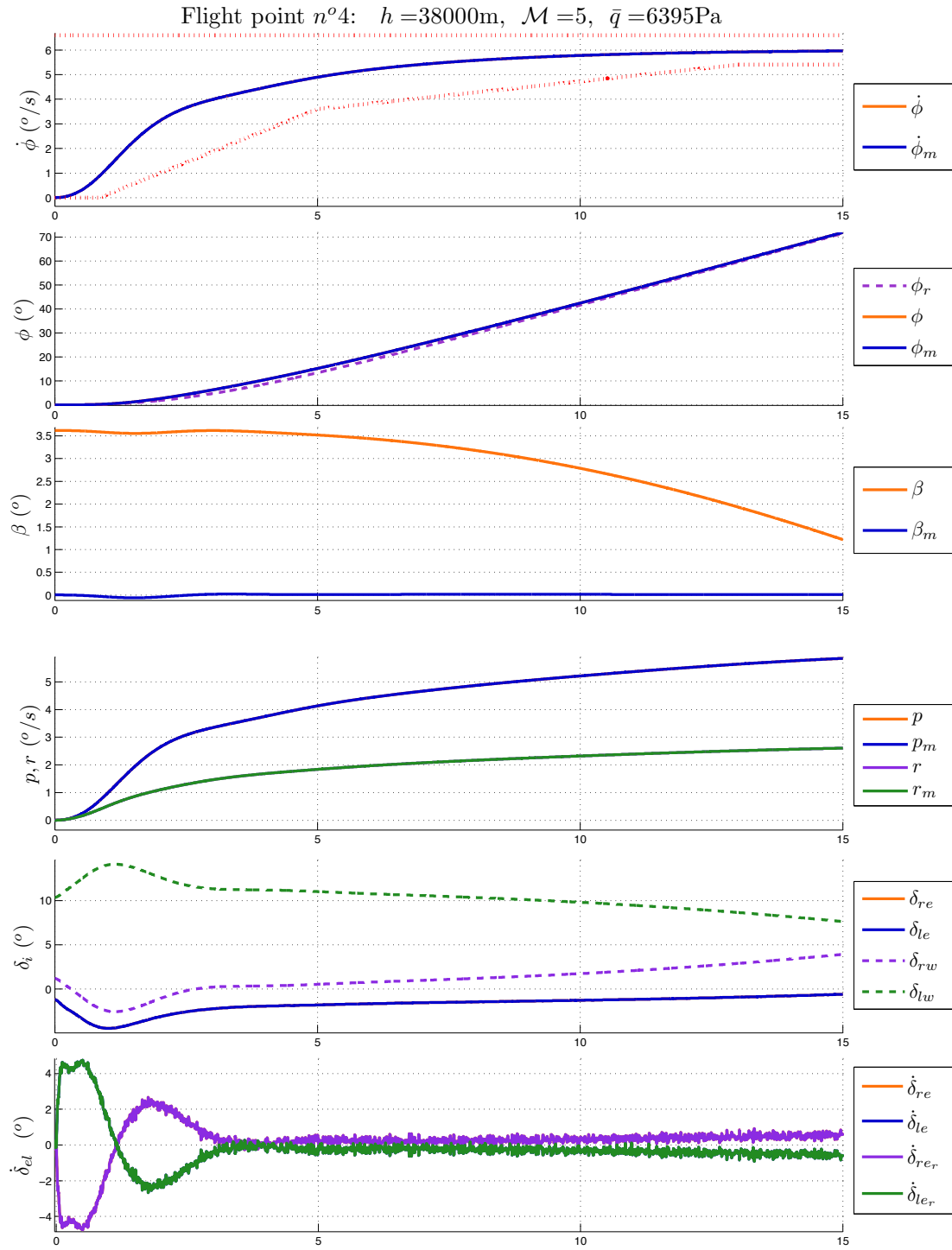
Figure E.78: Simulation with wind and saturated actuator and controller **n°10**.
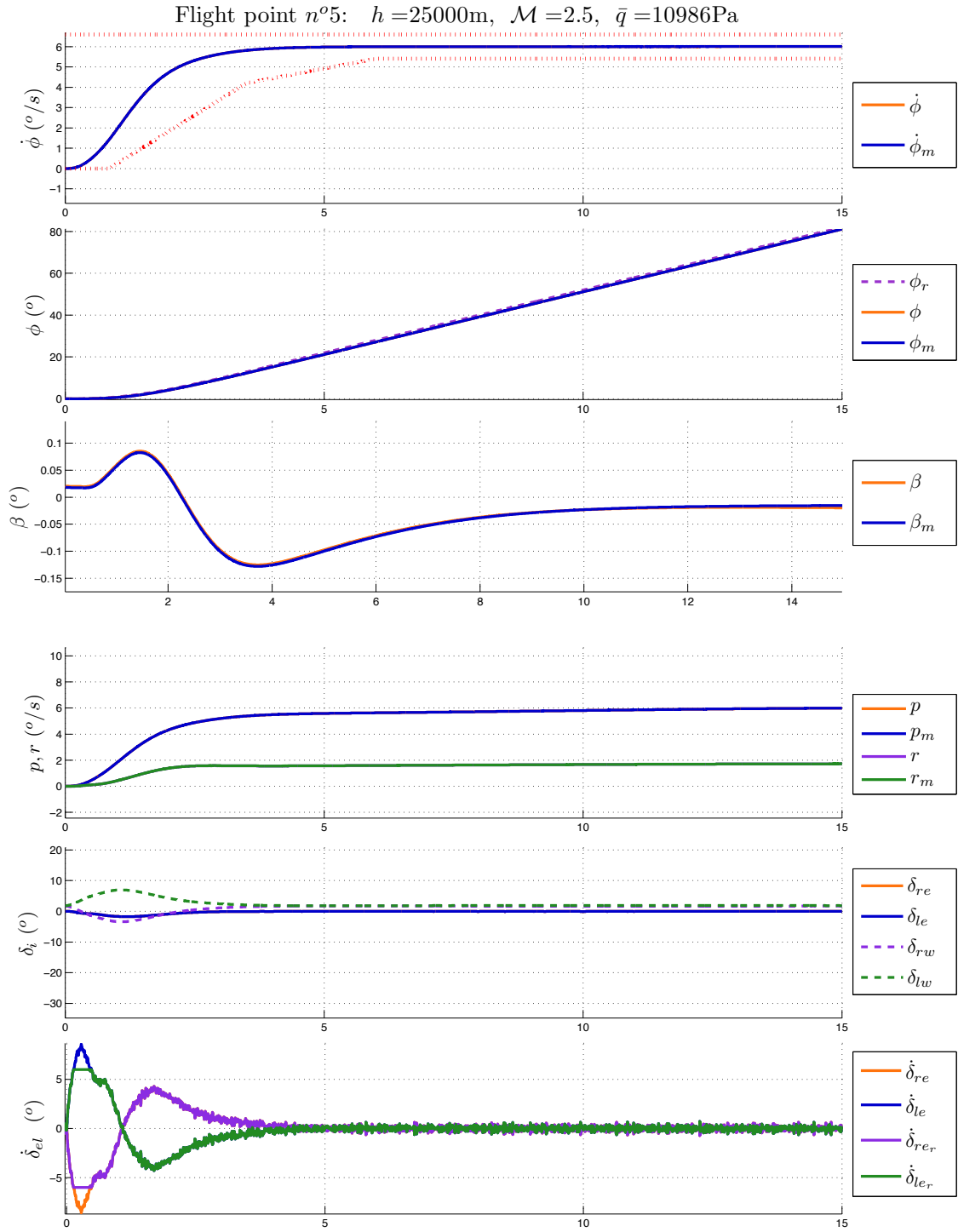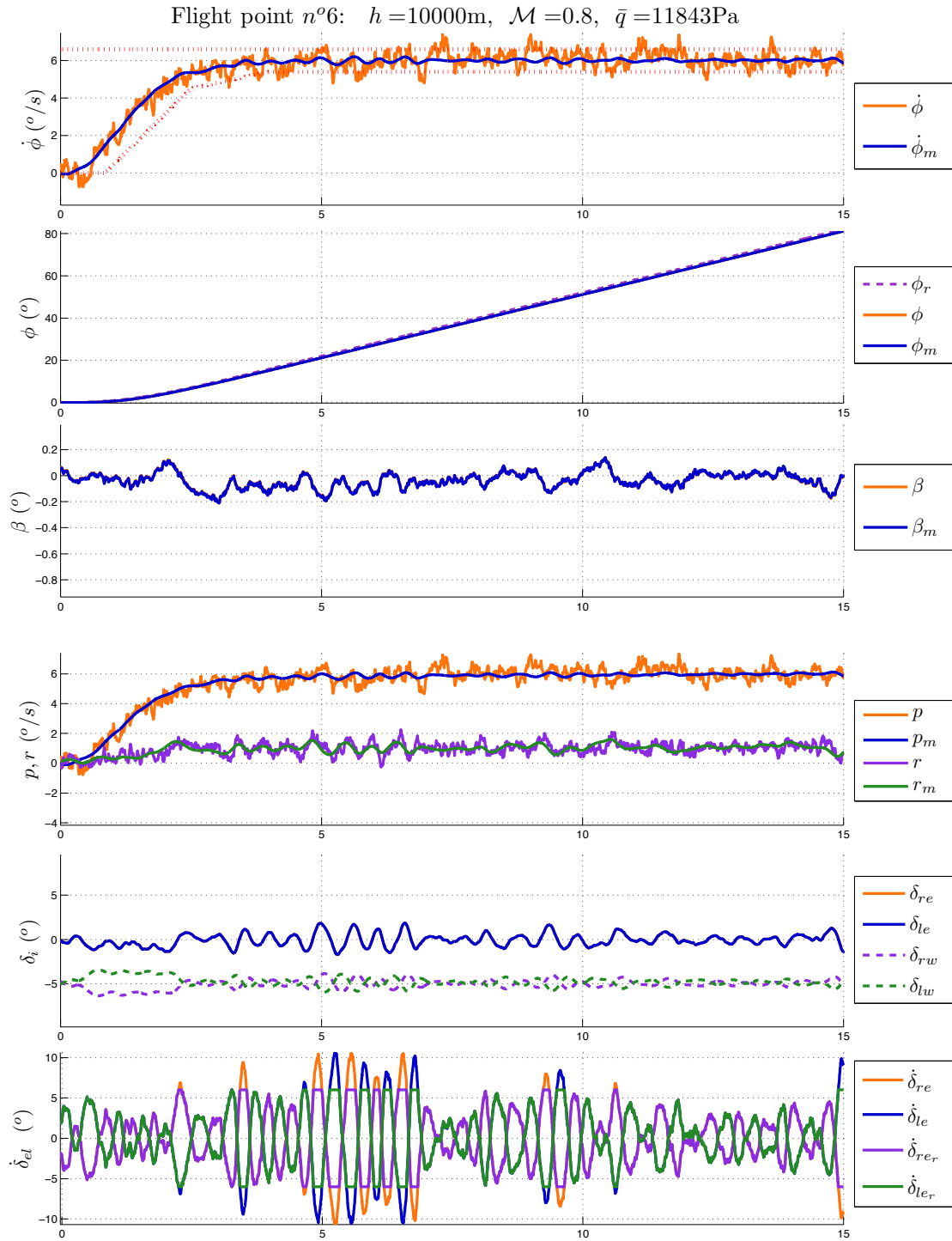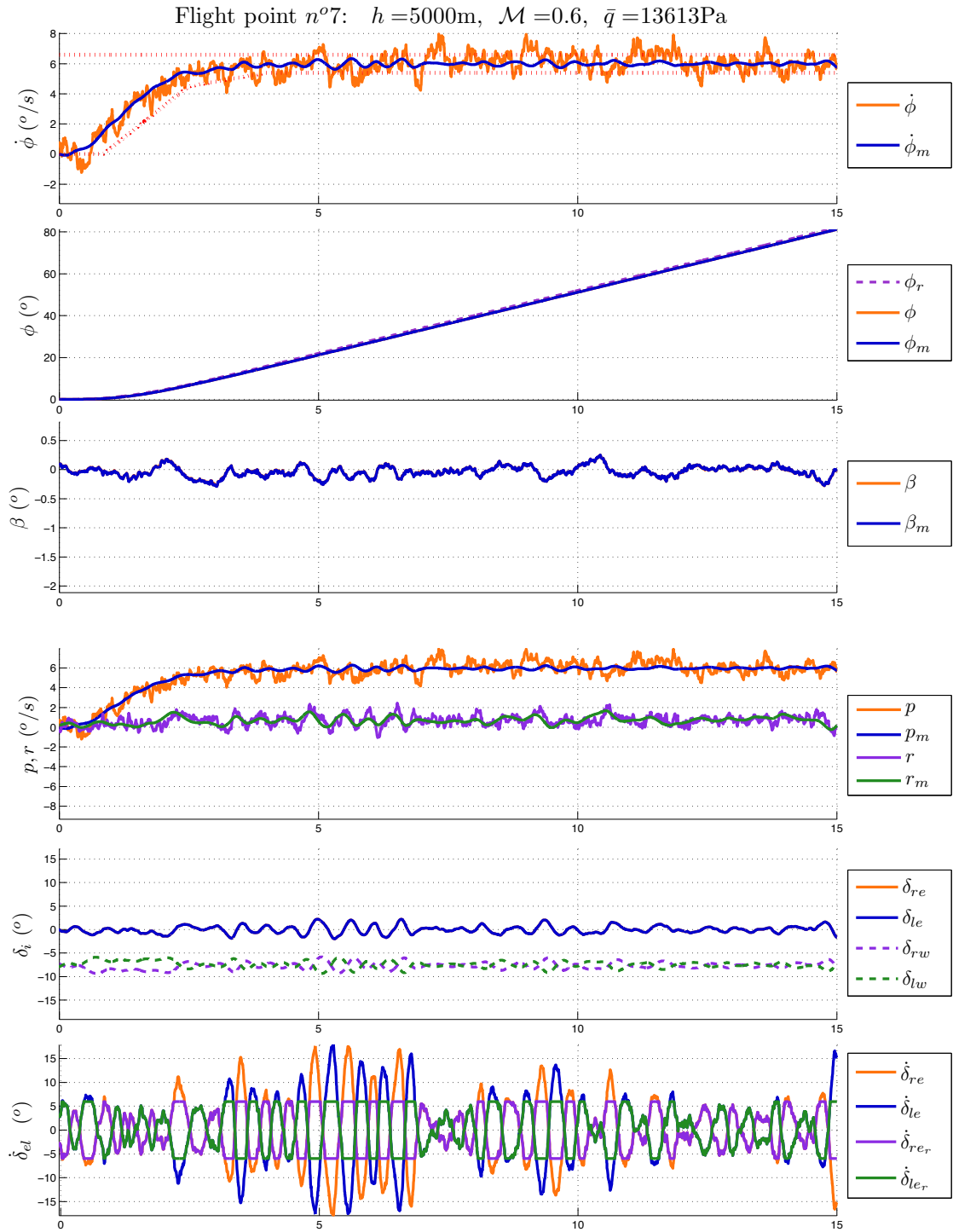
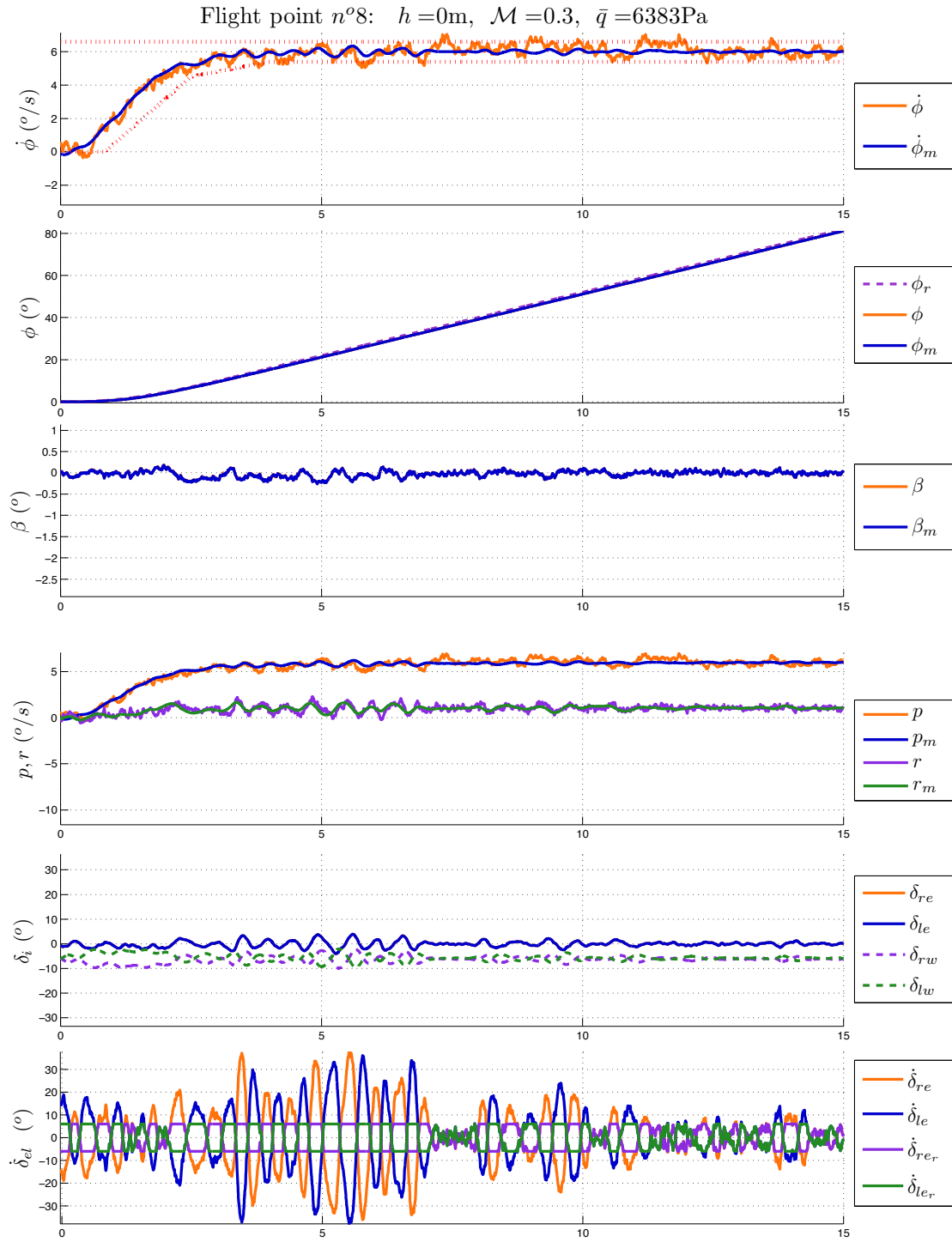Figure E.79: Simulation with wind and saturated actuator and controller **n°10**.

Figure E.80: Simulation with wind and saturated actuator and controller **n°10**.

Appendix F

An international conference paper

REENTRY FLIGHT-CONTROL DESIGN BY A NEW DYNAMIC INVERSION BASED APPROACH

Mario Hernandez – *ONERA/DCSD, Toulouse, France*

Frank Jouhaud – *ONERA/DCSD, Toulouse, France*

Jean-Marc Biannic – *ONERA/DCSD, Toulouse, France*

Abstract. *This paper focuses on the application of a new control design method to a reentry vehicle flight-control problem. Based on the well-known technique of Nonlinear Dynamic Inversion (NDI), we propose a more general framework that, despite input saturation and uncertainties, allows to compute flight-control laws capable of guaranteeing the stability of a reentry vehicle throughout its whole trajectory without requiring gain-scheduling. Considering different uncertain phenomenon and physical constraints, we then apply this approach to a reentry vehicle model to evaluate its stability and performance. The simulation results of the longitudinal dynamics of the reentry vehicle are presented to highlight the virtues of this approach.*

1 INTRODUCTION

For many reasons, control design for reentry vehicles still remains a challenging task. Typically, because the flight domain is extremely large, nonlinear and time-varying aspects introduce nontrivial issues. Most well-known linear control design techniques usually struggle to give a satisfying answer to the control problem, unless gain-scheduled controllers are used. In this contribution, an alternative methodology inspired by dynamic inversion schemes is proposed to avoid standard difficulties raised by gain-scheduling approaches, such as a lack of guarantee between interpolation points and a time-consuming tuning procedure.

After its mathematical formalization in the 1980's [1], NDI has been widely studied and applied in aeronautics and aerospace applications (e.g. [2],[3],[4] and [5]). The principle of NDI is simple: eliminate the nonlinear dynamics from the model and replace them with better-suited linear dynamics. This means that we can compute control laws able to linearize and decouple a nonlinear model at any operating point of its state envelope. Unfortunately, the technique was not originally conceived for models with input saturations and uncertainties. Thus, the technique is intrinsically not robust to physical constraints, to modeling errors and to environmental factors.

To address these flaws, different robust techniques can be applied. For example, in his outlines for applying a robust approach of NDI to the X-28 reentry vehicle, Ito (*et al.*) [6] uses a classic μ-synthesis technique that results in a high-order controller that unfortunately does not account for input saturations. Adaptive and evolutionary approaches have also been used to compensate for modeling errors and environmental factors but fail to incorporate input saturation effects in a single controller structure (e.g. [7] and [8]).

Unlike standard NDI approaches, our methodology can be viewed as a generalized nonlinear compensation framework which incorporates uncertainties and input saturations. The controller is computed through a two-step process. The first, thanks to recent advances in non-smooth optimization techniques [9], consists of optimizing a structured H_∞ controller. Then in a second phase, an anti-windup strategy [10] is used to enhance the controller properties despite saturations.

In order to validate the computed flight-control laws, we apply this new technique to a reentry vehicle simulation. This simulation model should therefore be the closest possible to a real case scenario. The simulation results presented are obtained by taking into consideration environmental factors and input saturations in addition to model uncertainties and measurement disturbances.

The paper is organized as follows: in Section 2, we will present the reentry vehicle's model and discuss the

flight control problem. The different disturbance sources considered for simulation will also be presented. Then in Section 3, after a preliminary analysis of a standard NDI controller, our generalized framework will be introduced. We will also explain in this section how the controller can be computed through two subsequent optimization processes. Section 4 will be then devoted to present the results obtained after applying the proposed method to the reentry vehicle simulator. Finally, we will conclude the paper in Section 5.

2   REENTRY VEHICLE MODEL

The analytic model of a reentry vehicle is nonlinear. We will briefly describe the equations used to represent the reentry vehicle dynamics.

2.1   EQUATIONS OF MOTION

The set of differential equations in (1) are obtained directly from Flight Mechanics. These are the equations of motion with 6 degrees-of-freedom for any flying, rigid body.

$$
\begin{cases}
\dot{\vec{r}} = \vec{V} \\
\dot{\vec{q}} = \frac{1}{2}\vec{q} \otimes \vec{\Omega} \\
m\dot{\vec{V}} = \Sigma\vec{F} + m\,\vec{g} \\
I\dot{\vec{\Omega}} = \Sigma\vec{M} - \vec{\Omega} \wedge I\vec{\Omega}
\end{cases}
\tag{1}
$$

The first equation describes the change in inertial position $\vec{r}$ of the body center of gravity. The second equation determines the inertial attitude of the body, using the quaternion $\vec{q}$ and by noting its non-commutable product $\otimes$. Next, the force equation contains the dynamics of the translational speed $\vec{V}$ of a body with mass m, under the action of the inertial gravity vector $\vec{g}$. Finally, the dynamics of the angular speed vector $\vec{\Omega}$ is described by the moments equation, where the matrix I represents the inertia tensor of the body.

By noting $\bar{q} = \frac{1}{2}\rho V_a^2$ the dynamic pressure, S_r the reference surface and l_r the reference wing span, the aerodynamic forces and moments that are created around the reentry vehicle can be expressed as:

$$
\vec{F}_a = \begin{bmatrix} C_{x_a}(\alpha, \mathcal{M}) \\ C_{y_a}(\alpha, \beta, \mathcal{M}, \delta_l, \delta_n) \\ C_{z_a}(\alpha, \mathcal{M}, \delta_m) \end{bmatrix} \bar{q}S_r \text{ and } \vec{M}_a = \begin{bmatrix} C_l(\alpha, \beta, \mathcal{M}, \delta_l, \delta_n) \\ C_m(\alpha, \mathcal{M}, \delta_m) \\ C_n(\alpha, \beta, \mathcal{M}, \delta_l, \delta_n) \end{bmatrix} \bar{q}S_r l_r
$$

The aerodynamic coefficients $C_\square$ of the reentry vehicle are nonlinear functions that evolve in a rather large flight domain. In this case, the aerodynamic coefficients depend mainly on the mach number $\mathcal{M}$, the angle-of-attack α, the side-slip angle β and the control surface deflection $\delta_\square$.

Under the assumption that the lateral and longitudinal dynamics can be decoupled, we will now focus on the longitudinal dynamics model. Our objective is to regulate the angle-of-attack α which is directly dependent on the pitch rate q of the vehicle. The dynamic equation of the pitch rate is obtained directly from the moment equation in (1). Then, from the definition of the angle-of-attack, we get the following state-space representation of the longitudinal dynamics:

$$
\begin{cases}
\dot{\alpha} = q + Z \\
I_{yy}\dot{q} = u + W
\end{cases}
\tag{3}
$$

with:

$$Z = -\tan\beta(p\cos\alpha + r\sin\alpha) + \frac{1}{V_a\cos\beta}\left[a_z\cos\alpha - a_x\sin\alpha + g\cos\gamma\cos\mu\right]$$

$$W = \bar{q}S_r l_r \left[C_{m_\alpha} + C_{m_q}\frac{l_r}{V_a}q + C_{z_\alpha}\frac{\Delta x}{l_r} - C_{x_\alpha}\frac{\Delta z}{l_r}\right] + (I_{zz} - I_{xx})pr + I_{xz}(r^2 - p^2)$$

$$u = \bar{q}S_r l_r \left[C_{m_{\delta_m}} + C_{z_{\delta_m}}\frac{\Delta x}{l_r} - C_{x_{\delta_m}}\frac{\Delta z}{l_r}\right] \approx B\delta_m$$

In general, the terms Z, W and B are nonlinear functions that can be estimate by means of measurements

(for example: the roll rate p, the yaw rate r, the flight path angle γ, the aerodynamic roll angle μ, the body axes accelerations $a_\square$, etc...) and a nominal model.

2.2 MODEL DISTURBANCE SOURCES

As mentioned before, the analytic model of the reentry vehicle is subject to a set of uncertain phenomenon that we need to consider in order to validate the flight-control laws that will be tested. The main model disturbance sources that were taken into consideration are the following:

- Variation of the atmosphere density as a function of the altitude ($\Delta\rho$)
- Wind. The wind $\vec{V}_w$ is decomposed into static wind ($\vec{V}_{sw}$) and turbulent wind ($\vec{V}_{tw}$).
- Aerodynamic coefficient modeling errors ($\Delta C_m, \Delta C_{m_{\delta_m}}, \Delta C_x, \Delta C_z$)
- Inertial constant modeling error (Δy)
- IMU measurement errors ($\Delta\psi, \Delta\theta, \Delta\phi, \Delta p, \Delta q, \Delta r, \Delta h$)
- Anemometer measurement errors ($\Delta\alpha, \Delta\beta, \Delta V_a$).

In general, we express these uncertainties as multiplicative even though they may be additive. The model uncertainties and disturbances are considered to be symmetrical and with maximum values $\pm\Delta_{max}$.

2.3 PERFORMANCE OBJECTIVE

One objective example for an angle-of attack maneuver of the reentry vehicle is defined by the time-response template with the upper and lower bounds shown on figure 1. This performance objective considers a reduced angle-of-attack starting at an initial angle α_0 and reaching the commanded angle α_c.
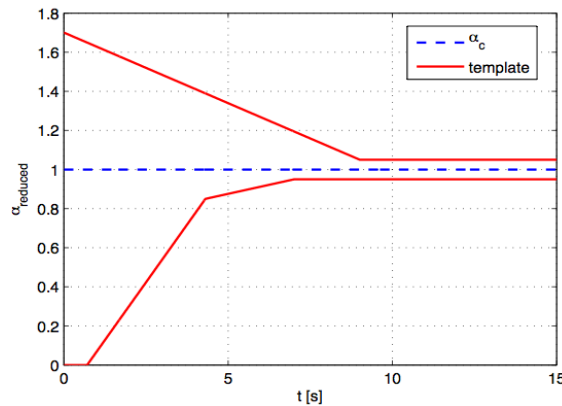

Fig. 1 – T*ime-response template for angle-of-attack maneuvers.*

By inspection of the template, it is clear that the time-response of the angle-of-attack objective is of about $T_r \approx 6.5\ s$. If we consider the first order desired dynamics $(\tau_d s + 1)^{-1}$, for example, that reaches 95% of its step response after a time $T_{r_{95\%}} = 3\tau_d$, then the natural frequency ω_d of such a first order is equivalent to $\omega_d = 1/\tau_d = 0.5\ rad/s$.

To establish second order desired dynamics, we can consider this natural frequency ω_d combined with a well-suited damping coefficient ξ_d allowing the angle-of-attack response to stay within the bounds of the template.

3 GENERALIZED NDI FRAMEWORK

Before presenting our generalized framework, we will briefly review the application of the classic NDI approach with time-scaling separation to the longitudinal dynamics of the reentry vehicle.

3.1 CLASSIC NDI REVIEW

We begin by assuming that the pitch rate dynamics are sufficiently faster than the angle-of-attack dynamics on

a time-scale basis. This assumption allows us to decouple both dynamics and treat the longitudinal model as two sub-systems: one containing the fast dynamics (the pitch rate q in this case) and the other containing the slow dynamics (angle-of-attack α). The dynamic inversion is then applied in two steps:

   a) Find the expression of the control input u that inverts the fast dynamics and that imposes first order dynamics to the fast sub-system.

$$u = I_{yy}\dot{q}_d - W \tag{4}$$

where:
$\dot{q}_d = \frac{1}{\tau_d}(q_c - q)$ and $u = B\delta_m$

   b) Find the commanded value of the pitch rate q_c that inverts the slow dynamics and establishes second order dynamics for the slow sub-system. In this case, the second order dynamics are obtained via a PI structure using a filtered commanded angle α_c of time constant $\tau_F = k_p/k_i$. We call the filter state α_F.

Finally, the dynamic inversion for the slow sub-systems is defined as follows:

$$q_c = \dot{\alpha}_d - Z \tag{5}$$

where:
$\dot{\alpha}_d = k_p(\alpha_F - \alpha) + k_i \int(\alpha_F - \alpha), \quad \alpha_F = \frac{1}{\tau_F s + 1}\alpha_c, \; k_p = 2\xi_d\omega_d$ and $k_i = \omega_d^2$.

By assembling equations (4) and (5), the expression of the control input u resulting from the dynamic inversion of the longitudinal model is obtained:

$$u = \frac{I_{yy}}{\tau_q}\left[k_p(\alpha_f - \alpha) + k_i\int(\alpha_f - \alpha) - Z - q\right] - W \tag{6}$$

If we chose to rewrite the longitudinal model described in (3) by adding the controlled input filter of state α_F and by adding the new state $\varepsilon = \int(\alpha_F - \alpha)$, the augmented longitudinal model can be represented by the state-space equation:

$$\dot{x} = Ax + B_1 w + B_2 u \tag{8}$$

where $x = [\alpha_F \; \varepsilon \; \alpha \; q]^T$ and $w = [\alpha_c \; Z \; W]^T$.

The control input u in (6) can now be written as a static state-feedback controller:

$$u = Kx + Hw \tag{9}$$

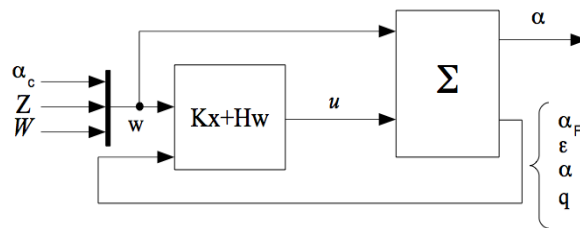This synthesis model scheme is represented on figure 2.

Fig. 2 – *Classic NDI synthesis scheme.*

The terms u and W are divided by I_{yy} to avoid introducing this constant in the static gains K and H:

$$\mathcal{U} = \begin{bmatrix} \frac{k_p}{\tau_q} & \frac{k_i}{\tau_q} & \frac{-k_p}{\tau_q} & \frac{-1}{\tau_q} \end{bmatrix} x + \begin{bmatrix} 0 & \frac{-1}{\tau_q} & -1 \end{bmatrix} w \tag{10}$$

where $\mathcal{U} = \frac{u}{I_{yy}}$.

The functions Z and $\mathcal{W} = W/I_{yy}$ will be now considered as "measured disturbances" of the flight-control problem. Thus, the controller can be interpreted as a state-feedback controller with injection of the commanded angle (α_c) and the measured disturbances (Z and $\mathcal{W}$). We can also highlight the fact that the

terms τ_q, k_p and k_i allowing to impose the longitudinal linear dynamics are included in the static gains K and H, which leads us to consider this classic NDI approach as a pole placement approach.

3.2 NDI GENERALIZATION

We recall that the model can be represented by the state-space equation (8). These types of linear representations are augmented plant models also known as *standard form*. They account for the "exogenous" input vector w affecting the system via the matrix B_1. In our generalized framework, the model nonlinear dynamics are regrouped in this vector to obtain a linear representation of the synthesis model. Then, the controller is obtained by a two step optimization process that will be detailed as follows.

3.2.1 STEP 1

The first advantage of this framework is that it allows to consider of a wide range of uncertainties Δ affecting the nonlinear functions regrouped in the input vector w. The control problem will be posed in a context of tracking in presence of disturbances. We aim to compute a controller capable of: stabilizing the system, rejecting the measured disturbances Z and $\mathcal{W}$, in the largest operation domain possible, while limiting the activity of the control input u at the same time.

Now, an optimization process that will seek to minimize the H_∞ norm of specific transfers of the synthesis model is used. More precisely, a structured H_∞ synthesis will be applied to the explicit model-tracking scheme presented on figure 3a. The reference model $R(s)$ contains the desired dynamics for the angle-of-attack. The "exogenous" input vector w and the weighted output vector z of the resulting standard form shown on figure 3b, are defined as: $w = [\alpha_c \ Z \ \mathcal{W}]^T$ and $z = [z_\alpha \ z_u]^T$. We respond to the synthesis requirements by minimizing the H_∞ norm of the multivariable transfer $T_{w \to z}$. The obtained control law can be expressed in general as:

$$u = K(s) \begin{bmatrix} w \\ y \end{bmatrix} \tag{11}$$

(a). Model-tracking synthesis scheme   (b). Resulting standard form with uncertainty block Δ
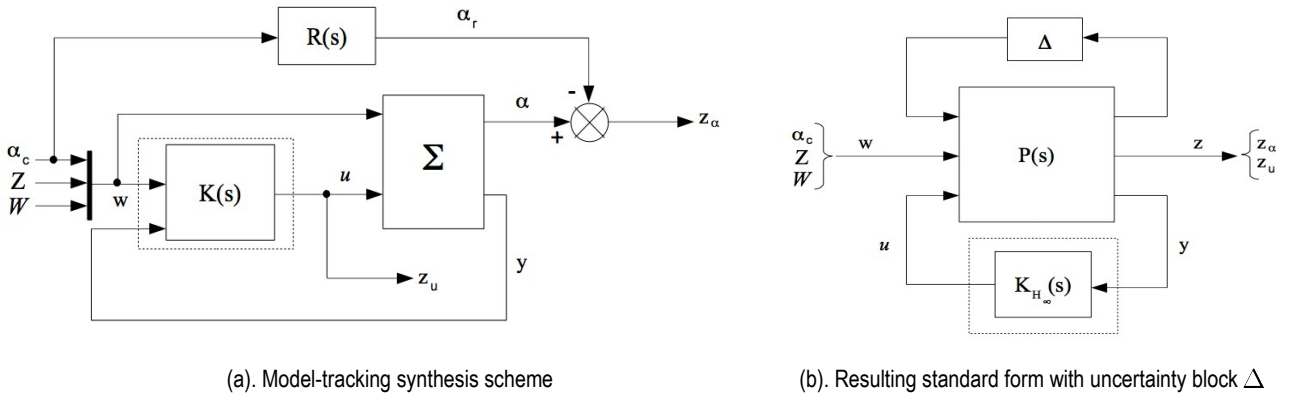
Fig. 3 – *Step 1 synthesis scheme.*

According to different weighing functions that can be used during the synthesis process, the resulting control law should be able to produce the following effects:

- The smaller $T_{\alpha_c \to z_\alpha}$, the better the model-tracking of $R(s)$
- The smaller $T_{[Z \ \mathcal{W}]^T \to z_\alpha}$, the larger the operation domain
- The smaller $T_{w \to z_u}$, the lower the control input activity.

3.2.2 STEP 2

The second advantage of this framework is that its formulation makes it easy to adapt Anti-windup control strategies for systems with saturating inputs. The idea is to compute a controller $J(s)$ capable of extending

the stability domain of the saturated closed-loop system by acting directly on the previously obtained controller $K(s)$.

The input of the controller, w_{AW}, is defined as: $w_{AW} = u - u_s$, where u is the non saturated control input and u_s is the saturated control input. From this definition, u_s can be expressed as: $u_s = u - w_{AW}$. By defining the saturated input this way, we are really transforming the saturation into a dead-zone Δ_{NL} acting over the non saturated input u as depicted on figure 4. Finally, in order to increase the stability domain of the saturated closed-loop system, an optimization process to minimize the H_∞ norm of the transfer $T_{w_\Delta \to z_\Delta}$ is used. Once again, a structured H_∞ synthesis can be employed for this purpose.

Fig. 4 – *Step 2 synthesis scheme.*

The obtained Anti-windup controller can be expressed as:

$$v = J(s)w_{AW} \tag{12}$$

While the enhanced controller becomes in general:

$$u = \tilde{K}(s) \begin{bmatrix} v \\ w \\ y \end{bmatrix} \tag{13}$$

4 RESULTS

We will now present the controller synthesis as well as the simulation results obtained. In this paper, simulation results will be shown for a fixed operation point of a possible trajectory of the reentry vehicle. The chosen operation point is defined by: its altitude $h = 46.5\,km$, mach number $\mathcal{M} = 7.5$ and trim angle-of-attack $\alpha_{trim} = 26.6°$.

The classic and the generalized methods were simulated considering the actuator model (14) and then considering the actuator model (15) that includes a saturation on the actuator rate. By contrasting the results on both cases, the impact of input saturations on the system stability will be illustrated.

$$\delta_m = \frac{1}{\tau_a s + 1}\delta_{m_c}, \qquad \tau_a = 0.2\,s \tag{14}$$

$$\dot{\delta}_m = sat\left(\frac{1}{\tau_a}\delta_{m_c} - \frac{1}{\tau_a}\delta_m\right), \qquad -6°/s < \dot{\delta} < 6°/s \tag{15}$$
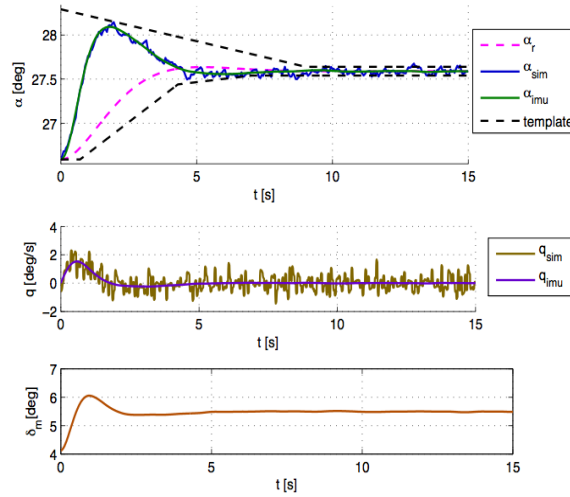
4.1 CLASSIC SOLUTION

Going back to controller (10) obtained in section 3.1, we will now fix the parameters of the static gains K and H. In this particular case, the slow dynamics are fixed in order to remain within the boundaries of the performance template of figure 1. Second order dynamics characterized by the natural frequency $\omega_d = 0.85\,rad/s$ and the damping coefficient $\xi_d = 0.7$, were chosen.

With this information, it is possible to fix the values of k_p and k_i of the controller (10). This leaves us with only one adjustable parameter τ_q, who's only constraint is that its inverse, τ_q^{-1}, stays sufficiently greater than the frequency ω_d in order to guarantee the assumption made by the time-scaling separation approach. It can be proven that, by reducing the value of the parameter τ_q, the tracking performance of the closed-loop system can be improved. It may be added that this reduction on the value of τ_q is followed by an increase of the activity in the control input u. For this case, a value of $\tau_q = 0.4\,s$ was chosen. The gain values of the controller (10) are:

$$K = [2.9\ 1.8 - 2.9 - 2.5] \text{ and } H = [0 - 2.5 - 1]$$

Considering actuator model (14), simulation results are shown on figure 5. The values with index *sim* correspond to the simulator computed values while those with index *imu* correspond to the IMU measurements. The results are considered satisfactory provided that the angle-of-attack α_{sim} stays within the performance template represented by the dark dotted lines. In this figure, we see that the simulation uncertainties and disturbances $+\Delta_{max}$ force the angle-of-attack to overshoot to the top of the performance template. Still, the response converges to the reference signal α_r.

Fig. 5 – *Time-response of the reentry vehicle with classic NDI controller ($+\Delta_{max}$).*

To prove that a closed solution to this classic NDI controller can be reproduced by our generalized approach, a singular value analysis of this classic solution, evaluated in our generalized framework, is done. The singular values of the multivariable transfer $T_{w \rightarrow z_\alpha}$ of figure 6a are shown on figure 6b. Results from this analysis will be used to determine the weighing functions allowing our generalized framework to obtain a similar solution.
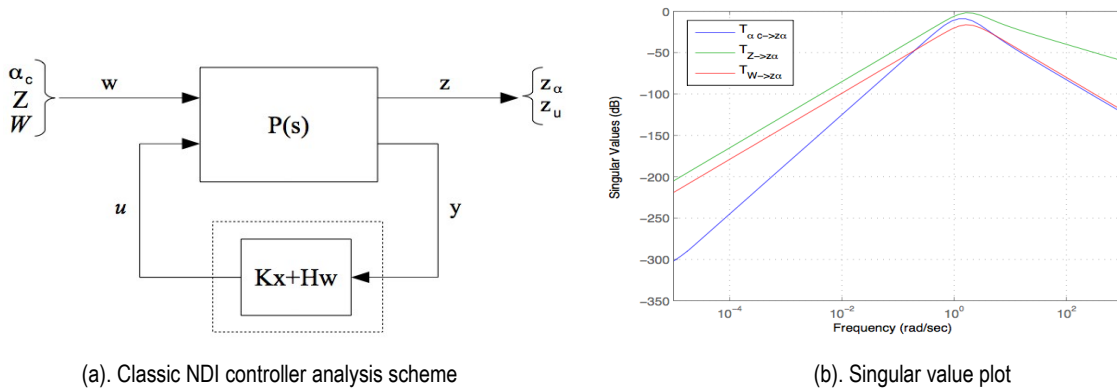
(a). Classic NDI controller analysis scheme

(b). Singular value plot

Fig. 6 – *Frequency domain analysis of the classic NDI controller.*

4.2 GENERALIZED SOLUTION

To generate a similar solution via our generalized framework, we look at the curves of figure 6b from which we can design a high-pass filter $F_{z_\alpha}(s)$ capable of wrapping the singular values obtained from the classic solution. The inverse of this filter, $F_{z_\alpha}(s)^{-1}$, is then used to weight the performance measurement z_α. To limit the controller output, we use a static gain g_{z_u} to weight the control input measurement z_u. In this particular case, a static gain, K_{H_∞}, is chosen as the controller structure and the same inputs and output of the classic solution are kept. After synthesis, we obtain the controller:

$$u = K_{H_\infty} \begin{bmatrix} w \\ y \end{bmatrix}, \text{ with } K_{H_\infty} = [0.9 - 3.7 - 0.9 \ \ 2.9 \ \ 2.1 - 3.8 - 4.4]$$

The simulation results of figure 7(a) and the singular value analysis of figure 7(b) show a clear resemblance to the previous results with the classic NDI controller.
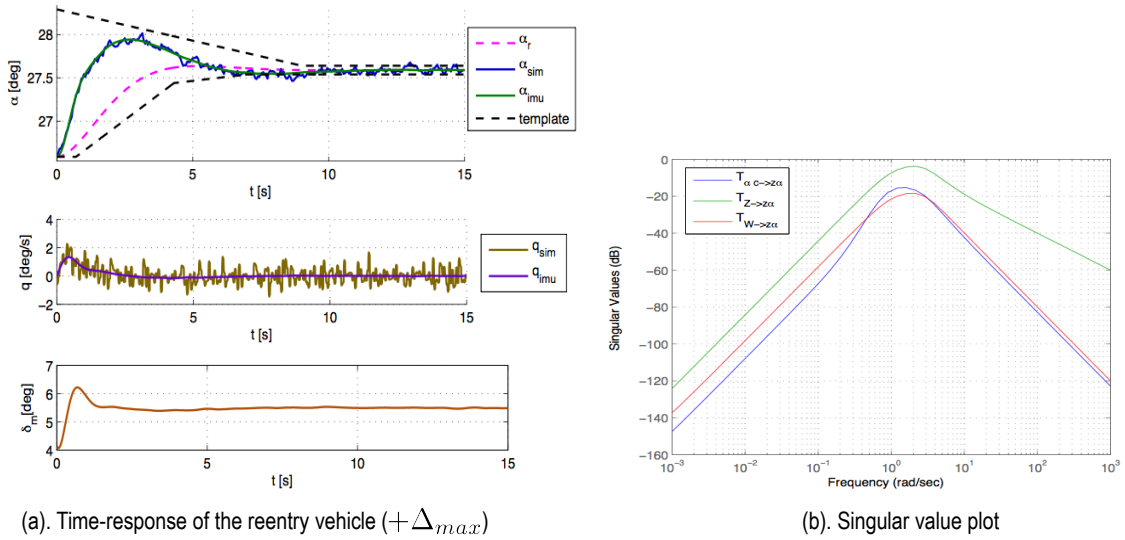

(a). Time-response of the reentry vehicle $(+\Delta_{max})$

(b). Singular value plot

Fig. 7 – *Closed-loop response of the generalized NDI controller.*

Referring to step 1 in section 3.2.1, an improved dynamic controller can be computed by considering model uncertainties and disturbances. At this particular flight point, it was determined that our model is affected by the multiplicative uncertainties $\Delta Z = 80\%$ and $\Delta \mathcal{W} = 50\%$.
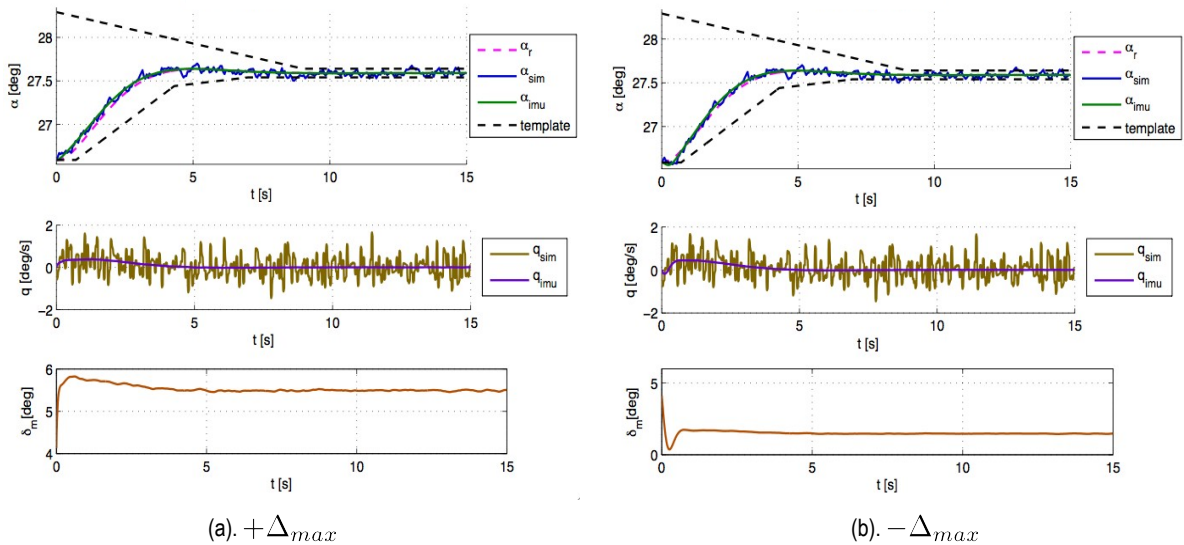

(a). $+\Delta_{max}$

(b). $-\Delta_{max}$

Fig. 8 – *Time-response of the generalized NDI controller (step 1).*

The synthesis scheme presented on figure 3 is used to obtain a second order controller $K_{H_\infty}(s)$. After synthesis and still considering the actuator model (14), the simulation responses of the reentry vehicle for positive and negative values of the simulation uncertainties Δ_{max}, are presented on figure 8. A clear performance improvement is observed in comparison to the former solution.

The controller is now tested in simulation with the actuator model (15). The time-responses of figure 9 show the effect of the actuator rate saturation. On figure 9a, a slight performance deterioration is observed in presence of the saturated rate, while on figure 9b the system has become unstable.

(a). $+\Delta_{max}$

(b). $-\Delta_{max}$
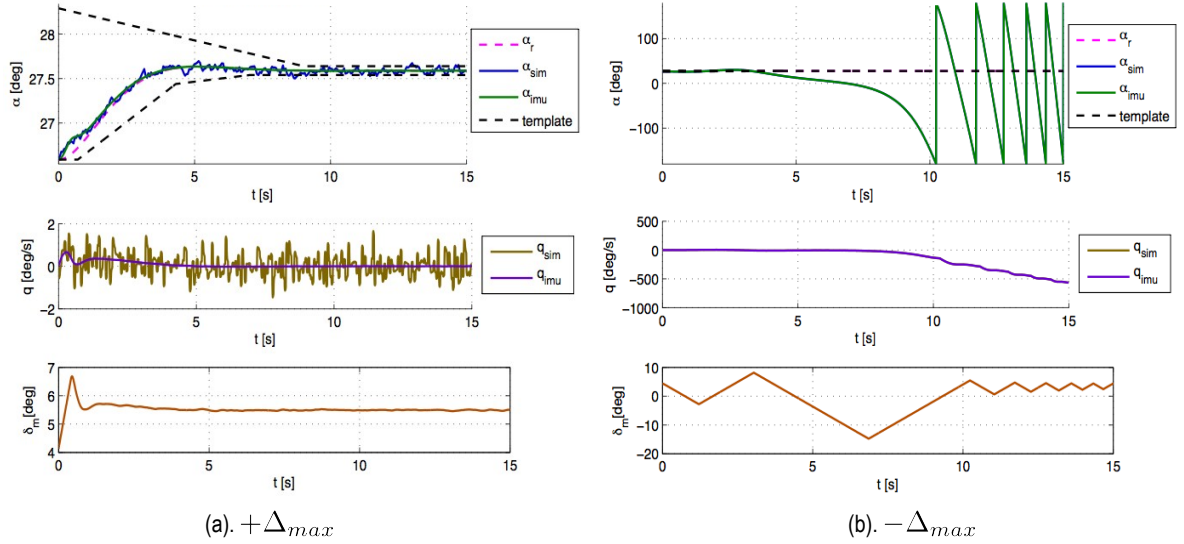
Fig. 9 – *Time-response of the generalized NDI controller with saturated actuator.*

To assess the lost of stability, we now go to step 2 of our generalized method described in section 3.2.2. Using the synthesis scheme of figure 5, a controller (12) that increases the system stability domain is computed. The output vector v of the controller $J(s)$ affects the dynamic equation of $\tilde{K}_{H_\infty}(s)$ to become:

$$\dot{x}_{\tilde{K}} = A_{\tilde{K}} x_{\tilde{K}} + B_{\tilde{K}} \begin{bmatrix} w \\ y \end{bmatrix} + v$$

(a). $-\frac{1}{4}\Delta_{max}$

(b). $-\Delta_{max}$
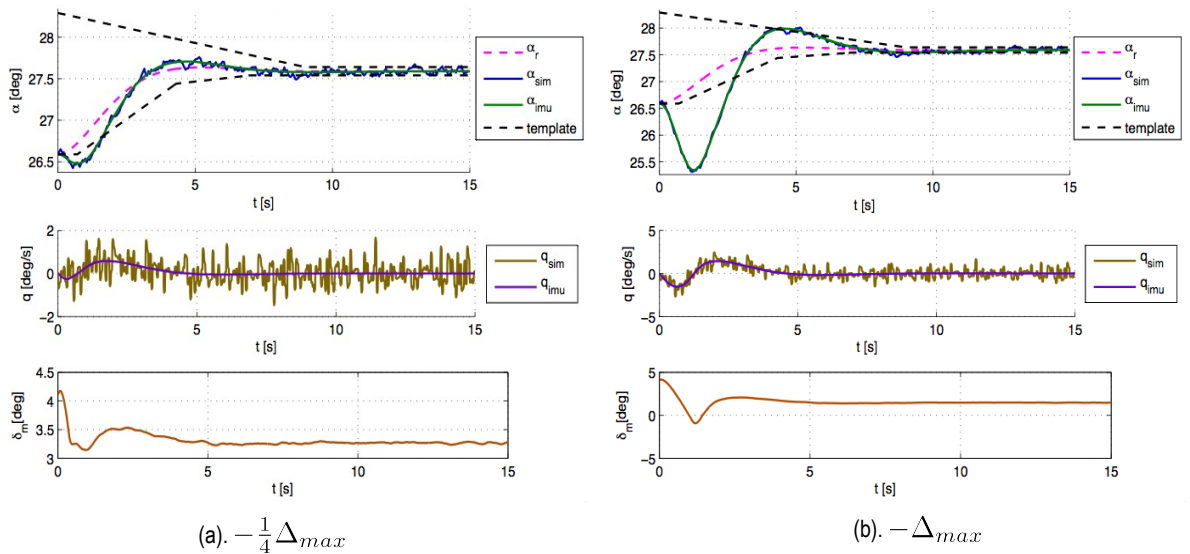
Fig. 10 – *Time-response of the generalized NDI controller (step 2).*

A first order controller structure was chosen for $J(s)$. The simulation results, obtained with this controller structure, are shown on figure 10. On figure 10a, the simulation results are shown with only one forth of the maximum uncertainty level $-\frac{1}{4}\Delta_{max}$. Then, figure 10b shows the response of the reentry vehicle under the full model uncertainty level $-\Delta_{max}$ which stands for the worst case possible.

The reentry vehicle response in both cases is clearly stable. This proves that the controller $\tilde{K}_{H_\infty}(s)$ along with the controller $J(s)$ can stabilize the system despite input saturation. It is also shown that as the model uncertainty level is increased, the system performance is deteriorated. This means that under the saturated input, this controller cannot master completely the worst modeled uncertainty level. Still, the synthesis objective of extending the stability domain is accomplished.

5 CONCLUSIONS

In this paper we have reformulated the classic nonlinear dynamic inversion technique to obtain a more general framework allowing to account for modeling errors and input saturations of a reentry vehicle. In this case, we were able to turn the nonlinear flight-control problem into a linear model-tracking problem for which more general solutions are available. From this general approach, not only were we able to reproduce a control law with similar characteristics as the one obtained via the classic NDI methodology, but we were also able to improve the system performance in presence of uncertain phenomena and to enhance its stability under input saturation. The results obtained in simulation proved to be very satisfactory even though a clear compromise between performance and stability arises at high levels of model uncertainty.

In this article, fixed structures for the flight-control law were tested. Yet, different combinations of structures for the two step synthesis scheme are conceivable and may present a variety of different results. Also, the performance of the control laws obtained with this generalized framework is yet to be tested on flexible models. The main concern in this case is that the control law might be such that the flexible modes of the vehicle may become resonant. One way to overcome this dilemma could be to limit, or even cut off, certain frequencies of the control law bandwidth to avoid exciting the flexible modes. Further studies on this subjects are still to be conducted.

REFERENCES

[1]   A. Isidori. *Nonlinear Control Systems*. Berlin: Springer-Verlag, Great Britain 1985.

[2]   F. Jouhaud. *Nonlinear attitude control law of a space plane*. IFAC Congress: Aerospace Control, Munich, Germany, 1992.

[3]   H. Lee, S. Reiman, C. Dillon, and H. Youssef. *Robust nonlinear dynamic inversion control for a hypersonic cruise vehicle*. AIAA Guidance, Navigation, and Control Conference and Exhibit, 2007.

[4]   J. Reiner, G. Balas, and L. Garrard. *Robust dynamic inversion for control of highly maneuverable aircraft*. Journal of Guidance, Control and Dynamics, Vol. 18, No. 1, January 1995.

[5]   C. Papageorgiou. *Robustness Analysis of Nonlinear Dynamic Inversion Control Laws for Flight Control Applications*. PhD thesis, University Of Cambridge, Cambridge, United Kingdom, 2003.

[6]   D. Ito, J. Georgie, J. Valasek, and D. Ward. *Reentry Vehicle Flight Controls Design Guidelines: Dynamic Inversion*. PhD thesis, Texas A&M University, Texas, USA, 2002.

[7]   M. Tandale. *Adaptive Dynamic Inversion Control Of Nonlinear Systems Subjected to Control Saturation Constraints*. PhD thesis, Texas A&M University, Texas, USA, 2006.

[8]   G. Plett. *Adaptive inverse control of linear and nonlinear systems using dynamic neural networks*. IEEE Transactions on Neural Networks, Vol. 14, No. 2, March 2003.

[9]   P. Apkarian and D. Noll. *Non-smooth H∞ synthesis*. IEEE Transactions in Automatic Control, Vol. 51, No. 1, pp. 71-86, January 2006.

[10] JM. Biannic and S. Tarboureich. *Optimization and implementation of dynamic anti-windup compensators with multiple saturations in flight control systems*. Control Engineering Practice, Vol. 17, No. 6, pp. 703-713, June 2009.

**Cadre de travail généralisé de compensation non-linéaire robuste :
application à la rentrée atmosphérique**

Ce travail de thèse est consacré à l'extension de l'Inversion Dynamique non-linéaire (NDI-Nonlinear Dynamic Inversion) pour un ensemble plus grand de systèmes non-linéaires, tout en garantissant des conditions de stabilité suffisantes.

La NDI a été étudiée dans le cas de diverses applications, y compris en aéronautique et en aérospatiale. Elle permet de calculer des lois de contrôle capables de linéariser et de découpler un modèle non-linéaire à tout point de fonctionnement de son enveloppe d'état. Cependant cette méthode est intrinsèquement non-robuste aux erreurs de modélisation et aux saturations en entrée. En outre, dans un contexte non-linéaire, l'obtention d'une garantie quantifiable du domaine de stabilité atteint reste à l'heure actuelle complexe.

Contrairement aux approches classiques de la NDI, notre méthodologie peut être considérée comme un cadre de compensation non-linéaire généralisé qui permet d'intégrer les incertitudes et les saturations en entrée dans le processus de conception. En utilisant des stratégies de contrôle anti-windup, la loi de pilotage peut être calculée grâce à un simple processus en deux phases.

Dans ce cadre de travail généralisé des transformations linéaires fractionnaires (LFT - Linear Fractional Transformations) de la boucle fermée non-linéaire peuvent être facilement déduites pour l'analyse de la stabilité robuste en utilisant des outils standards pour de systèmes linéaires.

La méthode proposée est testée pour le pilotage d'un véhicule de rentrée atmosphérique de type aile delta lors de ses phases hypersonique, transsonique et subsonique. Pour cette thèse, un simulateur du vol incluant divers facteurs externes ainsi que des erreurs de modélisation a été développé dans Simulink.

Mots-clés : Compensation Non-linéaire Généralisée, Inversion Dynamic Non-linéaire, Commande Anti-Windup, Commande Robuste, Transformations Linéaires Fractionnaires, Commande H-infinie Non-lisse, Rentrée Atmosphérique

**A generalized framework for robust nonlinear compensation:
application to an atmospheric reentry control problem.**

This thesis work is devoted to extending Nonlinear Dynamic Inversion (NDI) for a large scale of nonlinear systems while guaranteeing sufficient stability conditions.

NDI has been studied in a wide range of applications, including aeronautics and aerospace. It allows to compute nonlinear control laws able to decouple and linearize a model at any operating point of its state envelope. However, this method is inherently non-robust to modelling errors and input saturations. Moreover, obtaining a quantifiable guarantee of the attained stability domain in a nonlinear control context is not a very straightforward task.

Unlike standard NDI approaches, our methodology can be viewed as a generalized nonlinear compensation framework which allows to incorporate uncertainties and input saturations in the design process. Paralleling anti-windup strategies, the controller can be computed through a single multi-channel optimization problem or through a simple two-step process.

Within this framework, linear fractional transformations of the nonlinear closed-loop can be easily derived for robust stability analysis using standard tools for linear systems.

The proposed method is tested for the flight control of a delta wing type reentry vehicle at hypersonic, transonic and subsonic phases of the atmospheric reentry. For this thesis work, a Flight Mechanics simulator including diverse external factors and modelling errors was developed in Simulink.

Keywords: Generalized Nonlinear Compensation, Nonlinear Dynamic Inversion, Anti-Windup Control, Robust Control, Linear Fractional Transformation, Nonsmooth H-infinity control, Atmospheric Reentry